frontiers | Research Topics

Advanced technology for human movement rehabilitation and enhancement

Edited by
Longbin Zhang, Ruoli Wang, Yingbai Hu, Mingming Zhang, Wei Tech Ang and Elena Marie Gutierrez-Farewik

Published in
Frontiers in Neuroscience
Frontiers in Neurorobotics

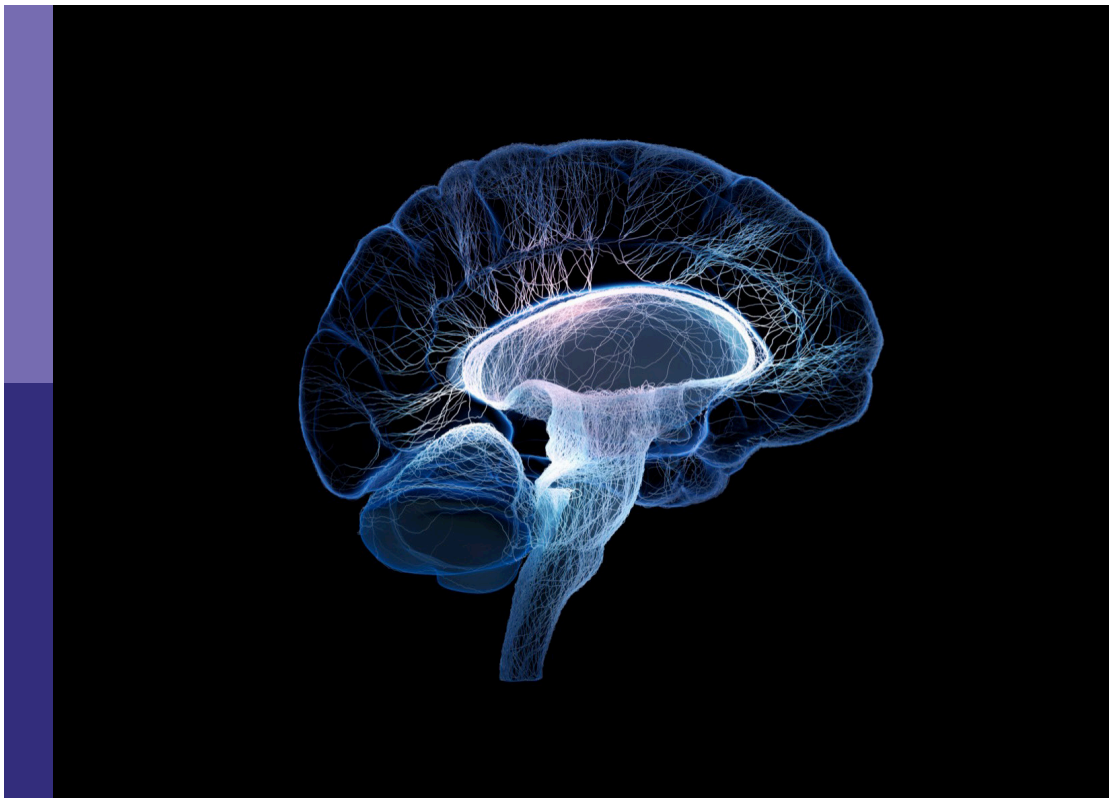

ISSN 1664-8714
ISBN 978-2-8325-6219-2
DOI 10.3389/978-2-8325-6219-2

About Frontiers

Frontiers is more than just an open access publisher of scholarly articles: it is a pioneering approach to the world of academia, radically improving the way scholarly research is managed. The grand vision of Frontiers is a world where all people have an equal opportunity to seek, share and generate knowledge. Frontiers provides immediate and permanent online open access to all its publications, but this alone is not enough to realize our grand goals.

Frontiers journal series

The Frontiers journal series is a multi-tier and interdisciplinary set of open-access, online journals, promising a paradigm shift from the current review, selection and dissemination processes in academic publishing. All Frontiers journals are driven by researchers for researchers; therefore, they constitute a service to the scholarly community. At the same time, the *Frontiers journal series* operates on a revolutionary invention, the tiered publishing system, initially addressing specific communities of scholars, and gradually climbing up to broader public understanding, thus serving the interests of the lay society, too.

Dedication to quality

Each Frontiers article is a landmark of the highest quality, thanks to genuinely collaborative interactions between authors and review editors, who include some of the world's best academicians. Research must be certified by peers before entering a stream of knowledge that may eventually reach the public - and shape society; therefore, Frontiers only applies the most rigorous and unbiased reviews. Frontiers revolutionizes research publishing by freely delivering the most outstanding research, evaluated with no bias from both the academic and social point of view. By applying the most advanced information technologies, Frontiers is catapulting scholarly publishing into a new generation.

What are Frontiers Research Topics?

Frontiers Research Topics are very popular trademarks of the *Frontiers journals series*: they are collections of at least ten articles, all centered on a particular subject. With their unique mix of varied contributions from Original Research to Review Articles, Frontiers Research Topics unify the most influential researchers, the latest key findings and historical advances in a hot research area.

Find out more on how to host your own Frontiers Research Topic or contribute to one as an author by contacting the Frontiers editorial office: frontiersin.org/about/contact

Advanced technology for human movement rehabilitation and enhancement

Topic editors

Longbin Zhang — Hunan University, China
Ruoli Wang — Royal Institute of Technology, Sweden
Yingbai Hu — The Chinese University of Hong Kong, China
Mingming Zhang — Southern University of Science and Technology, China
Wei Tech Ang — Nanyang Technological University, Singapore
Elena Marie Gutierrez-Farewik — KTH MoveAbility Lab, Royal Institute of Technology, Sweden

Citation

Zhang, L., Wang, R., Hu, Y., Zhang, M., Ang, W. T., Gutierrez-Farewik, E. M., eds. (2025). *Advanced technology for human movement rehabilitation and enhancement*. Lausanne: Frontiers Media SA. doi: 10.3389/978-2-8325-6219-2

Table of contents

frontiers | Frontiers in Neuroscience

TYPE Editorial
PUBLISHED 26 March 2025
DOI 10.3389/fnins.2025.1581451

OPEN ACCESS

EDITED AND REVIEWED BY
Karen L. Lankford,
Yale University, United States

*CORRESPONDENCE
Yingbai Hu
yingbaihu@cuhk.edu.hk

RECEIVED 22 February 2025
ACCEPTED 03 March 2025
PUBLISHED 26 March 2025

CITATION
Zhang L, Hu Y, Zhang M, Wang R, Gutierrez-Farewik EM and Ang WT (2025) Editorial: Advanced technology for human movement rehabilitation and enhancement. *Front. Neurosci.* 19:1581451. doi: 10.3389/fnins.2025.1581451

Editorial: Advanced technology for human movement rehabilitation and enhancement

Longbin Zhang[1,2], Yingbai Hu[3]*, Mingming Zhang[4], Ruoli Wang[5], Elena M. Gutierrez-Farewik[5] and Wei Tech Ang[2]

[1]School of Robotics, Hunan University, Changsha, China, [2]School of Mechanical and Aerospace Engineering, Nanyang Technological University, Singapore, Singapore, [3]Multi-Scale Medical Robotics Centre, The Chinese University of Hong Kong, Shatin, China, [4]Department of Biomedical Engineering, Southern University of Science and Technology, Shenzhen, China, [5]KTH MoveAbility Lab, Department of Engineering Mechanics, KTH Royal Institute of Technology, Stockholm, Sweden

KEYWORDS

wearable exoskeletons, artificial intelligence, virtual reality, advancing rehabilitation strategies, neuromuscular diseases

Editorial on the Research Topic
Advanced technology for human movement rehabilitation and enhancement

In the dynamic field of human movement science, the integration of cutting-edge technology with human physiology is driving a transformative shift in rehabilitation and enhancement. This research theme encompasses neurorehabilitation, assistive robotics, and human-machine interaction, offering exciting prospects for reshaping movement recovery. Translational research plays a key role by bridging scientific advancements with practical clinical applications, ensuring that breakthroughs in laboratories transition seamlessly into real-world treatments. Neurorehabilitation focuses on neuroplasticity and the brain's ability to adapt, while advanced imaging and neurophysiology guide interventions aimed at rewiring neural pathways for individuals with neurological injuries. Assistive robotics combine human potential with sophisticated devices, providing tailored support that aids recovery, enhances muscle activation, joint movement, and gait training, ultimately promoting functional independence. The intersection of human-machine interaction explores the blurring of lines between humans and technology, enabling seamless collaboration to guide and benefit patients through technological assistance.

This Research Topic provides a valuable platform for exploring key mechanisms of human movement rehabilitation, integrating physiological strategies with the design of assistive devices. It highlights the critical role of advanced algorithms, virtual reality, wearable sensors, and machine learning in addressing significant rehabilitation challenges. The studies in this Research Topic cover a broad spectrum of topics, from stroke-induced motor impairments and neurodegenerative conditions to pediatric mobility impairments and sports training. By showcasing groundbreaking technologies, this Research Topic emphasizes the importance of neurophysiological assessments and machine learning models in optimizing rehabilitation outcomes. Examples include motor unit estimation, surface electromyography, and electroencephalogram (EEG)-based movement intention detection to monitor and enhance recovery. Wearable sensors and artificial intelligence technologies are also leveraged to assess gait abnormalities, monitor knee osteoarthritis, and provide real-time feedback in sports training and swimming action recognition.

These innovations demonstrate the transformative potential of advanced technology in improving mobility, functional independence, and quality of life for patients across various conditions.

Stroke-induced impairments in gait and upper limb motor function significantly impact mobility, daily activities, and overall quality of life. Pan et al. conducted a case-control study analyzing the biomechanical deviations in gait patterns of post-stroke hemiplegic patients, using statistical parametric mapping to compare joint angles, moments, and ground reaction forces across the gait cycle. Their findings revealed significant abnormalities in both the affected and less-affected limbs, highlighting the need for targeted interventions that address bilateral impairments. Liu et al. conducted a randomized controlled trial comparing robot-assisted therapy (RT) with conventional therapy to enhance upper-limb motor function in post-stroke patients. Their results demonstrated that RT significantly accelerated improvements in Fugl-Meyer Assessment Upper Extremity scores, particularly in patients at Brunnstrom Stage III, although both groups showed similar improvements in functional independence as measured by the Modified Barthel Index. This suggests that robot-assisted therapy holds great potential for enhancing motor recovery in moderate impairment cases. Li et al. examined the predictive value of neuroelectrophysiological assessments, specifically motor unit number estimation (MUNE) and F-waves, for forecasting upper extremity motor function and long-term recovery in stroke patients. They found that MUNE provided more accurate predictions of motor recovery a year post-stroke, emphasizing the importance of incorporating neuroelectrophysiological evaluations into stroke rehabilitation to improve outcomes. Additionally, Lu et al. explored how spasticity confounds myoelectric pattern recognition in stroke rehabilitation. They suggested that botulinum toxin injections could reduce muscle overactivity and improve the effectiveness of myoelectric pattern recognition, supporting the use of this combined approach to enhance rehabilitation outcomes for stroke patients.

The integration of motor unit analysis and muscle synergy research is advancing rehabilitation strategies for neuromuscular diseases and mobility impairments. The loss of motor units in conditions like amyotrophic lateral sclerosis and muscular dystrophy leads to muscle weakness and atrophy, making tools like motor unit number estimation and compound muscle action potential (CMAP) valuable for tracking motor unit loss and compensatory reinnervation. Zhang D. et al. studied the impact of electrode recording areas on CMAP parameters, discovering that electrode size did not significantly affect CMAP data, which enhances the interpretation of CMAP scan results in rehabilitation contexts. Tsuchiya et al. explored how pedaling speed and direction influence the recruitment of muscle synergies, showing that specific muscle groups are recruited depending on the conditions, such as quadriceps and hip extensors at 30 revolutions per minute (RPM) and hamstring-dominant synergies at 60 RPM during forward pedaling. Their findings suggest that pedaling exercises tailored to different speeds and directions can better target specific muscles for rehabilitation, particularly for stroke patients and those with mobility impairments. These studies highlight the growing potential for personalized rehabilitation strategies that optimize recovery by considering individual muscle synergies and motor patterns.

Wearable robotic exoskeletons are increasingly recognized for their potential to assist rehabilitation in conditions like stroke-induced drop foot and pediatric mobility impairments such as cerebral palsy. Zhang X. et al. developed a soft ankle exoskeleton to assist with dorsiflexion and eversion, demonstrating its ability to significantly improve gait kinematics in both seated and gait tests with minimal errors. Bradley et al. assessed the clinical impact of the pediatric Trexo Plus exoskeleton, focusing on motor, neural, and muscular outcomes in children with severe mobility impairments. Their feasibility study highlighted the exoskeleton's potential to promote neuroplasticity and improve mobility, particularly in young patients with motor impairments. Miao et al. proposed a framework for robot-assisted upper-limb rehabilitation, using subject-specific workspace constraints and performance-based control strategies to enhance training effectiveness, natural motion, and patient engagement. Voß et al. emphasized the importance of intuitive control architectures for lower-limb prostheses, combining volitional control with proprioceptive feedback to improve user satisfaction and functionality. These studies demonstrate the promising potential of exoskeletons and advanced control systems to revolutionize rehabilitation, offering significant improvements across diverse patient populations.

Artificial intelligence and sensor technologies are at the forefront of human movement rehabilitation and performance enhancement, driving advancements in precision feedback and personalized interventions. LinLin et al. developed a system that combines Vision Transformers with Contrastive Language-Image Pretraining (CLIP) models to deliver real-time, context-aware feedback in sports training, outperforming traditional methods in accuracy, recall, and computational efficiency. Chen and Yue introduced Swimtrans Net, which uses Swin-Transformer and CLIP models to improve swimming action recognition and provide real-time feedback with exceptional accuracy. Sarmah et al. explored a non-invasive method for detecting knee osteoarthritis (Knee OA) and monitoring rehabilitation progress by integrating gait and muscle activity data with machine learning models. Their work demonstrated how wearable sensors and non-knee joint variables could be leveraged for early Knee OA detection and personalized interventions, illustrating the potential of artificial intelligence and sensor technologies to revolutionize both rehabilitation and sports performance through precision feedback and tailored solutions.

Virtual reality (VR)-based interventions are emerging as powerful tools in rehabilitation, offering cost-effective solutions for home-based recovery. Dai et al. developed a VR-based rehabilitation system that reconstructs full-body poses from sparse motion signals, providing real-time motion correction and allowing patients to undergo efficient therapy without frequent clinical visits. Dong et al. enhanced movement intention detection for neurological rehabilitation by using VR induction to improve EEG signal detectability, facilitating better activation of brain functional networks. These innovations highlight the growing role of VR in rehabilitation, demonstrating its potential to enhance motor recovery, engagement, and accessibility.

This Research Topic highlights the important role of advanced technologies in advancing human movement rehabilitation and enhancement. By exploring the intersection of assistive robotics, virtual reality, wearable sensors, and AI-powered systems, the research illustrates how engineering and human physiology work together to address a wide range of challenges in mobility and rehabilitation. Through a thoughtful integration of application, this body of work underscores the potential for impactful interventions that could contribute to the progression of rehabilitation science. By connecting theoretical advancements with practical implementations, these studies present opportunities to develop more personalized, accessible, and effective treatments for patients globally, shaping the future direction of rehabilitation.

Author contributions

LZ: Conceptualization, Writing – original draft, Writing – review & editing. YH: Conceptualization, Writing – original draft, Writing – review & editing. MZ: Conceptualization, Writing – review & editing. RW: Conceptualization, Writing – review & editing. EG-F: Conceptualization, Writing – review & editing. WA: Conceptualization, Writing – review & editing.

Funding

The author(s) declare that financial support was received for the research and/or publication of this article. We would like to thank the Agency for Science Technology and Research, and the National Healthcare Group.

Conflict of interest

The authors declare that the research was conducted in the absence of any commercial or financial relationships that could be construed as a potential conflict of interest.

Publisher's note

All claims expressed in this article are solely those of the authors and do not necessarily represent those of their affiliated organizations, or those of the publisher, the editors and the reviewers. Any product that may be evaluated in this article, or claim that may be made by its manufacturer, is not guaranteed or endorsed by the publisher.

frontiers | Frontiers in Neuroscience

TYPE Original Research
PUBLISHED 30 January 2024
DOI 10.3389/fnins.2023.1305850

OPEN ACCESS

EDITED BY
Longbin Zhang,
Nanyang Technological University, Singapore

REVIEWED BY
Debasish Nath,
Indian Institute of Technology Delhi, India
Zhiqiang Cao,
Singapore University of Technology and Design, Singapore

*CORRESPONDENCE
Runlin Dong
✉ dong_rl@stu.xjtu.edu.cn

RECEIVED 02 October 2023
ACCEPTED 28 December 2023
PUBLISHED 30 January 2024

CITATION
Dong R, Zhang X, Li H, Masengo G, Zhu A, Shi X and He C (2024) EEG generation mechanism of lower limb active movement intention and its virtual reality induction enhancement: a preliminary study. *Front. Neurosci.* 17:1305850. doi: 10.3389/fnins.2023.1305850

EEG generation mechanism of lower limb active movement intention and its virtual reality induction enhancement: a preliminary study

Runlin Dong[1]*, Xiaodong Zhang[1,2], Hanzhe Li[1], Gilbert Masengo[1], Aibin Zhu[1,2], Xiaojun Shi[1] and Chen He[3]

[1]School of Mechanical Engineering, Xi'an Jiaotong University, Xi'an, Shaanxi, China, [2]Shaanxi Key Laboratory of Intelligent Robots, Xi'an Jiaotong University, Xi'an, Shaanxi, China, [3]General Department, AVIC Creative Robotics Co., Ltd., Xi'an, Shaanxi, China

Introduction: Active rehabilitation requires active neurological participation when users use rehabilitation equipment. A brain-computer interface (BCI) is a direct communication channel for detecting changes in the nervous system. Individuals with dyskinesia have unclear intentions to initiate movement due to physical or psychological factors, which is not conducive to detection. Virtual reality (VR) technology can be a potential tool to enhance the movement intention from pre-movement neural signals in clinical exercise therapy. However, its effect on electroencephalogram (EEG) signals is not yet known. Therefore, the objective of this paper is to construct a model of the EEG signal generation mechanism of lower limb active movement intention and then investigate whether VR induction could improve movement intention detection based on EEG.

Methods: Firstly, a neural dynamic model of lower limb active movement intention generation was established from the perspective of signal transmission and information processing. Secondly, the movement-related EEG signal was calculated based on the model, and the effect of VR induction was simulated. Movement-related cortical potential (MRCP) and event-related desynchronization (ERD) features were extracted to analyze the enhancement of movement intention. Finally, we recorded EEG signals of 12 subjects in normal and VR environments to verify the effectiveness and feasibility of the above model and VR induction enhancement of lower limb active movement intention for individuals with dyskinesia.

Results: Simulation and experimental results show that VR induction can effectively enhance the EEG features of subjects and improve the detectability of movement intention.

Discussion: The proposed model can simulate the EEG signal of lower limb active movement intention, and VR induction can enhance the early and accurate detectability of lower limb active movement intention. It lays the foundation for further robot control based on the actual needs of users.

KEYWORDS

movement intention, electroencephalogram, virtual reality induction, movement-related cortical potential, event-related desynchronization, brain-computer interface

1 Introduction

With the aging population and the frequency of accidents, the number of individuals with lower limb dyskinesia is gradually increasing. Exercise therapy after surgery has been indicated as an effective way to help patients recover (McDonald et al., 2022). Human lower limbs support the weight of the body, which creates movement challenges for lower limb dyskinesia individuals, so they inevitably need external assistance. Exoskeleton robots can not only help the body stand upright but can also assist the user in walking. It has been extensively researched, designed, and implemented (Kalita et al., 2020; Xiang et al., 2020).

Exoskeleton robots are required to be able to personalize and intelligently assist the user. An important principle within the use of exoskeleton robots is that the robots assist lower limb dyskinesia people to actively undertake prescribed movements rather than their limbs moving passively. It is critical that robots perceive the user's movement intention (Qiu et al., 2021). Human active movement intention is the result of cognitive processes in the brain. The process of human brain cognition and its body expression can be described in two parts: "Uplink Pathway: Electroencephalogram (EEG) signal generation" and "Downlink Pathway: Electromyography (EMG) and other biological signal generation" (Zhang et al., 2021). EEG contains brain real-time information, which could be used to understand the current motor-related brain activity and further predict the next motor task. Furthermore, a brain–computer interface (BCI) could help researchers to investigate users' movement-related neurophysiological changes in a non-invasive way (Abiri et al., 2019). This technology would pave the way for intelligent assistance of exoskeleton robots.

Some scholars have studied the neurophysiological changes related to movement intention through BCI. Detection or prediction of movement intention via EEG signals is the ultimate goal. Sburlea et al. (2017) investigated the detection of gait intention; the results showed that the detector combines movement-related cortical potential (MRCP) amplitude and phase features of EEG signals and has 62.5% accuracy in healthy subjects and 59% in stroke patients. Lopez-Larraz et al. (2016) identified movement intention with the cue-guided paradigm; the accuracy of movement intention detection was 84.44% in healthy subjects and 77.61% in incomplete spinal cord injury patients. Jeong et al. (2017) validated a single-trial readiness potential performance in the lower limb exoskeleton environment and the average classification accuracy was 80.7% in healthy subjects. Hasan et al. (2020) employed a discrete wavelet transform-based method to detect the movement intention, the accuracy of detecting "rest vs. start" was 76.41% and "walk vs. stop" was 74%, with healthy subjects outperforming amputee subjects. In addition, there are some studies on filtering algorithms (Jeong et al., 2020; Mascolini et al., 2022), feature extraction methods (Wang et al., 2020; Jia et al., 2022), and detection methods (Chaisaen et al., 2020) to improve the performance of movement intention detection or prediction. The accuracy of lower limb movement intention detection in people with dyskinesia is lower than in healthy individuals with BCI intention detection. How to enhance the detectability of lower limb movement intention in people with dyskinesia based on BCI and enable them to accurately control exoskeleton robots is an urgent problem.

To solve this problem, the process by which the brain generates movement intentions and related EEG signals should be analyzed. The brain can filter and select the information, and only selectively filtered information can be perceived (Leone et al., 2017). The brain's generation of specific intentions is affected by facilitating and preventive factors, which is a process of competition. Individuals with lower limb dyskinesia experience physical discomfort during exercise, such as pain or fatigue, which generates a plethora of preventive factors that affect movement intentions. Although EEG signals have many advantages, they are inherently weak, non-stationary, and susceptible to interference. The brain of individuals with lower limb dyskinesia contains ambiguous and complex information, with a low signal-to-noise ratio and multiple confounding factors, which are not conducive to the analysis of movement-related neural signals (Jochumsen et al., 2015; Sburlea et al., 2016). Therefore, their movement intention detection accuracy is lower than that of healthy people. However, the current BCIs cannot address the impact of multiple factors on people with lower limb dyskinesia.

Cognitive neuroscience research suggests that human movement intention and preparation are greatly affected by their mental state of exercise (Van Overwalle et al., 2020). Some scholars have proposed to introduce virtual reality (VR) technology in rehabilitation training to build a three-dimensional audio-visual integrated virtual environment with multiple perceptions so that users can complete the two-way interaction between virtual and reality in a simulated environment. Immersive scenarios could help to filter out some of the external distractions and maximize the user's ability to focus on the movement task, promoting motor neurological rehabilitation. Berton et al. (2020) statistically analyzed the clinical data on the impact of VR technology on orthopedic patients from 2015 to 2020, the results showed that VR technology had a positive effect on the rehabilitation of patients. The case study by Chillura et al. (2020) showed that the combination of traditional rehabilitation under VR and robot-assisted rehabilitation could enhance functional recovery; the improvement effect of patients after combined treatment was significantly greater than that after conventional rehabilitation alone. Maggio et al. (2021) evaluated the usefulness of robot-aided gait training (RAGT) equipped with virtual reality augmented visuomotor feedback through EEG changes and confirmed that RAGT and VR can achieve better patient-tailored improvement in functional gait. These studies showed that VR technology plays a positive role in the rehabilitation of people with lower limb dyskinesia, but this is only a qualitative description, which does not indicate the impact of VR on brain or body changes in movement. Whether VR technology enhances movement intention or improves the detectability of movement intention is still unclear, and understanding the effect of VR on movement-related EEG potential change is important for movement intention detection based on BCI.

To study the mechanism of VR induction, it is necessary to analyze the brain information processing, establish a model for the generation of EEG signals, and then analyze the effect of different situations on its signal features. Some mathematical models of EEG generation were established and EEG signals have been simulated. Wendling et al. (2002) focused on the high-frequency EEG activity

and modeled EEG signals in epileptic patients. Zavaglia et al. (2008) built an EEG generation model by combining three neural mass models and simulated EEG power spectral density in some regions of interest during simple tasks. Chehelcheraghi et al. (2017) added external modulatory input and dynamic self-feedback to the Wendling neural mass model and simulated EEG signals in α, β, and γ bands. These models simulated macroscopic EEG signals by considering the brain regions of the sensing zone as a whole. However, brain information processing involves different regions and has a hierarchical relationship. Moreover, elements related to movement intention generation need to be added to the model to produce the corresponding EEG signal features. In this regard, the van der Pol oscillator is often used as a model for simulating EEG features. Baghdadi et al. (2018) modeled the ERD/ERS features of EEG signals using van der Pol oscillator simulations. Ghorbanian et al. (2015) simulated eyes-closed and eyes-open EEG based on the van der Pol oscillator, and the model showed that very good agreement exists between the model output and the EEG in terms of the power spectrum. Szuflitowska and Orlowski (2021) applied the Van der Pol model oscillator to study brain activity during temporal left lobe seizures. Therefore, to establish the EEG generation model of movement intention, it is necessary to combine the above different types of models and add more details. After modeling, the effect of the VR system on the EEG signal features can be analyzed by changing the parameters of the mathematical model.

In this study, we investigated the EEG generation of lower limb movement intention and its action expression mechanism and categorized brain information processing into primary and advanced processing. Then, an EEG signal generation model of lower limb active movement intention that fused the van der Pol oscillator and the neural mass model was established based on brain information processing laws. In addition, the model was simulated to investigate whether it is possible to enhance the movement intention significantly from EEG signals during leg lifts with VR induction. Finally, a comparative experiment was conducted on 12 healthy subjects to analyze EEG signal features and verify the correctness of the model. The rest of the paper is constructed in the following way. Section 2 describes the model and methods of the study. Section 3 describes the experiment. Section 4 contains the results of the model simulation and experiment. Section 5 is the discussion of the study. Section 6 is the limitations. Section 7 provides a conclusion to the study.

2 Methodology

2.1 Generation of lower limb movement intention and its virtual reality induction enhancement mechanism

The brain generates intention after cognition and decision-making. The process of movement intention generation is shown in **Figure 1A**. Human receptors continuously receive information from the body's internal or external environment, which is converted into electrical signals and transmitted to corresponding brain regions through specific nerve conduction pathways for primary processing. Then, the brain reprocesses and fuses the results with different primary processing regions, which can be regarded as an advanced processing process. Finally, the movement intention is generated and expressed in the EEG signals of the brain motor area.

For individuals with lower limb dyskinesia, pain during movement is the main factor that affects their movement intention. This is a prevention factor. However, psychological experimental research shows that visual information accounts for the largest proportion of the information received by the brain, which is 83% (An et al., 2017). In a VR induction system, virtual scenarios could provide an immersive and directional environment. It helps the users to perceive and focus on specific targets, generate selective attention, and enhance attention retention. Special scenarios could improve the competitiveness of the promoting factors for intention generation in the information-selective processing of the brain. In addition, individual willpower also affects the continuity of movement intention. The process of generating lower limb movement intention with the VR induction system is shown in **Figure 1B**. Pain irritation and individual willpower usually cannot be changed, while VR scenarios could provide positive visual information for generating movement intention and maximizing its benefits. Furthermore, attention enhancement and retention could enhance the efficiency of useful information, that is, enhancing motor control circuitry of the human brain, making movement-related neural associations easy to detect. Thus, the VR induction system increases the influence of specific signals in the brain's advanced processing process by altering the input signals.

2.2 Mathematical models

Brain neurons encode movement intention. The generation of neural oscillations is considered a marker of brain activity, it can be analyzed by mathematical models of brain dynamics. Two types of brain dynamics models are commonly used to describe the generation of EEG signals. The first type is the micro-level model, which describes the activity of a single neuron in detail; explicitly combines the properties of ion channels, axons, and dendrites; and explores the chemical properties of action potentials with the changes in intracellular ion concentrations (Abbott, 1999; Baladron et al., 2012). The model is computationally complex and ignores the interactions between cells, which cannot fully reveal the response characteristics of whole brain EEG signals (Bossy et al., 2015). The second type is the neural mass model (NMM), which is proposed due to the discovery that neurons with the same function can cluster and have similar dynamic properties (Wilson and Cowan, 1973). It assumes that neurons in the same population share similar inputs and synchronize their activity, reflecting the overall discharge behavior by describing the average characteristics of the neural population (such as average discharge rate, average membrane potential, etc.). The model uses multiple state variables to describe the dynamics of the entire neural population and its synapses, which has the advantages of low computational complexity, simple parameters, and clear physiological significance.

According to physiological research and the foregoing analysis, there are two stages between receiving various information from human receptors and generating movement intention. The goal of the primary processing model is to synchronize the generated signals with the external stimulus signals. The advanced processing

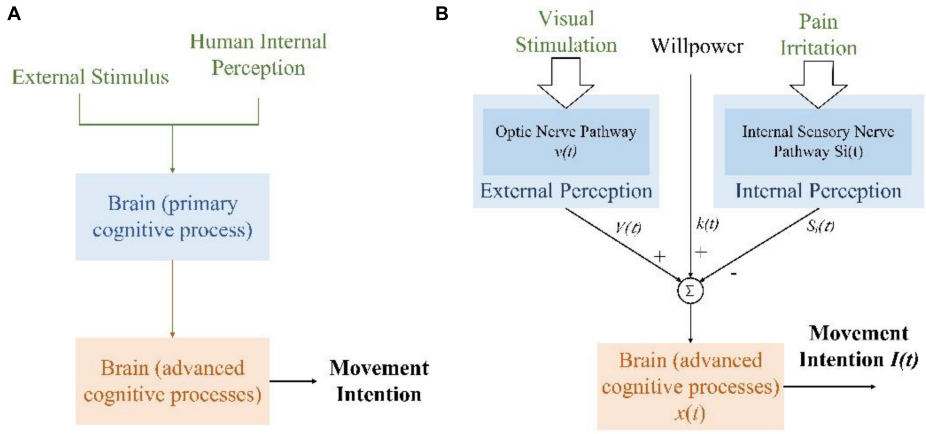

FIGURE 1
Generation of lower limb movement intention. **(A)** The generation of movement intention with secondary brain processing. **(B)** Various factors compete to produce movement intention for individuals with lower limb dyskinesia.

model couples the multiple types of signals obtained from the primary processing to output EEG signals indicating movement intention. Cascading these two models is the model proposed in this paper. In comparison with the universal model that simulates EEG at different frequencies, the proposed model could simulate not only spontaneous EEG signals but also the situation with external stimuli. Compared with the model that mimics the shape of EEG features, the proposed model has a clear physical significance. Overall, the proposed model is a model for movement intention generation that is more consistent with the physiological knowledge of brain processing and has good interpretability. The brain activity of movement intention generation could be expressed by the following two models.

2.2.1 Brain primary processing model

With the development of physiology and anatomy, researchers have segmented the brain according to its cell composition, arrangement, structure, and other characteristics. Each region plays a different role in processing information in the brain. Rhythmic neural electrical activity is the basis of brain cognitive function. This spontaneous neural electrical activity can be regarded as a dynamic self-excited oscillation process. When stimulated by the external environment, the endogenous neural activity in the brain is regulated by the external stimulus, the neural oscillation will be synchronized with the external rhythm (Thut et al., 2011). Thus, in primary brain processing, the neurons could be represented as oscillators, and synchronization is the oscillatory output.

A small oscillating neuronal assembly could be described by a van der Pol oscillator, as shown in **Equation 1**. Y is the output, λ is the bifurcation parameter, and $\dot{Y}$ determines the state variable of the oscillator. When $\lambda \leq 0$, there is no oscillation, when $\lambda > 1$, it enters a specific limit cycle with periodicity, and when $0 < \lambda < 1$, the oscillator oscillates at a frequency p with an amplitude of $2\sqrt{\lambda}$.

$$\ddot{Y} - (\lambda - Y^2)\dot{Y} + p^2 Y = 0 \quad (1)$$

When an external input (including the external input from the VR induction system) has the same frequency as the oscillator, the neural population could be affected by the oscillation. When the oscillator receives an input of the same frequency, the oscillator would not be affected when the input is the same as the oscillator phase, and the oscillator could gradually converge to the input through periodic stimulation when the phase is different. As the period increases, the average phase of the neuron oscillator gradually converges with the input, which is synchronization. The completion of synchronization means that information has been transmitted to corresponding brain regions through specific neural pathways.

2.2.2 Brain advanced processing model

The advanced processing of the brain is coordinated through the firing activity of a large number of widely interconnected neurons. It can be described in NMM. Based on the generation mechanism of nerve impulses, the classical NMM describes the interaction of different synaptic dynamics among pyramidal neurons, excitatory interneurons, and inhibitory interneurons (Wilson and Cowan, 1972; Jansen et al., 1993). It was initially used to study the mechanism of generation of alpha rhythms (Lopes da Silva et al., 1976) and the generation of simulated visual evoked potentials (Jansen and Rit, 1995). Physiological anatomy research suggests that the inhibitory synapses of pyramidal neurons in the hippocampus of the brain can be divided into slow inhibitory synaptic responses and fast inhibitory synaptic responses (Miles et al., 1996). Therefore, researchers divided inhibitory interneuron populations into slow inhibitory interneuron populations and fast inhibitory interneuron populations, and successfully simulated EEG signals that input targets were pyramidal cells (Wendling et al., 2002). However, input from neuronal populations can reach every interneuron. The results of a parameters sensitivity analysis showed that the model dynamics changes of excitatory interneurons and slow inhibitory interneurons were not obvious; thus, only the inputs to pyramidal neurons and fast inhibitory interneurons need to be considered. In addition, fast inhibitory interneurons exhibit self-inhibition (Ursino et al., 2010). Simulating brain parameters under different conditions (Vindiola et al., 2014; Mangia et al., 2017; Ferrat et al., 2018) and constructing a coupled brain network structure can clarify the changes in brain activities (Garnier et al., 2015; Chehelcheraghi et al., 2016).

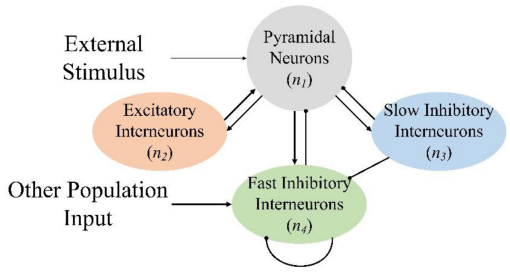

FIGURE 2
Neural mass model topology. The arrow line represents the excitatory transmission process, and the round-headed line represents the inhibitory process.

Based on previous research, the improved NMM topology is shown in Figure 2, where pyramidal neurons receive excitatory inputs from the excitatory interneurons and inhibitory inputs from the fast inhibitory interneurons and slow inhibitory interneurons. Pyramidal neurons transmit excitatory inputs to excitatory interneurons, fast inhibitory interneurons, and slow inhibitory interneurons. Slow inhibitory interneurons transmit inhibitory input to fast inhibitory interneurons and the fast inhibitory interneurons inhibit themselves. In the model, n is used to represent the neuron, and subscripts 1, 2, 3, and 4 of parameters represent pyramidal neurons, excitatory interneurons, slow inhibitory interneurons, and fast inhibitory interneurons, respectively. Attention enhancement and retention produced by the VR induction system affect the connectivity parameters of the various neuronal clusters, thereby enabling the brain to generate specific EEG signals.

2.2.3 Lower limb movement intention generation model

The primary processing and advanced processing of the brain are connected in series. According to the above method, the movement intention is generated when the promote factors are greater than the prevent factors; the motor areas of the cerebral cortex also display characteristic EEG signals. The model is shown in Figure 3.

In brain advanced processing, the primary processing results are collectively used as the input to the pyramidal neurons:

$$u_1(t) = u_{ev}(t) - u_{ip}(t) \tag{2}$$

Where $u_{ev}(t)$ represents the result of the primary processing of positive external visual information $U_{ev}(t)$ and $u_{ip}(t)$ represents the result of the primary processing of negative internal pain irritation $U_{ip}(t)$. The primary processing is simulated by the van der Pol oscillator.

Fast inhibitory interneurons could also receive input from other populations, which is recorded as $u_4(t)$. Here, it is assumed that they are connected through excitatory synapses.

Each population consists of a cascade of linear and nonlinear modules, receiving average postsynaptic membrane potential v_i from other neural populations, the average synaptic connection constant represents the coupling between neural populations. Then, the membrane potential is converted into the average peak density of the neurons, and the sigmoid function is used to simulate the existence of inhibition and saturation, denoted by z_i. Thus, $z_i = S(v_i)$. Changing the value could simulate the impulse responses of different synapses; the process is represented by $h_i(t)$.

By combining these two models, the brain's processing of movement intention generation could be simulated and corresponding EEG signals could be generated. The complete lower limb movement intention generation model corresponds to the following set of differential equations:

Pyramidal neurons

$$\begin{cases} \dfrac{dy_1(t)}{dt} = x_1(t) \\ \dfrac{dx_1(t)}{dt} = G_2\omega_2 z_1(t) - 2\omega_2 x_1(t) - \omega_2^2 y_1(t) \\ z_1(t) = \dfrac{2e_0}{1+e^{-rv_1}} - e_0 \\ v_1(t) = C_{12}y_2 - C_{13}y_3(t) - C_{14}y_4(t) \end{cases} \tag{3}$$

Excitatory interneurons

$$\begin{cases} \dfrac{dy_2(t)}{dt} = x_2(t) \\ \dfrac{dx_2(t)}{dt} = G_2\omega_2\left(z_2(t) + \dfrac{u_1(t)}{C_{12}}\right) - 2\omega_2 x_2(t) - \omega_2^2 y_2(t) \\ z_2(t) = \dfrac{2e_0}{1+e^{-rv_2}} - e_0 \\ v2(t) = C_{21}y_1(t) \end{cases} \tag{4}$$

Slow inhibitory interneurons

$$\begin{cases} \dfrac{dy_3(t)}{dt} = x_3(t) \\ \dfrac{dx_3(t)}{dt} = G_3\omega_3 z_3(t) - 2\omega_3 x_3(t) - \omega_3^2 y_3(t) \\ z_3(t) = \dfrac{2e_0}{1+e^{-rv_3}} - e_0 \\ v_3(t) = C_{31}y_1(t) \end{cases} \tag{5}$$

Fast inhibitory interneurons

$$\begin{cases} \dfrac{dy_4(t)}{dt} = x_4(t) \\ \dfrac{dx_4(t)}{dt} = G_4\omega_4 z_4(t) - 2\omega_4 x_4(t) - \omega_4^2 y_4(t) \\ \dfrac{dy_{4'}(t)}{dt} = x_{4'}(t) \\ \dfrac{dx_{4'}(t)}{dt} = G_2\omega_2 u_4(t) - 2\omega_2 x_{4'}(t) - \omega_2^2 y_{4'}(t) \\ z_4(t) = \dfrac{2e_0}{1+e^{-rv_4}} - e_0 \\ v_4(t) = C_{41}y_1(t) - C_{43}y_3(t) - C_{44}y_4(t) + y_{4'}(t) \end{cases} \tag{6}$$

In the model, $y_i(t)$ represents the output of the corresponding neuron, and the overall output of the model is $v_1(t)$. Moreover, the subscript 4' represents the negative self-loop of fast inhibitory interneurons. C_{ij} represents the synaptic constant from neuron j to neuron i. G_i represents the strength of the individual synapses and ω_i represents the reciprocal of the time constant. The sigmoidal function is centered on 0 and the parameters of the sigmoid function are represented by e_0 and r.

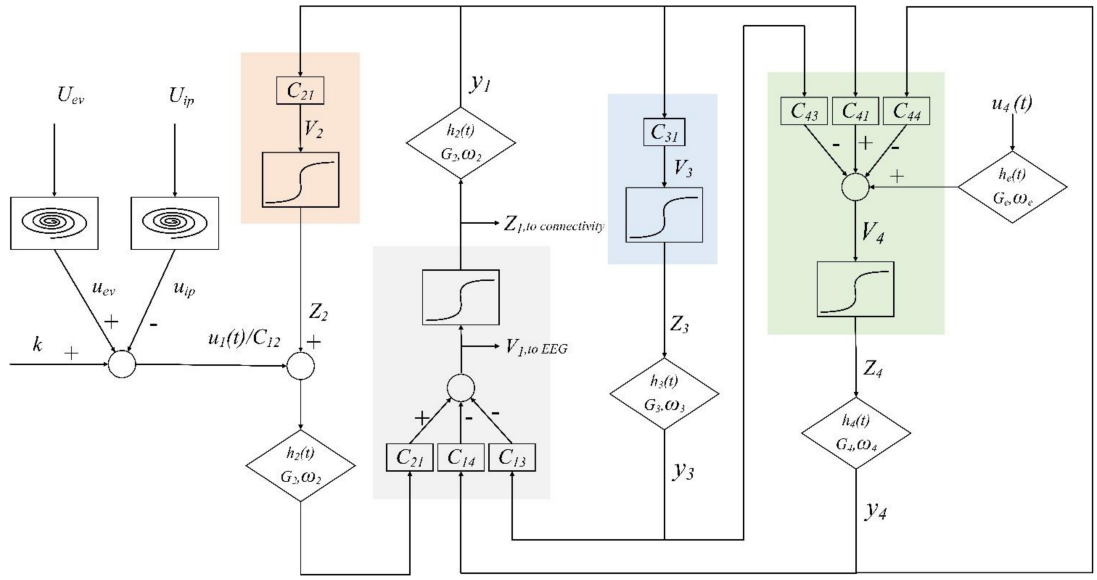

FIGURE 3
Layout of the lower limb movement intention generation model.

3 Experiment

3.1 Experimental system overview

In this study, an experimental platform was built to verify the above analysis. The experimental platform is built as shown in Figure 4A, including a VR module, an EEG signal acquisition module, an EMG signal acquisition module, and a host computer. HUAWEI VR Glasses were used to provide a VR environment. It adopts a dual fast LCD screen, with a field of view angle of 90 degrees and a binocular resolution of 3K and supports VR sound effects that move with the head. The advantage of VR glasses over VR helmets is that glasses do not need to be worn through the top of the head, which can reduce the adverse effects on EEG signals caused by friction between the device and the head. A Neuracle 32-channel EEG cap (Neusen W-EEG) was used to collect the EEG signals, and a Neuracle 16-channel EMG (NeuSen WM) acquisition instrument was used to collect the surface electromyography (sEMG) signals. The computer is used to receive and store the EEG and sEMG signals. Signal processing is carried out through MATLAB.

The construction of the virtual scenarios is shown in Figure 4B, which is implemented based on the Unity3D editor. The virtual character model induces the subjects to perform specified actions. The light source of the scene is the color of the sky, and the scene camera is bound to the virtual reality glasses. When the virtual characters in the scenarios start to move, the subjects need to follow them to move.

3.2 Subjects

A total of 12 college students were selected as subjects (marked as S1-S12), 10 male and 2 female, without any history of sensorimotor deficits or any psychological disorders. The demographic and physiological information of the subjects is summarized in Table 1. This study was approved by the Ethics Committee of Xi'an Jiaotong University (Ethics number: 2021-360). Before the start of the experiment, each of the subjects was introduced to the relevant tasks and signed the informed consent form.

3.3 Experimental protocol

The experiment was completed in the Bio-Mechatronics and Service Robot Laboratory of Xi'an Jiaotong University. The leg lift movement is the subject of movement because it is one of the important basic movements in lower limb movement. This experiment is a control experiment. The experimental group used the VR induction system to induce the subjects to perform the action, the control group did not use it and changed to a single-tone prompt. To ensure the single variable principle of the controlled experiment, the VR induction system included the same single-tone prompt as the control group. All subjects were required to complete two experiments, one for the experimental group and the other for the control group. The experiments were conducted on the same day with a long break in between to minimize variability caused by factors such as fatigue. During the experiment, the subjects should always maintain a natural standing state. There were a total of 5 sessions in this experiment, and the sequence diagram is shown in Figure 4C. Each session consisted of 10 trials. In each trial, the subjects first kept still for 5 s and then performed actions according to the prompts. Signals around and before the start moment of the movement were monitored so that the movement execution was not limited to but did not exceed 4 s (2 s to raise the leg and 2 s to lower it). After the actions were completed, there was a short rest to prepare for the next trial. Each of the sessions was 135 s long with a break of 2–5 min between two consecutive sessions. Finally,

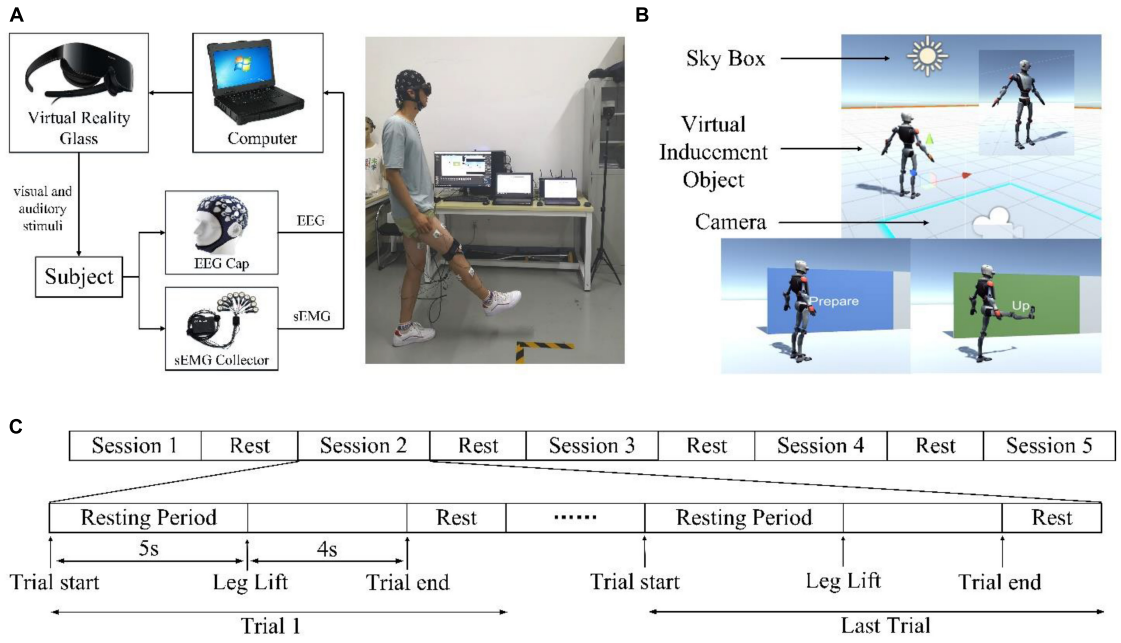

FIGURE 4
Experimental system. **(A)** The experimental platform. **(B)** Virtual scenarios. **(C)** Experimental Sequence Diagram.

TABLE 1 **Demographic characteristics of the subjects.**

Subjects	S1	S2	S3	S4	S5	S6	S7	S8	S9	S10	S11	S12	MEAN ± SDT
Age (years)	23	22	24	26	24	23	25	28	24	24	24	23	24.2 ± 1.5
Height (cm)	177	172	178	168	178	163	175	171	168	174	178	176	173 ± 4.7
Weight (kg)	71	73	74	63	64	53	67	68	57	72	64	69	66.3 ± 6.2

each subject's experimental and control group data were collected 50 times, respectively.

3.4 EEG data collection and movement evaluation

This experiment recorded the EEG signals of subjects during exercise. The measurement points of EEG electrodes under the international 10/20 system were FZ, FC1, FC2, CZ, C3, C4, CP1, CP2, and PZ. Before acquiring data, an appropriate conductive gel was applied to the scalp and ensure that the required impedance between the electrodes and the scalp was less than 5 kΩ. The sampling frequency was 1,000 Hz.

Lower limb movements were evaluated by surface EMG signals. Six surface EMG sensors were placed in the subjects' rectus femoris, vastus lateralis, vastus medialis, semitendinosus, tibialis anterior, and gastrocnemius. These EMG data provided the changes in lower limb muscle activation during the experiment. The sampling frequency of the sEMG sensor was 1,000 Hz.

3.5 Data analysis method

The Cz channel of the EEG cap corresponds to the lower limb motor-related cortex, so we selected the EEG signal data of the Cz for analysis (Li et al., 2018; Romero-Laiseca et al., 2020). Two major neural phenomena can be captured with EEG in relation to movement intention when human lower limbs are moving, event-related desynchronization (ERD), and MRCP. ERD is recognized as a decrease in the α (μ) band power (8–13 Hz) and in the β band power (14–25 Hz) with movement (Qiu et al., 2016). MRCP is a low-frequency negative shift in the EEG recording that takes place approximately 0.5–2 s before the movement production. MRCP is readily masked by higher frequency activity, and its amplitude is usually between 5 and 30 μV (Shakeel et al., 2015). These two features could be calculated from the original EEG data. The collected EEG signals contain artifacts such as noise, EMG, and power frequency interference, which need to be filtered out before analysis. This study used empirical mode decomposition and independent component analysis for artifact removal.

Short-time Fourier transform (STFT) is used to analyze the collected data in time-frequency domain. It multiplies a time-limited window function before Fourier transforms the signal instead of Fourier transforming the entire signal. It assumes that the signal is stationary in the short time interval of the analysis window, and the spectrum of the signal at each moment in the time domain is obtained by moving the window function on the time axis. To observe the EEG responses of different states in the time domain, event-related spectral perturbation (ERSP) is used to analyze the power

spectrum changes of EEG. The calculation of ERD features is as follows:

$$E_{i,j} = \frac{1}{n}\sum_{k=1}^{n} s_{i,j,k}^2 \tag{7}$$

$$E_{b_i} = \frac{1}{m}\sum_{j=1}^{m} E_{i,j} \tag{8}$$

$$ERD = \left(\frac{E_{i,j} - E_{b_i}}{E_{b_i}}\right) \times 100\% \tag{9}$$

Here, s represents the EEG signal. i, j, and k denote the trial number, epoch number, and sample number. E represents the mean power of the EEG data and n is the length of sub-epochs. E_b represents the baseline consisting of m epochs of each trial.

In STFT calculation, the choice of window function is crucial. The rectangular window has severe spectrum leakage. The BlackMan-harris window has an excessively wide main lobe that reduces the frequency resolution. The Hanning window has both good frequency resolution and less spectral leakage. Therefore, the Hanning window is used in this study. The EEG data were subdivided into 1-s-long epochs with a 200-ms overlap. Then, each epoch was processed for ERD extraction. Furthermore, the change of EEG power with frequency can be calculated by taking the ERSP power at different frequencies and then according to the mean value of the time dimension. Time-domain MRCP features could be extracted by filtering directly.

Moreover, a convolutional neural network (CNN) was used to detect the lower limb movement intention of the experimental group and the control group. Based on the convolutional neural network framework, this paper designed 13 convolutional layers, 5 pooling layers, 3 fully connected layers, and 1 normalization layer. The input data were filled with the "same" operation to ensure that the input and output sizes were the same after the convolution operation. The size of the convolution kernel was 3 × 3 and activated by the tanh function. The maximum pooling method was adopted for the pooling layer and the stride was 2 × 2.

4 Result

4.1 Simulation analysis

The central nervous system can always have rhythmic and spontaneous discharges without any external stimulation, so the input of the model can be simulated by a uniformly distributed random signal. The $u_4(t)$ during advanced brain processing is simulated by white Gaussian noise with mean 0 and variance 5. Referring to physiological knowledge, Sigmoid saturation (s^{-1}) e_0 = 2.5, Sigmoid steepness (mV^{-1}) r = 0.56, EEG signals of different states can be simulated by adjusting the connectivity constant and synaptic impulse response (Ursino et al., 2010).

The simulation results of the EEG signal during voluntary movement without external stimulus are shown in Figure 5A. When there is an external stimulus from the VR system, the stimulus can be represented by a sine curve at the moment of movement intention generation. The model input for this case is a uniformly distributed random signal superimposed on a sinusoidal signal. The simulation results of EEG signals during VR-based motion are shown in Figure 5B. Figures 5C, D are the simulated signals corresponding to the actual acquired EEG signals of S1 at the Cz channel. The simulated signal in the time domain is similar to the actual collected signal. Then, the features related to movement intention need to be extracted and analyzed from the simulated EEG signals.

Event-related desynchronization and MRCP features of the simulated EEG signals were extracted. The calculated EEG signal power in α and β frequency bands is shown in Figure 6A. It can be seen that the power is decreased in both α and β bands, and the power decrease is more pronounced with the stimulus from the VR induction system. The results of filtering the low frequency (0–10 Hz) EEG signal are shown in Figure 6B. It can be seen that during the preparation and execution of lower limb movements, the amplitude of the EEG signal decreases first and

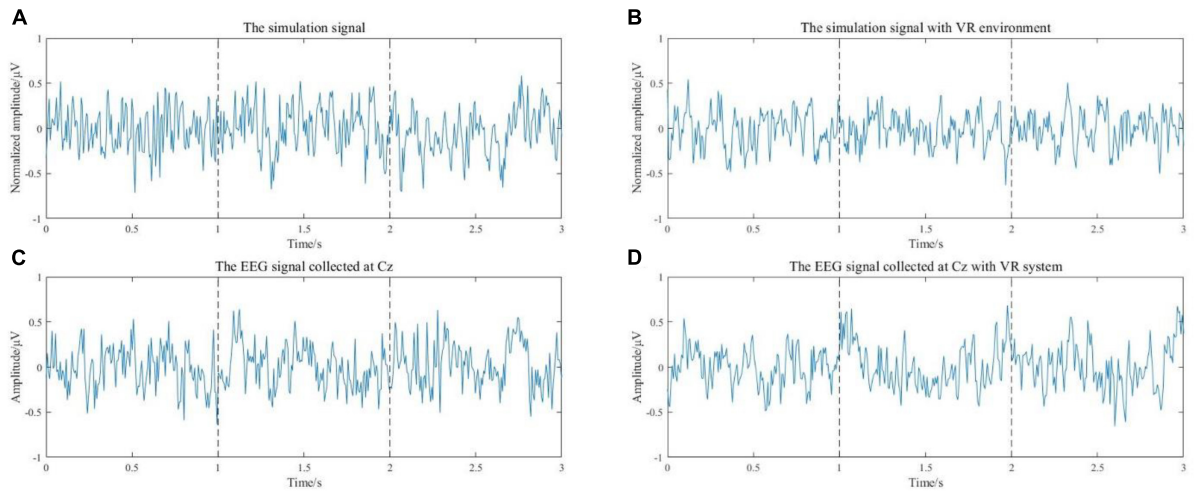

FIGURE 5
(A) The simulation results of the EEG signal during voluntary movement without external stimulus. **(B)** The simulation results of EEG signals during exercise with a VR environment. **(C)** The EEG signal of the Cz channel from S1. **(D)** The EEG signal of the Cz channel from subject 1 with VR induction system.

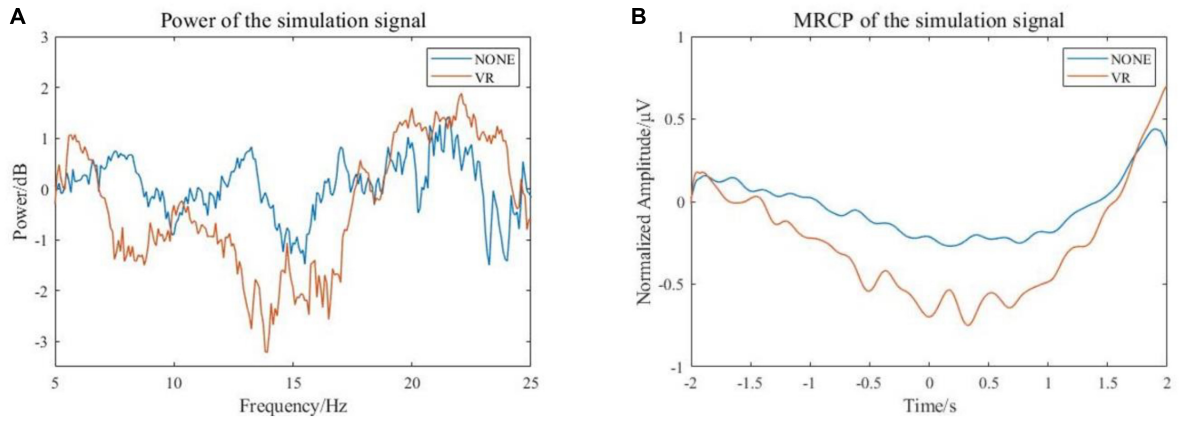

FIGURE 6
Characteristics of simulated EEG signal. **(A)** Frequency-domain features **(B)** Time domain features.

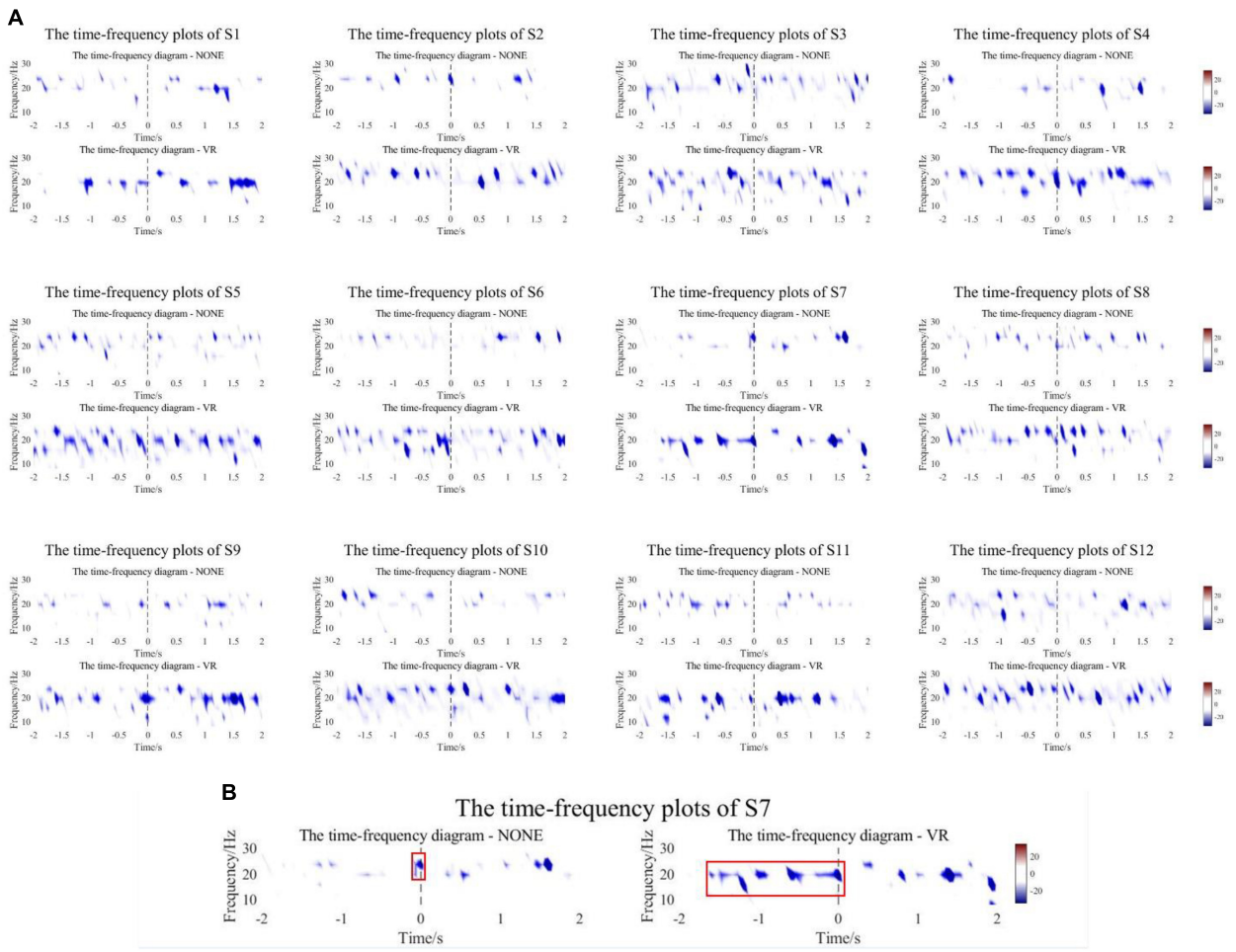

FIGURE 7
(A) The time-frequency plots of the experimental and control groups of subjects. **(B)** A representative subject. The starting position of the red box is the ERD onset time.

then increases. The signal is more negatively shifted with the stimulus from the VR induction system. In general, comparing the simulated EEG signals of VR induction or not, both MRCP and ERD features are more obvious when there is movement with the external stimuli from the VR induction system. This means that the use of a VR induction system would be more conducive to detecting/predicting movement intention from EEG signals.

TABLE 2 ERD onset time and peak value statistics.

Subject	ERD Onset Time (s)		Peak Value (dB)	
	Experimental Group	Control Group	Experimental Group	Control Group
S1	−1.133	−1.133	−30.237	−26.430
S2	−1.000	−0.933	−40.359	−31.113
S3	−1.809	−1.860	−27.831	−26.705
S4	−1.993	−1.867	−27.018	−23.066
S5	−2.015	−1.860	−31.345	−29.446
S6	−1.963	−1.603	−25.126	−24.293
S7	−1.600	−0.067	−30.964	−24.133
S8	−1.912	−1.037	−34.243	−24.264
S9	−1.860	−1.654	−32.932	−24.370
S10	−1.800	−1.867	−28.973	−23.279
S11	−1.654	−1.088	−29.010	−24.362
S12	−1.933	−1.067	−32.449	−22.621
MEAN ± STD	−1.723 ± 0.319	−1.336 ± 0.526	−30.874 ± 3.796	−25.340 ± 2.511

4.2 Neurophysiological data analysis

4.2.1 ERD time-frequency analysis

The collected EEG data of the experimental group and the control group were analyzed offline. Nerve conduction velocities ranged from approximately 50 to 70 m/s, and the nerve pathways involved in the reception of stimuli to intention generation were all on the millimeter scale. Therefore, the differences between the onset time of movement defined by the experimental group and the control group could be ignored. An epoch is 5 s before to 2 s after the motion. After preprocessing and filtering artifacts, 8–30 Hz fourth-order Butterworth band pass filtering was performed to obtain EEG signals in α and β frequency bands. The EEG data from −5 s to −2 s were regarded as the resting state, and the time-frequency plots of the 12 subjects at −2 s to 2 s were calculated and plotted based on this baseline. The signal was collected at the Cz channel. Figure 7 shows the time-frequency plots of the experimental and control groups of subjects.

Figure 7A shows that all subjects in the experimental group and control group had ERD phenomenon near the start of motion (−2∼2 s). The experimental group experienced a wider range of ERD phenomena and a more significant decrease in power compared to the control group. For quantitative analysis, the first occurrence −20 dB point is chosen as the point of initiation of ERD, and the ERD peaks of the experimental group and the control group were counted. As shown in Table 2, the mean onset time of ERD of subjects in the experimental group and control group was −1.723 ± 0.319 s and −1.336 ± 0.526 s, and the mean peak values were −30.874 ± 3.796 dB and −25.340 ± 2.511 dB. There was a significant difference in ERD Onset Time (p = 0.0191) and a highly significant difference in Peak Value (p = 0.0001) between the experimental and control groups. Most of the results yielded the same conclusion as the mean. All subjects in the experimental group had lower peaks than the control group, and most of the experimental group had ERD Onset Time earlier than the control group. However, the ERD onset time of the experimental group for S3 and S10 appeared slightly later than that of the control group, 0.051 s and 0.067 s, respectively, not exceeding 0.1 s. Nevertheless, the time-frequency plots clearly show that S3 and S10 produced a wider range of ERD phenomena in the experimental group, producing peaks that were 1.126 dB and 5.694 dB lower than in the control group, respectively. Figure 7B is a representative subject. The control group only showed a significant ERD phenomenon near the movement onset time, whereas the experimental group showed a wider range, especially before the start of the movement. The starting position of the red box is the ERD onset time.

Additionally, comparing the statistical significance of the difference in ERD between the experimental group and the control group, the compared test was calculated at the 95% significance level, and the results are shown in Figure 8A. All subjects showed differences near the onset of exercise at both the α and β frequency bands, especially for the α frequency band. Surprisingly, except for S1, S3, and S12, the other 9 subjects showed differences in early stages. Figure 8B is a representative subject. The major significant blocks are marked in red rectangles. It showed early significant differences even before the movement onset. Early features could be conducive to pre-movement intention pattern detection.

Moreover, to investigate how baseline EEG was affected by experimental and control groups, baseline EEG powers from all channels at α and β frequency band (8–25 Hz) were calculated and averaged across all subjects. The data conformed to a normal distribution according to the Shapiro–Wilk test. The experimental group had a kurtosis of −0.9 and a skewness of 0.8, while the control group had a kurtosis of 4.9 and a skewness of 2.1. Figure 9 shows the boxplot of the EEG baseline power, the average EEG baseline power of the experimental group was $5.66 \times 10^{-4}\ v^2$, and the control group was $3.89 \times 10^{-4}\ v^2$. Although the average EEG baseline power of the experimental group was slightly higher than that of the control group, the results of the t-test showed that the experimental group and the control group were not significantly different.

Therefore, in the overall ERD time-frequency analysis, the baseline EEG power of the experimental group and the control

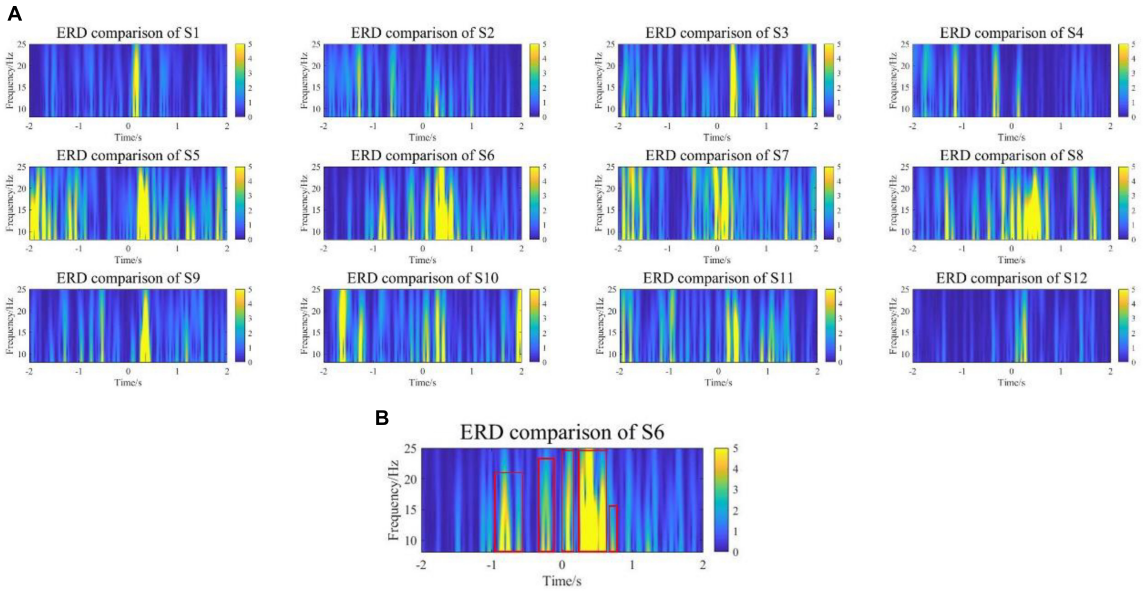

FIGURE 8
(A) The comparison results of ERD in the range of [−2,2] seconds between the experimental group and the control group. **(B)** A representative subject. The experimental group showed early significant differences in ERD even before the movement onset.

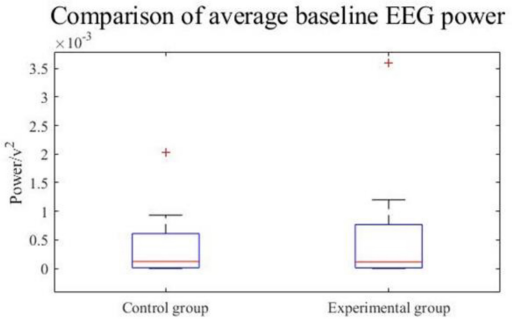

FIGURE 9
EEG baseline power.

group were consistent, which means that the VR induction system could not change EEG in the resting state. It could induce more obvious early ERD features to enhance the detectability of movement intention.

4.2.2 Frequency domain power analysis

The ERSP power of all subjects was calculated, and the frequency domain power of the experimental group and the control group was analyzed. The graph of the change of EEG power with frequency is shown in Figure 10. The red line is the frequency domain power of the experimental group and the blue line is the frequency domain power of the control group.

All subjects in the control group and the experimental group had the same trend of frequency domain power change. The power was dropped in the α and β Frequency bands. From the perspective of power attenuation, throughout the entire frequency range, the experimental group of most subjects had greater attenuation than the control group. Because of the opposite results presented at certain moments in some smaller ranges (such as the power of S9 at around 13 Hz), the characteristic frequencies of each frequency band need to be analyzed. The frequency corresponding to the minimum value in the figure was the characteristic frequency; detailed data is shown in Table 3.

The characteristic frequencies of the α band experimental group and the control group were 10.9 ± 1.4 Hz and 10.8 ± 2.0 Hz, respectively. The characteristic frequencies of the β band were 18.7 ± 1.7 Hz and 19.2 ± 1.9 Hz. The characteristic frequencies of the experimental group and the control group were correlated (R = 0.94), so the experimental group did not change the main frequency of feature generation. The power of characteristic frequency is shown in Figure 11. The power of the experimental group decreased more than that of the control group. In the α band, the average peak power of the experimental group was −3.679 ± 1.281 dB, and that of the control group was −2.156 ± 1.039 dB. In the β band, the average peak power was −3.490 ± 0.984 dB and −2.379 ± 0.835 dB, respectively.

The frequency domain power analysis shows that the characteristic frequencies generated by each frequency band in the experimental group and the control group are correlated. That means the VR induction system could generate more significant power attenuation in EEG to enhance the detectability of movement intention.

4.2.3 Time-domain MRCP feature analysis

The collected EEG data of two working conditions were analyzed. An epoch is 5 s before to 2 s after the motion. The epoch was preprocessed to eliminate the artifacts, and 0.1–10 Hz filtering was performed to obtain low-frequency signals. Figure 12 compares the MRCP features extracted from subjects in the experimental group and the control group. The red line is the MRCP of the experimental group and the blue line is the MRCP of the control group. It could be seen that all subjects in the

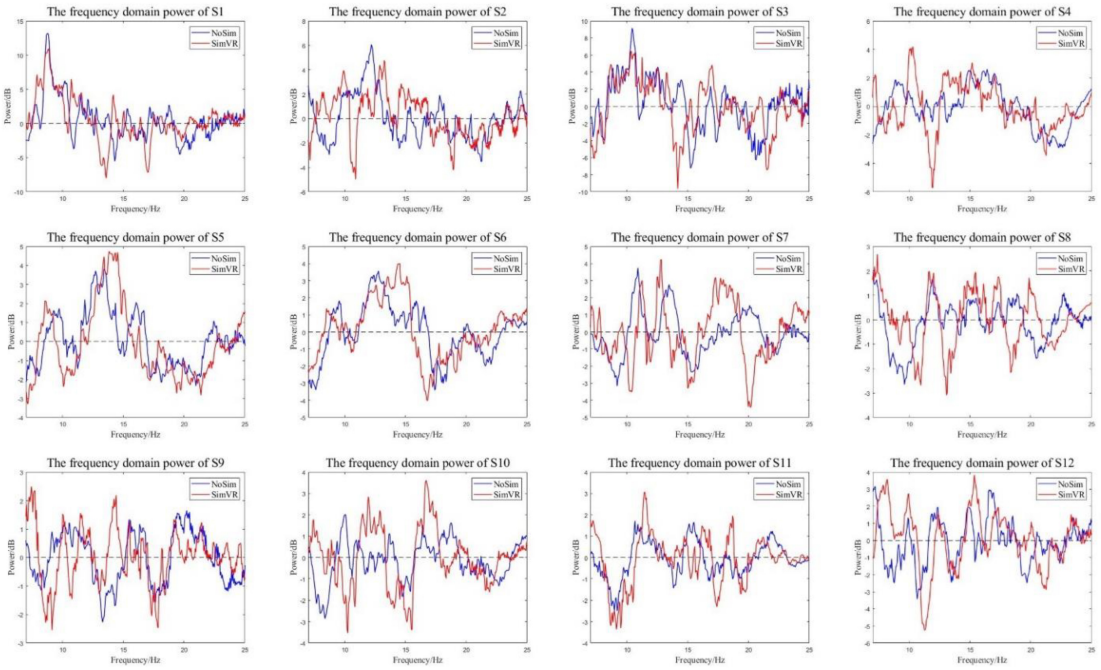

FIGURE 10
Energy curves in the frequency domain. The experimental group has more energy attenuation than the control group in α and β bands.

TABLE 3 Characteristic frequency in α and β band.

Subject	Experimental Group		Control Group	
	α Band (Hz)	β Band (Hz)	α Band (Hz)	β Band (Hz)
S1	13.0	17.0	14.0	20.0
S2	11.0	19.0	8.0	21.0
S3	14.0	19.0	14.0	19.0
S4	12.0	21.0	12.0	21.0
S5	10.0	21.0	11.0	20.0
S6	11.0	17.0	11.0	17.0
S7	10.0	20.0	9.0	22.0
S8	11.0	18.0	10.0	20.0
S9	9.0	18.0	13.0	18.0
S10	10.0	16.0	8.0	15.0
S11	9.0	17.0	9.0	17.0
S12	11.0	21.0	11.0	20.0
MEAN ± STD	10.9 ± 1.4	18.7 ± 1.7	10.8 ± 2.0	19.2 ± 1.9

experimental group showed obvious MRCP characteristics, and the amplitude of this potential began to decrease 2–3 s before the onset of motion and then rebounded. In total, 11 subjects in the control group showed MRCP characteristics, only S5 did not show obvious MRCP characteristics.

To compare the differences in the characteristics of the experimental group and the control group, the peak points of the MRCP characteristics were counted as shown in Figure 13A. The peak value of all experimental groups decreased more than that of the control group, with a significant statistical difference (p = 0.0082). The average peak value of the experimental group was −14.052 ± 8.757 μV and the control group was −7.855 ± 4.345 μV. Furthermore, comparing the peak time of the two groups, the time of peak appearance of the experimental group was −0.111 ± 0.343 s and the control group was −0.103 ± 0.412 s. Whether the peak time of the two groups came from the same distribution was verified through a quantile-quantile plot, as shown in Figure 13B, the red line is the distribution of the experimental group and the blue line is the distribution of the control group. The peak time of the experimental group and the control group follow different distributions, with statistical differences.

In time-domain MRCP feature analysis, the result means that the VR induction system could induce more significant MRCP features compared to enhancing the detectability of motion intention.

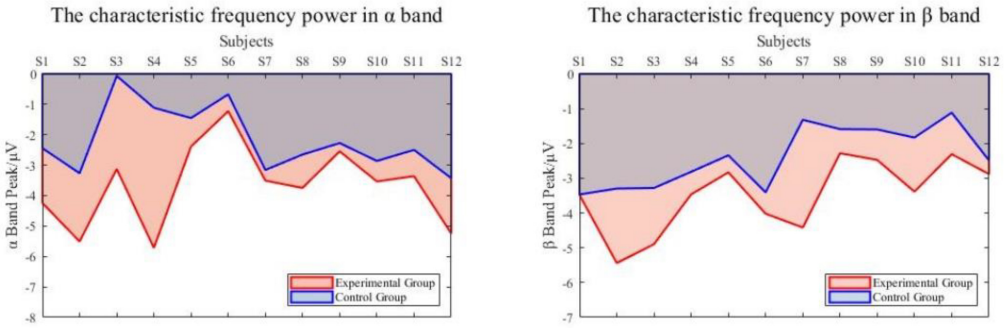

FIGURE 11
The power of characteristic frequency.

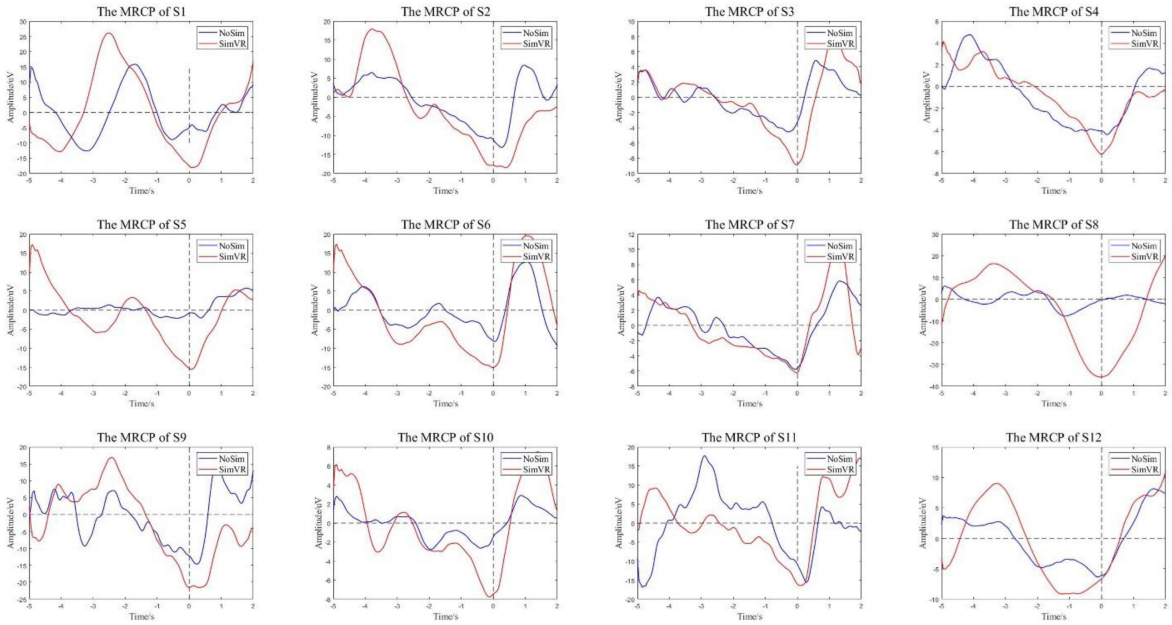

FIGURE 12
MRCP features. The experimental group showed obvious characteristics.

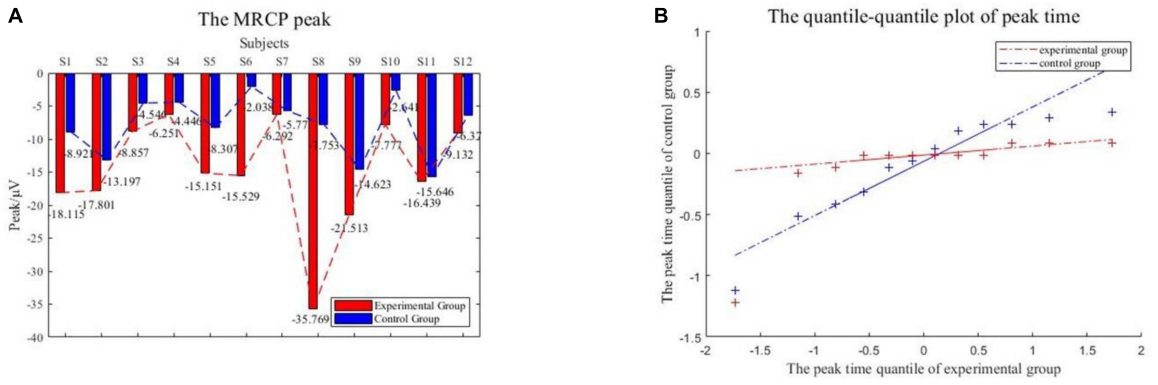

FIGURE 13
(A) The MRCP peak. **(B)** The quantile-quantile plot of peak time.

TABLE 4 Classification results.

Subject	Accuracy (%)		Sensitivity (%)		Specificity (%)	
	Experimental Group	Control Group	Experimental Group	Control Group	Experimental Group	Control Group
S1	83.50 ± 1.29	82.41 ± 2.81	82.14 ± 2.42	83.47 ± 2.96	87.50 ± 2.55	86.23 ± 5.89
S2	85.20 ± 2.84	79.81 ± 0.60	80.91 ± 1.64	76.92 ± 0.70	91.86 ± 5.18	84.62 ± 1.37
S3	83.26 ± 2.06	80.49 ± 1.52	81.45 ± 1.85	82.61 ± 2.49	90.72 ± 4.87	77.78 ± 1.24
S4	81.33 ± 2.14	80.17 ± 1.09	79.37 ± 1.42	81.20 ± 1.29	83.84 ± 3.07	78.85 ± 2.31
S5	84.88 ± 3.65	82.87 ± 2.56	85.22 ± 3.15	86.78 ± 2.64	85.56 ± 5.24	84.21 ± 5.71
S6	83.41 ± 1.14	81.25 ± 1.11	84.35 ± 2.49	79.49 ± 1.43	86.67 ± 2.07	85.71 ± 1.76
S7	84.50 ± 2.45	81.63 ± 1.67	83.04 ± 2.54	80.91 ± 1.76	86.36 ± 3.55	84.88 ± 3.14
S8	86.73 ± 3.35	84.91 ± 3.59	85.45 ± 3.18	83.19 ± 3.79	90.70 ± 4.21	88.17 ± 4.84
S9	86.34 ± 3.05	83.00 ± 2.88	84.35 ± 2.42	82.14 ± 2.55	88.89 ± 4.46	86.36 ± 4.47
S10	90.50 ± 6.74	84.18 ± 1.82	90.32 ± 6.13	81.82 ± 2.07	90.72 ± 8.06	88.37 ± 2.40
S11	85.85 ± 2.94	83.96 ± 1.68	86.96 ± 3.70	85.71 ± 2.91	85.56 ± 2.59	86.02 ± 3.78
S12	84.50 ± 2.52	81.94 ± 2.19	86.61 ± 3.20	80.99 ± 2.36	88.64 ± 4.65	86.32 ± 4.48
MEAN ± STD	85.00 ± 2.85	82.22 ± 1.96	84.18 ± 2.84	82.10 ± 2.25	88.08 ± 4.21	84.80 ± 3.32

4.3 Offline classification analysis

To maintain the optimal performance of CNN classifiers, it is necessary to adjust the parameters. The principle is to enable the validation set to be classified with no more than 95% specificity while maintaining at least a sensitivity of 75%. The calculation formulas for sensitivity and specificity are as follows:

$$\text{Sensitivity} = \frac{\text{True Positive}}{\text{True Positive} + \text{False Negative}} \tag{10}$$

$$\text{Specificity} = \frac{\text{True Negative}}{\text{True Negative} + \text{False Positive}} \tag{11}$$

Table 4 shows the offline classification results of 12 subjects in the experimental and control groups. Results for each subject were the mean after 10-fold cross-validation. The CNN classifier maintains a reasonable true positive detection rate while ensuring a minimal false positive detection. The accuracy rates for the experimental and control groups were 85 ± 2.85% and 82.22 ± 1.96%, respectively. Similarly, the sensitivity and specificity were 84.18 ± 2.84%, 82.1 ± 2.25% and 88.08 ± 4.21%, 84.8 ± 3.32%, respectively. The results showed that the accuracy (p = 0.0008) and specificity (p = 0.0097) of the experimental group were significantly higher than those of the control group, and the sensitivity (p = 0.0490) of the experimental group was significantly higher than that of the control group specificity. This means that the VR induction system could enhance the detectability of intentions.

4.4 Comparison of EMG activity

To further analyze the potential impact of the VR environment adopted by the experimental group on motor activity, muscle activation in the experimental and control groups was compared. Muscle activation can reflect the overall level of the movement execution process. The rectus femoris is an important muscle that reflects lower limb movements, therefore the EMG signal at the rectus femoris is used to calculate muscle activation. The

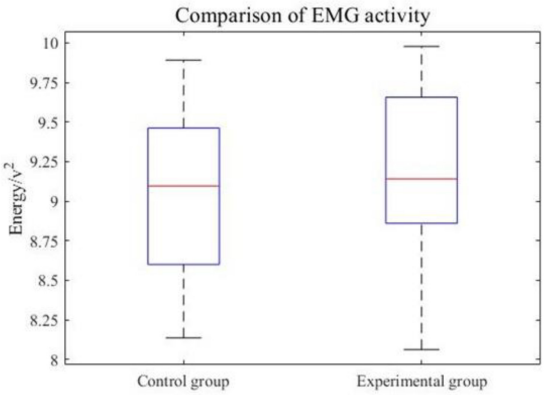

FIGURE 14
Comparison of EMG activity.

EMG power average for each trial of the subjects was calculated to obtain a global statistical representation of muscle activation energy. Figure 14 shows a boxplot of the EMG activity from all subjects. It can be seen that there was no significant difference in the EMG activity of the subjects in the experimental group and the control group. This indicates that the movement execution of the experimental group and the control group in the experiment was consistent.

5 Discussion

The above results show that the motion of the subject with the VR induction could enhance the detectability of movement intention via EEG signals compared with the general situation.

Most existing BCI control technologies have some shortcomings because they are based on empirical evidence or experimental results. Thus, mathematic modeling can further our understanding of the physiological mechanisms for the responses of EEG behavior. By simulating the lower limb

movement intention generation model in different conditions, the results show that the EEG signals related to movement intention had the corresponding features in the time and frequency domain, whatever the conditions. However, the VR induction could increase the significance of features. This provides a basis for feature selection during subsequent classification. The proposed model analyzes the mechanism of the brain's movement intention in sections and discusses the coupling of multiple neuronal clusters, which is of great practical significance for the study of the brain functional network. Movement intention with the VR induction enhanced mechanism provides a new method for the active regulation of nerves in patients' clinical rehabilitation.

In our experimental work, with ERD time-frequency analysis, we found that subjects' lower limb movement with VR induction leads to a more prevalent ERD phenomenon, which has a better time-frequency resolution. Significant peak drops could make it easier to detect. Some results showed a certain early saliency compared with the general situation, which indicates that it is easier to be detected before the movement occurs. However, the baseline power is not affected by different scenes. This suggests that VR induction could be an effective way to detect motion intention using EEG signals.

Moreover, the ERD in the β band is more significant than that in the α band, whether with VR induction or not. Further frequency domain power analysis demonstrates that the power of α and β bands had both decreased, and the characteristic frequencies were similar. Compared to the characteristic frequency power in the α and β bands, the power drop in the β band is obviously greater than in the α band. When using the VR induction system, the decline was enhanced in both the α and β bands, significantly so in the α band. This means that peak α power and peak β power could be used as a combined feature in movement intention detection with VR induction and peak β power was highly sensitive to detection.

Time domain MRCP feature analysis shows that the features generated are more obvious with VR-based motion, and the amplitude drops more. The MRCP consists of the readiness potential (RP), motor potential, and movement-monitoring potential (MMP). RP is considered to reflect the planning or preparation of the movement and motor potential and MMP is thought to reflect movement execution and control of performance. RP feature enhancement could help to decode pre-movement EEG signals.

The enhancement of the above features is of great significance for clinical practical applications. The offline classification results prove that the VR induction system could improve the detectability of the BCI system. The analysis is based on Cz sampling points and the region around Cz corresponds to lower limbs (Blanco-Diaz et al., 2023). In addition, there is no significant difference between the experimental group and the control group in muscle activation energy during movement. This means the VR induction system could improve the movement-related features of EEG signals and further enhance the detectability of lower limb movement intention based on BCI.

Furthermore, the enhancement of the VR system on the brain is multifaceted and may contribute to brain nerve remodeling (Namazi et al., 2021; Tan et al., 2021). The mathematical model we have developed is based on the physiological mechanisms of the brain information processing process. The focus of this study is on movement intention, so the simulation study was carried out for the EEG signals related to movement intention. During the simulation of the model, the intervention of the VR system was considered to have an effect on the selective attention process during brain information processing. When the input signal was changed, only the synaptic constants between the neuronal clusters were changed, and there was no specific change in the structure of the model, so we believe that the model has the ability to migrate to other similar tasks, which will be studied in the future. This study was conducted on EEG signals related to movement intention. Simulation results based on the model guided the analysis of the experimental data, and the consistent conclusions obtained from the experimental and simulation results can illustrate the validity of the model.

In summary, the time and frequency domain characteristics of subjects' EEG signals induced by VR are more obvious, the features appear earlier, and the intention detection accuracy is higher. Therefore, the intervention of VR induction can significantly improve the detectability of movement intention.

6 Limitations

Virtual reality scenarios make user interaction more natural when using rehabilitation robots, while immersion in the VR environment requires users to wear VR glasses or VR headsets, which may cause discomfort or visual fatigue. However, current research suggests that the help of an immersive VR environment can at least help increase movement intention, which in turn promotes neurorehabilitation. It could help people with impaired athletic ability to regain lost athletic ability to a certain extent with less effort and in less time. Additionally, to reduce the potential for hazards when moving while wearing a VR device, appropriate safety protocols should be designed and implemented so that users can be alerted to any tasks that require attention. This raises another interesting research question that should be investigated in future studies.

The limitation of this study is that the improved neural mass model in our study from a macroscopic point of view described the EEG generation mechanism of movement. Although the features of the simulated EEG signals had the same result as the experiment result, it still lacks some physiological validation. This should be refined in subsequent studies. In addition, EEG-EMG coherence analysis can respond to a certain extent to signal changes, which is a worthy topic for future research and contributes to the study of movement intention recognition methods based on the fusion of EEG and EMG signals. Furthermore, the experiment did not use subjects with lower limb dyskinesia, which will be resolved in future studies, but this study has been able to prove the effectiveness of VR induction in movement intention enhancement. The generation of active movement intention is the premise of active rehabilitation, and it is of great significance to improve the detectability of EEG related to the active motion intention of patients. To further improve the results, extensive research should be carried out on the details of the VR paradigm in the future.

7 Conclusion

In order to solve the problems of weak movement intention and low recognition accuracy in the rehabilitation process of people with lower limb motor dysfunction, this paper studied whether VR induction could enhance the detectability of lower limb active movement intention. The active movement intention generation process of individuals with lower limb dysfunction was analyzed, and an EEG generation theoretical model was established. A comparative experiment was conducted on 12 healthy subjects. Through simulation research and experimental results analysis of EEG signals, the multiple features were enhanced when subjects used VR induction so that VR induction could work as a tool to enhance the distinguishability of lower limb active movement intentions from EEG signals. Furthermore, offline classification proves that VR induction could enhance the detectability of movement intention. However, further work is necessary to quantify the effect of VR scenario stimuli on neural signals. Moreover, advanced signal processing and learning techniques could be employed to further enhance the results. In general, the current results show promising insights into VR scenarios and their effect on movement intention, preparation, and execution.

Data availability statement

The original contributions presented in the study are included in the article/supplementary material, further inquiries can be directed to the corresponding author.

Ethics statement

The studies involving humans were approved by the Ethics Committee of Xi'an Jiaotong University. The studies were conducted in accordance with the local legislation and institutional requirements. The participants provided their written informed consent to participate in this study. Written informed consent was obtained from the individual(s) for the publication of any potentially identifiable images or data included in this article. All the experiments were conducted in accordance with the Declaration of Helsinki.

Author contributions

RD: Writing—original draft, Writing—review and editing. XZ: Writing—review and editing. HL: Writing—original draft, Writing—review and editing. GM: Writing—review and editing. AZ: Writing—review and editing. XS: Writing—review and editing. CH: Writing—review and editing.

Funding

The author(s) declare financial support was received for the research, authorship, and/or publication of this article. This work was supported by grants from the National Key Research and Development Program of China (2023YFC3604903), the Qin Chuang Yuan "Scientist + Engineer" Team Construction Project of Shaanxi Province (2022KXJ-160), and the Fundamental Research Funds for the Central Universities (xzd012023018).

Conflict of interest

CH was employed by AVIC Creative Robotics Co., Ltd. The remaining authors declare that the research was conducted in the absence of any commercial or financial relationships that could be construed as a potential conflict of interest.

Publisher's note

All claims expressed in this article are solely those of the authors and do not necessarily represent those of their affiliated organizations, or those of the publisher, the editors and the reviewers. Any product that may be evaluated in this article, or claim that may be made by its manufacturer, is not guaranteed or endorsed by the publisher.

References

Abbott, L. F. (1999). Lapicque's introduction of the integrate-and-fire model Neuron (1907). *Brain Res. Bull.* 50, 303–304. doi: 10.1016/S0361-9230(99)00161-6

Abiri, R., Borhani, S., Sellers, E. W., Jiang, Y., and Zhao, X. P. (2019). A comprehensive review of eeg-based brain-computer interface paradigms. *J. Neural Eng.* 16:011001. doi: 10.1088/1741-2552/aaf12e

An, X., Cao, Y., Jiao, X., and Ming, D. (2017). Research on cognitive mechanism and brain-computer interface application in visual-auditory crossmodal stimuli. *J. Electronic Meas. Instrument* 31, 983–993.

Baghdadi, G., Towhidkhah, F., and Rostami, R. (2018). A mathematical model to mimic the shape of event related Desynchronization/Synchronization. *J. Theor. Biol.* 453, 117–124. doi: 10.1016/j.jtbi.2018.05.026

Baladron, J., Fasoli, D., Faugeras, O., and Touboul, J. (2012). Mean-field description and propagation of Chaos in networks of Hodgkin-Huxley and Fitzhugh-Nagumo Neurons. *J. Math. Neurosci.* 2:10. doi: 10.1186/2190-8567-2-10

Berton, A., Longo, U. G., Candela, V., Fioravanti, S., Giannone, L., Arcangeli, V., et al. (2020). Virtual reality, augmented reality, gamification, and telerehabilitation: psychological impact on orthopedic patients'. *Rehabil. J. Clin. Med.* 9:2567. doi: 10.3390/jcm9082567

Blanco-Diaz, C. F., Guerrero-Mendez, C. D., Delisle-Rodriguez, D., de Souza, A. F., Badue, C., and Bastos, T. F. (2023). Lower-limb kinematic reconstruction during pedaling tasks from Eeg signals using unscented Kalman filter. *Comput. Methods Biomech. Biomed. Eng.* Online ahead of print. doi: 10.1080/10255842.2023.2207705

Bossy, M., Faugeras, O., and Talay, D. (2015). Clarification and complement to "mean-field description and propagation of Chaos in networks of Hodgkin-Huxley and Fitzhugh-Nagumo neurons". *J. Math. Neurosci.* 5:19. doi: 10.1186/s13408-015-0031-8

Chaisaen, R., Autthasan, P., Mingchinda, N., Leelaarporn, P., Kunaseth, N., Tammajarung, S., et al. (2020). Decoding Eeg rhythms during action observation, motor imagery, and execution for standing and sitting. *IEEE Sensors J.* 20, 13776–13786. doi: 10.1109/JSEN.2020.3005968

Chehelcheraghi, M., Nakatani, C., Steur, E., and van Leeuwen, C. (2016). A neural mass model of phase-amplitude coupling. *Biol. Cybernetics* 110, 171–192. doi: 10.1007/s00422-016-0687-5

Chehelcheraghi, M., van Leeuwen, C., Steur, E., and Nakatani, C. (2017). A neural mass model of cross frequency coupling. *PLoS One* 12:e0173776. doi: 10.1371/journal.pone.0173776

Chillura, A., Bramanti, A., Tartamella, F., Pisano, M. F., and Naro, A. (2020). Advances in the rehabilitation of intensive care unit acquired weakness: a case report on the promising use of robotics and virtual reality coupled to physiotherapy. *Medicine* 99:e20939. doi: 10.1097/MD.0000000000020939

Ferrat, L. A., Goodfellow, M., and Terry, J. R. (2018). Classifying dynamic transitions in high dimensional neural mass models: a random forest approach. *PLoS Comput. Biol.* 14:e1006009. doi: 10.1371/journal.pcbi.1006009

Garnier, A., Vidal, A., Huneau, C., and Benali, H. (2015). A neural mass model with direct and indirect excitatory feedback loops: identification of bifurcations and temporal dynamics. *Neural Comput.* 27, 329–364. doi: 10.1162/NECO_a_00696

Ghorbanian, P., Ramakrishnan, S., Whitman, A., and Ashrafiuon, H. (2015). A phenomenological model of Eeg based on the dynamics of a stochastic Duffing-Van Der Pol Oscillator network. *Biomed. Signal Processing Control* 15, 1–10. doi: 10.1016/j.bspc.2014.08.013

Hasan, S. M. S., Siddiquee, M. R., Atri, R., Ramon, R., Marquez, J. S., and Bai, O. (2020). Prediction of gait intention from pre-movement Eeg signals: a feasibility study. *J. Neuroeng. Rehabil.* 17, 1–16. doi: 10.1186/s12984-020-00675-5

Jansen, B. H., and Rit, V. G. (1995). Electroencephalogram and visual-evoked potential generation in a mathematical-model of coupled cortical columns. *Biol. Cybernetics* 73, 357–366. doi: 10.1007/BF00199471

Jansen, B. H., Zouridakis, G., and Brandt, M. E. (1993). A neurophysiologically-based mathematical-model of flash visual evoked-potentials. *Biol. Cybernetics* 68, 275–283. doi: 10.1007/BF00224863

Jeong, J. H., Kwak, N. S., Guan, C. T., and Lee, S. W. (2020). Decoding movement-related cortical potentials based on subject-dependent and section-wise spectral filtering. *IEEE Trans. Neural Syst. Rehabil. Eng.* 28, 687–698. doi: 10.1109/TNSRE.2020.2966826

Jeong, J. H., Lee, M. H., Kwak, N. S., and Lee, S. W. (2017). "Single-trial analysis of readiness potentials for lower limb Exoskeleton control," in *Proceedings of the 5th International Winter Conference on Brain-Computer Interface (BCI)*, (South Korea). doi: 10.1109/IWW-BCI.2017.7858156

Jia, H., Sun, Z., Duan, F., Zhang, Y., Caiafa, C. F., and Solé-Casals, J. (2022). Improving pre-movement pattern detection with filter bank selection. *J. Neural Eng.* 19:066012. doi: 10.1088/1741-2552/ac9e75

Jochumsen, M., Niazi, I. K., Taylor, D., Farina, D., and Dremstrup, K. (2015). Detecting and classifying movement-related cortical potentials associated with hand movements in healthy subjects and stroke patients from single-electrode, singletrial Eeg. *J. Neural Eng.* 12:056013. doi: 10.1088/1741-2560/12/5/056013

Kalita, B., Narayan, J., and Dwivedy, S. K. (2020). Development of active lower limb robotic-based Orthosis and Exoskeleton devices: a systematic review. *Int. J. Soc. Robot.* 13, 775–793. doi: 10.1007/s12369-020-00662-9

Leone, C., Feys, P., Moumdjian, L., D'Amico, E., Zappia, M., and Patti, F. (2017). Cognitive-motor dual-task interference: a systematic review of neural correlates. *Neurosci. Biobehav. Rev.* 75, 348–360. doi: 10.1016/j.neubiorev.2017.01.010

Li, P., Wang, L., Liu, Y., Liu, B., and Ma, C. (2018). Study on Eeg rhythm features of lower limb motor imagery and motor performance. *Chinese J. Sci. Instrument* 39, 207–214.

Lopes da Silva, F. H., van Rotterdam, A., Barts, P., van Heusden, E., and Burr, W. (1976). Models of neuronal populations: the basic mechanisms of rhythmicity. *Progress Brain Res.* 45, 281–308. doi: 10.1016/S0079-6123(08)60995-4

Lopez-Larraz, E., Trincado-Alonso, F., Rajasekaran, V., Perez-Nombela, S., del-Ama, A. J., Aranda, J., et al. (2016). Control of an ambulatory Exoskeleton with a brain-machine interface for spinal cord injury gait rehabilitation. *Front. Neurosci.* 10:359. doi: 10.3389/fnins.2016.00359

Maggio, M. G., Naro, A., Manuli, A., Maresca, G., Balletta, T., Latella, D., et al. (2021). Effects of robotic neurorehabilitation on body representation in individuals with stroke: a preliminary study focusing on an Eeg-based approach. *Brain Topogr.* 34, 348–362. doi: 10.1007/s10548-021-00825-5

Mangia, A. L., Ursino, M., Lannocca, M., and Cappello, A. (2017). Transcallosal inhibition during motor imagery: analysis of a neural mass model. *Front. Comput. Neurosci.* 11:57. doi: 10.3389/fncom.2017.00057

Mascolini, A., Niazi, I. K., and Mesin, L. (2022). Non-linear optimized spatial filter for single-trial identification of movement related cortical potential. *Biocybernetics Biomed. Eng.* 42, 426–436. doi: 10.1016/j.bbe.2022.02.013

McDonald, C., Fingleton, C., Murphy, S., and Lennon, O. (2022). Stroke survivor perceptions of using an Exoskeleton during acute gait rehabilitation. *Sci. Rep.* 12:14185. doi: 10.1038/s41598-022-18188-7

Miles, R., Toth, K., Gulyas, A. I., Hajos, N., and Freund, T. F. (1996). Differences between somatic and dendritic inhibition in the Hippocampus. *Neuron* 16, 815–823. doi: 10.1016/S0896-6273(00)80101-4

Namazi, H., Babini, M. H., Kuca, K., and Krejcar, O. (2021). Information and memory-based analysis for decoding of the human learning between normal and Virtual Reality (Vr) conditions. *Fractals* 29:2150163. doi: 10.1142/S0218348X21501632

Qiu, S., Yi, W. B., Xu, J. P., Qi, H. Z., Du, J. G., Wang, C. F., et al. (2016). Event-related Beta Eeg changes during active, passive movement and functional electrical stimulation of the lower limb. *IEEE Trans. Neural Syst. Rehabil. Eng.* 24, 283–290. doi: 10.1109/TNSRE.2015.2476481

Qiu, S. Y., Guo, W., Caldwell, D., and Chen, F. (2021). Exoskeleton online learning and estimation of human walking intention based on dynamical movement primitives. *IEEE Trans. Cogn. Dev. Syst.* 13, 67–79. doi: 10.1109/TCDS.2020.2968845

Romero-Laiseca, M. A., Delisle-Rodriguez, D., Cardoso, V., Gurve, D., Loterio, F., Nascimento, J. H. P., et al. (2020). A low-cost lower-limb brain-machine interface triggered by pedaling motor imagery for post-stroke patients rehabilitation. *IEEE Trans. Neural Syst. Rehabil. Eng.* 28, 988–996. doi: 10.1109/TNSRE.2020.2974056

Sburlea, A. I., Montesano, L., and Minguez, J. (2016). Advantages of Eeg phase patterns for the detection of gait intention in healthy and stroke subjects Arxiv. *arXiv*

Sburlea, A. I., Montesano, L., and Minguez, J. (2017). Advantages of Eeg phase patterns for the detection of gait intention in healthy and stroke subjects. *J. Neural Eng.* 14:15. doi: 10.1088/1741-2552/aa5f2f

Shakeel, A., Navid, M. S., Anwar, M. N., Mazhar, S., Jochumsen, M., and Niazi, I. K. (2015). A review of techniques for detection of movement intention using movement-related cortical potentials. *Comput. Math. Methods Med.* 2015, 1–13. doi: 10.1155/2015/346217

Szuflitowska, B., and Orlowski, P. (2021). "Analysis of complex partial seizure using non-linear duffing Van Der Pol Oscillator model," in *Proceedings of the Computational Science - ICCS 2021. 21st International Conference. Lecture Notes in Computer Science*, (Berlin: Springer). doi: 10.1007/978-3-030-77970-2_33

Tan, W., Xu, Y., Liu, P., Liu, C., Li, Y., Du, Y., et al. (2021). A method of Vr-Eeg scene cognitive rehabilitation training. *Health Information Sci. Syst.* 9, 1–9. doi: 10.1007/s13755-020-00137-1

Thut, G., Schyns, P. G., and Gross, J. (2011). Entrainment of perceptually relevant brain oscillations by non-invasive rhythmic stimulation of the human brain. *Front. Psychol.* 2:170. doi: 10.3389/fpsyg.2011.00170

Ursino, M., Cona, F., and Zavaglia, M. (2010). The generation of rhythms within a cortical region: analysis of a neural mass model. *Neuroimage* 52, 1080–1094. doi: 10.1016/j.neuroimage.2009.12.084

Van Overwalle, F., Manto, M., Cattaneo, Z., Clausi, S., Ferrari, C., Gabrieli, J. D. E., et al. (2020). Consensus paper: cerebellum and social cognition. *Cerebellum* 19, 833–868. doi: 10.1007/s12311-020-01155-1

Vindiola, M. M., Vettel, J. M., Gordon, S. M., Franaszczuk, P. J., and McDowell, K. (2014). Applying Eeg phase synchronization measures to non-linearly coupled neural mass models. *J. Neurosci. Methods* 226, 1–14. doi: 10.1016/j.jneumeth.2014.01.025

Wang, K., Xu, M. P., Wang, Y. J., Zhang, S. S., Chen, L., and Ming, D. (2020). Enhance decoding of pre-movement Eeg patterns for brain-computer interfaces. *J. Neural Eng.* 17, 1–11. doi: 10.1088/1741-2552/ab598f

Wendling, F., Bartolomei, F., Bellanger, J. J., and Chauvel, P. (2002). Epileptic fast activity can be explained by a model of impaired Gabaergic dendritic inhibition. *Eur. J. Neurosci.* 15, 1499–1508. doi: 10.1046/j.1460-9568.2002.01985.x

Wilson, H. R., and Cowan, J. D. (1972). Excitatory and inhibitory interactions in localized populations of model neurons. *Biophys. J.* 12, 1–24. doi: 10.1016/S0006-3495(72)86068-5

Wilson, H. R., and Cowan, J. D. (1973). Mathematical theory of functional dynamics of cortical and thalamic nervous-tissue. *Kybernetik* 13, 55–80. doi: 10.1007/BF00288786

Xiang, X. N., Ding, M. F., Zong, H. Y., Liu, Y., Cheng, H., He, C. Q., et al. (2020). The safety and feasibility of a new rehabilitation robotic exoskeleton for assisting individuals with lower extremity motor complete lesions following spinal cord injury (Sci): an observational study. *Spinal Cord* 58, 787–794. doi: 10.1038/s41393-020-0423-9

Zavaglia, M., Astolfi, L., Babiloni, F., and Ursino, M. (2008). The effect of connectivity on Eeg rhythms, power spectral density and coherence among coupled neural populations: analysis with a neural mass model. *IEEE Trans. Biomed. Eng.* 55, 69–77. doi: 10.1109/TBME.2007.897814

Zhang, X. D., Li, H. Z., Lu, Z. F., and Yin, G. (2021). Homology characteristics of Eeg and Emg for lower limb voluntary movement intention. *Front. Neurorobot.* 15:642607. doi: 10.3389/fnbot.2021.642607

frontiers | Frontiers in Neuroscience

TYPE Brief Research Report
PUBLISHED 02 February 2024
DOI 10.3389/fnins.2024.1344841

OPEN ACCESS

EDITED BY
Yingbai Hu,
The Chinese University of Hong Kong, China

REVIEWED BY
Hongdong Wang,
Xuzhou University of Technology, China
Zeng Hx,
South China University of Technology, China

*CORRESPONDENCE
Zhen Wang
✉ wangz_21@sumhs.edu.cn

RECEIVED 26 November 2023
ACCEPTED 12 January 2024
PUBLISHED 02 February 2024

CITATION
Wang Z, Li X and Wang G (2024) Exploring wireless device-free localization technique to assist home-based neuro-rehabilitation. *Front. Neurosci.* 18:1344841. doi: 10.3389/fnins.2024.1344841

Exploring wireless device-free localization technique to assist home-based neuro-rehabilitation

Zhen Wang[1]*, Xiaoou Li[1] and Guoli Wang[2]

[1]College of Medical Instrumentation, Shanghai University of Medicine & Health Sciences, Shanghai, China, [2]School of Computer Science and Engineering, Sun Yat-sen University, Guangzhou, China

Home-based movement neuro-rehabilitation is quite necessary when the patient goes back home from hospital. Due to lack of supervision from doctors, rehabilitation at home is often forgotten. As an alternate to doctor-supervision, in this research, we explore the wireless device-free localization technique to assist the rehabilitation procedure. The localization technique can judge whether the patient is near the rehabilitation equipment and even obtain the movement trajectory. The most challenging problem in the wireless device-free localization system is that the received-signal-strength (RSS) of the electromagnetic-wave is unpredictable, which increases the localization error. How to select the informative RSS is pretty important. This research proposes a new criterion (i.e., fluctuation-level) to select the informative RSS. Experimental results show the effectiveness of the proposed fluctuation-level in reducing the localization error.

KEYWORDS

rehabilitation, localization, RTI, RSS, fluctuation-level

1 Introduction

For the patient who suffers from neuro-disabilities, he/she need to perform neuro-rehabilitation under the supervision of rehabilitation doctors. Usually, after he leaves the hospital, he is still required to do daily rehabilitation at home by himself (Maresca et al., 2020). However, due to lack of supervision from the rehabilitation doctors, the patient often forgets to take rehabilitation-exercises, leading to the degradation in health condition. To tackle this problem, technology-assisted movement-evaluation can be adopted (Zhang et al., 2020; Hu et al., 2023). One fundamental technique is to obtain the indoor location of the patient, which can judge whether the patient is near the rehabilitation equipment.

Currently, the indoor localization technique mainly adopts device-based strategy, meaning that the target needs to attach a device to obtain his location (Cao et al., 2020). Device-based strategy is inappropriate for the patient localization because the device hinders the patient to move and take rehabilitation-exercises. Therefore, this research explores the device-free localization technique to supervise the patient to take home-based rehabilitation.

Technically, many sensing strategies can be employed to achieve device-free localization, such as camera-based vision localization (Kim and Jun, 2008), infrared-based localization (Ngamakeur et al., 2022), ultrasound localization (Yoon and Park, 2016), RF (radio frequency) based wireless localization (Khan et al., 2021; Abdullah et al., 2023) etc. Camera-based localization somehow demands huge memory for video storage. Infrared-based localization is fragile to be interfered by fluorescent light, and the localization distance is limited. Ultrasound-based localization is easily influenced by Doppler effect and the localization area is comparably small.

By contrast, RF-based localization has the advantages of traveling long distance, not influenced by light, low data-storage, not violating the privacy etc., which attracts much more attention in the research community.

RF-based localization employs the principle that the wireless signal would change in received-signal-strength (RSS), channel state information (CSI), phase of arrival (POA) or angle of arrival (AOA) after the presence of the target. In which, RSS is the widely used pattern. Among different methods in RSS-based localization, radio-tomographic imaging (RTI) is an effective yet simple approach (Wilson and Patwari, 2010; Zhen et al., 2019a) which is the focus of this article.

RTI considers the located area as one shadowing image, each pixel has its pixel-value. The pixel-value equals to the attenuation-value occurring at the location of this pixel. RTI first computes one shadowing image from the RSS measurements. Then, the patient's location is estimated by finding the position with maximum pixel-value in the image (Zhen et al., 2019b).

However, there is one challenge which degrades the localization performance. The challenge is that not all the RSS measurements are contributive for patient-localization due to the multipath-noise in wireless propagation. How to select the informative RSS measurements that contribute to indoor-localization is the essential problem in RTI. Aiming at addressing this problem, current literatures mainly adopt the criterion of fade-level to select the informative RSS measurements (Wilson, 2012; Kaltiokallio et al., 2013; Mela et al., 2023). However, in practice, only using fade-level to select informative RSS measurements is unsatisfactory. In this article, in addition to fade-level, we propose another criterion (i.e., fluctuation-level) to select the informative RSS measurements. Experimental results show that combining fade-level and the proposed fluctuation-level can achieve better localization performance than just using fade-level.

2 Method

2.1 Wireless network deployment

Before implementing the device-free localization system, a wireless network should be deployed to cover the indoor area. Figure 1 illustrates one example of the wireless network. Each RF node adopts the off-the-shelf circuit-board which can guarantee the low system cost of the localization system. Each node-pair constitutes one RF-link. The area is divided into several pixel-grids, and each pixel has its coordinate. All the pixels constitute one shadowing image. The pixel-value denotes the attenuation-value occurring at the coordinate of this pixel. Intuitively, the pixel where the patient locates has maximum attenuation-value (or pixel-value). Therefore, we can obtain the location of the patient according to the pixel-value of the shadowing image. More RF nodes can contribute to enhance the localization accuracy. However, the trade-off should be made between localization accuracy and increased system cost in engineering practice.

In mathematics Equation (1), can be used to model RTI (Wilson and Patwari, 2010),

$$\boldsymbol{y} = \boldsymbol{H}\boldsymbol{x} + \boldsymbol{n}, \tag{1}$$

where $\boldsymbol{y} = [y_1, \cdots, y_M]^T$ represents the RSS measurements (i.e., the RSS variation before and after the patient presents in the room), M equals to the total number of RF-links in the wireless network. $\boldsymbol{x} = [x_1, \cdots, x_N]^T$ is the image-vector with each element denoting the attenuation-value, N is the pixel number. $\boldsymbol{n} = [n_1, \cdots, n_M]^T$ is the noise vector. $\boldsymbol{H} \in \mathbb{R}^{M \times N}$ is the weighting matrix, which can be determined by the ellipse model (Wilson and Patwari, 2010).

The aim of RTI is to compute the image-vector $\boldsymbol{x}$ given the measured RSS $\boldsymbol{y}$. Because not all the RSS is contributive for target localization, how to select the informative RSS constitutes one key problem in RTI-based device-free localization.

2.2 Selection of informative RSS by using fluctuation-level and fade-level

Currently, fade-level is the only criterion to evaluate whether the RSS from a particular link is informative or not. The computation of fade-level is shown as Equation (2),

$$F_l = \bar{z}_l - P(d_l) \tag{2}$$

where F_l represents fade-level of the *l-th* link, $\bar{z}$ is the average RSS of the *l-th* link when the room is without any person, $P(d_l)$ denotes the RSS computed by the path-loss model (Wilson, 2012). Previous research shows that the RSS with large-positive fade-level is more informative for localization (Wilson, 2012).

However, fade-level just reflects the deviation property of the RSS. In practice, the localization accuracy when just using fade-level to select informative RSS is usually unsatisfactory. Here we explore the fluctuation property of the RSS, and take it as a new criterion for informative RSS selection. We name the fluctuation property as fluctuation-level. The fluctuation-level can be obtained by computing the RSS variance. Mathematically, the fluctuation-level is shown as Equation (3),

$$v_l = \frac{1}{W} \sum_{i=1}^{W} (\tilde{r}_i - \bar{r}_l)^2 \tag{3}$$

where v_l denotes the fluctuation-level of the *l-th* link, W is the window length. $\tilde{r}_i$ denotes each RSS sample in this window, $\bar{r}_l$ is the mean of the RSS samples in this window for the *l-th* link. Intuitively, the RSS with lower fluctuation-level are more reliable than that with higher fluctuation-level.

In the localization system, we jointly use fluctuation-level and fade-level to select the informative RSS. Specifically, the fade-level and fluctuation-level are allocated with their respective threshold values F_{thr} and v_{thr}. In the joint-selection strategy, if $F > F_{thr}$ and $v < v_{thr}$ are satisfied for a particular link, the RSS from this link can be considered as informative. Otherwise, the RSS is filtered as being uninformative. Mathematically, this joint-selection strategy can be written as Equation (4),

$$link\_indicator = \begin{cases} 1 & if\ F > F_{thr}\ and\ v < v_{thr} \\ 0 & otherwise \end{cases} \tag{4}$$

where the variable *link_indicator* is a binary variable $\{0, 1\}$, indicating whether the RSS from a particular RF-link is informative.

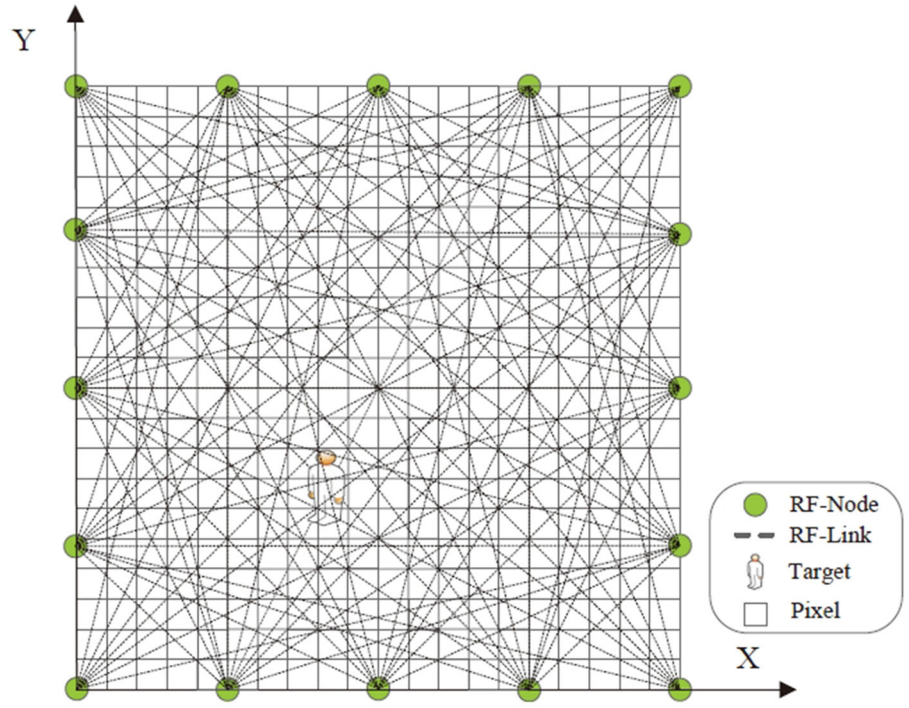

FIGURE 1
Wireless network deployment. Green circle represents the RF node. Dashed line denotes the RF link between two node-pairs. The target is within the located area covered by the wireless network. Square represents the pixel in the shadowing image.

Logic one indicates the link is informative, while zero denotes the contrary.

2.3 Shadowing image reconstruction and position inference

Based on the selected RSS, this section introduces how to compute the shadowing image and infer the patient's location. Because the image is sparse (Wilson and Patwari, 2010; Zhen et al., 2018), here the sparse Bayesian learning (SBL) method is adopted. In SBL, the image is allocated with zero-mean Gaussian prior-distribution having the variance constrained by inverse-Gamma distribution, which is expressed as Equation (5),

$$\begin{cases} P(\boldsymbol{x}|\boldsymbol{\lambda}) = \prod_{i=1}^{N} Gauss(x_i|0,\lambda_i) \\ P(\lambda_i) = InvGamma(\lambda_i|a,b) \end{cases} \tag{5}$$

where λ_i is the variance, a, b denote the shape and scale parameters respectively. For the noise, it is allocated with hierarchical prior-distribution shown as Equation (6),

$$\begin{cases} P(\boldsymbol{n}|\boldsymbol{\eta}) = \prod_{i=1}^{M} Gauss(n_i|0,\eta_i^{-1}) \\ P(\eta_i) = Gamma(\eta_i|c,d) \end{cases} \tag{6}$$

where η_i^{-1} denotes the variance, c, d represent the shape and scale parameters in Gamma distribution. The conditional distribution is assigned with Gaussian distribution shown as Equation (7),

$$P(\boldsymbol{y}|\boldsymbol{x},\boldsymbol{\eta}) = N(\boldsymbol{y}|\boldsymbol{H}\boldsymbol{x},\boldsymbol{D}^{-1}) \tag{7}$$

here $\boldsymbol{D} = diag(\boldsymbol{\eta})$, $\boldsymbol{\eta} = [\eta_1, \eta_2, \cdots, \eta_M]^T$.

Based on probability theorem (Tipping, 2001; Ying et al., 2023), the posterior estimation can be obtained as Equation (8),

$$\begin{aligned} P(\boldsymbol{x}|\boldsymbol{y};\boldsymbol{\lambda},\boldsymbol{\eta}) &= \frac{P(\boldsymbol{y}|\boldsymbol{x},\boldsymbol{\eta})P(\boldsymbol{x}|\boldsymbol{\lambda})}{\int P(\boldsymbol{y}|\boldsymbol{x};\boldsymbol{\eta})P(\boldsymbol{x}|\boldsymbol{\lambda})d\boldsymbol{x}} \\ &= (\frac{1}{\sqrt{2\pi}})^M |\boldsymbol{\Sigma}|^{-\frac{1}{2}} \exp\left[-\frac{1}{2}(\boldsymbol{x}-\boldsymbol{\mu})^T\boldsymbol{\Sigma}^{-1}(\boldsymbol{x}-\boldsymbol{\mu})\right] \end{aligned} \tag{8}$$

where $\boldsymbol{\mu}$ is the posterior-mean of the shadowing image, $\boldsymbol{\Sigma}$ is the covariance. Their respective expressions are stated in Equations (9, 10).

$$\boldsymbol{\mu} = \boldsymbol{\Sigma}\boldsymbol{H}^T\boldsymbol{D}\boldsymbol{y} \tag{9}$$

$$\boldsymbol{\Sigma} = [\boldsymbol{H}^T\boldsymbol{D}\boldsymbol{H} + \boldsymbol{C}]^{-1} \tag{10}$$

here $\boldsymbol{C} = diag(\boldsymbol{\lambda})$ with $\boldsymbol{\lambda} = [\lambda_1, \lambda_2, \cdots, \lambda_M]^T$.

As to $\boldsymbol{\lambda} = [\lambda_1, \lambda_2, \cdots, \lambda_N]^T$, $\boldsymbol{\eta} = [\eta_1, \eta_2, \cdots, \eta_M]^T$, they can be expressed as Equation (11),

$$\begin{cases} \lambda_i = \dfrac{2a + \theta_i - 2}{2b + \mu_i^2} \\ \eta_j = \dfrac{2c - 1}{2d + tr(\boldsymbol{\Sigma}\boldsymbol{H}_j^T\boldsymbol{H}_j) + (y_i - \boldsymbol{H}_j\boldsymbol{\mu})^2} \end{cases} \tag{11}$$

where $\theta_i = 1 - \lambda_i \Sigma_{ii}$, in which Σ_{ii} stands for the *i-th* diagonal element in $\boldsymbol{\Sigma}$. μ_i denotes the *i-th* number in $\boldsymbol{\mu}$. $\boldsymbol{H}_j$ is the *j-th* row of the weighting matrix $\boldsymbol{H}$. After the shadowing image is obtained, we can estimate the patient's location by finding the position where the maximum pixel-value locates. The localization algorithm is summarized in Algorithm 1.

Input: RSS change $\boldsymbol{y}$ from the selected links; the measurement matrix $\boldsymbol{H}$; shape and scale parameters a, b, c, d; the number of maximum iteration *max_Iter*.
Output: Reconstructed result of the shadowing image $\hat{\boldsymbol{x}}$

Initialization: $\boldsymbol{\mu} = \mathbf{0}$, $\boldsymbol{\Sigma} = \boldsymbol{I}$.
while *iter_num is less than max_Iter* **do**
  Update $\boldsymbol{\mu}$, $\boldsymbol{\Sigma}$ following Equations (9, 10).
  Update λ_i, η_j following Equation (11).
  iter_num $\Leftarrow$ *iter_num*+1.
end
Implement $\hat{\boldsymbol{x}} \Leftarrow \boldsymbol{\mu}$.
Transform image vector $\hat{\boldsymbol{x}}$ to 2-Dimensional matrix format.
Locate the target by searching for the pixel with maximum pixel-value.

Algorithm 1. Localisation algorithm

3 Experiment and result

3.1 Experiment setup

The localization experiment was carried out in an indoor 7.2 m * 7.5 m area (shown as Figure 2) with 24 nodes to constitute a wireless network. The RF nodes communicate following the ZigBee protocol with 2.4 GHz frequency-band. Every node has its node-identifier, which is used as the guidance of sequential transmission. At any instant, only one node transmit. Outside the wireless network, a special RF-node exists serving as the base-station. The base-station uploads the packet to the computer. The application program on the computer extracts the RSS from the received packet. In the experiment, the computer equips with Intel 2.4 GHz CPU and 4 GB RAM. In engineering practice, the localization algorithm can be run on the embedded system with low-cost.

3.2 Localization result

To evaluate the localization performance, the target sequentially stands at 31 different positions shown as Figure 2.

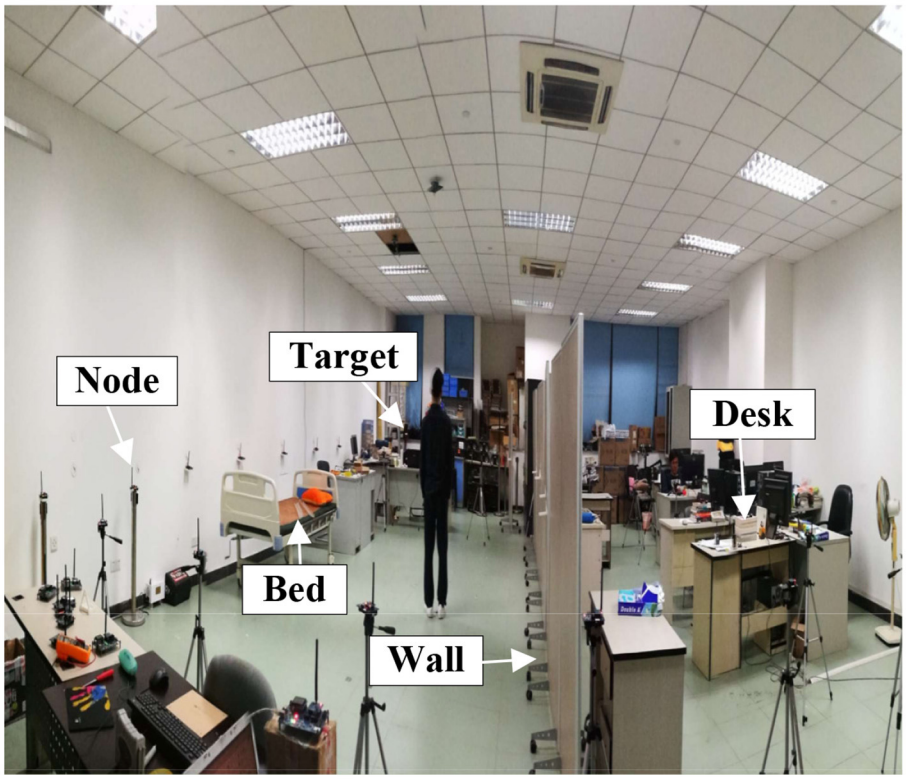

FIGURE 2
Experiment scenario. Lots of furniture are included in the room to constitute the environment with rich multipath propagation.

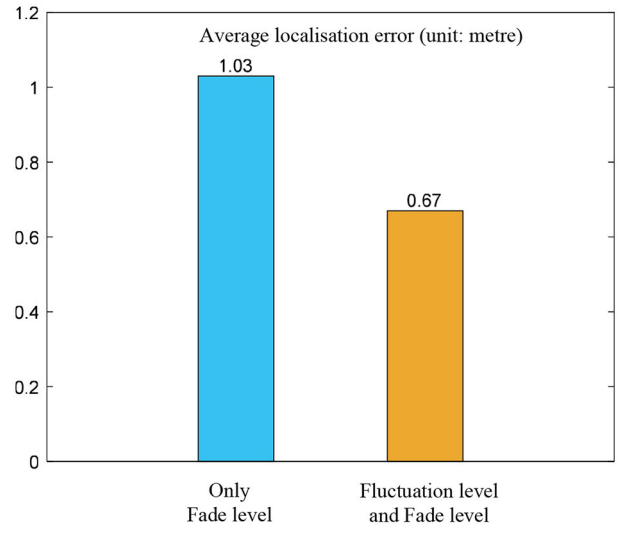

FIGURE 3
Comparison of localization error. Cyan represents the localization error only using fade level. Saffron yellow denotes the result when using both fluctuation level and fade level.

For each position, all the packets are uploaded to the computer and the RSS are extracted. Then, two different RSS selection strategies (i.e., only fade-level v.s combining fluctuation-level and fade-level) are adopted to select the informative RSS. The selected RSS measurements by two strategies are respectively used for the computation of target's position following the procedure in Algorithm 1.

To quantitatively examine the localization performance, the localization error is used which is defined as Equation (12),

$$e_{loc} = \|\hat{\boldsymbol{P}} - \boldsymbol{P}_{true}\|_{\ell_2} \tag{12}$$

where e_{loc} is the localization error, $\hat{\boldsymbol{P}}$ and $\boldsymbol{P}_{true}$ represent the estimated position and the true position respectively.

At each position, the localization error is computed following Equation (12). For being statistically effective, we compute the average localization error of all the positions as the metric for comparison. The average localization errors for two comparative strategies in selecting informative RSS (only fade-level vs. combining fluctuation-level and fade-level) are presented in Figure 3.

Obviously, the results in Figure 3 show that the strategy of combining fluctuation-level and fade-level can achieve lower localization error than that when just using fade-level.

4 Conclusion and discussion

For supervision of the patient to take home-based neuro-rehabilitation, this article explores the wireless device-free indoor localization technique to judge whether the patient is near the position of the rehabilitation-equipment. To reduce the localization error, this research proposes a new criterion (fluctuation-level) to combine with fade-level for the selection of informative RSS. Sparse Bayesian learning is used to reconstruct the shadowing image and estimate the position of the patient. Experimental results show that combining fluctuation-level and fade-level can achieve lower localization error than just using fade-level.

As to the mechanism, fluctuation-level shows the fluctuation property of the RSS measurements, this property is not reflected in fade-level. The combination of both can further filter the poor RSS that are ignored by using only fade-level. Future work will obtain the moving trajectory of the patient and build a rational formula from the amount of movement to the rehabilitation-efficacy, which is quite beneficial for neuro-rehabilitation evaluation.

Data availability statement

The raw data supporting the conclusions of this article will be made available by the authors, without undue reservation.

Ethics statement

The studies involving humans were approved by Ethics Committee of Shanghai University of Medicine & Health Sciences. The studies were conducted in accordance with the local legislation and institutional requirements. The participants provided their written informed consent to participate in this study.

Author contributions

ZW: Conceptualization, Formal analysis, Methodology, Software, Writing – original draft. XL: Writing – review & editing. GW: Writing – review & editing.

Funding

The author(s) declare that financial support was received for the research, authorship, and/or publication of this article. This research was funded in part by the project "Design and System Implementation of drug-AI generation algorithm" (hxxm-23-04-015), in part by Shanghai Municipal Science and Technology Plan Project (22010502400).

Conflict of interest

The authors declare that the research was conducted in the absence of any commercial or financial relationships that could be construed as a potential conflict of interest.

Publisher's note

All claims expressed in this article are solely those of the authors and do not necessarily represent those of their affiliated organizations, or those of the publisher,

the editors and the reviewers. Any product that may be evaluated in this article, or claim that may be made by its manufacturer, is not guaranteed or endorsed by the publisher.

References

Abdullah, O. A., Al-Hraishawi, H., and Chatzinotas, S. (2023). "Deep learning-based device-free localization in wireless sensor networks," in *2023 IEEE Wireless Communications and Networking Conference (WCNC)* (Glasgow: IEEE), 1–6. doi: 10.1109/WCNC55385.2023.10118744

Cao, Z., Wang, Z., Fei, H., Guo, X., and Wang, G. (2020). Generative model based attenuation image recovery for device-free localization with radio tomographic imaging. *Pervasive Mob. Comput.* 66:101205. doi: 10.1016/j.pmcj.2020.101205

Hu, Y., Chen, G., Li, Z., and Knoll, A. (2023). Robot policy improvement with natural evolution strategies for stable nonlinear dynamical system. *IEEE Trans. Cybern.* 53, 4002–4014. doi: 10.1109/TCYB.2022.3192049

Kaltiokallio, O., Bocca, M., and Patwari, N. (2013). A fade level-based spatial model for radio tomographic imaging. *IEEE Trans. Mob. Comput.* 13, 1159–1172. doi: 10.1109/TMC.2013.158

Khan, M. A., Khan, M. A., Driss, M., Boulila, W., and Ahmad, J. (2021). "Evolution of target localization in wireless sensor network (WSN): a review," in *2021 International Congress of Advanced Technology and Engineering (ICOTEN)* (Taiz: IEEE), 1–8. doi: 10.1109/ICOTEN52080.2021.9493510

Kim, J., and Jun, H. (2008). Vision-based location positioning using augmented reality for indoor navigation. *IEEE Trans. Consum. Electron* 54, 954–962. doi: 10.1109/TCE.2008.4637573

Maresca, G., Maggio, M. G., De Luca, R., Manuli, A., Tonin, A., Pignolo, L., et al. (2020). Tele-neuro-rehabilitation in Italy: state of the art and future perspectives. *Front. Neurol.* 11:563375. doi: 10.3389/fneur.2020.563375

Mela, L., Virrankoski, R., Korkeakoulu, S., and Jäntti, R. (2023). *Radio Tomographic Imaging with Drones*. Espoo: Aalto University, p. 1–68.

Ngamakeur, K., Yongchareon, S., Yu, J., and Islam, S. (2022). Passive infrared sensor dataset and deep learning models for device-free indoor localization and tracking. *Pervasive Mob. Comput.* 88:101721. doi: 10.1016/j.pmcj.2022.101721

Tipping, M. E. (2001). Sparse bayesian learning and the relevance vector machine. *J. Mach. Learn. Res.* 1, 211–244. doi: 10.1162/15324430152748236

Wilson (2012). A fade-level skew-laplace signal strength model for device-free localization with wireless networks. *IEEE Trans. Mob. Comput.* 11, 947–958. doi: 10.1109/TMC.2011.102

Wilson, J., and Patwari, N. (2010). Radio tomographic imaging with wireless networks. *IEEE Trans. Mob. Comput.* 9, 621–632. doi: 10.1109/TMC.2009.174

Ying, H., Wang, X., Liu, Y., Ding, W., and Knoll, A. (2023). PI-ELM: reinforcement learning-based adaptable policy improvement for dynamical system. *Inf. Sci.* 650:119700. doi: 10.1016/j.ins.2023.119700

Yoon, J.-W., and Park, T. (2016). Maximizing localization accuracy via self-configurable ultrasonic sensor grouping using genetic approach. *IEEE Trans. Instrum. Meas.* 65, 1518–1529. doi: 10.1109/TIM.2016.2534319

Zhang, L., Li, Z., Hu, Y., Smith, C., Farewik, E. M. G., Wang, R., et al. (2020). Ankle joint torque estimation using an emg-driven neuromusculoskeletal model and an artificial neural network model. *IEEE Trans. Autom. Sci. Eng.* 18, 564–573. doi: 10.1109/TASE.2020.3033664

Zhen, W., Hang, S., Xuemei, G., and Guoli, W. (2018). "Radio tomographic imaging with feedback-based sparse bayesian learning," in *2018 Eighth International Conference on Information Science and Technology (ICIST)* (Cordoba: IEEE), 50–56. doi: 10.1109/ICIST.2018.8426185

Zhen, W., Le, Q., Xuemei, G., and Guoli, W. (2019a). Dual-radio tomographic imaging with shadowing-measurement awareness. *IEEE Trans. Instrum. Meas.* 69, 4453–4464. doi: 10.1109/TIM.2019.2942171

Zhen, W., Xuemei, G., and Guoli, W. (2019b). Exploring the Laplace prior in radio tomographic imaging with sparse Bayesian learning towards the robustness to multipath fading. *Sensors* 19:5126. doi: 10.3390/s19235126

frontiers | Frontiers in Neuroscience

TYPE Opinion
PUBLISHED 29 February 2024
DOI 10.3389/fnins.2024.1364214

OPEN ACCESS

EDITED BY
Ruoli Wang,
Royal Institute of Technology, Sweden

REVIEWED BY
Pavel Lindberg,
INSERM U1266 Institut de Psychiatrie et Neurosciences de Paris, France

*CORRESPONDENCE
Ping Zhou
✉ dr.ping.zhou@outlook.com

RECEIVED 01 January 2024
ACCEPTED 14 February 2024
PUBLISHED 29 February 2024

CITATION
Lu Z, Zhang Y, Li S and Zhou P (2024) Botulinum toxin treatment may improve myoelectric pattern recognition in robot-assisted stroke rehabilitation. *Front. Neurosci.* 18:1364214. doi: 10.3389/fnins.2024.1364214

Botulinum toxin treatment may improve myoelectric pattern recognition in robot-assisted stroke rehabilitation

Zhiyuan Lu[1], Yingchun Zhang[2], Sheng Li[3] and Ping Zhou[1]*

[1]School of Rehabilitation Science and Engineering, University of Health and Rehabilitation Sciences, Qingdao, China, [2]Department of Biomedical Engineering, Desai Sethi Urology Institute, Miami Project to Cure Paralysis, University of Miami, Coral Gables, FL, United States, [3]Department of Physical Medicine and Rehabilitation, University of Texas Health Science Center at Houston, Houston, TX, United States

KEYWORDS

botulinum toxin, electromyography, myoelectric pattern recognition, robot-assisted rehabilitation, stroke

1 Introduction

Robot-assisted therapy is an effective treatment option for improving motor function in patients with neurological injury such as stroke, spinal cord injury, and cerebral palsy. Robot-assisted training facilitates improvements in motor performance necessary for completing activities of daily living. Active robotic training that takes the user's voluntary effort (or intent) into account can achieve better outcomes compared to passive training (Hu et al., 2009). Robots for active training are often driven by motion intents extracted from surface electromyography (EMG) signals. Compared with conventional proportional (Hu et al., 2009) or on-off (Hu et al., 2013) control strategies, myoelectric pattern recognition (Lu et al., 2017b) has the advantage of simultaneously controlling multiple degrees of freedom, an essential feature for increasing control of dexterity.

Unfortunately, despite the wide application of myoelectric pattern recognition in prosthesis control in amputees, relatively few have used it in patients with neurological injury, possibly because of the challenges associated with interference from spasticity. Spasticity and other types of muscle "overactivity" including spasms, clonus, and repetitive involuntary (spontaneous) motor unit activity associated with neurological injuries remain obstacles to robot-assisted therapy. For example, due to finger flexor spasticity and its associated involuntary activation, stroke survivors often flex their fingers during intended finger extension attempts (Kamper and Rymer, 2001). Among various treatment options, botulinum toxin therapy is often used and found to be effective at reducing spasticity. Although the relation between botulinum toxin treatment and motor function recovery is not clearly established (Ghasemi et al., 2013; Levy et al., 2019; Li et al., 2021), botulinum toxin therapy has demonstrated to be able to adequately suppress finger flexor spasticity and facilitate hand function in a subgroup of stroke survivors (Lee et al., 2018). Furthermore, the effectiveness of combining robot-assisted therapy and botulinum toxin treatment on motor function recovery has been reported (Gandolfi et al., 2019; Hung et al., 2021).

In the following sections, we discuss some of the confounding effects of spasticity (involuntary activity) and potential benefits of botulinum toxin treatment for facilitating myoelectric pattern recognition robot-assisted stroke rehabilitation.

2 Botulinum toxin treatment may improve voluntary muscle onset detection compromised by involuntary motor unit activity

After a stroke, involuntary motor unit activity is often observed at rest, particularly after a contraction, and may be interspersed with voluntary activity. It is technically challenging to selectively remove or reduce involuntary spikes using conventional signal processing methods because both involuntary and voluntary spikes have similar temporal and spatial characteristics. One common strategy for detection of voluntary muscle activity onset is based on amplitude measurements such as the root mean square or mean absolute value. A data instant with amplitude greater than a preset threshold is considered as the onset of muscle activity (Lu et al., 2017a,b). However, a resting data segment contaminated with involuntary discharges can be mistaken as active EMG and falsely trigger the robot. Although the chance of false triggering can be reduced by increasing the preset threshold, it may increase the rejection rate of voluntary motions, especially when there is severe muscle weakness.

Based on the observation that involuntary spikes sometimes have relatively stable firing rates and amplitude patterns (likely from the same motor units), several signal processing approaches have been proposed to overcome their influence on muscle onset detection (Zhang and Zhou, 2012; Liu et al., 2014a,b). These methods have not been tested in practical implementation of myoelectric control, due to some limitations. For example, sample entropy was reported to be able to detect muscle onset even if there are involuntary discharges (Zhang and Zhou, 2012). However, it is still unclear how to determine the global tolerance for the calculation of sample entropy in the case of real-time control. Therefore, muscle onset detection strategies applied in robot-assisted therapy are generally vulnerable to involuntary motor unit discharges, especially in patients with muscle weakness. Related to muscle onset detection, myoelectric pattern recognition is designed to extract motion intents from data segments that contain voluntary EMG signals. It is possible that involuntary motor unit discharges (either at rest or after the execution of a motion) are misclassified as voluntary motion intents. One strategy is to include the rest condition as a pattern in the candidate patterns, which are then recognized by the pattern recognition algorithm (Geng et al., 2013). Such a strategy can also be interfered because time domain (e.g., root mean square value) and frequency domain (e.g., mean and median power frequencies) features are sensitive to involuntary discharges.

Given the above, botulinum toxin treatment is expected to improve the performance of muscle onset detection due to its effectiveness in reducing involuntary muscle activity. Reliable muscle onset detection is essential for implementing myoelectric control.

3 Botulinum toxin treatment may improve classification performance

The myoelectric pattern recognition approach assumes that surface EMG features are consistent for a given muscle activation state associated with a particular task (motion intent) and different from one task to another. Surface EMG signals generated by the same motion intent in the presence or absence of spasticity may differ (i.e., increased time-variability or decreased stability of the EMG pattern). As a result, spasticity can degrade the performance of myoelectric pattern recognition. Our previous study suggests that EMG patterns extracted from post-stroke subjects are time-variant, and such time-variation compromises online myoelectric pattern recognition accuracy, whereas offline performance is less sensitive (Lu et al., 2019). Recognition accuracy was found to be less at low compared to moderate contraction strengths (Kopke et al., 2020), probably because the proportion of EMG power from involuntary discharges was higher at a low contraction strength. It is noteworthy that real-time myoelectric pattern recognition relies on EMG signals at the beginning of a motion intent (usually within 300 ms). During this period, the contraction level is relatively low and thus the performance of the muscle-machine interface is more likely to be affected by spasticity. This is consistent with our observation that the accuracy of real-time robot control (i.e., classification based on motion onset) was lower than the accuracy of offline recognition (i.e., classification throughout a motion) (Lu et al., 2019).

By reducing the muscle overactivity, botulinum toxin treatment is expected to facilitate myoelectric pattern recognition. In a study evaluating the effect of botulinum toxin injections on motor performance in chronic stroke subjects, it was found that both spasticity and muscle strength were reduced by the injections while motor performance of the weakened spastic muscle remained at similar levels before and after injections (Chen et al., 2020). Therefore, botulinum toxin treatment is promising to improve myoelectric pattern recognition performance for implementing real-time robotic control in stroke patients. It is likely that stroke patients with poor control of the robotic hand using myoelectric pattern recognition may achieve better control after botulinum toxin treatment.

4 Botulinum toxin treatment may improve range of motion

Some stroke patients have limited range of motion (ROM) on the affected side because of spasticity and contracture (Pandyan et al., 2003; Ro et al., 2020). Individual patients may have different combinations of spasticity and contracture (Lindberg et al., 2009). A longitudinal follow-up study of stroke patients using biomechanical measurements has suggested severe spasticity preceding contracture formation (Plantin et al., 2019). Attempts to stretch a patient's joint beyond the passive ROM may be resisted and painful. As a result, the robot ROM during therapy is usually set within the patient's passive ROM, although training with a larger ROM is potentially more beneficial. Depending on robot design, the ROM setting in a training task can be either preset (Lu et al., 2017b) or determined by the patient and the amount of assistance (Song et al., 2013). A patient may reach a larger ROM in both designs than through voluntary efforts (i.e., active ROM). Limb movements are primarily driven by the patient's voluntary muscle contraction within the active ROM (Feldman and Levin, 2016), whereas assistance becomes necessary or dominant beyond the active ROM. Botulinum toxin

treatment (on its own or with other treatments) may increase both passive and active ROM (Marciniak et al., 2017; Lee et al., 2018; Picelli et al., 2019; Santamato, 2022; Trompetto et al., 2023), due in part to suppression of spasticity and associated involuntary activation of spastic muscles (Ro et al., 2020; Lindsay et al., 2021). It is possible to achieve the full ROM or at least enlarge the ROM of the robot in both passive and active training tasks. Therefore, botulinum toxin treatment may help release muscle from the restrictions of spasticity and contractures. This release should allow for more effective robotic training driven by myoelectric pattern recognition, leading to better recovery outcomes in stroke patients.

5 Summary

By reducing spasticity (overactivity), botulinum toxin treatment is expected to improve muscle onset detection for myoelectric control, as well as the performance of myoelectric pattern recognition for implementing real-time robotic control in stroke patients. Increased range of motion through botulinum toxin treatment may similarly create better conditions for enhanced myoelectric pattern recognition. These potential benefits indicate that combined botulinum toxin and myoelectric pattern recognition robotic training may be a promising stroke rehabilitation therapy.

Author contributions

ZL: Conceptualization, Writing—original draft, Writing—review & editing, Funding acquisition. YZ: Conceptualization, Writing—review & editing. SL: Conceptualization, Writing—review & editing. PZ: Conceptualization, Funding acquisition, Writing—original draft, Writing—review & editing.

Funding

The author(s) declare financial support was received for the research, authorship, and/or publication of this article. This research was funded by the National Natural Science Foundation of China (Grant No. 82102179), the Taishan Scholar Project of Shandong Province, and the Shandong Provincial Natural Science Foundation (Grant No. ZR2021QH267).

Conflict of interest

The authors declare that the research was conducted in the absence of any commercial or financial relationships that could be construed as a potential conflict of interest.

The author(s) declared that they were an editorial board member of Frontiers, at the time of submission. This had no impact on the peer review process and the final decision.

Publisher's note

References

Chen, Y. T., Zhang, C., Liu, Y., Magat, E., Verduzco-Gutierrez, M., Francisco, G. E., et al. (2020). The effects of botulinum toxin injections on spasticity and motor performance in chronic stroke with spastic hemiplegia. *Toxins* 12:492. doi: 10.3390/toxins12080492

Feldman, A. G., and Levin, M. F. (2016). Spatial control of reflexes, posture and movement in normal conditions and after neurological lesions. *J. Hum. Kinet.* 52, 21–34. doi: 10.1515/hukin-2015-0191

Gandolfi, M., Valè, N., Dimitrova, E. K., Mazzoleni, S., Battini, E., Filippetti, M., et al. (2019). Effectiveness of robot-assisted upper limb training on spasticity, function and muscle activity in chronic stroke patients treated with botulinum toxin: a randomized single-blinded controlled trial. *Front. Neurol.* 10:41. doi: 10.3389/fneur.2019.00041

Geng, Y., Zhang, L., Tang, D., Zhang, X., and Li, G. (2013). "Pattern recognition based forearm motion classification for patients with chronic hemiparesis," in *Proceedings of the 35th Annual International Conference of the IEEE Engineering in Medicine and Biology Society (EMBC)* (Osaka), 5918–5921.

Ghasemi, M., Salari, M., Khorvash, F., and Shaygannejad, V. A. (2013). Literature review on the efficacy and safety of botulinum toxin: an injection in post-stroke spasticity. *Int. J. Prev. Med.* 4, S147–158.

Hu, X. L., Tong, K. Y., Song, R., Zheng, X. J., and Leung, W. W. F. A. (2009). Comparison between electromyography-driven robot and passive motion device on wrist rehabilitation for chronic stroke. *Neurorehabil. Neural Repair* 23, 837–846. doi: 10.1177/1545968309338191

Hu, X. L., Tong, K. Y., Wei, X. J., Rong, W., Susanto, E. A., Ho, S. K., et al. (2013). the effects of post-stroke upper-limb training with an electromyography (EMG)-driven hand robot. *J. Electromyogr. Kinesiol.* 23, 1065–1074. doi: 10.1016/j.jelekin.2013.07.007

Hung, J.-W., Chen, Y.-W., Chen, Y.-J., Pong, Y.-P., Wu, W.-C., Chang, K.C., eet al. (2021). the effects of distributed vs. condensed schedule for robot-assisted training with botulinum toxin A injection for spastic upper limbs in chronic post-stroke subjects. *Toxins* 13:539. doi: 10.3390/toxins13080539

Kamper, D. G., and Rymer, W. Z. (2001). Impairment of voluntary control of finger motion following stroke: role of inappropriate muscle coactivation. *Muscle Nerve* 24, 673–681. doi: 10.1002/mus.1054

Kopke, J. V., Ellis, M. D., and Hargrove, L. J. (2020). Determining user intent of partly dynamic shoulder tasks in individuals with chronic stroke using pattern recognition. *IEEE Transact. Neural Syst. Rehabil. Eng.* 28, 350–358. doi: 10.1109/TNSRE.2019.2955029

Lee, J. M., Gracies, J. M., Park, S. B., Lee, K. H., Lee, J. Y., Shin, J. H., et al. (2018). Botulinum toxin injections and electrical stimulation for spastic paresis improve active hand function following stroke. *Toxins* 10:426. doi: 10.3390/toxins10110426

Levy, J., Molteni, F., Cannaviello, G., Lansaman, T., Roche, N., Bensmail, D., et al. (2019). Does botulinum toxin treatment improve upper limb active function? *Ann. Phys. Rehabil. Med.* 62, 234–240. doi: 10.1016/j.rehab.2018.05.1320

Li, S., Francisco, G. E., and Rymer, W. Z. A. (2021). New definition of poststroke spasticity and the interference of spasticity with motor recovery from acute to chronic stages. *Neurorehabil. Neural Repair* 35, 601–610. doi: 10.1177/15459683211011214

Lindberg, P. G., Gäverth, J., Fagergren, A., Fransson, P., Forssberg, H., Borg, J., et al. (2009). Cortical activity in relation to velocity dependent movement resistance in the flexor muscles of the hand after stroke. *Neurorehabil. Neural Repair* 23, 800–810. doi: 10.1177/1545968309332735

Lindsay, C., Ispoglou, S., Helliwell, B., Hicklin, D., Sturman, S., Pandyan, A., et al. (2021). Can the early use of botulinum toxin in post stroke spasticity reduce

contracture development? A randomised controlled trial. *Clin. Rehabil.* 35, 399–409. doi: 10.1177/0269215520963855

Liu, J., Ying, D., Zev Rymer, W., and Zhou, P. (2014b). Subspace based adaptive denoising of surface EMG from neurological injury patients. *J. Neural Eng.* 11:056025. doi: 10.1088/1741-2560/11/5/056025

Liu, J., Ying, D., and Zhou, P. (2014a). Wiener filtering of surface EMG with a priori SNR estimation toward myoelectric control for neurological injury patients. *Med. Eng. Phys.* 36, 1711–1715. doi: 10.1016/j.medengphy.2014.09.008

Lu, Z., Chen, X., Zhang, X., Tong, K. Y., and Zhou, P. (2017a). Real-time control of an exoskeleton hand robot with myoelectric pattern recognition. *Int. J. Neural Syst.* 27:1750009. doi: 10.1142/S0129065717500095

Lu, Z., Tong, K., Shin, H., Li, S., and Zhou, P. (2017b). Advanced myoelectric control for robotic hand assisted training: outcome from a stroke patient. *Front. Neurol.* 8:107. doi: 10.3389/fneur.2017.00107

Lu, Z., Tong, K. Y., Zhang, X., Li, S., and Zhou, P. (2019). Myoelectric pattern recognition for controlling a robotic hand: a feasibility study in stroke. *IEEE Transact. Biomed. Eng.* 66, 365–372. doi: 10.1109/TBME.2018.2840848

Marciniak, C., McAllister, P., Walker, H., Brashear, A., Edgley, S., Deltombe, T., et al. (2017). Efficacy and safety of abobotulinumtoxina (dysport) for the treatment of hemiparesis in adults with upper limb spasticity previously treated with botulinum toxin: subanalysis from a phase 3 randomized controlled trial. *PM R* 9, 1181–1190. doi: 10.1016/j.pmrj.2017.06.007

Pandyan, A. D., Cameron, M., Powell, J., Stott, D. J., and Granat, M. H. (2003). Contractures in the post-stroke wrist: a pilot study of its time course of development and its association with upper limb recovery. *Clin. Rehabil.* 17, 88–95. doi: 10.1191/0269215503cr587oa

Picelli, A., Santamato, A., Chemello, E., Cinone, N., Cisari, C., Gandolfi, M., et al. (2019). Adjuvant treatments associated with botulinum toxin injection for managing spasticity: an overview of the literature. *Ann. Phys. Rehabil. Med.* 62, 291–296. doi: 10.1016/j.rehab.2018.08.004

Plantin, J., Pennati, G. V., Roca, P., Baron, J. C., Laurencikas, E., Weber, K., et al. (2019). Quantitative assessment of hand spasticity after stroke: imaging correlates and impact on motor recovery. *Front. Neurol.* 10:836. doi: 10.3389/fneur.2019.00836

Ro, T., Ota, T., Saito, T., and Oikawa, O. (2020). Spasticity and range of motion over time in stroke patients who received multiple-dose botulinum toxin therapy. *J. Stroke Cerebrovasc. Dis.* 29:104481. doi: 10.1016/j.jstrokecerebrovasdis.2019.104481

Santamato, A. (2022). High doses of botulinum toxin type A for the treatment of post-stroke spasticity: rationale for a real benefit for the patients. *Toxins* 14:332. doi: 10.3390/toxins14050332

Song, R., Tong, K. Y., Hu, X., and Zhou, W. (2013). Myoelectrically controlled wrist robot for stroke rehabilitation. *J. Neuroeng. Rehabil.* 10:52. doi: 10.1186/1743-0003-10-52

Trompetto, C., Marinelli, L., Mori, L., Bragazzi, N., Maggi, G., Cotellessa, F., et al. (2023). Increasing the passive range of joint motion in stroke patients using botulinum toxin: the role of pain relief. *Toxins* 15:335. doi: 10.3390/toxins15050335

Zhang, X., and Zhou, P. (2012). Sample entropy analysis of surface EMG for improved muscle activity onset detection against spurious background spikes. *J. Electromyogr. Kinesiol.* 22, 901–907. doi: 10.1016/j.jelekin.2012.06.005

frontiers | Frontiers in Neuroscience

TYPE Original Research
PUBLISHED 04 April 2024
DOI 10.3389/fnins.2024.1388742

OPEN ACCESS

EDITED BY
Yingbai Hu,
The Chinese University of Hong Kong, China

REVIEWED BY
Yinlong Liu,
Technical University of Munich, Germany
Huiqun Wu,
Nantong University, China
Jiaqi Hu,
Rice University, United States

*CORRESPONDENCE
Xueli Liu
✉ liuxueli@fudan.edu.cn
Xinrong Chen
✉ chenxinrong@fudan.edu.cn

†These authors have contributed equally to this work

RECEIVED 20 February 2024
ACCEPTED 15 March 2024
PUBLISHED 04 April 2024

CITATION
Dai X, Zhang Z, Zhao S, Liu X and Chen X (2024) Full-body pose reconstruction and correction in virtual reality for rehabilitation training. *Front. Neurosci.* 18:1388742. doi: 10.3389/fnins.2024.1388742

Full-body pose reconstruction and correction in virtual reality for rehabilitation training

Xiaokun Dai[1,2†], Zhen Zhang[3†], Shuting Zhao[1,2], Xueli Liu[4*] and Xinrong Chen[1,2*]

[1]Academy for Engineering & Technology, Fudan Universiry, Shanghai, China, [2]Shanghai Key Laboratory of Medical Image Computing and Computer Assisted Intervention, Shanghai, China, [3]Baoshan Branch of Ren Ji Hospital, Shanghai Jiao Tong University School of Medicine, Shanghai, China, [4]EYE & ENT Hospital of Fudan University, Shanghai, China

Existing statistical data indicates that an increasing number of people now require rehabilitation to restore compromised physical mobility. During the rehabilitation process, physical therapists evaluate and guide the movements of patients, aiding them in a more effective recovery of rehabilitation and preventing secondary injuries. However, the immutability of mobility and the expensive price of rehabilitation training hinder some patients from timely access to rehabilitation. Utilizing virtual reality for rehabilitation training might offer a potential alleviation to these issues. However, prevalent pose reconstruction algorithms in rehabilitation primarily rely on images, limiting their applicability to virtual reality. Furthermore, existing pose evaluation and correction methods in the field of rehabilitation focus on providing clinical metrics for doctors, and failed to offer patients efficient movement guidance. In this paper, a virtual reality-based rehabilitation training method is proposed. The sparse motion signals from virtual reality devices, specifically head-mounted displays hand controllers, is used to reconstruct full body poses. Subsequently, the reconstructed poses and the standard poses are fed into a natural language processing model, which contrasts the difference between the two poses and provides effective pose correction guidance in the form of natural language. Quantitative and qualitative results indicate that the proposed method can accurately reconstruct full body poses from sparse motion signals in real-time. By referencing standard poses, the model generates professional motion correction guidance text. This approach facilitates virtual reality-based rehabilitation training, reducing the cost of rehabilitation training and enhancing the efficiency of self-rehabilitation training.

KEYWORDS

rehabilitation training, virtual reality, full-body pose reconstruction, deep learning, Multilayer Perceptron (MLP)

1 Introduction

Existing statistical data indicate that an increasing number of people are now experiencing mobility impairments due to accidents, illness, or aging, thereby demanding the need for rehabilitation (Postolache et al., 2020). Rehabilitation training encompasses a series of intervention exercises aimed at aiding in the recovery of compromised motor functions. A pivotal aspect of this process involves tailored movement exercises conducted by a doctor or physical therapist. Early and intensive rehabilitation training proves more efficacious in facilitating the recovery of patients' motor abilities (Postolache et al., 2020). However, the demand for patients to attend hospitals or rehabilitation centers

for rehabilitation training presents additional challenges for those already grappling with mobility difficulties. Furthermore, the high cost associated with rehabilitation training becomes a financial impediment for certain patients. In this context, the emergence of virtual reality-based rehabilitation methods becomes apparent. These methods allow patients to engage in a more convenient and economical rehabilitation option through personalized virtual reality devices. By offering real-time user pose reconstruction and employing immersive interactive methods, virtual reality technology can provide patients with increased sensory stimulation and a more immersive environment during rehabilitation training (Adamovich et al., 2009). Existing research has shown that compared to conventional physical therapy, virtual reality-based rehabilitation training is more effective in promoting gait recovery in patients with Parkinson's disease (Feng et al., 2019).

However, common virtual reality devices can only accurately reconstruct the poses of user's head and hands through head-mounted displays and handheld controllers. This limitation is insufficient for full body rehabilitation training. Therefore, virtual reality-based rehabilitation methods often require additional wearable body measurement sensors to capture patients' movements (Huang et al., 2018; Jiang Y. et al., 2022), such as motion sensors for the legs and waist, gait detection devices, and more. Unfortunately, for patients, this not only represents an additional expense, but wearing extra sensors may also lead to physical discomfort. Moreover, patients' unprofessional handling of these sensors can result in tracking inaccuracies and affecting the effectiveness of the rehabilitation training. Hence, the studies that leverage the most prevalent virtual reality devices, using the sparse motion signals from the head and hands to reconstruct full body poses, demonstrate an effective solution for virtual reality-based rehabilitation training methods.

In addition, regardless of the form of rehabilitation, the quality assessment and precise guidance of patients' recovery movements are crucial (Qiu et al., 2022). This directly influences the effectiveness of patient's recovery. When patients participate in rehabilitation training at hospitals or rehabilitation facilities, doctors can assist by correcting their inaccurate movements, ensuring that their movements fall within the normal range to achieve the desired rehabilitation effects. This correction helps prevent secondary injuries resulting from incorrect movements. However, in virtual reality-based rehabilitation, there is currently no universally recognized solution to reasonably evaluate the quality of patients' rehabilitation movements (Qiu et al., 2022). Furthermore, there is no method to authentically simulate a doctor's supervision to aid patients in correcting rehabilitation movements. Therefore, proposing effective methods for correcting rehabilitation movements and providing appropriate movement guidance is crucial to advancing research in virtual reality-based rehabilitation.

To address the aforementioned issues, we propose a virtual reality-based rehabilitation method. As shown in Figure 1, this method utilizes commonly available virtual reality hardware devices to reconstruct full-body poses of patients. Then, a pose correction module based on a natural language model is employed to assess patients' movements, which generates specific movement correction guidance text by referencing standard movements. Specifically, to meet the requirement of accuracy, real-time performance and smoothness in full-body poses reconstruction, a deep learning-based model is introduced, comprising a multi-scale temporal feature switch module and a stacked MLP Blocks. The multi-scale temporal feature switch module expands the model's temporal receptive field, improving the accuracy and the smoothness of full-body poses reconstruction while ensuring real-time performance and model light-weighting. Subsequently, the reconstructed poses and the reference standard poses are input into the poss correction module, which assesses the reconstructed poses and outputs the movement correction guidance text by utilizing a natural language model. Comprehensive experimental results demonstrate that the proposed method can provide more accurate full-body poses reconstruction and more intelligent movement guidance for virtual reality-based rehabilitation training.

2 Related works

2.1 Full-body pose reconstruction from sparse motion signals

In recent years, the reconstruction of full-body poses using sparse motion signals from virtual reality devices, specifically head-mounted displays and handheld controllers, has become a focal point in research within the realms of virtual reality and the metaverse. Ahuja et al. introduced a convolutional neural network to extract features from sparse motion signals and utilized a K-nearest neighbors (KNN)—based method, employing interpolation algorithms to reconstruct the full-body poses from a limited motion database (Ahuja et al., 2021). However, this method heavily relies on the motion database, exhibiting poor generalization capabilities. In subsequent studies, novel deep learning models such as variational autoencoders (Pavlakos et al., 2019), long short-term memory networks (Yu et al., 2019), and transformers (Jiang J. et al., 2022; Luo et al., 2022; Zhang X. et al., 2023) have been applied to extract motion features from sparse motion signals, significantly enhancing the accuracy of full-body poses reconstruction. In recent studies, based on Multilayer Perceptron (MLP), a diffusion model has been employed to further optimize the reconstructed motion sequences, effectively alleviating the phenomenon of joint jitter (Du et al., 2023). However, the adoption of the diffusion model has substantially increased the computational demands and inference time of the model.

2.2 Pose evaluation for healthcare application

With the development of electronic information and computing technology, studies focusing on health applications, particularly the evaluation of human body poses during rehabilitation training, has been recently explored. Martınez et al. utilized depth cameras to capture the ground-truth human rehabilitation postures and quantitatively evaluated the accuracy of commonly used pose reconstruction algorithms (Martınez, 2019) in reconstructing rehabilitation postures (Hernández et al., 2021). Kidziński et al. (2020) introduced a neural network to quantitatively evaluate clinically relevant motion parameters from

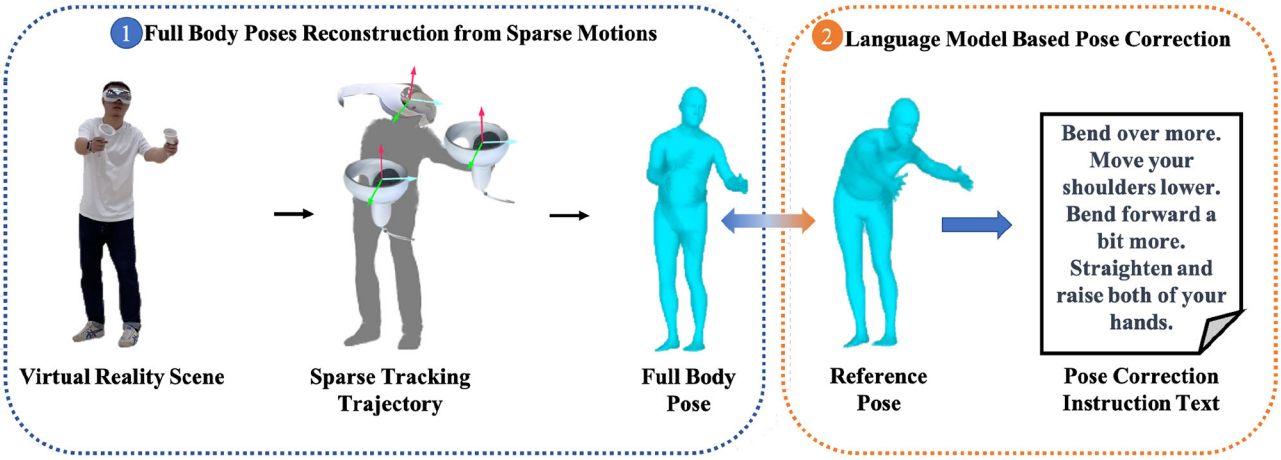

FIGURE 1
The pipeline of the proposed virtual reality-based rehabilitation training method.

patients' motion videos. Xu et al. (2022) employed multi-view videos for the evaluation of musculoskeletal patients' motion poses. Liao et al. (2020) combining the Long Short-Term Memory (LSTM), feature pyramids, and other deep learning methods, which designed the first rehabilitation posture quality evaluation method based on deep learning. Tang (2020) introduced a segmentation module to the posture evaluation network, significantly enhancing the accuracy of scores in evaluating the quality of rehabilitation postures. Bruce et al. employed graph convolutional networks to assess the severity of Alzheimer's disease in patients through motion videos (Bruce et al., 2021). However, the quantitative evaluation metrics of these methods are exclusive to proficient medical professionals for clinical evaluations, limiting their applicability for patients to comprehend the status of their rehabilitation training and make corrections.

To address the aforementioned issues, Qiu et al. (2022) devised a pose matching network, which achieves alignment and correction of poses between the trainers' pose and the standard poses, providing trainers with visualized movement guidance through Class Activation Maps (CAM). Despite having a certain foundation in research, the majority of these methods heavily rely on computer vision and are impractical for virtual reality-based rehabilitation. Moreover, there remains a dearth of intuitive and effective guidance for patients in evaluating their poses, such as the guidance provided by medical professional.

2.3 3D human poses and natural language models

In recent years, Transformer-based natural language processing models have achieved remarkable success in various fields. The following will introduce datasets that combine human poses with natural language processing models and showcase astonishing applications. The AMASS dataset (Mahmood et al., 2019) has collected motion data for numerous 3D human poses in the form of SMPL (Loper et al., 2023). Then, BABEL (Punnakkal et al., 2021) and HumanML3D (Guo et al., 2022), building on the AMASS dataset, provide free-from textual descriptions for its sequence data. These datasets focus more on describing the entire action sequences rather than the semantic information of each single-frame pose. Consequently, they are more suitable for tasks for generating action sequences (Zhang J. et al., 2023) or describing motions from videos. To address the gap in independent human pose semantic descriptions, PoseScript (Delmas et al., 2022) provides descriptions for each single-frame human poses from some subsets of the AMASS dataset. In further research, FixMyPose (Kim et al., 2021) and PoseFix (Delmas et al., 2023) can connect two different poses and generate textural information for pose correction. Unlike FixMyPose, which generates textual annotations from rendering 2D images, the PoseFix directly generates text explanations based on the 3D human pose data. This proves to be a more suitable and more potent solution for the virtual reality-based rehabilitation training.

3 Methods

3.1 Overview

Reconstructing full-body movements from sparse motion inputs is quite challenging. Sparse motion signals from the upper body cannot effectively constrain the movements of the lower body. As a result, the reconstruction of lower body poses may inevitably exhibit anomalies such as joint jitter and floor penetration, significantly affecting the user's experience in virtual reality. In previous studies (Du et al., 2023), one-dimensional convolution with temporal awareness-based diffusion models was employed to reduce joint jitter, noticeably enhancing the quality and fluency of full-body posture reconstruction. However, the diffusion model requires multiple inference steps, leading to longer model inference times that do not meet the real-time requirements of virtual reality applications. Moreover, when using only its MLP backbone network, joint jitter phenomena remain unresolved.

Therefore, as shown in Figure 2, a full-body pose reconstruction network based on a multi-scale temporal switch module is proposed. The sparse motion signals are input to an MLP

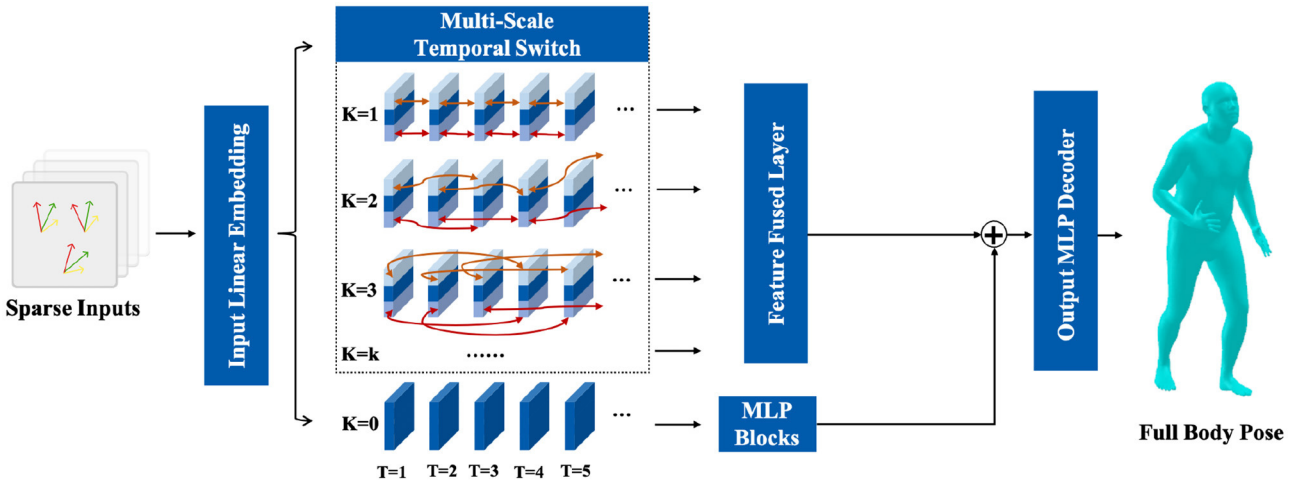

FIGURE 2
The detailed structure of proposed full-body pose reconstruct module and temporal switch module.

layer for feature embedding and then input into the multi-scale temporal switch module for aggregation of features across different time scales. Subsequently, the original features are fed into a stacked MLP module and the features aggregated at different time scales are fed into a MLP layer. Finally, the depth features from different scales are aggregated, fused with the original features, and input into an MLP layer for the reconstruction of full-body poses.

3.2 Full-body pose reconstruct module

3.2.1 Data preparation

To reconstruct the full body's poses, sparse motion signals are acquired from the Inertial Measurement Unit (IMU) devices on the virtual reality headset and handheld controllers. Each signal at every position includes global positional information $p^{1\times3}$ and rotational information $\theta^{1\times3}$ about the three axes. For a more refined reconstruction outcome, predicting the human body's motion posture at time t poses from a certain time interval T before time t is aggregated and jointly fed into the network. Therefore, the full-body joint pose $\mathcal{U}_{\text{full}}^{\text{joints}}$ is obtained by applying the mapping function Φ to the set of sparse inputs $\{p_i, \theta_i\}_{1:T}$, as shown in Equation 1:

$$\mathcal{U}_{\text{full}}^{\text{joints}} = \Phi\left(\bigcup_{i=1}^{n}\{p_i, \theta_i\}_{1:T}\right) \tag{1}$$

where n represents the number of sparse inputs, h is the quantity of full-body joints, and T is the count of continuous motion frames observed from the past.

To enable the model to comprehensively learn features from sparse motion signals, the following preprocessing steps are employed. The backward finite difference method is employed to initiate the calculation of linear velocity $v^{1\times3}$, as shown in Equation 2:

$$v_t = p_t - p_{t-1} \tag{2}$$

Subsequently, the angular velocity $\Omega_t^{1\times6}$ is defined by considering the orientation matrices $\mathbf{R}$ of the sparse input (Jiang J. et al., 2022), as shown in Equation 3:

$$\Omega_t = \mathbf{R}_{t-1}^{-1}\mathbf{R}_t \tag{3}$$

These matrices are initially derived from the $\theta^{1\times3}$ representation, which are converted to the rotation matrix $\mathbf{R}^{3\times3}$ using the conversion as previous studies (Zhou et al., 2019; Jiang J. et al., 2022). Following this, the last row of $\mathbf{R}$ is disregarded to yield the 6D rotation representation $w_t^{1\times6}$.

Consequently, each input at time frame t_i comprises four vectors: p_i, v_i, Ω_i, and w_i. This input feature is structured as Equation 4:

$$x_t = \left[p_t^1, v_t^1, w_t^1, \Omega_t^1, p_t^2, v_t^2, w_t^2, \Omega_t^2, p_t^3, v_t^3, w_t^3, \Omega_t^3\right] \tag{4}$$

As a result, all independent signals x_t within the time interval T are concatenated along the temporal dimension to form the input signal $\mathbf{X}$, as shown in Equation 5:

$$\mathbf{X} = [x_1, x_2, x_3, \ldots, x_T], \mathbf{X} \in \mathbb{R}^{B\times T\times F} \tag{5}$$

where B represent the batch size, T signifies the length of the temporal sequences, and F denotes the feature dimension. Therefore, the feature dimension F of the input tensor $\mathbf{X}$ amounts to 54.

3.2.2 Multi-scale temporal switch module

In previous research (Du et al., 2023), networks equipped with one-dimensional temporal convolutions are employed to enhance the model's temporal awareness, aiming for improving reconstruction of full-body poses. Additionally, the powerful generative ability of diffusion model is utilized to further optimize the reconstructed pose sequences, significantly reducing the occurrence of joint jitter. However, despite the application of Denoising Diffusion Implicit Model (DDIM) technology (Ho et al.,

2020), the diffusion model still necessitates five repeated inference steps to obtain the final predictions, which fails to meet the real-time requirements of virtual reality-based rehabilitation training.

To address these issues, a multi-scale temporal switch module based on two-dimensional time sequences is devised. This module comprises multiple branches at different temporal scales, aiding the model in capturing subtle temporal features within the sparse motion signals.

Initially, the preprocessed sparse motion signals $\mathbf{X}$ are fed into a Linear Layer for preliminary feature embedding, as shown in Equation 6:

$$F = LinearEmbedding(X) \tag{6}$$

where the *LinearEmbedding* is a linear layer with an input dimension of 54 and an output dimension of 256. As shown in Figure 2, the module comprises K branches representing different temporal switch scale. For each time slice $T = t$ alone the temporal dimension, the feature $\mathbf{F}^t$ is partitioned into three segments along the feature dimensions, such as f_1^t, f_2^t, and f_3^t. Here, as shown in Equation 7, the f_1^t and f_3^t are the first N features and the last N features alone the feature dimension, respectively:

$$F^t = (f_1^t, f_2^t, f_3^t) \tag{7}$$

where $\mathbf{F}^t \in \mathbb{R}^{B\times 1\times F}$, $f_1^t \in \mathbb{R}^{B\times 1\times F/8}$, $f_2^t \in \mathbb{R}^{B\times 1\times 3F/4}$, and $f_3^t \in \mathbb{R}^{B\times 1\times F/8}$.

Inspired by previous study (Zheng et al., 2022), we conduct $\mathbf{K}$ forward feature exchange modules alone the temporal direction for each feature slice $\mathbf{F}^t$. In the branch where $\mathbf{K} = k$, we exchange the features f_1^t and f_3^t in the feature slice $\mathbf{F}^t$ with the corresponding features f_1^{t+k} and f_3^{t+k} in the feature slice $\mathbf{F}^{t+k}$, where $\mathbf{F}^{t+k}$ represents the feature slice at a temporal distance of k frames, as shown in Equation 8:

$$F_k^t = (f_1^{t+k}, f_2^t, f_3^{t+k}) \tag{8}$$

After the exchange of features slice for all time frames $T = t$, we concatenate all the time slices along the temporal dimension to obtain the output $\mathbf{F}_k$ of the feature exchange module $\mathbf{K} = k$ in Equation 9:

$$F_k = \{F_k^1, F_k^2, \ldots, F_k^t\} \tag{9}$$

Finally, features from different branches are input into an MLP layer for feature fusion, as shown in Equation 10:

$$F_{switched} = OutPutLinear\{F_1 \odot F_2 \odot \ldots \odot F_k\} \tag{10}$$

where $\odot$ represents the concatenate operation and $\mathbf{F}_{switched} \in \mathbb{R}^B \times T \times F$, and the *OutPutLinear* is a linear layer with an input dimension of $\mathbf{K} * F$ and an output dimension of F and the *SiLu* activative function.

The difference between previous study and ours is that our approach solely employs forward switch along the temporal direction, refraining from bidirectional switch. Our rationale lies in the fact that bidirectional switch necessitates a greater number of feature switch operations for a limited enhancement. Given the constrained computational capacity of the virtual reality devices and the stringent demands for real-time processing, we opt for unidirectional propagation.

3.2.3 MLP based blocks

In the recent research (Du et al., 2023; Guo et al., 2023), the potential of MLP-based networks in full-body poses reconstruction tasks has been demonstrated. The MLP-based networks can effectively learn complex non-linear mapping relationships of input features, facilitating efficient feature learning and data representation (Guo et al., 2023). Additionally, the MLP networks possess the advantage of lightweight design, meeting the real-time requirements of our tasks. Considering the demands for both real-time processing and accuracy of the reconstructed poses, our model only employs several commonly used and effective modules in the field of deep learning, including fully connected layers, Silu activation function, one-dimensional convolution alone the temporal dimension with a size of 1, and the layer normalization. Specifically, the one-dimensional convolution layer is utilized to aggregate the temporal features from the entire pose sequence, while the other modules operate on the feature dimension to help the network alleviate gradient vanishing and overfitting phenomena. The structure of the MLP-based blocks is shown in Figure 3. To better extract features from sparse motion signals, the MLP-based blocks are stacked in M layers as in the study by Du et al. (2023).

As the proposed temporal switch module affects the spatial information of the original motion signals, the original feature f is preserved and fed into the aforementioned MLP-based Blocks for feature extraction in Equation 11:

$$F_0 = MLPBlocks(f) \tag{11}$$

where $\mathbf{F}_0 \in \mathbb{R}^B \times T \times F$.

Finally, the output feature $\mathbf{F}_0$ and the temporal switched feature $\mathbf{F}_{switched}$ are aggregated and input into the output MLP Layer to reconstruct the poses of 22 joints (excluding the joints of the palms) in the SMLP human pose model, achieving the reconstruction from sparse motion signals to full body poses, as shown in Equation 12:

$$F_{output} = Linear(F_0 \oplus F_{switched}) \tag{12}$$

where the $\oplus$ represents tensor addition operation and $\mathbf{F}_{output} \in \mathbb{R}^B \times T \times 132$.

3.3 NLP-based pose correction module

In this section, the state-of-the-art pose evaluation method, PoseFix (Delmas et al., 2023), is employed to compare the reconstructed full body poses and the standard poses, and generate professional motion correction guidance text. We will briefly elucidate how the reconstructed pose $Pose_A$ of the patient is matched to the target pose $Pose_B$ and modeled as correction guidance text. As shown in Figure 4, the rotation angles of the root joint of $Pose_A$ are aligned with the corresponding rotation angles of $Pose_B$. Subsequently, a Transformer-based auto encoder (Kingma and Welling, 2013) is utilized to extract independent 32-dimensional embedded features from $Pose_A$ and $Pose_B$. It is noteworthy that the $Pose_A$ and $Pose_B$ share the weights of the auto encoder. Next, the TIRG network (Vo et al., 2019), a widely applied module for compositional learning, is used to merge

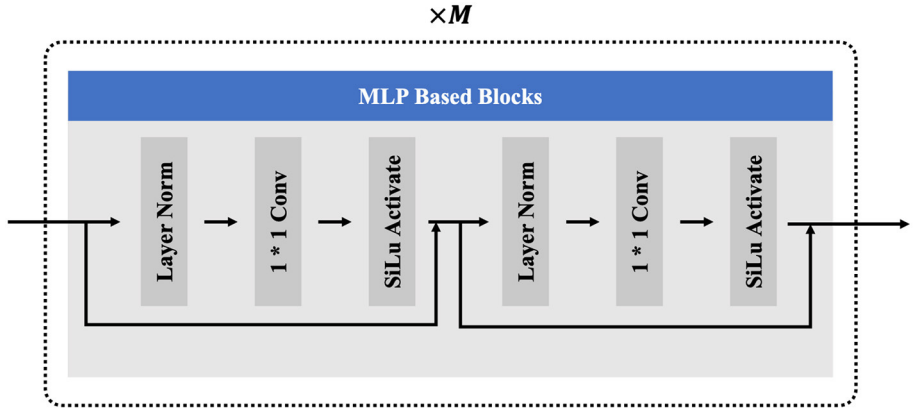

FIGURE 3
The components of the MLP based blocks.

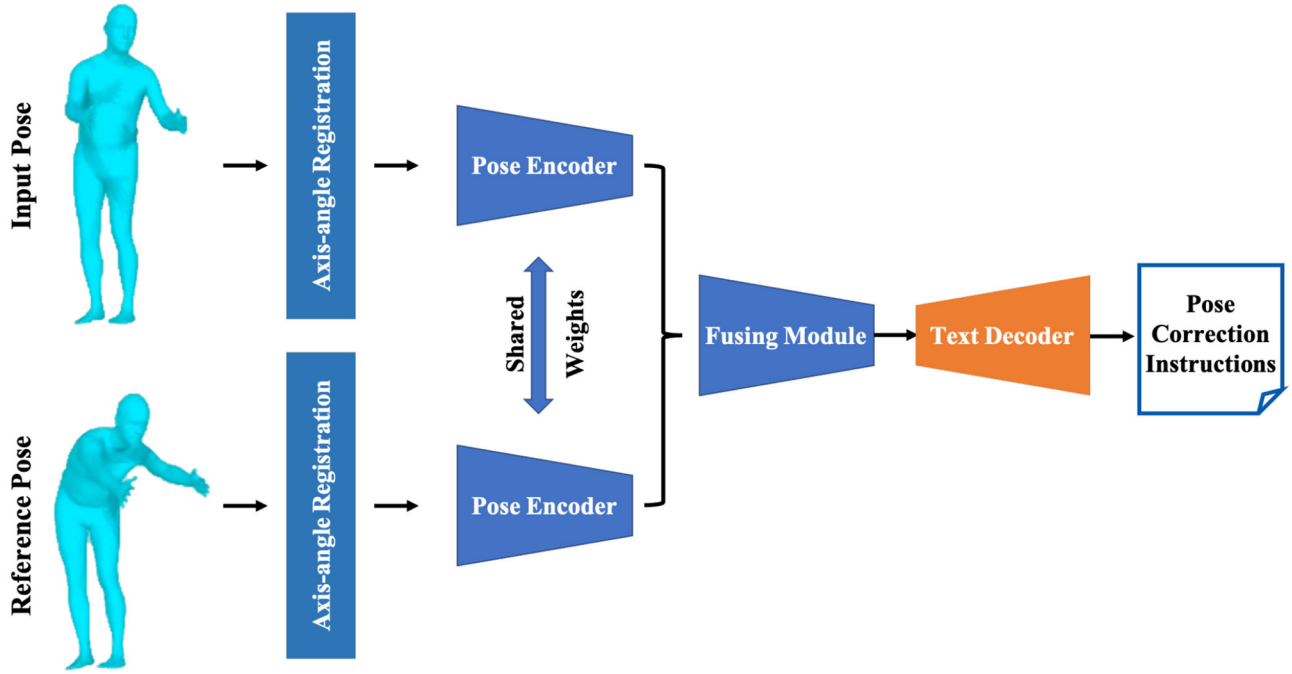

FIGURE 4
The structure of the pose correction module, which outputs pose correction guidance text for the users by contrasting the reconstructed pose with the standard reference pose.

latent features from the embedded features of $Pose_A$ and $Pose_B$. The TIRG (Vo et al., 2019) network comprises a gate network consisting of two MLP layers and two learnable weights, which is designed to retain the primary motion features and introduce additional improvement through residual connections. As shown in Equation 13:

$$F_{prompt} = w_f FC_f([\mathbf{a}, \mathbf{m}]) \odot \mathbf{a} + w_g FC_g([\mathbf{a}, \mathbf{m}]) \quad (13)$$

where FC_f and FC_g are MLP layers, and their weights are balanced by learnable parameters w_f and w_g.

Finally, the fused features $\mathbf{F}_{prompt}$ are fed into a Transformer-based auto-regressive model, serving as a prompt to guide the natural language processing model in generating motion correction guidance text. In the decoding process of the Transformer-based auto-regressive model, the input feature $\mathbf{F}_{prompt}$ is concatenated with a vector $F_{caption}$, composed entirely of ones, serving as additional positional encoding. This combined input is then fed into the Transformer model. Leveraging the attention mechanism of the Transformer, the prompt is decoded into a probability distribution of text embeddings, and the first text result T_1 is obtained through the softmax function. Subsequently, T_1 is integrated into $F_{caption}$, concatenated again with the input feature $\mathbf{F}_{prompt}$, and fed into the Transformer model to obtain the second text result T_2 with the highest probability. This iterative process

TABLE 1 Comparison of our approach with state-of-the-art methods on the subsets of AMASS.

Method	MPJPE	MPJRE	MPJVE	Jitter	Parameters (M)
AGRoL-MLP	3.93	2.69	22.85	13.01	3.73
AGRoL-Diffusion	3.71	2.66	18.59	7.26	7.48
Ours	3.79	2.69	20.94	11.53	4.52

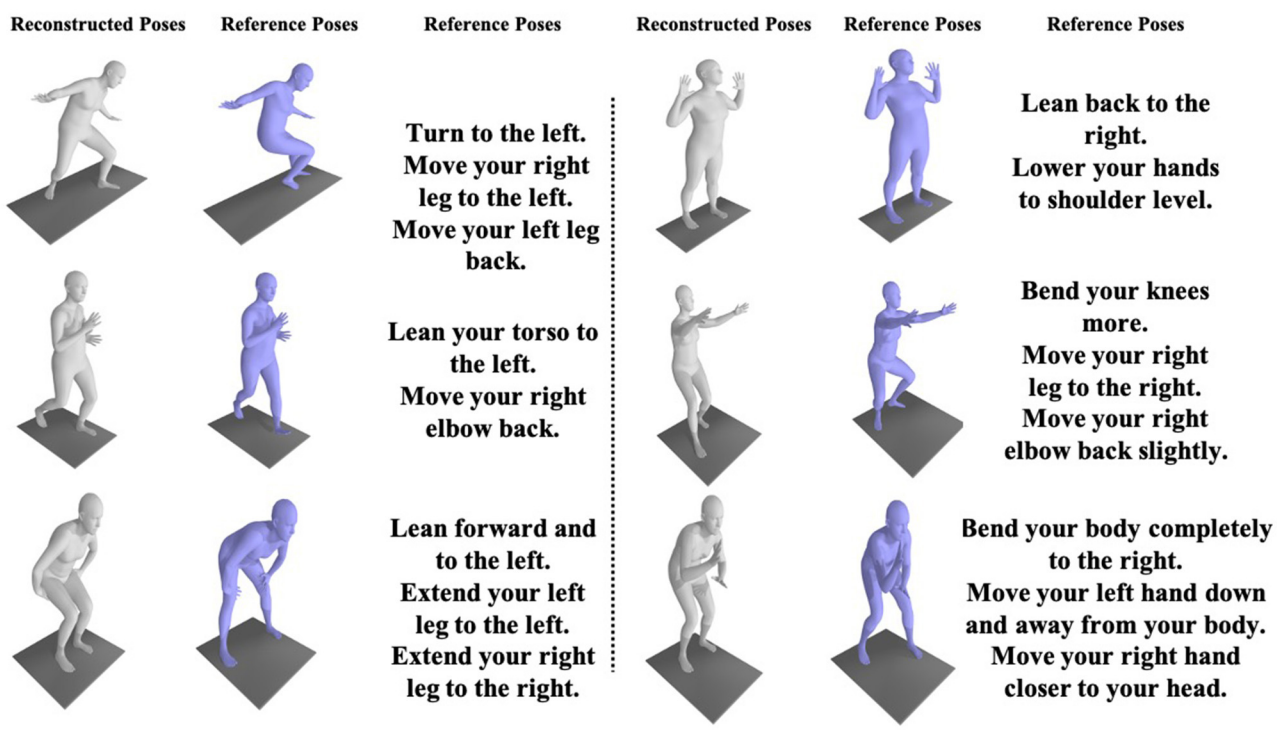

FIGURE 5
Partial results of the virtual reality-based rehabilitation training method indicate that users can correct their poses with guidance from the pose correction text.

continues, employing the method of iterative greedy decoding, until the entire sequence is decoded.

4 Experiments

4.1 Training details

To train the full-body pose reconstruction model based on sparse motion signals, three subsets of the AMASS dataset—CMU (Carnegie Mellon University), MPI-HDM05 (Max Planck Institute Human Motion Database 2005; Müller et al., 2007), and BioMotionLab-NTroje (Troje, 2002) are employed for model training and test. Specifically, we obtain 2,074, 215, and 3,061 motion sequences from these three subsets, covering commonly used actions in virtual reality such as walking, running, jumping, dancing, kicking, tool manipulation, and social behaviors and interpersonal interactions. Out of 5,350 motion sequences, 536 are randomly selected for model validation, with the remaining 4,814 used for model training. These motion sequences are stored in the format of SMPL model parameters, encompassing 156-dimensional joint motion parameters.

To emulate the hardware configuration of virtual reality devices, we extract the motion parameters of the head joint and wrists of both hands, inputting them into the model, and reconstruct the motion parameters of 22 body joints (excluding the joints of the palms). To ensure a fair comparison with previous methods, consistent experimental parameters are employed: the stacking layers of the MLP module M are set to 12, and the feature dimension F was set to 512. Both training and testing were conducted on an NVIDIA 4090 GPU using the PyTorch framework (Paszke et al., 2019).

For the natural language processing model-based pose correction module, we make no modifications and training to the PoseFix model. In PoseFix, a pipeline based on PoseScript is employed to compare the distance variations between multiple 3D keypoints for 135 k pairs of different actions. The resulting data are organized in structural order, forming the 135 k action correction guidance text dataset. This dataset is utilized for training the pose correction model. Additionally, the frozen DistillBERT (Sanh et al., 2019) is employed for word embedding. Instead, we directly

utilize publicly available model weights, as experimental results have already demonstrated that this method accurately evaluates differences between two poses and generates precise correction guidance text.

4.2 Evaluation metrics

To validate the effectiveness of the proposed method, the following evaluation metrics are employed to assess the model's performance and compare it with previous state-of-the-art methods (Du et al., 2023): Mean Per Joint Rotation Error (degrees; MPJRE) and Mean Per Joint Position Error (cm; MPJPE) measures the average relative rotation error and position error for each joints, which indicated the absolute errors of the model predictions. While the Mean Per Joint Velocity Error (cm/s; MPJVE) measures the average velocity error for the joints' positions, the Jitter (Yi et al., 2022) evaluates the mean jerk (change in acceleration over time; Du et al., 2023) of the joints in global space. These metrics can measure the smoothness of reconstructed poses, which directly relates to the user's overall experience. Specifically, jitter delineates the rate of change of acceleration in joint positions, serving as an indicator of the degree to which abrupt changes occur in joint positioning. Consequently, it proves valuable in characterizing and analyzing the dynamic aspects of motion, facilitating an evaluation metric of the smoothness of reconstructed poses (Flash and Hogan, 1985). The jitter is calculated as Equation 14:

$$Jitter = \frac{d^2p}{dt^2} \tag{14}$$

where p represents the joint position and t denotes the time. By computing the second derivative of each joint position with respect to time, jitter can be derived.

4.3 Evaluation results

In Table 1, we present the quantitative comparison results between our proposed model and the state-of-the-art method AGRoL (Du et al., 2023). As shown in Table 1, our approach demonstrates improvements across various metrics compared with the AGRoL's MLP-based backbone method. Moreover, the phenomenon of joint jitter has been noticeably mitigated. In comparison to AGRoL's diffusion model method, we maintain a comparable prediction accuracy, albeit with less pronounced joint jitter. However, our method requires only 60.4% of the model's parameters compared with this method, enhancing its practical applicability.

In Figure 5, we showcase comprehensive applications of virtual reality-based rehabilitation and partial action guidance. As shown in the figure, the reconstructed poses and target poses can be accurately evaluated by the PoseFix network, yielding intuitive, detailed, and precise action guidance.

5 Conclusion

Current rehabilitation training requires patients, who already face mobility challenges, to visit rehabilitation centers for treatment by physical therapists. This proves to be difficult and costly for patients. To enable patients to undergo precise, efficient, and cost-effective rehabilitation training in the comfort of their homes using their virtual reality devices, this study introduces a novel approach that utilizes sparse motion signals from VR devices, specifically head-mounted displays and hand controllers, to reconstruct full-body poses. Unlike existing methods that focus on clinical metrics for doctors, our method employs a natural language processing model to contrast reconstructed poses with standard poses. This process provides efficient pose correction guidance in the form of natural language, offering a more accessible and personalized approach to movement guidance for patients.

The quantitative and qualitative results demonstrate the effectiveness of the proposed method in real-time reconstruction of accurate full-body poses. By referencing standard poses, the model generates professional motion correction guidance text, facilitating virtual reality-based rehabilitation training. This approach not only reduces the cost of rehabilitation training but also enhances the efficiency of self-rehabilitation training, addressing the challenges faced by patients seeking timely and accessible rehabilitation.

Data availability statement

The original contributions presented in the study are included in the article/supplementary material, further inquiries can be directed to the corresponding authors.

Author contributions

XD: Conceptualization, Investigation, Methodology, Writing – original draft. ZZ: Investigation, Writing – original draft. SZ: Software, Visualization, Writing – original draft. XL: Supervision, Writing – review & editing. XC: Supervision, Writing – review & editing.

Funding

The author(s) declare financial support was received for the research, authorship, and/or publication of this article. This study was supported by the Renji Hospital Baoshan Branch Management Talent Program "Internet of Things Enhancing Clinical Efficiency and Usage Platform for Medical Equipment" (rbxxrc-2023-007), the Key Research and Development Plan of Ningxia Hui Autonomous Region (Grant No. 2023BEG03043), the Key Research and Development Plan of Ningxia Hui Autonomous Region (Grant No. 2023BEG02035), the Fudan University Medical Engineering Cross Research Project (yg2022-33), and the Shanghai Jiao Tong University School of Medicine

Affiliated Renji Hospital Baoshan Branch Fund (Grant No. 2023-rbcxjj-005).

Conflict of interest

The authors declare that the research was conducted in the absence of any commercial or financial relationships that could be construed as a potential conflict of interest.

Publisher's note

References

Adamovich, S. V., Fluet, G. G., Tunik, E., and Merians, A. S. (2009). Sensorimotor training in virtual reality: a review. *NeuroRehabilitation* 25, 29–44. doi: 10.3233/NRE-2009-0497

Ahuja, K., Ofek, E., Gonzalez-Franco, M., Holz, C., and Wilson, A. D. (2021). Coolmoves: user motion accentuation in virtual reality. *Proc. ACM Interact. Mob. Wear. Ubiquit. Technol.* 5, 1–23. doi: 10.1145/3463499

Bruce, X., Liu, Y., Chan, K. C., Yang, Q., and Wang, X. (2021). Skeleton-based human action evaluation using graph convolutional network for monitoring Alzheimer's progression. *Pat. Recogn.* 119:108095. doi: 10.1016/j.patcog.2021.108095

Delmas, G., Weinzaepfel, P., Lucas, T., Moreno-Noguer, F., and Rogez, G. (2022). "Posescript: 3D human poses from natural language," in *European Conference on Computer Vision* (Berlin: Springer), 346–362.

Delmas, G., Weinzaepfel, P., Moreno-Noguer, F., and Rogez, G. (2023). "Posefix: correcting 3D human poses with natural language," in *Proceedings of the IEEE/CVF International Conference on Computer Vision*, 15018–15028.

Du, Y., Kips, R., Pumarola, A., Starke, S., Thabet, A., and Sanakoyeu, A. (2023). "Avatars grow legs: generating smooth human motion from sparse tracking inputs with diffusion model," in *Proceedings of the IEEE/CVF Conference on Computer Vision and Pattern Recognition*, 481–490.

Feng, H., Li, C., Liu, J., Wang, L., Ma, J., Li, G., et al. (2019). Virtual reality rehabilitation versus conventional physical therapy for improving balance and gait in Parkinson's disease patients: a randomized controlled trial. *Med. Sci. Monit.* 25:4186. doi: 10.12659/MSM.916455

Flash, T., and Hogan, N. (1985). The coordination of arm movements: an experimentally confirmed mathematical model. *J. Neurosci.* 5, 1688–1703.

Guo, C., Zou, S., Zuo, X., Wang, S., Ji, W., Li, X., et al. (2022). "Generating diverse and natural 3D human motions from text," in *Proceedings of the IEEE/CVF Conference on Computer Vision and Pattern Recognition*, 5152–5161.

Guo, W., Du, Y., Shen, X., Lepetit, V., Alameda-Pineda, X., and Moreno-Noguer, F. (2023). "Back to MLP: a simple baseline for human motion prediction," in *Proceedings of the IEEE/CVF Winter Conference on Applications of Computer Vision*, 4809–4819.

Hernández, Ó. G., Morell, V., Ramon, J. L., and Jara, C. A. (2021). Human pose detection for robotic-assisted and rehabilitation environments. *Appl. Sci.* 11:4183. doi: 10.3390/app11094183

Ho, J., Jain, A., and Abbeel, P. (2020). Denoising diffusion probabilistic models. *Adv. Neural Inform. Process. Syst.* 33, 6840–6851.

Huang, Y., Kaufmann, M., Aksan, E., Black, M. J., Hilliges, O., and Pons-Moll, G. (2018). Deep inertial poser: learning to reconstruct human pose from sparse inertial measurements in real time. *ACM Trans. Graph.* 37, 1–15. doi: 10.1145/3272127.3275108

Jiang, J., Streli, P., Qiu, H., Fender, A., Laich, L., Snape, P., et al. (2022). "Avatarposer: articulated full-body pose tracking from sparse motion sensing," in *European Conference on Computer Vision* (Berlin: Springer), 443–460.

Jiang, Y., Ye, Y., Gopinath, D., Won, J., Winkler, A. W., and Liu, C. K. (2022). Transformer inertial poser: attention-based real-time human motion reconstruction from sparse IMUs. *arXiv e-prints, arXiv–2203*. doi: 10.48550/arXiv.2203.15720

Kidziński, Ł., Yang, B., Hicks, J. L., Rajagopal, A., Delp, S. L., and Schwartz, M. H. (2020). Deep neural networks enable quantitative movement analysis using single-camera videos. *Nat. Commun.* 11:4054. doi: 10.1038/s41467-020-17807-z

Kim, H., Zala, A., Burri, G., and Bansal, M. (2021). "Fixmypose: pose correctional captioning and retrieval," in *Proceedings of the AAAI Conference on Artificial Intelligence, Vol. 35*, 13161–13170.

Kingma, D. P., and Welling, M. (2013). Auto-encoding variational bayes. *arXiv preprint arXiv:1312.6114*. doi: 10.48550/arXiv.1312.6114

Liao, Y., Vakanski, A., and Xian, M. (2020). A deep learning framework for assessing physical rehabilitation exercises. *IEEE Trans. Neural Syst. Rehabil. Eng.* 28, 468–477. doi: 10.1109/TNSRE.2020.2966249

Loper, M., Mahmood, N., Romero, J., Pons-Moll, G., and Black, M. J. (2023). "SMPL: a skinned multi-person linear model," in *Seminal Graphics Papers: Pushing the Boundaries, Vol. 2*, 851–866.

Luo, J., Yuan, M., Fu, K., Wang, M., and Zhang, C. (2022). Deep graph matching based dense correspondence learning between non-rigid point clouds. *IEEE Robot. Automat. Lett.* 7, 5842–5849. doi: 10.1109/LRA.2022.3160237

Mahmood, N., Ghorbani, N., Troje, N. F., Pons-Moll, G., and Black, M. J. (2019). "AMASS: archive of motion capture as surface shapes," in *Proceedings of the IEEE/CVF International Conference on Computer Vision*, 5442–5451.

Martınez, G. H. (2019). *Openpose: Whole-Body Pose Estimation*. (Ph.D. thesis). Carnegie Mellon University, Pittsburgh, PA, United States.

Müller, M., Röder, T., Clausen, M., Eberhardt, B., Krüger, B., and Weber, A. (2007). *Mocap database HDM05*. (Bonn: Institut für Informatik II, Universität Bonn), 2.

Paszke, A., Gross, S., Massa, F., Lerer, A., Bradbury, J., Chanan, G., et al. (2019). PyTorch: an imperative style, high-performance deep learning library. *Adv. Neural Inform. Process. Syst.* 32:12. doi: 10.48550/arXiv.1912.01703

Pavlakos, G., Choutas, V., Ghorbani, N., Bolkart, T., Osman, A. A., Tzionas, D., et al. (2019). "Expressive body capture: 3D hands, face, and body from a single image," in *Proceedings of the IEEE/CVF Conference on Computer Vision and Pattern Recognition*, 10975–10985.

Postolache, O., Hemanth, D. J., Alexandre, R., Gupta, D., Geman, O., and Khanna, A. (2020). Remote monitoring of physical rehabilitation of stroke patients using IoT and virtual reality. *IEEE J. Select. Areas Commun.* 39, 562–573. doi: 10.1109/JSAC.2020.3020600

Punnakkal, A. R., Chandrasekaran, A., Athanasiou, N., Quiros-Ramirez, A., and Black, M. J. (2021). "Babel: bodies, action and behavior with english labels," in *Proceedings of the IEEE/CVF Conference on Computer Vision and Pattern Recognition*, 722–731.

Qiu, Y., Wang, J., Jin, Z., Chen, H., Zhang, M., and Guo, L. (2022). Pose-guided matching based on deep learning for assessing quality of action on rehabilitation training. *Biomed. Sign. Process. Contr.* 72:103323. doi: 10.1016/j.bspc.2021.103323

Sanh, V., Debut, L., Chaumond, J., and Wolf, T. (2019). Distilbert, a distilled version of bert: smaller, faster, cheaper and lighter. *arXiv preprint arXiv:1910.01108*. doi: 10.48550/arXiv.1910.01108

Tang, D. (2020). Hybridized hierarchical deep convolutional neural network for sports rehabilitation exercises. *IEEE Access* 8, 118969–118977. doi: 10.1109/ACCESS.2020.3005189

Troje, N. F. (2002). Decomposing biological motion: a framework for analysis and synthesis of human gait patterns. *J. Vis.* 2:2. doi: 10.1167/2.5.2

Vo, N., Jiang, L., Sun, C., Murphy, K., Li, L.-J., Fei-Fei, L., et al. (2019). "Composing text and image for image retrieval-an empirical Odyssey," in *Proceedings of the IEEE/CVF Conference on Computer Vision and Pattern Recognition*, 6439–6448.

Xu, W., Xiang, D., Wang, G., Liao, R., Shao, M., and Li, K. (2022). Multiview video-based 3-D pose estimation of patients in computer-assisted rehabilitation environment (CAREN). *IEEE Trans. Hum. Machine Syst.* 52, 196–206. doi: 10.1109/THMS.2022.3142108

Yi, X., Zhou, Y., Habermann, M., Shimada, S., Golyanik, V., Theobalt, C., et al. (2022). "Physical inertial poser (PIP): physics-aware real-time human motion tracking from sparse inertial sensors," in *Proceedings of the IEEE/CVF Conference on Computer Vision and Pattern Recognition*, 13167–13178.

Yu, Y., Si, X., Hu, C., and Zhang, J. (2019). A review of recurrent neural networks: LSTM cells and network architectures. *Neural Comput.* 31, 1235–1270. doi: 10.1162/neco_a_01199

Zhang, J., Zhang, Y., Cun, X., Zhang, Y., Zhao, H., Lu, H., et al. (2023). "Generating human motion from textual descriptions with discrete representations," in *Proceedings of the IEEE/CVF Conference on Computer Vision and Pattern Recognition*, 14730–14740.

Zhang, X., Chen, X., Dai, X., and Di, X. (2023). "Dual attention poser: dual path body tracking based on attention," in *Proceedings of the IEEE/CVF Conference on Computer Vision and Pattern Recognition*, 2794–2803.

Zheng, J., Liu, X., Gu, X., Sun, Y., Gan, C., Zhang, J., et al. (2022). "Gait recognition in the wild with multi-hop temporal switch," in *Proceedings of the 30th ACM International Conference on Multimedia*, 6136–6145.

Zhou, Y., Barnes, C., Lu, J., Yang, J., and Li, H. (2019). "On the continuity of rotation representations in neural networks," in *Proceedings of the IEEE/CVF Conference on Computer Vision and Pattern Recognition*, 5745–5753.

frontiers | Frontiers in Neuroscience

TYPE Brief Research Report
PUBLISHED 22 May 2024
DOI 10.3389/fnins.2024.1382871

OPEN ACCESS

EDITED BY
Mingming Zhang,
Southern University of Science and Technology, China

REVIEWED BY
Tugrul Artug,
Istanbul University-Cerrahpasa, Türkiye
Lin Wang,
Chinese Academy of Sciences (CAS), China

*CORRESPONDENCE
Zhiyuan Lu
✉ zhiyuan.lu@uor.edu.cn
Weijun Gong
✉ gwj197104@ccmu.edu.cn

RECEIVED 06 February 2024
ACCEPTED 17 April 2024
PUBLISHED 22 May 2024

CITATION
Zhang D, Lu Z, Gong W and Zhou P (2024) Effect of surface electrode recording area on compound muscle action potential scan processing for motor unit number estimation. *Front. Neurosci.* 18:1382871. doi: 10.3389/fnins.2024.1382871

Effect of surface electrode recording area on compound muscle action potential scan processing for motor unit number estimation

Dan Zhang[1], Zhiyuan Lu[2]*, Weijun Gong[1,3]* and Ping Zhou[2]

[1]School of Rehabilitation Medicine, Shandong Second Medical University, Weifang, Shandong, China, [2]School of Rehabilitation Science and Engineering, University of Health and Rehabilitation Sciences, Qingdao, Shandong, China, [3]Department of Neurological Rehabilitation, Beijing Rehabilitation Hospital, Capital Medical University, Beijing, China

Introduction: MScanFit is a model-based algorithm for motor unit number estimation (MUNE) from compound muscle action potential (CMAP) scan data. It is a clinically applicable tool because of its quick and automatic implementation. Electrodes with different recording areas were employed to record CMAP scan data in existing studies. However, the effect of electrode recording area on MScanFit MUNE and other CMAP scan parameters has not been studied.

Methods: CMAP scan was performed on the abductor pollicis brevis muscle of both hands on 14 healthy subjects using three different electrodes with recording areas of 10 mm × 10 mm, 11 mm × 14 mm, and 22 mm × 26 mm, respectively. Motor unit number was estimated using MScanFit for each CMAP scan. Two motor unit number index parameters, i.e., D50 and step index (STEPIX), were also derived from the CMAP scan data.

Results: No significant difference in D50, STEPIX, and MScanFit MUNE was observed across three different electrode recording areas, although the amplitude of CMAP decreased significantly when a larger electrode was used. Intraclass correlation coefficients of 0.792 and 0.782 were obtained for MScanFit MUNE and STEPIX, respectively.

Discussion: Compared with CMAP amplitude, D50, STEPIX, and MScanFit MUNE are less sensitive to variation in electrode recording area. However, the repeatability of MScanFit MUNE could be compromised by the inconsistency in the electrode recording area.

KEYWORDS

MScanFit, motor unit number estimation, compound muscle action potential scan, electromyography, electrode recording area

1 Introduction

The reduction of motor units may lead to muscle weakness and muscle atrophy in neuromuscular diseases. Motor unit number estimation (MUNE) is a powerful tool for tracking loss of motor units and the compensatory phenomenon of collateral reinnervation (Gooch et al., 2014). A variety of MUNE methods have been proposed in past decades, but those traditional MUNE methods such as incremental stimulation MUNE and multiple point

stimulation MUNE (de Carvalho et al., 2018; Wright et al., 2021) are likely biased to the sampling of motor units. By contrast, compound muscle action potential (CMAP) scan aims to gradually activate/deactivate all motor units by applying hundreds of transcutaneous stimuli to the motor nerve across a wide range of intensities (Blok et al., 2007). Compared with traditional MUNE methods, CMAP scan is less biased to the sampling of motor units, and various methods have been developed to process CMAP scan for examination of neuromuscular disorders (Sleutjes et al., 2014; Nandedkar et al., 2022; Chen et al., 2023a,b; Lu et al., 2023b). Of particular note, Bostock proposed a model-based MUNE algorithm named MScanFit, which estimates the number of motor units by fitting the detailed stimulus–response curve recorded from a CMAP scan (Bostock, 2016). MScanFit possesses the advantage of automated and quick (typically taking only a few minutes) implementation, making it so far the most often used CMAP scan processing method in basic and clinical electrophysiological studies (Kristensen et al., 2019; Zong et al., 2021; Schneider et al., 2023).

CMAP scan curve can be affected by experimental parameters including the number and the width of electrical stimuli. For example, our previous studies show that CMAP scan curve becomes denser when the number of stimuli is increased, which leads to an increase in derived step index (STEPIX; Lu et al., 2023a). Although MScanFit is not sensitive to the number of stimuli, it is significantly affected by the width of stimuli (Zong et al., 2020).

Electrode recording area (the area of the recording surface of an electrode) is another major factor affecting CMAP, especially on its shape and amplitude due to the different filtering effects (Wee and Ashley, 1990; Chang et al., 1993; Jonas et al., 1999; Barkhaus et al., 2006). The electrode recording area used for CMAP scan studies covered a wide range in literature from greater than 400 mm^2 (Sørensen et al., 2022, 2023) to around 100 mm^2 (Li et al., 2018; Song et al., 2023). Furthermore, inconsistent electrode recording areas were reported when examining the same muscle (Sleutjes et al., 2021). For example, when performing CMAP scan recordings on the abductor pollicis brevis (APB) muscle, square electrodes with the size of 30 mm × 22 mm (with the recording area of 474 mm^2) and 30 mm × 24 mm (detailed recording area was not reported) were used in Araújo et al. (2015) and Sørensen et al. (2023), respectively, while disk electrodes with the diameter of 10 mm (i.e., 79 mm^2) and 13 mm (i.e., 133 mm^2) were applied in Stikvoort García et al. (2022) and Song et al. (2023), respectively. Note that 2-dimensional electrode arrays up to 128 channels have also been used for MUNE, where electrodes with diameters smaller than 2 mm are commonly used (Sleutjes et al., 2016).

The effect of electrode recording area on CMAP implies that the CMAP scan curves could also vary with different surface electrodes. However, it still remains unclear how the different surface electrode recording areas may affect CMAP scan processing parameters, such as MScanFit MUNE. The objective of this study was, therefore, to assess the effect of electrode recording area on MScanFit MUNE and other CMAP scan parameters. In addition, the repeatability of these parameters using different electrode recording areas was quantified.

2 Methods

2.1 Experimental protocol

Three electrodes with different recording areas were used for CMAP scan recording in this study. Their recording areas are 10 mm × 10 mm (denoted as E1), 11 mm × 14 mm (denoted as E2), and 22 mm × 26 mm (denoted as E3), respectively.

Fourteen right-handed healthy subjects (7 males and 7 females, aged 30.6 ± 9.5 years) participated in this study. Each subject's bilateral APB muscles were recorded. The order of the left and right hand was randomized. In the experiment, each subject was seated comfortably in a chair with his/her testing hand rested on a table and restrained in the pronation position. CMAP scan was performed three times on each hand using one of the three active electrodes in a random order, while all the other experimental parameters remained the same. Before each recording, the subject was given sufficient rest to avoid mental and muscle fatigue.

2.2 CMAP scan recording

Before each recording, the range of stimulating current intensity was determined by performing an automatic search. The range of current intensity was then manually tuned in order to cover the entire motor unit recruitment range. The pulse duration was set to 0.1 ms, the number of stimuli was set to 500, and the frequency of stimuli was set to 2 Hz. All the data were collected using Nicolet EDX system (Natus Neurology Incorporated, Middleton, WI, United States).

As shown in Figure 1, the active electrode was placed on the abdominal eminence of the APB muscle, and the reference electrode was placed on the metacarpophalangeal joint of the thumb. The ground electrode was placed on the bony protuberance on the back of the hand between the active electrode and the reference electrode. The stimulating electrode (Ag/AgCl electrode) with two contact surfaces spaced 20 mm apart and each having a diameter of 9 mm, was placed 1–2 cm proximal to the wrist to activate the median nerve. The electrode was coated with conductive paste and the cathode was oriented distally. Both recording and stimulating electrodes were carefully tuned in order to optimize electrode positions where the largest CMAP amplitude can be evoked with a relatively low stimulating current intensity. Once the stimulating site was determined, the electrode was fixed with surgical tape or self-adherent wrap. Alcohol pads were used to clean the thumb, thenar, wrist, and back of the hand before the electrodes were attached.

2.3 CMAP scan data analysis

The MScanFit program (free version 2016; Bostock, 2016) was applied to estimate motor unit number. Each recording was analyzed multiple times until three valid estimations were obtained (i.e., percentage error < 7%), and the one with the smallest error was accepted. The pre-scan and post-scan limits were manually selected each time, while all the other settings remained at their default values.

D50, step index, S0, S100, and the difference between S0 and S100 (i.e., S100 − S0) were also derived from each scan using a customized Matlab script. D50 is the number of largest consecutive differences from each scan that are required to build up 50% of the maximum CMAP amplitude (Sleutjes et al., 2014). STEPIX, which is a recently proposed index based on the logarithmic relation between the step amplitude and step number in a CMAP scan, reflects the number of motor units (Nandedkar et al., 2022). S0 is the maximum electrical intensity that cannot activate any motor unit. S100 is the minimum electrical intensity that can activate all the motor units.

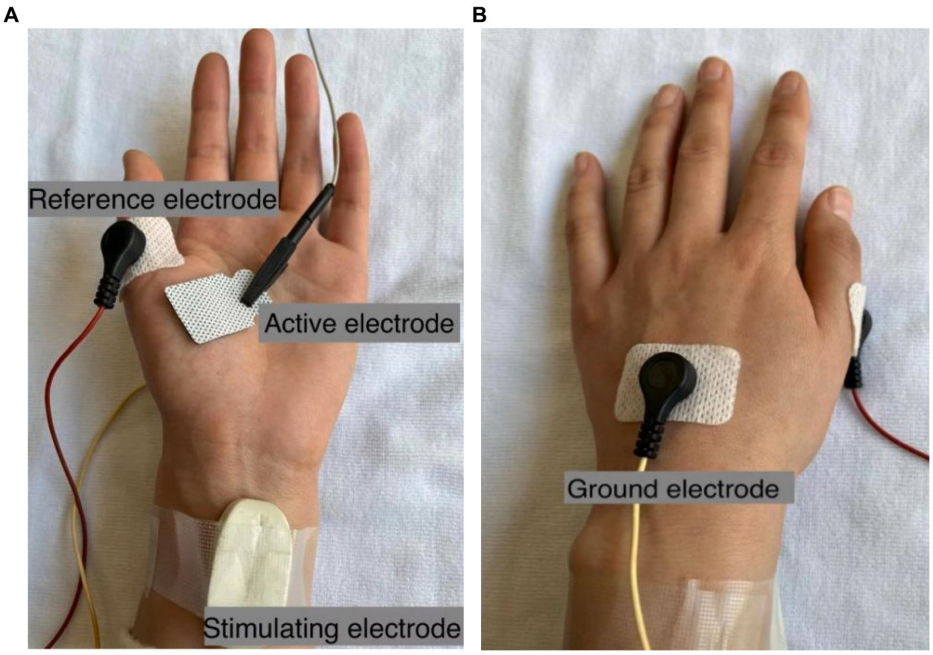

FIGURE 1
Electrode configurations for CMAP scan recording of the APB muscle. The active electrode E3 with the size of 22 mm × 26 mm is shown as an example in **(A)**, and the ground electrode is shown in **(B)**.

2.4 Statistical analysis

One-way repeated measures analysis of variance was performed to examine the differences in the maximum CMAP amplitude, S0, S100, S100 − S0, D50, STEPIX, and MScanFit MUNE parameters for different electrode recording areas. Statistical significance was set as $p < 0.05$. Repeatability was quantified using consistency intraclass correlation coefficient (ICC) if significant difference was observed; otherwise, absolute agreement ICC was used. Results are presented as mean ± standard error.

3 Results

Mild or tolerable pain was reported by the subjects in our experiment. The CMAP amplitude of one subject's left hand was lower than 50% of the amplitude of his right hand, and thus CMAP scan data from his left hand was excluded. As a result, a total of 81 CMAP scan curves (3 trials per hand × 27 hands) recorded from 14 subjects were analyzed.

The maximum CMAP amplitude of the APB muscle was 10.18 ± 0.58 mV for electrode E1, 9.65 ± 0.56 mV for electrode E2, and 8.54 ± 0.50 mV for electrode E3 (as shown in Table 1). Significant difference was observed across the three electrodes ($p < 0.0001$), and the maximum CMAP amplitude decreased at a larger electrode recording area. No significant difference was observed across the three electrode recording areas in S0 ($p = 0.592$), S100 ($p = 0.482$), S100 − S0 ($p = 0.536$), D50 ($p = 0.463$), STEPIX ($p = 0.654$), or MScanFit MUNE ($p = 0.155$). The ICC of MScanFit MUNE (0.792) was greater than that of the other two indexes (0.782 for STEPIX and 0.686 for D50). The median value of difference in D50, STEPIX, and MScanFit MUNE between individual subject's CMAP scan curves recorded using electrodes with different recording areas was distributed close to 0 (i.e., no significant difference across three electrodes). However, it was observed that the difference in these parameters between two electrodes could be distributed in a large range, as shown in Figure 2.

Three CMAP scan curves recorded using electrode E1, E2, and E3 from the APB muscle of a representative subject are demonstrated in Figure 3. It is worth noting that the curves recorded using electrode E2 and E3 demonstrate a close pattern, and there is only a difference of 2 (or 1.7%) in MScanFit MUNE although the difference in maximum CMAP amplitude is as high as 1.13 mV (or 9.5%).

4 Discussion

This study presents a novel analysis of CMAP scan parameters with respect to the different electrode recording areas. By testing three different electrodes on CMAP scan recordings of the APB muscle we observed that changes in the electrode recording area had no significant impact on the examined CMAP processing parameters including D50, STEPIX and MScanFit MUNE. In recent years, different electrodes or recording areas have been used in CMAP scan experiments on various muscles. For example, a disk electrode with 11 mm in diameter was used to examine the abductor hallucis muscle (Li et al., 2018); a smaller disk electrode with 10 mm in diameter was used to collect CMAP scan data from the first dorsal interosseous (FDI) muscle (Zong et al., 2020). Additionally, some researchers used 13 mm diameter disk electrodes to examine the FDI and abductor digiti minimi (ADM) muscles (Song et al., 2023). For the APB muscle examined in this study, literature shows that the surface electrode used for CMAP scan recording ranged from 10 mm to 15 mm in diameter (i.e., 79 mm^2 to 177 mm^2; Farschtschi et al., 2017; Stikvoort García et al., 2022; Zong et al., 2022c; Song et al., 2023). Square electrodes

TABLE 1 Parameters derived from CMAP scan of the APB muscle on healthy subjects using electrodes with different recording areas.

	10 mm × 10 mm	11 mm × 14 mm	22 mm × 26 mm	Significance	ICC*
Maximum CMAP (mV)	10.18 ± 0.58	9.65 ± 0.56	8.54 ± 0.50	$p < 0.0001$	0.934
S0 (mA)	10.01 ± 0.51	10.06 ± 0.56	10.23 ± 0.54	$p = 0.592$	0.914
S100 (mA)	19.21 ± 0.88	19.00 ± 0.80	19.53 ± 0.88	$p = 0.482$	0.867
S100 − S0 (mA)	9.19 ± 0.58	8.95 ± 0.51	9.31 ± 0.58	$p = 0.536$	0.831
D50	38.85 ± 1.64	39.37 ± 1.64	40.44 ± 1.63	$p = 0.463$	0.686
STEPIX	103.67 ± 5.50	106.59 ± 6.00	103.37 ± 5.81	$p = 0.654$	0.782
MScanFit MUNE	107.37 ± 7.33	109.07 ± 6.57	115.52 ± 6.75	$p = 0.155$	0.792

*All these ICC values are the absolute agreement type, except the ICC of the maximum CMAP, which is the consistency type.

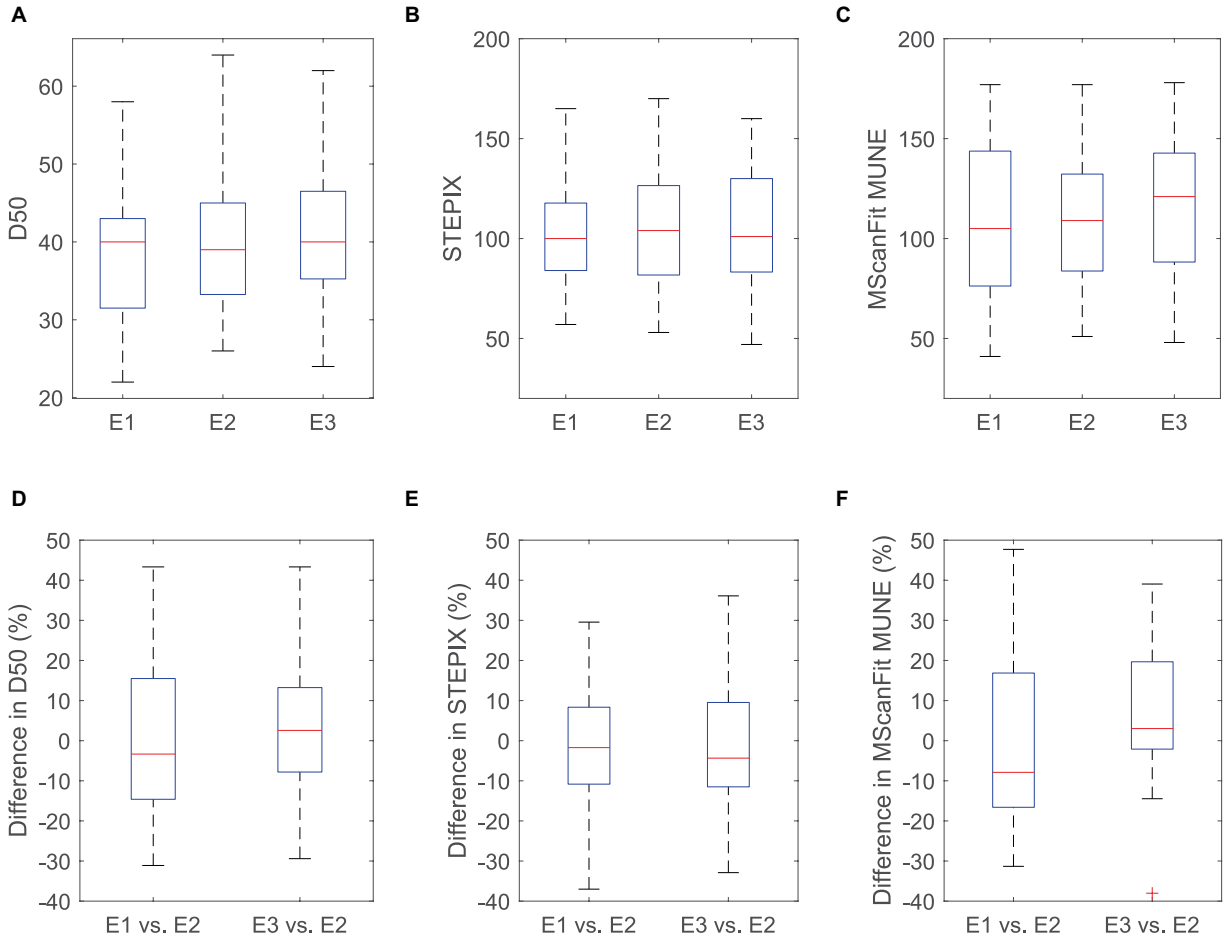

FIGURE 2
D50 **(A)**, STEPIX **(B)**, MScanFit MUNE **(C)**, and the difference in D50 **(D)**, STEPIX **(E)**, and MScanFit MUNE **(F)** between CMAP scan curves of the APB muscle of healthy subjects recorded using electrodes with different recording areas. The difference was calculated as (Parameter derived from E1 or E3–Parameter derived from E2)/Parameter derived from E2 for each subject. One outlier (above 50% in both STEPIX and MScanFit) is not shown in this figure.

with different recording areas were also reported for APB muscle CMAP scan recordings (Araújo et al., 2015; Sørensen et al., 2023). Considering various recording areas reported in previous CMAP scan studies, we chose to use three electrodes with recording areas of 100 mm^2, 154 mm^2, and 572 mm^2, respectively. The three electrode recording areas used in this study can cover the commonly used surface electrodes in research and clinical practice.

In addition to motor unit number parameters (e.g., MScanFit MUNE), it was also observed that the three different electrode recording areas had no significant impact on CMAP scan's stimulus intensity parameters including S0, S100, and S100 − S0. This is not surprising since the stimulus intensities that elicit motor unit responses are independent of the electrode size. Our results indicate that both large and small electrode recording areas have a similar

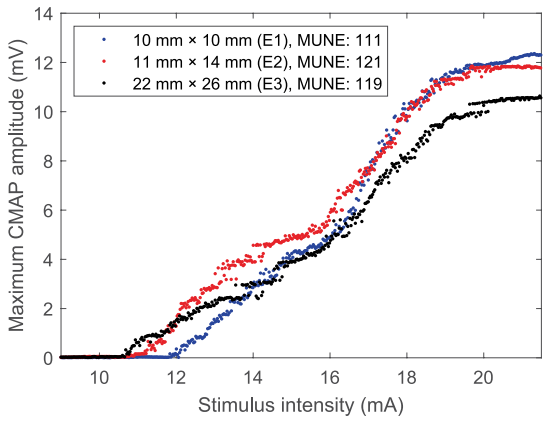

FIGURE 3
CMAP scan curves of the APB muscle of a representative healthy subject recorded using three electrodes with different recording areas.

sensitivity in capturing the recruited motor unit activity of the examined muscle.

The only observed significant difference across three different electrode recording areas was CMAP amplitude. Our results indicated that increased electrode recording area significantly reduced CMAP amplitude of the APB muscle. This is consistent to previous experimental (Wee and Ashley, 1990; Barkhaus et al., 2006) and theoretical findings (Fuglevand et al., 1992). The same tendency was also reported by Chang et al. (1993) although the significance level was not reached. Large surface electrodes can capture relatively more muscle volume but impose an increased low pass filtering effect on the recorded signal compared with small ones. These two factors have opposite effects on the CMAP amplitude. For the examined APB muscle in this study, it seems the difference in low pass filtering effect caused by different surface electrodes was more dominant than the difference in captured muscle volume, thus the CMAP amplitude was reduced with increased recording surface area. Nonetheless, the alterations in CMAP amplitude did not have a significant influence on its processing parameters, such as MScanFit MUNE. This is likely because MScanFit MUNE applies a number of operations to refine the CMAP scan model to meet the predefined error score, including adjusting individual motor unit parameters, splitting or merging motor units, etc. This is different from conventional MUNE methods, calculated as the ratio of the CMAP measurement to the mean motor unit action potential measurement estimated from a small sample of motor units.

The repeatability of CMAP scan parameters was also examined in this study across three different surface electrodes. The repeatability of MScanFit MUNE across the three different electrodes was observed to be slightly higher than that of the two index parameters (i.e., D50 and STEPIX). The repeatability of MScanFit MUNE can be exemplified by Figure 3, as it indicates a relative large variation in CMAP scan amplitude (induced from different electrodes) does not necessarily impose a similar extent of variation in MScanFit MUNE. Existing studies reported that the test–retest repeatability of MScanFit MUNE was excellent using the same electrode for CMAP scan recordings. For example, the ICC of test–retest repeatability achieved 0.93, 0.90, and 0.96 in our previous studies on the abductor hallucis (Li et al., 2018), the anconeus (Zong et al., 2022b), and the second lumbrical (Zong et al., 2022a) muscles, respectively. ICCs greater than 0.8 were also reported for MScanFit MUNE in three repeated tests on the APB, FDI, and ADM muscles (Higashihara et al., 2020). In this study, as expected, although MScanFit MUNE values were not significantly different across three different surface electrode recording areas, the repeatability of MScanFit MUNE was not as high as previously reported numbers, due to inconsistency in surface electrode recording area.

As an important neuromuscular electrophysiological method, MUNE is often used to compare the difference between two groups (for example, between healthy control subjects and subjects with neuromuscular diseases) in a cross-sectional study or track the same muscle in a longitudinal study. Although group analysis revealed no significant difference in MScanFit MUNE of the APB muscle across three different surface electrodes, variation up to ±50% in individual subject was observed between two different electrode recording areas. Such a variation may reduce the reliability of tracking motor unit loss. Therefore, we advocate the same experimental settings (including the same recording electrode) should be used in MUNE studies for both research and clinical settings. This can help to avoid confounding factors for comparing MUNE and other CMAP scan parameters in different situations.

The current study is limited by only examining the APB muscle of neurologically intact subjects. It remains to be determined whether the findings can be generalized to other muscles, particularly to those large muscles. In addition, it is important in the future work to investigate how different electrode recording areas may affect the sensitivity of MScanFit and other CMAP scan processing parameters in quantifying motor unit number and size changes in clinical application.

5 Conclusion

The effect of electrode recording area on MScanFit MUNE and other parameters derived from a CMAP scan was assessed by testing three different electrode recording areas. The experimental results from APB muscles indicate that although CMAP amplitude was sensitive to surface electrode recording area, CMAP scan processing parameters including D50, STEPIX, and MScanFit MUNE were not significantly affected by the changes in electrode recording area. However, inconsistency in electrode recording area may compromise the repeatability of CMAP scan processing. The findings of the study can help to understand the effect of experimental factors on different CMAP scan parameters, thus facilitating their analysis and interpretation.

Data availability statement

The raw data supporting the conclusions of this article will be made available by the authors, without undue reservation.

Ethics statement

The studies involving humans were approved by the Ethics Committee of the University of Health and Rehabilitation Sciences. The studies were conducted in accordance with the local legislation

and institutional requirements. Written informed consent for participation in this study was provided by the participants.

Author contributions

DZ: Data curation, Formal analysis, Investigation, Software, Visualization, Writing – original draft. ZL: Conceptualization, Funding acquisition, Investigation, Methodology, Project administration, Resources, Software, Validation, Writing – original draft. WG: Methodology, Project administration, Validation, Resources, Supervision, Writing – review & editing. PZ: Conceptualization, Funding acquisition, Methodology, Resources, Supervision, Validation, Writing – review & editing.

Funding

The author(s) declare that financial support was received for the research, authorship, and/or publication of this article. This research was funded by the National Natural Science Foundation of China (grant no. 82102179), the Shandong Provincial Natural Science Foundation (grant no. ZR2021QH267), and the Taishan Scholar of Shandong Province (tsqn202211226 and tstp20221144).

Conflict of interest

The authors declare that the research was conducted in the absence of any commercial or financial relationships that could be construed as a potential conflict of interest.

The author(s) declared that they were an editorial board member of Frontiers, at the time of submission. This had no impact on the peer review process and the final decision.

Publisher's note

References

Araújo, T., Candeias, R., Nunes, N., and Gamboa, H. (2015). Evaluation of motor neuron excitability by CMAP scanning with electric modulated current. *Neurosci J* 2015, 1–5. doi: 10.1155/2015/360648

Barkhaus, P. E., Periquet, M. I., and Nandedkar, S. D. (2006). Influence of the surface EMG electrode on the compound muscle action potential. *Electromyogr. Clin. Neurophysiol.* 46, 235–239.

Blok, J. H., Ruitenberg, A., Maathuis, E. M., and Visser, G. H. (2007). The electrophysiological muscle scan. *Muscle Nerve* 36, 436–446. doi: 10.1002/mus.20838

Bostock, H. (2016). Estimating motor unit numbers from a CMAP scan: CMAP scan MUNE. *Muscle Nerve* 53, 889–896. doi: 10.1002/mus.24945

Chang, H., Chan, R. C., and Hsu, T. C. (1993). The effect of surface area of active recording electrode to CMAP parameters. *Zhonghua Yi Xue Za Zhi* 51, 419–424.

Chen, M., Lu, Z., Li, X., Zong, Y., Xie, Q., Li, S., et al. (2023a). Compound muscle action potential (CMAP) scan examination of paretic and contralateral muscles reveals motor unit alterations after stroke. *Sci. China Life Sci.* 66, 2604–2613. doi: 10.1007/s11427-022-2308-8

Chen, M., Lu, Z., Zong, Y., Li, X., and Zhou, P. (2023b). A novel analysis of compound muscle action potential scan: staircase function fitting and StairFit motor unit number estimation. *IEEE J. Biomed. Health Inform.* 27, 1579–1587. doi: 10.1109/JBHI.2022.3229211

de Carvalho, M., Barkhaus, P. E., Nandedkar, S. D., and Swash, M. (2018). Motor unit number estimation (MUNE): where are we now? *Clin. Neurophysiol.* 129, 1507–1516. doi: 10.1016/J.CLINPH.2018.04.748

Farschtschi, S., Gelderblom, M., Buschbaum, S., Bostock, H., Grafe, P., and Mautner, V. F. (2017). Muscle action potential scans and ultrasound imaging in neurofibromatosis type 2: CMAP scans and nerve imaging in NF2. *Muscle Nerve* 55, 350–358. doi: 10.1002/mus.25256

Fuglevand, A. J., Winter, D. A., Patla, A. E., and Stashuk, D. (1992). Detection of motor unit action potentials with surface electrodes: influence of electrode size and spacing. *Biol. Cybern.* 67, 143–153. doi: 10.1007/BF00201021

Gooch, C. L., Doherty, T. J., Chan, K. M., Bromberg, M. B., Lewis, R. A., Stashuk, D. W., et al. (2014). Motor unit number estimation: a technology and literature review. *Muscle Nerve* 50, 884–893. doi: 10.1002/mus.24442

Higashihara, M., Menon, P., Bos, M., Pavey, N., and Vucic, S. (2020). Reproducibility of motor unit number index and MScanFit motor unit number estimation across intrinsic hand muscles. *Muscle Nerve* 62, 192–200. doi: 10.1002/mus.26839

Jonas, D., Bischoff, C., and Conrad, B. (1999). Infuence of different types of surface electrodes on amplitude, area and duration of the compound muscle action potential. *Clin. Neurophysiol.* 110, 2171–2175. doi: 10.1016/S1388-2457(99)00116-9

Kristensen, R. S., Bostock, H., Tan, S. V., Witt, A., Fuglsang-Frederiksen, A., Qerama, E., et al. (2019). MScanFit motor unit number estimation (MScan) and muscle velocity recovery cycle recordings in amyotrophic lateral sclerosis patients. *Clin. Neurophysiol.* 130, 1280–1288. doi: 10.1016/j.clinph.2019.04.713

Li, X., Zong, Y., Klein, C. S., and Zhou, P. (2018). Motor unit number estimation of human abductor Hallucis from a CMAP scan. *Muscle Nerve* 58, 735–737. doi: 10.1002/mus.26295

Lu, Z., Chen, M., Zong, Y., Huang, C., Li, X., and Zhou, P. (2023a). Sensitivity analysis of CMAP scan step index to different stimulation parameters and examination of muscles affected by spinal cord injury. *IEEE Trans. Biomed. Eng.* 70, 2834–2840. doi: 10.1109/TBME.2023.3266327

Lu, Z., Chen, M., Zong, Y., Li, X., and Zhou, P. (2023b). A novel analysis of CMAP scans from perspective of information theory: CMAP distribution index (CDIX). *I.E.E.E. Trans. Biomed. Eng.* 70, 1182–1188. doi: 10.1109/TBME.2022.3212312

Nandedkar, S. D., Barkhaus, P. E., and Stålberg, E. V. (2022). Analysis of the compound muscle action potential scan: step index (STEPIX) and amplitude index (AMPIX). *Clin. Neurophysiol.* 139, 119–127. doi: 10.1016/j.clinph.2022.04.011

Schneider, C., Svačina, M. K. R., Kohle, F., Sprenger-Svačina, A., Fink, G. R., and Lehmann, H. C. (2023). Motor unit number estimation by MScanFit in myotonic dystrophies. *J. Neurol. Sci.* 451:120728. doi: 10.1016/j.jns.2023.120728

Sleutjes, B. T. H. M., Jacobsen, A. B., Tankisi, H., Sirin, N. G., Oge, A. E., Henderson, R. D., et al. (2021). Advancing disease monitoring of amyotrophic lateral sclerosis with the compound muscle action potential scan. *Clin. Neurophysiol.* 132, 3152–3159. doi: 10.1016/j.clinph.2021.09.014

Sleutjes, B. T. H. M., Maathuis, E. M., van Doorn, P. A., Blok, J. H., and Visser, G. H. (2016). Electrically evoked multiplet discharges are associated with more marked clinical deterioration in motor neuron disease. *Muscle Nerve* 53, 222–226. doi: 10.1002/mus.24700

Sleutjes, B. T. H. M., Montfoort, I., Maathuis, E. M., Drenthen, J., Van Doorn, P. A., Visser, G. H., et al. (2014). CMAP scan discontinuities: automated detection and relation to motor unit loss. *Clin. Neurophysiol.* 125, 388–395. doi: 10.1016/j.clinph.2013.07.016

Song, X., Cui, L., Zong, Y., Chen, M., Lu, Z., Xie, Q., et al. (2023). A single center report of MScanFit motor unit number estimation in five muscles of healthy subjects. *Front. Hum. Neurosci.* 16:1078848. doi: 10.3389/fnhum.2022.1078848

Sørensen, D. M., Bostock, H., Abrahao, A., Alaamel, A., Alaydin, H. C., Ballegaard, M., et al. (2023). Estimating motor unit numbers from a CMAP scan: repeatability study on three muscles at 15 centres. *Clin. Neurophysiol.* 151, 92–99. doi: 10.1016/j.clinph.2023.04.008

Sørensen, D. M., Bostock, H., Ballegaard, M., Fuglsang-Frederiksen, A., Graffe, C. C., Grötting, A., et al. (2022). Assessing inter-rater reproducibility in MScanFit MUNE in a 6-subject, 12-rater "round Robin" setup. *Neurophysiol. Clin.* 52, 157–169. doi: 10.1016/j.neucli.2021.11.002

Stikvoort García, D. J. L., Kovalchuk, M. O., Goedee, H. S., van Schelven, L. J., van den Berg, L. H., Franssen, H., et al. (2022). Motor unit integrity in multifocal motor

neuropathy: a systematic evaluation with CMAP scans. *Muscle Nerve* 65, 317–325. doi: 10.1002/mus.27469

Wee, A. S., and Ashley, R. A. (1990). Relationship between the size of the recording electrodes and morphology of the compound muscle action potentials. *Electromyogr. Clin. Neurophysiol.* 30, 165–168.

Wright, R. D., Sivak, A., Abrahão, A., and Jones, K. E. (2021). Fifty years of motor unit number estimation. *Can. J. Neurol. Sci.* 50, 109–111. doi: 10.1017/cjn.2021.500

Zong, Y., Lu, Z., Chen, M., Deng, L., Xie, Q., and Zhou, P. (2022a). Motor unit number estimation of the second Lumbrical muscle in human hand. *Front. Physiol.* 13:854385. doi: 10.3389/fphys.2022.854385

Zong, Y., Lu, Z., Chen, M., Li, X., Stampas, A., Deng, L., et al. (2021). CMAP scan examination of the first dorsal interosseous muscle after spinal cord injury. *IEEE Trans. Neural Syst. Rehabil. Eng.* 29, 1199–1205. doi: 10.1109/TNSRE.2021.3088061

Zong, Y., Lu, Z., Chen, M., Xie, Q., and Zhou, P. (2022b). MScanFit motor unit number estimation of human anconeus muscle. *Muscle Nerve* 65, 460–463. doi: 10.1002/mus.27487

Zong, Y., Lu, Z., Xu, P., Chen, M., Deng, L., Li, S., et al. (2022c). MScanFit motor unit number estimation of abductor pollicis brevis: findings from different experimental parameters. *Front. Aging Neurosci.* 14:953173. doi: 10.3389/fnagi.2022.953173

Zong, Y., Lu, Z., Zhang, L., Li, X., and Zhou, P. (2020). Motor unit number of the first dorsal interosseous muscle estimated from CMAP scan with different pulse widths and steps. *J. Neural Eng.* 17:014001. doi: 10.1088/1741-2552/ab57cc

frontiers | Frontiers in Neurorobotics

TYPE Perspective
PUBLISHED 20 June 2024
DOI 10.3389/fnbot.2024.1410760

OPEN ACCESS

EDITED BY
Ruoli Wang,
Royal Institute of Technology, Sweden

REVIEWED BY
Kamran Iqbal,
University of Arkansas at Little Rock,
United States

*CORRESPONDENCE
Matthias Voß
matthias.voss@fau.de

RECEIVED 01 April 2024
ACCEPTED 06 June 2024
PUBLISHED 20 June 2024

CITATION
Voß M, Koelewijn AD and Beckerle P (2024) Intuitive and versatile bionic legs: a perspective on volitional control. *Front. Neurorobot.* 18:1410760. doi: 10.3389/fnbot.2024.1410760

Intuitive and versatile bionic legs: a perspective on volitional control

Matthias Voß[1]*, Anne D. Koelewijn[1] and Philipp Beckerle[1,2]

[1]Chair of Autonomous Systems and Mechatronics, Department Electrical Engineering, Friedrich-Alexander-Universität Erlangen-Nürnberg, Erlangen, Germany, [2]Department Artificial Intelligence in Biomedical Engineering, Friedrich-Alexander-Universität Erlangen-Nürnberg, Erlangen, Germany

Active lower limb prostheses show large potential to offer energetic, balance, and versatility improvements to users when compared to passive and semi-active devices. Still, their control remains a major development challenge, with many different approaches existing. This perspective aims at illustrating a future leg prosthesis control approach to improve the everyday life of prosthesis users, while providing a research road map for getting there. Reviewing research on the needs and challenges faced by prosthesis users, we argue for the development of versatile control architectures for lower limb prosthetic devices that grant the wearer full volitional control at all times. To this end, existing control approaches for active lower limb prostheses are divided based on their consideration of volitional user input. The presented methods are discussed in regard to their suitability for universal everyday control involving user volition. Novel combinations of established methods are proposed. This involves the combination of feed-forward motor control signals with simulated feedback loops in prosthesis control, as well as online optimization techniques to individualize the system parameters. To provide more context, developments related to volitional control design are touched on.

KEYWORDS

lower limb prostheses, bionic legs, voluntary control, electromyography, human-in-the-loop optimization

1 Introduction

Research in active lower limb prostheses has recently received increasingly more attention. While passive prostheses only restore and return energy during the movement of the user and semi-active devices modulate this energy return by changing system dynamics, active prostheses are able to provide net positive energy to their wearer. Besides the energetic benefit and more possible movement applications, active leg prostheses have been shown to improve balance (Berry, 2006), functional performance, satisfaction and quality of life compared to passive devices (Burçak et al., 2021). Meanwhile, the design of device controllers that benefit users in locomotor tasks amounts to one of the main challenges in the development of active prostheses (Voloshina and Collins, 2020).

To maximize the potential benefits of active prosthesis hardware in the long term, wearers should be able and eager to use them as often as possible, which necessitates user satisfaction. In general, prosthesis usefulness is strongly associated with embodiment, which itself correlates with user satisfaction (Bekrater-Bodmann, 2021). More specifically, certain aspects to prosthesis usage satisfaction are directly affected by the control architecture in place. Versatility and intuitiveness in leg prostheses support independence, confidence and safety, which are key user desires (Manz et al., 2022).

A lack of voluntary motor functionality can lead to user dissatisfaction (Christ et al., 2011). A recent systematic review identified users' ability to perform different movements as a factor for satisfaction with lower limb prostheses, amongst others (Baars et al., 2018). These relations call for control methods allowing users to modulate the prosthesis behavior according to certain movement tasks and environments or, more universally, at will. We refer to this approach as volitional control.

The most practical and technologically matured, noninvasive way to transfer control commands from the user to a prosthetic device is electromyography (EMG) (Zheng, 2019). People with lower limb amputations are able to volitionally use their residual muscles for EMG-based control (Huang and Huang, 2018, 2019). There are challenges to EMG control, like differing muscle activation profiles between individuals (Huang and Ferris, 2012), as well as varying abilities to volitionally create activation patterns, including unintended coactivation of antagonistic muscles (Huang and Huang, 2019). However, users are able to learn and improve their control capabilities over time (Alcaide-Aguirre et al., 2013; Fleming et al., 2018).

To date, the majority of lower-limb prostheses is autonomously controlled based on state prediction (Fleming et al., 2021), which constitutes a discrepancy between the potential benefit of intuitive volitional control to the users and the control strategies implemented in research and commercial prosthesics. Currently, there are no commercially available devices using EMG (Fleming et al., 2021; Ahkami et al., 2023) and even in research, only half of EMG leg prosthesis are volitionally controllable at most, as recent reviews show (Fleming et al., 2021; Cimolato et al., 2022; Ahkami et al., 2023). Besides numerous experiments involving pointing tasks or virtual lower limbs, only a few studies cover initial trials with volitional control during gait. When considering the enabling of gait the primary function of a leg prosthesis, the state of the art of volitionally controllable leg prostheses is deficient. Therefore, we argue for the development of a universally applicable volitional control architecture suitable for everyday use. For this purpose, this perspective offers an overview of existing control strategies and assesses their respective applicability. The combination of these control approaches is discussed to point out directions in future research in this field. Additionally, other potential methods to advance volitional control, namely restoration of proprioception and human-in-the-loop optimization, are examined.

2 Lower limb prosthesis control strategies

This section summarizes existing control strategies for active lower limb prostheses and discusses their suitability for volitional control to derive the novel control architecture proposed in Section 3. As suggested by Martin et al. (2010), we divide the control approaches in two categories, depending on how they incorporate inputs from the user's nervous system. Interactive extrinsic control (IEC) assigns the prosthesis user immediate and continuous control of the device's behavior, with the commonly used interface being surface EMG from the muscles in the residual limb. In contrast to IEC, computational intrinsic control (CIC) does not receive direct volitional input by the user and instead determines prosthesis movement autonomously (Cimolato et al., 2022). Device-specific low-level controllers setting torque, position, or speed on the prosthetic hardware are not affected by this distinction and not discussed here. The presented categories and their proposed consideration in volitional prosthesis control are shown in Figure 1. The examples mentioned focus on implementations that enable gait, whereas non-weight-bearing tasks and virtual devices are not discussed.

2.1 Interactive extrinsic control (IEC)

Since IEC enables the user to continuously and directly modulate the prosthesis state, its inclusion in a volitional control architecture appears obvious. A general detriment to IEC is its constant reliance on user input. One can assume this increases cognitive user load compared to autonomously controlled devices, but this has yet to be quantified (Fleming et al., 2021). This potential downside applies to both IEC variants presented in the following.

2.1.1 Direct EMG control

Direct EMG control uses mathematical functions to calculate a desired prosthesis state such as joint angle or torque from EMG input, with only a few papers discussing its application for gait. Huang et al. (2014, 2016) used EMG-proportional pressure in artificial pneumatic muscles to control an ankle prosthesis, which allowed level-ground walking under the provision of visual feedback. Other studies implemented direct control with an electromechanical knee prosthesis (Hoover et al., 2012; Dawley et al., 2013). Here, for level-ground walking and stair ascend, the stiffness and equilibrium point of impedance controllers were modulated via recorded EMG signals, producing a compliant volitional position control.

An advantage of direct control is its relatively low computational cost (Ahkami et al., 2023), especially for simple approaches like proportional control. Since the method does not inherently mimic any biological example, it might at times generate unnatural relations between muscle activity and prosthesis behavior (e.g., proportional joint torque), that are hard to learn for users. Though, to point out a clear tendency here, the number of conducted experiments with this approach is too small.

2.1.2 Muscle-model-based EMG control

In muscle-model-based EMG prosthesis control, a simplified simulation of EMG-driven muscles acting on a joint is employed to calculate a resulting joint torque. Wu et al. (2011) presented a simple model with two antagonistic muscles in a knee prosthesis, each consisting of a source of immediate force and one adaptive spring-damper pair in parallel. Here, EMG amplitudes modulated the spring stiffness, damper coefficient, and a proportional force to calculate the desired knee torque. This enabled level-ground walking by an able-bodied individual wearing a prosthesis adapter. Shah et al. (2022) used two Hill-type-muscles driven by gastrocnemius and tibialis anterior EMG recordings to control an ankle prosthesis for a symmetrical balancing task.

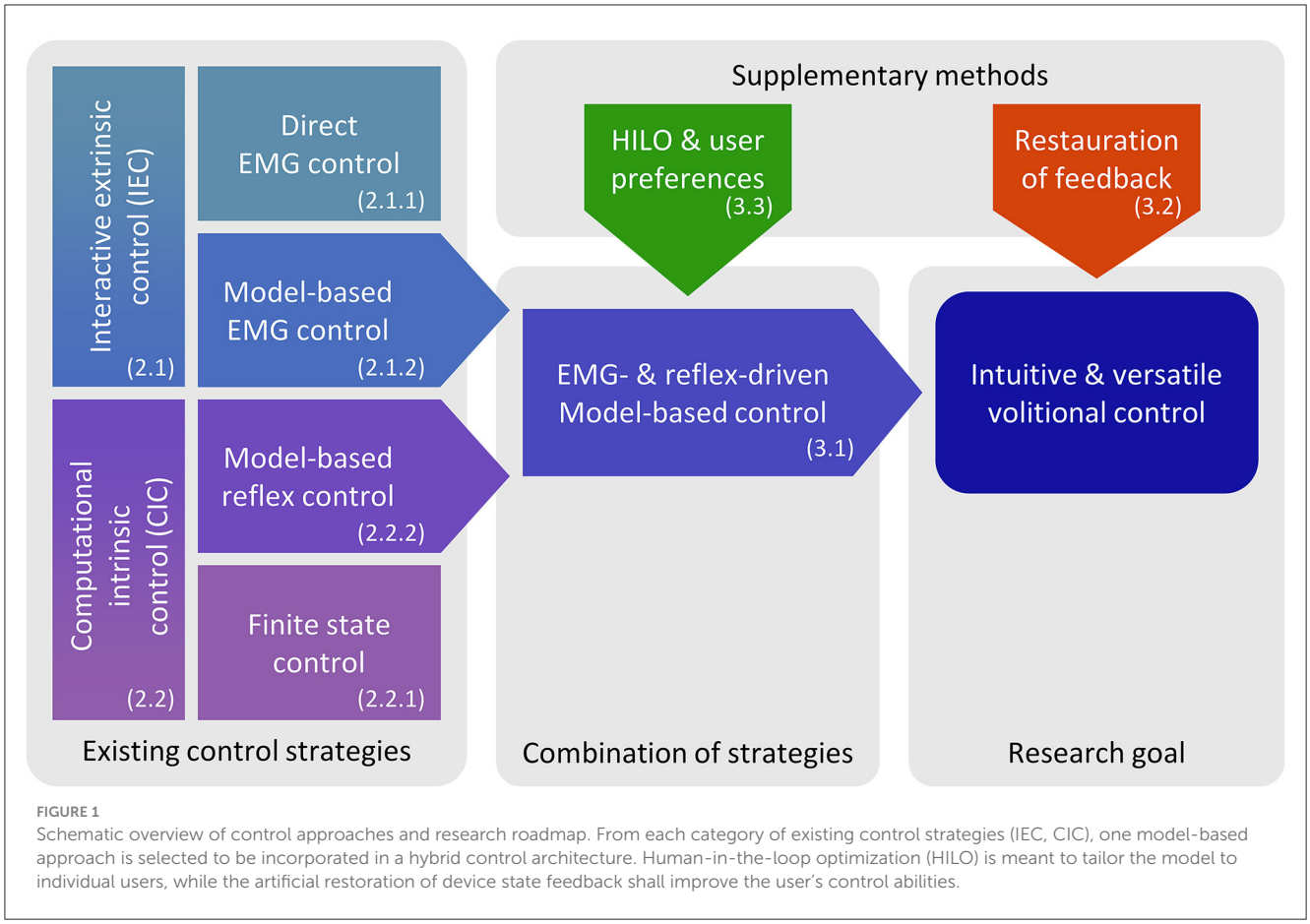

FIGURE 1
Schematic overview of control approaches and research roadmap. From each category of existing control strategies (IEC, CIC), one model-based approach is selected to be incorporated in a hybrid control architecture. Human-in-the-loop optimization (HILO) is meant to tailor the model to individual users, while the artificial restoration of device state feedback shall improve the user's control abilities.

In model-based EMG control, the natural joint behavior depending on muscle activity is emulated and driven by a volitional input. Compared to direct EMG control, a downside of this approach is a rather complex model. This likely leads to increased computational demand and higher numbers of model parameters to be determined.

2.2 Computational intrinsic control (CIC)

The lack of immediate user authority over the device offered by CIC seems to rule this control approach out for volitional control at first glance. We still discuss CIC variants to get a comprehensive view on existing control approaches and evaluate their suitability to maybe be partially incorporated in a volitional approach.

2.2.1 Finite state controllers

Finite state controllers choose between a finite number of operation modes, target trajectories, set points or other system parameters to tackle a given task. To make the system adaptable to changing walking speeds, gait modes or environments, a recognition of gait phases or user intend is required. Besides sensors for non-biosignals like inertial or force sensors, EMG can also be incorporated for this classification task (Cimolato et al., 2022). With modern machine learning approaches, low single-digit percentage classification errors have been achieved (Voloshina and Collins, 2020).

For prosthesis users, classification errors are hard to comprehend and hard to compensate for, since the mapping of EMG input to the prosthesis behavior is a complex black box (Fleming et al., 2021). Depending on their type and timing, these errors can lead to gait instability (Zhang et al., 2015) and therefore to falls. To safely classify thousands of daily steps in everyday use, a near-perfect classification performance is needed. Furthermore, the finite number of operation modes limits the user's ability to intuitively and spontaneously use a prosthesis in varying situations. Therefore, we consider state-dependent controllers not suitable for the volitional control system proposed in Section 3 and do not further discuss them.

2.2.2 Reflex-driven muscle model based control

Reflexive, involuntary responses to stimuli are present in a large variety of human motor tasks and are believed to play a role in able-bodied gait (Kandel et al., 2012). Following preceding simulation studies (Geyer and Herr, 2010), some studies employed muscle and joint models driven by simulated reflexes instead of EMG signals. In this way, walking with an ankle prosthesis was proven possible, while enabling adaption to changes in slope (Eilenberg et al., 2010) and speed (Markowitz et al., 2011). Thatte et al. (2018) extended the concept to a knee and ankle prosthesis. Here, five able-bodied

individuals using an adapter were able to walk with the prosthesis on level-ground. All three studies only implemented reflex control in stance phase and relied on predetermined trajectories during swing.

Like other CIC methods, this control strategy lacks volitional input from the user, and the presented implementations rely on state detection for gait. The reflex models used in the presented papers do not resemble actual biolocial control schemes (Markowitz et al., 2011), as reflexes in the human body are task-dependent and adapt to afferent neural signals from the brain (Kandel et al., 2012). Therefore, more complex reflexive networks with more detailed state distinctions are likely needed to enable different tasks like postural balance or sit-to-stand transitions.

2.3 Hybrid approaches

Some studies combine IEC and CIC elements in hybrid prosthesis control strategies. For stair ascent with a knee prosthesis, Hoover et al. (2013) modulated the stiffness and equilibrium point of an impedance controller via both EMG input and predefined values for stance and swing phases. Wang et al. (2013) used EMG to manipulate plantarflexion force during push-off with an otherwise intrinsic controller in an ankle prosthesis, which enabled level-ground walking. This was adapted to also support stair ambulation by Kannape and Herr (2014). Shu et al. (2022) applied a similar control approach with an offline optimization method to map EMG inputs to the virtual muscles.

Hybrid control approaches allow for some volitional adjustments to the assistance given by the device. Because they do not solely rely on volitional input, they feature a potential reduction in cognitive load compared to full IEC. On the contrary, the presented methods still carry the disadvantages of finite state controllers. They rely on the detection of gait phases and are limited to predetermined movements and activities.

3 Promising research directions

Considering the previously analyzed control strategies, this section proposes future research directions to improve volitional lower limb prosthesis control. This suggestion includes parameterization approaches as well as the restoration of feedback and proprioception to prosthesis users. Figure 2 shows the proposed overall control structure in comparison with the motor control present in a healthy limb.

3.1 Combining EMG input and simulated reflexes

Human motor control signals are believed to consist of feed-forward and feedback components (Kandel et al., 2012). Markowitz et al. (2011) recognize this circumstance, but do not incorporate any user-controllable feed-forward signals in their control approach. Likewise, Shu et al. (2022) call reflexes essential for physiological gait and lament its absence in amputation musculature, but their device control relies on feed-forward signals alone. To our knowledge, the combination of muscle reflexes with feed-forward signals has only been tested in gait simulation, where it improved the model's robustness against perturbations compared to pure reflex control (Haeufle et al., 2018).

To facilitate compliant device behavior while limiting the cognitive demand on the user, we propose the development of a hybrid controller that combines EMG-based volitional input and simulated reflexes for the virtual muscle excitation in a model-based prosthesis control architecture. The structure of the proposed control approach is shown in Figure 2. Via EMG readings from residual muscles, the simulated muscles can be volitionally driven by the user, which subsequently command a desired torque to the prosthesis. Compared to the healthy limb, the afferent signals reporting muscle length (muscle spindles) and force (Golgi tendon organs) as well as cutaneous sensing to the spinal cord and brain (Kandel et al., 2012) are missing. This is substituted by incorporating virtual muscle states as well as sensory signals from the prosthesis hardware into simulated reflexes, which leads to an additional, non-volitional activation of the virtual muscles.

While this combined approach entails a high parameter count, it also allows for extensive individualization. Similar to the simulations conducted by Haeufle et al. (2018), the emphasis could be shifted between reflexes and volitional input by varying signal gains, depending on the wearer and their abilities to cognitively and physically handle the input responsibility. It is important to note that the studies mentioned here and in Section 2.2.2 mostly simulate monosynaptic stretch reflexes with a positive feedback of muscle force. This approach is self-reinforcing and would quickly lead to a maximum contraction of all muscles in a volitionally controllable prosthesis. Therefore, the reflex model needs to be adapted.

3.2 Restoration of feedback

The lack of haptic and proprioceptive sensing in prostheses limits the natural and intuitive movement dexterity of users. Supplementary feedback can improve immediate control performance and promote the learning of internal motor models (Sensinger and Dosen, 2020). Feedback of the device state to the user is suggested to facilitate embodiment, device acceptance and dexterity (Beckerle et al., 2019).

Providing position feedback in an EMG-controlled position tracking task can heavily improve performance. Canino and Fite (2016) demonstrated this in a knee prosthesis with both, static pressure and vibratory feedback. The presented studies examining prosthetic gait did not employ such feedback mechanisms, while some mention the necessity of visual feedback. A completely different approach to proprioception restoration is the agonist-antagonist myoneural interface, which aims to recreate natural co-dependencies by attaching residual muscles to their respective antagonist in the residual limb (Clites et al., 2018). In addition to improved volitional muscle activation, this also enables the introduction of perceived passive movement by electrically stimulating the muscles. This surgical construct has enabled great

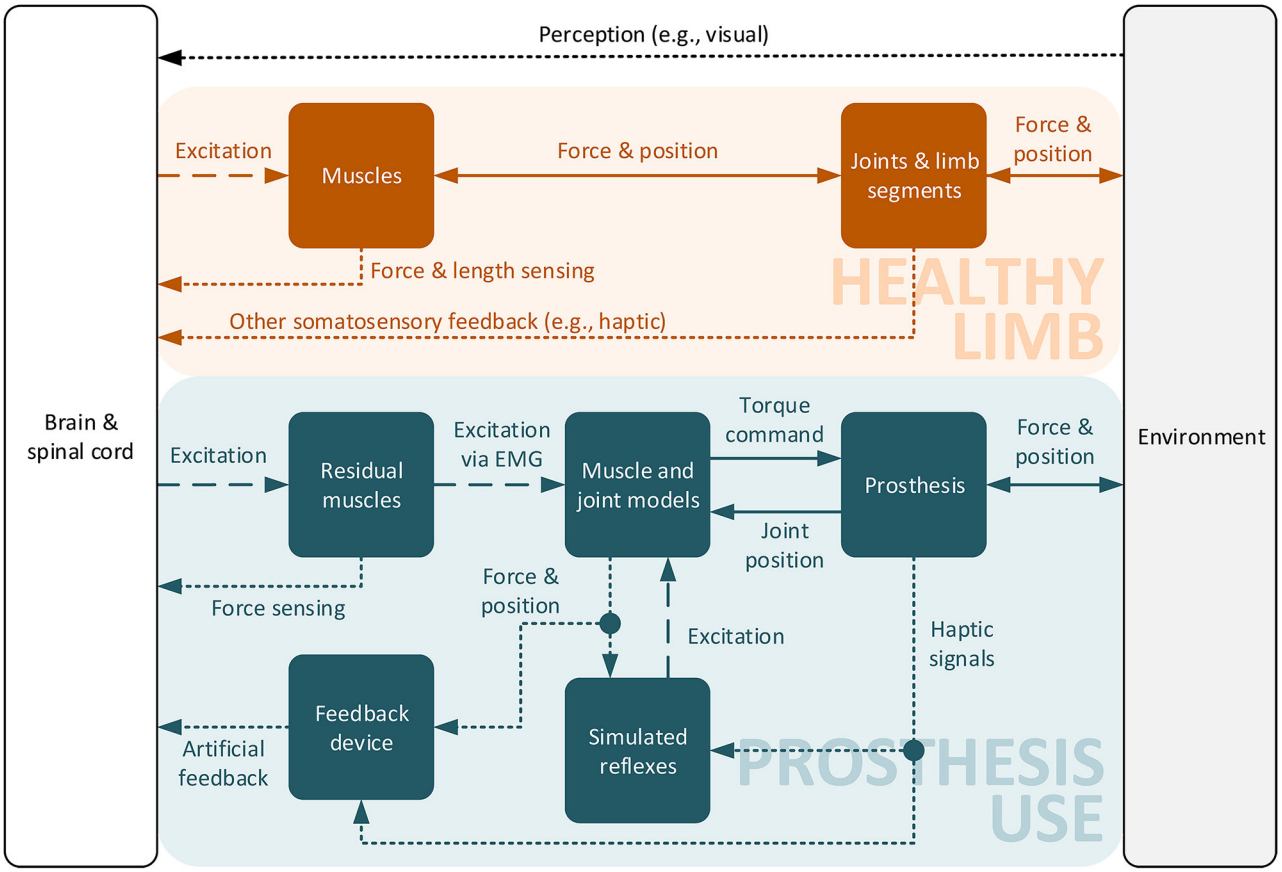

FIGURE 2
Diagram of control and excitation signals in the proposed control structure compared to a healthy limb. Elements and signals are orange for a healthy limb and blue in case of using a prosthesis. Black elements are present in both. Solid lines depict physical interaction or its virtual emulation. In the same way, dashed and dotted lines show efferent and afferent neural signals or their simulation.

control performance for individuals with an amputation, including the presented hybrid approach by Shu et al. (2022).

Given the discovered benefits of prosthesis state feedback to the user, it should receive more attention in lower-limb prosthesis research. Since advanced and novel surgery procedures will likely not be available to or suitable for everyone, feedback mechanisms built into devices need to be investigated and developed further. Current solutions for artificial feedback do not match natural fidelity, while selecting the appropriate feedback signals remains a challenge (Seminara et al., 2023). As pictured by Beckerle et al. (2017), the form and extent of the provided artificial feedback should be thoroughly assessed to ensure actual improvements in a given task. To enable conscious reactions to changes in the artificial limb state, the structure given in Figure 2 contains a feedback device, which receives the same simulated and sensor feedback as the artificial reflexes. It is ceded to future research to design the feedback derived from these signals.

3.3 Human-in-the-loop optimization

Finding control parameters is a key challenge and choosing universal parameters for multiple users often does not appear suitable. The assistance required for a certain objective varies between individual users (Koller et al., 2015). People respond differently to active assistance and small changes can have large effects on energy expenditure (Voloshina and Collins, 2020). Thatte et al. (2018) observed that individual users prefer different gait characteristics and control parameter sets and called for methods to individualize prosthesis control.

Human-in-the-loop optimization (HILO) is a procedure of varying system parameters during user experiments to optimize for a given objective. It has been shown to successfully improve performance for exoskeletons and prostheses in a variety of tasks (Díaz et al., 2022) and offers the possibility to individualize prosthesis control (Voloshina and Collins, 2020). A common goal is the reduction of metabolic cost, which can be estimated from respiratory data (Zhang et al., 2017). An example for kinematic objectives is gait symmetry (Wen et al., 2020), which is especially interesting in the case of unilateral amputations. While HILO has been tested on a variety of control approaches for assistive devices, the combination with volitional control in lower-limb prostheses has yet to be realized.

We propose the use of HILO to determine control parameters that suit the individual needs of prosthesis users. Besides helping to manage large parameter spaces, HILO allows reseachers

to pick different optimization objectives for different users or usecases. This can include desired gait kinetics, gait symmetry, metabolic cost, or user comfort and preference. For the last two, manual user input can be incorporated (Ingraham et al., 2020). Likewise, HILO allows to optimize for different tasks, like walking, stair-ascent and -descent or standing balance, depending on what is considered most important or most challenging by the user. To find initial parameters, anthropometric features and isometric torque and EMG measurements (Durandau et al., 2019) or predictive simulations of the human-machine interaction (Koelewijn and Selinger, 2022) can be used.

3.4 Consideration of model complexity

The studies on model-based EMG control mentioned in Section 2.1.2 all base their control on two simulated muscles in one degree of freedom (DoF) prostheses (plantar-/dorsiflexion for the ankle, flexion/extension for the knee). More elaborate models find use in CIC approaches (Markowitz et al., 2011; Thatte et al., 2018) and are being investigated for volitional control (Cimolato et al., 2020), but are not yet employed. Considering the example of an ankle prosthesis, active inversion/eversion was shown to reduce metabolic (Kim and Collins, 2017) and the lack of this DoF limits the adaption to uneven grounds. The use of only one plantarflexor muscle neglects the influence of the knee angle on the gastrocnemius length and hence the joint torque.

Challenging this common level of modeling depth could reveal potential benefits of more complex musculoskeletal models, though increase computational demands and parameter count. Therefore, the benefit of modeling certain biological anatomical features should be assessed and evaluated against the associated costs.

4 Conclusion

While active lower limb prostheses offer a multitude of potential benefits to users, their control remains challenging. In this perspective, we present arguments for the development of prostheses that are intuitively and volitionally controllable. Existing control approaches are summarized and evaluated regarding their suitability for that objective, laying out their advantages and disadvantages.

Overall, we propose the combination of EMG-based volitional control signals with simulated muscle reflexes in a model-based high level prosthesis control, aided by a feedback of the device's state to the user. We argue to strive for individualizing the assistance given by this control scheme to individual users and their respective needs. To this end and to tackle the potentially large number of model parameters influencing the control behavior, we argue for the use of HILO. We believe that this combination of methods will substantially advance the field of volitional control of lower limb prostheses and facilitate the development of intuitive to use leg prostheses in the future.

Data availability statement

The original contributions presented in the study are included in the article/supplementary material, further inquiries can be directed to the corresponding author.

Author contributions

MV: Conceptualization, Investigation, Visualization, Writing – original draft, Writing – review & editing. AK: Writing – review & editing. PB: Conceptualization, Supervision, Writing – review & editing.

Funding

The author(s) declare that financial support was received for the research, authorship, and/or publication of this article. This research was conducted in the context of setting up the Interactive Gait Assistance Experience Lab supported by a major research instrumentation grant of the German Research Foundation (DFG; INST 90/1477-1 FUGG).

Acknowledgments

We thank Daniel Häufle for reviewing the paper concept and inspiring discussions.

Conflict of interest

The authors declare that the research was conducted in the absence of any commercial or financial relationships that could be construed as a potential conflict of interest.

The author(s) declared that they were an editorial board member of Frontiers, at the time of submission. This had no impact on the peer review process and the final decision.

Publisher's note

References

Ahkami, B., Ahmed, K., Thesleff, A., Hargrove, L., and Ortiz-Catalan, M. (2023). Electromyography-based control of lower limb prostheses: a systematic review. *IEEE Trans. Med. Robot. Bionics* 5, 547–562. doi: 10.1109/TMRB.2023.3282325

Alcaide-Aguirre, R. E., Morgenroth, D. C., and Ferris, D. P. (2013). Motor control and learning with lower-limb myoelectric control in amputees. *J. Rehabil. Res. Dev.* 50:687. doi: 10.1682/JRRD.2012.06.0115

Baars, E. C., Schrier, E., Dijkstra, P. U., and Geertzen, J. H. B. (2018). Prosthesis satisfaction in lower limb amputees: a systematic review of associated factors and questionnaires. *Medicine* 97:e12296. doi: 10.1097/MD.0000000000012296

Beckerle, P., Castellini, C., and Lenggenhager, B. (2019). Robotic interfaces for cognitive psychology and embodiment research: a research roadmap. *WIREs Cognit. Sci.* 10:e1486. doi: 10.1002/wcs.1486

Beckerle, P., Salvietti, G., Unal, R., Prattichizzo, D., Rossi, S., Castellini, C., et al. (2017). A human-robot interaction perspective on assistive and rehabilitation robotics. *Front. Neurorobot.* 11:24. doi: 10.3389/fnbot.2017.00024

Bekrater-Bodmann, R. (2021). Factors associated with prosthesis embodiment and its importance for prosthetic satisfaction in lower limb amputees. *Front. Neurorobot.* 14:604376. doi: 10.3389/fnbot.2020.604376

Berry, D. (2006). Microprocessor prosthetic knees. *Phys. Med. Rehabil. Clin. N. Am.* 17, 91–113. doi: 10.1016/j.pmr.2005.10.006

Burçak, B., Kesikburun, B., Köseoğlu, B. F., Öken, Ö., and Doğan, A. (2021). Quality of life, body image, and mobility in lower-limb amputees using high-tech prostheses: a pragmatic trial. *Ann. Phys. Rehabil. Med.* 64:101405. doi: 10.1016/j.rehab.2020.03.016

Canino, J. M., and Fite, K. B. (2016). "Haptic feedback in lower-limb prosthesis: Combined haptic feedback and EMG control of a powered prosthesis," in *2016 IEEE EMBS International Student Conference (ISC)* (Ottawa, ON: IEEE), 1–4.

Christ, O., Beckerle, P., Rinderknecht, S., and Vogt, J. (2011). Usability, satisfaction and appearance while using lower limb prostheses: implications for the future. *Neurosci. Lett.* 500:e50. doi: 10.1016/j.neulet.2011.05.214

Cimolato, A., Driessen, J. J. M., Mattos, L. S., De Momi, E., Laffranchi, M., and De Michieli, L. (2022). EMG-driven control in lower limb prostheses: A topic-based systematic review. *J. Neuroeng. Rehabil.* 19:43. doi: 10.1186/s12984-022-01019-1

Cimolato, A., Milandri, G., Mattos, L. S., De Momi, E., Laffranchi, M., and De Michieli, L. (2020). "Hybrid machine learning-neuromusculoskeletal modeling for control of lower limb prosthetics," in *2020 8th IEEE RAS/EMBS International Conference for Biomedical Robotics and Biomechatronics (BioRob)* (New York, NY: IEEE), 557–563.

Clites, T. R., Carty, M. J., Ullauri, J. B., Carney, M. E., Mooney, L. M., Duval, J.-F., et al. (2018). Proprioception from a neurally controlled lower-extremity prosthesis. *Sci. Transl. Med.* 10:eaap8373. doi: 10.1126/scitranslmed.aap8373

Dawley, J. A., Fite, K. B., and Fulk, G. D. (2013). "EMG control of a bionic knee prosthesis: Exploiting muscle co-contractions for improved locomotor function," in *2013 IEEE 13th International Conference on Rehabilitation Robotics (ICORR)* (Seattle, WA: IEEE), 1–6.

Díaz, M. A., Voß, M., Dillen, A., Tassignon, B., Flynn, L., Geeroms, J., et al. (2022). Human-in-the-loop optimization of wearable robotic devices to improve human-robot interaction: a systematic review. *IEEE Trans. Cybernet.* 53, 7483–7496. doi: 10.1109/TCYB.2022.3224895

Durandau, G., Farina, D., Asín-Prieto, G., Dimbwadyo-Terrer, I., Lerma-Lara, S., Pons, J. L., et al. (2019). Voluntary control of wearable robotic exoskeletons by patients with paresis via neuromechanical modeling. *J. Neuroeng. Rehabil.* 16:91. doi: 10.1186/s12984-019-0559-z

Eilenberg, M. F., Geyer, H., and Herr, H. (2010). Control of a powered ankle-foot prosthesis based on a neuromuscular model. *IEEE Trans. Neural Syst. Rehabili. Eng.* 18, 164–173. doi: 10.1109/TNSRE.2009.2039620

Fleming, A., Huang, S., and Huang, H. (2018). "Coordination of voluntary residual muscle contractions in transtibial amputees: a pilot study," in *2018 40th Annual International Conference of the IEEE Engineering in Medicine and Biology Society (EMBC)* (Honolulu, HI: IEEE), 2128–2131.

Fleming, A., Stafford, N., Huang, S., Hu, X., Ferris, D. P., and Huang, H. H. (2021). Myoelectric control of robotic lower limb prostheses: a review of electromyography interfaces, control paradigms, challenges and future directions. *J. Neural Eng.* 18:041004. doi: 10.1088/1741-2552/ac1176

Geyer, H., and Herr, H. (2010). A muscle-reflex model that encodes principles of legged mechanics produces human walking dynamics and muscle activities. *IEEE Trans. Neural Syst. Rehabil. Eng.* 18, 263–273. doi: 10.1109/TNSRE.2010.2047592

Haeufle, D. F. B., Schmortte, B., Geyer, H., Müller, R., and Schmitt, S. (2018). The benefit of combining neuronal feedback and feed-forward control for robustness in step down perturbations of simulated human walking depends on the muscle function. *Front. Comput. Neurosci.* 12:80. doi: 10.3389/fncom.2018.00080

Hoover, C. D., Fulk, G. D., and Fite, K. B. (2012). The design and initial experimental validation of an active myoelectric transfemoral prosthesis. *J. Med. Device.* 6:011005. doi: 10.1115/1.4005784

Hoover, C. D., Fulk, G. D., and Fite, K. B. (2013). Stair ascent with a powered transfemoral prosthesis under direct myoelectric control. *IEEE/ASME Trans. Mechatron.* 18, 1191–1200. doi: 10.1109/TMECH.2012.2200498

Huang, S., and Ferris, D. (2012). Muscle activation patterns during walking from transtibial amputees recorded within the residual limb-prosthetic interface. *J. Neuroeng. Rehabil.* 9:55. doi: 10.1186/1743-0003-9-55

Huang, S., and Huang, H. (2018). Voluntary control of residual antagonistic muscles in transtibial amputees: feedforward ballistic contractions and implications for direct neural control of powered lower limb prostheses. *IEEE Trans. Neural Syst. Rehabil. Eng.* 26, 894–903. doi: 10.1109/TNSRE.2018.2811544

Huang, S., and Huang, H. (2019). Voluntary control of residual antagonistic muscles in transtibial amputees: reciprocal activation, coactivation, and implications for direct neural control of powered lower limb prostheses. *IEEE Trans. Neural Syst. Rehabil. Eng.* 27, 85–95. doi: 10.1109/TNSRE.2018.2885641

Huang, S., Wensman, J. P., and Ferris, D. P. (2014). An experimental powered lower limb prosthesis using proportional myoelectric control. *J. Med. Device.* 8:024501. doi: 10.1115/1.4026633

Huang, S., Wensman, J. P., and Ferris, D. P. (2016). Locomotor adaptation by transtibial amputees walking with an experimental powered prosthesis under continuous myoelectric control. *IEEE Trans. Neural Syst. Rehabil. Eng.* 24, 573–581. doi: 10.1109/TNSRE.2015.2441061

Ingraham, K. A., Remy, C. D., and Rouse, E. J. (2020). "User preference of applied torque characteristics for bilateral powered ankle exoskeletons," in *2020 8th IEEE RAS/EMBS International Conference for Biomedical Robotics and Biomechatronics (BioRob)* (New York City, NY: IEEE), 839–845.

Kandel, E. R., Schwartz, J. H., Jessell, T. M., Siegelbaum, S. A., and Hudspeth, A. J. (2012). *Principles of Neural Science*. New York: McGraw-Hill Education Ltd.

Kannape, O., and Herr, H. (2014). Volitional control of ankle plantar flexion in a powered transtibial prosthesis during stair-ambulation. *Annu. Int. Conf. IEEE Eng. Med. Biol. Soc.* 2014, 1662–1665. doi: 10.1109/EMBC.2014.6943925

Kim, M., and Collins, S. H. (2017). Step-to-step ankle inversion/eversion torque modulation can reduce effort associated with balance. *Front. Neurorobot.* 11:62. doi: 10.3389/fnbot.2017.00062

Koelewijn, A. D., and Selinger, J. C. (2022). Predictive simulations to replicate human gait adaptations and energetics with exoskeletons. *IEEE Trans. Neural Syst. Rehabil. Eng.* 30, 1931–1940. doi: 10.1109/TNSRE.2022.3189038

Koller, J., Jacobs, D., Ferris, D., and Remy, C. (2015). Learning to walk with an adaptive gain proportional myoelectric controller for a robotic ankle exoskeleton. *J. Neuroeng. Rehabil.* 12:5. doi: 10.1186/s12984-015-0086-5

Manz, S., Valette, R., Damonte, F., Avanci Gaudio, L., Gonzalez-Vargas, J., Sartori, M., et al. (2022). A review of user needs to drive the development of lower limb prostheses. *J. Neuroeng. Rehabil.* 19, 119. doi: 10.1186/s12984-022-01097-1

Markowitz, J., Krishnaswamy, P., Eilenberg, M., Endo, K., Barnhart, C., and Herr, H. (2011). Speed adaptation in a powered transtibial prosthesis controlled with a neuromuscular model. Philosophical transactions of the Royal Society of London. *Series B, Biol. Sci.* 366, 1621–1631. doi: 10.1098/rstb.2010.0347

Martin, J., Pollock, A., and Hettinger, J. (2010). Microprocessor lower limb prosthetics: review of current state of the art. *JPO: J. Prosthet. Orthot.* 22:183. doi: 10.1097/JPO.0b013e3181e8fe8a

Seminara, L., Dosen, S., Mastrogiovanni, F., Bianchi, M., Watt, S., Beckerle, P., et al. (2023). A hierarchical sensorimotor control framework for human-in-the-loop robotic hands. *Sci. Robot.* 8:eadd5434. doi: 10.1126/scirobotics.add5434

Sensinger, J. W., and Dosen, S. (2020). A review of sensory feedback in upper-limb prostheses from the perspective of human motor control. *Front. Neurosci.* 14:345. doi: 10.3389/fnins.2020.00345

Shah, C., Fleming, A., Nalam, V., Liu, M., and Huang, H. H. (2022). "Design of EMG-driven musculoskeletal model for volitional control of a robotic ankle prosthesis," in *2022 IEEE/RSJ International Conference on Intelligent Robots and Systems (IROS)* (Kyoto: IEEE), 12261–12266.

Shu, T., Shallal, C., Chun, E., Shah, A., Bu, A., Levine, D., et al. (2022). Modulation of prosthetic ankle plantarflexion through direct myoelectric control of a subject-optimized neuromuscular model. *IEEE Robot. Automat. Lett.* 7, 7620–7627. doi: 10.1109/LRA.2022.3183762

Thatte, N., Duan, H., and Geyer, H. (2018). "A method for online optimization of lower limb assistive devices with high dimensional parameter spaces," in *2018 IEEE International Conference on Robotics and Automation (ICRA)* (Brisbane, QLD: IEEE), 5380–5385.

Voloshina, A. S., and Collins, S. H. (2020). "Lower limb active prosthetic systems—overview," in *Wearable Robotics* (London: Elsevier), 469–486.

Wang, J., Kannape, O. A., and Herr, H. M. (2013). "Proportional EMG control of ankle plantar flexion in a powered transtibial prosthesis," in *2013 IEEE 13th International Conference on Rehabilitation Robotics (ICORR)* (Seattle, WA. IEEE).

Wen, Y., Li, M., Si, J., and Huang, H. (2020). Wearer-prosthesis interaction for symmetrical gait: a study enabled by reinforcement learning prosthesis control. *IEEE Trans. Neural Syst. Rehabil. Eng.* 28, 904–913. doi: 10.1109/TNSRE.2020.2979033

Wu, S.-K., Waycaster, G., and Shen, X. (2011). Electromyography-based control of active above-knee prostheses. *Control Eng. Pract.* 19, 875–882. doi: 10.1016/j.conengprac.2011.04.017

Zhang, F., Liu, M., and Huang, H. (2015). Effects of locomotion mode recognition errors on volitional control of powered above-knee prostheses. *IEEE Trans. Neural Syst. Rehabil. Eng.* 23, 64–72. doi: 10.1109/TNSRE.2014.2327230

Zhang, J., Fiers, P., Witte, K. A., Jackson, R. W., Poggensee, K. L., Atkeson, C. G., et al. (2017). Human-in-the-loop optimization of exoskeleton assistance during walking. *Science* 356, 1280–1284. doi: 10.1126/science.aal5054

Zheng, X. (2019). *Neural Interface: Frontiers and Applications, volume 1101 of Advances in Experimental Medicine and Biology*. Singapore: Springer Singapore.

frontiers | Frontiers in Neuroscience

TYPE Original Research
PUBLISHED 22 July 2024
DOI 10.3389/fnins.2024.1425183

OPEN ACCESS

EDITED BY
Yingbai Hu,
The Chinese University of Hong Kong, Hong Kong SAR, China

REVIEWED BY
Yu Song,
University of Kansas, United States
Xiaoyu Wu,
National University of Singapore, Singapore
Zixiang Gao,
Eötvös Loránd University, Hungary

*CORRESPONDENCE
Jing Wen Pan
✉ nie173748@e.ntu.edu.sg

RECEIVED 29 April 2024
ACCEPTED 11 July 2024
PUBLISHED 22 July 2024

CITATION
Pan JW, Sidarta A, Wu T-L, Kwong WHP, Ong PL, Tay MRJ, Phua MW, Chong WB, Ang WT and Chua KSG (2024) Unraveling stroke gait deviations with movement analytics, more than meets the eye: a case control study.
Front. Neurosci. 18:1425183.
doi: 10.3389/fnins.2024.1425183

Unraveling stroke gait deviations with movement analytics, more than meets the eye: a case control study

Jing Wen Pan[1,2]*, Ananda Sidarta[1], Tsung-Lin Wu[1], Wai Hang Patrick Kwong[3], Poo Lee Ong[4], Matthew Rong Jie Tay[4,5], Min Wee Phua[4], Wei Binh Chong[4], Wei Tech Ang[1,5,6] and Karen Sui Geok Chua[1,4,5]

[1]Rehabilitation Research Institute of Singapore, Nanyang Technological University, Singapore, Singapore, [2]Department of Sports Science and Physical Education, Chinese University of Hong Kong, Hong Kong, Hong Kong SAR, China, [3]Department of Rehabilitation Sciences, Hong Kong Polytechnic University, Kowloon, Hong Kong SAR, China, [4]Institute of Rehabilitation Excellence (IREx), Tan Tock Seng Hospital Rehabilitation Centre, Singapore, Singapore, [5]Lee Kong Chian School of Medicine, Nanyang Technological University, Singapore, Singapore, [6]School of Mechanical and Aerospace Engineering, Nanyang Technological University, Singapore, Singapore

Background: This study aimed to identify and quantify the kinematic and kinetic gait deviations in post-stroke hemiplegic patients with matched healthy controls using Statistical Parametric Mapping (SPM).

Methods: Fifteen chronic stroke patients [4 females, 11 males; age 53.7 (standard deviation 12.2) years; body mass 65.4 (10.4) kg; standing height 168.5 (9.6) cm] and 15 matched healthy controls [4 females, 11 males; age 52.9 (11.7) years; body weight 66.5 (10.7) years; standing height 168.3 (8.8) cm] were recruited. In a 10-m walking task, joint angles, ground reaction forces (GRF), and joint moments were collected, analyzed, and compared using SPM for an entire gait cycle.

Results: Generally, when comparing the stroke patients' affected (hemiplegic) and less-affected (contralateral) limbs with the control group, SPM identified significant differences in the late stance phase and early swing phase in the joint angles and moments in bilateral limbs (all $p < 0.005$). In addition, the vertical and anteroposterior components of GRF were significantly different in various periods of the stance phase (all $p < 0.005$), while the mediolateral component showed no differences between the two groups.

Conclusion: SPM was able to detect abnormal gait patterns in both the affected and less-affected limbs of stroke patients with significant differences when compared with matched controls. The findings draw attention to significant quantifiable gait deviations in the less-affected post-stroke limb with the potential impact to inform gait retraining strategies for clinicians and physiotherapists.

KEYWORDS

biomechanics, gait analysis, Statistical Parametric Mapping, mobility, kinematic, kinetic, hemiplegia

1 Introduction

Gait impairments affect more than 70% of stroke survivors, who usually exhibit hemiparetic patterns of weakness (Lawrence et al., 2001). A stroke survivor's ability to independently ambulate a distance of 10 m is indicative of lower limb function and overall motor performance (Kwakkel et al., 2017), and walking speed is often used to evaluate gait performance (Kollen et al., 2006). Furthermore, functional assessments have been applied clinically to evaluate gait performance, lower extremity joint strength, and muscle force (Goldie et al., 1996; Kollen et al., 2006; Smith et al., 2017; Selves et al., 2020). To better characterize post-stroke hemiplegic gait, biomechanical measurements have been extensively conducted. Generally, stroke survivors had a slower walking speed (Tamaya et al., 2020) compared with the controls. In addition, joint range of motion (ROM) or maximum joint angles of the affected limb were smaller in multiple periods in a gait cycle (Tamaya et al., 2020; Nesi et al., 2023). While the existing literature focuses on the affected limb displaying abnormal movement patterns, specific descriptions of the kinematics or kinetics of the contralateral (less-affected) limb are sparse. Given the possible maladaptation of the less-affected limb, precise measurements may provide valuable insights towards understanding the gait patterns (Patterson et al., 2008).

Recent research has highlighted the significance of correctly measuring the nature of impairment and disability in heterogenous stroke populations, intending to prescribe individualized and effective treatments (French et al., 2022). Recent technologies, such as motion capture systems, can systematically examine gait deviations and track rehabilitation outcomes objectively and accurately. While the abovementioned studies have examined the discrete (zero-dimensional, 0D) variables in stroke survivors using instrumented gait analysis systems or motion capture devices (Teixeira-Salmela et al., 2001; Bijleveld-Uitman et al., 2013; Tamaya et al., 2020; Nesi et al., 2023), information about the time-history of these biomechanical variables in a full gait cycle is unclear.

Statistical Parametric Mapping (SPM), as a statistical analysis tool, is able to detect differences in one-dimensional (1D) datasets (e.g., time-varying waveforms for forces, joint angles, joint moments, and electromyography amplitudes) between two or more conditions/groups (Pataky, 2010, 2012). This method has been applied in gait analysis for able-bodied and athletic populations (Mei et al., 2019; Gao et al., 2020), however, data pertaining to stroke gait are sparse. A recent study examined the gait variables using SPM in hemiplegic gait, and observed greater thorax flexion/extension angle during stance phase and greater thorax internal/external rotation angle during the terminal stance phase in the stroke group than the control group (Tamaya et al., 2020).

In gait analysis, a gait cycle has been usually treated as an entire phase from a heel strike (initial contact) of one foot to the next of the same foot, labeled temporally as 0–100%. In the literature, some found significant differences and interpreted the results into certain periods, e.g., 'during the pre-swing and initial swing phases (55.2–66.5%)' (Fernández-Vázquez et al., 2023) and 'terminal-stance phase (31–50%)' (Park and Yoon, 2021). They may have accepted the fixed cut-off value of 60% to split an entire gait cycle (stance phase: 0–60%, swing phase: 60–100%). While this is valid for a normal population, it can be problematic for stroke survivors, who usually display individual differences in gait impairments, including prolonged stance phase and a higher ratio of stance-to-swing duration (Olney and Richards, 1996). Hence, splitting an entire gait cycle is warranted in SPM analysis (Tamaya et al., 2020), which may provide more focused information regarding abnormal gait patterns. This present study, therefore, aimed to apply SPM to compare the biomechanical variables of both the affected and less-affected limbs in the stance and swing phases of a gait cycle during a 10-m walking task between the stroke and control groups. It was hypothesized that stroke patients' both limbs would exhibit different biomechanics compared with the control group.

2 Method

2.1 Study design and setting

This was a cross-sectional, case control study, comparing the gait patterns of a group of chronic stroke patients with an equal number of matched healthy controls (trial registered with www.clinicaltrials.gov, NCT04169594). The latter comprised retrospective data from an Asian-centric movement database of activities of daily living (ADLs) (Liang et al., 2020). The measurements for both the stroke group and control group (the database) were conducted in the same gait laboratory. Stroke participants were referred from an ambulatory rehabilitation clinic of a public rehabilitation hospital.

2.2 Participants

All methods of this study were performed in accordance with the Declaration of Helsinki and the ethical approvals were granted by the National Healthcare Group Domain Specific Review Board, Singapore (DSRB reference number: NHG DSRB 2019/00879). The study was registered with www.clinicaltrials.gov, NCT04169594. All participants provided written informed consent. All stroke participants had a history of stroke with a duration exceeding 6 months, and their minimal ambulatory status was indicated by a Functional Ambulation Category (FAC) score (Holden et al., 1984) greater than 4. The detailed inclusion/exclusion criteria can be found in the Supplementary material. This study recruited 15 stroke patients with 1 data point (Table 1, stroke group). The recruitment flowchart (Supplementary Figure S1) and individual demographic and clinical characteristics for the stroke group (Supplementary Table S1). For each stroke patient, one healthy participant, matched by age, gender, height, body mass, and ethnicity, was selected for analysis (Table 1, control group). The matching method was conducted based on the weighted nearest neighbors-based algorithm (Szekér and Vathy-Fogarassy, 2020).

2.3 Data acquisition

All 15 stroke patients and 15 control participants were instructed to perform a 10-m walk (Liang et al., 2020) at a comfortable speed, whereby the data of the 15 controls were retrospectively collected. Only the trials with sufficient marker trajectories and the entire foot planting on the force platforms were used for analysis. The mean (standard deviation) speeds were 0.90 (0.24) m/s for the stroke group

TABLE 1 Participants' physical characteristics and demographic information ($n = 30$).

	Stroke	Control	*p* value
n	Females ($n = 4$)	Females ($n = 4$)	--
	Males ($n = 11$)	Males ($n = 11$)	--
Ethnicity	Chinese ($n = 12$)	Chinese ($n = 14$)	--
	Indian ($n = 1$)	Indian ($n = 1$)	--
	Others** ($n = 2$)	Others ($n = 0$)	--
Age (years)	53.7 (12.2)	52.9 (11.7)	0.844
Body mass (kg)	65.4 (10.4)	66.5 (10.7)	0.764
Standing height (cm)	168.5 (9.6)	168.3 (8.8)	0.936
Body mass index (kg/m^2)	22.9 (2.3)	23.4 (2.1)	0.562
Stroke side*	Left ($n = 5$)	--	--
	Right ($n = 10$)	--	--
Stroke diagnosis	Hemorrhage ($n = 7$)	--	--
	Infarct ($n = 8$)	--	--

*Stroke side refers to the body side affected (paretic side). Data are expressed as mean (standard deviation). Differences between the stroke group and control group were compared using independent *t*-tests. **Others: Myanmarese ($n = 1$) and Nepalese ($n = 1$).

and 1.62 (0.27) m/s for the control group, respectively. A certified physiotherapist was present with all 15 stroke participants throughout all trials but did not need to assist them. Participants were able to walk independently with their own footwear and lower limb orthotics (e.g., ankle foot orthoses) as needed.

To facilitate data collection, a 3D motion capture system with 16 two-megapixel Miqus M3 cameras (200 Hz, Qualisys AB, Göteborg, Sweden) was employed with a modified Calibrated Anatomical System Technique (CAST) marker set (Liang et al., 2020). There were 30 retro-reflective markers (12.5 mm) placed on the anatomical landmarks on the trunk, hip, and both lower limbs, and 16 markers as the tracking markers (4 on each of the 4 marker clusters) on the thighs and shanks bilaterally (Liang et al., 2020). Two adjacent force platforms (2000 Hz, type 9260AA6, Kistler Instruments AG, Winterthur, Switzerland) were synchronized with the Qualisys system to record ground reaction forces (GRF). Kinematic data were identified for both lower limbs for the stroke group and control group, and kinematic data were obtained for the torso.

2.4 Data analyses

Raw marker trajectories and GRF data were low-pass filtered using a fourth-order Butterworth filter at the cut-off frequencies of 15 Hz (Alhossary et al., 2022) and 50 Hz, respectively on Visual3D (v2021.04.1, C-Motion Inc., Germantown, MD, United States). For each foot, the first initial contact and foot-off events used for analysis were determined according to the vertical GRF threshold of 20 N (Park and Yoon, 2021). As the subsequent initial contact occurred when the foot stepped out of the force platforms, it was determined based on the heel marker trajectories (Tamaya et al., 2020). Two sub-phases in a gait cycle, namely stance and swing phases, were subsequently obtained. Biomechanical variables, including GRF, joint angles, and joint moments, were then calculated using the data obtained through the 3D motion capture system and force platforms, and exported into three planes, respectively, i.e., sagittal (e.g., flexion/extension), frontal (e.g., adduction/abduction), and transverse planes (e.g., internal/external rotation). Joint angles were calculated as Euler angles in accordance with a Cardan rotation sequence of "X-Y-Z" (Cole et al., 1993; Wu et al., 2002). Torso angle was computed as the thorax segment with respect to the pelvis. Due to the stroke impacting one body side, the torso movements are usually asymmetric among stroke patients during ambulation (Van Criekinge et al., 2017), and hence, the torso angle was only analyzed for the gait cycle of the affected limb (Yen et al., 2019). For example, if a stroke patient had the left limb paretic, the torso angle was obtained in the stance and swing phases of the left leg. GRF data were normalized to the individual body weight (N/N), and joint moments were normalized to the individual body mass (Nm/kg) (Park and Yoon, 2021).

2.5 Statistical analyses

All kinematic and kinetic data were time normalized to 101 data points for each of the stance and swing phases. Subsequently, the time-normalized variables for each participant were averaged across repetitions to obtain a subject-level dataset. These variables were compared between the stroke and control groups using the t-test function of SPM on Python. Matched right and left limbs of the stroke patients and control participants were selected for analysis. For example, if a stroke participant's affected limb was the left limb, the left limb of the matched participant was selected for comparison, and vice versa. All statistical tests were set at $\alpha = 0.05$.

3 Results

All 15 stroke and 15 control participants completed the 10-m walking task. The time-varying joint angles for the lower limbs (Figure 1) and torso (Figure 2), GRF (Figure 3), and joint moments (Figure 4) are presented for both the stroke and control groups.

When comparing the joint angles and moments between the stroke patients' affected limb and control group, SPM identified significant differences in various periods in both the stance phase and swing phase for the ankle, knee, and hip joints (all $p < 0.05$). Differences in torso angles were seen primarily not in the sagittal plane but in the frontal plane, where the torso exhibited greater downward angles in the early and terminal stance phases ($p = 0.050$ and $p = 0.049$, respectively) and entire swing phase ($p = 0.001$), indicating the stroke patients leaning towards their affected limb compared with the control group (Figure 2).

In the stance phase, significant differences in the vertical component of GRF were identified when contrasting the stroke and control groups (Figure 3). For the affected limb, the differences ranged from 0.4 to 7.8% ($p = 0.001$), from 8.3 to 26.7% ($p < 0.001$), from 41.2 to 61.6% ($p < 0.001$), and from 68.2 to 94.5% ($p < 0.001$). Similarly, for the less-affected limb, from 0.1 to 4.8% ($p = 0.009$), from 13.3 to 30.9% ($p < 0.001$), from 35.4 to 61.3% ($p < 0.001$), and from 67.6 to 81.7% ($p < 0.001$). Additionally, significant deviations from the control group in the anteroposterior component of GRF were noted. The differences were found for the affected limb to be from 2.3 to 35.5%, ($p < 0.001$)

and from 64.6 to 99.9% ($p < 0.001$), while for the less-affected limb, the differences ranged from 1.3 to 49.5% ($p < 0.001$) and from 64.3 to 94.4% ($p < 0.001$).

4 Discussion

This study conducted a comprehensive comparison of kinematic and kinetic variables during a 10-meter walking task between a group of stroke patients and appropriately matched healthy controls. SPM was employed to assess biomechanical variables for both the stance and swing phases in the gait cycle. The findings indicated notable disparities in joint angles (Figure 1) and moments (Figure 4) during both the stance and swing phases when comparing the affected limb with the control group. Importantly, differences were also evident between the less-affected limb of the stroke group and the control participants' matched limb. Furthermore, significant differences emerged in the amplitudes of the vertical and anteroposterior components of GRF during the stance phase (Figure 3). In contrast, no statistically significant difference was observed in the mediolateral component throughout the stance phase.

4.1 Joint angles

The lower limb joint angle profiles were similar to the ones reported in previous studies (Balaban and Tok, 2014; Tamaya et al., 2020). Significant differences between stroke and control participants were observed in the ankle, knee, and hip joints (Figure 1), primarily in the sagittal plane during the early stance phase, and the period from late stance to early swing phase. The former differences were likely related to weight acceptance, and the latter could be associated with foot push-off (Perry and Burnfield, 2010). During the early swing phase (0–69%, Figure 1), the affected knee displayed much smaller ROM of flexion/extension angle (< 10°) than the control group (~20°). This is consistent with stroke-related stiff knee gait or an extensor gait pattern, characterized by reduced flexion during the swing phase (Woolley, 2001; Perry and Burnfield, 2010). Thus, joint ROM recovery, in particular for the period from late stance phase to early swing phase, can be meaningful for the enhancement of walking performance (Teixeira-Salmela et al., 2001; Nesi et al., 2023).

Abnormalities were also observed in the early and late stance phases, and early swing phase of the contralateral less-affected lower limb (Figure 1). This is in line with one prior study which reported a decrease in lower limb extension angles in the late stance phase for both affected and less-affected limbs (Teixeira-Salmela et al., 2001). However, that study solely analyzed the maximum joint angles, which makes it difficult to diagnose abnormality at different period during ambulation. Hence, this reaffirms the merits of SPM in identifying differences in time-varying data (Pataky, 2010, 2012). On average, torso angles in the frontal plane demonstrated significant differences in the terminal stance phase and the entire swing phase, i.e., leaning more toward the affected side (shown as a downward angle, Figure 2), presumably as a form of compensatory strategy, soft-tissue architecture restriction, or hemi-body spasticity for the hemiplegic gait. Future studies are recommended to include electromyography (EMG) analysis to help better understand stroke patients' torso movement deviations.

4.2 Ground reaction forces

The control group exhibited two obvious peaks in the vertical component of the GRF (black lines in Figure 3), which correspond to the moment of body weight transfer and the foot pushing off the ground (ankle plantarflexion). In contrast, stroke patients' affected foot displayed significant reductions in both peaks during the stance phase, especially for the second peak, which is important for the pre-swing. This parallels the findings from the pediatric cerebral palsy research (Williams et al., 2011), which also noted reduced vertical GRF at the second peak. This also aligns patients' reduced weight transfer to the affected foot and diminished ankle ROM during late stance compared with the controls, as shown in the present study. Interestingly, the vertical component of the GRF of the less-affected side also showed a significant reduction similar to the affected side (Figure 3). Hence, the decline of the vertical GRF of both feet may together contribute to stroke patients' impaired dynamic gait function.

4.3 Joint moments

For the controls, an ankle dorsiflexion moment was generated primarily by the ankle dorsiflexor muscles (e.g., tibialis anterior) immediately after initial foot contact (early stance phase, black lines in Figure 4), serving as weight acceptance (Sloot and Van Der Krogt, 2016) when the body weight is transferred to the standing leg. However, smaller ankle dorsiflexion moments were found in both the affected limb (from 0.6 to 14.3%, $p < 0.001$) and less-affected limb (from 0.9 to 15%, $p < 0.001$) in the stroke group. This could also be reflected by the missing first vertical GRF peak in the stroke patients (Figure 3). Then, when pushing off the ground, a great plantarflexion moment was seen in the late stance phase for the control group (Sloot and Van Der Krogt, 2016). However, the affected limb of the stroke group showed smaller peak plantarflexion moments during the late stance phase (Figure 4, approximately 0.5 and 1.5 Nm/kg, respectively). This may also explain the lack of the obvious second vertical GRF peak for the stroke group (Figure 3). Clinicians, based on the current research findings, may prescribe personalized exercises, such as concentric training focusing on the ankle muscles, to improve the patients' walking performance (Perez et al., 2024).

Similar to the ankle joint moment, a knee flexion moment (negative in value) was seen in a very short period, as shown in the early stance phase for the control group (black lines in Figure 4), which is also related to weight acceptance. Subsequently, a great extension moment (positive in value) was shown to extend the knee forward. However, consistent with the ankle joint, the stroke patients displayed smaller knee flexion and extension moments than the control group. During the stance phase, knee abduction moment is associated with stabilizing the knee joint. Hence, the stroke patients' lower knee abduction moments than the control group (from 6 to 8%, $p = 0.043$; from 84.4 to 89.9%, $p = 0.016$; from 97.2 to 100%, $p = 0.038$) may induce an unstable knee joint during ambulation.

The controls exhibited a hip extension moment in the early stance (positive in value, black lines in Figure 4) in response to weight acceptance. After that, a hip flexion moment (negative in value) was seen in the late stance phase, which prepared the leg for push-off. However, the stroke patients' affected limb (from 4.4

10.3389/fnins.2024.1425183

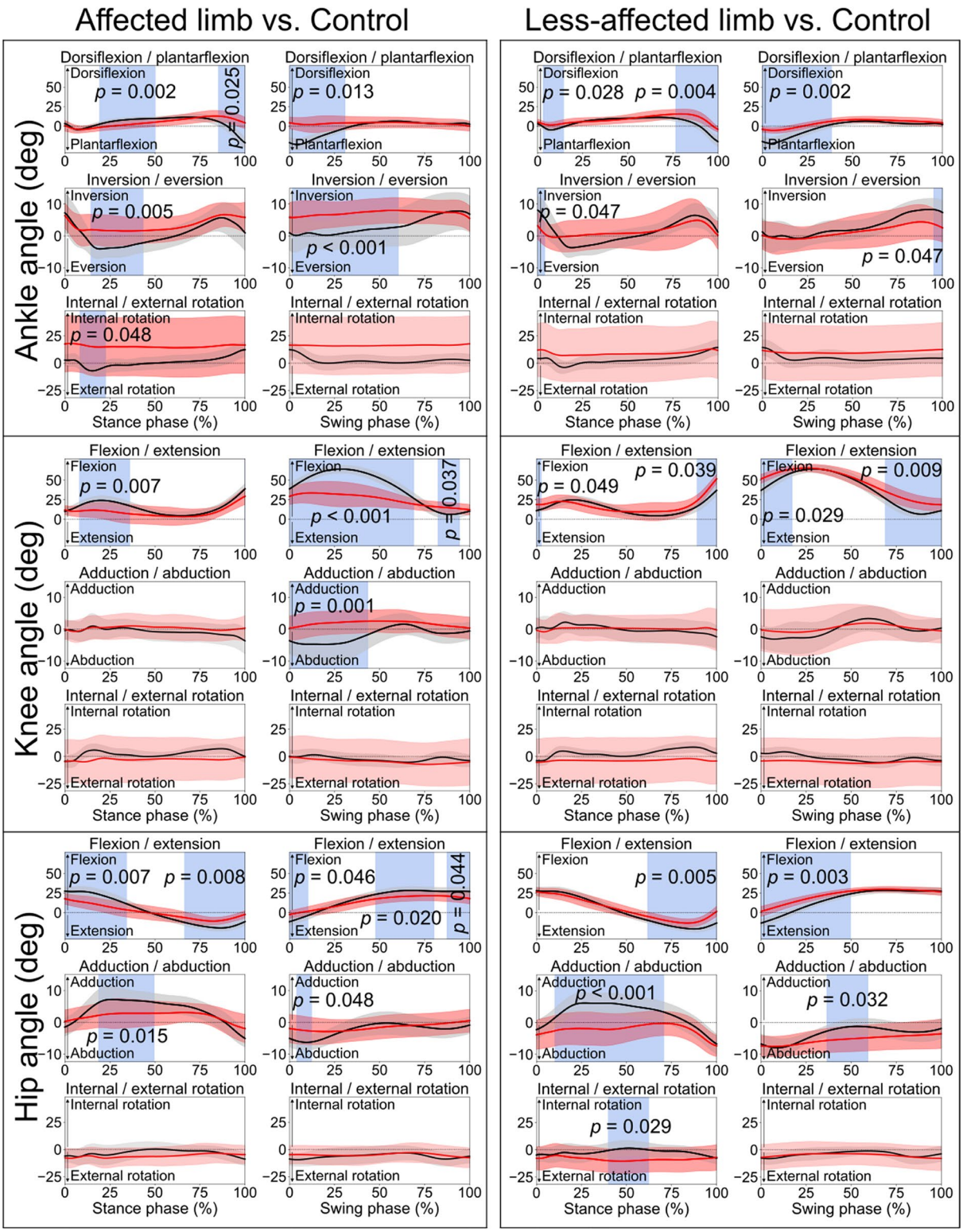

FIGURE 1
Lower limb joint angles. Comparisons between the stroke group (red lines) and control group (black lines) in the stance phase and swing phase of a gait cycle. Blue shades indicate the time clusters with significant differences between the two groups ($p < 0.05$).

to 10%, $p = 0.005$, from 69.2 to 93.9%, $p < 0.001$) showed smaller moment amplitudes than the control group. This is consistent with the findings in a previous study that hip extension strength could be one of the most important indicators regarding stroke patients' ability to walk independently (Smith et al., 2017). As the hip could be the leading joint while walking, stroke patients'

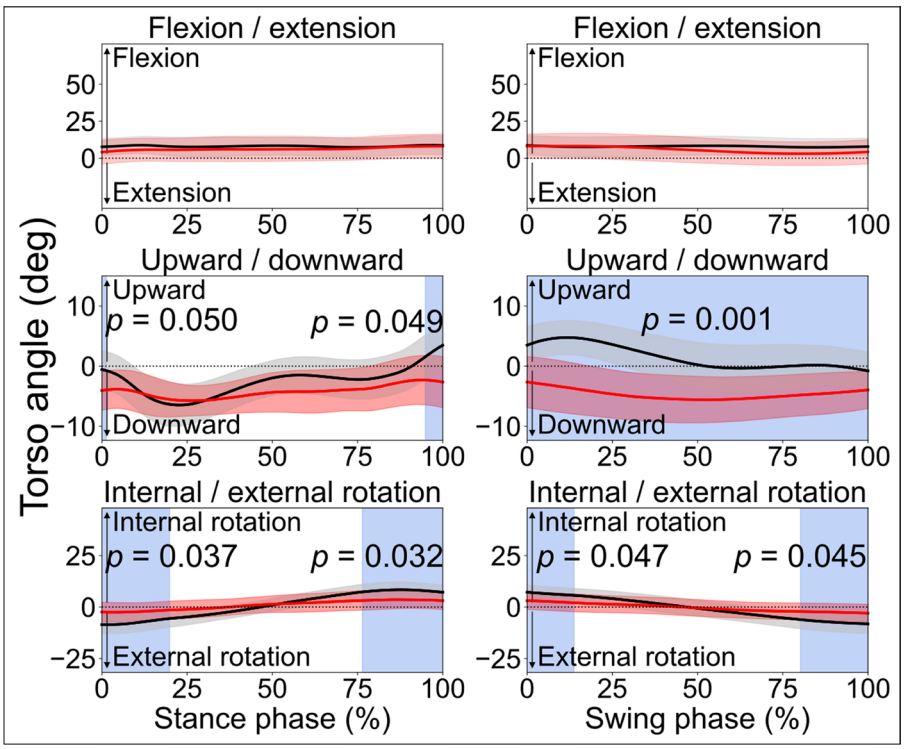

FIGURE 2
Torso angles. Comparisons between the stroke group (red lines) and control group (black lines) in the stance phase and swing phase of a gait cycle. In the frontal plane, leaning downward indicates leaning towards the affected side, while leaning upward indicates leaning toward the less-affected side. Blue shades indicate the time clusters with significant differences between the two groups ($p < 0.05$).

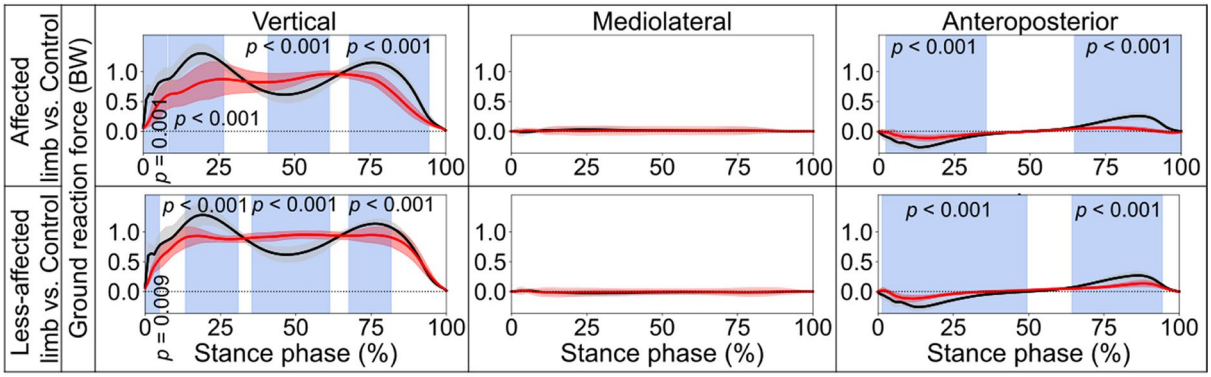

FIGURE 3
Ground reaction forces. Comparisons between the stroke group (red lines) and control group (black lines) in the stance phase of a gait cycle. Blue shades indicate the time clusters with significant differences between the two groups ($p < 0.05$). Data were normalized to the individual body weight (BW).

reduced hip extension/flexion moments may lead to weak interaction torques at the lower joints (e.g., knee and ankle) (Dounskaia, 2005). Hence, the decreased moments of the lower limb joints on both affected and less affected limbs may together contribute to the slower walking speed after stroke. This may confirm the relationship between the increases in lower limb joint moments and improved gait performance. Thus, the findings of this current study suggest that gait rehabilitation, such as joint force or muscle force recovery, should take both limbs into consideration.

Concerning the kinetic aspect in gait analysis, stroke patients exhibited diminished dorsiflexion after initial foot contact, reflected by a missing first vertical GRF peak (Figure 3), and smaller peak plantarflexion moments during late stance (Figure 4), potentially explaining the absence of the second vertical GRF peak. Additionally, stroke patients displayed reduced knee flexion and extension

10.3389/fnins.2024.1425183

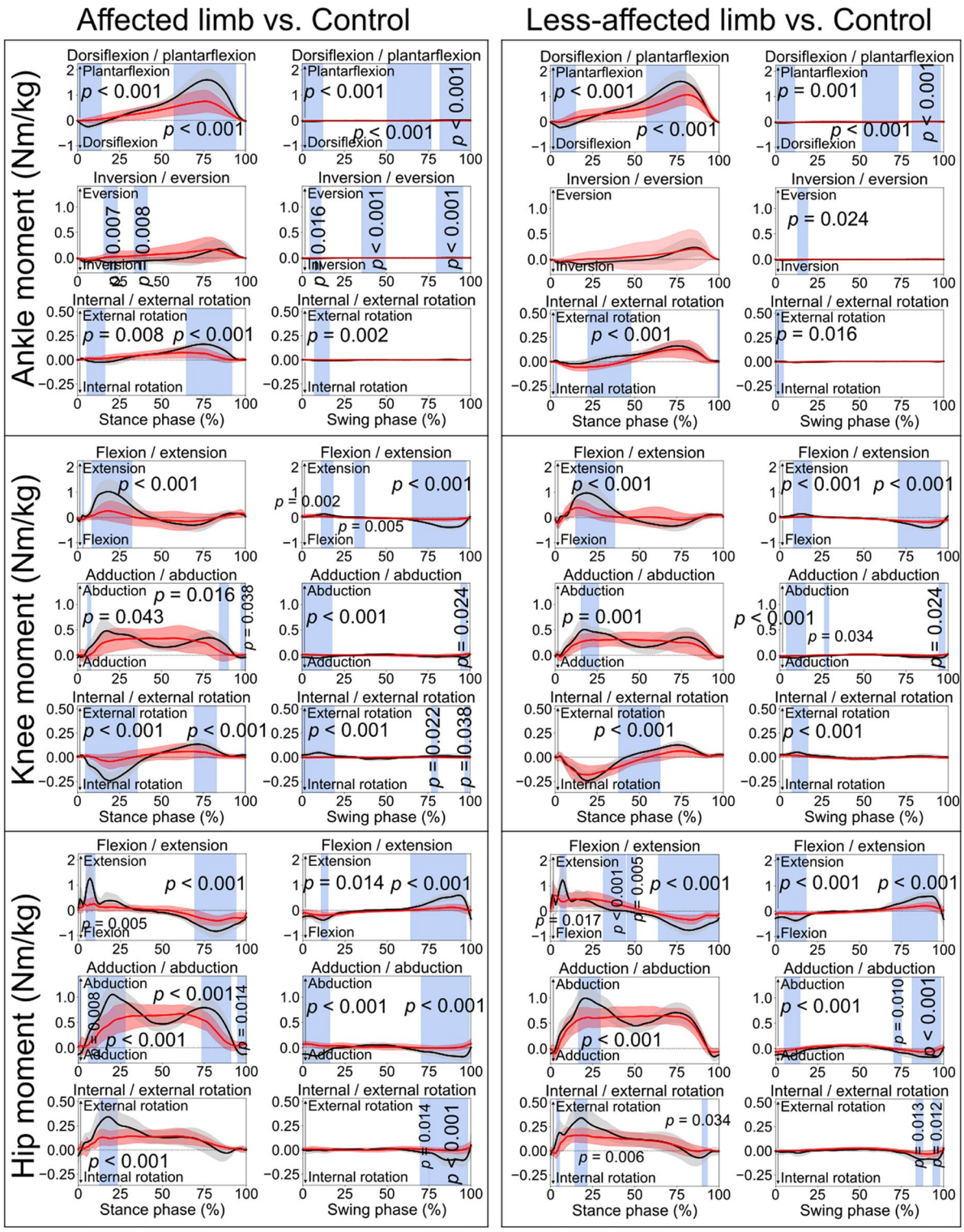

FIGURE 4
Lower limb joint moments. Comparisons between the stroke group (red lines) and control group (black lines) in the stance phase and swing phase of a gait cycle. Blue shades indicate the time clusters with significant differences between the two groups ($p < 0.05$).

moments, possibly leading to unstable knee joints during ambulation. Furthermore, stroke patients exhibited lower hip extension/flexion moments, suggesting weakened interaction torques at subordinate joints and contributing to slower walking speeds in both affected and less-affected limbs. These findings emphasize the complex interplay of joint moments and GRF in stroke patients' gait mechanics, highlighting potential targets for rehabilitation interventions aimed at improving walking function and independence.

4.4 Limitations

There are several limitations to this present study. Firstly, inconsistent gait patterns may be exhibited across the small sample of 15 stroke patients, and hence, future studies are recommended to recruit stroke patterns in similar status and conditions to improve group homogeneity for analysis. Secondly, since the inherent difficulty existed in obtaining valid walking trials for the stroke patients (e.g., planting the whole foot on the force platform without touching its edge), only 2 strides for each left and right foot were used for analysis. For the control group, 3 strides were included, which is in line with the previous literature (Teixeira-Salmela et al., 2001). Hence, in the future, more valid strides/trials should be included to reach a more stable mean value.

5 Conclusion

This study compared the kinematics (joint angles) and kinetics (GRF and joint moments) for a group of chronic stroke patients against their matched healthy controls in a 10-m walking task. SPM detected significant differences in joint angles and moments in various periods during the stance and swing phases between the stroke and controls. Between-group differences were also revealed in GRF during the stance phase. The findings reveal that in addition to the affected limb which have been extensively investigated in previous studies, the less-affected limb also exhibited abnormal biomechanics variables compared with the control group in this study. This suggests that post-stroke gait rehabilitation should take both limbs into consideration, and clinicians can prescribe personalized exercises to improve stroke patients' walking performance. The present study illustrates that 3D motion capture technology and SPM analyses can offer clinicians valuable insights into gait pattern deviations across different phases in the gait cycle. The research findings may draw attention to specific periods within the gait cycle (e.g., early stance phase for the knee, and early swing phase for the ankle), and potentially enhances rehabilitation therapy by monitoring the responses to therapeutic modalities.

Data availability statement

The raw data supporting the conclusions of this article will be made available by the authors, without undue reservation.

Ethics statement

The studies involving humans were approved by National Healthcare Group Domain Specific Review Board, Singapore. The studies were conducted in accordance with the local legislation and institutional requirements. The participants provided their written informed consent to participate in this study.

Author contributions

JP: Data curation, Formal analysis, Visualization, Writing – original draft, Writing – review & editing. AS: Methodology, Supervision, Writing – original draft, Writing – review & editing. T-LW: Formal analysis, Methodology, Visualization, Writing – review & editing. WK: Conceptualization, Resources, Writing – review & editing, Investigation. PO: Conceptualization, Writing – review & editing. MT: Conceptualization, Writing – review & editing. MP: Conceptualization, Writing – review & editing. WC: Data curation, Investigation, Writing – review & editing. WA: Conceptualization, Supervision, Writing – review & editing. KC: Conceptualization, Funding acquisition, Resources, Writing – review & editing, Supervision.

Funding

The author(s) declare that financial support was received for the research, authorship, and/or publication of this article. This study was funded by the Rehabilitation Research Grant (RRG3/19002) 2019.

Conflict of interest

The authors declare that the research was conducted in the absence of any commercial or financial relationships that could be construed as a potential conflict of interest.

Publisher's note

All claims expressed in this article are solely those of the authors and do not necessarily represent those of their affiliated organizations, or those of the publisher, the editors and the reviewers. Any product that may be evaluated in this article, or claim that may be made by its manufacturer, is not guaranteed or endorsed by the publisher.

Supplementary material

The Supplementary material for this article can be found online at: https://www.frontiersin.org/articles/10.3389/fnins.2024.1425183/full#supplementary-material

References

Alhossary, A., Ang, W. T., Chua, K. S. G., Tay, M. R. J., Ong, P. L., Murakami, T., et al. (2022). Identification of secondary biomechanical abnormalities in the lower limb joints after chronic transtibial amputation: a proof-of-concept study using SPM1D analysis. *Bioengineering* 9:293. doi: 10.3390/bioengineering9070293

Balaban, B., and Tok, F. (2014). Gait disturbances in patients with stroke. *PMR* 6, 635–642. doi: 10.1016/j.pmrj.2013.12.017

Bijleveld-Uitman, M., van de Port, I., and Kwakkel, G. (2013). Is gait speed or walking distance a better predictor for community walking after stroke? *J. Rehabil. Med.* 45, 535–540. doi: 10.2340/16501977-1147

Cole, G. K., Nigg, B. M., Ronsky, J. L., and Yeadon, M. R. (1993). Application of the joint coordinate system to three-dimensional joint attitude and movement representation: a standardization proposal. *J. Biomech. Eng.* 115, 344–349. doi: 10.1115/1.2895496

Dounskaia, N. (2005). The internal model and the leading joint hypothesis: implications for control of multi-joint movements. *Exp. Brain Res.* 166, 1–16. doi: 10.1007/s00221-005-2339-1

Fernández-Vázquez, D., Calvo-Malón, G., Molina-Rueda, F., López-González, R., Carratalá-Tejada, M., Navarro-López, V., et al. (2023). Kinematic gait analysis in people

with mild-disability multiple sclerosis using statistical parametric mapping: a cross-sectional study. *Sensors* 23:7671. doi: 10.3390/s23187671

French, M. A., Roemmich, R. T., Daley, K., Beier, M., Penttinen, S., Raghavan, P., et al. (2022). Precision rehabilitation: optimizing function, adding value to health care. *Arch. Phys. Med. Rehabil.* 103, 1233–1239. doi: 10.1016/j.apmr.2022.01.154

Gao, Z., Mei, Q., Xiang, L., and Gu, Y. (2020). Difference of walking plantar loadings in experienced and novice long-distance runners. *Acta Bioeng. Biomech.* 22, 1–21. doi: 10.37190/ABB-01627-2020-02

Goldie, P. A., Matyas, T. A., and Evans, O. M. (1996). Deficit and change in gait velocity during rehabilitation after stroke. *Arch. Phys. Med. Rehabil.* 77, 1074–1082. doi: 10.1016/S0003-9993(96)90072-6

Holden, M. K., Gill, K. M., Magliozzi, M. R., Nathan, J., and Piehl-Baker, L. (1984). Clinical gait assessment in the neurologically impaired. *Phys. Ther.* 64, 35–40. doi: 10.1093/ptj/64.1.35

Kollen, B., Kwakkel, G., and Lindeman, E. (2006). Hemiplegic gait after stroke: is measurement of maximum speed required? *Arch. Phys. Med. Rehabil.* 87, 358–363. doi: 10.1016/j.apmr.2005.11.007

Kwakkel, G., Lannin, N. A., Borschmann, K., English, C., Ali, M., Churilov, L., et al. (2017). Standardized measurement of sensorimotor recovery in stroke trials: consensus-based core recommendations from the stroke recovery and rehabilitation roundtable. *Int. J. Stroke* 12, 451–461. doi: 10.1177/1747493017711813

Lawrence, E. S., Coshall, C., Dundas, R., Stewart, J., Rudd, A. G., Howard, R., et al. (2001). Estimates of the prevalence of acute stroke impairments and disability in a multiethnic population. *Stroke* 32, 1279–1284. doi: 10.1161/01.STR.32.6.1279

Liang, P., Kwong, W. H., Sidarta, A., Yap, C. K., Tan, W. K., Lim, L. S., et al. (2020). An Asian-centric human movement database capturing activities of daily living. *Scient. Data* 7:290. doi: 10.1038/s41597-020-00627-7

Mei, Q., Gu, Y., Xiang, L., Baker, J. S., and Fernandez, J. (2019). Foot pronation contributes to altered lower extremity loading after long distance running. *Front. Physiol.* 10:573. doi: 10.3389/fphys.2019.00573

Nesi, B., Taviani, A., D'Auria, L., Bardelli, R., Zuccarello, G., Platano, D., et al. (2023). The relationship between gait velocity and walking pattern in hemiplegic patients. *Appl. Sci.* 13:934. doi: 10.3390/app13020934

Olney, S. J., and Richards, C. (1996). Hemiparetic gait following stroke part I: characteristics. *Gait Posture* 4, 136–148. doi: 10.1016/0966-6362(96)01063-6

Park, S., and Yoon, S. (2021). Validity evaluation of an inertial measurement unit (imu) in gait analysis using statistical parametric mapping (SPM). *Sensors* 21:3667. doi: 10.3390/s21113667

Pataky, T. C. (2010). Generalized n-dimensional biomechanical field analysis using statistical parametric mapping. *J. Biomech.* 43, 1976–1982. doi: 10.1016/j.jbiomech.2010.03.008

Pataky, T. C. (2012). One-dimensional statistical parametric mapping in python. *Comput. Methods Biomech. Biomed. Engin.* 15, 295–301. doi: 10.1080/10255842.2010.527837

Patterson, K. K., Parafianowicz, I., Danells, C. J., Closson, V., Verrier, M. C., Staines, W. R., et al. (2008). Gait asymmetry in community-ambulating stroke survivors. *Arch. Phys. Med. Rehabil.* 89, 304–310. doi: 10.1016/j.apmr.2007.08.142

Perez, N., Morales, C., Reyes, A., Cruickshank, T., and Penailillo, L. (2024). Effects of eccentric strength training on motor function in individuals with stroke: a scoping review. *Top. Stroke Rehabil.* 1, 1–14. doi: 10.1080/10749357.2024.2330040

Perry, J., and Burnfield, J. M. (2010). Gait analysis: Normal and pathological function. *2nd* Edn. Thorofare, NJ, United States: Slack Incorporated.

Selves, C., Stoquart, G., and Lejeune, T. (2020). Gait rehabilitation after stroke: review of the evidence of predictors, clinical outcomes and timing for interventions. *Acta Neurol. Belg.* 120, 783–790. doi: 10.1007/s13760-020-01320-7

Sloot, L. H., and Van Der Krogt, M. M. (2016). "Interpreting joint moments and powers in gait" in Handbook of human motion. eds. B. Müller, S. I. Wolf, G.-P. Brueggemann, Z. Deng, A. McIntosh and F. Milleret al. (Cham, Switzerland: Springer International Publishing), 1–19.

Smith, M.-C., Barber, P. A., and Stinear, C. M. (2017). The TWIST algorithm predicts time to walking independently after stroke. *Neurorehabil. Neural Repair* 31, 955–964. doi: 10.1177/1545968317736820

Szekér, S., and Vathy-Fogarassy, Á. (2020). Weighted nearest neighbours-based control group selection method for observational studies. *PLoS One* 15:e0236531. doi: 10.1371/journal.pone.0236531

Tamaya, V. C., Wim, S., Herssens, N., Van De Walle, P., Willem, D. H., Steven, T., et al. (2020). Trunk biomechanics during walking after sub-acute stroke and its relation to lower limb impairments. *Clin. Biomech.* 75:105013. doi: 10.1016/j.clinbiomech.2020.105013

Teixeira-Salmela, L. F., Nadeau, S., Mcbride, I., and Olney, S. J. (2001). Effects of muscle strengthening and physical conditioning training on temporal, kinematic and kinetic variables during gait in chronic stroke survivors. *J. Rehabil. Med.* 33, 53–60. doi: 10.1080/165019701750098867

Van Criekinge, T., Saeys, W., Hallemans, A., Velghe, S., Viskens, P.-J., Vereeck, L., et al. (2017). Trunk biomechanics during hemiplegic gait after stroke: a systematic review. *Gait Posture* 54, 133–143. doi: 10.1016/j.gaitpost.2017.03.004

Williams, S. E., Gibbs, S., Meadows, C. B., and Abboud, R. J. (2011). Classification of the reduced vertical component of the ground reaction force in late stance in cerebral palsy gait. *Gait Posture* 34, 370–373. doi: 10.1016/j.gaitpost.2011.06.003

Woolley, S. M. (2001). Characteristics of gait in hemiplegia. *Top. Stroke Rehabil.* 7, 1–18. doi: 10.1310/JB16-V04F-JAL5-H1UV

Wu, G., Siegler, S., Allard, P., Kirtley, C., Leardini, A., Rosenbaum, D., et al. (2002). ISB recommendation on definitions of joint coordinate system of various joints for the reporting of human joint motion—part I: ankle, hip, and spine. *J. Biomech.* 35, 543–548. doi: 10.1016/S0021-9290(01)00222-6

Yen, C.-L., Chang, K.-C., Wu, C.-Y., and Hsieh, Y.-W. (2019). The relationship between trunk acceleration parameters and kinematic characteristics during walking in patients with stroke. *J. Phys. Ther. Sci.* 31, 638–644. doi: 10.1589/jpts.31.638

frontiers | Frontiers in Neuroscience

TYPE Study Protocol
PUBLISHED 31 July 2024
DOI 10.3389/fnins.2024.1398459

OPEN ACCESS

EDITED BY
Yingbai Hu,
The Chinese University of Hong Kong, Hong Kong SAR, China

REVIEWED BY
Xiao Luo,
The Chinese University of Hong Kong, Hong Kong SAR, China
Konstantinos Chandolias,
University of Thessaly, Greece

*CORRESPONDENCE
F. Virginia Wright
✉ vwright@hollandbloorview.ca

RECEIVED 09 March 2024
ACCEPTED 17 July 2024
PUBLISHED 31 July 2024

CITATION
Bradley SS, de Holanda LJ, Chau T and Wright FV (2024) Physiotherapy-assisted overground exoskeleton use: mixed methods feasibility study protocol quantifying the user experience, as well as functional, neural, and muscular outcomes in children with mobility impairments. *Front. Neurosci.* 18:1398459. doi: 10.3389/fnins.2024.1398459

Physiotherapy-assisted overground exoskeleton use: mixed methods feasibility study protocol quantifying the user experience, as well as functional, neural, and muscular outcomes in children with mobility impairments

Stefanie S. Bradley[1,2], Ledycnarf Januario de Holanda[1], Tom Chau[1,2] and F. Virginia Wright[1,3]*

[1]Bloorview Research Institute, Holland Bloorview Kids Rehabilitation Hospital, Toronto, ON, Canada, [2]Institute of Biomedical Engineering, University of Toronto, Toronto, ON, Canada, [3]Department of Physical Therapy, University of Toronto, Toronto, ON, Canada

Background: Early phase research suggests that physiotherapy paired with use of robotic walking aids provides a novel opportunity for children with severe mobility challenges to experience active walking. The Trexo Plus is a pediatric lower limb exoskeleton mounted on a wheeled walker frame, and is adjustable to fit a child's positional and gait requirements. It guides and powers the child's leg movements in a way that is individualized to their movement potential and upright support needs, and can provide progressive challenges for walking within a physiotherapy-based motor learning treatment paradigm.

Methods: This protocol outlines a single group mixed-methods study that assesses the feasibility of physiotherapy-assisted overground Trexo use in school and outpatient settings during a 6-week physiotherapy block. Children ages 3–6 years (n = 10; cerebral palsy or related disorder, Gross Motor Function Classification System level IV) will be recruited by circle of care invitations to participate. Study indicators/outcomes will focus on evaluation of: (i) clinical feasibility, safety, and acceptability of intervention; (ii) pre-post intervention motor/functional outcomes; (iii) pre-post intervention brain structure characterization and resting state brain connectivity; (iv) muscle activity characterization during Trexo-assisted gait and natural assisted gait; (v) heart rate during Trexo-assisted gait and natural assisted gait; and (vi) user experience and perceptions of physiotherapists, children, and parents.

Discussion: This will be the first study to investigate feasibility indicators, outcomes, and experiences of Trexo-based physiotherapy in a school and outpatient context with children who have mobility challenges. It will explore the possibility of experience-dependent neuroplasticity in the context of gait rehabilitation, as well as associated functional and muscular outcomes. Finally, the study will address important questions about clinical utility and future

adoption of the device from the physiotherapists' perspective, comfort and engagement from the children's perspective, and the impressions of parents about the value of introducing this technology as an early intervention.

Clinical trial registration: https://clinicaltrials.gov, identifier NCT05463211

KEYWORDS

lower limb exoskeleton, overground gait training, cerebral palsy, GMFCS IV, robotic training, pediatric, mobility, physiotherapy

1 Introduction

While wheelchairs are essential for supporting mobility and participation in the daily activities of individuals who have severe motor impairments (Gibson et al., 2012), they do not offer supported upright positioning of the body. Many individuals with limited mobility use a combination of assistive devices for different intentions or circumstances, such as wheelchairs, standing frames, and supported walkers (Moen and Østensjø, 2023). Walking (or assisted standing) confers a multitude of health benefits including improved bone health (Kim et al., 2017), respiration (Lee and Kim, 2014), circulation (Eng et al., 2001), urination (Houle et al., 1998; Walter et al., 1999), bowel function (Walter et al., 1999), joint range of motion (Paleg et al., 2013), sleep (Eng et al., 2001), as well as psychosocial (McKeever et al., 2013; Livingstone and Paleg, 2023) and mental health benefits (Kenyon et al., 2021). Growing recognition across rehabilitation sectors about the possibility of technology to facilitate enhanced upright mobility and independence has stimulated the engineering advancement of assistive gait devices from simple wheeled walkers (Tao et al., 2020), to supported stepping devices (Livingstone and Paleg, 2023), to non-robotic mechanically facilitated walkers (Wright and Jutai, 2006; Paleg and Livingstone, 2015), to treadmill mounted (tethered) gait trainers (Cherni and Ziane, 2022), and most recently to powered exoskeletons that move overground (Owens et al., 2020).

Overground lower-limb powered exoskeletons afford earth vertical weight-bearing positioning that is coupled with augmented mobility (De Luca et al., 2019), giving novel upright movement opportunities when foundational gross motor skills (e.g., learning to walk) are delayed or when disease or injury has resulted in loss of independent walking abilities (Hunt, 2021). These exoskeletons can be used in conjunction with other gait aids such as wheeled walkers, or tethered on a treadmill (Kim et al., 2021) to fit the individual's support needs. They can also be built as freestanding robotically guided mobile walking frames (De Luca et al., 2019; Sarajchi et al., 2021).The added value of exoskeleton use within gait-based physiotherapy sessions is that they provide: the option of hands-free body weight support (thereby freeing the arms/hands for other activities), sensors that respond to biological feedback, natural joint movements and activation of weak or spastic muscles by modulating forces on body segments, normalization of the gait cycle by standardizing step length and range of motion, reduced cost of walking to allow meaningful periods of exercise during intervention sessions, quantified session progress to provide real-time feedback, and supported use of motor learning protocols (intensity, repetition, variability, and task-specificity) to optimize gait training (Molteni et al., 2018; De Luca et al., 2019).

Increased clinical adoption of mobile exoskeletons such as the Angel-legs (Angel Robotics Co., Ltd., Seoul, Korea), ReWalk (ReWalk Robotics Inc., Marlborough, MA, USA), and Ekso (Ekso Bionics, Richmond, CA, USA) has occurred over the last decade in adult rehabilitation, and there is an emerging body of evidence of the physical and health benefits of exoskeleton use by adults with neuromotor conditions (Louie and Eng, 2016; Bruni et al., 2018; Rojek et al., 2020; Karunakaran et al., 2021; Rodríguez-Fernández et al., 2021). However, development and access to smaller sized exoskeletons for pediatric populations, and associated clinical experience with using them, currently lags far behind that of adults (Fosch-Villaronga et al., 2020). As a result, there is limited knowledge on the neurological and neuromuscular effects of exoskeleton use in children, as well as the training considerations and user perspectives that are essential to facilitate best practice use. The majority of research to date on robotic walkers in pediatrics has been with treadmill-based tethered models such as the Lokomat robotic gait trainer (Hocoma AG, Volketswil, Switzerland) (Aurich-Schuler et al., 2015; Cumplido et al., 2021; Kim et al., 2021; Cherni and Ziane, 2022). While tethered exoskeletons offer weightbearing and gait training benefits (Kim et al., 2021), they do not provide the functional and participation opportunities obtained from the added experience of moving overground with mobile exoskeletons like Ekso, Trexo pediatric frame-mounted exoskeleton (Trexo Robotics, 2022), or similar devices.

The Trexo Plus (hereafter referred to as the Trexo), designed specifically for use with children with motor impairments, has been commercially available since 2017. Thus far it has been investigated in the context of home use with children's caregivers operating the device after orientation provided by the Trexo team (Diot et al., 2021, 2023). Benefits in the areas of sleep quality, bowel function, postural function, and positive affect associated with Trexo use have been documented (Diot et al., 2023). At the time of writing,

Abbreviations: O_0, baseline phase; X, intervention phase; O_1, follow-up phase; O_2, follow-up 2 phase; SR, study researcher; SI, study interviewer GMFM-88, gross motor function measure 88; COPM, Canadian Occupational Performance Measure; GAS, Goal Attainment Scaling; MRI, magnetic resonance imaging; MMG, mechanomyography; ROM, range of motion; PPAS, Posture and Postural Ability Scale; LSS, Level of Sitting Scale; PEDI-CAT, Pediatric Evaluation of Disability Inventory; 1MWT, 1-minute walk test; DMA, Directional Mobility Assessment; MACS, Manual Ability Classification System; CFCS, Communication Function Classification System.

Trexo use is being evaluated in a follow-up crossover feasibility RCT (4-week Trexo home program [prescribed/taught by a PT and facilitated by the child's caregiver 4–5 times/week] compared with a 4-week identical frequency functional therapy program [prescribed/taught by a PT and facilitated by the child's caregiver]) (McCormick et al., 2023).

There are no published studies to date that focus on integration of the Trexo into clinical settings, specifically physiotherapist-led therapy sessions. There is evidence though of adoption-related challenges for rehabilitation teams using exoskeletons in adult rehabilitation, such as extensive knowledge requirements and hands-on skill demands to handle the operation of these advanced new technologies for competent goal-based therapeutic use, while ensuring patient safety and comfort (Read et al., 2020). There is also the need for strong teamwork within a facility to collaboratively develop therapy protocols for each patient that will optimize outcomes (Gilardi et al., 2020).

Paradigmatic shifts in thinking about possible walking-based outcomes for minimally ambulatory children (van Hedel et al., 2016; Livingstone and Paleg, 2023) are occurring in tandem with assistive device developments. For example, typical physiotherapy and occupational therapy goals for children with cerebral palsy (CP) who are minimally ambulatory or non-ambulatory (i.e., Gross Motor Function Classification System [GMFCS] levels IV and V respectively) have traditionally focused on achieving their highest degree of independence within the context of their physical constraints (Goswami et al., 2021). The recent introduction of overground robotic devices (such as the Trexo) has been encouraging a transition in practice toward providing more active focus on upright assisted walking within home and community environments, especially in children's younger years, using a physiotherapy intervention approach that is based on principles of motor learning and neuroplasticity. However, from a best practice perspective, there is an urgent responsibility to gather clinical evidence both on intervention processes and associated outcomes before making them a part of regular clinical care (Phelan et al., 2015).

The primary aim of this study is to investigate the feasibility, user perspectives, and body-wide outcomes associated with institutionally based overground exoskeleton gait training in children 3–6 years of age with a functional presentation of GMFCS level IV. The Trexo will be the overground lower limb exoskeleton used. It is listed as a Class I medical device by Health Canada and Class II medical device by the FDA.

The study aims will be completed through a study protocol with the following objectives:

i) Assess aspects of clinical feasibility, safety, and acceptability of Trexo gait training within an outpatient center and school
ii) Capture the Trexo user experience of children and physiotherapists during exoskeleton gait training, as well as physiotherapists' and parents' perspectives of outcomes associated with use
iii) Assess motor and functional outcomes pre/post Trexo gait training (including any carryover effects)
iv) Examine brain anatomy and brain connectivity pre/post Trexo gait training
v) Evaluate muscle activations, particularly indicating muscle fatigue, during Trexo gait training (compare with muscle activations during use of regular assistive mobility devices)
vi) Capture heart rate and heart rate variability during Trexo gait training (compare with heart rate during use of regular assistive mobility devices).

2 Methods and analysis

2.1 Study design

This mixed methods feasibility study protocol [phase IIa; Orbit Model (Czajkowski et al., 2015) uses an $\mathbf{O_0\ X\ O_1\ O_2}$ design (Figure 1), with participants (n = 10) acting as their own controls (within a longitudinal intervention consisting of O_0, O_1, and O_2 = study assessment phases, and X = physiotherapy intervention with the Trexo]. The protocol follows Standard Protocol Items: Recommendations for Interventional Trials (SPIRIT Checklist; Chan et al., 2013a,b). All study team members' roles are outlined in Table 1.

During '**O' phases (pre/post intervention)**, participants will do their usual physiotherapy regimen (with their usual assistive device, where applicable) and associated home program, and will undergo the set of study assessments (gross motor/functional assessments and neuroimaging) in this approximately 2–3-week period pre- and post-Trexo use (Phase X). One-month post O_1, participants will have one final motor/functional assessment and neuroimaging visit (O_2). They will continue with their usual physiotherapy regimen during the month between O_1 and O_2.

Intervention 'X' phase will consist of the Trexo physiotherapy block: physiotherapy sessions twice weekly (30-min sessions

TABLE 1 Research team member designations and corresponding roles in the study.

Designation	Role
Principal investigators	Responsible for study oversight and adverse event management.
Study researchers	Non-PT team members that are responsible for coordinating recruitment, scheduling, non-PT data collection, and data analysis.
Study physician	Center-affiliated pediatrician that helps with diagnostic expertise, recruitment, eligibility, and adverse event management.
Treating PTs/PTAs	Physiotherapy team members that are Trexo-trained and complete the 12 Trexo (twice weekly) intervention sessions.
PT assessors	Independent PTs (different from treating PTs) that complete the physical screening and motor/functional assessments.
Study interviewer	Independent team member that hosts all Zoom-based interviews.
MRI technician	Centre-affiliated technician that operates MRI scanner.

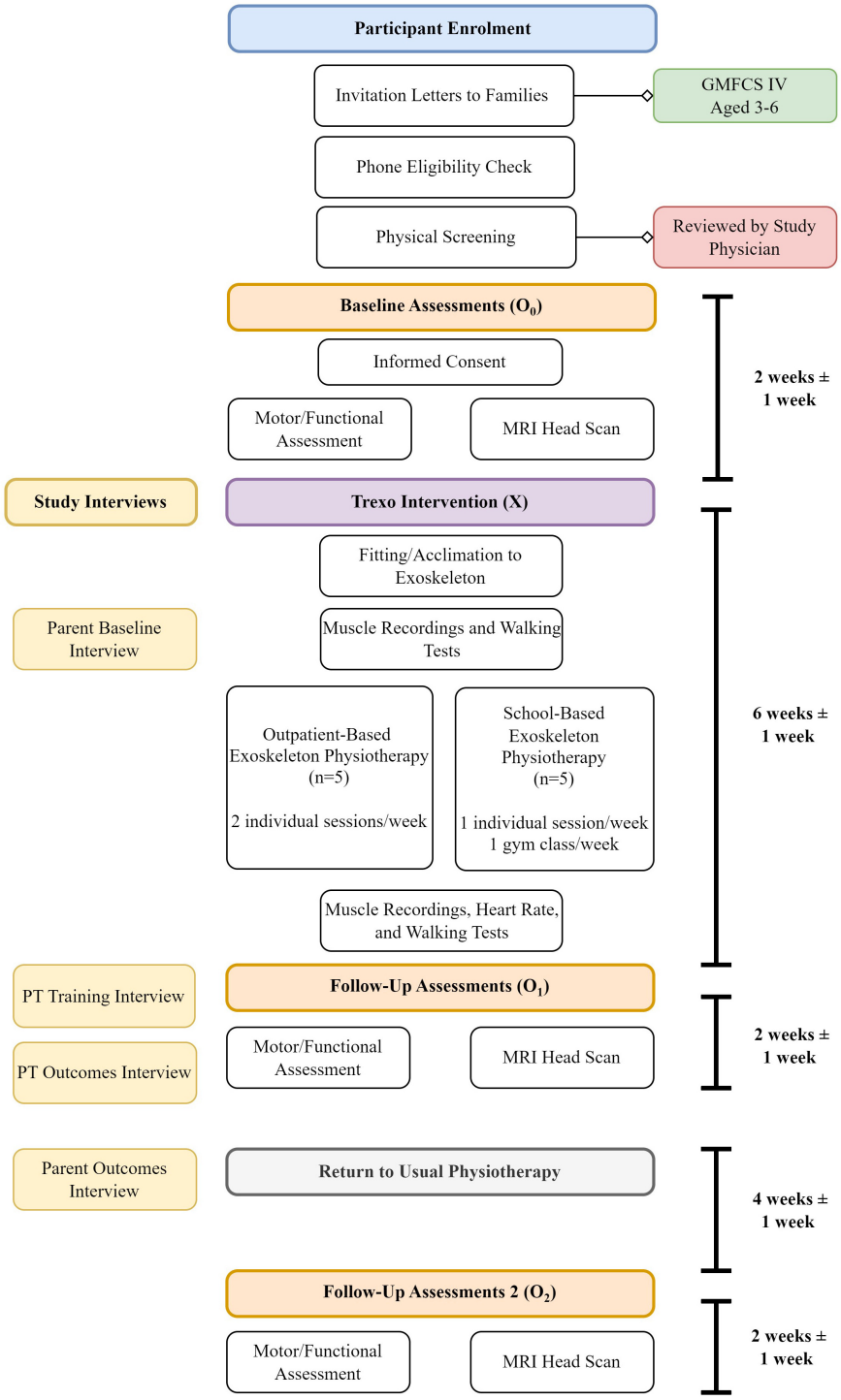

FIGURE 1
Flow chart of study visits and timeline, reflecting O_0 X O_1 O_2 design.

excluding initial set-up time) for 6 weeks provided by a study-trained PT/ Physiotherapist Assistant (PTA) team within a goal-based training program that is grounded in motor learning principles. Trexo physiotherapy will be integrated within a school-based program for half of the study cohort (n = 5), and within an outpatient program for the other half (n = 5). Each child will receive 1–2 acclimatization/fitting sessions in the Trexo before starting physiotherapy sessions. Walking tests and muscle recordings at the start and end of this phase will be done in the Trexo and in the child's usual non-robotic wheeled walker (if they use one) for comparison and for assessment of potential carryover effects from Trexo use to their wheeled walker.

Independent PT assessors (different from the intervention PTs) will perform motor/functional assessments, with the same assessor

assigned to a child for each assessment. They will be blinded to the results of their previous assessment(s). Treating Trexo PTs and PTAs may choose to share their experience of using the Trexo as an intervention via optional qualitative interviews pertaining to: (i) their Trexo training/learning process, and (ii) the treatment process specific to each of the children who is assigned to them. Parents may choose to share their expectations and impressions of the Trexo treatment block via optional qualitative interviews pertaining to: (i) baseline study expectations, and (ii) post-intervention impressions and any associated outcomes of their child's use.

2.2 Participant eligibility

2.2.1 Age range justification

We decided to acquire a medium-sized Trexo, which fits children aged 3–6 years old (height and weight requirements). We aim to work with children at an early intervention point where there is still considerable developmental potential for change and capitalize on the developing brain's neuroplastic nature (Novak et al., 2017). According to GMFM Motor Growth Curves for children with CP (GMFCS IV) there is still potential for motor gains for children under the age of 6 (Rosenbaum et al., 2002).

2.2.2 Inclusion criteria

(a) Age 3–6 years inclusive at the time of receiving the study invitation; (b) mobility impairment caused by a non-progressive neuromuscular disorder, classified as **GMFCS Level IV** or equivalent: uses a wheelchair (pushed by others or powered) most of the time, and walking is very limited even with use of assistive devices (Palisano et al., 2008) and able to sit on chair but need adaptive seating for trunk control and to maximize hand function, can move in and out of chair with assistance from an adult or a stable surface to push or pull up on with their arms, can walk no more than short distances with a maximum support walker/stepping device and caregiver assistance (Rosenbaum et al., 2008); (c) weight: 20–100 lbs to fit within our medium size Trexo; (d) leg length with specific measurement of the hip to the knee of 17–27 cm and knee to floor of 18–32 cm while wearing shoes; (e) able to indicate pain, fear, or discomfort verbally or non-verbally; (f) able to respond to one or two-step commands; and (g) at least 2 months after any lower limb Botulinum Toxin injections. Children may have a maximum support manual walker (e.g., a supported stepping device such as the Rifton Pacer Gait Trainer[1] - a wheeled "walking" frame or support walker that provides trunk and pelvic support and has a soft strap or solid seat and arm support as needed) that they use as their gait device at home/school, but this will not be necessary to be eligible to participate in the study.

2.2.3 Exclusion criteria

(a) As per the Trexo Plus Operations manual (Trexo Robotics, 2022), unless cleared by study physician: knee flexion contracture $> 20°$; knee valgus $> 40°$; hip extension $< -10°$; hip subluxation $> 40\%$; (b) dynamic spasticity or behavioral concerns that interfere with the use of the Trexo; (c) weight-bearing restrictions (d) osteogenesis imperfecta; (e) orthopedic surgery within the last 6 months (if muscle) or 12 months (if bone), or planned within the next 6 months; (f) seizure disorder that's not controlled by medication; (g) unable to pass MRI screening; (h) involved in another interventional study (reviewed on a case-by-case basis); (i) received robotic exoskeleton training in the past; (j) neurological, respiratory, cardiac, and orthopedic medical conditions that would restrict physical activity as reported by parents; (k) open skin lesions or vascular disorders of the lower extremities; and (l) not able to discontinue Botulinum Toxin injections for 6-week period during study intervention.

2.2.4 Sample size justification

The planned sample size of 10 children for this feasibility study will be sufficient to give an initial group picture through descriptive statistics and summary graphs of feasibility indicators and quantitative outcomes. This aligns with other quantitative pediatric therapy technology-based intervention studies that have successfully provided meaningful feasibility study results with 4 to 20 participants: (Richards et al., 1997; Wallen et al., 2008; Weightman et al., 2011; Radtka et al., 2013). This sample size will also elucidate how a single robotic assistive device may be shared (i.e., fitting adaptations to support use) among multiple children for use as a physiotherapy intervention within a center.

For the qualitative user perspective data, there is no agreed-upon sample size to achieve saturation in qualitative research (Saunders et al., 2018), instead depending collectively on sample homogeneity, interaction quality, and theoretical framework (Malterud et al., 2016).

Previous qualitative descriptive studies with children, parents, or clinicians reporting on user experiences of applying new technology or outcome measures have produced meaningful results with samples of 5 to 13 participants (Rich et al., 2014; Beveridge et al., 2015; Phelan et al., 2015; Kahlon et al., 2019; Vaughan-Graham et al., 2020; Giancolo et al., 2022; Hadj-Moussa et al., 2022; Torchia et al., 2023).

2.3 Participant enrolment

2.3.1 Invitation letters from circle of care

Pediatricians, PTs, and clinic staff affiliated with the hospital-based outpatient program and the school integrated education therapy program will share study invitation letters with parents of the children on their caseload who meet the main eligibility criteria. Interested parents will have an initial phone conversation with the study's research coordinator who will provide them with full details on the study, and if they are interested in moving ahead, will then review the study's basic eligibility questions. If these criteria are met, they will be added to a candidate list that will be capped by a predetermined date deadline. If the list exceeds capacity, names will be drawn by a random number system (randomizer.org) to schedule an in-person physical screening visit to confirm eligibility.

2.3.2 Physical screening

A PT assessor will perform the child's in-person physical screening following receipt of written informed consent from the parent, and will document the following: height (body and leg lengths), range of motion, orthopedic/medical suitability,

1 www.rifton.com

cognitive ability to participate in physiotherapy, current home program, method of communicating discomfort or pain, and parent's willingness to commit to the treatment frequency and to refrain from commencing other new therapies during O_0, X, and O_1 phases the study. The study physician will review the results of this screening and confirm the child's eligibility to proceed with the study.

2.3.3 Informed consent

Informed consent will be obtained from: child's parent, child (assent; contingent on capacity assessment determination prior to the consent session) for the Trexo intervention and associated assessments, PT/PTAs for study interviews (post child's Trexo use), and parent for study interviews (pre and post child's Trexo use). Consent for neuroimaging will be obtained separately.

2.4 Study intervention

2.4.1 Trexo plus pediatric exoskeleton

The Trexo Plus lower limb exoskeleton (Figure 2) comprises powered orthotic legs which work cohesively within a Rifton Pacer wheeled walker that has been adapted to accommodate the exoskeleton attached to its frame. The Trexo's robotic legs are a multi-joint system with two actuated degrees of freedom per lower limb for hip flexion-extension and knee flexion-extension. This design makes the device responsive to the child's ability to initiate steps, and able to provide proportional support needed for leg movement as provided through more mechanically active "endurance mode" or more passive "strength mode". It can also be used in "standing mode" for upright activity facilitation. Trexo settings are adjusted via a user-friendly tablet interface that monitors walking time, step count, and initiation (Trexo Robotics, 2022). The Trexo requires a person outside of the user to facilitate steering and turning via the guide bar attached to the Rifton frame. For this study protocol, the Trexo robotic legs will be oriented outward (facing out of the open side of the Rifton Pacer frame), to maximize the child's hands-free participation during physiotherapy (Tao et al., 2020).

2.4.2 Physiotherapy team training and treatment strategy

The Trexo device will be a new physiotherapy intervention tool for physiotherapists. As such, to ensure safe, effective, and competent use that aligns with the child's abilities and individualized gait goals, PT/PTA training will include: (i) vendor-created technical materials and virtual training from the Trexo company; (ii) in-person shadowing of Trexo use at a community clinic; (iii) motor-learning strategies online educational materials created at our center and based on the Motor Learning Strategies Rating Instrument (Ryan et al., 2019, 2020; Spivak et al., 2021); (iv) Trexo piloting with typically developing children; and (v) ongoing peer-mentoring process within our center.

Trexo physiotherapy sessions will use an incremental progression process consistent with a motor learning approach, with increasingly challenging tasks presented over time (Figure 3). Participants may also perform exercises (i.e., stretching) to a maximum of 10 additional minutes at the start of the session that may be helpful in these sessions to facilitate the child's comfort in the Trexo. Principles of motor learning (intensity, repetition, variability, task-specificity, etc.), and the parent's and PT's structured goals (described in section "2.6.2 Functional priority goals") will be prioritized during sessions. In each session, the PT/PTA team will work together with the child and Trexo. The PT/PTA will self-select between the roles of (i) steering the exoskeleton and (ii) operating the Trexo tablet and motivating the child. A safety monitoring plan will be in place throughout each Trexo session to mitigate and/or respond to any adverse events (section "2.10 Adverse events").

2.4.3 Outpatient physiotherapy program

Participants in the outpatient cohort will receive two individual Trexo-based physiotherapy sessions per week (30-min sessions active treatment time excluding initial Trexo set-up time). The session will be led by one of the study's Trexo-trained PTs along with a Trexo-trained assisting PTA. These clinicians will not necessarily be previously familiar with the child, being assigned instead according to family and PT/PTA availability. To ensure safe and effective communication with the child, parents will be present at all sessions and will help interpret communication and fatigue as needed while the child is in the Trexo. For each session, 60 min will be allocated to setup, Trexo-based physiotherapy, and session feedback documentation by the PT/PTA. Sessions will occur in the center's gait lab, hallways, or outdoors in the summer months.

2.4.4 In-school physiotherapy program

Participants in the school cohort will receive two Trexo-based sessions per week (20-min sessions active treatment time excluding initial Trexo set-up time) from their school-affiliated physiotherapy team, to be integrated within a typical school week. The PT/PTA feedback documentation will be done at the end of the school day. One Trexo session will be done in gym class (participation opportunities for peer-based activities), and one done individually in the school's activity center. Parents are not typically present at regular physiotherapy sessions in this school setting. Thus, the child's usual school PT will provide the Trexo intervention to ensure that the child has a familiar service provider. This PT will have undergone the Trexo user training. The Trexo-trained PTA for these sessions will be assigned based on availability and will not necessarily be previously known to the child.

2.5 Feasibility and acceptability indicators

Feasibility and safety will be quantitatively measured by a set of key process, management, and resource indicators (Tickle-Degnen, 2013; Ameis et al., 2020; Ayoub et al., 2020; Hilderley et al., 2022) with associated targets set for this study protocol. A priori targets for feasibility and acceptability are: (i) ability to enroll 80% of eligible participants that are invited to participate in the study; (ii) study retention rate of $\geq$ 90%; (iii) completion of awake MRIs $\geq$ 50%; (iv) tolerance (of setup and wear) and retention of muscle recording sensors during walking tests $\geq$ 75%; (v) tolerance and retention of heart rate sensor chest strap wear during gait (Trexo walker and regular walker) and motor/functional assessment $\geq$ 75%; (vi) tolerance of

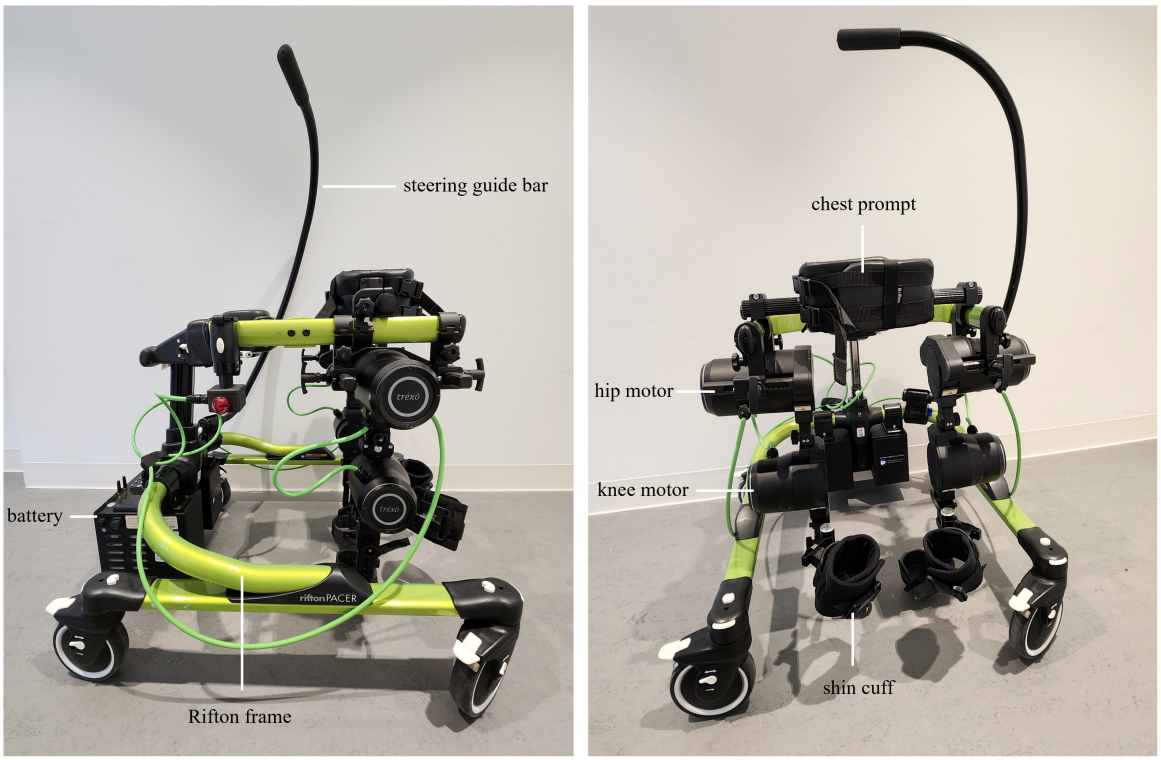

FIGURE 2
Trexo Plus pediatric lower-limb exoskeleton, mounted on a medium-sized Rifton Pacer Gait trainer. Lateral **(left)** and anterior **(right)** views are shown. Exoskeleton battery, motors at the hip and knee, and shin cuffs are indicated. Rifton frame, steering guide bar, and chest prompt are also indicated. Trexo orientation is set-up for child to be facing out of the open side of Rifton frame. Tablet interface for controlling the robotic legs is not shown.

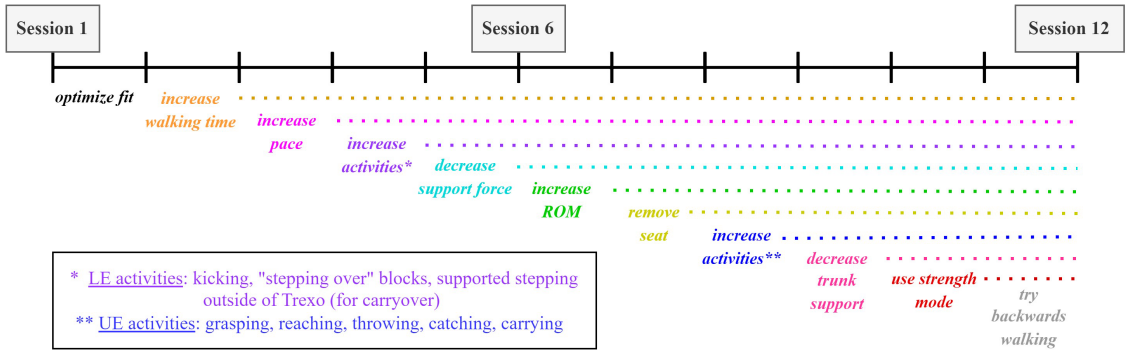

FIGURE 3
Sample of physiotherapy progression throughout duration of 12 Trexo intervention sessions. Choice of incremental challenges (through Rifton or exoskeleton adjustments) can be tailored to the participant and their individual response to therapy.

motor/functional assessments ≥ 90%; (vii) completion of parent and PT/PTA interviews ≥ 75%; (viii) adverse events "mild" severity at most and occur in ≤ 10% of physiotherapy sessions; (ix) Trexo set-up time and pauses due to adjustments significantly decrease over 12 physiotherapy session duration; (x) Trexo software or device glitches occur in ≤ 5% of sessions; (xi) motor learning strategies used "often" (25–49% of time) by PT/PTA team during physiotherapy sessions; (xii) child comfort and task enjoyment self-ratings during physiotherapy sessions reflect ≥ 80% positive scoring; (xiii) perceived study benefit by parent/clinician ≥ 80% positive scoring; and (xiv) PT/PTA training and session satisfaction ratings ≥ 80%.

2.5.1 Recruitment, retention and adherence

Recruitment rate will be calculated as the percentage of participants enrolled as a function of the number of participants invited. Study retention will be calculated as the enrolled participants who complete all required parts of the study as a function of total enrolled participants. Tolerance will be defined as procedural adherence for each methodology, whereby completion

of each of the various measurement and intervention components will be carefully considered for planning of future interventions. The acceptability of physiotherapy intervention frequency of twice per week will be assessed based on attendance and family feedback.

2.5.2 Safety

Potential risks for Trexo physiotherapy may include the usual risk of muscle soreness when doing walking-based activities, skin irritation from the exoskeleton's shin cuffs or other parts of the Trexo's walking frame, or falling when transitioning child in/out of the Trexo device. Of note, there were no adverse events documented during a 3-month case study of Trexo use at home and in the community (Diot et al., 2021).

To support close monitoring of any negative physical impacts associated with Trexo use, the treating PT will document the presence of any skin irritation experienced by the participant before and immediately after each treatment session. If pain is indicated by the child, the PT will check the identified area for bruising, redness or other skin/tenderness issues that might be associated with exoskeleton wear and/or the previous Trexo session. The child's own method of discomfort/pain communication will be taken into account when quantifying the discomfort. Body location, discomfort type (muscle vs. skin), severity (mild to severe), duration (temporary vs. sustained) of pain will be tracked thoroughly, with recommendations made for next steps (section "2.10 Adverse events"). These safety categories will be summarized when assessing the acceptability of the Trexo intervention.

2.5.3 Session tracking and documentation

All of the Trexo-based physiotherapy sessions will have associated content summary sheets (completed by the treating PT) that will permit systematic documentation of motor tasks undertaken, successes, challenges, adjustments, strategies applied, and next session planning. Additionally, a non-PT member of the research team will document the following at each session: attending staff roles, extra equipment/props used, Trexo setup time, Trexo tablet modes used, changes to range of motion or robotic support force, physical adjustments, walking and standing activities, total step count and walking time, timing and rationale for all session pauses (i.e. rest, adjustment, discomfort, standing activity), socialization opportunities, child communication modes, and observable fatigue (Supplementary Material 1).

Documentation of the active ingredients of PT interventions using exoskeleton treatments (i.e., device parameter changes and activities undertaken) has been largely missing in the literature to date. There is strong advocacy now to include tracking and reporting of device usage parameters in future trials to aid in the understanding of how best to apply the technology and better support the translation of best practice protocols into clinical practice (Cherni and Ziane, 2022; van Dellen and Labruyère, 2022). Thus, one session per child (the 10^{th} or 11^{th}) will be videorecorded to allow documentation of the extent to which motor learning approaches were taken by the PT/PTA team, assessed by an external rater using the *Motor Learning Strategies Rating Instrument* (MLSRI; Spivak et al., 2021).

2.5.4 Child, parent, and physiotherapy team satisfaction

At the end of each session, child-rated Trexo session satisfaction will be assessed using a picture-format (smiley-o-meter based) rating scale (Zaman et al., 2013). The child will be given picture scales formatted as a choice of a happy/neutral/sad face to rate how they felt in the Trexo (comfort), level of exertion (tiredness at end of session), and their level of enjoyment for each of the Trexo activities done. Summaries of each experience category (comfort, tiredness, task enjoyment) will be quantified across all 12 sessions for each participant.

Optional qualitative interviews will capture parent and PT/PTA team perspectives on the Trexo use with the child (section "2.7.2 Postural control assessments"). This will be an opportunity to solicit feedback on study design, tolerance, and opinions on different study aspects from a clinical and family perspective. PT/PTA teams will have the opportunity to reflect on the Trexo training process and the rollout of the intervention itself, so that this process can be optimized for future PT/PTA cohorts.

2.6 Primary study outcomes

Primary study outcomes will be assessed at multiple timepoints (Table 2) pre- and post-intervention.

2.6.1 Gross motor skills

The *Gross Motor Function Measure* (GMFM-88; Russell et al., 2000) will be administered by an independent PT assessor during the motor/functional assessment at baseline and immediately post-intervention. It will also be used 1-month post-intervention to gauge maintenance/progression of any functional gains. PT assessors will be trained on the GMFM-88 and all other PT assessment measures by the study's co-principal investigator prior to their first study assessment. All PTs will already have extensive clinical experience administering the GMFM with children with CP, and variable experience with the other measures. The full 88-item version of the GMFM will be used as it more comprehensively captures a range of abilities in its lowest dimensions (Lie/Roll and Sit) than the abbreviated GMFM-66. This will be important as better trunk and head control are anticipated to be goals and potential outcomes associated with Trexo use in children in GMFCS Level IV. The GMFM-88 testing will be captured on video to enable post-assessment review by PTs. Pre/post change scores will be calculated with descriptive statistics representing results of the group. The GMFM has excellent test-retest reliability (Bjornson et al., 1998), and responsiveness to change (Vos-Vromans et al., 2005).

2.6.2 Functional priority goals

The PT assessor will guide the attending parent(s) through the *Canadian Occupational Performance Measure* (COPM; Law et al., 1990) during the baseline functional assessment visit to set priority outcome goals for their child. These 3–4 goals will be guided from a menu prepared by the investigators of walking-based or other functional outcomes that may arise from Trexo use. These goals can relate to the child's abilities in home, school, or community environments. The parent(s) will use the COPM's

TABLE 2 Outcome measures across timepoints.

		Timepoint			
Measures	Completed by	O_0	X	O_1	O_2
Primary outcome measure					
GMFM-88*	PT assessor	•		•	•
COPM *	Parent with PT assessor	•		•	•
GAS	Treating PT/PTA		**T** (†); **T** (‡)		
MRI	SR with MRI technician	•		•	•
MMG	SR		**T, W** (†); **T, W** (‡)		
Secondary outcome measure					
ROM and Tardieu Spasticity*	PT assessor	•		•	•
PPAS and LSS*	PT assessor	•		•	•
PEDI-CAT*	Parent	•		•	•
1WT and DMA	Treating PT/PTA		**T, W** (†); **T, W** (‡)		
Heart rate	SR		**T, W** (‡)		
Participant characterization					
MACS*	PT assessor with parent	•			
CFCS	Treating PT and SR			**T**	
Dimensions of mastery*	Parent	•			
Trexo physical adjustments	Treating PT and SR		**T**		
PT and parent perspectives					
Parent baseline interview	Parent with SI		•		
Parent outcomes interview	Parent with SI			•	
PT training interview	Treating PT/PTA with SI			•	
PT outcomes interview	Treating PT/PTA with SI			•	

*Completed during motor/functional assessment visit. **T** = done in Trexo; **W** = done in regular walker; • = done without any device. (†) denotes the beginning of the intervention phase and (‡) denotes the end of the intervention phase.

10-point response scales to rate the importance of each goal, as well as satisfaction and performance of each at baseline. COPM goals will be rated by the parent(s) again at the post-intervention assessment, as well as the 1-month post intervention assessment. All efforts will be made to have the same parent attend each assessment to maintain consistency. The parent(s) and assessor will be blinded to previous COPM scores. Pre/post mean change scores will be calculated for each child. The COPM has been adapted for use with children and has demonstrated strong internal consistency, construct validity, and responsiveness to change (Cusick et al., 2007).

Goal Attainment Scaling (GAS) goals and achievement levels will be set by the treating PTs, and will be Trexo-directed or regular walker-associated. GAS will serve as an individualized measure of change for each child and will link to the parent-chosen COPM goals to allow evaluation of the targeted subcomponents of COPM's higher level functional priority goals (King et al., 2000; Ostensjo et al., 2008). These two or three goals will be set by the 3rd physiotherapy session, allowing the PT team to first form a realistic idea of the child's functional abilities and potential areas of improvement. GAS outcomes will be scored per goal by the child's treating PT upon completion of the child's last physiotherapy session, and a summary T-score will also be calculated. GAS is commonly used with children with CP who use walkers, and has demonstrated strong internal consistency, construct validity, and responsiveness to change (Paleg and Livingstone, 2016).

2.6.3 Neuroimaging

Awake magnetic resonance imaging (MRI) head scanning will be done in the Siemens Prisma MAGNETOM 3-Tesla MRI scanner with a 36-channel head coil at Holland Bloorview Kids Rehabilitation Hospital (Figure 4). If tolerated, these will be done at baseline and immediately post-intervention, with an option for a third scan 1-month post-intervention. Prior to the baseline scan, families will be provided with MRI resources intended to prepare and educate them for an awake scan with their child. Resources include a child-friendly MRI explanation book, video links to a tour of the center's MRI suite, links to MRI cartoons, links to MRI sound samples, and a link to the resting state fMRI video. This is meant to ease any apprehension or stress associated with the MRI process.

Total MRI acquisition time will be kept under 40 min for this young demographic. MRI scanning will include T1-weighted scanning, T2-weighted scanning for incidental findings, diffusion kurtosis imaging (DKI), and resting state functional MRI (fMRI) (scan parameters: Supplementary Material 2). Participants will wear noise-canceling headphones and watch videos of their choice during the structural scans, and the visual paradigm Inscapes video

FIGURE 4
The MRI suite at Holland Bloorview Kids Rehabilitation Hospital (Toronto, Canada). This suite is fully accessible, child-friendly, research-focused, immersive, and customizable. Awake MRI head scanning occurs pre- and post-intervention.

(headspacestudios.org/inscapes) during the fMRI scan. Incidental reviews of all scans will be completed by a pediatric radiologist.

2.6.4 Muscle recordings

Mechanomyography (MMG) muscle recordings (Plewa et al., 2017) from each child will be recorded at baseline and post-intervention, concurrently with walking assessments (section "2.8.3 Motivation-related traits") in their regular maximum support walker (if they have one) and the Trexo walker.

Bilateral MMG data will be collected using tri-axial ADXL335 accelerometers (2.0 cm x 1.5cm; sampling rate 1000 hz/channel), powered by a 3.3V regulator. 8 accelerometers will be placed on muscle sites bilaterally to record muscle vibrations: erector spinae (longissimus thoracis), biceps femoris, vastus lateralis and gluteus maximus. These muscles were selected based on their role in gait (Hesse and Uhlenbrock, 2000; Jonkers et al., 2003; Sousa and Tavares, 2012; Di Nardo et al., 2015) and body surface accessibility for muscle sensors while in the Trexo. Accelerometers will be attached with medical tape on the skin above the largest part of the muscle belly (Figure 5). All selected muscle sites are above the knee as Trexo shin cuffs preclude access to below-knee locations. An additional (9^{th}) sensor will be attached to the knee joint of the Trexo device to record robotic leg movement.

Each accelerometer will be wired to a data collection unit comprised of two National Instruments USB-6210 data acquisition cards. The data acquisition cards will plug into a laptop computer via USB, which will be fitted into a backpack that travels with the walkers (hung on the back of the Trexo or carried by a member of the research team). A second computer will connect remotely to the laptop, allowing the researcher to start and stop the data collection as well as remotely mark the data in real time during significant events (e.g., pauses for adjustments, start/stop of walking assessments).

MMG data collection will take place in 25-min testing sessions (including setup; per walker) that will encompass the 1-min walk and dynamic mobility assessment (section "2.7.4 Gait assessments") followed by a free (unstructured) walking period with the child.

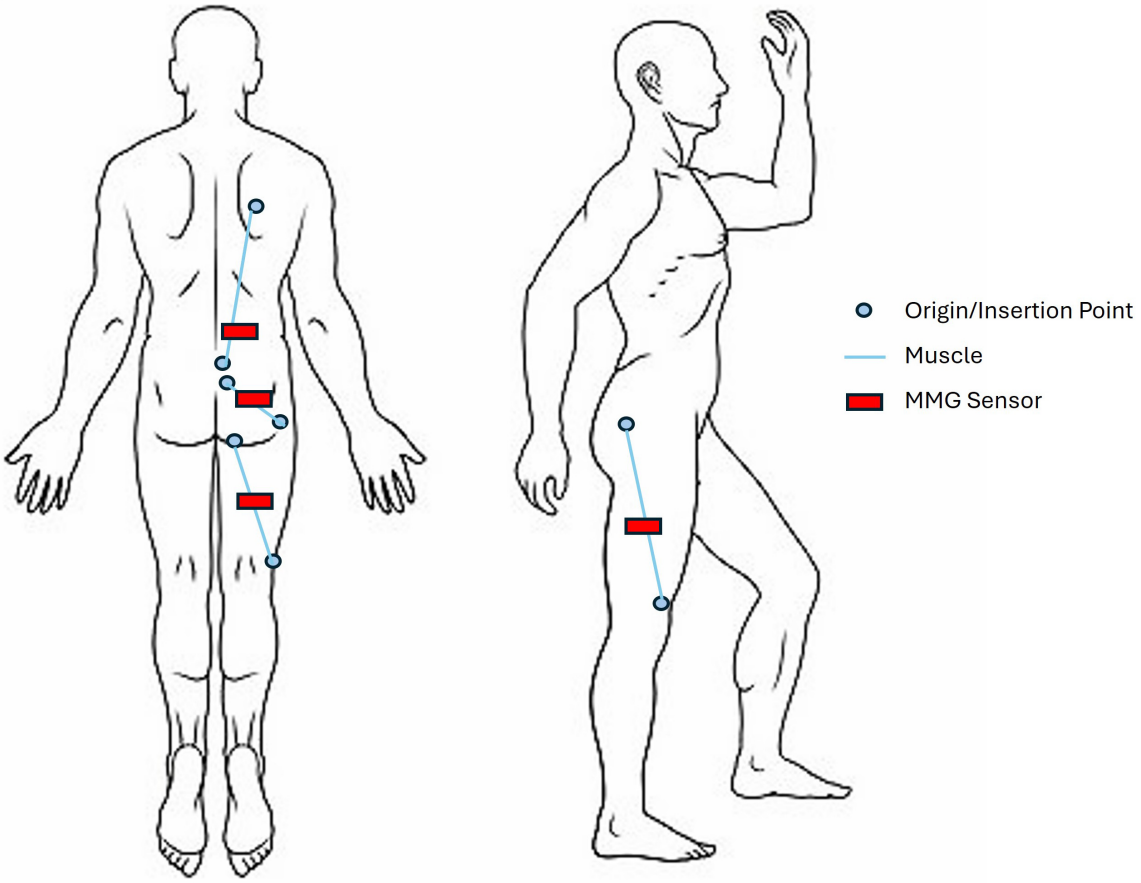

FIGURE 5
Mechanomyography sensor layout, shown on the right side of the body. Target muscles include vastus lateralis, biceps femoris (long head), gluteus maximus, and erector spinae (longissimus thoracis). Sensors will be secured on top of the skin with medical tape and located according to origin and insertion points of the muscles.

Each participant will walk for a minimum of 5 min (or until fatigue to a maximum of 20 min) in their regular maximum support walker and the Trexo exoskeleton. Baseline MMG readings will be taken during quiet standing for 30 s at the start of each testing session – these readings will be used to normalize signals.

2.7 Secondary study outcomes

Secondary study outcomes will be assessed at multiple timepoints (Table 2) pre- and post-intervention.

2.7.1 Body structure and function

Passive range of motion (ROM) of selected movements (hip flexion contracture; hip abduction; popliteal angle; knee flexion contracture; ankle dorsiflexion with knee flexed or extended), and evaluation of resting and dynamic spasticity as measured by the *Tardieu Scale* (Scholtes et al., 2006) at knee and ankle (hip adductors, hamstrings, gastrocnemius with knee flexed and extended) will be conducted at all functional assessment timepoints. This is important to establish at baseline (excerpted from screening session data where ROM eligibility was confirmed) to monitor adverse events, and permit evaluation of changes in ROM associated with Trexo use.

2.7.2 Postural control assessments

Two postural assessments will be administered by the physiotherapist assessor, and scored from video that will be captured during the assessment by a research assistant using a standardized camera angle protocol.

The *Posture and Postural Ability Scale (*PPAS; Rodby-Bousquet et al., 2016*)* is a validated measure for children with CP in GMFCS levels II to V. It will rate the symmetry and alignment of the child's head, trunk, pelvis, legs, arms, and weight distribution in frontal and sagittal planes. The child will be guided into prone, supine, sitting and supported standing positions (30 s in each) by the assessor. Scoring will be done from the video of the assessment.

The *Level of Sitting Scale* (LSS) (Fife et al., 1991; Field and Roxborough, 2011) is designed for children who are wheelchair users and require some degree of external support (GMFCS IV and V). The LSS will classify a child's sitting ability without feet supported. It will serve as both a descriptive measure of children enrolled in the study and also an outcome measure in tandem with the PPAS. It will be scored from the PPAS video.

2.7.3 Functional abilities parent-report questionnaire

The *Pediatric Evaluation of Disability Inventory* (PEDI-CAT) (Haley et al., 2011; Shore et al., 2017) parent-report questionnaire's Daily Activities (speedy version), Mobility (content version) and Social/Cognitive (speedy version) domains will be completed by the child's parent at each of the functional assessments, via a secure weblink on a study tablet. If both the parents are present, they may complete it together.

2.7.4 Gait assessments

Functional gait will be assessed via a *1-minute walk test* (1MWT) (Hassani et al., 2014) and the *Directional Mobility Assessment* (DMA) (Wright and Jutai, 2006; Livingstone and Paleg, 2016), done in the child's regular walking device (if they use one) and the Trexo walker. The 1MWT will measure the distance walked down a straight wide hallway within 60 s with the Trexo and with the child's regular walker, with support from the child's PT/PTA team as needed for steering (Trexo and regular walker) and facilitating steps (regular walker). The DMA incorporates a functional walking course: straight walking, turns, obstacles, narrow path, and backing up.

These walking tasks will be administered by the child's treating PT/PTA simultaneously during MMG/heart rate monitoring (facilitated by study researchers). Involvement of the PT/PTA in this testing is essential as they are Trexo-trained and aware of the child's functional abilities and safety considerations. A video recording will be made of these walking tests to permit their rating by an independent PT assessor to maintain independence of scoring from the clinical team.

2.7.5 Heart rate

Heart rate during gait will be captured using a Polar H10 Heart Rate Sensor (wireless chest strap placed around the torso) which will transmit data (beats per minute, RR intervals, and heart rate variability taken continuously) via Bluetooth to a secure device. Heart rate will be captured post-intervention (end of Phase X) concurrently with muscle recordings (section "2.6.4 Muscle recordings") during Trexo and regular walker use at the timed walk and DMA assessments since robotically facilitated walking may impact heart rate differently than would a manual walker. Resting heart rate will be captured initially in each instance. Heart rate will also be captured in the absence of walking, during the post-intervention functional assessment.

2.8 Participant characterization

The following assessments will be completed only once during the child's study participation as they portray a fixed trait/ability (i.e., not outcome measures). These assessments will help characterize each participant and may serve as predictors or correlates for feasibility and outcome measure results.

2.8.1 Upper extremity function

The *Manual Ability Classification System* (MACS or MiniMACS; Eliasson et al., 2006) will be completed by a PT assessor at the end of the baseline motor/functional assessment as they reflect the child's hand function observed during upper and lower body tasks in the assessment and confirm child's day to day hand function in conversation with the parent- at the assessment. Children in GMFCS IV may have hand function at a different level than that of their gross motor function, and these hand and arm abilities may have an impact on what the child will be able to do during Trexo physiotherapy. Hence this information may be important in the interpretation of sessional data and ultimate goal accomplishment.

2.8.2 Communication ability

The *Communication Function Classification System* (CFCS; Hidecker et al., 2011) will be used after all 12 Trexo physiotherapy sessions have been completed, to capture the child's communication style over time while in the Trexo.

2.8.3 Motivation-related traits

The *Dimensions of Mastery* questionnaire (Morgan et al., 2006; Igoe et al., 2011) will be completed by parents at the baseline motor/functional assessment only. This information about the child's underlying motivation traits may help identify personal characteristics related to engagement and learning that maybe contribute to Trexo session success.

2.8.4 Individualized Trexo physical adjustment templates

Each child will have their own baseline Trexo adjustment template (Supplementary Material 3) created during their pre-physiotherapy fitting session and updated through the course of the child's Trexo use. This template will compile Rifton Pacer settings (chest prompt size/tilt, Rifton frame height, seat height, seat angle, and seat position), Trexo leg settings (robotic leg width, knee-to-floor length, hip-to-knee length, and footplate size), and Trexo tablet settings (range of motion and optimal support forces for hip and knee joints). These settings will be selected by the treating PT to ensure good postural alignment, comfort, and adequate heel strike during walking. Since a single Trexo device will be shared across the children in the study, the research team will refer to this profile prior to each child's physiotherapy session to make sure all child-specific physical adjustments are made to the Trexo before the session starts.

2.9 PT and parent perspectives

Qualitative interviews will be scheduled separately with the PT/PTA team and parents with an independent study interviewer using semi-structured interview guides. These interviews will be scheduled proximal to the pre- and post-intervention study timepoints.

Participating PTs and PTAs will have the opportunity to share their perspectives via two optional interviews: (i) reflection on the strengths and limitations of the Trexo training process used following the completion of their training and a round of Trexo physiotherapy sessions for at least one child (~30–60 min); and (ii) Trexo user experience for each participant, following the end of that child's physiotherapy intervention (60–90 min).

Parents' study expectations and goals will be collected at two optional interview timepoints: (i) baseline; about Trexo

outcomes goals and hopes (~20 min); and (ii) post-Trexo intervention; focusing on observed outcomes, impressions about study methodologies, and individualized goal accomplishment including questions about overall quality of life in addition to the questions about mobility (~45 min). Since the research team will see the child for only 2 h a week, parent feedback will be essential to capture functional changes observed in the daily living context of their child. This will also be an opportunity to solicit parental feedback on study design, tolerance, and opinions on different study aspects.

2.10 Adverse events

In the case of an adverse event, the study physician will be contacted for the recommended course of action, which will depend on the severity and circumstances of the adverse event. Documentation of the event will be completed by the treating PT, principal investigator, and study physician as per the study's adverse event form. A treatment plan will be made at the discretion of the study physician. If the study team concludes that the Trexo presents a possible continuing risk to the child, Trexo treatment will be discontinued for that child and the post-Trexo outcomes assessment will be completed at that time. Additionally, the parent or child can decide to discontinue the study at any point for any reason. They will be invited to complete the next follow-up assessment at that point but are free to decline this as well. If any children drop out of the study, no children will be recruited in their place since this discontinuation of participation could point to an underlying acceptability or safety issue.

2.11 Data analysis

2.11.1 Quantitative data analysis

Feasibility/safety/acceptability indicators (section "2.5 Feasibility and acceptability indicators") will be summarized for each child's sessions and the group descriptive statistics will be compared to *a priori* target values.

Motor/functional assessment measures and functional priority goals will have total/dimension scores summarized via descriptive statistics. Paired *t*-tests or non-parametric equivalents will be conducted for baseline and post-intervention time points for the co-primary measures (GMFM-88 and COPM goals), and then with each of the secondary outcomes. Correlational analyses (Pearson's r) will also be undertaken to investigate associations between primary and secondary outcomes or with MRI results. Each clinical measure will be graphically inspected for any patterns from baseline to the optional 1-month post-intervention timepoint. For a subsample of children (undetermined subgroup 'n' at this point), comparisons will also be made between walking performance in the child's regular walker and the Trexo at baseline and post-intervention.

MRI scans will be processed with Freesurfer Software (surfer.nmr.mgh.harvard.edu), employing a longitudinal pipeline. Automated segmentation of structural T1-weighted images will be performed, followed by quality control steps to ensure image clarity. Any neuroimaging data with excessive motion artifact will be excluded from the study. Regions of interest (ROI) will be selected based on brain areas that are most associated with gait, motor function, and motor learning. From T1 anatomical data, mean cortical thickness per brain region, and white and gray matter volumes will be calculated. Diffusion data will be used to identify and reconstruct relevant white matter tracts as well as derive DKI and DTI mean metric maps, kurtosis fractional anisotropy (FA) values, and mean kurtosis (MK), as outcome measures. From the fMRI data, ROI-specific time courses of the BOLD signal will be computed by averaging time courses across voxels within each ROI. fMRI outcome measures will include functional connectivity (FC) correlation matrices and a structural-decoupling index.

MMG signals will be calculated as the magnitude of the vector sum of the tri-axial ADXL335 accelerations. Data will be segmented according to periods of activity and normalized to the initial period of quiet standing for each participant. Accelerometer data will be processed using Matlab Software (Natick, Massachusetts: The MathWorks Inc.): bandpass filtered between 5 and 100 Hz (4^{th} order Butterworth filter) and processed with a symlet wavelet transform (Alves and Chau, 2010; Achmamad and Jbari, 2020). Device-induced noise will be compared in the Trexo and the child's regular walker. Heel strike will be identified based on video recordings to demarcate phases of the gait cycle and changes in magnitude and slope of the force. We will extract and select features in time, frequency, and time-frequency domain for classification.

2.11.2 Qualitative data analysis

Anonymized individual physiotherapy summary profiles will be created from the session documentation, detailing goals worked on, Trexo settings used, activities undertaken, things that went well, and challenges that presented during sessions. Collective data profiles across children from their first, mid-point, and last sessions will be analyzed via a content analysis approach (settings/activities/challenges) to summarize the operational details related to Trexo use and elucidate any patterns of progression of Trexo settings, walk distances and activities undertaken within the Trexo treatment block.

All interviews will be transcribed within Zoom, checked afterward by the interviewer for accuracy and then de-identified prior to thematic analysis. Data will be analyzed using NVivo Software (QSR International Inc., Burlington, Canada), and an inductive content analysis approach will be taken to generate the initial codebook (Braun and Clarke, 2006). Parent and PT/PTA interviews will undergo separate thematic analysis to support within-group development of preliminary codes. Specific wording used by participants will be included in the codes to assist in preserving the meaning participants attribute to their actions and processes (Maher et al., 2018). Research team meetings will advance code-to-category-theme development and propose alternate/refined themes and interpretations until group consensus is reached.

A concurrent mixed methods approach will be taken where qualitative and quantitative data will be presented together by theme, and results reported in a narrative joint display (Fetters et al., 2013; Guetterman et al., 2015). Transferability of the results will be facilitated by reporting relevant study participant demographics to contextualize the findings.

3 Discussion

Overground exoskeleton use offers children who have restricted ambulatory abilities the opportunity to uniquely access their surrounding environment within a device that provides safety and stability (Diot et al., 2021) while also offering the opportunity to incorporate hand and arm use during walking-based activities. To our knowledge, this will be the first study to investigate feasibility indicators, outcomes, and experiences of Trexo-based physiotherapy in school and outpatient contexts for children with severe mobility impairments. Our rehabilitation protocol is based on motor learning principles that may promote experience-dependent neuroplasticity (Gassert and Dietz, 2018; Berger et al., 2019) and changes in functional, neural, and muscular outcomes.

Compared to conventional gait training, the preparation and execution of physiotherapy treatment blocks using new gait technologies is more cognitively demanding for PTs (Read et al., 2020; Ouendi et al., 2022; van Dellen et al., 2023; Murphy et al., 2024). This added aspect underscores the importance of evaluating the feasibility and acceptability of the "typical" Trexo session itself. In our pediatric context, quantitative and qualitative data captured during Trexo physiotherapy sessions will provide user-based information that may address questions related to clinical adoption and utility from the PT perspective. Specifically, stakeholder feedback (child, parents, clinician) from interviews and feasibility/session data overall will guide the creation of future training materials, and evidence-based implementation protocols for PTs. It will also facilitate realistic goal setting and capture impressions of parents about the value of this technology for their preambulatory children and any extended associated impact on performance in routine activity or on quality of life more broadly.

Understanding the body-wide outcomes associated with gait training in children with CP is essential for safety and maximizing positive functional results. The characterization of therapy-dependent neuroplasticity (Peters et al., 2020) may provide indications about how responses to exoskeleton-assisted gait therapy may have some association with a child's neurological profile (Schwartz and Meiner, 2015), and may be associated with different changes in functional and muscular behavior (Snodgrass et al., 2014; Sczesny-Kaiser et al., 2015; Perpetuini et al., 2022). Quantifying muscle behavior and heart rate during robotic gait training can help establish any training limit thresholds that might need to be put in place to prevent injury and over-exertion in physiotherapy treatments (Brunton and Rice, 2012; Puce et al., 2021), especially for nonverbal children. Future overground exoskeleton development can be paired with this knowledge of body-wide outcomes to advance mechanical feedback responses to the child's physiological signals, thereby integrating with the child's existing motor abilities while also compensating for skill deficiencies.

This study will contribute evidence-based knowledge to guide clinical decisions about the introduction of the Trexo or similar lower-limb exoskeletons within pediatric rehabilitation settings, and serve as an empirical foundation for a progressive program of multi-center research. In addition to the field of CP, this research could be broadened to include individuals with other non-progressive neuromotor conditions which impair the lower body, including those in GMFCS V (non-ambulatory children), if adequate safety and acceptability are established.

4 Ethics and dissemination

4.1 Ethics approval and consent to participate

This study protocol was approved by the research ethics board of Holland Bloorview Kids Rehabilitation Hospital (no. 0523), and the University of Toronto (no. 00044118), according to Resolution 466/12 of the National Health Council and the Declaration of Helsinki. Researchers will invite children and parents to participate voluntarily and sign the informed consent forms to be included in the study.

4.2 Consent for publication and confidentiality

Participation information will be kept confidential and stored securely in the hospital database. Only researchers will access the database, ensuring anonymity, respect, and human dignity. Results will be published in peer-reviewed journals and presented at scientific meetings. In case of significant changes in the protocol, we will inform participants, Clinicaltrials.gov, and journals. If requested, we will provide a copy of the informed consent form.

4.3 Availability of protocol and data

This protocol information is registered and available: [https://clinicaltrials.gov], identifier NCT05463211.The corresponding author will provide the study protocol and data on reasonable request to achieve study goals.

Ethics statement

The studies involving humans were approved by the Research ethics committees at Holland Bloorview Kids Rehabilitation Hospital REB (no. 0523), University of Toronto (no. 00044118). The studies were conducted in accordance with the local legislation and institutional requirements. Written informed consent for participation in this study was provided by the participants' legal guardians/next of kin.

Author contributions

SB: Conceptualization, Data curation, Formal analysis, Funding acquisition, Methodology, Project administration, Resources, Validation, Visualization, Writing – original draft, Writing – review and editing. LH: Writing – original draft, Writing – review and editing. TC: Conceptualization, Funding acquisition, Methodology, Resources, Supervision, Writing – original draft, Writing –

review and editing, Validation. FVW: Conceptualization, Funding acquisition, Methodology, Resources, Supervision, Writing – original draft, Writing – review and editing.

Funding

The author(s) declare that financial support was received for the research, authorship, and/or publication of this article. This study is funded by the Cerebral Palsy Alliance Foundation Doctoral Grant to SB (PHD00421), FVW's SPARK Lab Research Support fund and TC's Natural Sciences and Engineering Research Council grant (RGPIN-2019-06033), the Bloorview Research Institute within Holland Bloorview Kids Rehabilitation Hospital: Center for Leadership Grant, Kimel Graduate Student Scholarship in Pediatric Disability to SB, and Whipper Watson Graduate Studentship Award to SB. SB was also funded by the Ontario Graduate Scholarship (2021).

Acknowledgments

We would like to thank the Holland Bloorview Kids Rehabilitation Hospital Foundation for funding the acquisition of the Trexo exoskeleton to be used in this study. For help in protocol design, we would like to acknowledge: Dr. Anne Kawamura for eligibility and diagnostic criteria guidance, Dr. Donald Mabbott for protocol design feedback, Ka Lun Tam for technical help (MMG hardware/software design), Kevin Chung and Julie Tseng for MRI scan parameter selection, and SMILE Therapy for Kids for Trexo physiotherapy consultation.

Conflict of interest

The authors declare that the research was conducted in the absence of any commercial or financial relationships that could be construed as a potential conflict of interest.

Publisher's note

Supplementary material

The Supplementary Material for this article can be found online at: https://www.frontiersin.org/articles/10.3389/fnins.2024.1398459/full#supplementary-material

References

Achmamad, A., and Jbari, A. (2020). A comparative study of wavelet families for electromyography signal classification based on discrete wavelet transform. *Bull. EEI* 9, 1420–1429. doi: 10.11591/eei.v9i4.2381

Alves, N., and Chau, T. (2010). Automatic detection of muscle activity from mechanomyogram signals: A comparison of amplitude and wavelet-based methods. *Physiol. Meas.* 31:461. doi: 10.1088/0967-3334/31/4/001

Ameis, S. H., Blumberger, D. M., Croarkin, P. E., Mabbott, D. J., Lai, M.-C., Desarkar, P., et al. (2020). Treatment of executive function deficits in autism spectrum disorder with repetitive transcranial magnetic stimulation: A double-blind, sham-controlled, pilot trial. *Brain Stimul.* 13, 539–547. doi: 10.1016/j.brs.2020.01.007

Aurich-Schuler, T., Warken, B., Graser, J., Ulrich, T., Borggraefe, I., Heinen, F., et al. (2015). Practical recommendations for robot-assisted treadmill therapy (Lokomat) in children with cerebral palsy: Indications, goal setting, and clinical implementation within the WHO-ICF framework. *Neuropediatrics* 46, 248–260. doi: 10.1055/s-0035-1550150

Ayoub, R., Ruddy, R. M., Cox, E., Oyefiade, A., Derkach, D., Laughlin, S., et al. (2020). Assessment of cognitive and neural recovery in survivors of pediatric brain tumors in a pilot clinical trial using metformin. *Nat. Med.* 26, 1285–1294. doi: 10.1038/s41591-020-0985-2

Berger, A., Horst, F., Müller, S., Steinberg, F., and Doppelmayr, M. (2019). Current state and future prospects of EEG and fNIRS in robot-assisted gait rehabilitation: A brief review. *Front. Hum. Neurosci.* 13:172. doi: 10.3389/fnhum.2019.00172

Beveridge, B., Feltracco, D., Struyf, J., Strauss, E., Dang, S., Phelan, S., et al. (2015). "You gotta try it all": Parents' experiences with robotic gait training for their children with cerebral palsy. *Phys. Occup. Ther. Pediatr.* 35, 327–341. doi: 10.3109/01942638.2014.990547

Bjornson, K. F., Graubert, C. S., McLaughlin, J. F., Kerfeld, C. I., and Clark, E. M. (1998). Test-retest reliability of the gross motor function measure in children with cerebral palsy. *Phys. Occup. Ther. Pediatr.* 18, 51–61.

Braun, V., and Clarke, V. (2006). Qualitative research in psychology using thematic analysis in psychology using thematic analysis in psychology. *Qual. Res. Psychol.* 3, 77–101.

Bruni, M. F., Melegari, C., Cola, M. C. D., Bramanti, A., Bramanti, P., and Calabrò, R. S. (2018). What does best evidence tell us about robotic gait rehabilitation in stroke patients: A systematic review and meta-analysis. *J. Clin. Neurosci.* 48, 11–17. doi: 10.1016/j.jocn.2017.10.048

Brunton, L. K., and Rice, C. L. (2012). Fatigue in cerebral palsy: A critical review. *Dev. Neurorehabil.* 15, 54–62.

Chan, A.-W., Tetzlaff, J. M., Altman, D. G., Laupacis, A., Gøtzsche, P. C., Krleža-Jerić, K., et al. (2013a). SPIRIT 2013 statement: Defining standard protocol items for clinical trials. *Ann. Intern. Med.* 158, 200–207. doi: 10.7326/0003-4819-158-3-201302050-00583

Chan, A.-W., Tetzlaff, J. M., Gøtzsche, P. C., Altman, D. G., Mann, H., Berlin, J. A., et al. (2013b). SPIRIT 2013 explanation and elaboration: Guidance for protocols of clinical trials. *BMJ* 346:e7586. doi: 10.1136/bmj.e7586

Cherni, Y., and Ziane, C. (2022). A narrative review on robotic-assisted gait training in children and adolescents with cerebral palsy: Training parameters, choice of settings, and perspectives. *Disabilities* 2, 293–303.

Cumplido, C., Delgado, E., Ramos, J., Puyuelo, G., Garcés, E., Destarac, M. A., et al. (2021). Gait-assisted exoskeletons for children with cerebral palsy or spinal muscular atrophy: A systematic review. *Neuro Rehabil.* 49, 333–348.

Cusick, A., Lannin, N. A., and Lowe, K. (2007). Adapting the Canadian occupational performance measure for use in a paediatric clinical trial. *Disabil. Rehabil.* 29, 761–766. doi: 10.1080/09638280600929201

Czajkowski, S. M., Powell, L. H., Adler, N., Naar-King, S., Reynolds, K. D., Hunter, C. M., et al. (2015). From ideas to efficacy: The ORBIT model for developing behavioral treatments for chronic diseases. *Health Psychol.* 34, 971–982. doi: 10.1037/hea0000161

De Luca, A., Bellitto, A., Mandraccia, S., Marchesi, G., Pellegrino, L., Coscia, M., et al. (2019). Exoskeleton for gait rehabilitation: Effects of assistance, mechanical structure, and walking aids on muscle activations. *Appl. Sci.* 9:2868. doi: 10.3390/app9142868

Di Nardo, F., Maranesi, E., Mengarelli, A., Ghetti, G., Burattini, L., and Fioretti, S. (2015). Assessment of the variability of vastii myoelectric activity in young healthy females during walking: A statistical gait analysis. *J. Electromyogr. Kinesiol.* 25, 800–807. doi: 10.1016/j.jelekin.2015.07.004

Diot, C. M., Thomas, R. L., Raess, L., Wrightson, J. G., and Condliffe, E. G. (2021). Robotic lower extremity exoskeleton use in a non-ambulatory child with cerebral palsy: A case study. *Disabil. Rehabil. Assist. Technol.* 18, 497–501. doi: 10.1080/17483107.2021.1878296

Diot, C. M., Youngblood, J. L., Friesen, A. H., Wong, T., Santos, T. A., Norman, B. M., et al. (2023). Robot-assisted gait training with Trexo home: Users, usage and initial impacts. *Children (Basel)* 10:437. doi: 10.3390/children10030437

Eliasson, A.-C., Krumlinde-Sundholm, L., Rösblad, B., Beckung, E., Arner, M., Öhrvall, A.-M., et al. (2006). The Manual Ability Classification System (MACS) for children with cerebral palsy: Scale development and evidence of validity and reliability. *Dev. Med. Child Neurol.* 48, 549–554. doi: 10.1017/S0012162206001162

Eng, J. J., Levins, S. M., Townson, A. F., Mah-Jones, D., Bremner, J., and Huston, G. (2001). Use of prolonged standing for individuals with spinal cord injuries. *Phys. Ther.* 81, 1392–1399. doi: 10.1093/ptj/81.8.1392

Fetters, M. D., Curry, L. A., and Creswell, J. W. (2013). Achieving integration in mixed methods designs - principles and practices. *Health Serv. Res.* 48, 2134–2156.

Field, D. A., and Roxborough, L. A. (2011). Responsiveness of the seated postural control measure and the level of sitting scale in children with neuromotor disorders. *Disabil. Rehabil. Assist. Technol.* 6, 473–482.

Fife, S. E., Roxborough, L. A., and Armstrong, R. W. (1991). Development of a clinical measure of postural control for assessment of adaptive seating in children with neuromotor disabilities. *Phys. Ther.* 71, 981–993. doi: 10.1093/ptj/71.12.981

Fosch-Villaronga, E., Čartolovni, A., and Pierce, R. L. (2020). Promoting inclusiveness in exoskeleton robotics: Addressing challenges for pediatric access. *J. Behav. Robot.* 11, 327–339.

Gassert, R., and Dietz, V. (2018). Rehabilitation robots for the treatment of sensorimotor deficits: A neurophysiological perspective. *J. Neuroeng. Rehabil.* 15:46. doi: 10.1186/s12984-018-0383-x

Giancolo, J., McWilliam, K., Wright, F. V., and Ryan, J. (2022). Exploring motor learning strategies use in occupational therapy for children and youth with acquired brain injury. *Phys. Occup. Ther. Pediatr.* 42, 30–45.

Gibson, B. E., Teachman, G., Wright, V., Fehlings, D., Young, N. L., and McKeever, P. (2012). Children's and parents' beliefs regarding the value of walking: Rehabilitation implications for children with cerebral palsy. *Child Care Health* 38, 61–69.

Gilardi, F., De Falco, F., Casasanta, D., Andellini, M., Gazzellini, S., Petrarca, M., et al. (2020). Robotic technology in pediatric neurorehabilitation. A pilot study of human factors in an Italian pediatric hospital. *Int. J. Environ. Res. Public Health* 17:3503. doi: 10.3390/ijerph17103503

Goswami, J. N., Sankhyan, N., and Singhi, P. (2021). Add-on home-centered activity-based therapy vs conventional physiotherapy in improving walking ability at 6-months in children with diplegic cerebral palsy: A randomized controlled rrial. *Indian Pediatr.* 58, 826–832.

Guetterman, T. C., Fetters, M. D., and Creswell, J. W. (2015). Integrating quantitative and qualitative results in health science mixed methods research through joint displays. *Ann. Fam. Med.* 13, 554–561. doi: 10.1370/afm.1865

Hadj-Moussa, F., Zahid, H. B., Wright, F. V., Kelland, K., and Andrysek, J. (2022). 'It's more than just a running leg': A qualitative study of running-specific prosthesis use by children with lower limb absence. *Disabil. Rehabil.* 44, 7190–7198. doi: 10.1080/09638288.2021.1986748

Haley, S. M., Coster, W. J., Dumas, H. M., Fragala-Pinkham, M. A., Kramer, J., and Ni, P. (2011). Accuracy and precision of the pediatric evaluation of disability inventory computer-adaptive tests PEDI-CAT. *Dev. Med. Child Neurol.* 53, 1100–1106. doi: 10.1111/j.1469-8749.2011.04107.x

Hassani, S., Krzak, J. J., Johnson, B., Flanagan, A., Gorton III, G., Bagley, A., et al. (2014). One-Minute Walk and modified Timed Up and Go tests in children with cerebral palsy: Performance and minimum clinically important differences. *Dev. Med. Child Neurol.* 56, 482–489. doi: 10.1111/dmcn.12325

Hesse, S., and Uhlenbrock, D. (2000). A mechanized gait trainer for restoration of gait. *J. Rehabil. Res. Dev.* 37, 701–708.

Hidecker, M. J. C., Paneth, N., Rosenbaum, P. L., Kent, R. D., Lillie, J., Eulenberg, J. B., et al. (2011). Developing and validating the communication function classification system for individuals with cerebral palsy. *Dev. Med. Child Neurol.* 53, 704–710. doi: 10.1111/j.1469-8749.2011.03996.x

Hilderley, A. J., Fehlings, D., Chen, J. L., and Wright, F. V. (2022). Comparison of sports skills movement training to lower limb strength training for independently ambulatory children with cerebral palsy: A randomised feasibility trial. *Disabil. Rehabil.* 44, 3039–3047. doi: 10.1080/09638288.2020.1851779

Houle, A. M., Vernet, O., Jednak, R., Pippi Salle, J. L., and Farmer, J. P. (1998). Bladder function before and after selective dorsal rhizotomy in children with cerebral palsy. *J. Urol.* 160, 1088–1091.

Hunt, P. F. (2021). Inclusive education: The case for early identification and early intervention in assistive technology. *Assist. Technol.* 1, S94–S101. doi: 10.1080/10400435.2021.1974122

Igoe, D., Peralta, C., Jean, L., Vo, S., Ngan Yep, L., Zabjek, K., et al. (2011). Evaluation of the test-retest reliability of the dimensions of mastery questionnaire (DMQ) in preschool-aged children. *Inf. Young Child.* 24, 280–291.

Jonkers, I., Stewart, C., and Spaepen, A. (2003). The complementary role of the plantarflexors, hamstrings and gluteus maximus in the control of stance limb stability during gait. *Gait Post.* 17, 264–272. doi: 10.1016/S0966-6362(02)00102-9

Kahlon, S., McKellar, K., Caron, E., Ramonov, K., Brubacher-Cressman, K., Taubman, R., et al. (2019). Opening the door to physical activity for children with cerebral palsy: Experiences of participants in the BeFAST and BeSTRONG program. *Adap. Phys. Act. Q.* 36, 202–222. doi: 10.1123/apaq.2018-0048

Karunakaran, K. K., Gute, S., Ames, G. R., Chervin, K., Dandola, C. M., and Nolan, K. J. (2021). Effect of robotic exoskeleton gait training during acute stroke on functional ambulation. *Neuro Rehabil.* 48, 493–503. doi: 10.3233/NRE-210010

Kenyon, L. K., Harrison, K. L., Huettner, M. K., Johnson, S. B., and Miller, W. C. (2021). Stakeholder perspectives of pediatric powered wheelchair standing devices: A qualitative study. *Dev. Med. Child Neurol.* 63, 969–975.

Kim, S. J., Kim, S.-N., Yang, Y.-N., Lee, I.-S., and Koh, S.-E. (2017). Effect of weight bearing exercise to improve bone mineral density in children with cerebral palsy: A meta-analysis. *J. Musculoskelet. Neuronal Interact.* 17, 334–340.

Kim, S. K., Park, D., Yoo, B., Shim, D., Choi, J.-O., Choi, T. Y., et al. (2021). Overground robot-assisted gait training for pediatric cerebral palsy. *Sensors* 21:2087. doi: 10.3390/s21062087

King, G. A., McDougall, J., Palisano, R. J., Gritzan, J., and Tucker, M. A. (2000). Goal attainment scaling: Its use in evaluating pediatric therapy programs. *Phys. Occup. Ther. Pediatr.* 19, 31–52.

Law, M., Baptiste, S., McColl, M., Opzoomer, A., Polatajko, H., and Pollock, N. (1990). The Canadian occupational performance measure: An outcome measure for occupational therapy. *Can. J. Occup. Ther.* 57, 82–87.

Lee, H. Y., and Kim, K. (2014). Can walking ability enhance the effectiveness of breathing exercise in children with spastic cerebral palsy? *J. Phys. Ther. Sci.* 26, 539–542. doi: 10.1589/jpts.26.539

Livingstone, R. W., and Paleg, G. S. (2023). Use of overground supported-stepping devices for non-ambulant children, adolescents, and adults with cerebral palsy: A scoping review. *Disabilities* 3, 165–195. doi: 10.3390/disabilities3020012

Livingstone, R., and Paleg, G. (2016). Measuring outcomes for children with cerebral palsy who use gait rrainers. *Technologies* 4:22. doi: 10.3390/technologies4030022

Louie, D. R., and Eng, J. J. (2016). Powered robotic exoskeletons in post-stroke rehabilitation of gait: A scoping review. *J. Neuroeng. Rehabil.* 13:53. doi: 10.1186/s12984-016-0162-5

Maher, C., Hadfield, M., and Hutchings, M. (2018). Ensuring rigor in qualitative data analysis: A design research approach to coding combining NVivo with traditional material methods. *Int. J. Qual. Methods* 17, 1–13.

Malterud, K., Siersma, V. D., and Guassora, A. D. (2016). Sample size in qualitative interview studies: Guided by information power. *Qual. Health. Res.* 26, 1753–1760.

McCormick, A. M., Alazem, H., Zaidi, S., Barrowman, N. J., Ward, L. M., McMillan, H. J., et al. (2023). A randomized, cross-over trial comparing the effect of innovative robotic gait training and functional clinical therapy in children with cerebral palsy; a protocol to test feasibility. *Contemp. Clin. Trials* 127:107086. doi: 10.1016/j.cct.2023.107086

McKeever, P., Rossen, B. E., Scott, H., Robinson-Vincent, K., and Wright, V. (2013). The significance of uprightness: Parents' reflections on children's responses to a hands-free walker for children. *Disabil. Soc.* 28, 380–392.

Moen, R. D., and Østensjø, S. (2023). Understanding the use and benefits of assistive devices among young children with cerebral palsy and their families in Norway: A cross-sectional population-based registry study. *Disabil. Rehabil. Assist. Technol.* 19, 1454–1462. doi: 10.1080/17483107.2023.2198563

Molteni, F., Gasperini, G., Cannaviello, G., and Guanziroli, E. (2018). Exoskeleton and end-effector robots for upper and lower limbs rehabilitation: Narrative review. *PM R* 10, S174–S188. doi: 10.1016/j.pmrj.2018.06.005

Morgan, G., Busch-Rossnagel, N., Barrett, K., and Harmon, R. (2006). *The dimensions of mastery questionnaire: A manual about its development, psychometrics and use*. Fort Collins, CO: Colorado State University.

Murphy, M., Pradhan, S., Levin, M. F., and Hancock, N. J. (2024). Uptake of technology for neurorehabilitation in clinical practice: A scoping review. *Phys. Ther.* 104:zad140. doi: 10.1093/ptj/pzad140

Novak, I., Morgan, C., Adde, L., Blackman, J., Boyd, R. N., Brunstrom-Hernandez, J., et al. (2017). Early, accurate diagnosis and early intervention in cerebral palsy: Advances in diagnosis and treatment. *JAMA Pediatr.* 171, 897–907.

Ostensjo, S., Oien, I., and Fallang, B. (2008). Goal-oriented rehabilitation of preschoolers with cerebral palsy–a multi-case study of combined use of the Canadian occupational performance measure (COPM) and the goal attainment scaling (GAS). *Dev. Neurorehabil.* 11, 252–259. doi: 10.1080/17518420802525500

Ouendi, N., Hubaut, R., Pelayo, S., Anceaux, F., and Wallard, L. (2022). The rehabilitation robot: Factors influencing its use, advantages and limitations in clinical rehabilitation. *Disabil. Rehabil. Assist. Tech.* 25, 1–12. doi: 10.1080/17483107.2022.2107095

Owens, J. G., Rauzi, M. R., Kittelson, A., Graber, J., Bade, M. J., and Johnson, J. (2020). How new technology is improving physical therapy. *Curr. Rev. Musculoskelet. Med.* 13, 200–211.

Paleg, G. S., Smith, B. A., and Glickman, L. B. (2013). Systematic review and evidence-based clinical recommendations for dosing of pediatric supported standing programs. *Pediatr. Phys. Ther.* 25, 232–247. doi: 10.1097/PEP.0b013e318299d5e7

Paleg, G., and Livingstone, R. (2015). Outcomes of gait trainer use in home and school settings for children with motor impairments: A systematic review. *Clin. Rehabil.* 29, 1077–1091. doi: 10.1177/0269215514565947

Paleg, G., and Livingstone, R. (2016). Evidence-informed clinical perspectives on selecting gait trainer features for children with cerebral palsy. *Int. J. Ther. Rehabil.* 23, 444–454.

Palisano, R. J., Rosenbaum, P., Bartlett, D., and Livingston, M. H. (2008). Content validity of the expanded and revised gross motor function classification system. *Dev. Med. Child Neurol.* 50, 744–750. doi: 10.1111/j.1469-8749.2008.03089.x

Perpetuini, D., Russo, E. F., Cardone, D., Palmieri, R., Filippini, C., Tritto, M., et al. (2022). Identification of functional cortical plasticity in children with cerebral palsy associated to robotic-assisted gait training: An fNIRS study. *JCM* 11:6790. doi: 10.3390/jcm11226790

Peters, S., Lim, S. B., Louie, D. R., Ling, Y. C., and Eng, J. J. (2020). Passive, yet not inactive: Robotic exoskeleton walking increases cortical activation dependent on task. *J. Neuroeng. Rehabil.* 17:107.

Phelan, S. K., Gibson, B. E., and Wright, F. V. (2015). What is it like to walk with the help of a robot? Children's perspectives on robotic gait training technology. *Disabil. Rehabil.* 37, 2272–2281. doi: 10.3109/09638288.2015.1019648

Plewa, K., Samadani, A., and Chau, T. (2017). Comparing electro- and mechano-myographic muscle activation patterns in self-paced pediatric gait. *J. Electromyogr. Kinesiol.* 36, 73–80. doi: 10.1016/j.jelekin.2017.07.002

Puce, L., Pallecchi, I., Chamari, K., Marinelli, L., Innocenti, T., Pedrini, R., et al. (2021). Systematic review of fatigue in individuals with cerebral palsy. *Front. Hum. Neurosci.* 15:598800. doi: 10.3389/fnhum.2021.598800

Radtka, S., Hone, R., Brown, C., Mastick, J., Melnick, M. E., and Dowling, G. A. (2013). Feasibility of computer-based videogame therapy for children with cerebral palsy. *Games Health J.* 2, 222–228. doi: 10.1089/g4h.2012.0071

Read, E., Woolsey, C., McGibbon, C. A., and O'Connell, C. (2020). Physiotherapists' experiences using the Ekso bionic exoskeleton with patients in a neurological rehabilitation hospital: A qualitative study. 9, 1–8. doi: 10.1155/2020/2939573

Rich, D., Rigby, P., and Wright, V. (2014). Mothers' experiences with the pediatric evaluation of disability inventory (PEDI). *Phys. Occup. Ther. Pediatr.* 34, 271–288. doi: 10.3109/01942638.2013.823473

Richards, C. L., Malouin, F., Dumas, F., Marcoux, S., Lepage, C., and Menier, C. (1997). Early and intensive treadmill locomotor training for young children with cerebral palsy: A feasibility study. *Pediatr. Phys. Ther.* 9:158.

Rodby-Bousquet, E., Persson-Bunke, M., and Czuba, T. (2016). Psychometric evaluation of the Posture and Postural Ability Scale for children with cerebral palsy. *Clin. Rehabil.* 30, 697–704.

Rodríguez-Fernández, A., Lobo-Prat, J., and Font-Llagunes, J. M. (2021). Systematic review on wearable lower-limb exoskeletons for gait training in neuromuscular impairments. *J. Neuroeng. Rehabil.* 18:22. doi: 10.1186/s12984-021-00815-5

Rojek, A., Mika, A., Oleksy, Ł, Stolarczyk, A., and Kielnar, R. (2020). Effects of exoskeleton gait training on balance, load distribution, and functional status in stroke: A randomized controlled trial. *Front. Neurol.* 10:1344. doi: 10.3389/fneur.2019.01344

Rosenbaum, P. L., Palisano, R. J., Bartlett, D. J., Galuppi, B. E., and Russell, D. J. (2008). Development of the gross motor function classification system for cerebral palsy. *Dev. Med. Child Neurol.* 50, 249–253.

Rosenbaum, P., Walter, S., Hanna, S., Palisano, R., Russell, D., Raina, P., et al. (2002). Prognosis for gross motor function in cerebral palsy: Creation of motor development curves. *J. Am. Med. Assoc.* 288, 1357–1363. doi: 10.1001/jama.288.11.1357

Russell, D. J., Avery, L. M., Rosenbaum, P. L., Raina, P. S., Walter, S. D., and Palisano, R. J. (2000). Improved scaling of the gross motor function measure for children with cerebral palsy: Evidence of reliability and validity. *Phys. Ther.* 80, 873–885.

Ryan, J. L., Wright, F. V., and Levac, D. E. (2020). Exploring physiotherapists' use of motor learning strategies in gait-based interventions for children with cerebral palsy. *Phys. Occup. Ther. Pediatr.* 40, 79–92. doi: 10.1080/01942638.2019.1622623

Ryan, J., Levac, D. E., and Wright, F. V. (2019). Inter- and intra-rater reliability of the motor learning strategies rating instrument in physiotherapy intervention for children with cerebral palsy. *Dev. Med. Child Neurol.* 16, 1061–1066. doi: 10.1111/dmcn.14177

Sarajchi, M., Al-Hares, M. K., and Sirlantzis, K. (2021). Wearable lower-limb exoskeleton for children with cerebral palsy: A systematic review of mechanical design, actuation type, control strategy, and clinical evaluation. *IEEE Trans. Neural Syst. Rehabil. Eng.* 29, 2695–2720. doi: 10.1109/TNSRE.2021.3136088

Saunders, B., Sim, J., Kingstone, T., Baker, S., Waterfield, J., and Bartlam, B. (2018). Saturation in qualitative research: Exploring its conceptualization and operationalization. *Qual. Quant.* 52, 1893–1907. doi: 10.1007/s11135-017-0574-8

Scholtes, V. A. B., Becher, J. G., Beelen, A., and Lankhorst, G. J. (2006). Clinical assessment of spasticity in children with cerebral palsy: A critical review of available instruments. *Dev. Med. Child Neurol.* 48, 64–73. doi: 10.1017/S0012162206000132

Schwartz, I., and Meiner, Z. (2015). Robotic-assisted gait training in neurological patients: Who may benefit? *Ann. Biomed. Eng.* 43, 1260–1269. doi: 10.1007/s10439-015-1283-x

Sczesny-Kaiser, M., Höffken, O., Aach, M., Cruciger, O., Grasmücke, D., and Meindl, R. (2015). HAL® exoskeleton training improves walking parameters and normalizes cortical excitability in primary somatosensory cortex in spinal cord injury patients. *J. Neuroeng. Rehabil.* 20:68. doi: 10.1186/s12984-015-0058-9

Shore, B. J., Allar, B. G., Miller, P. E., Matheney, T. H., Snyder, B. D., and Fragala-Pinkham, M. A. (2017). Evaluating the discriminant validity of the pediatric evaluation of disability inventory: Computer adaptive test in children with cerebral palsy. *Phys. Ther.* 97, 669–676. doi: 10.1093/ptj/pzx033

Snodgrass, S. J., Heneghan, N. R., Tsao, H., Stanwell, P. T., Rivett, D. A., and Van Vliet, P. M. (2014). Recognising neuroplasticity in musculoskeletal rehabilitation: A basis for greater collaboration between musculoskeletal and neurological physiotherapists. *Manual Ther.* 19, 614–617. doi: 10.1016/j.math.2014.01.006

Sousa, A. S. P., and Tavares, J. M. (2012). Effect of gait speed on muscle activity patterns and magnitude during stance. *Motor Control.* 16, 480–492. doi: 10.1123/mcj.16.4.480

Spivak, M. R., Chan, J. R., Cooper, M. S., Petrucci, C., Sheridan, A. M., Tang, T. Y., et al. (2021). Reliability of the revised motor learning strategies rating instrument and its role in describing physiotherapy session motor learning strategy content in pediatric acquired brain injury. *Physiother. Can.* 73, 381–390. doi: 10.3138/ptc-2020-0014

Tao, R., Feng, L., and Xiao, Z. (2020). Posterior versus anterior walkers for children with cerebral palsy-biomechanical analysis and energy consumption: A systematic review. *J. Dev. Phys. Disabil.* 32, 877–892. doi: 10.1007/s10882-020-09731-3

Tickle-Degnen, L. (2013). Nuts and bolts of conducting feasibility studies. *Am. J. Occup. Ther.* 67, 171–176. doi: 10.5014/ajot.2013.006270

Torchia, K., Mirzazada, S., Wright, F. V., and Ryan, J. L. (2023). Clinicians' perspectives on motor learning strategy selection and application in occupational therapy and speech-language pathology interventions for children with acquired brain injury. *Disabil. Rehabil.* 22, 1–10. doi: 10.1080/09638288.2023.2269863

Trexo Robotics (2022). *Trexo plus user manual version 0.9*. Mississauga, ON: Trexo Robotics Inc.

van Dellen, F., and Labruyère, R. (2022). Settings matter: A scoping review on parameters in robot-assisted gait therapy identifies the importance of reporting standards. *J. Neuroeng. Rehabil.* 19:40. doi: 10.1186/s12984-022-01017-3

van Dellen, F., Aurich-Schuler, T., and Labruyère, R. (2023). Within- and between-therapist agreement on personalized parameters for robot-assisted gait therapy: The challenge of adjusting robotic assistance. *J. Neuroeng. Rehabil.* 20:81. doi: 10.1186/s12984-023-01176-x

van Hedel, H. J. A., Meyer-Heim, A., and Rüsch-Bohtz, C. (2016). Robot-assisted gait training might be beneficial for more severely affected children with cerebral palsy. *Dev. Neurorehabil.* 19, 410–415. doi: 10.3109/17518423.2015.1017661

Vaughan-Graham, J., Brooks, D., and Rose, L. (2020). Exoskeleton use in post-stroke gait rehabilitation: A qualitative study of the perspectives of persons post-stroke and physiotherapists. *J. Neuroeng. Rehabil.* 17:123. doi: 10.1186/s12984-020-00750-x

Vos-Vromans, D. C. W. M., Ketelaar, M., and Gorter, J. W. (2005). Responsiveness of evaluative measures for children with cerebral palsy: The gross motor function measure and the pediatric evaluation of disability inventory. *Disabil. Rehabil.* 27, 1245–1252. doi: 10.1080/09638280500076178

Wallen, M., Ziviani, J., Herbert, R., Evans, R., and Novak, I. (2008). Modified constraint-induced therapy for children with hemiplegic cerebral palsy: A feasibility study. *Dev. Neurorehabil.* 11, 124–133. doi: 10.1080/17518420701640897

Walter, S. J., Sola, G. P., Sacks, J., Lucero, Y., Langbein, E., and Weaver, F. (1999). Indications for a home standing program for individuals with spinal cord injury. *J. Spinal Cord Med.* 22, 152–158. doi: 10.1080/10790268.1999.11719564

Weightman, A., Preston, N., Levesley, M., Holt, R., Mon-Williams, M., Clarke, M., et al. (2011). Home based computer-assisted upper limb exercise for young children with cerebral palsy: A feasibility study investigating impact on motor control and functional outcome. *J. Rehabil. Med.* 43, 359–363. doi: 10.2340/16501977-0679

Wright, F. V., and Jutai, J. W. (2006). Evaluation of the longer-term use of the David Hart Walker Orthosis by children with cerebral palsy: A 3-year prospective evaluation. *Disabil. Rehabil. Assist. Tech.* 1, 155–166. doi: 10.1080/17483100600627382

Zaman, B., Vanden Abeele, V., and Grooff, D. (2013). Measuring product liking in preschool children: An evaluation of the Smileyometer and this or that methods. *Int. J. Child Comput. Interact.* 1, 61–70.

frontiers | Frontiers in Bioengineering and Biotechnology

TYPE Original Research
PUBLISHED 31 July 2024
DOI 10.3389/fbioe.2024.1401153

OPEN ACCESS

EDITED BY
Longbin Zhang,
Nanyang Technological University, Singapore

REVIEWED BY
Areerat Suputtitada,
M. D., Chulalongkorn University, Thailand
Asuka Takai,
Advanced Telecommunications Research Institute International (ATR), Japan

*CORRESPONDENCE
Arnab Sarmah,
sarmah18@iitg.ac.in

RECEIVED 21 March 2024
ACCEPTED 01 July 2024
PUBLISHED 31 July 2024

CITATION
Sarmah A, Boruah L, Ito S and Kanagaraj S (2024), Integrative approach to pedobarography and pelvis-trunk motion for knee osteoarthritis detection and exploration of non-radiographic rehabilitation monitoring. *Front. Bioeng. Biotechnol.* 12:1401153. doi: 10.3389/fbioe.2024.1401153

Integrative approach to pedobarography and pelvis-trunk motion for knee osteoarthritis detection and exploration of non-radiographic rehabilitation monitoring

Arnab Sarmah[1,2]*, Lipika Boruah[3], Satoshi Ito[4] and Subramani Kanagaraj[1,3]

[1]Department of Mechanical Engineering, Indian Institute of Technology Guwahati, Guwahati, India, [2]Graduate School of Engineering, Gifu University, Gifu, Japan, [3]Center for Intelligent Cyber Physical Systems, Indian Institute of Technology Guwahati, Guwahati, India, [4]Faculty of Engineering, Gifu University, Gifu, Japan

Background: Osteoarthritis (OA) is a highly prevalent global musculoskeletal disorder, and knee OA (KOA) accounts for four-fifths of the cases worldwide. It is a degenerative disorder that greatly affects the quality of life. Thus, it is managed through different methods, such as weight loss, physical therapy, and knee arthroplasty. Physical therapy aims to strengthen the knee periarticular muscles to improve joint stability.

Methods: Pedobarographic data and pelvis and trunk motion of 56 adults are recorded. Among them, 28 subjects were healthy, and 28 subjects were suffering from varying degrees of KOA. Age, sex, BMI, and the recorded variables are used together to identify subjects with KOA using machine learning (ML) models, namely, logistic regression, SVM, decision tree, and random forest. Surface electromyography (sEMG) signals are also recorded bilaterally from two muscles, the rectus femoris and biceps femoris caput longus, bilaterally during various activities for two healthy and six KOA subjects. Cluster analysis is then performed using the principal components obtained from time-series features, frequency features, and time–frequency features.

Results: KOA is successfully identified using the pedobarographic data and the pelvis and trunk motion with the highest accuracy and sensitivity of 89.3% and 85.7%, respectively, using a decision tree classifier. In addition, sEMG data have been successfully used to cluster healthy subjects from KOA subjects, with wavelet analysis features providing the best performance for the standing activity under different conditions.

Conclusion: KOA is detected using gait variables not directly related to the knee, such as pedobarographic measurements and pelvis and trunk motion captured by pedobarography mats and wearable sensors, respectively. KOA subjects are also distinguished from healthy individuals through clustering analysis using sEMG data from knee periarticular muscles during walking and standing. Gait data and sEMG complement each other, aiding in KOA identification and rehabilitation monitoring. It is important because wearable sensors simplify

data collection, require minimal sample preparation, and offer a non-radiographic, safe method suitable for both laboratory and real-world scenarios. The decision tree classifier, trained with stratified k-fold cross validation (SKCV) data, is observed to be the best for KOA identification using gait data.

KEYWORDS

knee osteoarthritis, rehabilitation, disease identification, pedobarography, wearable sensor, surface electromyography, non-radiographic

1 Introduction

Osteoarthritis (OA) is the most prevalent type of musculoskeletal disorder globally and is the leading cause of chronic pain and disability in adults (Singh et al., 2022). Knee osteoarthritis (KOA) accounts for four-fifths of the burden of OA worldwide. The pooled global prevalence of KOA is 16% in individuals aged 15 and over and 22.9% in individuals 40 and over. The ratio of prevalence and incidence in women and men is found to be 1.69 and 1.39, respectively (Cui et al., 2020). In India, the prevalence is reported to be 28.7%. The prevalence is higher in women at 31.6% than in men at 28.1% (Pal et al., 2016). KOA is a degenerative disorder and requires total knee replacement, i.e., knee arthroplasty at an advanced stage of the disease. It, however, results in substantial health costs. Thus, an important aspect of managing the disease is early identification and, hence, early intervention (Cui et al., 2020). The diagnosis of KOA can be confirmed based on clinical and/or radiological features. The current gold standard for diagnosing OA is X-ray imaging, which is cost-efficient and widely available. However, it is insensitive to detecting early OA changes (Tiulpin et al., 2018) and involves high-energy electromagnetic radiation. MRI has also been increasingly employed to diagnose KOA. However, it can detect OA with high specificity and moderate sensitivity. Thus, it is more useful for ruling out OA than ruling it in (Menashe et al., 2012). Thus, early diagnosis of OA is particularly challenging as it relies heavily on the subjective judgment of the practitioner due to the lack of a precise grading system. The widely employed Kellgren–Lawrence (KL) grading scale is semi-quantitative and suffers from ambiguity. Such ambiguity poses an obstacle to early OA diagnosis, thus affecting millions of people globally (Tiulpin et al., 2018). Machine learning (ML) has been employed for the diagnosis of KOA using kinematics (Yang et al., 2020; Kwon et al., 2019; Kwon et al., 2020) and kinetics (Kwon et al., 2019) of the hip, knee, and ankle joints. They have also been employed along with radiographic images (Kwon et al., 2020) to identify KOA subjects from healthy subjects (Yang et al., 2020) and differentiate between the different grades of KOA subjects (Kwon et al., 2019; Kwon et al., 2020). However, the data are collected using either a 3D motion capture system (Kwon et al., 2019; Kwon et al., 2020) or multiple IMUs (Yang et al., 2020), which require a post-processing step before the data can be used for classification. In addition, classification is performed using only one type of classifier. Surface electromyography (sEMG) has also been employed in recent years for the diagnosis of KOA, with a high accuracy of 92% (Chen et al., 2019) and 96.3% (Khader et al., 2024). Data considered for diagnosis were collected considering walking at a self-selected pace as an activity. The different muscles considered are the quadriceps femoris (Khader et al., 2024), medial gastrocnemius (Khader et al., 2024), rectus femoris (Khader et al., 2024), semi-tendinous (Chen et al., 2019; Khader et al., 2024), biceps femoris (Chen et al., 2019; Khader et al., 2024), and vastus lateralis (Chen et al., 2019; Khader et al., 2024).

The diagnosis is followed by an intervention regimen, which revolves around a combination of non-pharmacological and pharmacological methods. One of the initial measures is weight reduction, which can help slow down the progression of KOA. Another most widely implemented remedy is physical therapy and rehabilitation. It has been useful for patients with pain and mobility. Specific useful programs include strength training, Tai Chi, aerobics, electrotherapy, and hydrotherapy, among which strength training is the most common approach. It improves the muscular strength and joint stability of the individual, thus improving Western Ontario and McMaster Universities (WOMAC) pain scores and overall health benefits (Bhatia et al., 2013). Increased rectus femoris muscle force is related to thinner knee joint cartilage in KOA (Yagi et al., 2022), and increased muscle activations of the biceps femoris have been reported in KOA subjects compared to healthy subjects while performing activities of daily life (Hortobágyi et al., 2005). Thus, the strength of the contraction of periarticular muscles (i.e., the quadriceps and hamstrings for the knee joint) is an important contributing factor to the quality of the cartilage. In addition to increasing the strength of the muscles surrounding the knee, it also increases the intra- and intermuscular coordination of the knee extensor muscles, which results in lower impact and impulsive loading being transmitted through the joint (Beckwée et al., 2013). The assessment of the effectiveness of the physical therapy further enables us to plan the intervention regimen and understand the progress. One of the approaches includes the use of the QQ index (Brouwer et al., 1999), where the subjects' effective working hours during a day are compared to those of the previous day (Reijonsaari et al., 2012). Another approach is through a video system or a mobile application through which the physiotherapist can remotely monitor a patient in real time and provide instant feedback (Saraee et al., 2017; Vaish et al., 2017)).

Since the assessment of the effectiveness of physical therapy for KOA is subjective and relies on the clinician's expertise, employing a quantitative approach becomes highly beneficial in achieving more objective results. The effectiveness of physical therapy on KOA has been reported to be monitored in a case study that showed improvements in temporal parameters such as stride length, mean velocity, and cadence. Root mean square (RMS) values of EMG are also used to infer the improvement of the condition post-treatment (Liang et al., 2019). Physical therapy has also been monitored using a pedometer, Fitbit, and accelerometer to assess the influence of physical activity on a wide range of subjects with different pathologies (de Leeuwerk et al., 2022). However, it only

utilizes kinematic variables and does not consider the kinetic variables associated with human movement. Thus, there is a need for the identification of kinetic and kinematic variables that can be used for KOA diagnosis and also for monitoring the effectiveness of any intervention.

The highly interdependent nature of human movement allows us to employ variables associated with other joints and muscles to assess their effect on other parts and *vice versa*. It has been reported that the quadriceps and hamstring muscles weaken and have delayed reaction time in subjects suffering from plantar fasciitis (Lee et al., 2020). Increased hamstring tightness also induces prolonged forefoot loading (Harty et al., 2005). In addition, hamstring length significantly influences the pelvic angle and flexion range of motion (ROM), lumbar angle flexion ROM, and thoracic angle flexion ROM. Short hamstrings are associated with decreased flexion ROMs of the pelvic and lumbar angles and increased flexion ROM of the thoracic angle (Gajdosik et al., 1994). This shows that there exists a relationship between the muscular strength of the periarticular muscles of the knee, the plantar pressure, and the ROM of the pelvis and lumbar region.

This work thus aims to identify KOA subjects using both kinetic and kinematic non-knee joint parameters, which are the pedobarographic measurements and the pelvis and trunk ROM variables. In addition, the effect of KOA on the periarticular muscles of the knee is studied through sEMG, and using these data, the kinetic and kinematic variables are to be established as potential biomarkers for monitoring the effectiveness of any neuromuscular rehabilitation intervention technique for addressing KOA. This is possible as knee health has been associated with hamstring and quadriceps muscle strength and is also associated with pelvis and trunk ROM along with plantar pressure distribution. The variables considered for KOA identification are dynamic in nature and require minimal subject preparation.

2 Methodology

Figure 1 shows us an overview of the various steps undertaken during the study. It includes a two-fold methodology to investigate KOA identification and monitoring through gait and muscle data. Initially, gait data from 56 subjects (28 healthy and 28 KOA) are analyzed using supervised ML algorithms to demonstrate the ability to identify KOA using beyond knee-related gait data. The effect of KOA on the periarticular muscles of the knee is then studied through the analysis of sEMG data from the rectus femoris and bicep femoris caput longus bilaterally. The features obtained are then used for cluster analysis. Successful clustering will indicate the effect of KOA on the muscular activity of the periarticular muscles. Integrating the two studies, we can propose using gait data to monitor muscle strengthening to rehabilitate KOA subjects. Data are collected using the wearable sensor, pedobarographic mat, and sEMG sensors. Pelvis ROM is captured using the wearable sensors while the subjects walk comfortably at a self-selected speed for 20 m. The wearable sensor was also used to conduct the Timed Up and Go (TUG), which provides the trunk ROM in the sagittal plane during the sit-to-stand and stand-to-sit parts of TUG and the total TUG time. TUG is considered because it is recommended by the Osteoarthritis Research Society International (OARSI) as an assessment tool in KOA, which is necessary to detect functional mobility and the risk of falls. Measuring trunk movement during these steps helps health workers and physiotherapists provide a proper rehabilitation strategy for KOA (Dobson et al., 2013). The subjects walk at a self-selected speed over the pedobarography mat to capture the 56 kinetic and kinematic features. There is evidence of neuromuscular adaptations associated with even early stages of KOA and without gait adaptations (Duffell et al., 2014). Thus, sEMG data are collected from two muscles, namely, the rectus femoris and the biceps femoris caput longus, while the subjects walk at a self-selected speed. sEMG data are also collected while standing under different stability conditions. Walking is chosen because it has been reported that individuals with KOA exhibit higher gait deviations than healthy subjects (Mills et al., 2013). KOA has also been reported to cause deficits in balance control, with its severity increasing in moderate to severe KOA (Kim et al., 2011). In addition, standing data under different stability conditions have been reported to be useful in classifying balance-related disorders (Sarmah et al., 2024). Hence, standing under different stability conditions are considered for sEMG data collection.

2.1 Participants

The study was approved by the Institute Human Ethics Committee (IHEC), IIT Guwahati, and conducted in compliance with the relevant regulations. Written informed consent is obtained from all the study participants. Pedobarography and wearable sensor data from the pelvis are collected from KOA subjects with different degrees of severity, as well as from healthy subjects. Age, sex, and BMI are recorded for each subject and are summarized in Table 1. Data are collected for 28 able bodied subjects and 28 subjects with KOA. The inclusion criteria for healthy subjects are (i) age greater than 18 years and (ii) ability to perform normal activities of daily life. For KOA subjects, the inclusion criteria are (i) age greater than 18 years, (ii) being diagnosed with KOA and referred by an orthopedic doctor, and (iii) being able to walk and stand without the need for any support. The exclusion criteria in both healthy and KOA cases are (i) diagnosed with neurological disorders like Parkinson's disorder. The 28 KOA subjects contain 11 subjects with Grade 1 severity, 13 subjects with Grade 2 severity, and 4 subjects with Grade 3 severity according to KL grade.

2.2 Gait data collection

All the gait data are collected in the Gait and Motion Analysis Laboratory at IIT Guwahati. The subjects are, at first, familiarized with the experimental setup and protocol. They are instructed to walk over a dynamic pedobarographic mat from Zebris Medical GmbH (FDM-2) at a self-selected speed, as shown in Figure 2. This mat captures the plantar pressure experienced by the subject during walking, along with the spatiotemporal variables such as stride length, step length, cadence, and speed.

The dynamic variables captured include the force and pressure experienced in the three sections of the foot, namely, the forefoot, midfoot, and heel. In addition, butterfly parameters such as gait line length and velocity, single-stance line, anterior–posterior position, and mediolateral position are reported. A representation of the dynamic variables is shown in Figure 3. Thereafter, data are collected

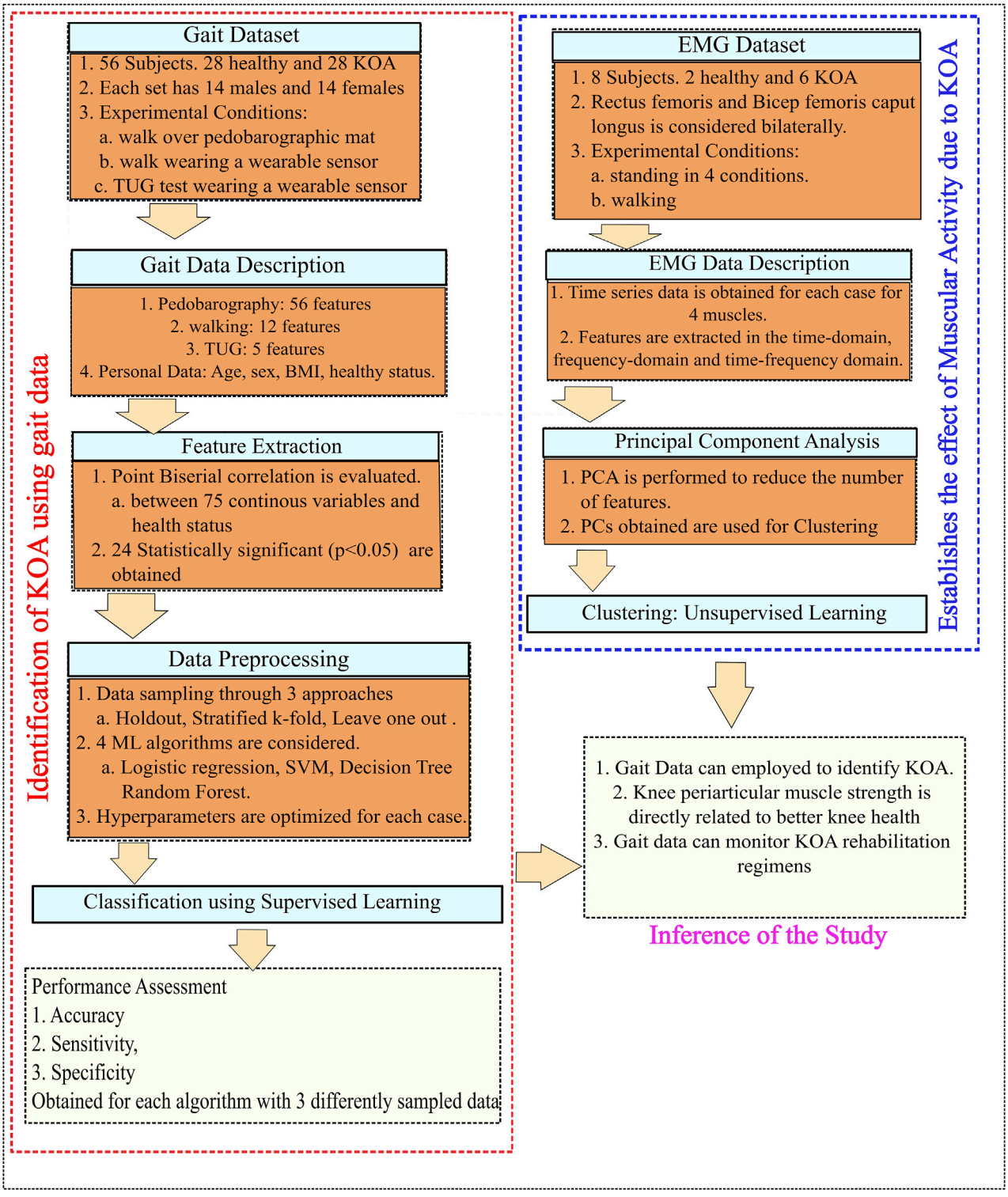

FIGURE 1
Flowchart of the methodology.

using the wearable sensor GWALK from BTS Bioengineering for two activities: normal walking and TUG. In the normal walk test, the wearable sensor is placed on the level of the subject's sacrum (Supplementary Material S1) and then asked to walk at a self-selected speed for a distance of 20 m. Figure 4 shows the placement of the wearable sensor and the representation of the pelvis motion in the three planes. The variables captured during the normal walking test are pelvis tilt right (PTR), pelvis tilt left (PTL), pelvis obliquity right (POR), pelvis obliquity left (POL), pelvis rotation right (PRR), and pelvis rotation left (PRL) with respect to gait cycle percent.

TABLE 1 Summary of the subject characteristics in two categories.

	Age	Sex	BMI
Healthy subjects	30.3 ± 7.8	14 male and 14 female subjects	24.1 ± 3.8
KOA subjects	53.8 ± 11.7	14 male and 14 female subjects	27.5 ± 4.3

FIGURE 2
Sample subject walking over the pedobarographic mat.

During the measurement of plantar pressure and pelvis ROM, the experimental condition is walking at a self-selected speed. However, ROM was not measured while the participant was walking over the foot pressure mat. It is because the GWALK requires the subject to walk at least 7 m, while the foot pressure mat is 2 m in length.

In the TUG test, the wearable sensor was placed on the lumbar 2 (L2) vertebrae. The test starts with the subject in a seated posture, getting up and walking for 3 m, then turning around, and returning to the starting seated posture. A subject undergoing the test is shown in Figure 5. The variables captured from this experiment are the trunk flexion-extension (F/E) in the sagittal plane with respect to normalized time and the TUG time.

3 Data analysis

3.1 Data description

The data analysis and classification were performed using Python 3.11. Pelvis angles are obtained with respect to the gait cycle percent, and the mean and standard deviation (SD) are evaluated for each subject under six conditions (considering the cardinal planes and the side of the body) using Eqs 1, 2. A total of 12 features, namely, the mean and SD of PTR, PTL, POR, POL, PRR, and PRL, are evaluated, which represent the pelvis angles in three planes during a normal walk. The mean and standard deviation (SD) are also evaluated for the trunk F/E angles in sit-to-stand and stand-to-sit conditions using Eqs 1, 2. Four trunk motion features, two mean and two SD values, which represent the trunk F/E during sit-to-stand and stand-to-sit activity, and TUG time are obtained from the TUG test. The mean and SD of different gait variables are considered as they have been successfully employed as a feature to classify between healthy and neuromusculoskeletal disorders, which result in gait deviation (Xia et al., 2015; Nandy, 2019). In addition, this approach reduces the computational complexity of the analysis due to the reduced dataset dimensionality.

$$\text{Angle}_{\text{mean}} = \sum(Angle_i)/N, \tag{1}$$

$$\text{Angle}_{\text{stddev}} = \sqrt{\sum(Angle_i - Angle_{mean})^2/N - 1}, \tag{2}$$

where Angle_i is the angle (pelvis or trunk) at each interval and N = 100 (gait cycle percentage).

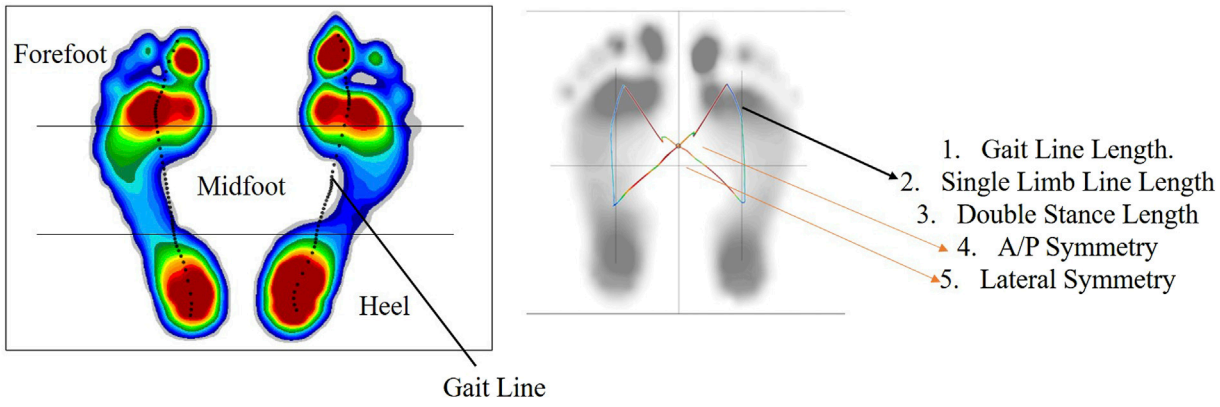

FIGURE 3
Representation of the dynamic variables obtained from the pedobarographic mat.

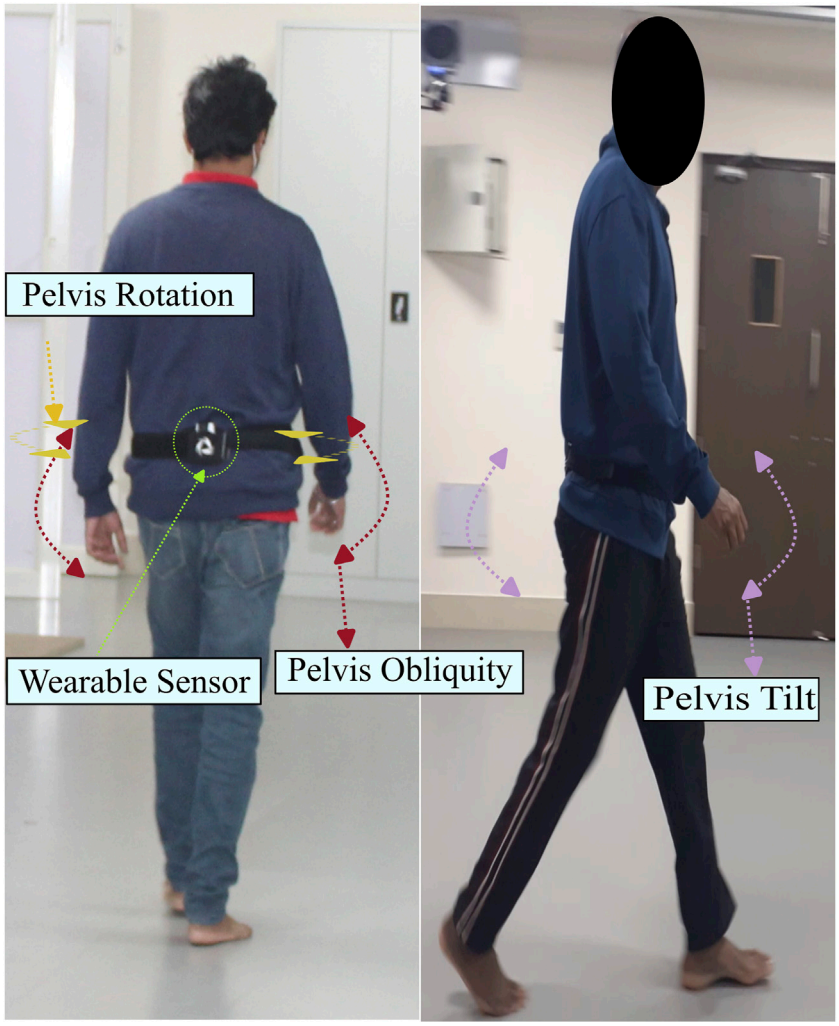

FIGURE 4
Pelvis motion in three planes during normal walking.

In addition, 56 features are obtained from the pedobarographic mat, which includes 19 spatiotemporal features, 13 butterfly features, and 24 dynamic features. The spatiotemporal variables include the mean and SD of the foot progression angle (left and right side), step length (left and right side), stride length, mean and SD of step width, stance phase percent (left and right side), swing phase percent (left and right side), double stance phase percent, step time (left and right side), stride time, cadence, and velocity. The Foot progression angle is considered because gait training with a specific foot progression angle increases the lateral knee muscle co-activity, thereby unloading the medial knee compartment (Gholami et al., 2022). This implies that any change in knee joint loading will be reflected in the foot progression angles. The butterfly parameters consist of the mean and SD of the gait line length (left and right side), single limb support line (left and right side), anterior–posterior (A/P) position, and lateral symmetry and the maximum gait line velocity. The dynamic parameters obtained are the mean and SD of the forefoot, midfoot, and heel force and pressure (left and right side).

3.2 Feature selection using point-biserial correlation

Two personal features (age and BMI), 56 features from the pedobarographic data (19 spatiotemporal features, 13 butterfly features, and 24 dynamic features), 12 features from the Pelvis motion during normal walk, four features from the trunk movement during TUG, and TUG time are considered for analysis. At first, point-biserial correlation is evaluated between the 75 features and the health status of the subject by considering healthy as 0 and KOA as 1. Point-biserial correlation is performed when one of the variables is continuous and the other is a dichotomous variable. It is performed to find the variables strongly affected by KOA. The correlation coefficients obtained give us variables that are most affected by KOA. A total of 24 statistically significant ($p < 0.05$) variables that relate the variables to the health status of the subject are obtained from the point-biserial correlation, which can then be employed for the identification of subjects with KOA. The variables obtained after point-biserial correlation are shown in Table 2 in descending order

FIGURE 5
Sample subject during the TUG test.

of correlation coefficient. A total of 10 of the features are positively correlated with KOA, and 14 are negatively correlated. Age, SD of trunk F/E (sit to stand), and mean of trunk F/E (stand to sit) are the most positively correlated variables; and velocity, step length (left), and stride length are the most negatively correlated variables employed for classification.

3.3 Data preprocessing

The 24 statistically significant variables, obtained after point-biserial correlation, include two personal features (age and BMI), 17 features from the pedobarographic data (11 spatiotemporal features, 4 butterfly features, and 2 dynamic features), 2 features from the pelvis motion during a normal walk, and 2 features from the trunk movement during TUG and TUG time. The statistically significant variables, sex, and pathological condition of the subject are used to identify subjects with KOA.

Data preprocessing is to be conducted before it can be used for identification. When applying a classification model, it is crucial to convert the dataset into numerical form. The pathology of the subject is already assigned in binary form. Binary data are then extracted from the other categorical variables, which results in an increase in the number of unique features such as sex, which gets split into two independent features, female and male. The "sex" column and one of the independent features are then dropped. In this case, the "female" column was dropped. In the "male" column, 0 indicates female subjects and 1 indicates male subjects. This method is called one-hot encoding. The "StandardScaler" function from Python's scikit-learn library is then employed to normalize the data, ensuring a mean of 0 and a standard deviation of 1.

The data sampling for training and testing uses three approaches, namely, holdout method, stratified k-fold cross-validation (SKCV) method, and leave-one-out cross-validation (LOOCV) method. In the holdout method, the dataset is divided into training and test sets, which are to be used for training and testing, respectively. In this case, training and test sets comprise 75% and 25% of the total data, respectively. Stratified k-fold splits the dataset randomly into 'k' groups while ensuring that each fold has the same proportion of the different classes as the entire dataset. The models are then trained on the training set and analyzed on the testing set. The process is repeated k-times until each set/fold has been utilized as a test set. The data are divided into "5" folds or groups in this case. In the leave-one-out approach, each observation is considered the test set, and the remaining (N-1) observations are considered the training set. The process is repeated N times until each observation has been used as the testing set. Different types of sampling are employed to make the trained and tested models applicable to classify data from several different datasets, which may be unbalanced. Different sampling methods are utilized for the analysis to ensure the quality and reliability of the models. The stratified k-fold approach provides more reliable performance estimates and is crucial for imbalanced datasets. The leave-one-out approach is suitable for small datasets and assesses the model's stability.

TABLE 2 Point-biserial correlation relating the variables with the health status of the subjects.

Sl. No.	Variable	Point-biserial correlation coefficient	*p*-value
1	Age	0.708968	9.68E-10
2	Trunk F/E (sit-to-stand) SD	0.411328	0.001636
3	Trunk F/E (stand-to-sit) mean	0.343412	0.009564
4	TUG time	0.318584	0.016711
5	Double-stance phase %	0.314555	0.018221
6	Stance phase (right)%	0.29898	0.025197
7	BMI	0.281456	0.035606
8	Stance phase (left)%	0.27304	0.041748
9	Stride time (sec)	0.272102	0.042484
10	Gait line right SD	0.26594	0.047585
11	Swing phase (left) %	−0.27304	0.041748
12	Cadence (steps/min)	−0.28389	0.033977
13	Swing phase (right) %	−0.29898	0.025197
14	Single-limb support line right (mm)	−0.30409	0.022695
15	Heel left (pressure)	−0.30774	0.021037
16	PRL SD	−0.32316	0.015126
17	PRR SD	−0.3259	0.014239
18	Heel right (pressure)	−0.33572	0.011422
19	Single limb support line left (mm)	−0.34601	0.008998
20	Gait line right	−0.34897	0.008388
21	Step length right (cm)	−0.41402	0.001514
22	Stride length (cm)	−0.4395	0.000702
23	Step length left (cm)	−0.44234	0.000641
24	Velocity (km/hr)	−0.45057	0.000493

3.4 Hyperparameter optimization

Hyperparameters serve as crucial external configuration variables in managing machine learning models and are set before the model's training. The process of finding the right set of hyperparameters is known as hyperparameter tuning or optimization. It involves experimenting with different combinations to maximize or minimize a target variable, often accuracy. Among the approaches employed, grid search stands out, systematically exploring all possible hyperparameter combinations from a predefined list to find the best fit. The optimization process aims to enhance the model's performance on unseen data, thereby enhancing its overall predictive accuracy. The grid search approach is employed for hyperparameter search in all the models.

In logistic regression, different combinations of regularization parameters (which control the bias-variance trade-off to develop more generalized models), penalty terms, and the maximum number of iterations are scrutinized to optimize the logistic regression model's performance. The tuning process optimizes the logistic regression model and makes it more generalized and resistant to overfitting. The optimized model is then trained and tested on three differently sampled datasets and provides insight into its effectiveness across various validation scenarios.

In the support vector machine (SVM), the different combinations of regularization parameters, kernel types (linear, polynomial, radial bias function, and sigmoid), degree (only for polynomial kernels), and gamma (only for polynomial, radial bias function, and sigmoid kernels) are explored. The choice of the optimal kernel depends on the dataset's characteristics, such as linearity or non-linearity. The best kernel type selected might differ between the sampling methods (holdout, stratified K-fold, and leave one out) due to the distinct subsets they provide for training and testing, influencing the hyperparameter selection.

In the case of the decision tree classifier, key hyperparameters such as maximum depth (which is a limit to stop further splitting of nodes when the specified tree depth is reached), criterion for data splitting, cost complexity pruning (which addresses the problem of overfitting by selectively removing certain parts of the decision tree), minimum sample leaf (the minimum number of samples required

TABLE 3 Hyperparameters obtained for logistic regression.

Hyperparameter	Holdout-sampled data	Stratified K-fold-sampled data (K = 5)	Leave-one-out-sampled data
Regularization parameter (C)	0.1	10	10
Penalty	L2	L2	L2
Maximum number of iterations	100	100	100

TABLE 4 Hyperparameters obtained for SVM.

Hyperparameter	Holdout-sampled data	Stratified K-fold-sampled data (K = 5)	Leave-one-out-sampled data
Regularization parameter (C)	1	1	10
Kernel	Linear	Linear	rbf
Degree	Not applicable	Not applicable	Not applicable
Gamma	Not applicable	Not applicable	0.01

for a leaf node or external node and hence do not have any further splits), and minimum sample split (the minimum number of samples required to split an internal split) are adjusted to find the combination that maximizes the model's performance. These adjustments enhance the model's performance by finding the right combination that maximizes accuracy.

In a random forest, the key hyperparameters include the number of estimators, which represents the number of trees in the random forest, maximum depth, minimum sample leaf, and minimum sample split. Collectively, these hyperparameters shape the structure and complexity of each decision tree within the random forest ensemble.

3.5 Classification

Eleven spatiotemporal variables, four butterfly features, and two dynamic features from pedobarography, namely, double stance phase %, right and left stance phase %, stride time, right and left swing phase %, cadence, right and left step length, stride length, velocity, mean and SD of right gait line, right and left single limb support line, right and left heel pressure along with two features from normal walking pelvis motion, namely, SD of PRL and PRR; two trunk motion features, namely, mean of trunk F/E during the stand-to-sit condition and SD of trunk F/E during the sit-to-stand condition and TUG time during TUG test, and personal details including BMI, age, sex, and the health status of the subject are used to identify subjects with KOA. The models considered for classification are logistic regression, SVM, decision tree, and random forest. These models are trained and tested on the three differently sampled datasets. Logistic regression explains the relationship between the dependent variable, i.e., the pathology of the subject, and the remaining independent input variables, i.e., the pedobarographic data, pelvis and trunk motion, and personal details, to classify subjects with KOA. The threshold for classification is considered to be $\geq$ 0.5. The optimized hyperparameter values for logistic regression are shown in Table 3.

SVM classifies the data points by finding a hyperplane in an N-dimensional space. The "best" hyperplane is chosen among the several hyperplanes developed. The optimized hyperparameters for SVM are shown in Table 4. After determining the 'optimal' hyperplane, the data points situated on either side of it are assigned to distinct classes. The classification of an unknown data point is then based on its relative position to this established hyperplane. SVM with a linear kernel is used for the holdout- and stratified k-mean-sampled data and SVM with a radial bias function (rbf) kernel is employed for leave-one-out-sampled data.

A decision tree is constructed as a flowchart-like tree structure and employs internal nodes to test different attributes; branches represent the results of those tests, and each leaf node represents the class the feature falls into. The decision tree is built through a recursive process that involves dividing the training data into subsets according to attribute values. This recursive splitting continues until a predefined stopping criterion is satisfied, such as reaching the maximum tree depth or fulfilling the minimum number of samples needed to split a node. The decision tree is constructed by recursively splitting training data into subsets based on the values of the attributes until a stopping criterion is met, such as the maximum depth of the tree or the minimum number of samples required to split a node. During the training process, the algorithm selects the optimal attribute for data splitting using metrics such as entropy or gini impurity, aiming to maximize information gain or minimize impurity after each split. To achieve the best results, hyperparameters, namely, the maximum depth, criterion, cost complexity pruning, minimum sample leaf, and minimum sample split, are optimized. The hyperparameters obtained for the different sampled data for the decision tree are listed in Table 5.

A random forest classifier is an ensemble method where a collection of decision trees is trained on different subsets of the data. It employs the "bagging" approach for ensemble, in which each tree trains a random subset of the dataset, sampled with replacement. The final classification is determined by a majority vote among the individual trees. The different hyperparameters associated with the random forest classifier are the number of trees, minimum sample leaf, and minimum sample split. The hyperparameters obtained for the different sampled data for the random forest are listed in Table 6.

TABLE 5 Hyperparameters obtained for decision tree.

Hyperparameter	Holdout-sampled data	Stratified K-fold-sampled data (K = 5)	Leave-one-out-sampled data
Maximum depth	7	7	3
Criterion	Entropy	Gini	Entropy
Cost complexity pruning	0.05	0	0.025
Minimum sample leaf	1	3	1
Minimum sample split	4	6	2

TABLE 6 Hyperparameters obtained for random forest.

Hyperparameter	Holdout-sampled data	Stratified K-fold-sampled data (K = 5)	Leave-one-out-sampled data
Number of trees	100	100	50
Minimum sample leaf	1	1	1
Minimum sample split	2	5	2

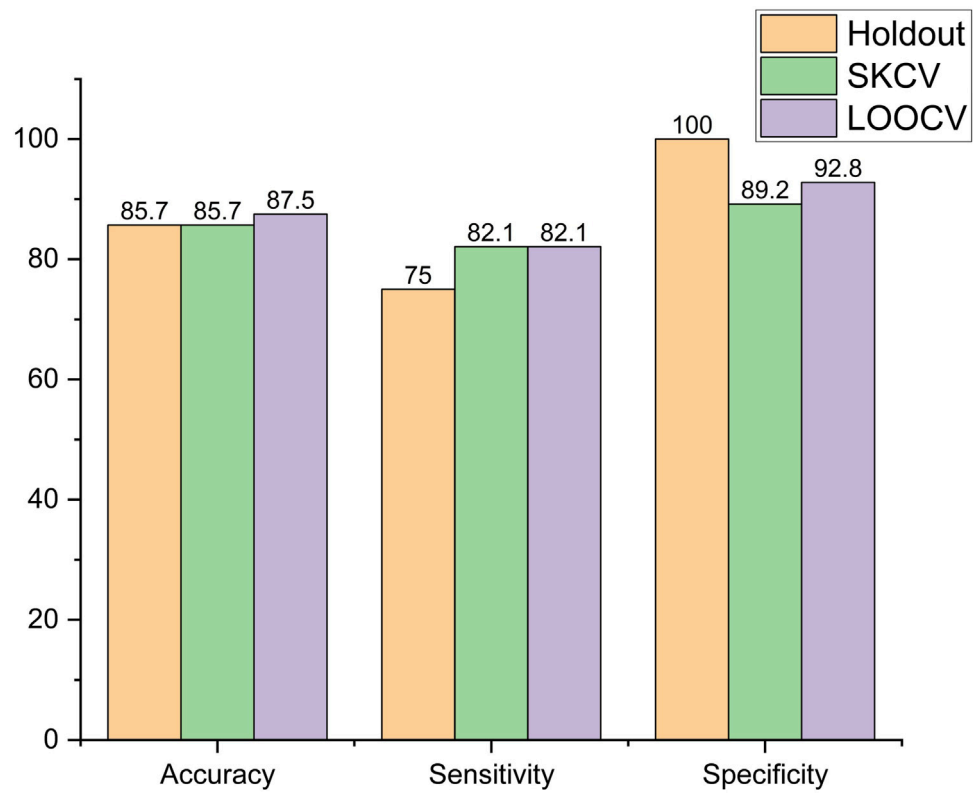

FIGURE 6
Performance metric of logistic regression.

3.6 Performance assessment

Accuracy, sensitivity, and specificity metrics are used to assess the performance of the classifiers. True positive (TP) signifies the correct identification of KOA (positive) cases, while true negative (TN) indicates the accurate exclusion of healthy (negative) cases. False positive (FP) occurs when the classifier wrongly identifies a negative (healthy) case as positive (KOA), and false negative (FN) arises when a positive (KOA) case is incorrectly classified as negative (healthy). The overall accuracy is computed by (TP + TN)/TCT, where TCT represents the total number of classification tests. Sensitivity and specificity are expressed by TP/(TP + FN) and TN/(TN + FP), respectively. Accuracy provides an overall measure of model performance, sensitivity gauges the model's ability to detect positive

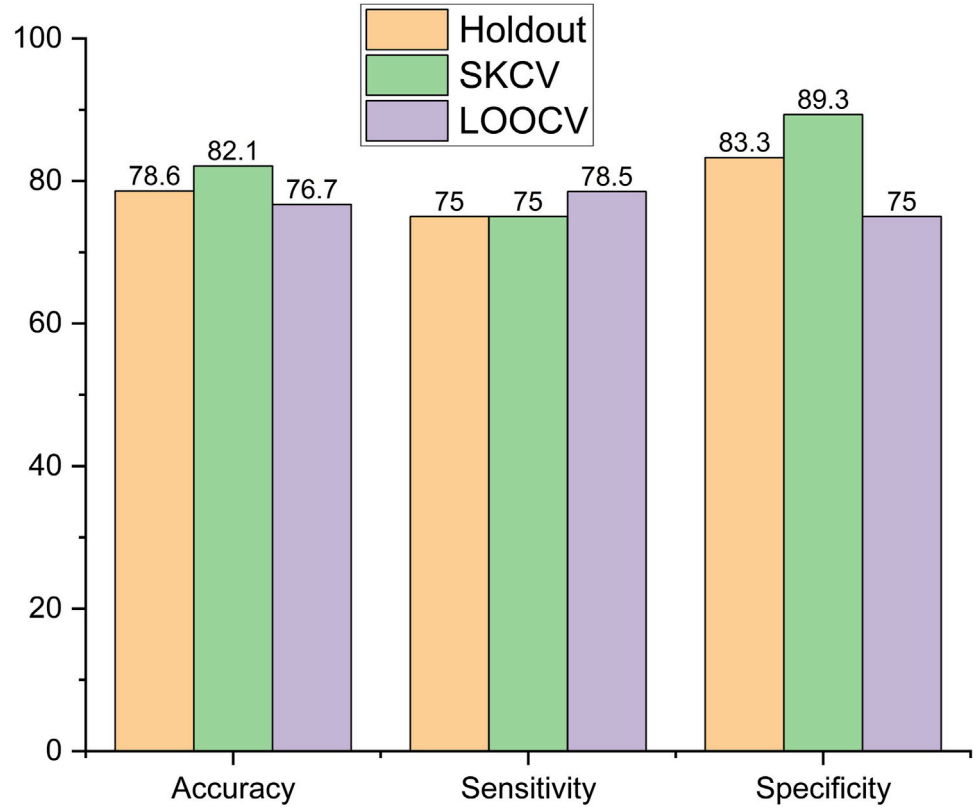

FIGURE 7
Performance metric of SVM.

cases, and specificity assesses the accuracy of identifying negative outcomes. Evaluation is conducted across three datasets sampled using holdout, SKCV, and leave-one-out LOOCV approaches.

3.7 Results

The performance metrics of the models, viz., logistic regression, SVM, decision tree, and random forest, are shown in Figures 6–9, respectively.

It is observed that in logistic regression, as shown in Figure 6, accuracy remained the same when the sampling method was changed from holdout to SKCV and increased by 2.1% from 85.7% to 87.5% when it was changed to LOOCV. Sensitivity increased by 9.46% from 75% to 82.1% when the sampling method was changed from holdout to SKCV or LOOCV. Specificity, however, decreased by 10.8% and 7.2% from 100% to 89.8% and from 100% to 92.8%, respectively, when the sampling method was changed from holdout to SKCV and LOOCV, respectively. The specificity obtained by the LOOCV sample was 3.87% higher than that obtained using the SKCV sample.

In the SVM, accuracy increased by 4.45%, from 78.6% to 82.1%, when the sampling method was changed from holdout to SKCV, and decreased by 2.41%, from 78.6% to 76.7%, when the sampling method was changed from holdout to LOOCV. Sensitivity remained the same for holdout- and SKCV-sampled data, while it increased by 4.6%, from 75% to 78.5%, when LOOCV sampled data were employed. Specificity for the SKCV sampled data increased by 6.7% and 16.01% in comparison to that of the data sampled by the holdout and LOOCV methods, respectively, as shown in Figure 7.

In the decision tree model, accuracy was highest for the data sampled using SKCV, with a decrease of 4%, from 89.3% to 85.7%, for data sampled by holdout and a larger decrease of 18%, from 89.3% to 73.2%, for data sampled by LOOCV, as shown in Figure 8. The trend was also similar for sensitivity, which peaked at 85.7% for data sampled by SKCV but decreased by 12.48% for data sampled by holdout and LOOCV. Specificity is the highest for data sampled by the Holdout method but decreased by 7.2% and 17.9% for data sampled by SKCV and LOOCV, respectively.

In the random forest, accuracy was highest for the holdout-sampled data, with a decrease of 4.2%, from 85.7% to 78.5%, and 8.4%, from 85.7% to 82.1%, for data sampled by LOOCV and SKCV, respectively. Sensitivity is highest for the LOOCV-sampled data but decreased by 8.64%, from 82.1% to 75%, for both holdout- and SKCV-sampled data, as shown in Figure 9. Sensitivity is highest for the holdout-sampled data but decreased by 17.9%, from 100% to 82.1%, for both SKCV- and LOOCV-sampled data.

4 Muscular activity of the periarticular muscles in KOA and healthy subjects

The identification of KOA through pedobarographic variables and pelvis and trunk motion variables can be inferred from the above section. Effectively monitoring rehabilitation therapies for

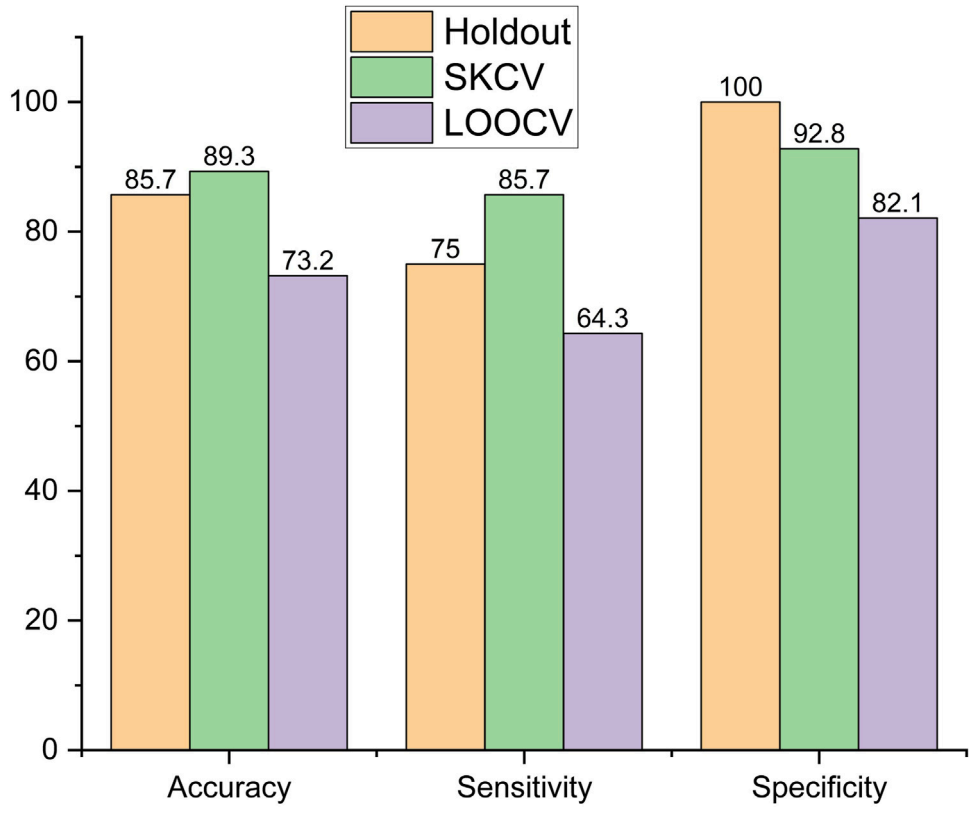

FIGURE 8
Performance metric of decision tree.

KOA using these variables necessitates establishing the impact of KOA on the strength of the periarticular muscles around the knee, which are part of the prime movers of knee flexion and extension (Levangie et al., 2011), and the rectus femoris and biceps femoris are part of the muscle group. Increased muscle force in the rectus femoris (Yagi et al., 2022) and increased muscle activation in the biceps femoris (Hortobágyi et al., 2005) for KOA subjects make it suitable for sEMG studies to differentiate between KOA and healthy subjects. In addition, sEMG features from the rectus femoris (Khader et al., 2024) and biceps femoris (Chen et al., 2019; Khader et al., 2024) have been previously employed in the identification of KOA. Thus, rectus femoris and biceps femoris are employed for the collection of sEMG data from healthy and KOA subjects, using them for the identification of KOA subjects. It is conducted by clustering analysis utilizing sEMG signals collected from the rectus femoris and biceps femoris caput longus bilaterally from two healthy subjects and six KOA subjects from the dataset. Prior to clustering, sEMG signals are filtered and analyzed to extract features in time, frequency, and time–frequency domains. The number of features is reduced using principal component analysis (PCA), which is then used for clustering analysis.

4.1 sEMG data collection

sEMG data of six subjects with varying degrees of KOA and two healthy subjects are collected to assess the muscle activity of the subjects during different activities. The various activities considered are standing under four different conditions for 60 s and walking. The standing conditions include walking at a self-selected speed and standing on firm ground with eyes open (Firm EO), firm ground with eyes closed (Firm EC), foam with eyes open (Foam EO), and foam with eyes closed (Foam EC). Table 7 provides us with a summary of the condition of the subjects along with the activities undertaken by each subject.

Data collection is done using wireless sEMG sensors from BTS Bioengineering, as shown in Figure 10. The muscles considered are the bilateral rectus femoris and biceps femoris caput longus, which are part of the quadriceps and hamstring group of muscles.

4.2 Feature selection using time-series, frequency, and time–frequency analysis

Along with sEMG signals, various noises and movement artifacts are also detected, so the required information remains together with the raw sEMG signal. It is thus difficult to assess the subjects using raw signals. Thus, sEMG features from different domains, which include time, frequency, and time–frequency domain features, are to be employed for the assessment (Chowdhury et al., 2013). Time domain features are considered as they have been reported to successfully classify healthy and knee-pathological subjects (Naik et al., 2018). The time domain features extracted here include "the Hudgins' features," i.e., the mean absolute value (MAV), MAV slope, slope sign changes (SSC),

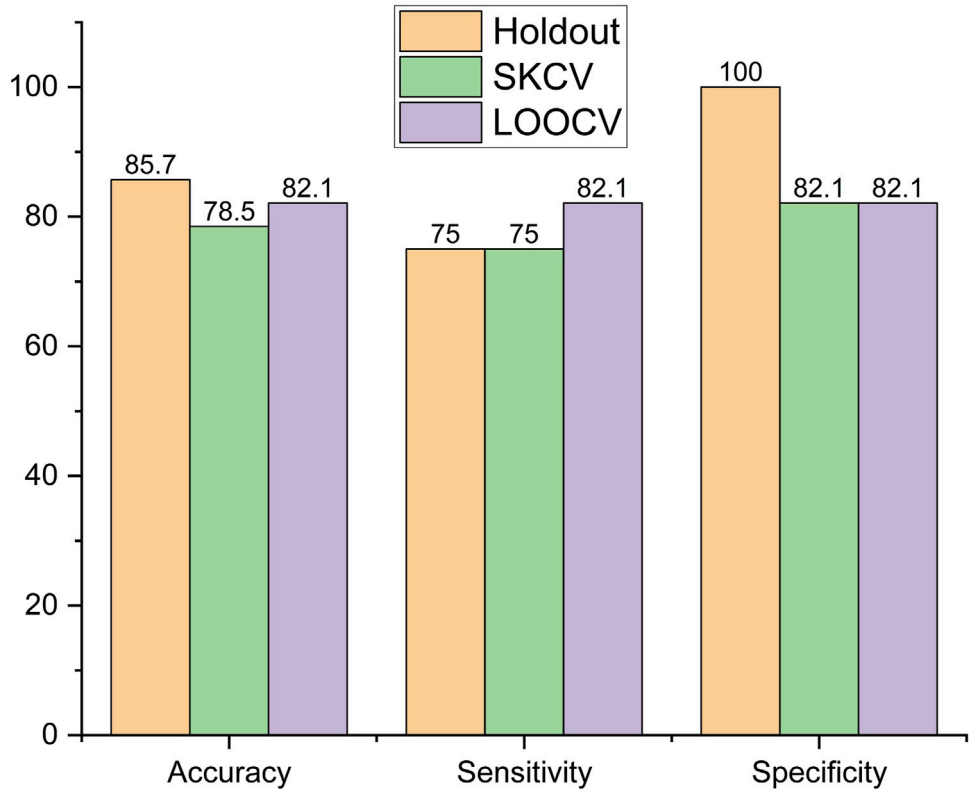

FIGURE 9
Performance metric of random forest.

TABLE 7 Summary of the subjects' condition during sEMG analysis.

Subject	Health condition	Activities undertaken
Subject 1	Healthy (H1)	Firm EO, Firm EC, Foam EO, Foam EC, and walking
Subject 2	Healthy (H2)	Firm EO, Firm EC, Foam EO, Foam EC, and walking
Subject 3	KOA Grade 3 (OA1_G3)	Firm EO, Firm EC, and Foam EO.
Subject 4	KOA Grade 1 (OA2_G1)	Firm EO, Foam EO, and Foam EC.
Subject 5	KOA Grade 2 (OA3_G2)	Firm EO, Firm EC, Foam EO, Foam EC, and walking
Subject 6	KOA Grade 1 (OA4_G1)	Firm EO, Firm EC, and walking
Subject 7	KOA Grade 1 (OA5_G1)	Walking
Subject 8	KOA Grade 1 (OA6_G1)	Walking

waveform length (WL), and zero crossings (ZCs) (Hudgins et al., 1993). In addition to that, average amplitude change (AAC), difference absolute standard deviation value (DASDV), integrated EMG (iEMG), kurtosis, log, root mean square (RMS) value, variance (var), and skewness are also evaluated in the time domain. Thus, 13 features are considered in the time domain. Frequency domain features have been established to be the best for assessing muscle fatigue (Cifrek et al., 2009). A time-domain EMG signal is transformed to the frequency domain using periodogram analysis, where the square of the absolute value of the Fourier transform of the EMG signal is divided by the signal length (Phinyomark et al., 2012). Thus, five frequency features, namely, the mean frequency (MNF), median frequency (MDF), mean power (MNP), and total power (TTP), are extracted from the EMG signal. MNF is the average frequency of the power spectrum of the EMG signal. MDF is the frequency at which the EMG power spectrum is divided into two regions with equal amplitudes. TTP is the aggregate of the EMG power spectrum and is also known as energy and the zero spectral moment. TTP and MNP are the frequency domain features that extract the same information as time domain features such as iEMG, RMS, and MAV based on the energy information as muscle fatigue results in an increase in EMG signal amplitude

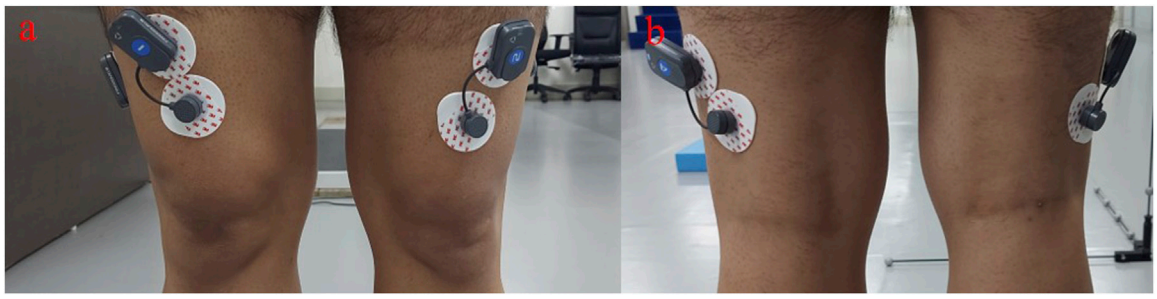

FIGURE 10
sEMG electrodes placed on **(A)** rectus femoris and **(B)** bicep femoris caput longus.

(Phinyomark et al., 2012). In addition to time and frequency analyses, time–frequency analysis is performed using the continuous wavelet transform (CWT) as it has been reported to effectively document quadriceps fatigue during knee extension exercise (So et al., 2009). In addition, wavelet neural network models using sEMG have been employed to estimate knee joint angles (Li et al., 2020). In CWT, one of the crucial steps is the selection of the "mother wavelet," which depends on the study application. The 5th order of coiflet is reported to provide the perfect reconstruction of the sEMG signal. Furthermore, symlet4 and symlet5 have been employed to determine muscle failure. Daubechies's functions (db2, db4, db6, db44, and db45) have been reported to be successfully applied for analyzing sEMG signals (Chowdhury et al., 2013). Thus, we have employed coiflet5, symlet4, symlet5, db2, and db4 as mother wavelets for the analysis of the sEMG signals and obtained five features, namely, the zero crossing rate (ZRC), root mean square (RMS), maximum amplitude, phase duration, and number of peaks for each signal.

4.3 Cluster analysis

Using the features obtained from each analysis, cluster analysis is performed in each experimental condition, namely, Firm EO, Firm EC, Foam EO, Foam EC, and walking. Using the time-series analysis, each muscle is found to have 13 features. As data are collected from four muscles, a total of 13 × 4, i.e., 52 features for each subject, are obtained in each experimental condition. The large number of features is reduced by employing PCA. The number of principal components (PCs) extracted is based on the condition that the maximum variance is explained by the least number of PCs. The 52 features are reduced to 5, 4, 4, 3, and 5 PCs for Firm EO, Firm EC, Foam EO, Foam EC, and walking condition, respectively. Using PCs, the K-nearest neighbor (KNN) algorithm is employed unsupervised to divide the subjects into clusters. Table 8 shows the clustering pattern obtained under the different experimental conditions for time-series features. It can be seen that PCs from time-series features were able to cluster the subjects accurately only for the Foam EC condition, with two healthy subjects and two OA subjects, one with Grade 1 and the Grade 2 severity. In the Firm EC condition, which contains five subjects, the OA subjects with Grade 1 and Grade 2 severity were clustered together with healthy subjects, while the OA subjects with Grade 3 severity were clustered separately. In the Firm EO condition, six subjects (two healthy and four OA) are considered. Two healthy subjects and two OA subjects with Grade 1 and Grade 2 severity are clustered together, and two OA subjects with Grade 1 and Grade 3 severity are then clustered separately. In the FOAM EO condition, five subjects (two healthy and three OA) are considered. One healthy and one OA Grade 2 subject are clustered together, and one healthy subject and two OA subjects with Grade 1 and Grade 3 are clustered together separately. In the walking condition, six subjects (two healthy and four OA subjects) are considered. Two healthy and two OA subjects with Grade 1 are clustered together, and two OA subjects, one with Grade 1 and one with Grade 2, are clustered together separately.

Frequency analysis provides five features for each muscle. Thus, a total of 5 × 4, i.e., 20 features for each subject, is obtained in each experimental condition. In each case, PCA is conducted to reduce the number of features. PCA reduces the 20 features to 4, 4, 4, 3, and 4 PCs for Firm EO, Firm EC, Foam EO, Foam EC, and walking condition, respectively. Using the PCs, the KNN algorithm is employed unsupervised to divide the subjects into clusters. Table 9 shows the clustering pattern obtained under the different experimental conditions for the frequency features. The PCs from the frequency features also cluster the subjects similarly, with the accurate cluster available with Foam EC condition. The clustering behavior for the other experimental conditions is similar to that of the time-series features except for the Foam EO condition, where the healthy subjects and the OA subject with Grade 1 severity are clustered together, and the OA subjects with Grade 2 and Grade 3 severity are clustered together separately.

Similarly, wavelet analysis, i.e., time–frequency analysis, also provides us with five features for each muscle. Thus, we have a total of 5 × 4, i.e., 20 features for each subject in each experimental condition. In each case, at first, PCA is conducted to reduce the number of features. PCA reduces the 20 features to 5, 4, 3, 3, and 5 PCs for Firm EO, Firm EC, Foam EO, Foam EC, and walking condition, respectively, with coif5 as the mother wavelet. In the case of the db2 mother wavelet, PCA reduces the 20 features to 5, 4, 4, 3, and 5 PCs for Firm EO, Firm EC, Foam EO, Foam EC, and walking condition, respectively. Considering the db4 mother wavelet, PCA reduces the 20 features to 5, 4, 4, 3, and 5 PCs for Firm EO, Firm EC,

TABLE 8 Cluster analysis on the time-series features.

	Subject name	Subject 1	Subject 2	Subject 3	Subject 4	Subject 5	Subject 6	Subject 7	Subject 8
	Actual condition	H1	H2	OA1_G3	OA2_G1	OA3_G2	OA4_G1	OA5_G1	OA6_G1
Cluster assigned with data from different experimental conditions	Firm EO	1	1	0	0	1	1	-	-
	Firm EC	1	1	0	—	1	1	-	-
	Foam EO	1	0	0	0	1	-	-	-
	Foam EC	0	0	—	1	1	-	-	-
	Walking	1	1	—	—	0	1	1	0

TABLE 9 Cluster analysis on the frequency features.

	Subject name	Subject 1	Subject 2	Subject 3	Subject 4	Subject 5	Subject 6	Subject 7	Subject 8
	Actual condition	H1	H2	OA1_G3	OA2_G1	OA3_G2	OA4_G1	OA5_G1	OA6_G1
Cluster assigned with data from different experimental conditions	Firm EO	1	1	0	0	1	1	—	—
	Firm EC	1	1	0	—	1	1	—	—
	Foam EO	1	1	0	1	0	—	—	—
	Foam EC	0	0	—	1	1	—	—	—
	Walking	1	1	—	—	0	1	1	0

Foam EO, Foam EC, and walking condition, respectively. With the sym4 mother wavelet, PCA reduces the 20 features to 5, 4, 4, 3, and 5 PCs for Firm EO, Firm EC, Foam EO, Foam EC, and walking condition, respectively. With the sym5 mother wavelet, PCA reduces the 20 features to 5, 4, 4, 3, and 5 PCs for Firm EO, Firm EC, Foam EO, Foam EC, and walking condition, respectively. Using PCs, the KNN algorithm is employed unsupervised to divide the subjects into clusters. Table 10 shows the clustering pattern obtained under the different experimental conditions using wavelet features. The clustering behavior of the PCs obtained from wavelet features is the same, irrespective of the choice of the mother wavelet. Accurate clustering is obtained for Firm EO, Foam EO, and Foam EC conditions. In the Firm EO condition, six subjects (two healthy and four OA) are considered. The healthy subjects are clustered together, and the four OA subjects with varying severity are clustered together separately. In the Firm EO condition, five subjects (two healthy and three OA) are considered. The healthy subjects are clustered together, and the three OA subjects with varying severity are clustered together separately. In the Foam EC condition, four subjects (two healthy and two OA) are considered. The healthy subjects are clustered together, and two OA subjects with varying severity are clustered together separately. In the case of Firm EC condition, five subjects (two healthy and three OA) are considered. One healthy subject is clustered together, and the other subjects (one healthy and three OA) are clustered together separately. In the walking condition, six subjects (two healthy and four OA) are considered. Two healthy subjects, one OA subject with Grade 2 severity and one OA subject with Grade 1 severity, are clustered together; and two OA subjects with Grade 1 are clustered together separately.

5 Discussion

With a worldwide high prevalence, KOA has significantly affected the quality of life of a large population. Because of its degenerative nature, early identification and, thus, early intervention greatly affect the management of KOA. The current gold standard to identify KOA is X-ray imaging, which is best suited for assessing the progression of the disorder, and MRI is more effective in ruling out OA but is expensive. In addition, there is a risk of radiation exposure in the case of X-rays. Hence, it is not effective for continuous monitoring of any rehabilitation regimens. The interdependency of the kinetic and kinematic variables of human movement with the muscle activity of the associated joints provides an alternate, non-invasive knee health monitoring technique. It is conducted by monitoring the pedobarographic data and pelvis and trunk motion as they are reported to be affected by the condition of the muscles around the knee (Gajdosik et al., 1994; Harty et al., 2005; Lee et al., 2020), which are in turn reported to be provided as physical therapy for the management of KOA (Bhatia et al., 2013).

Point-biserial correlation gives us 24 statistically significant features that are affected by KOA. Age is the most positively correlated variable, which is because of the nature of the disease, i.e., a chronic degenerative disorder (Anderson and Loeser, 2010). The TUG variables, which include one feature from the trunk F/E

TABLE 10 Cluster analysis on the wavelet features.

	Subject name		Subject 1	Subject 2	Subject 3	Subject 4	Subject 5	Subject 6	Subject 7	Subject 8
	Actual condition		H1	H2	OA1_G3	OA2_G1	OA3_G2	OA4_G1	OA5_G1	OA6_G1
Cluster assigned with data from different experimental conditions	Firm EO	coif5	1	1	0	0	0	0	—	-
		db2	1	1	0	0	0	0	—	-
		db4	1	1	0	0	0	0	—	-
		sym4	1	1	0	0	0	0	—	-
		sym5	1	1	0	0	0	0	—	-
	Firm EC	coif5	0	1	1	—	1	1	—	-
		db2	0	1	1	—	1	1	—	-
		db4	0	1	1	—	1	1	—	-
		sym4	0	1	1	—	1	1	—	-
		sym5	0	1	1	—	1	1	—	-
	Foam EO	coif5	1	1	0	0	0	—	—	-
		db2	1	1	0	0	0	—	—	-
		db4	1	1	0	0	0	—	—	-
		sym4	1	1	0	0	0	—	—	-
		sym5	1	1	0	0	0	—	—	-
	Foam EC	coif5	0	0	—	1	1	—	—	-
		db2	0	0	—	1	1	—	—	-
		db4	0	0	—	1	1	—	—	-
		sym4	0	0	—	1	1	—	—	-
		sym5	0	0	—	1	1	—	—	-
	Walking	coif5	1	1	—	—	1	0	1	0
		db2	1	1	—	—	1	0	1	0
		db4	1	1	—	—	1	0	1	0
		sym4	1	1	—	—	1	0	1	0
		sym5	1	1	—	—	1	0	1	0

during sit-to-stand and stand-to-sit conditions, and the TUG time are the next most positively correlated variables. This is because KOA has been reported to affect both gait and gaze during TUG (Rossignol et al., 2023). The positive correlation between the double-stance phase % and the stance phase (right and left) % is probably because of the impaired balance control due to KOA (Kim et al., 2011). The increased double-stance phase also results in a reduction of the swing phase and single-limb support line. BMI is found to be positively correlated with KOA because obesity has been associated with high risks of KOA (Zheng and Chen, 2015). Heel pressure is negatively correlated with KOA, thus inferring low heel pressure in KOA subjects. It is because of the insufficient knee extension during the heel-contact phase (Saito et al., 2013). A negative correlation is also observed for the spatiotemporal variables such as step length, stride length, and effective velocity, which are indicative of the abnormal knee joint loading adaptations due to the KOA (Chen et al., 2003). The SD of pelvis rotation on both the right and left sides is found to be negatively correlated with KOA, which suggests reduced variation in the pelvis rotation due to KOA. This is because there is reduced pelvic rotation in KOA subjects (Tanaka et al., 2007; Van Der Esch et al., 2011), which is a compensatory change adapted to minimize the load on the affected knee (Van Der Esch et al., 2011). Thus, pelvic rotation exercises can be part of the rehabilitation regimen targeted to address KOA (Tanaka et al., 2007). Age and SD of trunk F/E (sit to stand) are the most positively affected variables due to KOA, and velocity is the most negatively affected variable due to KOA.

ML models, namely, logistic regression, SVM, decision tree, and random forest, have been successful in classifying KOA with the highest accuracy of 89.3% and the highest sensitivity of 85.7% with

decision tree as a classifier and SKCV as the data sampling method. A specificity of 100% is obtained for three classifiers, namely, logistic regression, decision tree, and random forest with holdout as the sampling method. However, SKCV or LOOCV data sampling methods provide more robust results and are more adaptive to overfitting problems. Not considering the holdout sampling method, the specificity is the highest at 92.8% using decision tree as a classifier and SKCV as the data sampling method. The best performance is obtained with SKCV-sampled data because it ensures that each fold maintains the same distribution as the original dataset. This helps the model learn equally in all the folds and makes it sensitive to imbalances in the dataset. In addition, decision tree excels at extracting meaningful interactions between features, especially if they are non-linear in nature, compared to logistic regression and SVM. The better performance of decision tree in comparison to random forest may seem counterintuitive as random forest is an ensemble method that builds multiple decision trees; however, it may be because decision trees can capture interactions between features at a finer level compared to random forest and in the absence of excessive noise in the data, it may lead to better-performing decision trees. Thus, decision tree is the best-performing algorithm for the identification of subjects with KOA using pedobarographic data and pelvis and trunk motion. This reaffirms the possibility of the identification of KOA using variables from joints other than the knee, which was also reported by Kobsar et al. (2017), in which KOA rehabilitation responses were classified according to their effectiveness using wearable sensors in the back, thigh, and shank.

KOA greatly affects the muscle activity of the rectus femoris and biceps femoris caput longus. PCs from time-series features can distinguish between Grades 1 and 2 of KOA and healthy subjects during the Foam EC standing condition. They can also distinguish between Grade 3 KOA and other grades of KOA and healthy subjects during the Firm EC condition. They, thus, can distinguish between the early stages of KOA and healthy subjects. PCs from time-series features are not effective in distinguishing between KOA subjects and healthy subjects during Firm EO and Foam EO standing conditions and walking. In addition to Foam EC and Firm EC conditions, PCs from the frequency features are also able to distinguish between KOA with Grade 2 or higher severity and healthy subjects. It may be due to the fact that frequency domain features are sensitive to the effect of muscle fatigue (Cifrek et al., 2009) during any activity and hence are able to detect the strain on muscles due to KOA of Grade 2. However, Grade 1 KOA and healthy subjects are indistinguishable by this feature. PCs from the wavelet features performed the best in distinguishing between KOA subjects of different grades and healthy subjects for Firm EO, Foam EO, and Foam EC, by perfect distinction. It may be because time–frequency domain analysis provides a deeper understanding of the electrophysiological processes behind the neuromuscular activations (Di Nardo et al., 2022), and continuous wavelet transforms have also been reported to outperform other time–frequency analyses for both simulated and real EMG recordings (Karlsson and Gerdle, 2001). However, muscle activity from the rectus femoris and biceps femoris caput longus during walking is not found to distinguish between KOA subjects and healthy subjects. This is because during walking, balance, support, and progression are mostly contributed by five muscle groups, namely, the gluteus maximus, gluteus medius, vasti, gastrocnemius, and soleus (Lim et al., 2022).

Thus, KOA is diagnosed using gait variables for joints other than the knee, such as pedobarographic data and pelvis and trunk motion, along with the comparison of muscular activity in the bilateral rectus femoris and biceps femoris caput longus muscles for a section of the KOA and healthy subjects. Data are collected using wearable sensors, except for pedobarographic data, which can also be collected using wearable flexible insoles (Stassi et al., 2013). This allows for the identification of KOA through variables that can be captured using wearable sensors in real-world scenarios. Moreover, the establishment of the effect on muscular activity of knee periarticular muscles due to KOA through clustering analysis shows the complementary relationship between the gait variables and sEMG data. This opens up the possibility of monitoring hamstring and quadriceps strengthening as part of rehabilitation therapy to address KOA. The effect of KOA on the periarticular muscles of the knee is also reported by Ghazwan et al. (2022).

6 Limitations

A limitation of this study is that the EMG analysis was performed on only a few subjects and sEMG data were collected only for two major muscles responsible for knee joint movement. The periarticular muscles surrounding the knees contribute majorly during standing; however, the major muscles contributing during other activities of daily life are from different groups. Thus, the inclusion of at least one muscle from each of the major muscle groups in the lower limb will encompass and translate the study into more activities and also help us consider the synergistic behavior of the muscles.

7 Conclusion

This study establishes the capability of detecting KOA using gait variables from joints other than the knee. It employs pedobarographic data and pelvis and trunk ROM for the analysis. This offers a non-invasive and accessible method for the detection of KOA. The variables most affected by KOA are the SD of trunk F/E (sit to stand) and velocity. In addition, the study associated KOA with reduced pelvic rotation and thus suggests pelvis rotation exercises as part of a rehabilitation regimen targeted to address the effects of KOA. Furthermore, evidence of altered muscle activity in the rectus femoris and biceps femoris caput longus, which are part of the quadriceps and hamstring group of muscles, is found in subjects affected by KOA through cluster analysis. Thus, it can be inferred that KOA affects both mobility and muscle condition simultaneously, and both datasets complement each other. Hence, gait data can be employed to identify KOA subjects and perform a preliminary assessment and monitoring approach to gauge the effectiveness of rehabilitation therapies aimed at addressing KOA through muscle strengthening. Given the feasibility of collecting pedobarographic data and pelvis and trunk motion using wearable sensors with minimal sample preparation and its non-radiographic nature, the proposed method can be seamlessly integrated not only in a laboratory setting but also in real-world environments. Different combinations of machine learning models and data sampling methods have been employed to understand this behavior, and the decision tree with data sampled using SKCV is found to be the best classifier of KOA using gait data. The activities to be considered for

monitoring the assessment include walking and standing under different conditions, such as Firm EO, Foam EO, and Foam EC.

Data availability statement

The original contributions presented in the study and the data used for classification in the study are included in the article/Supplementary Material; further inquiries can be directed to the corresponding author.

Ethics statement

The studies involving humans were approved by the Institute Human Ethics Committee of Indian Institute of Technology, Guwahati. The studies were conducted in accordance with the local legislation and institutional requirements. The participants provided their written informed consent to participate in this study.

Author contributions

AS: writing–review and editing, writing–original draft, visualization, software, methodology, investigation, formal analysis, data curation, and conceptualization. LB: writing–review and editing, writing–original draft, methodology, investigation, and data curation. SI: funding acquisition, writing–review and editing, writing–original draft, and supervision. SK: writing–review and editing, writing–original draft, supervision, and funding acquisition.

Funding

The author(s) declare that financial support was received for the research, authorship, and/or publication of this article. The authors acknowledge the support provided by NECBH through the DBT project (BT/NER/143/SP44675/2023), IIT Guwahati, for the establishment of Gait and Motion Analysis Laboratory, IIT Guwahati.

Conflict of interest

The authors declare that the research was conducted in the absence of any commercial or financial relationships that could be construed as a potential conflict of interest.

Publisher's note

All claims expressed in this article are solely those of the authors and do not necessarily represent those of their affiliated organizations, or those of the publisher, the editors, and the reviewers. Any product that may be evaluated in this article, or claim that may be made by its manufacturer, is not guaranteed or endorsed by the publisher.

Supplementary material

The Supplementary Material for this article can be found online at: https://www.frontiersin.org/articles/10.3389/fbioe.2024.1401153/full#supplementary-material

References

Anderson, A. S., and Loeser, R. F. (2010). Why is OA an age-related disease. *Best. P. R. Res. Clin. Rheumatol.* 24 (1), 1–18.

Beckwée, D., Vaes, P., Cnudde, M., Swinnen, E., and Bautmans, I. (2013). Osteoarthritis of the knee: why does exercise work? A qualitative study of the literature. *Ageing Res. Rev.* 12 (1), 226–236. doi:10.1016/j.arr.2012.09.005

Bhatia, D., Bejarano, T., and Novo, M. (2013). Current interventions in the management of knee osteoarthritis. *J. Pharm. Bioallied Sci.* 5 (1), 30–38. doi:10.4103/0975-7406.106561

Brouwer, W. B. F., Koopmanschap, M. A., and Rutten, F. F. H. (1999). Productivity losses without absence: measurement validation and empirical evidence. *Health Policy (New York)* 48 (1), 13–27. doi:10.1016/s0168-8510(99)00028-7

Chen, C. P. C., Chen, M. J. L., Pei, Y.-C., Lew, H. L., Wong, P.-Y., and Tang, S. F. T. (2003). Sagittal plane loading response during gait in different age groups and in people with knee osteoarthritis. *Am. J. Phys. Med. Rehabil.* 82, 307–312. doi:10.1097/01.phm.0000056987.33630.56

Chen, X., Chen, J., Liang, J., Li, Y., Courtney, C. A., and Yang, Y. (2019). Entropy-based surface electromyogram feature extraction for knee osteoarthritis classification. *IEEE Access* 7, 164144–164151. doi:10.1109/access.2019.2950665

Chowdhury, R. H., Reaz, M. B. I., Bin Mohd Ali, M. A., Bakar, A. A. A., Chellappan, K., and Chang, T. G. (2013). Surface electromyography signal processing and classification techniques. *Sensors Switz.* 13 (9), 12431–12466. doi:10.3390/s130912431

Cifrek, M., Medved, V., Tonković, S., and Ostojić, S. (2009). Surface EMG based muscle fatigue evaluation in biomechanics. *Clin. Biomech.* 24 (4), 327–340. doi:10.1016/j.clinbiomech.2009.01.010

Cui, A., Li, H., Wang, D., Zhong, J., Chen, Y., and Lu, H. (2020). Global, regional prevalence, incidence and risk factors of knee osteoarthritis in population-based studies. *EClinicalMedicine.* 29–30, 100587. doi:10.1016/j.eclinm.2020.100587

de Leeuwerk, M. E., Bor, P., van der Ploeg, H. P., de Groot, V., van der Schaaf, M., van der Leeden, M., et al. (2022). The effectiveness of physical activity interventions using activity trackers during or after inpatient care: a systematic review and meta-analysis of randomized controlled trials. *Int. J. Behav. Nutr. Phys. Act.* 19 (1), 59–19. doi:10.1186/s12966-022-01261-9

Di Nardo, F., Basili, T., Meletani, S., and Scaradozzi, D. (2022). Wavelet-based assessment of the muscle-activation frequency range by EMG analysis. *IEEE Access* 10, 9793–9805. doi:10.1109/access.2022.3141162

Dobson, F., Hinman, R. S., Roos, E. M., Abbott, J. H., Stratford, P., Davis, A. M., et al. (2013). OARSI recommended performance-based tests to assess physical function in people diagnosed with hip or knee osteoarthritis. *Osteoarthr. Cartil.* 21 (8), 1042–1052. doi:10.1016/j.joca.2013.05.002

Duffell, L. D., Southgate, D. F. L., Gulati, V., and McGregor, A. H. (2014). Balance and gait adaptations in patients with early knee osteoarthritis. *Gait Posture* 39 (4), 1057–1061. doi:10.1016/j.gaitpost.2014.01.005

Gajdosik, R. L., Albert, C. R., and Mitman, J. J. (1994). Influence of hamstring length on the standing position and flexion range of motion of the pelvic angle, lumbar angle, and thoracic angle. *J. Orthop. Sports Phys. Ther.* 20 (4), 213–219. doi:10.2519/jospt.1994.20.4.213

Ghazwan, A., Wilson, C., Holt, C. A., and Whatling, G. M. (2022). Knee osteoarthritis alters peri-articular knee muscle strategies during gait. *PLoS One* 17, e262816. doi:10.1371/journal.pone.0262798

Gholami, S., Torkaman, G., Bahrami, F., and Bayat, N. (2022). Gait modification with subject-specific foot progression angle in people with moderate knee osteoarthritis: Investigation of knee adduction moment and muscle activity. *Knee* 35, 124–132. doi:10.1016/j.knee.2022.03.001

Harty, J., Soffe, K., O'Toole, G., and Stephens, M. M. (2005). The role of hamstring tightness in plantar fasciitis. *Foot and Ankle Int.* 26 (12), 1089–1092. doi:10.1177/107110070502601215

Hortobágyi, T., Westerkamp, L., Beam, S., Moody, J., Garry, J., Holbert, D., et al. (2005). Altered hamstring-quadriceps muscle balance in patients with knee osteoarthritis. *Clin. Biomech.* 20 (1), 97–104. doi:10.1016/j.clinbiomech.2004.08.004

Hudgins, B., Parker, P., and Scott, R. N. (1993). A new strategy for multifunction myoelectric control. *IEEE Trans. Biomed. Eng.* 40 (1), 82–94. doi:10.1109/10.204774

Karlsson, S., and Gerdle, B. (2001). Mean frequency and signal amplitude of the surface EMG of the quadriceps muscles increase with increasing torque - a study using the continuous wavelet transform. *J. Electromyogr. Kinesiol* 11 (2), 131–140. doi:10.1016/s1050-6411(00)00046-8

Khader, A., Zyout, A., and Al Fahoum, A. (2024). Combining enhanced spectral resolution of EMG and a deep learning approach for knee pathology diagnosis. *PLoS One.* 19 (5 May), e0302707–e0302715. doi:10.1371/journal.pone.0302707

Kim, H.-S., Yun, D. H., Yoo, S. D., Kim, D. H., Jeong, Y. S., Yun, J.-S., et al. (2011). Balance control and knee osteoarthritis severity. *Ann. Rehabil. Med.* 35 (5), 701. doi:10.5535/arm.2011.35.5.701

Kobsar, D., Osis, S. T., Boyd, J. E., Hettinga, B. A., and Ferber, R. (2017). Wearable sensors to predict improvement following an exercise intervention in patients with knee osteoarthritis. *J. Neuroeng Rehabil.* 14 (1), 94–10. doi:10.1186/s12984-017-0309-z

Kwon, S. B., Han, H. S., Lee, M. C., Kim, H. C., Ku, Y., and Ro, D. H. (2020). Machine learning-based automatic classification of knee osteoarthritis severity using gait data and radiographic images. *IEEE Access* 8, 120597–120603. doi:10.1109/access.2020.3006335

Kwon, S. B., Ro, D. H., Song, M. K., Han, H. S., Lee, M. C., and Kim, H. C. (2019). Identifying key gait features associated with the radiological grade of knee osteoarthritis. *Osteoarthr. Cartil.* 27 (12), 1755–1760. doi:10.1016/j.joca.2019.07.014

Lee, J. H., Jung, H. W., and Jang, W. Y. (2020). A prospective study of the muscle strength and reaction time of the quadriceps, hamstring, and gastrocnemius muscles in patients with plantar fasciitis. *BMC Musculoskelet. Disord.* 21 (1), 722–727. doi:10.1186/s12891-020-03740-1

Levangie, P. K., Norkin, C. C., and Levangie, P. K. (2011). *Joint structure and function: a comprehensive analysis*. Philadelphia: F.A. Davis Co.

Li, W., Liu, K., Sun, Z., Wang, G., Li, F., Zhang, X., et al. (2020). "Continuous estimation of human knee-joint angles from SEMG using wavelet neural network," in *Proc 2020 IEEE 9th data driven control learn syst conf DDCLS 2020*, 606–611.

Liang, J., Lang, S., Zheng, Y., Wang, Y., Chen, H., Yang, J., et al. (2019). The effect of anti-gravity treadmill training for knee osteoarthritis rehabilitation on joint pain, gait, and EMG: case report. *Med. Baltim.* 98 (18), e15386. doi:10.1097/md.0000000000015386

Lim, Y. P., Lin, Y. C., and Pandy, M. G. (2022). Lower-limb muscle function in healthy young and older adults across a range of walking speeds. *Gait Posture* 94, 124–130. doi:10.1016/j.gaitpost.2022.03.003

Menashe, L., Hirko, K., Losina, E., Kloppenburg, M., Zhang, W., Li, L., et al. (2012). The diagnostic performance of MRI in osteoarthritis: a systematic review and meta-analysis. *Osteoarthr. Cartil.* 20 (1), 13–21. doi:10.1016/j.joca.2011.10.003

Mills, K., Hunt, M. A., and Ferber, R. (2013). Biomechanical deviations during level walking associated with knee osteoarthritis: a systematic review and meta-analysis. *Arthritis Care Res. Hob.* 65 (10), 1643–1665. doi:10.1002/acr.22015

Naik, G. R., Selvan, S. E., Arjunan, S. P., Acharyya, A., Kumar, D. K., Ramanujam, A., et al. (2018). An ICA-EBM-based sEMG classifier for recognizing lower limb movements in individuals with and without knee pathology. *IEEE Trans. Neural Syst. Rehabil. Eng.* 26 (3), 675–686. doi:10.1109/tnsre.2018.2796070

Nandy, A. (2019). Statistical methods for analysis of Parkinson's disease gait pattern and classification. *Multimed. Tools Appl.* 78 (14), 19697–19734. doi:10.1007/s11042-019-7310-4

Pal, C. P., Singh, P., Chaturvedi, S., Pruthi, K. K., and Vij, A. (2016). Epidemiology of knee osteoarthritis in India and related factors. *Indian J. Orthop.* 50 (5), 518–522. doi:10.4103/0019-5413.189608

Phinyomark, A., Thongpanja, S., Hu, H., Phukpattaranont, P., and Limsakul, C. (2012). *The usefulness of mean and median frequencies in electromyography analysis*. Comput Intell Electromyogr Anal - A Perspect Curr Appl Futur Challenges.

Reijonsaari, K., Vehtari, A., Kahilakoski, O. P., van Mechelen, W., Aro, T., and Taimela, S. (2012). The effectiveness of physical activity monitoring and distance counseling in an occupational setting - results from a randomized controlled trial (CoAct). *BMC Public Health* 12 (1), 344. doi:10.1186/1471-2458-12-344

Rossignol, S. Le, Fraser, E., Grant, A., Doma, K., Wilkinson, M., Morse, L., et al. (2023). Patients with knee osteoarthritis have altered gait and gaze patterns compared to age-matched controls: a pilot study. *PLoS One.* 18 (11 November), 1–14. doi:10.1371/journal.pone.0283451

Saito, I., Okada, K., Nishi, T., Wakasa, M., Saito, A., Sugawara, K., et al. (2013). Foot pressure pattern and its correlation with knee range of motion limitations for individuals with medial knee osteoarthritis. *Arch. Phys. Med. Rehabil.* 94 (12), 2502–2508. doi:10.1016/j.apmr.2013.07.017

Saraee, E., Singh, S., Hendron, K., Zheng, M., Joshi, A., Ellis, T., et al. ExerciseCheck: remote monitoring and evaluation platform for home based physical therapy. *ACM Int. Conf. Proceeding Ser.* 2017;Part F1285:87–90.

Sarmah, A., Aggarwal, R., Vitekar, S. S., Katao, S., Boruah, L., Ito, S., et al. (2024). Framework for early detection and classification of balance pathologies using posturography and anthropometric variables. *Clin. Biomech.* 113, 106214. doi:10.1016/j.clinbiomech.2024.10621

Singh, A., Das, S., Chopra, A., Danda, D., Paul, B. J., March, L., et al. (2022). Burden of osteoarthritis in India and its states, 1990–2019: findings from the Global Burden of disease study 2019. *Osteoarthr. Cartil.* 30 (8), 1070–1078. doi:10.1016/j.joca.2022.05.004

So, R. C. H., Ng, J. K. F., Lam, R. W. K., Lo, C. K. K., and Ng, G. Y. F. (2009). EMG wavelet analysis of quadriceps muscle during repeated knee extension movement. *Med. Sci. Sports Exerc* 41 (4), 788–796. doi:10.1249/mss.0b013e31818cb4d0

Stassi, S., Canavese, G., Cauda, V., Fallauto, C., Corbellini, S., Motto, P., et al. (2013). Wearable and flexible pedobarographic insole for continuous pressure monitoring. *Proc. IEEE Sensors.*, 1–4.

Tanaka, K., Miyashita, K., Urabe, Y., Koshida, S., Takemoto, Y., and Ijiri, T. (2007). Relationship between pelvic rotation and trunk lean motion during walking in patients with symptomatic knee osteoarthritis. *J. Biomech.* 40, S508. doi:10.1016/s0021-9290(07)70498-0

Tiulpin, A., Thevenot, J., Rahtu, E., Lehenkari, P., and Saarakkala, S. (2018). Automatic knee osteoarthritis diagnosis from plain radiographs: a deep learning-based approach. *Sci. Rep.* 8 (1), 1727–1810. doi:10.1038/s41598-018-20132-7

Vaish, A., Ahmed, S., and Shetty, A. (2017). Remote physiotherapy monitoring using the novel D+R Therapy iPhone application. *J. Clin. Orthop. Trauma* 8 (1), 21–24. doi:10.1016/j.jcot.2016.08.008

Van Der Esch, M., Steultjens, M. P., Harlaar, J., Van Den Noort, J. C., Knol, D. L., and Dekker, J. (2011). Lateral trunk motion and knee pain in osteoarthritis of the knee: a cross-sectional study. *BMC Musculoskelet. Disord.* 12, 141–147. doi:10.1186/1471-2474-12-141

Xia, Y., Gao, Q., and Ye, Q. (2015). Classification of gait rhythm signals between patients with neuro-degenerative diseases and normal subjects: experiments with statistical features and different classification models. *Biomed. Signal Process Control* 18, 254–262. doi:10.1016/j.bspc.2015.02.002

Yagi, M., Taniguchi, M., Tateuchi, H., Hirono, T., Yamagata, M., Umehara, J., et al. (2022). Relationship between individual forces of each quadriceps head during low-load knee extension and cartilage thickness and knee pain in women with knee osteoarthritis. *Clin. Biomech.* 91, 105546. doi:10.1016/j.clinbiomech.2021.105546

Yang, J. H., Park, J. H., Jang, S. H., and Cho, J. (2020). Novel method of classification in knee osteoarthritis: machine learning application versus logistic regression model. *Ann. Rehabil. Med.* 44 (6), 415–427. doi:10.5535/arm.20071

Zheng, H., and Chen, C. (2015). Body mass index and risk of knee osteoarthritis: systematic review and meta-analysis of prospective studies. *BMJ open.* 5 (12), e007568. doi:10.1136/bmjopen-2014-007568

frontiers | Frontiers in Neurorobotics

TYPE Original Research
PUBLISHED 21 August 2024
DOI 10.3389/fnbot.2024.1372763

OPEN ACCESS

EDITED BY
Alois C. Knoll,
Technical University of Munich, Germany

REVIEWED BY
Xinxing Chen,
Southern University of Science and Technology, China
Yingbai Hu,
The Chinese University of Hong Kong, China
Xiaoyu Wu,
National University of Singapore, Singapore

*CORRESPONDENCE
Elena M. Gutierrez-Farewik
✉ lanie@kth.se

RECEIVED 18 January 2024
ACCEPTED 05 August 2024
PUBLISHED 21 August 2024

CITATION
Zhang X, Liu Y-X, Wang R and Gutierrez-Farewik EM (2024) Soft ankle exoskeleton to counteract dropfoot and excessive inversion.
Front. Neurorobot. 18:1372763.
doi: 10.3389/fnbot.2024.1372763

Soft ankle exoskeleton to counteract dropfoot and excessive inversion

Xiaochen Zhang[1], Yi-Xing Liu[1], Ruoli Wang[1] and Elena M. Gutierrez-Farewik[1,2]*

[1]KTH MoveAbility, Department of Engineering Mechanics, KTH Royal Institute of Technology, Stockholm, Sweden, [2]Department of Women's and Children's Health, Karolinska Institutet, Stockholm, Sweden

Introduction: Wearable exoskeletons are emerging technologies for providing movement assistance and rehabilitation for people with motor disorders. In this study, we focus on the specific gait pathology dropfoot, which is common after a stroke. Dropfoot makes it difficult to achieve foot clearance during swing and heel contact at early stance and often necessitates compensatory movements.

Methods: We developed a soft ankle exoskeleton consisting of actuation and transmission systems to assist two degrees of freedom simultaneously: dorsiflexion and eversion, then performed several proof-of-concept experiments on non-disabled persons. The actuation system consists of two motors worn on a waist belt. The transmission system provides assistive force to the medial and lateral sides of the forefoot via Bowden cables. The coupling design enables variable assistance of dorsiflexion and inversion at the same time, and a force-free controller is proposed to compensate for device resistance. We first evaluated the performance of the exoskeleton in three seated movement tests: assisting dorsiflexion and eversion, controlling plantarflexion, and compensating for device resistance, then during walking tests. In all proof-of-concept experiments, dropfoot tendency was simulated by fastening a weight to the shoe over the lateral forefoot.

Results: In the first two seated tests, errors between the target and the achieved ankle joint angles in two planes were low; errors of $<1.5^\circ$ were achieved in assisting dorsiflexion and/or controlling plantarflexion and of $<1.4^\circ$ in assisting ankle eversion. The force-free controller in test three significantly compensated for the device resistance during ankle joint plantarflexion. In the gait tests, the exoskeleton was able to normalize ankle joint and foot segment kinematics, specifically foot inclination angle and ankle inversion angle at initial contact and ankle angle and clearance height during swing.

Discussion: Our findings support the feasibility of the new ankle exoskeleton design in assisting two degrees of freedom at the ankle simultaneously and show its potential to assist people with dropfoot and excessive inversion.

KEYWORDS

assistive device, biomechanics, gait impairment, gait analysis, soft robotics

1 Introduction

Dropfoot, or the inability to lift the foot during gait, is a common secondary gait disorder after a stroke (Kluding et al., 2013) or other neurological injuries (Nori and Das, 2019) resulting from weakness and/or atypical motor control. People with dropfoot often exhibit two gait pathologies (Blaya and Herr, 2004): steppage gait and excessive subtalar inversion. Steppage gait is a condition where people demonstrate the inability to lift

the forefoot during the swing phase adequately and initially contact the floor with the whole foot or forefoot (Perry and Burnfield, 2010), making a high risk of tripping or even falling; excessive subtalar inversion after a stroke is primarily caused by spasticity in tibialis posterior. It can further influence foot clearance, leading to an unstable base of support and a high risk of ankle injury during walking (DeMers et al., 2017), and is associated with gait asymmetry and slow walking speed (Deltombe et al., 2017; Li, 2020). In dropfoot gait, typical compensatory movements to achieve foot clearance include ipsilateral pelvic elevation or "hiking" and increased hip abduction or "circumduction." Together, these movements generally reduce walking efficiency and endurance (Schmid et al., 2013), influence walking independence (Awad et al., 2017) and confidence (Yeung et al., 2021), and generally make daily activities challenging and inconvenient (Gil-Castillo et al., 2020).

Orthotic devices, such as ankle-foot orthoses that compensate for dropfoot gait by restricting plantarflexion, are widely used and positively impact the mobility and balance of the user (Tyson and Kent, 2013; Winstein et al., 2016; Awad et al., 2017). However, orthoses that restrict ankle movement inhibit any remaining ability of the plantarflexors to forward propel the leg during the preswing phase (Vistamehr et al., 2014) and may induce dependence on the devices (de Sèze et al., 2011; Daryabor et al., 2018).

Powered wearable exoskeletons are with increasing frequency being developed for movement assistance and rehabilitation (Blaya and Herr, 2004; Wu et al., 2019; Hu et al., 2023; Zhang L. et al., 2023). Rigid powered ankle exoskeletons may be able to provide adequate and timely assistance with movements, showing better performance than passive orthotic devices (Shorter et al., 2011; Yeung et al., 2018; Kim et al., 2020). The implementation of an actuation and control systems may achieve this, but rigid structures tend to be heavy and bulky, and may thus have limited feasibility and efficacy (Liu et al., 2021). It is also challenging to customize rigid exoskeletons for individual users as alignment of the device's ankle joint with the user's ankle joint can be challenging.

To this end, exoskeletons are increasingly designed to be lighter and more compliant, with the aim of achieving natural interactions between them and their users (Bae et al., 2015; Thalman et al., 2019). Many soft exoskeletons consist of an actuation system and a cable transmission system with a compact size and high transmission efficiency (Bae et al., 2015). The actuation system, which is often the heaviest part, should be positioned near the body's center of mass instead of distally near the ankle to minimize the user's additional metabolic demand associated with its weight (Browning et al., 2007; Lerner et al., 2018). Ankle exoskeletons with cable-driven transmission can have a substantial effect on both plantarflexion and dorsiflexion for people with disabilities, showing potential to improve gait kinematics (Bae et al., 2018), mobility, and energy expenditure (Lerner et al., 2018; Han et al., 2021). Nowadays, most soft ankle exoskeletons have focused solely on assisting the ankle in the sagittal plane (Bae et al., 2018; Lerner et al., 2018), providing assistance with toe clearance and push-off to fulfill the basic requirements for walking. However, they often overlook the critical need for assistance in the frontal plane, which is also vital for maintaining foot clearance and landing stability, thus impacting gait safety, especially in cases of excessive inversion. Although few attempts have been made to address multi-degree-of-freedom (DoF) requirements, these solutions typically involve complex structures and control strategies (Park et al., 2014).

The aims of this study were therefore to design and fabricate a 2-DoF powered soft ankle exoskeleton specifically intended to assist both dropfoot and excessive inversion, with features of lightweight, natural interaction, and reasonably simple mechanical design, and, in non-disabled subjects with simulated dropfoot impairment, to test its feasibility in assisting dorsiflexion and subtalar eversion, resisting plantarflexion, and compensating for device resistance in seated subjects, and in improving ankle and foot kinematics during gait.

2 Design

2.1 Hardware design

Inspired by the Harvard exosuits (Awad et al., 2017; Bae et al., 2018), the design of our active soft ankle exoskeleton consisted of four parts: a waist belt, a calf wrap, a pair of shoes, and sensors, with a total mass of 3.1 kg (Figure 1).

The design principles and selection of components were guided by the goal to develop a compliant and lightweight structure, with minimal burden on the user, maximal comfort, and flexibility to accommodate for different body sizes.

2.1.1 Waist belt

The actuation module was attached to the waist belt, consisting of actuators, controllers, and power supplies.

The actuator module contains two motors. In each actuator, a brushless DC motor (EC-4pole 22, 90W, Maxon Inc, Switzerland) with a planetary gearbox (GP 32, HP 123:1, Maxon Inc, Switzerland) was used, which can provide up to 5.54 Nm torque. Through a 3D printed pulley with a radius of 14 mm, the inner Bowden cable was attached to the actuators, with a possible retraction force of up to 396 N, which fulfilled the application requirements in our design.

A microcomputer (Raspberry Pi 4B, Raspberry Pi Foundation, UK) was used to control the actuators by sending control signals to motor drivers (EPOS4 Compact 50/8 CAN, Maxon Inc, Switzerland). The microcomputer was monitored and controlled by a laptop via Virtual Network Computing, through which the controller settings and the exoskeleton parameters could be tuned and adjusted remotely. By processing the movement information extracted from the load sensors, the microcomputer sent the control signal to the motor drivers, and the actuator was then driven to follow the control profiles.

The power supply was comprised of two batteries (Li-ion)—one with a capacity of 24 V and 144 Wh and the other at 18V—as well as a power bank with an output of 5 V and 3 A, which powered the actuators, load cells, and microcomputer, respectively.

2.1.2 Calf wrap

The calf wrap is made of Neoprene, secured with Velcro straps and elastic bands, and is able to fit different shank dimensions. Two anchors were assembled on the bottom of the calf wrap, positioned on both the medial and lateral sides, and were used to connect to the sheath of Bowden cables.

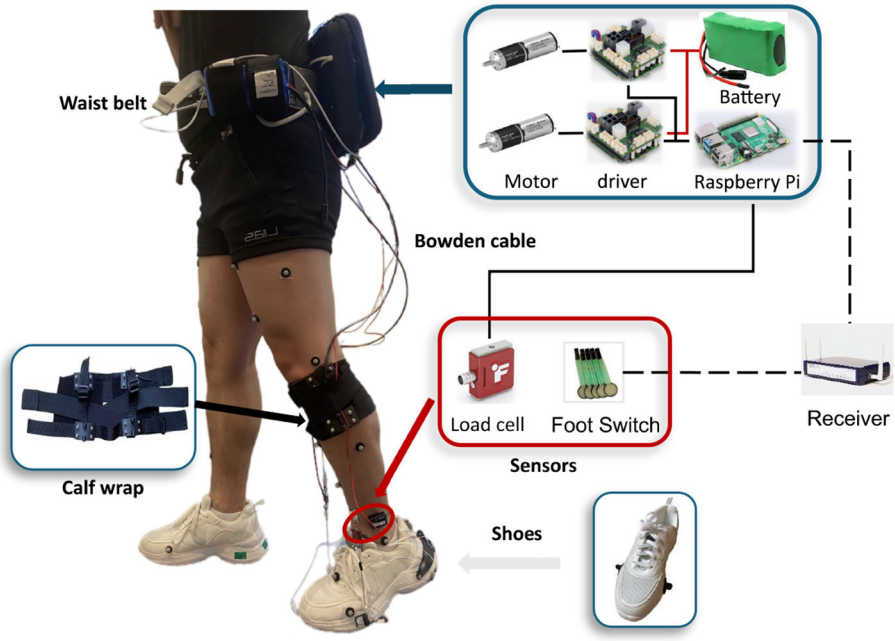

FIGURE 1
Overview of the soft ankle exoskeleton designed to counteract dropfoot and excessive inversion.

2.1.3 Shoe

Anchors were fixed on the lateral and medial sides of the forefront of the shoes. The distal end of each of the two inner Bowden cables was attached to these anchors.

2.1.4 Sensors

Two load cells (LSB205, FUTEK) with amplifiers (A100, FUTEK) were aligned in series with the Bowden cables to measure cable tensile forces, and the measured data were transferred to the controller through the cables. Encoders (16 EASY, 1024 CPT, 3 channels, Maxon Inc, Switzerland) mounted on motors were used to monitor motor positions. Two pairs of foot switches (Cometa, Italy) with four transducers each were attached to the bottom of shoes. The foot switch signal was transmitted from the receiver to the microcomputer via the TCP/IP protocol, at a frequency of 100 Hz. This signal was used to detect gait events, thereby identifying stance and swing phases.

The device was designed with both electrical and mechanical stops. For the electrical stop, the position of the cable and motor can be detected during the trials, and if the motor's position is out of a safe range, the motor will be stopped. In the mechanical stop, there is a physical stop in the cable to make sure it cannot be over-retracted.

2.2 Controller

A hierarchical controller that consists of a high-level, a mid-level, and a low-level controller was developed in this study (Figure 2). The high-level controller detects the gait phase based on foot switches on the bottom of the shoes. The mid-level controller has two modes—position control to achieve the desired ankle joint profile (Figure 2A) and force-free control to compensate for the resistance generated in the actuation system (Figure 2B). The low-level controller has a configuration with position control and current control loops embedded in the motor driver that aims to precisely direct the actuator to follow the profiles from the mid-level controller.

2.2.1 Position trajectory generator

On the exoskeleton, one anchor located on the calf wrap, one on the shoe, and one along the ankle joint axis formed a triangular structure, on both medial and lateral sides. When the actuator is activated, the interior angles of the triangle undergo alterations followed by the cable retraction or release, driving the ankle joint moving in the sagittal plane. Different alterations can be realized in the two triangular structures by setting different profiles for the two motors, which then trigger the kinematic change of the ankle joint in the sagittal and frontal planes simultaneously.

We generated the position trajectory that characterized the desired ankle motion with a smooth property at the initial and end stages. The position trajectory was defined by relative position p_{rel} and phase time t_{phase}, as well as a three-phase velocity profile (Figure 3). The function of the trajectory generator is to translate this predefined profile to the parameters that the low-level controller can read.

Relative position p_{rel} was obtained by subtracting initial position p_{ini} from target position p_{tar}. The positions were measured as the motor shaft positions by the encoders. The phase time t_{phase} was predefined and divided into three equal phases: ramp up t_{up},

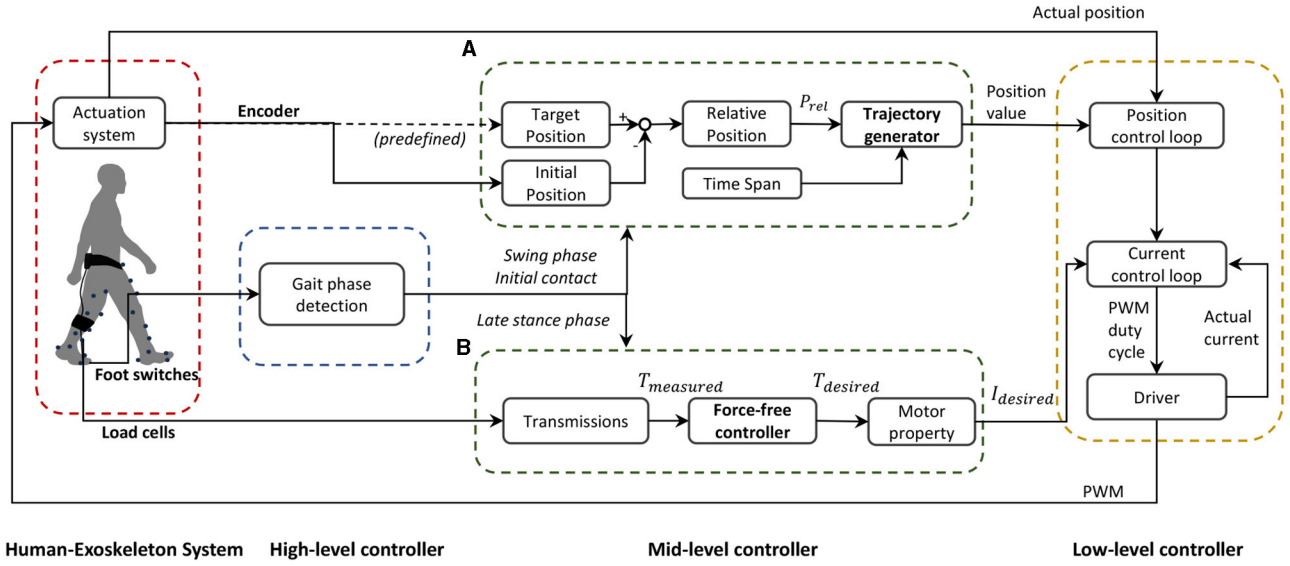

FIGURE 2
Schematic block diagram of the soft ankle exoskeleton controller. The frame presents a human-exoskeleton system, a high-level controller, a mid-level controller, and a low-level controller. The mid-level controller consists of two different modes: **(A)** position trajectory generator and **(B)** force-free controller.

maximum speed t_{max}, and ramp down t_{down}. With the relative position p_{rel} and specified intervals of t_{phase}, maximum velocity v_{max}, acceleration a_{max}, and deceleration a_{min} were computed. The position trajectory was then determined accordingly (Figure 2A).

To ensure precise motor performance along the predefined trajectory, the motor driver used a nested control loop structure wherein the position controller generated a desired current command based on the error between the desired and actual positions. The current control loop then tracked this current command using a finely tuned PID controller.

2.2.2 Force-free controller

A force-free controller, which aimed to compensate for the effect of gravity, device friction, and inertial forces (Dong et al., 2019; Hu et al., 2024), was used to achieve the desired ankle joint under a non-constraint condition during plantarflexion (Figure 2B).

In this study, the soft exoskeleton's weight and inertia around the ankle were considered negligible. The controller was simplified as follows:

The output torque of the motor T_m was computed using Equation 1:

$$T_m = (1 - K_t) \cdot T \tag{1}$$

where T_m and T represent the output torque of the motor and measured torque, respectively; K_t is a constant value.

Cable tensile force F_{cable} was measured with a load cell, and the measured torque was computed as per Equation 2:

$$T = F_{cable} \cdot R_{pulley}/r_{gear} \tag{2}$$

where R_{pulley} is the radius of the pulley, and r_{gear} is the ratio of the gear box.

For the constant value K_t, the relationship between the external torque, the constant value, and the inertia and friction torques can be expressed as per Equation 3:

$$T_{ext} = K_t^{-1}(J\ddot{\theta} + T_f) \tag{3}$$

where T_{ext} is the external torque; $J\ddot{\theta}$ is the inertia torque of the motor rotor, and T_f is the friction torque.

It can be seen that if $K_t > 1$, the external torque that is needed to overcome the inertia and friction torques will decrease by a multiple of K_t.

The current input I to the controller can be expressed as per Equation 4:

$$I = T_m/k_\tau \tag{4}$$

where k_τ represents the torque constant of the motor.

After computing the current input, the low-level current control loop utilized a finely tuned PID controller to track the current input. By continuously adjusting based on the error between the actual and target current, the system maintained accurate motor operation (Figure 2). This ensured the motor was driven to achieve the desired performance in the force-free application.

3 Experiments

Proof-of-concept experiments were conducted in two sessions and with different non-disabled subjects. The first three tests were performed on subjects in a seated position, and the fourth test was performed on subjects walking in an instrumented gait laboratory. These experiments were conducted to test the exoskeleton's feasibility and basic functionality to:

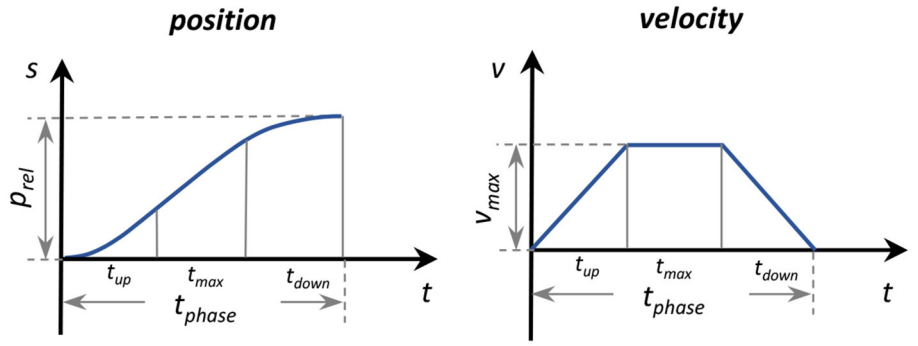

FIGURE 3
Parameterization of the position trajectory three-phase velocity profile.

1. Achieve two-DoF assistance simultaneously, specifically ankle dorsiflexion and eversion, from an initially plantarflexed and inverted ankle position.

2. Control speed and final position during a passive plantarflexion motion.

3. Compensate for device resistance from cable release during plantarflexion movement.

4. Normalize foot and ankle kinematics during walking.

3.1 Participants and experimental setup

Five non-disabled subjects (2M / 3F, (Mean ± SD) height: 166.4 ± 6.2 cm, weight: 60.6 ± 7.9 kg, age: 28.4 ± 1.4 years) participated in the seated tests, and three non-disabled subjects (1M / 2F, (Mean ± SD) height: 166.3 ± 5.8 cm, weight: 57.5 ± 3.9 kg, age: 27.4 ± 0.6 years) participated in the gait text. Inclusion criteria were no musculoskeletal disorders or recent lower-limb injuries that can influence gait or ankle movement. All subjects provided written informed consent, and the experiment was approved by the Swedish Ethical Review Authority (Dnr. 2023-02891-01).

Experiments were conducted in the Promobilia MoveAbility Lab, equipped with a 10-camera motion capture system (Vicon V16, UK). Thirty-six reflective markers were placed on each subject, and joint angles were computed according to a common lower-limb marker set (CGM2.4). Marker data were collected at 100 Hz. Two surface electromyography (EMG) sensors (Aktos Nano, Myon, Schwarzenberg, Switzerland) were placed on each subject's tibialis anterior (TA) and peroneus longus (PL) according to SENIAM recommendations (Hermens et al., 1999). Maximum voluntary isometric contraction (MVIC) of the two muscles was measured as per (Konrad, 2005), with the subject in a supine position on an examination table with heel contact.

In the first session, Tests 1–3, each subject, donning the exoskeleton and a 1-kg weight secured to the show over the lateral forefoot, sat on a chair with the shank and foot suspended in the sitting test. The purpose of the weight was to create an external plantarflexion and inversion moment, as a proxy to simulate dropfoot and excessive inversion impairments. The order of the three tests was randomized for each subject.

In the second session, Test 4, each subject donned the exoskeleton and the 1-kg weight over the lateral forefoot and walked on level ground at their preferred speed in a gait laboratory.

3.2 Test 1: assisting ankle dorsiflexion and eversion

This test focused on the functionality of assisting the ankle joint to dorsiflex and evert to a target position from an initially plantarflexed and inverted position. This test approximates dropfoot during the swing phase.

Prior to the data collection in Test 1, the target position was defined as the neutral position of the ankle during standing, and the initial position was defined from an earlier trial with wedges placed under the foot that placed the ankle in ∼18° plantarflexion and 10° inversion. Just prior to data collection, the ankle was moved to the initial position, confirmed via 3D motion capture, while suspended. Motor positions were recorded at both ankle joint position setups by the encoders.

During the test, position control was used to assist ankle dorsiflexion and eversion of the ankle joint from the initial to the target position during two different time intervals—fast: 0.5 s and slow: 0.75 s. These were repeated three times in a randomized order.

3.3 Test 2: controlling plantarflexion

This test focused on efficacy in controlling and preventing excessive plantarflexion and inversion, approximating loading response in early stance, beginning at initial contact and ending at a plantigrade foot position. This test involved controlling a passive plantarflexion movement. Subjects were seated with feet suspended and the ankle initially in a neutral position. The 1-kg weight on the lateral forefoot then passively plantarflexed and inverted the ankle. The exoskeleton's objective was to control this motion to a target position in a predetermined duration.

The initial position was defined as the neutral position during standing, and the target position was set to 8° plantarflexion.

During the test, position control was used to control ankle plantarflexion by following the predefined cable release trajectory, determined by initial and target positions, during a 0.4 s duration ("with exo" mode). As a reference, subjects were also tested in this procedure with the exoskeleton, while the cables were detached ("no cables" mode).

With the exoskeleton donned, subjects were asked to relax and not to not perform any active dorsi- or plantarflexion. However, in the "no cables" mode, they were required to activate dorsiflexors prior to the test to hold up the foot to the neutral position and then asked to relax them to initiate the test.

The trials were each repeated three times, and the order of the two modes was randomized.

3.4 Test 3: resistance compensation during plantarflexion

This test focused on evaluating the efficacy of the force-free controller to compensate for device resistance during plantarflexion motion, approximating the preswing phase of gait. The exoskeleton's objective was to restrict desired plantarflexion as little as possible.

The initial position was defined as the neutral ankle position during standing. The 1-kg weight was placed on the lateral forefoot, and each subject passively planterflexed the ankle from a neutral position during three different conditions:

- The cables were detached from exoskeleton to measure natural plantarflexion movement without any resistance ("no cables" mode),
- The exoskeleton was unpowered, and the cables were stretched passively to measure the effects of resistance ("passive" mode),
- The exoskeleton was powered with the force-free controller, aiming to compensate for resistance and restore natural plantarflexion motion ("resistance compensation" mode).

Subjects were asked to be as relaxed as possible during the trials, so that plantarflexion was induced by gravity and the weight. As in Test 2, however, in the "no cables" mode, subjects were required to use dorsiflexor muscles to maintain ankle position prior to the test and then to relax them to initiate the test.

Each mode was repeated three times in a randomized order.

3.5 Test 4: assisting ankle and foot kinematics during gait

This test focused on the exoskeleton's efficacy in correcting the altered ankle and foot kinematics associated with the simulated dropfoot, specifically its ability to resist the passive plantarflexion and inversion from the simulated impairment, while not limiting the plantarflexion movement during stance.

Subjects walked on level ground at their preferred walking speeds in three different conditions:

- Walking without the exoskeleton and without the weight on the shoe. Parameters measured in this condition were set as reference ("Reference").
- Walking without the exoskeleton and with the weight on the shoe. The simulated impairments were measured in this condition ("Simulated Impairment").
- Walking with the powered exoskeleton ("With Exoskeleton") and the weight on the shoe. Position control was used in swing and loading response phases, and the force-free controller was used in late stance. In the swing phase, the target position and phase time of the position control were defined as the neutral position during standing, similar to Test 1, and the average swing phase duration during the previous three steps. In loading response, the parameters were set to 8° plantarflexion and 0.2 s, respectively.

The order of conditions was randomized.

3.6 Data processing and outcome parameters

Recorded raw EMG signals were processed using a band-pass filter (Butterworth 20–400 Hz), rectified, low-pass filter (Butterworth 4 Hz), and then normalized by MVICs (MATLAB R2020b, Mathworks, US). Kinematics were calculated through inverse kinematics (Nexus, Vicon).

The device's functionality in the different seated tests was evaluated with three outcome parameters:

- Tracking accuracy, defined as the error between measured and target ankle angles in the sagittal and frontal planes, was computed for Tests 1 and 2.
- Resistance reduction, defined as the rate of ankle plantarflexion and inversion, was computed for each of the three modes—resistance compensation, passive, and no cables.
- Muscle activity, specifically the normalized EMG signals with and without resistance compensation for each subject, was computed.

Paired t-tests were used to compare velocities and normalized EMG in different modes in Test 3.

The devices' functionality to normalize foot and ankle kinematics during gait was evaluated with five outcome parameters:

- Foot inclination angle at initial contact
- Ankle inversion angle at initial contact
- Foot clearance height during the swing phase, defined as the minimal height of the fifth metatarsal head marker
- Maximum plantarflexion angle in preswing, defined as the maximum plantarlexion angle between 50 and 60 % gait cycle
- Average ankle angle in late swing, defined as the average sagittal ankle angle in 90%–100 % gait cycle.

No statistical tests were performed in Test 4, since there they only include data on three subjects.

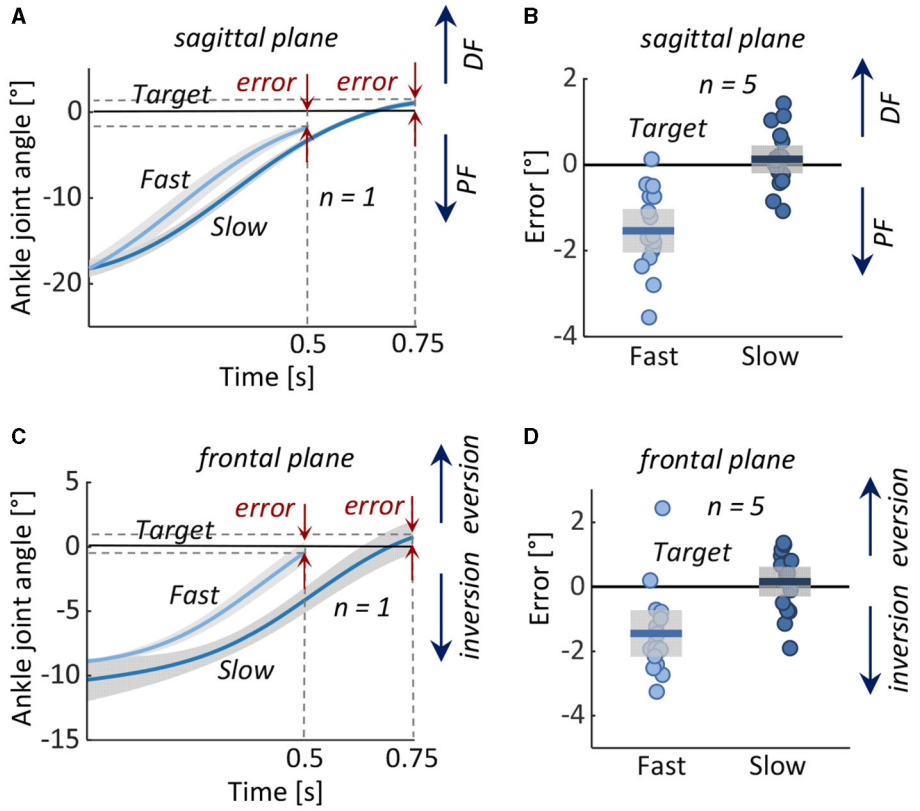

FIGURE 4
Test 1: Assisting dorsiflexion and eversion from an initial position of ankle plantarflexion and inversion to a neutral target position in 0.5 s (Fast) and 0.75 s (Slow). Left: Measured ankle joint angles (mean ± 1 standard deviation) during fast and slow movements in **(A)** representative subject in the **(A)** sagittal and **(C)** frontal planes. Right: Error in reaching the target angle in all five subjects in the **(B)** sagittal and **(D)** frontal planes. Boxes represent the standard deviation, the horizontal lines represent the mean value of the five subjects in the two conditions, and data from individual subjects are overlaid. DF, dorsiflexion; PF, plantarflexion.

4 Results

4.1 Test 1: performance in assisting dorsiflexion and eversion

The subjects' average initial ankle positions were ∼18° plantarflexion and 10° inversion, and target positions were 0° in both planes. With the exoskeleton, the subjects were able to approximate the target position, in both fast and slow conditions (Figure 4). In both anatomical planes, slightly greater accuracy was achieved in the slow condition. Among subjects, the mean ± standard deviation (SD) of the target position in the sagittal plane were −1.5° ± 0.5° in the fast condition and 0.1° ± 0.3° in the slow condition and in the frontal plane, −1.4° ± 0.7° in the fast condition, and 0.2° ± 0.5° in slow condition, respectively.

4.2 Test 2: performance in controlling plantarflexion

In the no cables condition, the ankles rapidly and exaggeratedly plantarflexed and inverted. With the exoskeleton, ankle motion was decelerated and reduced in both sagittal and frontal planes (Figure 5).

Among subjects, with the exoskeleton, the mean ± SD ankle final angles were −7.2° ± 0.5° (with target position errors of 0.8° ± 0.5°) in the sagittal plane and −1.2° ± 0.5° (target position error 1.2° ± 0.5°) in the frontal plane. Without the exoskeleton, mean ± SD final angle was −30.8° ± 5.7° in the sagittal plane and −4.0° ± 1.7° in the frontal plane.

4.3 Test 3: performance in resistance compensation

The device's natural resistance decelerated the desired plantarflexion motion. The resistance compensation was partially able to compensate for this resistance but not fully. The rate of ankle motion was lowest in the passive mode, with an average of 16.6 deg s^{-1} in the sagittal plane and 1.1 deg s^{-1} in the frontal plane. With the exoskeleton in force-free control mode, the average rate of ankle motion was significantly higher; it more than doubled in both the sagittal plane (44.4 deg s^{-1}, $p < 0.01$) and in the frontal plane (4.4 deg s^{-1}, $p < 0.05$). However, even with the force-free control, the ankle motion was approximately half as fast as in the no-cable mode (Figure 6).

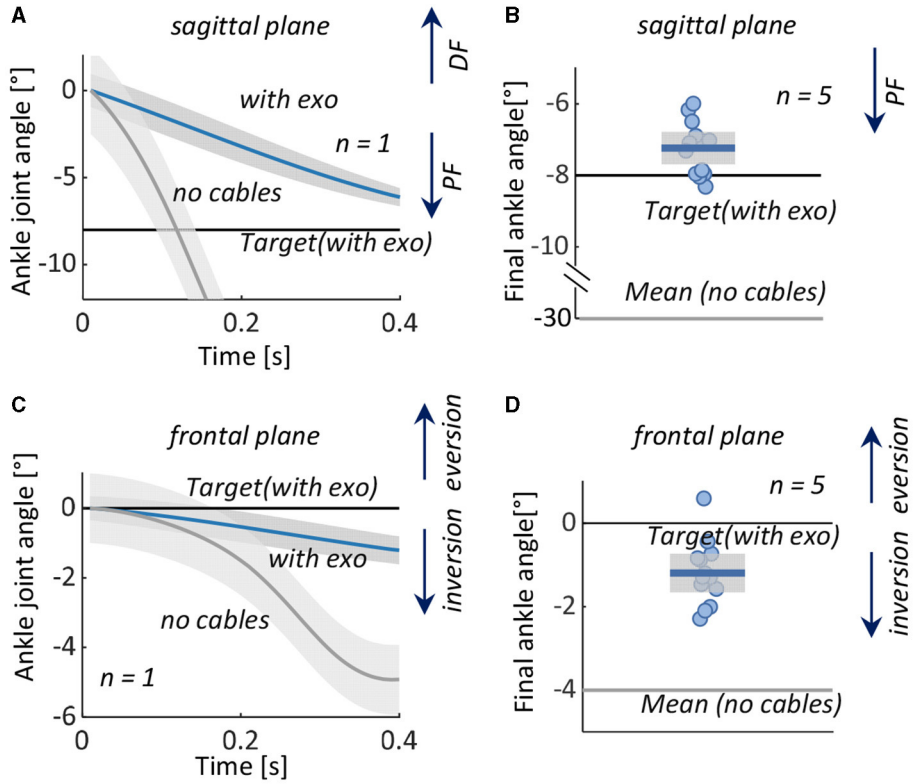

FIGURE 5
Test 2: Controlling plantarflexion from an initial neutral position to a plantarflexed position. Left: Measured ankle joint angles (mean ± 1 standard deviation) with the exoskeleton (with exo) and with cabled detached (no cables) in a representative subject in the **(A)** sagittal and **(C)** frontal planes. Right: Ankle angle at the final position in all five subjects and target angles in the **(B)** sagittal and **(D)** frontal planes. Boxes represent the standard deviation with data from individual subjects overlaid, the horizontal black lines represent the target angles of the five subjects with the exoskeleton, and the horizontal gray lines represent the mean value in the condition without the exoskeleton. DF, dorsiflexion; PF, plantarflexion.

There were no significant differences in muscle activities of the TA and PL during the trials between passive and force-free conditions ($p = 0.618$ and $p = 0.836$).

4.4 Test 4: performance in normalizing foot and ankle kinematics during gait

Compared to the reference condition, the simulated impairment resulted in decreased ankle dorsiflexion in late swing and loading response, wherein the foot segment was both more plantarflexed and inverted at initial contact. The exoskeleton normalized these angles (Figure 7); with the exoskeleton, the average foot inclination angle at initial contact increased from 11.6° to 16.9° (reference 20.8°), and the ankle inversion decreased from 1.0° inversion to 0.4° eversion (reference 0.6° eversion). Average foot clearance height increased from 36.7 to 49.7 mm (reference 54.3 mm), and ankle angle in late swing changed from 6.2° of plantarflexion to 0.7° of dorsiflexion (reference 2.7° of dorsiflexion).

With the exoskeleton, minor restriction of maximum plantarflexion in preswing was observed; compared to the reference condition, the maximum plantarflexion angle in preswing with the exoskeleton (9.8°) was largely unchanged (reference 13.1°).

5 Discussion

In this study, we have designed and developed a new powered soft exoskeleton to assist people with dropfoot, with or without a tendency for excessive inversion. We tested the device's overall feasibility and efficacy in a small group of non-disabled adults, first in several seated tests that simulate problematic gait phases for persons with dropfoot, specifically foot clearance in swing and early foot contact in loading response, then during gait. As a proxy for the associated atypical motor control in persons with dropfoot, external plantarflexion and inversion moment were created in the non-disabled subjects by a weight on the superior, distal, and lateral side of the foot, inspired by previous studies that simulated gait deviations in non-disabled subjects (Hong et al., 2021; Zhang Q. et al., 2023). The purpose of the third test in our study was to evaluate the ability of the controller to compensate for the inherent resistance in the exoskeleton system.

The novelty of our device is its ability to control both the sagittal and frontal motion of the ankle, achieved with the relatively simple design of placing an anchor for the cable on the lateral and another on the medial sides of the forefoot. The assistance force and design

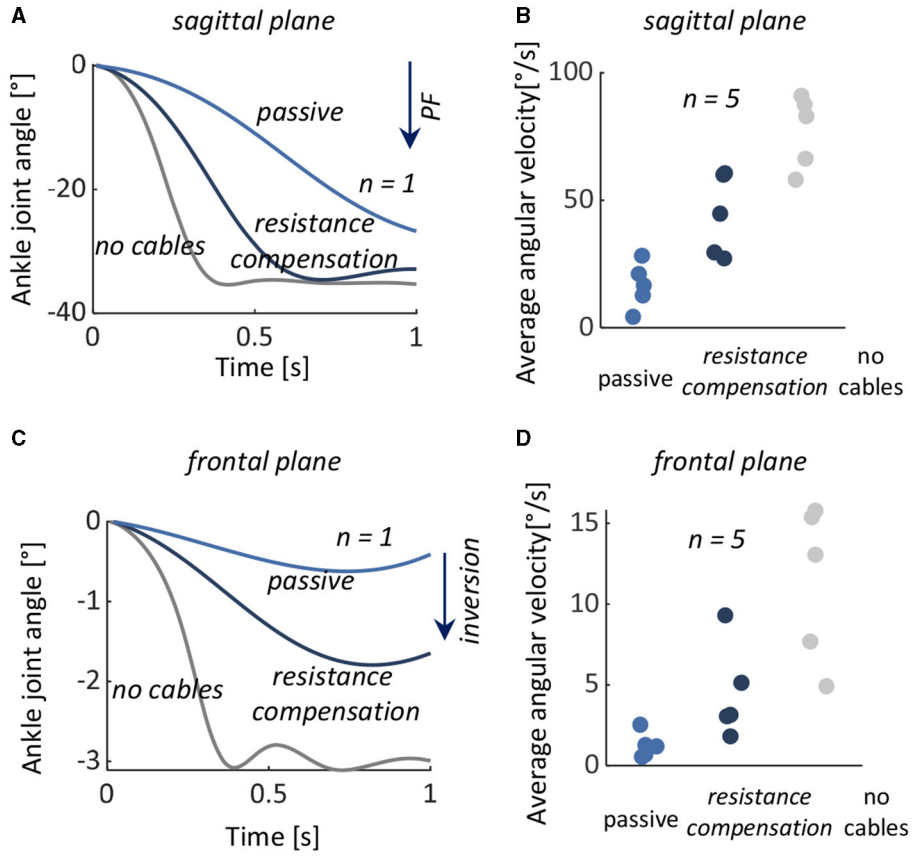

FIGURE 6
Test 3: Resistance compensation during a desired plantarflexion motion. Left: Measured ankle joint angles with the exoskeleton's natural resistance (passive), with the exoskeleton and force-free controller (resistance compensation), and with the cables detached from the exoskeleton (no cables) from a representative subject in the **(A)** sagittal and **(C)** frontal planes. Left: Average plantarflexion angular velocity in all five subjects during passive (light blue), resistance compensation (dark blue), and no cables (gray) in **(B)** sagittal and **(D)** frontal planes. The data from individual subjects are overlaid. PF, plantarflexion.

with motors in the waist belt and Bowden cables were inspired from previous designs (Awad et al., 2017; Bae et al., 2018; Lerner et al., 2018), with the feature of being lightweight and compact. Our design was able to control forefoot kinematics with low errors, notably in the frontal plane, compared with a design described by Xia et al. (2020). Instead of employing a rigid structure on the foot segment (Zhong et al., 2023) or controlling the movements in the sagittal and frontal planes separately (Xia et al., 2020), our device uses two motors to lift the medial and lateral sides of the foot and thus adjust in both planes in a relatively simple but effective control strategy.

The two-mode controller in our design includes position control. The controller's accuracy of ankle kinematics is a common yet important performance metric to evaluate a device's effectiveness, particularly for people with disabilities (Yeung et al., 2017; Bae et al., 2018; Xia et al., 2020). In the first two tests, we found that the dorsiflexion and eversion assistance tracked the target position with relatively low errors, which demonstrates that our exoskeleton is capable of guiding the ankle motion well with the cable retraction/release mechanism.

Soft exoskeletons commonly have lower tracking accuracy than rigid exoskeletons (Asbeck et al., 2013; Bae et al., 2018), partly attributable to movement and/or deformation of the textiles and other soft materials subjected to interaction force. In our experiments, we did not observe any slippage of the calf wrap. It did, of course, deform, however, but this effect was mitigated to a good extent by setting the target ankle position and corresponding cable length before the experiment with the exoskeleton on. However, in Test 1, tracking errors were higher in the fast condition than in the slow condition, which might be due in part to more textile deformation with the larger interaction forces.

The second mode of the controller was the force-free controller. The simplicity of the design with both cable anchors on the forefoot also presents a challenge in assisting ankle motion as it introduces device resistance during plantarflexion. Bae et al. (2018) have suggested an approach to address this issue, specifically a cable slackness management method, which involved updating a baseline position and then releasing the cable to the position during each stride. For our implementation, this approach would not be appropriate, particularly as ankle kinematics may deviate in each stride, making it difficult to adjust cable tension for each step. We implemented the force-free controller, aiming at compensating for the inherent drag from the system friction and cable slack and making the exoskeleton follow natural ankle plantarflexion

10.3389/fnbot.2024.1372763

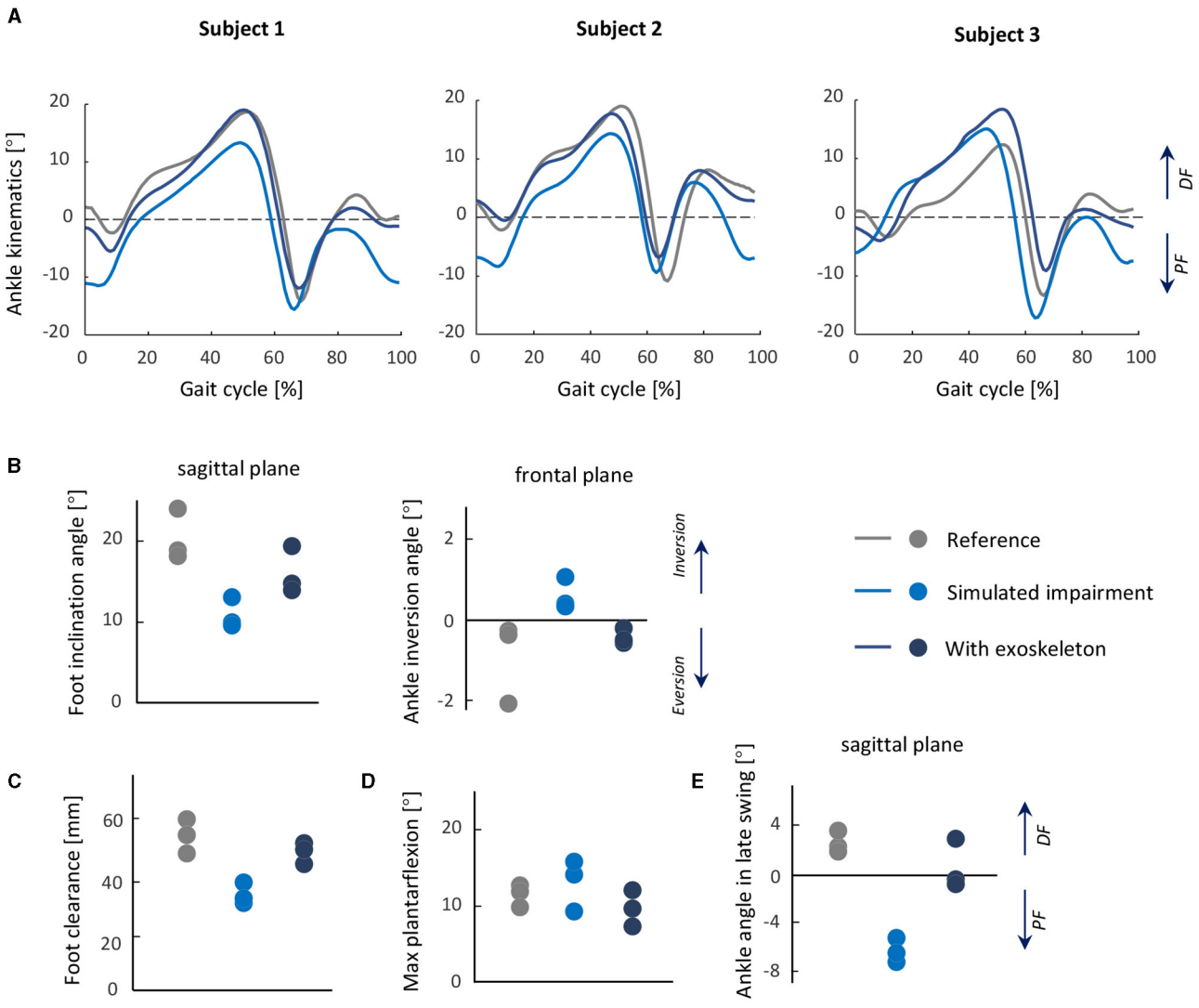

FIGURE 7
Test 4: Normalizing foot and ankle kinematics during gait from a simulated dropfoot condition. Top row: **(A)** Ankle joint kinematics during gait in each subject in three conditions: reference, simulated impairment, and with exoskeleton, shown as averages of each trial. **(B)** Foot inclination angle and ankle inversion angle at initial contact. **(C)** Foot clearance height during the swing phase. **(D)** Maximum plantarflexion during gait. **(E)** The average ankle joint angle in the late swing phase. From **(B)** to **(E)**, the mean value of each subject is shown for all metrics, and the data from individual subjects are overlaid.

as smoothly as possible. The experimental result showed that the force-free controller was able to reduce the inherent drag of the system resistance, apparent as higher angle velocity in passive plantarflexion in Test 3, but not to eliminate it entirely.

In the gait tests, the exoskeleton showed potential in normalizing the altered ankle and foot kinematics induced by the simulated gait impairment; specifically, it was able to lift the foot during swing and orient the foot segment similarly to the reference condition, without limiting the plantarflexion motion during preswing. Switching between control modes involves a 3–5 ms delay, which is unlikely to have much influence on the device's efficacy. Further exploration of other control profiles and optimization methods for ideal assistance is warranted.

There are some limitations and simplifications in this study. In Test 3, the force-free controller could reduce some of the effects of drag in plantarflexion in both seating and gait tests but not entirely. In addition, it did not constrain the ankle from inverting. This could be problematic for persons with a tendency to invert the ankle; more tension in the lateral Bowden cable may be required. For the parameter K_t in the force-free controller, we selected a constant value to balance the flexibility and stability for all subjects in both seating and gait tests. Future investigations are necessary to determine the optimal value to provide adequate assistive and balance plantarflexion and inversion control. It is also possible that optimal values of K_t may be subject-specific, based on motor control and subject anthropometry. We did not examine the device on persons with dropfoot in the current study; the aim of the study was instead to propose the device and perform proof-of-concept tests prior to testing on a subject population with gait disability. By adding the weight over the foot to simulate dropfoot

gait, we were able to capture several gait characteristics similar to those observed spontaneously in persons with dropfoot, though of course the two scenarios are not identical. Testing exoskeletons on subjects with simulated impairments is a common practice before their application, often involving the addition of resistance, such as springs (Xia et al., 2020; Hong et al., 2021), to specific joints or segments. These limitations will be addressed in future study involving individuals with a tendency for dropfoot and excessive ankle inversion.

6 Conclusion

In this study, a 2-DoF powered soft ankle exoskeleton was developed to assist the ankle in movements that simulate dropfoot and excessive inversion. The device's features are its low weight and minimal movement restriction. In the pilot study population of non-disabled persons, the exoskeleton was able to accurately guide the ankle in active dorsiflexion and eversion, as well as in controlled plantarflexion and inversion. The force-free control was able to compensate for a significant portion of the inherent device resistance, though not all. The exoskeleton showed promise in normalizing dropfoot-related ankle and foot kinematics in swing and initial contact while not restricting plantarflexion in preswing. Altogether, these demonstrated its feasibility for use to control foot and ankle kinematics, and its potential to counteract dropfoot with or without excessive inversion. Future study will address its efficacy during gait in a population with these gait deviations.

Data availability statement

The original contributions presented in the study are included in the article/supplementary material, further inquiries can be directed to the corresponding author.

Ethics statement

The studies involving humans were approved by the Swedish Ethical Review Authority. The studies were conducted in accordance with the local legislation and institutional requirements. The participants provided their written informed consent to participate in this study. Written informed consent was obtained from the individual(s) for the publication of any potentially identifiable images or data included in this article.

Author contributions

XZ: Conceptualization, Data curation, Investigation, Methodology, Software, Validation, Writing – original draft, Formal analysis. Y-XL: Conceptualization, Data curation, Methodology, Writing – review & editing. RW: Conceptualization, Methodology, Writing – review & editing. EG-F: Conceptualization, Funding acquisition, Methodology, Supervision, Writing – review & editing, Data curation, Project administration.

Funding

The author(s) declare financial support was received for the research, authorship, and/or publication of this article. This study was generously funded by the Promobilia Foundation (ref 20300, 21300, 22000), the Swedish Research Council (ref 2018-00750), and Digital Futures (ref KTH-RPROJ-0146472). The work of XZ was also supported by the China Scholarship Council (CSC).

Acknowledgments

We would like to express our gratitude to Susanne Palmcrantz for her valuable suggestions during the development of the exoskeleton and Antea Destro for her help during data collection.

Conflict of interest

The authors declare that the research was conducted in the absence of any commercial or financial relationships that could be construed as a potential conflict of interest.

Publisher's note

References

Asbeck, A. T., Dyer, R. J., Larusson, A. F., and Walsh, C. J. (2013). "Biologically-inspired soft exosuit," in *2013 IEEE 13th International Conference on Rehabilitation Robotics (ICORR)* (Seattle, WA: IEEE), 1–8. doi: 10.1109/ICORR.2013.6650455

Awad, L. N., Bae, J., O'donnell, K., De Rossi, S. M., Hendron, K., Sloot, L. H., et al. (2017). A soft robotic exosuit improves walking in patients after stroke. *Sci. Transl. Med.* 9:eaai9084. doi: 10.1126/scitranslmed.aai9084

Bae, J., De Rossi, S. M. M., O'Donnell, K., Hendron, K. L., Awad, L. N., Dos Santos, T. D., et al. (2015). "A soft exosuit for patients with stroke: feasibility study with a mobile off-board actuation unit," in *2015 IEEE International Conference on Rehabilitation Robotics (ICORR)* (Singapore: IEEE), 131–138. doi: 10.1109/ICORR.2015.7281188

Bae, J., Siviy, C., Rouleau, M., Menard, N., O'Donnell, K., Geliana, I., et al. (2018). "A lightweight and efficient portable soft exosuit for paretic ankle assistance in walking after stroke," in *2018 IEEE International Conference on Robotics and Automation (ICRA)* (Brisbane, QLD: IEEE), 2820–2827. doi: 10.1109/ICRA.2018.8461046

Blaya, J. A., and Herr, H. (2004). Adaptive control of a variable-impedance ankle-foot orthosis to assist drop-foot gait. *IEEE Trans. Neural Syst. Rehabil. Eng.* 12, 24–31. doi: 10.1109/TNSRE.2003.823266

Browning, R. C., Modica, J. R., Kram, R., and Goswami, A. (2007). The effects of adding mass to the legs on the energetics and biomechanics of walking. *Medi. Sci. Sports Exerc*. 39, 515–525. doi: 10.1249/mss.0b013e31802b3562

Daryabor, A., Arazpour, M., and Aminian, G. (2018). Effect of different designs of ankle-foot orthoses on gait in patients with stroke: a systematic review. *Gait Posture* 62, 268–279. doi: 10.1016/j.gaitpost.2018.03.026

de Sèze, M.-P., Bonhomme, C., Daviet, J.-C., Burguete, E., Machat, H., Rousseaux, M., et al. (2011). Effect of early compensation of distal motor deficiency by the chignon ankle-foot orthosis on gait in hemiplegic patients: a randomized pilot study. *Clin. Rehabil*. 25, 989–998. doi: 10.1177/0269215511410730

Deltombe, T., Wautier, D., De Cloedt, P., Fostier, M., and Gustin, T. (2017). Assessment and treatment of spastic equinovarus foot after stroke: guidance from the mont-godinne interdisciplinary group. *J. Rehabil. Med*. 49, 461–468. doi: 10.2340/16501977-2226

DeMers, M. S., Hicks, J. L., and Delp, S. L. (2017). Preparatory co-activation of the ankle muscles may prevent ankle inversion injuries. *J. Biomech*. 52, 17–23. doi: 10.1016/j.jbiomech.2016.11.002

Dong, K., Liu, H., Zhu, X., Wang, X., Xu, F., Liang, B., et al. (2019). Force-free control for the flexible-joint robot in human-robot interaction. *Comput. Electr. Eng*. 73, 9–22. doi: 10.1016/j.compeleceng.2018.10.014

Gil-Castillo, J., Alnajjar, F., Koutsou, A., Torricelli, D., and Moreno, J. C. (2020). Advances in neuroprosthetic management of foot drop: a review. *J. Neuroeng. Rehabil*. 17, 1–19. doi: 10.1186/s12984-020-00668-4

Han, H., Wang, W., Zhang, F., Li, X., Chen, J., Han, J., et al. (2021). Selection of muscle-activity-based cost function in human-in-the-loop optimization of multi-gait ankle exoskeleton assistance. *IEEE Trans. Neural Syst. Rehabil. Eng*. 29, 944–952. doi: 10.1109/TNSRE.2021.3082198

Hermens, H. J., Freriks, B., Merletti, R., Stegeman, D., Blok, J., Rau, G., et al. (1999). European recommendations for surface electromyography. *Roessingh Res. Dev*. 8, 13–54.

Hong, J.-C., Cheng, H., Yasuda, K., Ohashi, H., and Iwata, H. (2021). Effects of assisted dorsiflexion timing on voluntary efforts and compensatory movements: a feasibility study in healthy participants. *IEEE Trans. Neural Syst. Rehabil. Eng*. 29, 2222–2231. doi: 10.1109/TNSRE.2021.3119873

Hu, Y., Li, Z., and Yen, G. G. (2023). A knee-guided evolutionary computation design for motor performance limitations of a class of robot with strong nonlinear dynamic coupling. *IEEE Trans. Syst. Man. Cybern. Syst*. 53, 4429–4441. doi: 10.1109/TSMC.2023.3249123

Hu, Y., Zhou, W., Liu, Y., Zeng, M., Ding, W., Li, S., et al. (2024). Efficient online planning and robust optimal control for nonholonomic mobile robot in unstructured environments. *IEEE Trans. Emerg. Top. Comput. Intellig*. doi: 10.1109/TETCI.2024.3424527. [Epub ahead of print].

Kim, S. J., Na, Y., Lee, D. Y., Chang, H., and Kim, J. (2020). Pneumatic afo powered by a miniature custom compressor for drop foot correction. *IEEE Trans. Neural Syst. Rehabil. Eng*. 28, 1781–1789. doi: 10.1109/TNSRE.2020.3003860

Kluding, P. M., Dunning, K., O'Dell, M. W., Wu, S. S., Ginosian, J., Feld, J., et al. (2013). Foot drop stimulation versus ankle foot orthosis after stroke: 30-week outcomes. *Stroke* 44, 1660–1669. doi: 10.1161/STROKEAHA.111.000334

Konrad, P. (2005). *The ABC of EMG. A Practical Introduction to Kinesiological Electromyography, version. 1*. Scottsdale, AZ: Noraxon INC, 30–35.

Lerner, Z. F., Gasparri, G. M., Bair, M. O., Lawson, J. L., Luque, J., Harvey, T. A., et al. (2018). An untethered ankle exoskeleton improves walking economy in a pilot study of individuals with cerebral palsy. *IEEE Trans. Neural Syst. Rehabil. Eng*. 26, 1985–1993. doi: 10.1109/TNSRE.2018.2870756

Li, S. (2020). Ankle and foot spasticity patterns in chronic stroke survivors with abnormal gait. *Toxins* 12:646. doi: 10.3390/toxins12100646

Liu, Y.-X., Zhang, L., Wang, R., Smith, C., and Gutierrez-Farewik, E. M. (2021). Weight distribution of a knee exoskeleton influences muscle activities during movements. *IEEE Access* 9, 91614–91624. doi: 10.1109/ACCESS.2021.3091649

Nori, S. L., and Das, J. M. (2019). *Steppage Gait*. Treasure Island, FL: StatPearls Publishing.

Park, Y.-L., Chen, B.-r., Pérez-Arancibia, N. O., Young, D., Stirling, L., Wood, R. J., et al. (2014). Design and control of a bio-inspired soft wearable robotic device for ankle-foot rehabilitation. *Bioinspir. Biomim*. 9:016007. doi: 10.1088/1748-3182/9/1/016007

Perry, J., and Burnfield, J. M. (2010). *Gait Analysis. Normal and Pathological Function*, 2nd Edn. San Francisco, CA: Slack.

Schmid, S., Schweizer, K., Romkes, J., Lorenzetti, S., and Brunner, R. (2013). Secondary gait deviations in patients with and without neurological involvement: a systematic review. *Gait Posture* 37, 480–493. doi: 10.1016/j.gaitpost.2012.09.006

Shorter, K. A., Kogler, G. F., Loth, E., Durfee, W. K., and Hsiao-Wecksler, E. T. (2011). A portable powered ankle-foot orthosis for rehabilitation. *J. Rehabil. Res. Dev*. 48, 459–472. doi: 10.1682/JRRD.2010.04.0054

Thalman, C. M., Hsu, J., Snyder, L., and Polygerinos, P. (2019). "Design of a soft ankle-foot orthosis exosuit for foot drop assistance," in *2019 International Conference on Robotics and Automation (ICRA)* (Montreal, QC: IEEE), 8436–8442. doi: 10.1109/ICRA.2019.8794005

Tyson, S. F., and Kent, R. M. (2013). Effects of an ankle-foot orthosis on balance and walking after stroke: a systematic review and pooled meta-analysis. *Arch. Phys. Med. Rehabil*. 94, 1377–1385. doi: 10.1016/j.apmr.2012.12.025

Vistamehr, A., Kautz, S. A., and Neptune, R. R. (2014). The influence of solid ankle-foot-orthoses on forward propulsion and dynamic balance in healthy adults during walking. *Clin. Biomech*. 29, 583–589. doi: 10.1016/j.clinbiomech.2014.02.007

Winstein, C. J., Stein, J., Arena, R., Bates, B., Cherney, L. R., Cramer, S. C., et al. (2016). Guidelines for adult stroke rehabilitation and recovery: a guideline for healthcare professionals from the American heart association/American stroke association. *Stroke* 47, e98-e169. doi: 10.1161/STR.0000000000000098

Wu, X., Li, Z., Kan, Z., and Gao, H. (2019). Reference trajectory reshaping optimization and control of robotic exoskeletons for human-robot co-manipulation. *IEEE Trans. Cybern*. 50, 3740–3751. doi: 10.1109/TCYB.2019.2933019

Xia, H., Kwon, J., Pathak, P., Ahn, J., Shull, P. B., Park, Y.-L., et al. (2020). "Design of a multi-functional soft ankle exoskeleton for foot-drop prevention, propulsion assistance, and inversion/eversion stabilization," in *2020 8th IEEE RAS/EMBS International Conference for Biomedical Robotics and Biomechatronics (BioRob)* (New York, NY: IEEE), 118–123. doi: 10.1109/BioRob49111.2020.9224420

Yeung, L.-F., Lau, C. C., Lai, C. W., Soo, Y. O., Chan, M.-L., Tong, R. K., et al. (2021). Effects of wearable ankle robotics for stair and over-ground training on sub-acute stroke: a randomized controlled trial. *J. Neuroeng. Rehabil*. 18, 1–10. doi: 10.1186/s12984-021-00814-6

Yeung, L.-F., Ockenfeld, C., Pang, M.-K., Wai, H.-W., Soo, O.-Y., Li, S.-W., et al. (2017). Design of an exoskeleton ankle robot for robot-assisted gait training of stroke patients. *Int. Conf. Rehabil. Robot. 2017*, 211–215. doi: 10.1109/ICORR.2017.8009248

Yeung, L.-F., Ockenfeld, C., Pang, M.-K., Wai, H.-W., Soo, O.-Y., Li, S.-W., et al. (2018). Randomized controlled trial of robot-assisted gait training with dorsiflexion assistance on chronic stroke patients wearing ankle-foot-orthosis. *J. Neuroeng. Rehabil*. 15, 1–12. doi: 10.1186/s12984-018-0394-7

Zhang, L., Zhang, X., Zhu, X., Wang, R., and Gutierrez-Farewik, E. M. (2023). Neuromusculoskeletal model-informed machine learning-based control of a knee exoskeleton with uncertainties quantification. *Front. Neurosci*. 17:1254088. doi: 10.3389/fnins.2023.1254088

Zhang, Q., Tu, X., Si, J., Lewek, M. D., and Huang, H. (2023). "A robotic assistance personalization control approach of hip exoskeletons for gait symmetry improvement," in *IEEE/RSJ International Conference on Intelligent Robots and Systems (IROS)* (Detroit, MI: IEEE), 6125–6132. doi: 10.1109/IROS55552.2023.10341440

Zhong, B., Shen, M., Liu, H., Zhao, Y., Qian, Q., Wang, W., et al. (2023). A cable-driven exoskeleton with personalized assistance improves the gait metrics of people in subacute stroke. *IEEE Trans. Neural Syst. Rehabil. Eng*. 31, 2560–2569. doi: 10.1109/TNSRE.2023.3281409

frontiers | Frontiers in Neurology

TYPE Original Research
PUBLISHED 20 September 2024
DOI 10.3389/fneur.2024.1466252

OPEN ACCESS

EDITED BY
Mingming Zhang,
Southern University of Science and Technology, China

REVIEWED BY
Łukasz Rzepiński,
10th Military Research Hospital and Polyclinic, Poland
Anjing Zhang,
Shanghai First Rehabilitation Hospital, China
Xu-Yun Hua,
Shanghai University of Traditional Chinese Medicine, China

*CORRESPONDENCE
Hongxing Wang
✉ 101012648@seu.edu.cn

RECEIVED 17 July 2024
ACCEPTED 10 September 2024
PUBLISHED 20 September 2024

CITATION
Li X, Shao Z, Li Z, Wei X, Zong L, Wang P, Zhou T and Wang H (2024) The relationship between the functional status of upper extremity motor neurons and motor function and prognosis in stroke patients.
Front. Neurol. 15:1466252.
doi: 10.3389/fneur.2024.1466252

The relationship between the functional status of upper extremity motor neurons and motor function and prognosis in stroke patients

Xiaoyi Li[1], Zhen Shao[2], Zhi Li[1], Xiupan Wei[1], Lijuan Zong[1], Pei Wang[1], Ting Zhou[1] and Hongxing Wang[1]*

[1]Department of Rehabilitation Medicine, Zhongda Hospital Southeast University, School of Medicine, Southeast University, Nanjing, China, [2]Department of Rehabilitation Medicine, Affiliated Hospital of Xuzhou Medical University, Xuzhou, China

Introduction: This study investigates the correlation between neuroelectrophysiological assessments such as motor unit number estimation (MUNE) and F-waves with upper extremity motor function and one-year prognosis in stroke patients.

Methods: Neuroelectrophysiological assessments of the abductor pollicis brevis muscle, including MUNE and F-waves, were conducted. Upper extremity motor function was evaluated using the Fugl-Meyer Assessment of Upper Extremity (FMA-UE) and the Modified Ashworth Scale (MAS). Pearson correlation and multiple linear regression analyses were performed to explore the relationship between upper extremity motor function and variables such as MUNE and F-waves. ROC curve analysis assessed the predictive ability of MUNE and F-waves for upper extremity motor function, and binary logistic regression analysis examined factors related to motor function improvement 1 year post-discharge.

Results: A total of 130 patients were ultimately included. Significant differences in MUNE and occupancy rate of non-repeater F-waves (non-ORF) were found between hemiplegic and unaffected sides ($p < 0.001$), with a significant difference in F-wave mean latency ($p < 0.05$). Pearson correlation analysis showed a positive correlation between FMA-UE at admission and hemiplegic side's MUNE and non-ORF ($p < 0.001$). Multiple linear regression indicated that hemiplegic side's MUNE ($\beta = 0.88$, $p < 0.001$) and non-ORF ($\beta = 0.275$, $p = 0.005$) influenced FMA-UE. ROC analysis demonstrated higher predictive ability for hemiplegic side's MUNE (AUC = 0.696, $p < 0.001$) than non-ORF (AUC = 0.622, $p = 0.018$). Binary logistic regression showed that hemiplegic side's MUNE was associated with FMA-UE improvement 1 year post-discharge.

Conclusion: MUNE and F-waves are correlated with upper extremity motor function in patients, reflecting their motor function status. These indicators have good predictive value for motor function and are associated with the prognosis of upper extremity motor function to a certain extent.

KEYWORDS

stroke, motor neurons, repeater F-waves, MUNE, upper extremity motor function

1 Introduction

Stroke is one of the leading causes of disability and death worldwide. Research indicates that approximately 80% of acute stroke patients experience upper extremity motor dysfunction, and 50–60% of these patients continue to suffer from this dysfunction 6 months post-stroke (1). This significantly impacts patients' quality of life and daily living abilities, placing a heavy burden on patients, their families, and society (2). Evidence-based medicine has proven that rehabilitation plays a crucial role in optimizing functional recovery, with rehabilitation assessment being the foundation of treatment. Therefore, accurately and systematically quantifying upper extremity motor dysfunction in patients is a complex yet critical issue in rehabilitation (3).

Stroke primarily affects the upper motor neuron regions. However, studies have shown that post-stroke, patients often exhibit secondary lower motor neuron dysfunction (4, 5). This dysfunction is related to damage to the upper motor neurons (corticospinal tract) and the loss of trophic support to the target organs (skeletal muscles), with the extent of lower motor neuron damage potentially corresponding to the severity of corticospinal tract damage and muscle paralysis (6). Although changes in lower motor neuron function are crucial for post-stroke skeletal muscle and motor control capabilities, current stroke treatment and rehabilitation guidelines pay limited attention to lower motor neuron dysfunction, and clinical assessments rarely evaluate related indicators. Thus, accurately assessing lower motor neurons is vital for understanding the recovery of motor dysfunction post-stroke.

The commonly used physical examinations and functional scales in clinical practice focus on muscle function assessment but cannot accurately reflect lower motor neuron dysfunction. They are also subjective and prone to biases influenced by personal experience (7, 8). In contrast, neuroelectrophysiological assessment is an extension of the nervous system examination, capable of evaluating the integrity of lower motor neurons (9). As a non-invasive and repeatable method, it aids in developing rehabilitation treatment plans and provides quantitative reference data for functional evaluation (10). Among them, the abductor pollicis brevis, innervated by the median nerve, is frequently selected for nerve electrophysiological examination due to its high responsiveness to electrical stimulation and excellent reproducibility of results. Moreover, this muscle often exhibits pathological spontaneous activity during needle electromyography (EMG), a phenomenon commonly observed in the distal muscles of the hemiplegic upper limb and hand (11, 12).

In recent years, neuroelectrophysiological assessment such as motor unit number estimation (MUNE) and F-waves have been increasingly used for quantitative measurement of motor units and motor neuron functional status (13, 14). However, there are currently few studies on the relationship between motor neuron functional status and patients' motor function and prognosis post-stroke. Therefore, this study aims to investigate the correlation between neuroelectrophysiological assessment (MUNE and F-waves) of the median nerve in the upper extremity of stroke patients and their motor function and one-year prognosis after discharge, exploring the predictive value of these indicators for patients' upper extremity motor function and prognosis.

2 Methods

2.1 Subjects

From November 2020 to May 2023, 190 stroke patients admitted to the Rehabilitation Medicine Department of Zhongda Hospital Southeast University, were consecutively selected for this study. The inclusion criteria were as follows: (1) first-time diagnosis of cerebral infarction or cerebral hemorrhage, confirmed by cranial CT or MRI, with lesions confined to one cerebral hemisphere according to WHO standards; (2) unilateral limb motor dysfunction of varying degrees; (3) age between 16 and 80 years, with stable vital signs, clear consciousness, and no severe cognitive impairment; (4) disease duration of 0 to 6 months; (5) good cardiopulmonary function, with no swelling or skin damage in the upper extremities; and (6) voluntary participation with signed informed consent. The exclusion criteria included: (1) unstable condition or non-cooperation; (2) previous damage to the central nervous system other than stroke; (3) previous peripheral neuropathy, radiculopathy, neuromuscular junction disorders, or motor neuron diseases, and other diseases those may affect peripheral nerves or peripheral neuropathy as assessed by history, neurologic examination, and electrodiagnosis; (4) other conditions causing increased muscle tone or previous use of medications affecting muscle tone; (5) previous upper extremity motor dysfunction due to trauma or osteoarthropathy; and (6) participation in other clinical trials. Patients who were found to not meet the inclusion criteria after enrollment or had incomplete case data that precluded efficacy evaluation were excluded. Patients who could not continue participation or voluntarily withdrew during the evaluation process were considered dropouts. This study was approved by the Clinical Research Ethics Committee of Zhongda Hospital Southeast University (approval number: 2022ZDSYLL397-P01).

Study Procedures All eligible inpatients or their immediate family members were interviewed to obtain consent. General information, including age, gender, type of stroke, hemiplegic UE, right handed or left handed and disease duration, were collected and recorded. In this study, following rehabilitation assessment, individualized routine rehabilitation training programs were developed for patients based on their existing functional impairments. These programs included physical therapy, occupational therapy, acupuncture,and other treatments. The aforementioned treatments were administered one time daily, 6 days per week, for 3 weeks totally. After discharge, professional healthcare personnel followed up with patients through outpatient visits, telephone calls, or community visits 1 year post-discharge. The primary outcome measure was the Fugl-Meyer Assessment of Upper Extremity (FMA-UE) score 1 year after discharge.

2.2 Motor function assessment

2.2.1 FMA-UE

The FMA-UE consists of 33 items, each scored up to 2 points. Except for the "presence of upper extremity reflex activity," which is scored as 0 or 2 points, the remaining 31 items are scored as 0, 1, or 2 points, with a total possible score of 66. Higher scores indicate better upper extremity motor function. The difference between the first assessment (at hospital admission) and the final follow-up assessment (1 year after discharge) in the FMA-UE score was used to determine

improvement in upper extremity motor function. In this study, the minimal clinically important difference (MCID) for the FMA-UE (defined as an FMA-UE change score = 6) was used as the threshold (15). Patients with an FMA-UE change score of 6 or more were classified as having improved function, while those with a score of less than 6 were classified as having unimproved function. The MCID was chosen as the binary classification threshold because it represents a meaningful clinical improvement for patients (16).

2.2.2 MAS

The MAS was used to assess muscle tone in the hemiplegic side's wrist flexors. Only changes in muscle tone during passive wrist extension in the hemiplegic upper extremity were evaluated. Patients were seated with their bodies upright, elbows flexed at 90°, and forearms in pronation. Muscle tone was graded as 0, 1, 1+, 2, 3 and 4, with higher scores indicating greater muscle tone.

2.3 Neuroelectrophysiological assessment

Neuroelectrophysiological assessment was conducted using a Haishen NDI-094 electromyography evoked potential instrument in a quiet room at a temperature of 22–25°C. The patient's skin temperature was maintained above 32°C, and the local skin of the recording and stimulation sites was cleaned. The patient was placed in a supine or sitting position, with the muscles to be tested kept relaxed.

2.3.1 MUNE examinations

Routine sensory and motor conduction studies were performed before MUNE testing to rule out neural variations. The MUNE program in the electromyography instrument was used, with the stimulating electrode placed between the flexor carpi radialis and palmaris longus tendons at the wrist. The recording electrode was placed on the belly of the abductor pollicis brevis muscle, and the reference electrode was positioned at the distal tendon of the abductor pollicis brevis. The ground electrode was placed between the recording and stimulating electrodes. After identifying the optimal stimulation and recording points, stimulation was performed using a handle electrode, and recordings were made using surface electrodes. The incremental method was employed, providing increasing intensity nerve stimulation from sub-threshold levels to obtain compound muscle action potentials (CMAP) in the abductor pollicis brevis. The mean amplitude of single motor-unit action potentials (S-MUAPs) was derived from the incrementally increased amplitudes. The MUNE was calculated as the ratio of the maximum CMAP amplitude to the mean S-MUAPs amplitude, with the computer program automatically computing the MUNE.

2.3.2 F-wave examinations

The positions of the stimulating and recording electrodes were the same as in the MUNE examination. Supramaximal electrical stimulation was administered 20 times consecutively to record F-waves. The study used the mean latency and mean amplitude of F-waves. Repeater F-waves (17) were defined as F-waves with identical waveform, latency difference not exceeding 0.5 ms, and amplitude difference not exceeding 0.1 mV. Repeater F-waves were identified through visual inspection, requiring the superimposition of 20 traces to identify consistent shapes, with the entire waveform from start to return to baseline needing to be identical. Any interruptions or extra phases disqualified the waveform from being a repeater F-wave. A-waves, characterized by 4–8 unchanged waveforms with almost constant latency (within 1.5–4.0 ms), were excluded from this study. The occupancy rate of repeater F-waves (ORF) was calculated as the number of repeater F-waves divided by the total number of F-waves, expressed as a percentage. The occupancy rate of non-repeater F-waves (non-ORF) was derived by subtracting the ORF from 100%.

2.4 Statistical methods

Data were processed using SPSS 25.0 software. Measurement data conforming to a normal distribution were expressed as mean ± standard deviation ($x \pm s$), and intergroup differences were analyzed using *t*-tests or one-way ANOVA. Measurement data not conforming to a normal distribution were expressed as median (lower quartile, upper quartile), with differences analyzed using the rank-sum test. Multiple comparisons were corrected using the Bonferroni method. Count data were presented as frequency and percentage, with intergroup comparisons made using the χ^2 test. Pearson correlation analysis was used to explore correlations between indicators, and multiple linear regression and binary logistic regression were employed for multifactor regression analysis. ROC curve analysis was conducted to assess the predictive ability of various indicators for the improvement of FMA-UE 1 year after discharge. The significance level (α) was set at 0.05.

3 Results

3.1 Baseline characteristics

According to the inclusion and exclusion criteria, 16 patients were excluded due to a disease course exceeding 6 months. During the follow-up process, 41 patients were lost to follow-up, and 3 patients died. Ultimately, 130 stroke patients were included in the study (Table 1). All participants included in the study were confirmed right-hand dominant. The average age of the patients was 60.62 ± 13.48 years. Among them, 95 were male (73%) and 35 were female (27%); 109 had cerebral infarction (84%) and 21 had cerebral hemorrhage (16%). The disease duration was less than 1 month in 77 patients (59%), 1–3 months in 36 patients (28%), and 3–6 months in 17 patients (13%). There were 63 patients (48%) with left-sided hemiplegia and 67 patients (52%) with right-sided hemiplegia. Muscle tone was decreased in 21 patients (16%), normal in 59 patients (45%), and increased in 50 patients (39%).

3.2 Comparison of upper extremity neuroelectrophysiological assessment

We first analyzed the changes in neuroelectrophysiological assessment between the hemiplegic and unaffected sides (Table 2 and Figure 1). The results showed significant statistical differences in MUNE and non-ORF between the hemiplegic and unaffected sides ($p < 0.001$). The difference in the mean latency of F-waves was also statistically significant ($p < 0.05$). However, there was no statistically

TABLE 1 Baseline characteristics of the patients ($n = 130$).

Variable	Values
Age (years)	
Mean ± SD	60.62 ± 13.48
Gender, *n*	
Male/Female	95/35
Stroke, *n*	
Ischemic/Hemorrhagic	109/21
Disease duration (month), *n*	
Average (range)	0.85 (0.43, 1.63)
<1	77
1–3	36
3–6	17
Hemiplegic UE, *n*	
Left/right	63/67
MAS, *n*	
Decreased	21
0	59
1	25
1+	16
2	8
3	1

TABLE 2 Comparison of the results of the UE neuroelectrophysiological assessment.

	Hemiplegic side	Unaffected side	Statistic	*p* value
MUNE	49.12 ± 13.71	56.34 ± 11.49	$t = 4.607$	<0.001
Non-ORF (%)	47.92 ± 14.56	72.21 ± 13.21	$t = 14.086$	<0.001
F-wave mean latency (ms)	27.18 ± 2.10	26.57 ± 2.01	$t = -3.337$	0.016
F-wave mean amplitude (mV)	0.23 (0.14, 0.37)	0.24 (0.16, 0.35)	$z = -0.224$	0.822

significant difference in the mean amplitude of F-waves between the hemiplegic and unaffected sides ($p > 0.05$).

3.3 Correlation between admission FMA-UE and neuroelectrophysiological assessment

Pearson correlation analysis showed that the FMA-UE at admission was significantly correlated with the hemiplegic side's MUNE ($r = 0.640$, $p < 0.001$) and the hemiplegic side's non-ORF ($r = 0.347$, $p < 0.001$) (Table 3 and Figure 2). There was no significant correlation between FMA-UE and the unaffected side's MUNE ($r = 0.097$, $p = 0.270$), the hemiplegic side's mean latency of F-waves ($r = 0.156$, $p = 0.076$), the unaffected side's mean latency of F-waves ($r = 0.211$, $p = 0.060$), or the unaffected side's non-ORF ($r = 0.064$, $p = 0.473$).

3.4 Multiple linear regression analysis

Based on the correlation analysis results, multiple linear regression analysis was conducted with age, gender, disease duration, type of stroke, side of hemiplegia, MAS, hemiplegic side MUNE, and hemiplegic side non-ORF as independent variables, and FMA-UE at admission as the dependent variable. The results indicated that the hemiplegic side's MUNE ($\beta = 0.88$, $p < 0.001$) and the hemiplegic side's non-ORF ($\beta = 0.275$, $p = 0.005$) were influencing factors for FMA-UE (Table 4). This suggests that, after adjusting for confounding factors, the hemiplegic side's MUNE and non-ORF significantly impact the FMA-UE at admission.

3.5 FMA-UE at one-year follow-up

Follow-up results showed that among the 130 patients, 76 exhibited significant improvement (ΔFMA-UE ≥ 6 points). ROC curve analysis was used to assess the predictive ability of the hemiplegic side's MUNE and non-ORF for FMA-UE improvement 1 year after discharge. The results (Figure 3) indicated that both the hemiplegic side's MUNE and non-ORF could predict the improvement in FMA-UE 1 year post-discharge. Additionally, the predictive ability of the hemiplegic side's MUNE for FMA-UE improvement (AUC = 0.696, $p < 0.001$) was higher than that of the hemiplegic side's non-ORF (AUC = 0.622, $p = 0.018$).

3.6 Binary logistic regression analysis

Binary logistic regression analysis was conducted on the variables to determine the improvement in FMA-UE 1 year after discharge. After adjusting for confounding factors such as age, the analysis showed that the hemiplegic side's MUNE was a significant risk factor for FMA-UE improvement 1 year post-discharge ($p < 0.05$) (Table 5).

4 Discussion

Stroke is characterized by high incidence, high mortality, and high disability rates, making it a serious global healthcare issue (18). In recent years, with the advancements in neurophysiology and imaging, researchers have been focusing on how to use precise, quantitative, non-invasive methods to assess and predict the recovery of motor dysfunction after stroke (19). Neuroelectrophysiological techniques, as an extension of nervous system examinations, offer high sensitivity and detect changes before clinical signs appear. These techniques provide relatively objective indicators for estimating prognosis, evaluating treatment efficacy, and selecting treatment plans for stroke (20). This study explored the neuroelectrophysiological data of stroke patients, analyzing the functional status of motor neurons post-stroke and its association with upper extremity motor function. This helps in understanding the extent of upper extremity motor function at an early stage and implementing effective rehabilitation interventions promptly.

Currently, clinical assessment of motor neuron function relies heavily on functional scales, lacking quantitative, reproducible evaluation evidence that accurately reflects the functional status of motor neurons. The MUNE indicator used in this study quantitatively evaluates the total number of functional motor units in a muscle or muscle group innervated by a nerve from a macro perspective. MUNE

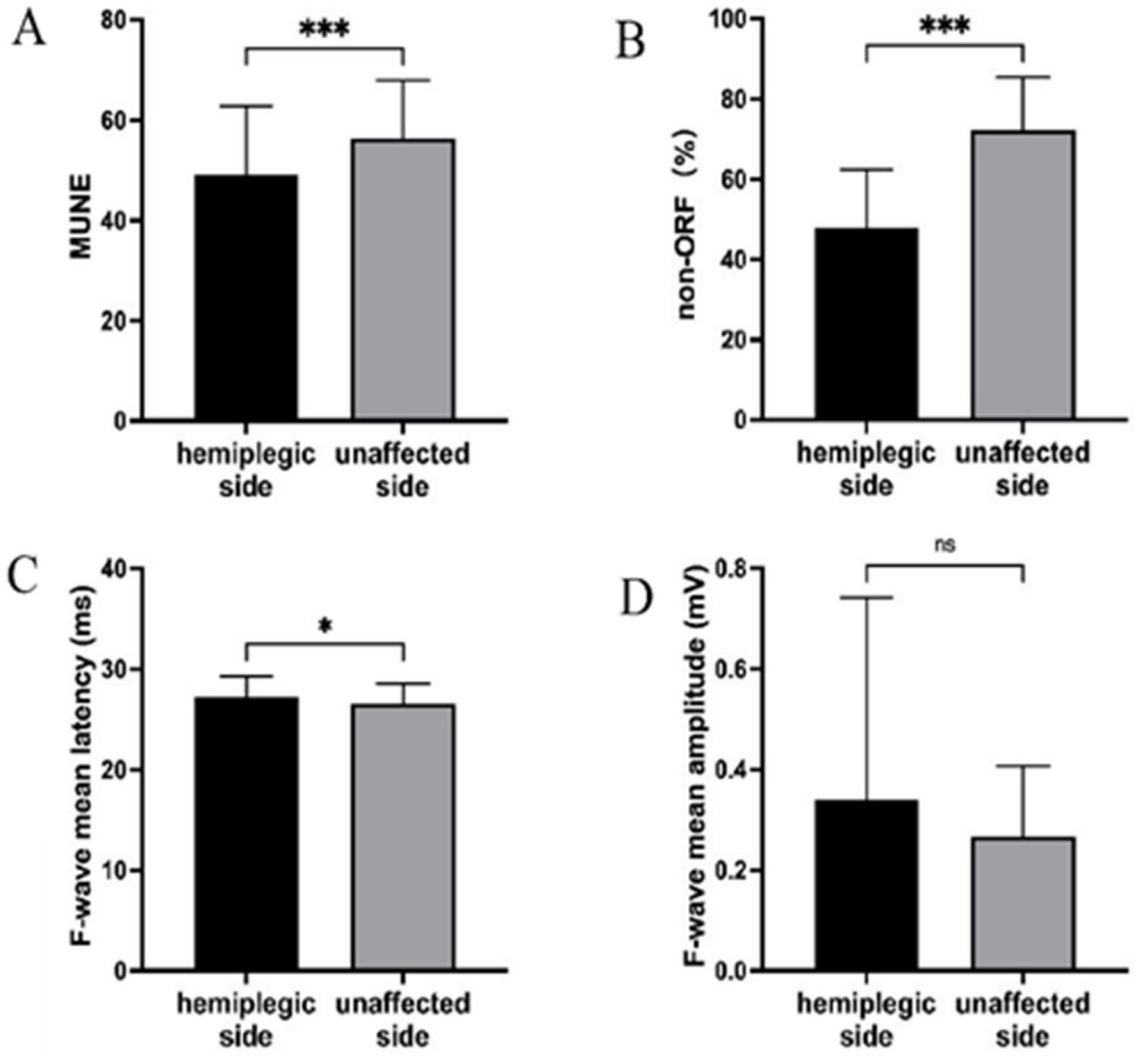

FIGURE 1
The results of the UE neuroelectrophysiological assessment. **(A)** MUNE; **(B)** non-ORF; **(C)** F-wave mean latency; **(D)** F-wave mean amplitude. *** Indicates the hemiplegic side is significant lower ($p < 0.001$) than the unaffected side. * Indicates the hemiplegic side is higher ($p < 0.05$) than the unaffected side. ns, Indicates the hemiplegic side is not significant the unaffected side.

TABLE 3 Pearson correlation analysis between FMA-UE and UE neuroelectrophysiological assessment.

	MUNE		F-wave mean latency (ms)		Non-ORF (%)	
	Hemiplegic side	Unaffected side	Hemiplegic side	Unaffected side	Hemiplegic side	Unaffected side
r	0.640	0.097	0.156	0.211	0.347	0.064
P	<0.001	0.270	0.076	0.060	<0.001	0.473

values represent the number of functional motor units, which is crucial for predicting the prognosis of motor function recovery in patients (21, 22). The abductor pollicis brevis muscle is often chosen for MUNE due to its responsiveness to electrical stimulation and good reproducibility. Our findings align with those of Hara et al. (12), who found a reduction in the number of motor units in the hemiplegic abductor pollicis brevis muscle post-stroke, confirming the difference in motor unit numbers between the hemiplegic and unaffected sides. This reduction in motor units post-stroke may result from transsynaptic degeneration of lower motor neurons caused by upper motor neuron damage. Another study by Hara et al. (23) indicated that the reduction in motor units on the hemiplegic side might occur in the second week after upper motor neuron lesions and is closely related to the severity of motor dysfunction. Patients with severe hemiplegia experience a greater reduction, which persists up to 1 year post-stroke. This reduction in functional motor units may affect the patient's ability to generate muscle force and control fine movements, thereby impacting the motor function of the upper limb. Future research should focus on finding methods to prevent the reduction of functional motor units due to transsynaptic degeneration of lower motor neurons in the acute phase of stroke, which could enhance functional recovery and improve daily living abilities.

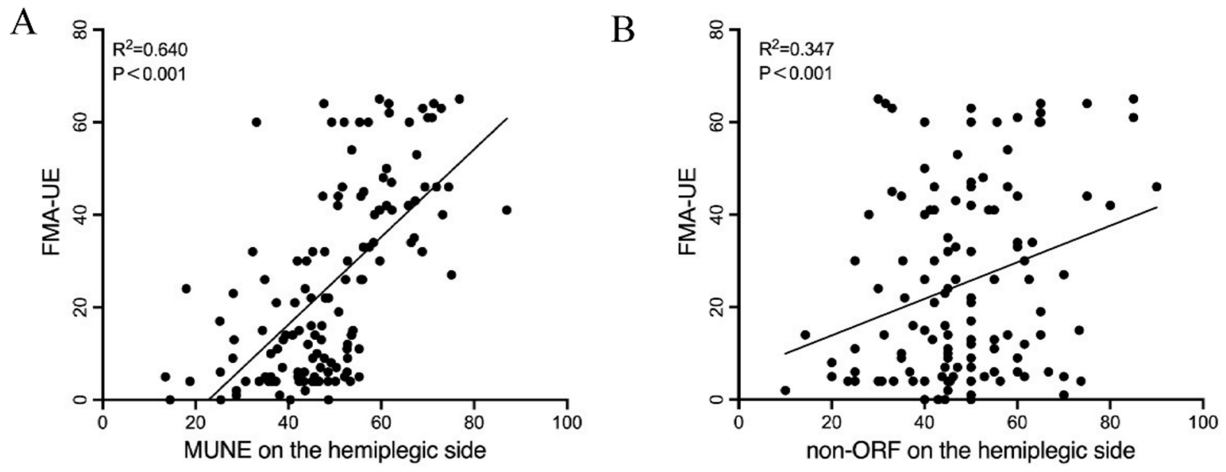

FIGURE 2
Pearson correlation analysis between FMA-UE and UE neuroelectrophysiological assessment in patients. **(A)** MUNE on the hemiplegic side; **(B)** non-ORF on the hemiplegic side.

TABLE 4 **Multiple linear regression analysis of influencing factors of FMA-UE in patients at admission.**

Variant	Standard error	B (95%CI)	*t* value	*P* value
Constant	9.771		−3.222	0.002
Age	0.108	−0.074 (−0.287, 0.139)	−0.689	0.492
Gender	3.161	0.982 (−5.277, 7.241)	0.311	0.757
Disease duration	1.266	2.164 (−0.343, 4.672)	1.709	0.09
Stroke type	3.701	2.405 (−4.923, 9.733)	0.65	0.517
Hemiplegic UE	2.793	0.312 (−5.217, 5.841)	0.112	0.911
MAS	1.413	−2.383 (−5.181, 0.414)	−1.687	0.094
MUNE on the hemiplegic side	0.103	0.88 (−0.676, 1.085)	8.518	<0.001
non-ORF on the hemiplegic side	0.097	0.275 (−0.084, 0.467)	2.844	0.005

SE, Standard error; β, Standardized coefficient; CI, Confidence interval.

Lower motor neurons mainly include anterior horn motor neurons of the spinal cord and their subsequent nerve roots and peripheral nerves (24). After losing higher central control, anterior horn motor neurons can transition from early inhibition to excitation, clinically presenting as a progression from flaccid paralysis with decreased muscle tone to increased muscle tone, spasticity, and eventual recovery of voluntary motor control (25). Studies have shown that the functional status of anterior horn motor neurons post-stroke reflects the physiological basis of muscle function in the hemiplegic limbs. Terao et al. (26) demonstrated that the loss of trophic support from upper motor neurons in stroke patients can alter the functional status of cells in the hemiplegic anterior horn of the spinal cord without losing the cells themselves. Qiu et al. (6) found no significant difference in the number of anterior horn cells between the hemiplegic and unaffected sides in stroke patients compared to normal subjects, but the cross-sectional area of the hemiplegic anterior horn cells was significantly reduced. Therefore, anterior horn motor neurons might be in a state of functional inhibition. Reactivating these inhibited anterior horn motor neurons could potentially aid in the functional improvement of stroke patients (27).

Studies have shown that F-waves can reflect the excitability of anterior horn motor neurons and assess the integrity of motor neurons and motor pathways (28). Measuring the mean latency of F-waves provides a sensitive and reliable method for examining the conduction properties of the proximal segment of motor axons. In this study, the mean latency of F-waves on the hemiplegic side was significantly different from that on the unaffected side, with the latency being prolonged on the hemiplegic side. This indicates that the conduction of functionally active motor neurons may be impaired after a stroke, consistent with previous findings (29, 30). Post-stroke, synaptic degeneration of upper motor neurons and increased excitability of anterior horn motor cells result in prolonged mean latency of F-waves, demonstrating the high sensitivity of F-waves to spinal excitability changes. This makes F-waves a probe for excitability changes in anterior horn cells, serving as an objective indicator of anterior horn motor cell excitability (31, 32).

Additionally, our research team conducted a statistical analysis of repeater F-waves in stroke patients. Repeater F-waves are generated by repetitive impulses from a single motor neuron. Their presence has been confirmed in conditions like carpal tunnel syndrome (33), motor neuron diseases, cervical spondylosis (34), lumbosacral radiculopathy

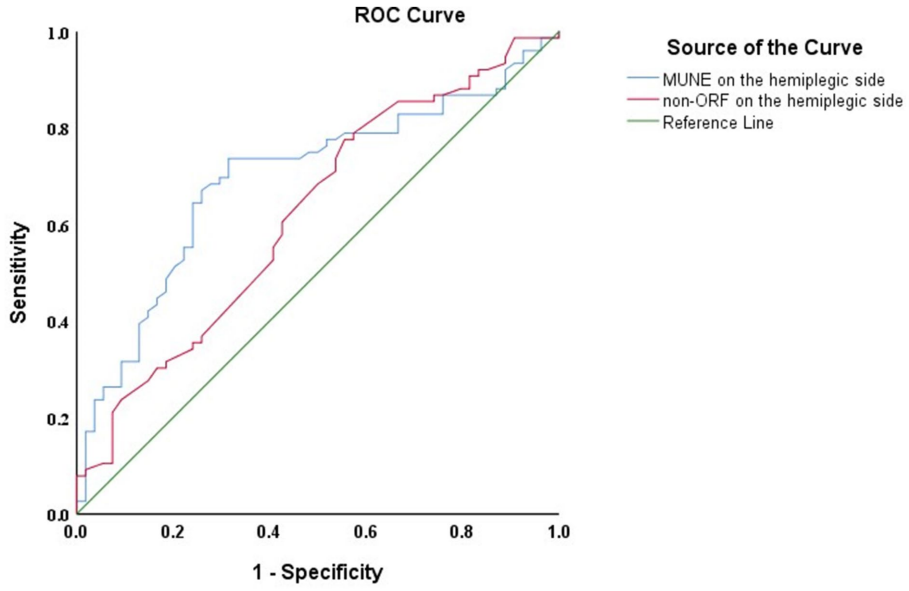

FIGURE 3
ROC curves of the hemiplegic side MUNE and non-ORF for predicting FMA—UE 1 year after discharge in patients.

TABLE 5 Binary logistic regression analysis of FMA-UE improvement in patients one year after discharge.

Variant	Define	*b*	SE	OR (95%CI)	*p* value
Constant	–	−2.994	1.466	0.05	0.041
Age	<62 = 0, ≥62 = 1	−0.003	0.016	0.997 (0.967, 1.027)	0.822
Gender	Female = 0, Male = 1	0.527	0.445	1.695 (0.708, 4.055)	0.236
Disease duration	<0.87 = 0, ≥0.87 = 1	−0.059	0.185	0.943 (0.656, 1.355)	0.75
Stroke	Hemorrhagic = 0, Ischemic = 1	−0.024	0.538	0.977 (0.34, 2.805)	0.965
Hemiplegic UE	Left side = 0, right side = 1	0.515	0.406	1.674 (0.755, 3.71)	0.204
MAS	<1 = 0, ≥1 = 1	−0.278	0.204	0.757 (0.508, 1.128)	0.172
MUNE on the hemiplegic side	<48.6 = 0, ≥48.6 = 1	0.043	0.016	1.044 (1.012, 1.076)	0.006
Non-ORF on the hemiplegic side	<47.1 = 0, ≥47.1 = 1	0.023	0.014	1.023 (0.995, 1.053)	0.114

(35), and poliomyelitis (36). Repeater F-waves can enhance the sensitivity of diagnosing certain neuromuscular disorders. Despite their recognized importance, quantitative evaluation of repeater F-waves in stroke patients is uncommon. This study found a decrease in non-ORF on the hemiplegic side, indicating an increase in the proportion of repeater F-waves. This suggests that fewer motor neurons generate F-waves, possibly due to the central release of functionally active neurons exhibiting enhanced repetitive impulse generation (37, 38). As the number of motor neurons decreases, the proportion of F-waves with different shapes diminishes, while repeater F-waves from single motor neurons increase. Our findings indicate a reduction in the number of functional motor neurons on the hemiplegic side post-stroke, with the remaining neurons showing abnormally increased excitability, further validating the MUNE results. This increased excitability may represent a compensatory mechanism for the reduced descending motor input, suggesting that we can enhance motor function plasticity by modulating motor neuron excitability. Through changes in neurophysiological indicators such as MUNE and F-waves, we can observe alterations in both structural (loss of motor units) and functional (changes in spinal excitability) adaptations following stroke.

The correlation analysis between neuroelectrophysiological assessment and motor function showed a significant association between FMA-UE and the hemiplegic side's MUNE and non-ORF. This indicates that a higher abundance of motor neurons generating impulses correlates with better motor function on the hemiplegic side. Multiple linear regression analysis revealed that, after adjusting for confounding factors, the hemiplegic side's MUNE and non-ORF were significant influencing factors for FMA-UE at admission. ROC curve analysis suggested that the hemiplegic side's MUNE and non-ORF have good predictive value for upper extremity motor function, with MUNE having a superior predictive ability compared to non-ORF.

One year post-discharge, follow-up analysis showed that the hemiplegic side's MUNE remained a significant factor for the improvement in upper extremity motor function after excluding confounding factors like age. This indicates that MUNE is a good predictor of upper extremity motor function and is associated with motor function prognosis to some extent. Based on the results of this

study, future research directions could explore neuroprotective strategies to mitigate transsynaptic degeneration of lower motor neurons in patients during the acute phase. Research could also focus on neuromodulation techniques to reactivate functionally inhibited anterior horn motor neurons in the spinal cord. Additionally, utilizing a multimodal assessment system that integrates neurophysiological evaluations and neuroimaging techniques could provide a more comprehensive understanding of structural and functional changes in both central and peripheral motor systems following stroke. This approach may lead to the development of more targeted and effective therapeutic interventions. However, this study has several limitations. First, it lacks electrophysiological and ultrasound evaluations of other peripheral nerves in the lower and upper extremities, which could provide additional information about the entire peripheral nervous system. Simultaneously, we did not consider the impact of disease severity, such as lesion size, location, and whether the patient had undergone cranial surgery, or other potential confounding factors on neurophysiological assessments. Additionally, comorbidities such as hypertension and coronary heart disease may also influence neurophysiological assessments and the recovery of upper limb motor function. Second, we did not perform needle electromyography, which could show denervation activity or evaluate motor unit potentials. Finally, more stroke patients and longer follow-up periods are needed to further investigate the relationship between neuroelectrophysiological assessment and upper extremity motor function.

In summary, neuroelectrophysiological assessment such as MUNE and F-waves of the median nerve are associated with FMA-UE, reflecting upper extremity motor function in stroke patients. These indicators have good predictive value for upper extremity motor function and are associated with motor function prognosis to some extent. The results suggest that MUNE and F-waves have potential predictive value for early assessment of motor function in stroke patients and support further related neuroelectrophysiological research.

Data availability statement

The raw data supporting the conclusions of this article will be made available by the authors, without undue reservation.

Ethics statement

The studies involving humans were approved by the Clinical Research Ethics Committee of Zhongda Hospital Southeast University. The studies were conducted in accordance with the local legislation and institutional requirements. The participants provided their written informed consent to participate in this study.

Author contributions

XL: Conceptualization, Data curation, Formal analysis, Methodology, Writing – original draft, Writing – review & editing. ZS: Data curation, Formal analysis, Writing – original draft. ZL: Methodology, Software, Writing – original draft. XW: Investigation, Validation, Writing – original draft. LZ: Data curation, Resources, Writing – original draft. PW: Investigation, Visualization, Writing – original draft. TZ: Writing – review & editing. HW: Funding acquisition, Methodology, Project administration, Supervision, Writing – original draft, Writing – review & editing.

Funding

The author(s) declare financial support was received for the research, authorship, and/or publication of this article. This research was supported by the National Key Research and Development Program of China, (2022YFC2009700); Key Project of Jiangsu Province's Key Research and Development Program (BE2023023-4); Key Project of Jiangsu Province's Key Research and Development Program (BE2023034); Jiangsu Province Capability Improvement Project through Science, Technology and Education, Jiangsu Provincial Medical Key Discipline Cultivation Unit, (JSDW202202); Jiangsu Province Capability Improvement Project through Science, Technology and Education (ZDXYS202210).

Conflict of interest

The authors declare that the research was conducted in the absence of any commercial or financial relationships that could be construed as a potential conflict of interest.

Publisher's note

References

1. Dawson J, Liu CY, Francisco GE, Cramer SC, Wolf SL, Dixit A, et al. Vagus nerve stimulation paired with rehabilitation for upper limb motor function after Ischaemic stroke (Vns-rehab): a randomised, blinded, pivotal, device trial. *Lancet*. (2021) 397:1545–53. doi: 10.1016/s0140-6736(21)00475-x

2. Chen J, Or CK, Chen T. Effectiveness of using virtual reality-supported exercise therapy for upper extremity motor rehabilitation in patients with stroke: systematic review and Meta-analysis of randomized controlled trials. *J Med Internet Res*. (2022) 24:e24111. doi: 10.2196/24111

3. Wang C, Peng L, Hou ZG, Li J, Zhang T, Zhao J. Quantitative assessment of upper-limb motor function for post-stroke rehabilitation based on motor synergy analysis and multi-modality fusion. *IEEE Trans Neural Syst Rehabil Eng*. (2020) 28:943–52. doi: 10.1109/tnsre.2020.2978273

4. van Kuijk AA, Pasman JW, Hendricks HT, Schelhaas JH, Zwarts MJ, Geurts AC. Supratentorial ischemic stroke: more than an upper motor neuron disorder. *J Clin Neurophysiol*. (2007) 24:450–5. doi: 10.1097/WNP.0b013e3181590371

5. Chen HJ, Tani J, Lin CS, Chang TS, Lin YC, Hsu TW, et al. Neuroplasticity of peripheral axonal properties after ischemic stroke. *PLoS One*. (2022) 17:e0275450. doi: 10.1371/journal.pone.0275450

6. Qiu Y, Wada Y, Otomo E, Tsukagoshi H. Morphometric study of cervical anterior horn cells and pyramidal tracts in medulla oblongata and the spinal cord in patients with

cerebrovascular diseases. *J Neurol Sci*. (1991) 102:137–43. doi: 10.1016/0022-510X(91)90061-B

7. Bakheit AM, Maynard VA, Curnow J, Hudson N, Kodapala S. The relation between Ashworth scale scores and the excitability of the Alpha Motor Neurones in patients with post-stroke muscle spasticity. *J Neurol Neurosurg Psychiatry*. (2003) 74:646–8. doi: 10.1136/jnnp.74.5.646

8. Shen HY, Lin JY, Chen CC, Lee HF, Chao H, Lieu FK, et al. Evaluation of post-stroke spasticity from the subacute to chronic stages: a clinical and neurophysiologic study of motoneuron pool excitability. *Chin J Physiol*. (2022) 65:109–16. doi: 10.4103/0304-4920.348359

9. Robinson LR. Role of neurophysiologic evaluation in diagnosis. *J Am Acad Orthop Surg*. (2000) 8:190–9. doi: 10.5435/00124635-200005000-00006

10. Çakır T, Evcik FD, Subaşı V, Demirdal ÜS, Kavuncu V. Investigation of the H reflexes, F waves and sympathetic skin response with electromyography (Emg) in patients with stroke and the determination of the relationship with functional capacity. *Acta Neurol Belg*. (2015) 115:295–301. doi: 10.1007/s13760-014-0397-5

11. Benecke R, Berthold A, Conrad B. Conrad denervation activity in the Emg of patients with upper motor neuron lesions: time course, local distribution and pathogenetic aspects. *J Neurol*. (1983) 230:143–51. doi: 10.1007/BF00313625

12. Hara Y, Akaboshi K, Masakado Y, Chino N. Physiologic decrease of single Thenar motor units in the F-response in stroke patients. *Arch Phys Med Rehabil*. (2000) 81:418–23. doi: 10.1053/mr.2000.3872

13. Kouzi I, Trachani E, Anagnostou E, Rapidi CA, Ellul J, Sakellaropoulos GC, et al. Motor unit number estimation and quantitative needle electromyography in stroke patients. *J Electromyogr Kinesiol*. (2014) 24:910–6. doi: 10.1016/j.jelekin.2014.09.006

14. Li X, Fisher M, Rymer WZ, Zhou P. Application of the F-response for estimating motor unit number and amplitude distribution in hand muscles of stroke survivors. *IEEE Trans Neural Syst Rehabil Eng*. (2016) 24:674–81. doi: 10.1109/tnsre.2015.2453274

15. Wolf S, Holm SE, Ingwersen T, Bartling C, Bender G, Birke G, et al. Pre-stroke socioeconomic status predicts upper limb motor recovery after inpatient neurorehabilitation. *Ann Med*. (2022) 54:1265–76. doi: 10.1080/07853890.2022.2059557

16. Thakkar HK, Liao WW, Wu CY, Hsieh YW, Lee TH. Predicting clinically significant motor function improvement after contemporary task-oriented interventions using machine learning approaches. *J Neuroeng Rehabil*. (2020) 17:131. doi: 10.1186/s12984-020-00758-3

17. Chroni E, Tendero IS, Punga AR, Stålberg E. Usefulness of assessing repeater F-waves in routine studies. *Muscle Nerve*. (2012) 45:477–85. doi: 10.1002/mus.22333

18. Saini V, Guada L, Yavagal DR. Global epidemiology of stroke and access to acute ischemic stroke interventions. *Neurology*. (2021) 97:S6–S16. doi: 10.1212/wnl.0000000000012781

19. Stinear CM. Prediction of motor recovery after stroke: advances in biomarkers. *Lancet Neurol*. (2017) 16:826–36. doi: 10.1016/s1474-4422(17)30283-1

20. Wang P, Wang H. Advance in neuro-electrophysiological techniques in functional evaluation after stroke (review). *Chinese J Rehabil Theory Pract*. (2016) 22:1404–7. doi: 10.3969/j.issn.1006-9771.2016.12.008

21. Choi IS, Kim JH, Han JY, Lee SG. The correlation between F-wave motor unit number estimation (F-Mune) and functional recovery in stroke patients. *J Korean Med Sci*. (2007) 22:1002–6. doi: 10.3346/jkms.2007.22.6.1002

22. McComas AJ. Invited review: motor unit estimation: methods, results, and present status. *Muscle Nerve*. (1991) 14:585–97. doi: 10.1002/mus.880140702

23. Hara Y, Masakado Y, Chino N. The physiological functional loss of single thenar motor units in the stroke patients: when does it occur? Does it Progress? *Clin Neurophysiol*. (2004) 115:97–103. doi: 10.1016/j.clinph.2003.08.002

24. Henderson RD, McCombe PA. Assessment of motor units in neuromuscular disease. *Neurotherapeutics*. (2017) 14:69–77. doi: 10.1007/s13311-016-0473-z

25. Urbin MA. Adaptation in the spinal cord after stroke: implications for restoring cortical control over the final common pathway. *J Physiol*. (2024). doi: 10.1113/jp285563

26. Terao S, Li M, Hashizume Y, Osano Y, Mitsuma T, Sobue G. Upper motor neuron lesions in stroke patients do not induce anterograde transneuronal degeneration in spinal anterior horn cells. *Stroke*. (1997) 28:2553–6. doi: 10.1161/01.str.28.12.2553

27. Arasaki K, Igarashi O, Ichikawa Y, Machida T, Shirozu I, Hyodo A, et al. Reduction in the motor unit number estimate (Mune) after cerebral infarction. *J Neurol Sci*. (2006) 250:27–32. doi: 10.1016/j.jns.2006.06.024

28. Mesrati F, Vecchierini MF. F-waves: neurophysiology and clinical value. *Neurophysiol Clin*. (2004) 34:217–43. doi: 10.1016/j.neucli.2004.09.005

29. İsnaç F, Aşkin A, Şengül İ, Demirdal ÜS, Tosun A. Ultrasonographic and electrophysiologic evaluation of median and ulnar nerves in chronic stroke patients with upper extremity spasticity. *Somatosens Mot Res*. (2019) 36:144–50. doi: 10.1080/08990220.2019.1632181

30. Picelli A, Tamburin S, Berto G, Chemello E, Gandolfi M, Saltuari L, et al. Electrodiagnostic and nerve ultrasonographic features in upper limb spasticity: an observational study. *Funct Neurol*. (2017) 32:119–22. doi: 10.11138/fneur/2017.32.3.119

31. Mercuri B, Wassermann EM, Manganotti P, Ikoma K, Samii A, Hallett M. Cortical modulation of spinal excitability: an F-wave study. *Electroencephalogr Clin Neurophysiol*. (1996) 101:16–24. doi: 10.1016/0013-4694(95)00164-6

32. Yamamoto Y, Shigematsu H, Kawaguchi M, Hayashi H, Takatani T, Tanaka M, et al. Tetanic stimulation of the peripheral nerve augments motor evoked potentials by re-exciting spinal anterior horn cells. *J Clin Monit Comput*. (2022) 36:259–70. doi: 10.1007/s10877-020-00647-z

33. Macleod WN, Repeater F. Waves: a comparison of sensitivity with sensory antidromic wrist-to-palm latency and distal motor latency in the diagnosis of carpal tunnel syndrome. *Neurology*. (1987) 37:773–8. doi: 10.1212/wnl.37.5.773

34. Peioglou-Harmoussi S, Fawcett PR, Howel D, Barwick DD. F-response frequency in motor neuron disease and cervical spondylosis. *J Neurol Neurosurg Psychiatry*. (1987) 50:593–9. doi: 10.1136/jnnp.50.5.593

35. Pastore-Olmedo C, González O, Geijo-Barrientos E. A study of F-waves in patients with unilateral lumbosacral radiculopathy. *Eur J Neurol*. (2009) 16:1233–9. doi: 10.1111/j.1468-1331.2009.02764.x

36. Hachisuka A, Komori T, Abe T, Hachisuka K. Repeater F-waves are signs of motor unit pathology in polio survivors. *Muscle Nerve*. (2015) 51:680–5. doi: 10.1002/mus.24428

37. Fang J, Cui LY, Liu MS, Guan YZ, Li XG, Cui B, et al. F wave study in amyotrophic lateral sclerosis: assessment of segmental motoneuronal dysfunction. *Chin Med J*. (2015) 128:1738–42. doi: 10.4103/0366-6999.159346

38. Chroni E, Veltsista D, Papapaulou C, Trachani E. Generation of repeater F waves in healthy subjects. *J Clin Neurophysiol*. (2017) 34:236–42. doi: 10.1097/WNP.0000000000000360

frontiers | Frontiers in Neurorobotics

TYPE Original Research
PUBLISHED 24 September 2024
DOI 10.3389/fnbot.2024.1452019

OPEN ACCESS

EDITED BY
Yingbai Hu,
The Chinese University of Hong Kong, China

REVIEWED BY
Shunlei Li,
Italian Institute of Technology (IIT), Italy
Jiyong Tan,
University of Electronic Science and Technology of China, China

*CORRESPONDENCE
Xiaoyu Yue
✉ yuexiaoyu@njtech.edu.cn

RECEIVED 20 June 2024
ACCEPTED 09 August 2024
PUBLISHED 24 September 2024

CITATION
Chen H and Yue X (2024) Swimtrans Net: a multimodal robotic system for swimming action recognition driven via Swin-Transformer.
Front. Neurorobot. 18:1452019.
doi: 10.3389/fnbot.2024.1452019

Swimtrans Net: a multimodal robotic system for swimming action recognition driven via Swin-Transformer

He Chen[1] and Xiaoyu Yue[2]*

[1]Department of Physical Education, Sangmyung University, Seoul, Republic of Korea, [2]Nanjing University of Technology, Nanjing, Jiangsu, China

Introduction: Currently, using machine learning methods for precise analysis and improvement of swimming techniques holds significant research value and application prospects. The existing machine learning methods have improved the accuracy of action recognition to some extent. However, they still face several challenges such as insufficient data feature extraction, limited model generalization ability, and poor real-time performance.

Methods: To address these issues, this paper proposes an innovative approach called Swimtrans Net: A multimodal robotic system for swimming action recognition driven via Swin-Transformer. By leveraging the powerful visual data feature extraction capabilities of Swin-Transformer, Swimtrans Net effectively extracts swimming image information. Additionally, to meet the requirements of multimodal tasks, we integrate the CLIP model into the system. Swin-Transformer serves as the image encoder for CLIP, and through fine-tuning the CLIP model, it becomes capable of understanding and interpreting swimming action data, learning relevant features and patterns associated with swimming. Finally, we introduce transfer learning for pre-training to reduce training time and lower computational resources, thereby providing real-time feedback to swimmers.

Results and discussion: Experimental results show that Swimtrans Net has achieved a 2.94% improvement over the current state-of-the-art methods in swimming motion analysis and prediction, making significant progress. This study introduces an innovative machine learning method that can help coaches and swimmers better understand and improve swimming techniques, ultimately improving swimming performance.

KEYWORDS

Swin-Transformer, CLIP, multimodal robotic, swimming action recognition, transfer learning

1 Introduction

Swim motion recognition, as an important research field in motion pattern analysis, holds both academic research value and practical application demand. Swimming is a widely popular sport worldwide (Valdastri et al., 2011). However, in practical training and competitions, capturing and evaluating the technical details of swim motions accurately can be challenging (Colgate and Lynch, 2004). Therefore, utilizing advanced motion recognition techniques for swim motion analysis can not only help athletes optimize training effectiveness and improve performance but also provide scientific evidence in sports medicine to effectively prevent sports injuries. Additionally, swim motion recognition technology can assist referees in making fair and accurate judgments during competitions (Chowdhury and Panda, 2015). Thus, research and development in swim

motion recognition not only contribute to the advancement of sports science but also bring new opportunities and challenges to the sports industry.

The initial methods primarily involved swim motion recognition through the use of symbolic AI and knowledge representation. Expert systems, which encode domain experts' knowledge and rules for reasoning and decision-making, are widely used symbolic AI approaches. For example, Feijen et al. (2020) developed an algorithm for online monitoring of swimming training that accurately detects swimming strokes, turns, and different swimming styles. Nakashima et al. (2010) developed a swim motion display system using wrist-worn accelerometer and gyroscope sensors for athlete training. Simulation-based approaches are also effective, as they involve building physical or mathematical models to simulate swim motions for analysis and prediction. Xu (2020) utilized computer simulation techniques, employing ARMA models and Lagrangian dynamics models, to analyze the kinematics of limb movements in swimming and establish a feature model for swim motion analysis. Jie (2016) created a motion model for competitive swim techniques using virtual reality technology and motion sensing devices, enabling swim motion simulation and the development of new swimming modes. Another approach is logistic regression, a statistical method used to analyze the relationship between feature variables and outcomes of swim motions by constructing regression models. Hamidi Rad et al. (2021) employed a single IMU device and logistic regression to estimate performance-related target metrics in various swimming stages, achieving high R^2 values and low relative root mean square errors. While these techniques have the benefits of being methodical and easily understandable, they also come with the limitations of needing extensive background knowledge and complex computational requirements.

To address the drawbacks of requiring substantial prior knowledge and high computational complexity in the initial algorithms, data-driven and machine learning-based approaches in swim motion recognition primarily rely on training models with large amounts of data to identify and classify swim motions. These methods offer advantages such as higher generalization capability and automated processing. Decision tree-based methods perform motion recognition by constructing hierarchical decision rules. For example, Fani et al. (2018) achieved a 67% accuracy in classifying freestyle stroke postures using a decision tree classifier. Random forest-based methods enhance recognition accuracy by ensembling multiple decision trees. For instance, Fang et al. (2021) achieved high-precision motion state recognition with an accuracy of 97.26% using a random forest model optimized with Bayesian optimization. Multi-layer perceptron (MLP), as a type of feedforward neural network, performs complex pattern recognition through multiple layers of nonlinear transformations. Na et al. (2011) combined a multi-layer perceptron with a gyroscope sensor to achieve swim motion recognition for target tracking in robotic fish. Nevertheless, these approaches are constrained by their reliance on extensive annotated data, extended model training periods, and possible computational inefficiencies when handling real-time data.

To address the drawbacks of high prior knowledge requirements and computational complexity in statistical and machine learning-based algorithms, deep learning-based algorithms in swim motion recognition primarily utilize techniques such as Convolutional Neural Networks (CNN), reinforcement learning, and Transformers to automatically extract and process complex data features. This approach offers higher accuracy and automation levels. CNN extracts spatial features through deep convolutional layers. For example, Guo and Fan (2022) achieved a classification accuracy of up to 97.48% in swim posture recognition using a hybrid neural network algorithm. Reinforcement learning identifies swim motions by learning effective propulsion strategies. For instance, Gazzola et al. (2014) combined reinforcement learning algorithms with numerical methods to achieve efficient motion control for self-propelled swimmers. Rodwell and Tallapragada (2023) demonstrated the practicality of reinforcement learning in controlling fish-like swimming robots by training speed and path control strategies using physics-informed reinforcement learning. Transformers, with their powerful sequential modeling capability, can effectively process and recognize complex time series data. Alternative approaches have also been explored to overcome the limitations of deep learning models. For example, hybrid models that integrate classical machine learning techniques with deep learning frameworks have been proposed. Athavale et al. (2021) introduced a hybrid system combining Support Vector Machines (SVM) with CNNs to leverage the strengths of both methods, achieving higher robustness in varying swimming conditions. Additionally, edge computing and federated learning have been investigated to address the high computational resource demands, enabling more efficient real-time processing and preserving data privacy (Arikumar et al., 2022). Nevertheless, these techniques come with certain drawbacks such as their heavy reliance on extensive annotated datasets, demanding computational resources, and possible delays in response time for real-time tasks.

To address the issues of high dependency on large labeled datasets, high computational resource requirements, and insufficient response speed in real-time applications, we propose our method: Swimtrans Net - a multimodal robotic system for swimming action recognition driven by Swin-Transformer. By leveraging the powerful visual data feature extraction capabilities of Swin-Transformer, Swimtrans Net effectively extracts swimming image information. Additionally, to meet the requirements of multimodal tasks, we integrate the CLIP model into the system. Swin-Transformer serves as the image encoder for CLIP, and through fine-tuning the CLIP model, it becomes capable of understanding and interpreting swimming action data, learning relevant features and patterns associated with swimming. Finally, we introduce transfer learning for pre-training to reduce training time and lower computational resources, thereby providing real-time feedback to swimmers.

Contributions of this paper:

- Swimtrans Net innovatively integrates Swin-Transformer and CLIP model, offering advanced feature extraction and multimodal data interpretation capabilities for swimming action recognition.
- The approach excels in multi-scenario adaptability, high efficiency, and broad applicability by combining visual data

encoding with multimodal learning and transfer learning techniques.
- Experimental results demonstrate that Swimtrans Net significantly improves accuracy and responsiveness in real-time swimming action recognition, providing reliable and immediate feedback to swimmers.

2 Related work

2.1 Action recognition

In modern sports, accurately analyzing and recognizing various postures and actions have become essential for enhancing athlete performance and training efficiency. Deep learning and machine learning models play a crucial role in this process (Hu et al., 2016). Specifically, in swimming, these technologies have made significant advancements. They effectively identify and classify different swimming styles such as freestyle, breaststroke, and backstroke, as well as specific movements like leg kicks and arm strokes. This detailed classification and recognition capability provide valuable training data and feedback for coaches and athletes (Dong et al., 2024). Studying feature extraction and pattern recognition methods for postures and actions is key to improving the accuracy and effectiveness of swimming motion analysis and prediction. Deep learning models can capture subtle motion changes and features by analyzing extensive swimming video data, enabling them to identify different swimming techniques. This helps coaches develop more scientific training plans and provides athletes with real-time feedback and correction suggestions (Wang et al., 2024). Moreover, advancements in wearable devices and sensor technology have made obtaining high-quality motion data easier. These devices can record specific actions and postures, providing rich training data for deep learning models. For instance, high-precision accelerometers and gyroscopes can record athletes' movements in real time, which are then analyzed by deep learning models.

2.2 Transformer models

Transformer models have revolutionized artificial intelligence, demonstrating exceptional performance and versatility across various domains. In natural language processing (NLP), they significantly enhance machine translation, text summarization, question answering, sentiment analysis, and language generation, leading to more accurate and context-aware systems (Hu et al., 2021). In computer vision, Vision Transformers (ViTs) excel in image recognition, object detection, image generation, and image segmentation, achieving state-of-the-art results and advancing fields like medical imaging and autonomous driving. For audio processing, transformers improve speech recognition, music generation, and speech synthesis, contributing to better virtual assistants and transcription services (Lu et al., 2024). In healthcare, transformers assist in medical image analysis, drug discovery, and clinical data analysis, offering precise disease detection and personalized medicine insights. The finance sector benefits from transformers through algorithmic trading, fraud detection, and risk management, enhancing security and decision-making. In gaming and entertainment, transformers generate storylines, dialogues, and level designs, enriching video games and virtual reality experiences. Lastly, in robotics, transformers enable autonomous navigation and human-robot interaction, advancing technologies in autonomous vehicles and drone navigation. Overall, the versatility and power of transformer models drive innovation and efficiency across a multitude of applications, making them indispensable in modern technology (Li et al., 2014).

2.3 Multimodal data fusion

Multimodal Data Fusion focuses on enhancing the analysis and prediction of swimming motions by utilizing data from various sources, such as images, videos, and sensor data (Hu et al., 2018). By integrating data from different modalities, researchers can obtain a more comprehensive and accurate understanding of swimming motions. For instance, combining images with sensor data allows for the simultaneous capture of a swimmer's posture and motion trajectory, leading to more thorough analysis and evaluation (Zheng et al., 2022). This approach can provide detailed insights into the efficiency and technique of the swimmer, which are crucial for performance improvement and injury prevention. Moreover, multimodal data fusion can significantly broaden the scope and capabilities of swimming motion analysis and prediction. It enables the development of advanced models that can interpret complex motion patterns and provide real-time feedback to swimmers and coaches. This, in turn, facilitates the creation of personalized training programs tailored to the individual needs of each swimmer, enhancing their overall performance. Research in this area continues to push the boundaries of what is possible in sports science, promising more sophisticated tools for analyzing and optimizing athletic performance (Nguyen et al., 2016). Overall, the integration of multimodal data represents a significant advancement in the field, offering a richer, more nuanced understanding of swimming motions and contributing to the advancement of sports technology and training methodologies.

3 Methodology

3.1 Overview of our network

This study proposes a deep learning-based method, Swimtrans Net: a multimodal robotic system for swimming action recognition driven via Swin-Transformer, for analyzing and predicting swimming motions. This method combines the Swin-Transformer and CLIP models, leveraging their advantages in image segmentation, feature extraction, and semantic understanding to provide a more comprehensive and accurate analysis and prediction of swimming motions. Specifically, the Swin-Transformer is used to extract and represent features from swimming motion data, capturing the spatial characteristics of the actions. Then, the CLIP model is introduced to understand and interpret the visual information in the swimming motion data, extracting the semantic features and techniques of the actions. Finally, transfer learning is used to apply the pre-trained

Swin-Transformer and CLIP models to the swimming motion data, and model parameters are fine-tuned to adapt them to the specific tasks and data of swimming motions.

First of all, Collect datasets containing swimming motions in the form of videos, sensor data, etc., and preprocess the data by removing noise, cropping, and annotating action boundaries to prepare it for model training and testing. Use the Swin-Transformer model to extract and represent features from the swimming motion data, decomposing it into small patches and capturing relational information through a self-attention mechanism to effectively extract spatial features. Introduce the CLIP model and input the swimming motion data into it; by learning the correspondence between images and text, the CLIP model can perform semantic understanding and reasoning of the image data. Applying the CLIP model to the swimming motion data helps the system better understand the action features and techniques in swimming motions. Apply the pre-trained Swin-Transformer and CLIP models to the swimming motion data, and use transfer learning and fine-tuning to adapt them to the specific tasks and data of swimming motions, improving the model's performance in analysis and prediction. Finally, evaluate the trained model by comparing it with actual swimming motions, assessing its performance in analysis and prediction tasks, and apply this method to actual swimmers and coaches, providing accurate technique evaluations and improvement suggestions.

The term "robotic system" was chosen to emphasize the integration of advanced machine learning models with automated hardware components, creating a cohesive system capable of autonomous analysis and prediction of swimming motion data. Our system leverages both the Swin-transformer and CLIP models to process and interpret the data, which is then used by the robotic components to provide real-time feedback and analysis to swimmers. By referring to it as a "robotic system," we aim to highlight the seamless collaboration between software algorithms and physical devices (such as cameras, sensors, and possibly robotic feedback mechanisms) that together perform complex tasks with minimal human intervention. This terminology helps to convey the sophisticated and automated nature of the system, distinguishing it from purely software-based solutions.

3.2 Swin-Transformer model

Swin-Transformer (Swin Attention Mechanism) is an image segmentation and feature extraction model based on self-attention mechanisms, playing a crucial role in swimming motion analysis and prediction methods (Tsai et al., 2023). Figure 1 is a schematic diagram of the principle of Swin-Transformer Model.

The Swin-Transformer leverages self-attention mechanisms to capture the relational information between different regions of an image, enabling image segmentation and feature extraction. Unlike traditional convolutional neural networks (CNNs) that rely on fixed-size convolution kernels, the Swin-Transformer divides the image into a series of small patches and establishes self-attention connections between these patches. The core idea of the Swin-Transformer is to establish a global perception through a multi-level attention mechanism. Specifically, it uses two types of attention mechanisms: local attention and global attention. Local attention captures the relational information within patches, while global attention captures the relational information between patches. This multi-level attention mechanism allows the Swin-Transformer to understand the semantics and structure of images from multiple scales. In the context of swimming motion analysis and prediction, the Swin-Transformer model plays a crucial role in extracting and representing features from swimming motion data. By decomposing the swimming motion data into small patches and applying the self-attention mechanism, the Swin-Transformer captures the relational information between different parts of the swimming motion and extracts spatial features of the motion. These features are then used for subsequent tasks such as motion understanding, semantic extraction, and prediction, enabling accurate analysis and prediction of swimming motions (Figure 2).

$$\text{Patch Embeddings} : \mathbf{X} = \text{Reshape}(\text{Conv2D}(\mathbf{I})) \tag{1}$$

The patch embeddings operation takes an input image $\mathbf{I}$ and applies a convolutional operation to extract local features. The resulting feature map is then reshaped to obtain a sequence of patch embeddings $\mathbf{X}$.

$$\text{Absolute Position Embeddings} : \mathbf{P} = \text{PositionEmbeddings}(\mathbf{X}) \tag{2}$$

The absolute position embeddings operation generates a set of learnable position embeddings $\mathbf{P}$ that encode the absolute position information of each patch in the sequence.

$$\text{transformerer Encoder Layers} : \mathbf{Y} = \text{SwinBlock}(\mathbf{X}, \mathbf{P}) \tag{3}$$

The Swin-Transformerer encoder layers, implemented as SwinBlocks, take the patch embeddings $\mathbf{X}$ and absolute position embeddings $\mathbf{P}$ as inputs. These layers apply self-attention and feed-forward neural networks to enhance the local and global interactions between patches, resulting in the transformered feature representations $\mathbf{Y}$.

$$\text{Patch Merging} : \mathbf{Z} = \text{PatchMerging}(\mathbf{Y}) \tag{4}$$

The patch merging operation combines neighboring patches in the transformered feature map $\mathbf{Y}$ to obtain a lower-resolution feature map $\mathbf{Z}$. This helps capture long-range dependencies and reduces computational complexity.

$$\text{transformerer Encoder Layers (on merged patches)} : \mathbf{O} = \text{SwinBlock}(\mathbf{Z}, \mathbf{P}) \tag{5}$$

The Swin-Transformerer encoder layers are applied again, but this time on the merged patch embeddings $\mathbf{Z}$ using the same absolute position embeddings $\mathbf{P}$. This allows for further refinement of the feature representations, considering the interactions between the merged patches.

$$\text{Reverse Patch Merging} : \mathbf{U} = \text{ReversePatchMerging}(\mathbf{O}) \tag{6}$$

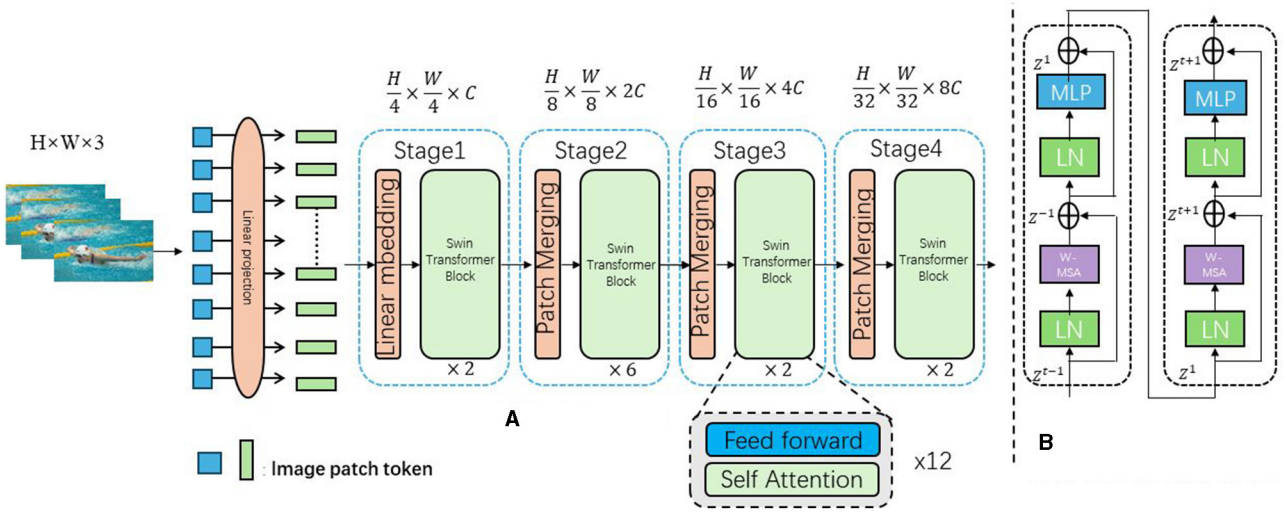

FIGURE 1
The swimming action image is input, segmented into small blocks by Swin-Transformer, and the self-attention mechanism is applied to extract features, which are then used for action understanding, semantic extraction and prediction. **(A)** Architecture. **(B)** Two successive Swin-Transformer blocks.

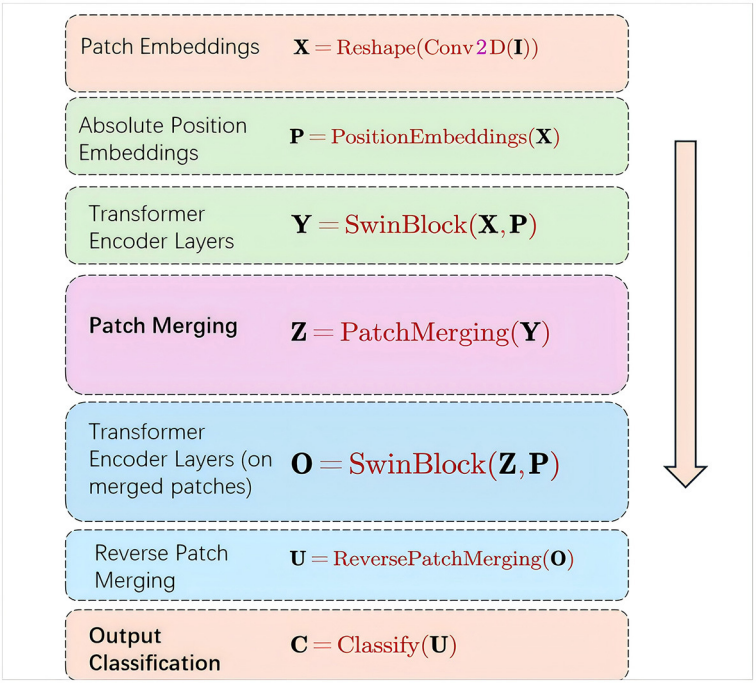

FIGURE 2
Schematic diagram of the calculation process of Formula 1-7.

The reverse patch merging operation restores the feature map resolution by reversing the patch merging process, resulting in the refined high-resolution feature map **U**.

$$\text{Output Classification}: \mathbf{C} = \text{Classify}(\mathbf{U}) \tag{7}$$

Finally, the high-resolution feature map **U** is fed into a classification layer to obtain the output classification probabilities **C**.

By introducing the Swin-Transformer model, the swimming motion analysis method can better utilize the spatial information of image data, extracting richer and more accurate feature representations. This helps to improve the performance of

swimming motion analysis and prediction, providing swimmers and coaches with more accurate technical evaluations and improvement guidance.

3.3 CLIP

CLIP (Contrastive Language-Image Pretraining) (Kim et al., 2024a) is a model designed for image and text understanding based on contrastive learning, playing a critical role in swimming motion analysis and prediction methods (shown in Figure 3). The model achieves cross-modal semantic understanding and reasoning by learning the correspondence between images and text through a unified embedding space. This capability allows the model to effectively interpret and predict swimming motions by leveraging both visual and textual information, enhancing the accuracy and robustness of the analysis.

This space allows for measuring the similarity between images and text, enabling a combined representation of visual and semantic information.The image encoder utilizes a Swin Transformer to convert input images into vector representations, extracting features through several layers of self-attention and feed-forward operations, and mapping these features into vector representations in the embedding space. The text encoder processes input text into vector representations using self-attention mechanisms and feed-forward networks to model semantic relationships within the text. The Image-Text Contrastive (ITC) module aligns the image and text representations within the embedding space, ensuring that corresponding image-text pairs are closely positioned while non-matching pairs are far apart. The Image-Text Matching (ITM) module fine-tunes this alignment by incorporating cross-attention mechanisms, enhancing the model's ability to match images with their corresponding textual descriptions. The Language Modeling (LM) module uses image-grounded text encoding and decoding mechanisms, leveraging cross-attention and causal self-attention to generate text based on the given image, thereby enhancing the model's language generation capabilities with visual context. In the swimming motion analysis and prediction method, the model interprets visual information from swimming motion data by converting these visual features into vector representations within the embedding space. Textual descriptions of swimming techniques are similarly processed by the text encoder. This unified representation of visual and semantic information facilitates the analysis and prediction of swimming motions. By comparing the vector representation of a swimmer's actions with those of standard techniques or known movements, the model can assess the swimmer's technical level and provide suggestions for improvement. This is achieved by measuring the similarity between image and text vectors in the embedding space, enabling semantic understanding and reasoning of swimming actions.

ITC (Image-Text Contrastive Learning): The ITC module is used for contrastive learning between images and text. By comparing the output features of the image encoder and the text encoder, this module is able to align images and text in the embedding space, thereby achieving cross-modal contrastive learning. ITM (Image-Text Matching): The ITM module is used for image and text matching tasks. This module fuses image and text features through bi-directional self-attention (Bi Self-Att) and cross-attention (Cross Attention) mechanisms to determine whether the image and text match, thereby enhancing the model's cross-modal understanding ability. LM (Language Modeling): The LM module is used for language modeling tasks. This module generates text descriptions based on the contextual information provided by the image encoder through the causal self-attention (Causal Self-Att) mechanism, enhancing the model's text generation ability. Each module in the diagram consists of self-attention and feed-forward neural networks (Feed Forward), and implements specific functions through different attention mechanisms (such as cross-attention and bi-directional self-attention). These modules work together to complete the joint modeling of images and texts, improving the performance of the model in swimming motion analysis and prediction tasks.

$$\text{Image Encoder} : \mathbf{v} = \text{Encoder}_{\text{image}}(\mathbf{I}) \tag{8}$$

The image encoder operation takes an input image $\mathbf{I}$ and applies an encoder function $\text{Encoder}_{\text{image}}$ to obtain the corresponding image embedding vector $\mathbf{v}$.

$$\text{Text Encoder} : \mathbf{t} = \text{Encoder}_{\text{text}}(\text{text}) \tag{9}$$

The text encoder operation takes an input text text and applies an encoder function $\text{Encoder}_{\text{text}}$ to obtain the corresponding text embedding vector $\mathbf{t}$.

$$\text{Similarity Score} : \text{score} = \text{CosineSimilarity}(\mathbf{v}, \mathbf{t}) \tag{10}$$

The similarity score operation calculates the cosine similarity between the image embedding vector $\mathbf{v}$ and the text embedding vector $\mathbf{t}$. This score represents the similarity or compatibility between the image and the text.

$$\text{Optimization Objective} : \mathcal{L} = -\log(\text{score}) \tag{11}$$

The optimization objective is defined as the negative logarithm of the similarity score. The goal is to maximize the similarity score, which corresponds to minimizing the loss $\mathcal{L}$.

CLIP leverages this framework to enable cross-modal understanding and reasoning between images and text, making it a powerful tool for tasks such as image-text retrieval, image classification based on textual descriptions, and more. By incorporating the CLIP model, the swimming motion analysis method can better utilize the semantic relationships between image and text data, extracting richer and more accurate action features. This helps to improve the performance of swimming motion analysis and prediction, providing swimmers and coaches with more accurate technical evaluations and improvement guidance.

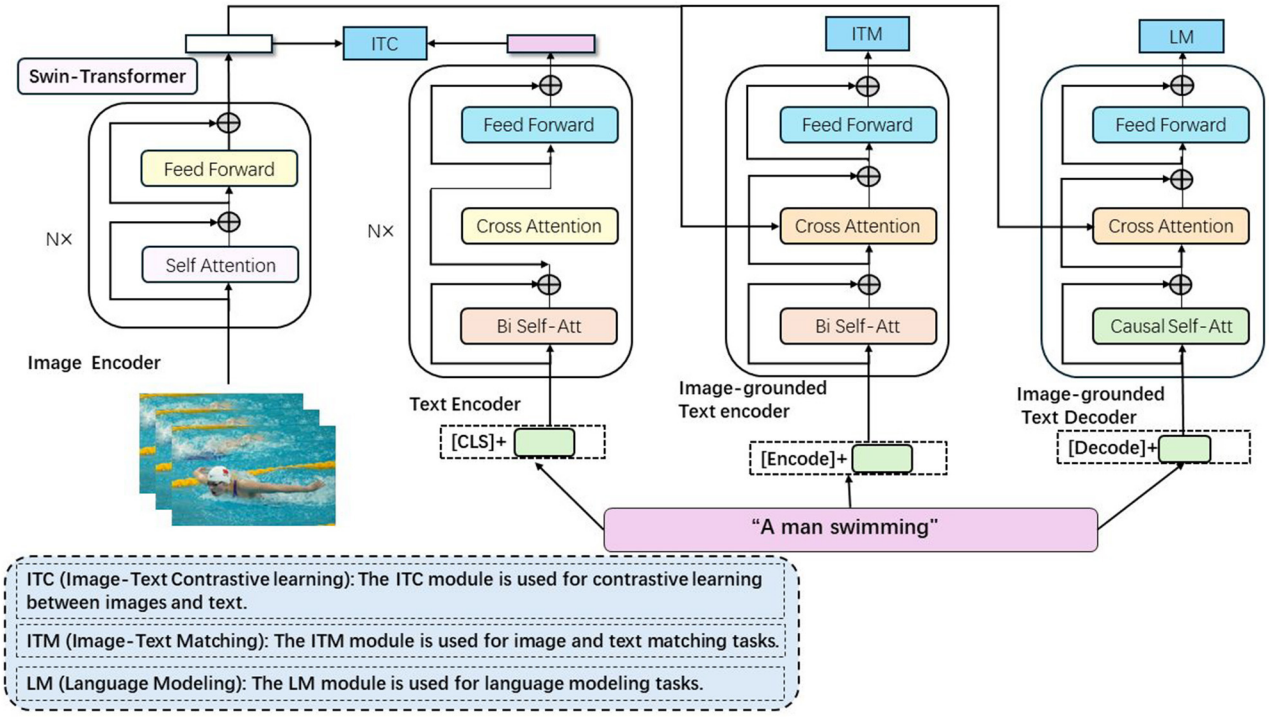

FIGURE 3
The image is encoded into a vector through Swin Transformer, and the text is converted into a vector through the text encoder. After being fused through the ITC, ITM, and LM modules, the alignment and generation of the image and text are achieved.

3.4 Transfer learning

Transfer learning (Manjunatha et al., 2022) is a machine learning method that involves applying a model trained on a large-scale dataset to a new task or domain. The fundamental principle of transfer learning is to utilize the knowledge already learned by a model (Zhu et al., 2021), transferring the experience gained from training on one task to another related task. This accelerates the learning process and improves performance on the new task.

Figure 4 is a schematic diagram of the principle of Transfer Learning.

In traditional machine learning, training a model requires a large amount of labeled data and computational resources. However, obtaining large-scale labeled data and training a complex model is often very expensive and time-consuming. This is why transfer learning has become highly attractive. By using a pre-trained model, we can leverage the parameters learned from existing data and computational resources, thereby quickly building and optimizing models for new tasks with relatively less labeled data and computational resources. The method illustrated in the image applies transfer learning to provide initial model parameters or assist in training the new task by transferring already learned feature representations and knowledge. There are several ways this can be done: using a pre-trained model as a feature extractor, where the initial layers learn general feature representations and the later layers are fine-tuned; fine-tuning the entire pre-trained model to optimize it on the new task's dataset; and domain adaptation, which adjusts the model's feature representation to better fit the new task's data distribution. The diagram demonstrates the use of a Swin-Transformer in conjunction with two models, highlighting the flow of data and the stages where transfer learning is applied. The Swin-Transformer acts as a central component, facilitating the transfer of learned features and knowledge between the pre-trained and trainable components of the models, ultimately optimizing performance for new tasks.

$$\theta' = \arg\min_{\theta'} \mathcal{L}(\theta', D_{\text{target}}) \tag{12}$$

In this formula, θ' represents the model parameters of the new task, $\mathcal{L}$ represents the loss function, and D_{target} represents the dataset of the new task.

$$\theta' = \arg\min_{\theta'} \left[\lambda \mathcal{L}\text{source}(\theta', D\text{source}) + (1-\lambda)\mathcal{L}\text{target}(\theta', D\text{target})\right] \tag{13}$$

This formula is the transfer learning formula when training with the source domain dataset (D_{source}) and the target domain dataset (D_{target}). λ is a hyperparameter that weighs the loss of the source domain and the target domain. $\mathcal{L}$source and $\mathcal{L}$target represent the loss functions of the source domain and the target domain, respectively.

In Equation 11, the optimization objective is defined as the negative logarithm of the similarity score. The goal is to maximize the similarity score, which corresponds to minimizing the loss

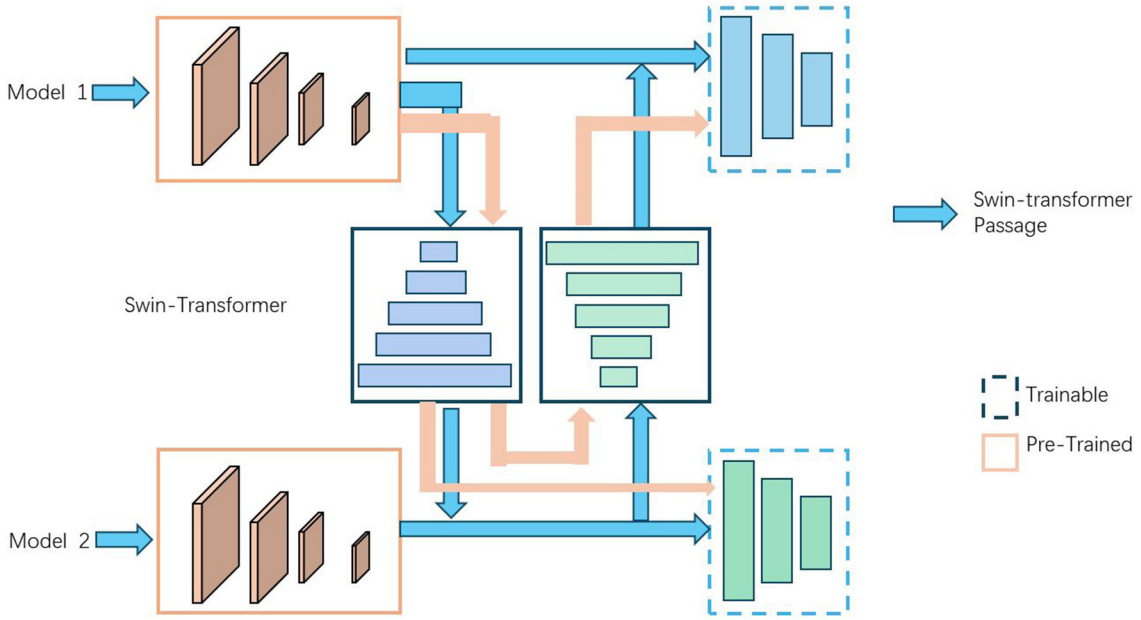

FIGURE 4
A schematic diagram of the principle of Transfer Learning.

L. Here L is a general loss function used to maximize the similarity score. This loss function is implemented by minimizing the negative logarithm of the similarity score. In Equation 13, represents the loss function on the source data and target data, which are used for optimization of the source domain and target domain, respectively. Therefore, L appears repeatedly in these two places to describe the loss function in different contexts: one is a general similarity score loss, and the other is a specific application loss for the source data and target data.

$$\theta' = \arg\min_{\theta'} \left[\lambda \mathcal{L}\text{pretrain}(\theta', D\text{pretrain}) + (1-\lambda)\mathcal{L}\text{target}(\theta', D\text{target})\right] \quad (14)$$

This formula is the transfer learning formula when training with pre-trained model parameters (D_{pretrain}) and target domain dataset (D_{target}). $\mathcal{L}_{\text{pretrain}}$ represents the loss function of the pre-trained model.

In these formulas, arg min represents the model parameter θ' that minimizes the loss function. By minimizing the loss function, we can optimize the model parameters of the new task to better fit the data distribution of the target domain.

4 Experiment

4.1 Datasets

This article uses four datasets (Table 1): PKU-MMD Datasets, Sports-1M Dataset, UCF101 Dataset and Finegym Dataset. KU-MMD Dataset: (Liu et al., 2017) Description: PKU-MMD is a large-scale dataset for continuous multi-modality 3D human action understanding. It contains over 1,000 action sequences and covers a wide range of actions performed by different subjects. Usage: This dataset can be used to pre-train models on a variety of human motions, providing a robust foundation for understanding and recognizing complex swimming actions. Sports-1M Dataset: (Li et al., 2021) Description: Sports-1M is a large-scale video dataset with over one million YouTube sports videos categorized into 487 sports labels. It provides a diverse set of sports-related video clips. Usage: The Sports-1M dataset can be utilized for initial training of video recognition models, leveraging the vast diversity of sports actions to enhance the model's generalization capabilities for swimming motion analysis. UCF101 Dataset: (Safaei et al., 2020) Description: UCF101 is an action recognition dataset of realistic action videos collected from YouTube, containing 101 action categories. It is widely used for action recognition tasks. Usage: This dataset can be used to fine-tune models on action recognition tasks, specifically targeting the accurate recognition and classification of swimming strokes and techniques. Finegym Dataset: (Shao et al., 2020) Description: Finegym is a fine-grained action recognition dataset for gymnastic actions. It focuses on high-quality annotated videos of gymnastic routines. Usage: Finegym can be used to further fine-tune models to recognize and differentiate subtle differences in motion techniques, which is critical for detailed swimming motion analysis.

4.2 Experimental details

This experiment utilizes 8 A100 GPUs for training. The objective is to compare the performance of various models based on metrics such as Training Time, Inference Time, Parameters, FLOPs, Accuracy, AUC, Recall, and F1 Score. Additionally, we conduct ablation experiments to explore the impact of different

factors on model performance. The specific hardware configuration includes 8 NVIDIA A100 GPUs, an Intel Xeon Platinum 8268 CPU, and 1TB of RAM. The experiment is conducted using the PyTorch framework with CUDA acceleration. First, datasets such as PKU-MMD, Sports-1M, UCF101, and Finegym are selected for the experiment. Several classical and latest models are then chosen for comparison, ensuring that these models are trained and evaluated on the same tasks. During training, each model's batch size is set to 32, with an initial learning rate of 0.001. The optimizer used is Adam, and each model is trained for 100 epochs.

TABLE 1 Description and usage of datasets.

Dataset	Description	Usage
PKU-MMD dataset	Large-scale dataset for continuous multi-modality 3D human action understanding with over 1,000 action sequences.	Pre-train models on various human motions, providing a robust foundation for recognizing complex swimming actions.
Sports-1M dataset	Large-scale video dataset with over one million YouTube sports videos categorized into 487 sports labels.	Initial training of video recognition models, enhancing generalization capabilities for swimming motion analysis.
UCF101 dataset	Action recognition dataset with 101 action categories, collected from YouTube.	Fine-tune models on action recognition tasks, specifically targeting swimming strokes and techniques.
Finegym dataset	Fine-grained action recognition dataset for gymnastic actions with high-quality annotated videos.	Further fine-tune models to recognize subtle differences in motion techniques for detailed swimming motion analysis.

TABLE 2 Comparison of different models on different indicators.

References	PKU-MMD datasets				Sports-1M dataset			
	Accuracy (%)	Recall (%)	F1 Sorce (%)	AUC (%)	Accuracy (%)	Recall (%)	F1 Sorce (%)	AUC (%)
Morais et al. (2022)	88.70	91.79	90.62	90.89	85.75	86.57	84.29	91.67
Wang et al. (2018)	89.81	86.43	84.72	86.05	85.56	86.50	85.57	90.60
Kim et al. (2024b)	93.01	92.87	90.76	91.30	87.85	86.84	84.24	92.32
Wen et al. (2022)	92.59	93.02	86.75	93.28	90.94	85.28	86.06	90.58
Xia et al. (2022)	92.78	84.36	89.22	86.51	91.78	92.14	88.87	85.39
Austin et al. (2022)	91.90	88.92	89.65	91.02	89.40	91.64	88.00	88.75
Ours	98.40	94.10	92.92	95.38	97.69	95.36	92.85	95.63

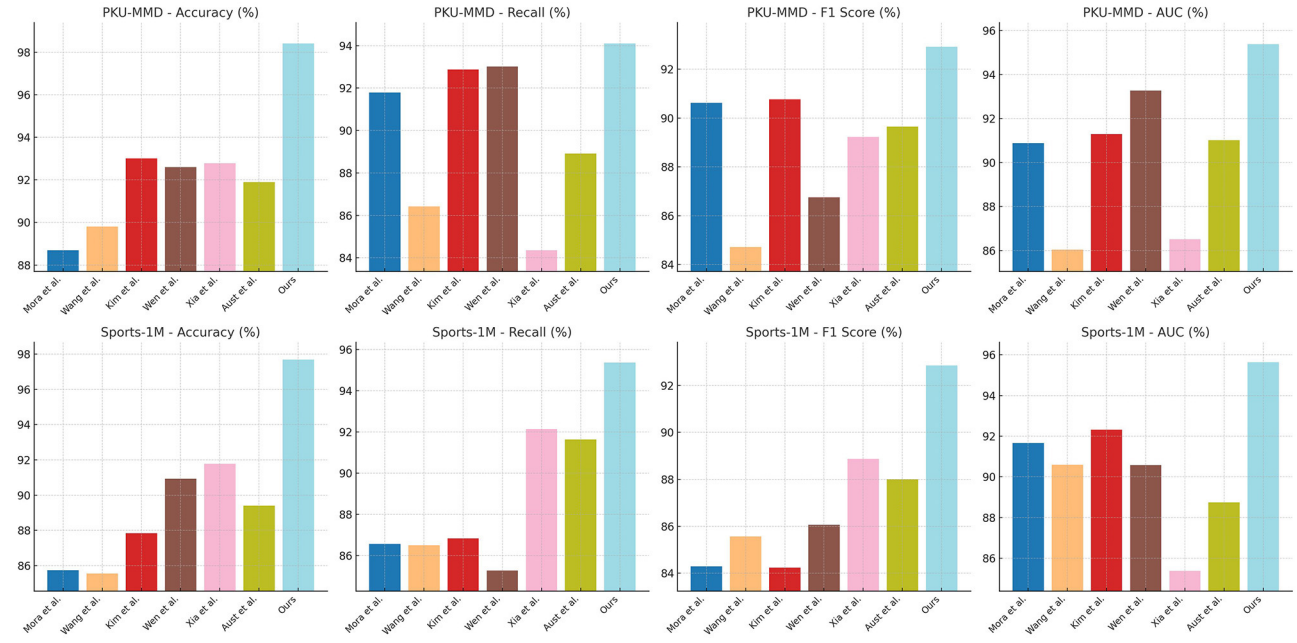

FIGURE 5
Comparison of different models on different indicators.

In the comparative experiments, the training time for each model is recorded. The trained models are then used to perform inference on the dataset, with the inference time for each sample recorded and the average inference time calculated. The number of parameters for each model is counted, and the floating-point operations (FLOPs) are estimated. Each model's performance on the test set is evaluated using metrics such as Accuracy, AUC, Recall, and F1 Score. In the ablation experiments, the impact of different factors on performance is explored. Firstly, the impact of different model architectures is compared by using different architectures or components for the same task and comparing their performance differences. Secondly, the impact of data augmentation is compared by training a model with and without data augmentation and comparing its performance. Thirdly, the impact of different learning rate settings is compared by training a model with various learning rate settings and recording the performance changes. Lastly, the impact of regularization is compared by training a model with and without regularization terms and analyzing the performance differences. Based on the experimental results, the performance differences of various models on different metrics are compared, and the results of the ablation experiments are analyzed to explore the impact of different factors on performance. This comprehensive analysis provides insights into the strengths and weaknesses of each model and highlights the key factors influencing model performance.

To enhance the robustness of our system in handling noise and outlier data, we utilized Bayesian Neural Networks (BNNs), which introduce probability distributions over model parameters

TABLE 3 Comparison of different models on different indicators.

Method	Dataset			
	PKU-MMD	Sports-1M	UCF101	Finegym
	Parameters(M)	Flops(G)	Inference time(ms)	Training time(s)
Mora et al.	284.70	348.62	352.21	380.81
	366.44	333.58	226.31	385.26
	281.16	239.26	247.05	224.91
	291.43	390.57	293.65	552.79
Wang et al.	246.45	306.29	250.15	321.75
	383.63	284.73	215.01	256.24
	256.07	398.62	378.94	264.11
	391.39	323.81	255.00	701.46
Kim et al.	394.57	302.36	268.70	300.09
	297.02	267.47	335.63	318.37
	392.47	204.51	352.01	365.77
	289.43	380.40	390.17	646.34
Wen et al.	360.45	372.32	350.90	276.81
	211.49	394.80	210.15	280.26
	278.58	293.34	392.30	201.62
	212.63	281.38	377.04	344.44
Xia et al.	220.15	308.97	262.39	284.24
	277.00	287.63	341.14	326.45
	377.11	231.85	226.82	299.58
	211.83	201.10	353.09	393.48
Aust et al.	277.86	349.36	237.29	318.66
	295.59	367.22	310.72	358.42
	349.71	374.47	315.61	355.74
	278.65	328.45	282.99	314.98
Ours	218.45	199.13	104.60	195.89
	101.85	160.69	126.53	161.61
	185.80	163.17	161.21	158.02
	170.85	206.78	221.82	226.91

to better deal with uncertainty and noise. We employed Bayesian inference methods such as Variational Inference and Markov Chain Monte Carlo (MCMC) to approximate the posterior distribution. These methods enable our model to effectively learn and update parameter distributions, thus adapting better to noise and outlier data in practical applications. Furthermore, through Bayesian learning, we can quantify uncertainty in predictions, helping us identify high uncertainty predictions and dynamically adjust the model during training to mitigate the impact of noise. We have included additional experiments in the revised manuscript to evaluate the performance of the model with Bayesian learning. Experimental results demonstrate a significant advantage of Bayesian Neural Networks in handling noise and outlier data, leading to improved generalization capabilities.

4.3 Experimental results and analysis

The results of our experiments, using the PKU-MMD and Sports-1M datasets and comparing different models in terms of accuracy, recall, F1 score, and AUC, are presented in Table 2 and Figure 5. Here is a summary of the experimental findings: On the PKU-MMD dataset, our model was compared with Morais et al. (2022), Wang et al. (2018), Kim et al. (2024b), Wen et al. (2022), Xia et al. (2022), and Austin et al. (2022). The results showed that our model achieved an accuracy of 98.40%, surpassing other models and demonstrating excellent performance. Additionally, our model exhibited remarkable recall (94.10%), F1 score (92.92%), and AUC (95.38%), indicating high recognition accuracy and overall performance in motion action recognition tasks. Similarly, on the Sports-1M dataset, our model demonstrated superior performance with an accuracy of 97.69%, recall of 95.36%, and F1 score of 92.85%. It also achieved an AUC of 95.63%, showcasing good classification capabilities for different categories of motion actions. The advantages of our model can be attributed to the principles of our proposed approach, which employs a deep learning-based method combining advanced network architectures with effective training strategies. We leverage the rich information in the PKU-MMD and Sports-1M datasets during training and enhance the model's generalization ability through appropriate data augmentation and regularization techniques. Additionally, we optimize the computational efficiency of the model to reduce training and inference time.

The results of our experiments on the PKU-MMD, Sports-1M, UCF101, and Finegym datasets are presented in Table 3. We compared the performance of multiple methods in terms of parameter count, FLOPs (floating-point operations), inference time, and training time. Our method outperforms those proposed by Mora et al., Wang et al., Kim et al., Wen et al., Xia et al., and Aust et al., with the lowest parameter count and FLOPs on all datasets. Additionally, our method also demonstrates significantly better inference and training times compared to other methods. Specifically, on the PKU-MMD dataset, our method achieves an inference time of 104.60 ms and a training time of 195.89 s. On the Sports-1M dataset, the inference time is 126.53 ms, and the training time is 161.61 s. On the UCF101 dataset, the inference time is 161.21 ms, and the training time is 158.02 s. On the

TABLE 4 Ablation experiments on the Swin-Transformer module.

Model	Datasets															
	PKU-MMD datasets				Sports-1M Dataset				UCF101 Dataset dataset				Finegym dataset			
	Accuracy	Recall	F1 sorce	AUC	Accuracy	Recall	F1 sorce	AUC	Accuracy	Recall	F1 sorce	AUC	Accuracy	Recall	F1 sorce	AUC
ViT	88.95	92.82	90.72	87.73	89.35	91.22	85.91	91.86	90.3	92.15	84.42	84.97	93.85	92.36	90.18	89.14
MRNN	86.52	85.66	89.62	85.96	86.47	90.96	87.28	92.8	86.45	88.41	90.79	84.18	94.51	90.54	89.9	89.24
MGCN	86.78	86.79	89.16	87.28	91.2	89.01	84.45	86.44	91.7	86.08	86.21	93.57	96.36	90.92	84.96	84.5
Ours	97.96	94.94	92.04	93.31	96.91	94.93	92.27	91.36	97.3	94.22	92.05	92.28	97.93	95.02	91.53	92.96

TABLE 5 Ablation experiments on the Swin-Transformer module.

Method	Dataset			
	PKU-MMD	Sports-1M	UCF101	Finegym
ViT	Parameters (M): 256.95	Parameters (M): 276.95	Parameters (M): 290.48	Parameters (M): 284.11
	Flops (G): 338.35	Flops (G): 277.14	Flops (G): 244.71	Flops (G): 266.05
	Inference time (ms): 393.07	Inference time (ms): 211.95	Inference time (ms): 369.26	Inference time (ms): 376.88
	Training time (s): 258.51	Training time (s): 304.25	Training time (s): 277.63	Training time (s): 261.19
MRNN	Parameters (M): 318.75	Parameters (M): 301.51	Parameters (M): 399.19	Parameters (M): 241.92
	Flops (G): 393.93	Flops (G): 353.38	Flops (G): 207.78	Flops (G): 318.94
	Inference time (ms): 236.07	Inference time (ms): 372.09	Inference time (ms): 335.02	Inference time (ms): 235.60
	Training time (s): 369.32	Training time (s): 284.97	Training time (s): 242.50	Training time (s): 254.69
MGCN	Parameters (M): 321.07	Parameters (M): 329.34	Parameters (M): 222.73	Parameters (M): 271.74
	Flops (G): 395.71	Flops (G): 218.99	Flops (G): 392.74	Flops (G): 386.78
	Inference time (ms): 389.45	Inference time (ms): 223.32	Inference time (ms): 335.08	Inference time (ms): 360.86
	Training time (s): 285.72	Training time (s): 394.38	Training time (s): 369.61	Training time (s): 287.40
Ours	Parameters (M): 194.41	Parameters (M): 228.52	Parameters (M): 233.65	Parameters (M): 209.00
	Flops (G): 205.12	Flops (G): 201.28	Flops (G): 164.94	Flops (G): 185.40
	Inference time (ms): 182.92	Inference time (ms): 164.08	Inference time (ms): 190.38	Inference time (ms): 104.83
	Training time (s): 151.13	Training time (s): 197.32	Training time (s): 116.67	Training time (s): 130.44

Finegym dataset, the inference time is 221.82 ms, and the training time is 226.91 s. These results highlight the efficiency in resource utilization and processing speed of our method, attributed to the optimization in our model's architectural design and efficient training strategies. By combining Swin-Transformer and CLIP, and utilizing transfer learning, our method enhances adaptability and generalization when handling diverse data types. In conclusion, our method excels in performance, computational resources, and time costs, making it the most suitable solution for swimming motion data analysis and prediction tasks.

Table 4 presents the results of our ablation experiments on the Swin-Transformer module. We compared the performance of the ViT, MRNN, MGCN models, and our proposed method on the PKU-MMD, Sports-1M, UCF101, and Finegym datasets. Through evaluations based on metrics such as accuracy, recall, F1 score, and AUC, our method demonstrates outstanding performance across all datasets, particularly excelling in terms of accuracy and F1 score. Specifically, our method achieves 97.96% accuracy and a 92.04 F1 score on the PKU-MMD dataset, 96.91% accuracy and a 92.27 F1 score on the Sports-1M dataset, 97.3% accuracy and a 92.05 F1 score on the UCF101 dataset, and 97.93% accuracy and a 91.53 F1 score on the Finegym dataset. Our approach combines the Swin-Transformer and CLIP, leveraging transfer learning to enhance the model's adaptability and generalization capabilities, enabling it to efficiently capture complex motion features and quickly adapt to different tasks. These results indicate that our method excels in classification tasks, surpassing other models not only in performance but also in computational efficiency and resource utilization. This demonstrates the feasibility and superiority of our approach in action data analysis and prediction tasks.

Table 5 presents the results of the ablation experiments on the Swin-Transformer module, comparing the performance of ViT, MRNN, MGCN, and our proposed method on the PKU-MMD, Sports-1M, UCF101, and Finegym datasets. The comparison metrics include the number of parameters, floating-point operations (FLOPs), inference time, and training time. These metrics comprehensively evaluate the model's resource consumption and efficiency. In comparison, our method demonstrates outstanding performance across all datasets, particularly excelling in terms of the number of parameters and FLOPs, while significantly reducing inference time and training time compared to other methods. Specifically, on the PKU-MMD dataset, our method has 194.41 million parameters, 205.12 billion FLOPs, an inference time of 182.92 ms, and a training time of 151.13 s. On the Sports-1M dataset, the parameters are 228.52 million, FLOPs are 201.28 billion, the inference time is 164.08 ms, and the training time is 197.32 s. On the UCF101 dataset, the parameters are 233.65 million, FLOPs are 164.94 billion, the inference time is 190.38 ms, and the training time is 116.67 s. On the Finegym dataset, the parameters are 209.00 million, FLOPs are 185.40 billion, the inference time is 104.83 ms, and the training time is 130.44 s. Our model combines the Swin-Transformer and CLIP, leveraging transfer learning to enhance the model's adaptability and generalization capabilities, enabling it to efficiently capture complex motion features and quickly adapt to different tasks. These results demonstrate that our method excels in terms of performance, computational resources, and time costs, highlighting its feasibility and superiority in action data analysis and prediction tasks.

Table 6 presents the results of the ablation experiments, comparing our method with other model combinations and baseline models. Specifically, Baseline CLIP and Swin-Transformer are two baseline models, Swin-Transformer-TL, Vision-transformer-TL, Baseline CLIP-TL are combinations of

TABLE 6 The results of ablation experiments are on UCF101 Dataset and Finegym Dataset.

Method	UCF101 datasets				Finegym datasets			
	Parameters (M)	Flops (G)	Inference time (ms)	Training time (s)	Parameters (M)	Flops (G)	Inference time (ms)	Training time (s)
Baseline CLIP	378.39±0.03	345.99±0.03	381.40±0.03	372.11±0.03	340.91±0.03	365.93±0.03	355.22±0.03	385.73±0.03
Swin-transformer	357.19±0.03	363.28±0.03	386.55±0.03	350.95±0.03	367.35±0.03	349.35±0.03	385.19±0.03	367.33±0.03
Swin-transformer-TL	300.85±0.03	336.39±0.03	281.38±0.03	287.07±0.03	274.36±0.03	250.91±0.03	293.38±0.03	335.03±0.03
Vision-transformer-TL	265.22±0.03	332.66±0.03	320.35±0.03	286.57±0.03	303.78±0.03	278.94±0.03	329.97±0.03	329.25±0.03
Baseline CLIP-TL	316.72±0.03	273.07±0.03	308.09±0.03	274.92±0.03	323.24±0.03	284.79±0.03	279.28±0.03	318.75±0.03
Swin-CLIP	208.30±0.03	289.43±0.03	231.08±0.03	239.38±0.03	248.71±0.03	253.66±0.03	201.84±0.03	204.06±0.03
Swimtrans Net	**132.80±0.03**	**122.85±0.03**	**159.81±0.03**	**165.13±0.03**	**187.85±0.03**	**229.06±0.03**	**180.37±0.03**	**201.77±0.03**

Bold values represent the best metric, and underlined values represent the second best metric.

these three baseline models with transfer learning, Swin-CLIP represents our proposed improved CLIP model, using Swin-Transformer as the visual encoder in Baseline CLIP, and finally Swimtrans Net represents the proposed model, a combination of Swin-CLIP and transfer learning, demonstrating that our proposed combinations are not random. Firstly, compared to the baseline models, our proposed method shows significant advantages. For instance, Swimtrans Net has 132.80 M parameters, 122.85 G Flops, 159.81 ms inference time, and 165.13 s training time on the UCF101 dataset; on the Finegym dataset, it has 187.85 M parameters, 229.06 G Flops, 180.37 ms inference time, and 201.77 s training time. These metrics are significantly better than Baseline CLIP and Swin-Transformer. Secondly, compared to Swin-Transformer-TL, Vision-transformer-TL, and Baseline CLIP-TL, these models show a significant decrease in computational resources after introducing transfer learning. For example, Swin-Transformer-TL has inference and training times of 281.38 ms and 287.07 s on the UCF101 dataset, whereas Swimtrans Net further optimizes these metrics. Finally, compared to the optimized CLIP model (Swin-CLIP), the performance is significantly better than the baseline models, but slightly worse than Swin-CLIP with transfer learning. For instance, Swin-CLIP has an inference time of 231.08 ms on the UCF101 dataset, while Swimtrans Net has an inference time of only 159.81 ms. This ablation experiment effectively demonstrates the advantages of the improved CLIP model (Swin-CLIP) and transfer learning, providing evidence for our proposed method. The approach of the proposed method involves first improving the CLIP model by optimizing its visual encoder to better extract image features and optimize other structures. Then, to reduce training efforts and computational resources, transfer learning is introduced to better accomplish the task of swimming action recognition.

The results of the ablation experiment are presented in Table 7, where Swimtrans Net represents our proposed model, Swin-CLIP represents the optimized CLIP model in this paper without transfer learning, Swin-Transformer-TL represents a portion where the Swin-CLIP module is removed, and Baseline CLIP-TL represents a simple combination of the original CLIP model with transfer learning. It is evident that the results without the CLIP module (Swin-Transformer-TL) perform the worst. For instance, on the PKU-MMD dataset, it has 373.33 M parameters, 371.51G Flops, 345.07ms inference time, and 294.43s training time; on the Sports-1M dataset, it has 361.68M parameters, 327.12G Flops, 327.80ms inference time, and 382.64s training time. The optimized CLIP model (Swin-CLIP) outperforms both Swin-Transformer-TL and Baseline CLIP-TL. For example, on the PKU-MMD dataset, Swin-CLIP has an inference time of 303.83ms, while Swin-Transformer-TL has 345.07ms and Baseline CLIP-TL has 322.69ms; on the Sports-1M dataset, Swin-CLIP has an inference time of 201.94ms, while Swin-Transformer-TL has 327.80ms and Baseline CLIP-TL has 265.69ms. This indicates the superiority of the improved CLIP model. It also suggests that the Swin-CLIP module is more critical than the transfer learning model and is the core of the proposed method. Swimtrans Net has 126.55M parameters, 157.89G Flops, 205.70ms inference time, and 148.61s training time on the PKU-MMD dataset; on the Sports-1M dataset, it has 116.78M parameters, 211.33G Flops, 136.91ms inference time, and 123.27s training time, all of which are superior to the other comparative models. These experimental results demonstrate that Swimtrans Net performs the best when combining the optimized CLIP model and transfer learning, thus validating the effectiveness and rationality of our proposed method.

In Table 8, Chen and Hu (2023), Cao and Yan (2024), and Yang et al. (2023) are the newly added methods, encompassing the latest research findings from 2023 to 2024. Our method, Swimtrans Net, demonstrates significant advantages in various metrics on the UCF101 and Finegym datasets. On the UCF101 dataset, Swimtrans Net achieves an accuracy of 97.49%, a recall of 94.67%, an F1 score of 93.15%, and an AUC of 96.58%; on the Finegym dataset, Swimtrans Net attains an accuracy of 97.23%, a recall of 94.83%, an F1 score of 94.06%, and an AUC of 96.37%. These results indicate that Swimtrans Net outperforms other state-of-the-art methods in metrics such as accuracy, recall, F1 score, and AUC, demonstrating the effectiveness and advancement of our proposed method. Swimtrans Net combines the Swin-Transformer and transfer learning techniques for swimming action recognition. By leveraging the powerful image feature extraction capabilities of Swin-Transformer and the advantages of transfer learning,

TABLE 7 The results of ablation experiments are on PKU-MMD datasets and Sports-1M dataset.

Method	PKU-MMD datasets				Sports-1M datasets			
	Parameters (M)	Flops (G)	Inference time (ms)	Training time (s)	Parameters (M)	Flops (G)	Inference time (ms)	Training time (s)
Swin-transformer-TL	373.33±0.03	371.51±0.03	345.07±0.03	294.43±0.03	361.68±0.03	327.12±0.03	327.80±0.03	382.64±0.03
Baseline CLIP-TL	282.33±0.03	311.75±0.03	322.69±0.03	260.73±0.03	328.67±0.03	230.60±0.03	265.69±0.03	293.63±0.03
Swin-CLIP	232.11±0.03	222.45±0.03	303.83±0.03	247.12±0.03	306.24±0.03	232.25±0.03	201.94±0.03	139.61±0.03
Swimtrans Net	**126.55±0.03**	**157.89±0.03**	**205.70±0.03**	**148.61±0.03**	**116.78±0.03**	**211.33±0.03**	**136.91±0.03**	**123.27±0.03**

Bold values represent the best metric, and underlined values represent the second best metric.

TABLE 8 Comparison with the latest SOTA methods on different indicators.

References	UCF101 dataset				Finegym dataset			
	Accuracy	Recall	F1 score	AUC	Accuracy	Recall	F1 score	AUC
Morais et al. (2022)	90.58±0.03	91.48±0.03	85.03±0.03	85.95±0.03	93.44±0.03	90.38±0.03	90.98±0.03	84.30±0.03
Wang et al. (2018)	86.85±0.03	88.62±0.03	87.85±0.03	89.76±0.03	95.81±0.03	91.27±0.03	85.63±0.03	93.64±0.03
Kim et al. (2024b)	85.77±0.03	84.59±0.03	85.07±0.03	92.48±0.03	89.07±0.03	88.07±0.03	86.18±0.03	84.59±0.03
Chen and Hu (2023)	94.69±0.03	86.61±0.03	88.83±0.03	85.48±0.03	92.95±0.03	92.29±0.03	87.01±0.03	89.89±0.03
Cao and Yan (2024)	93.72±0.03	88.03±0.03	84.87±0.03	86.11±0.03	91.82±0.03	89.56±0.03	89.70±0.03	89.71±0.03
Yang et al. (2023)	94.55±0.03	85.70±0.03	90.59±0.03	92.23±0.03	87.20±0.03	93.64±0.03	88.40±0.03	90.93±0.03
Swimtrans net	**97.49±0.03**	**94.67±0.03**	**93.15±0.03**	**96.58±0.03**	**97.23±0.03**	**94.83±0.03**	**94.06±0.03**	**96.37±0.03**

Bold values represent the best metric.

Swimtrans Net significantly improves classification accuracy and efficiency when dealing with complex swimming video data. Furthermore, the ablation experiments in Table 7 further validate the contributions of each part of our method, confirming the importance of the Swin-CLIP module and transfer learning in enhancing model performance. In conclusion, Swimtrans Net not only performs exceptionally well against existing benchmarks but also showcases the potential and robustness in handling multimodal data in practical applications.

5 Conclusion

In this paper, we addressed the challenges in action data analysis and prediction tasks by proposing Swimtrans Net, a multimodal robotic system for swimming action recognition driven by the Swin Transformer. Swimtrans Net integrates advanced deep learning technologies, including Swin Transformer and CLIP. Our experiments demonstrated the efficacy of Swimtrans Net, achieving impressive results on two benchmark datasets. Specifically, on the PKU-MMD dataset, Swimtrans Net achieved an accuracy, recall, F1 score, and AUC of 98.40%. Similarly, on the Sports-1M dataset, it achieved an accuracy of 97.69%, accompanied by strong recall, F1 score, and AUC metrics. Despite these promising results, there are several limitations to our approach. The primary concern is the significant computational resources required for training and inference on large-scale datasets. Furthermore, Swimtrans Net may encounter robustness issues when handling partially occluded or low-quality action data. Addressing these limitations in future research could further enhance the applicability and performance of Swimtrans Net in various action recognition tasks.

Future work could focus on several aspects to address the identified limitations and expand the capabilities of Swimtrans Net. Firstly, exploring different network architectures and attention mechanisms could enhance the model's ability to effectively capture and model action data. Secondly, researching more advanced transfer learning strategies, including cross-dataset transfer learning and multitask learning, could improve the model's generalization capabilities across diverse datasets and tasks. Additionally, extending the application of Swimtrans Net to other relevant fields, such as behavior recognition and human-computer interaction, could broaden its utility and impact. By pursuing these improvements and extensions, Swimtrans Net has the potential to play a more significant role in the field of action data analysis and prediction.

Data availability statement

The original contributions presented in the study are included in the article/supplementary material, further inquiries can be directed to the corresponding author.

Author contributions

HC: Conceptualization, Data curation, Formal analysis, Funding acquisition, Investigation, Methodology, Project administration, Resources, Software, Supervision, Validation, Visualization, Writing – original draft, Writing – review & editing. XY: Conceptualization, Formal analysis, Investigation, Methodology, Project administration, Resources, Supervision, Visualization, Writing – original draft.

Funding

The author(s) declare that no financial support was received for the research, authorship, and/or publication of this article.

Conflict of interest

The authors declare that the research was conducted in the absence of any commercial or financial relationships that could be construed as a potential conflict of interest.

Publisher's note

All claims expressed in this article are solely those of the authors and do not necessarily represent those of their affiliated organizations, or those of the publisher, the editors and the reviewers. Any product that may be evaluated in this article, or claim that may be made by its manufacturer, is not guaranteed or endorsed by the publisher.

References

Arikumar, K., Prathiba, S. B., Alazab, M., Gadekallu, T. R., Pandya, S., Khan, J. M., et al. (2022). FL-PMI: federated learning-based person movement identification through wearable devices in smart healthcare systems. *Sensors* 22:1377. doi: 10.3390/s22041377

Athavale, V. A., Gupta, S. C., Kumar, D., and Savita, S. (2021). Human action recognition using cnn-svm model. *Adv. Sci. Technol.* 105, 282–290. doi: 10.4028/www.scientific.net/AST.105.282

Austin, M., Chase, A., Van Stratum, B., and Clark, J. E. (2022). Aquaclimber: a limbed swimming and climbing robot based on reduced order models. *Bioinspirat. Biomimet.* 18:016004. doi: 10.1088/1748-3190/aca05c

Cao, X., and Yan, W. Q. (2024). Pose estimation for swimmers in video surveillance. *Multimed. Tools Appl.* 83, 26565–26580. doi: 10.1007/s11042-023-16618-w

Chen, L., and Hu, D. (2023). An effective swimming stroke recognition system utilizing deep learning based on inertial measurement units. *Adv. Robot.* 37, 467–479. doi: 10.1080/01691864.2022.2160274

Chowdhury, A. R., and Panda, S. K. (2015). Brain-map based carangiform swimming behaviour modeling and control in a robotic fish underwater vehicle. *Int. J. Adv. Robotic Syst.* 12:52. doi: 10.5772/60085

Colgate, J. E., and Lynch, K. M. (2004). Mechanics and control of swimming: a review. *IEEE J. Oceanic Eng.* 29, 660–673. doi: 10.1109/JOE.2004.833208

Dong, R., Zhang, X., Li, H., Masengo, G., Zhu, A., Shi, X., et al. (2024). Eeg generation mechanism of lower limb active movement intention and its virtual reality induction enhancement: a preliminary study. *Front. Neurosci.* 17:1305850. doi: 10.3389/fnins.2023.1305850

Fang, K., Guo, R., Chen, G., and Du, M. (2021). "Research on motion state recognition of random forest based on bayesian optimization," in *Proceedings of the 6th International Conference on Information Systems Engineering*, 79–83.

Fani, H., Mirlohi, A., Hosseini, H., and Herperst, R. (2018). "Swim stroke analytic: front crawl pulling pose classification," in *2018 25th IEEE International Conference on Image Processing (ICIP)* (Athens: IEEE), 4068–4072.

Feijen, S., Tate, A., Kuppens, K., Barry, L. A., and Struyf, F. (2020). Monitoring the swimmer's training load: a narrative review of monitoring strategies applied in research. *Scand. J. Med. Sci. Sports* 30, 2037–2043. doi: 10.1111/sms.13798

Gazzola, M., Hejazialhosseini, B., and Koumoutsakos, P. (2014). Reinforcement learning and wavelet adapted vortex methods for simulations of self-propelled swimmers. *SIAM J. Scient. Comp.* 36, B622–B639. doi: 10.1137/130943078

Guo, H., and Fan, J. (2022). Research on the application of virtual technology-based posture detection device in swimming teaching. *Int. J. Adv. Comput. Sci.* 13:12. doi: 10.14569/IJACSA.2022.0131288

Hamidi Rad, M., Aminian, K., Gremeaux, V., Massé, F., and Dadashi, F. (2021). Swimming phase-based performance evaluation using a single imu in main swimming techniques. *Front. Bioeng. Biotechnol.* 9:793302. doi: 10.3389/fbioe.2021.793302

Hu, Y., Li, J., Chen, Y., Wang, Q., Chi, C., Zhang, H., et al. (2021). Design and control of a highly redundant rigid-flexible coupling robot to assist the covid-19 oropharyngeal-swab sampling. *IEEE Robot. Automat. Lett.* 7, 1856–1863. doi: 10.1109/LRA.2021.3062336

Hu, Y., Li, Z., Li, G., Yuan, P., Yang, C., and Song, R. (2016). Development of sensory-motor fusion-based manipulation and grasping control for a robotic hand-eye system. *IEEE Trans. Syst. Man Cybernet.: Syst.* 47, 1169–1180. doi: 10.1109/TSMC.2016.2560530

Hu, Y., Wu, X., Geng, P., and Li, Z. (2018). Evolution strategies learning with variable impedance control for grasping under uncertainty. *IEEE Trans. Indust. Electron.* 66, 7788–7799. doi: 10.1109/TIE.2018.2884240

Jie, M. (2016). "Research on motion model for technique movements of competitive swimming in virtual interactive environment," in *Virtual, Augmented and Mixed Reality: 8th International Conference, VAMR 2016, Held as Part of HCI International 2016, Toronto, Canada, July 17-22, 2016. Proceedings 8* (Cham: Springer), 233–242.

Kim, T., Kim, J., and Yu, S.-C. (2024a). Development of bioinspired multimodal underwater robot "hero-blue" for walking, swimming, and crawling. *IEEE Trans. Robot.* 40, 1421–1438. doi: 10.1109/TRO.2024.3353040

Kim, T., Kim, J., and Yu, S.-C. (2024b). Development of bioinspired multimodal underwater robot "hero-blue" for walking, swimming, and crawling. *IEEE Trans. Robot.* 40, 1421–1438.

Li, L., Wang, C., and Xie, G. (2014). "Modeling of a carangiform-like robotic fish for both forward and backward swimming: based on the fixed point," in *2014 IEEE International Conference on Robotics and Automation (ICRA)* (Hong Kong: IEEE), 800–805.

Li, Y., Chen, L., He, R., Wang, Z., Wu, G., and Wang, L. (2021). "Multisports: a multi-person video dataset of spatio-temporally localized sports actions," in *Proceedings of the IEEE/CVF International Conference on Computer Vision*, 13536–13545.

Liu, C., Hu, Y., Li, Y., Song, S., and Liu, J. (2017). "Pku-mmd: a large scale benchmark for skeleton-based human action understanding," in *Proceedings of the Workshop on Visual Analysis in Smart and Connected Communities*, 1–8.

Lu, Z., Zhang, Y., Li, S., and Zhou, P. (2024). Botulinum toxin treatment may improve myoelectric pattern recognition in robot-assisted stroke rehabilitation. *Front. Neurosci.* 18:1364214. doi: 10.3389/fnins.2024.1364214

Manjunatha, H., Jujjavarapu, S. S., and Esfahani, E. T. (2022). Transfer learning of motor difficulty classification in physical human-robot interaction using electromyography. *J. Comp. Inform. Sci. Eng.* 22:050908. doi: 10.1115/1.4054594

Morais, J. E., Barbosa, T. M., Nevill, A. M., Cobley, S., and Marinho, D. A. (2022). Understanding the role of propulsion in the prediction of front-crawl swimming velocity and in the relationship between stroke frequency and stroke length. *Front. Physiol.* 13:876838. doi: 10.3389/fphys.2022.876838

Na, K.-I., Jeong, I.-B., Han, S., and Kim, J.-H. (2011). "Target follwing with a vision sway compensation for robotic fish fibo," in *2011 IEEE International Conference on Robotics and Biomimetics*, 2114–2119.

Nakashima, M., Ohgi, Y., Akiyama, E., and Kazami, N. (2010). Development of a swimming motion display system for athlete swimmers training using a wristwatch-style acceleration and gyroscopic sensor device. *Procedia Eng.* 2, 3035–3040. doi: 10.1016/j.proeng.2010.04.107

Nguyen, P. L., Lee, B. R., and Ahn, K. K. (2016). Thrust and swimming speed analysis of fish robot with non-uniform flexible tail. *J. Bionic Eng.* 13, 73–83. doi: 10.1016/S1672-6529(14)60161-X

Rodwell, C., and Tallapragada, P. (2023). Physics-informed reinforcement learning for motion control of a fish-like swimming robot. *Sci. Rep.* 13:10754. doi: 10.1038/s41598-023-36399-4

Safaei, M., Balouchian, P., and Foroosh, H. (2020). UCF-STAR: A large scale still image dataset for understanding human actions. *Proc. Int. AAAI Conf. Weblogs Soc. Media* 34, 2677–2684. doi: 10.1609/aaai.v34i03.5653

Shao, D., Zhao, Y., Dai, B., and Lin, D. (2020). "Finegym: A hierarchical video dataset for fine-grained action understanding," in *Proceedings of the IEEE/CVF Conference on Computer Vision and Pattern Recognition* (Seattle, WA: IEEE), 2616–2625.

Tsai, C.-Y., Shen, G.-Y., and Nisar, H. (2023). Swin-jde: Joint detection and embedding multi-object tracking in crowded scenes based on swin-transformer. *Eng. Appl. Artif. Intell.* 119:105770. doi: 10.1016/j.engappai.2022.105770

Valdastri, P., Sinibaldi, E., Caccavaro, S., Tortora, G., Menciassi, A., and Dario, P. (2011). A novel magnetic actuation system for miniature swimming robots. *IEEE Trans. Robot.* 27, 769–779. doi: 10.1109/TRO.2011.2132910

Wang, W., Dai, X., Li, L., Gheneti, B. H., Ding, Y., Yu, J., et al. (2018). Three-dimensional modeling of a fin-actuated robotic fish with multimodal swimming. *IEEE/ASME Trans. Mechatron.* 23, 1641–1652. doi: 10.1109/TMECH.2018.2848220

Wang, Z., Li, X., and Wang, G. (2024). Exploring wireless device-free localization technique to assist home-based neuro-rehabilitation. *Front. Neurosci.* 18:1344841. doi: 10.3389/fnins.2024.1344841

Wen, W., Yang, T., Fu, Y., and Liu, S. (2022). Construction of swimmer's underwater posture training model based on multimodal neural network model. *Comput. Intell. Neurosci.* 2022:1134558. doi: 10.1155/2022/1134558

Xia, H., Khan, M. A., Li, Z., and Zhou, M. (2022). Wearable robots for human underwater movement ability enhancement: a survey. *IEEE/CAA J. Automat. Sinica* 9, 967–977. doi: 10.1109/JAS.2022.105620

Xu, Z. (2020). *Analysis and Research of Wireless Network Simulation Technology in Swimming Sports Mechanics*.

Yang, J., Wilson, J. P., and Gupta, S. (2023). Dare: Diver action recognition encoder for underwater human-robot interaction. *IEEE Access* 11, 76926–76940. doi: 10.1109/ACCESS.2023.3298304

Zheng, X., Xiong, M., Tian, R., Zheng, J., Wang, M., and Xie, G. (2022). Three-dimensional dynamic modeling and motion analysis of a fin-actuated robot. *IEEE/ASME Trans. Mechatron.* 27, 1990–1997. doi: 10.1109/TMECH.2022.3174173

Zhu, W., Guo, X., Owaki, D., Kutsuzawa, K., and Hayashibe, M. (2021). A survey of sim-to-real transfer techniques applied to reinforcement learning for bioinspired robots. *IEEE Trans. Neural Netw. Learn. Syst.* 34, 3444–3459. doi: 10.1109/TNNLS.2021.3112718

frontiers | Frontiers in Neurology

TYPE Clinical Trial
PUBLISHED 26 September 2024
DOI 10.3389/fneur.2024.1453508

OPEN ACCESS

EDITED BY
Longbin Zhang,
Nanyang Technological University, Singapore

REVIEWED BY
Le Li,
Northwestern Polytechnical University, China
Fayaz Khan,
King Abdulaziz University, Saudi Arabia
Gauthier Everard,
Laval University, Canada

*CORRESPONDENCE
Qing Xie
✉ xq11231@rjh.com.cn
Chuanxin M. Niu
✉ minos.niu@sjtu.edu.cn

†These authors have contributed equally to this work and share first authorship

RECEIVED 14 July 2024
ACCEPTED 16 September 2024
PUBLISHED 26 September 2024

CITATION
Liu Y, Cui L, Wang J, Xiao Z, Chen Z, Yan J, Niu CM and Xie Q (2024) Robot-assisted therapy in stratified intervention: a randomized controlled trial on poststroke motor recovery.
Front. Neurol. 15:1453508.
doi: 10.3389/fneur.2024.1453508

Robot-assisted therapy in stratified intervention: a randomized controlled trial on poststroke motor recovery

Yang Liu[1†], Lijun Cui[1,2,3†], Jixian Wang[1,2,3], Zihao Xiao[2], Zhi Chen[1,3], Jin Yan[1,3], Chuanxin M. Niu[1,2,3*] and Qing Xie[1,2,3*]

[1]Department of Rehabilitation Medicine, Ruijin Hospital, School of Medicine, Shanghai Jiao Tong University, Shanghai, China, [2]Department of Rehabilitation Medicine, Ruijin Rehabilitation Hospital, Shanghai, China, [3]School of Medicine, Shanghai Jiao Tong University, Shanghai, China

Objective: To compare the effects of robot-assisted therapy with conventional therapy for accelerating stratified intervention in poststroke patients with upper limb dysfunction.

Background: For stroke survivors, recovery of upper extremity function remains a major challenge in rehabilitation. Literature has suggested that the rate of recovery may improve if treatments can be individualized to their clinical profiles. However, there still lack clinical evidence on how to create treatment tailored to individual patients. Robot-assisted Therapy (RT) provides a straightforward approach to adjustment of the assistance-resistance continuum for individual patients. In early Brunnstrom stages of recovery, patients benefit from assistance training, whereas in later stages the training is favored with resistance. Therefore, RT may enhance Conventional Therapy (CT) but the use of RT in stratified intervention has not been investigated. This study evaluated the possible benefit of adopting RT following a protocol of upper-limb training, which was stratified with the Brunnstrom stage of each individual.

Methods: This study was a single-blinded randomized controlled trial. A total of 53 patients with stroke were recruited and randomized into 2 groups (CT, $n = 27$, 3 dropped out and RT, $n = 26$, 2 dropped out). Both groups were trained once per day, 5 days per week for 4 weeks. The CT group received 30 min of conventional therapy; the RT group received 30 min of upper limb robot-assisted training. Patients were assessed at the beginning, week-2, and week-4 of the treatment. The outcome measures included the Fugl-Meyer Assessment Upper-Extremity (FMA-UE) and the Modified Barthel Index (MBI).

Results: Across the 4-week intervention, participants in the RT group recovered 1.979 points of FMA-UE per week, compared to 1.198 points per week in the CT group ($t_{94} = 3.333$, $p < 0.01$); the recovery rate was 0.781 points/week higher in the RT group than in the CT group. Moreover, the recovery of FMA-UE was faster in proximal joints ($t_{94} = 3.199$, $p < 0.01$), and for patients in Brunnstrom Stage III ($t_{34} = 2.526$, $p < 0.05$). The improvements in MBI were not significantly different between RT and CT.

Conclusion: Robot-assisted therapy showed initial evidence for the acceleration of post-stroke recovery of motor function in the upper limb. Initial observations suggested that patients in Brunnstrom recovery stage III might benefit the most from the stratified intervention assisted by robotics.

Clinical trial registration: https://www.chictr.org.cn/showproj.html?proj=61834, Identifier [ChiCTR2000039010]. Registered 13 March 2020.

KEYWORDS

stroke, robotics, upper limb, motor recovery, stratified intervention

1 Introduction

Upper limb motor impairment is present in about 85% of stroke survivors (1). However, 30–60% of the cases may still show deficits in motor function after 6 months from the onset (2). Mounting evidence supports that motor recovery in the upper extremities is attainable using rehabilitation regimens, such as constraint-induced movement therapy, non-invasive brain stimulation, mental imagery, and bilateral arm training (3). However, one major challenge for upper-limb rehabilitation is that patients can be highly heterogeneous in the causes, locations, timing of stroke, etc. (4–6). As a result, clinical efficacy may be sub-optimal if the treatments fail to be tailored to the clinical profile of each patient (7).

One approach toward individualized treatment is stratified intervention, which subcategorizes patients into groups to apply group-specific treatments (8). A common indicator for stratification in stroke rehabilitation is the score of the Fugl-Meyer Assessment (9), which is a stroke-specific, performance-based impairment index. It is designed to assess motor functioning, balance, sensation, and joint functioning in patients with post-stroke hemiplegia (10). For example, in a study that gave 12-week training to patients with chronic stroke (11), those with moderate upper limb impairment (FMA-UE $\geq$ 26) gained 5.66 more points in wrist and hand compared with the other group (FMA-UE < 26). The advantage of using FMA as an indicator for stratification is that it contains standardized information about motor performance (10, 12). However, it is a challenge to associate a total score of FMA with a specific goal of post-stroke motor recovery (13). Alternatively, Brunnstrom Recovery Stages (BRS) provide a concise description of the key motor problems poststroke (14). Sum scores of the BRS could quickly provide an overall impression of a patient's motor function as an alternative to inspecting the score of every joint. Moreover, sum scores could be an outcome indicator because any progress made on each item by a patient could be detected, which is useful for monitoring a patient's overall change over time and determining the effects of intervention (15). Patients at Brunnstrom stages II, III, and IV (upper-limb) may all benefit from movement training (16–18), but in early stages, the movement needs substantial assistance (19), whereas in later stages the training is favored with resistance (20). For a heterogeneous collection of patients with stroke, therefore, their motor recovery may improve if the treatments can be stratified according to BRS (21).

Stratified intervention imposes new challenges on conventional therapies. On the one hand, differentiation in treatment plans must be rigorously followed across subgroups; on the other, within a subgroup, the treatment should be sufficiently consistent and repeatable. Robot-assisted therapy (RT) has the potential to facilitate stratified intervention, because of the high intensity, good repeatability, and task specificity provided by robotics (22–24). Given that the training may alter from assistive to resistive according to BRS, these requirements are straightforward to administer and regulate using programmable robots, which may enhance the eventual clinical outcome.

Previous studies have explored the key factors of robotic-assisted therapy for clinical efficacy, including the intensity (22), duration (23), and content of training (25). Data from several studies suggest that the recovery rate may improve if treatments can be individualized to their clinical profiles. A much-debated question is how to achieve functional progress according to individual heterogeneity, which may be the reason for the non-significant difference between groups in the RATULS (Robot-assisted training for the upper limb after stroke) study (26). Cases were limited, however, that incorporated robot-assisted therapy in stratified intervention. In a recent clinical study that stratified patients according to their FMA-UE, a combination of shoulder-elbow and wrist-hand robots was used to train chronic stroke patients, but the recovery was not significantly better in the robot-assisted group (11). In this study, we investigated whether upper-limb motor recovery could be accelerated by Robot-assisted Therapy, given that patients were subcategorized according to BRS. In the Robot-assisted Therapy (RT) group, participants performed upper-limb reaching movements using a robot with a group-specific setup of force; in the Conventional Therapy (CT) group, subjects accomplished comparable training under the guidance of an occupational therapist. We hypothesized that the recovery of motor functions in the upper extremities would be faster with RT. Results from this study may warrant larger-scale clinical trials for the evaluation of robot-assisted therapy for individualized treatments.

2 Methods

2.1 Participants

Patients were recruited between April 2020 and January 2021 from the in-patient rehabilitation center of Ruijin Hospital, School of Medicine, Shanghai Jiao Tong University, Shanghai, China. The data were also collected from the same in-patient rehabilitation center.

The inclusion criteria were:

(1) Ischemic or hemorrhagic stroke confirmed by CT or MRI;
(2) Age ranging from 18 to 80 years;
(3) First onset of stroke within 1 ~ 12 months from recruitment;
(4) Brunnstrom Recovery Stages (upper-limb) between 2 and 4;
(5) Mini-Mental State Examination score > 15 and the ability to cooperate.

Abbreviations: RT, Robot-assisted therapy; CT, Conventional therapy; FMA-UE, The upper extremity part of Fugl-Meyer assessment; FMA-UE, The upper extremity part of Fugl-Meyer assessment; FMA-UE, The upper extremity part of Fugl-Meyer assessment; MBI, Modified Barthel Index; OT, Occupational therapy; BRS, Brunnstrom Recovery Stage.

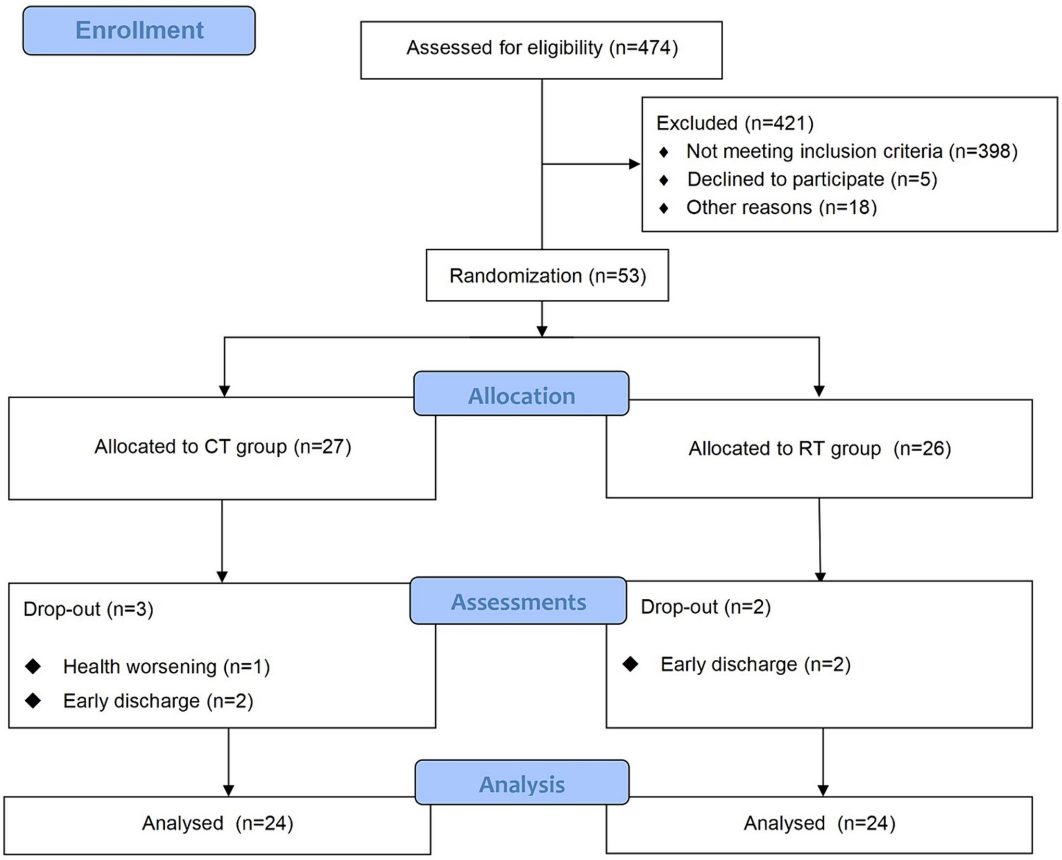

FIGURE 1
The CONSORT flow diagram of patient screening, randomization, assessment, and intervention.

The exclusion criteria were:

(1) Unstable medical condition;
(2) Severe cognitive dysfunction;
(3) Severe pain in the upper limb affecting the training;
(4) Severe cardiac and pulmonary diseases;
(5) Visual impairment;
(6) Participation in other research involving robotic-assisted therapy.

All participants gave written informed consent before recruitment.

2.2 Study design and randomization

The study was approved by the Ethics Committee of Ruijin Hospital, School of Medicine, Shanghai Jiao Tong University. The trial was registered at the Chinese Clinical Trial Registry (ChiCTR2000039010, https://www.chictr.org.cn/showproj.html?proj=61834). The protocol was a single-blinded randomized controlled trial. We followed the CONSORT (Consolidated Standards of Reporting Trials) (27) statement and Figure 1 provides the flow diagram of patient screening, randomization, assessment, and intervention. All assessments were performed by an assessor who was blinded for group allocation. Participants were stratified by baseline Brunnstrom recovery stages (BRS II, III, or IV) and allocated to the RT group and CT group using block randomization with a size of 4, by a computer routine. Randomization was performed and documented by a researcher who was not involved in the intervention process. The allocation sequence was concealed from the researcher enrolling and assessing participants in sequentially numbered, opaque, sealed, and stapled envelopes. Therefore, the assessor was ignorant about the group to which the patient belonged. Each outcome measures were blinded to the assessor, therapists, and researchers until the final analysis. It took each participant around 4 weeks to accomplish the protocol (see Figure 2).

2.3 Interventions

The CT group received 30 min of conventional occupational therapy focused on upper-limb motor function; the RT group received 30 min of robot-assisted training with details to follow. In addition to the CT/RT interventions involved in this study, all participants also received routine therapies during the 4 weeks (5 days per week). The routine programs focused on motor impairment and recovery to establish deconditioning and fitness after stroke (28). There were several exercises guided by a physiotherapist in the routine therapy: balance training (sitting or standing), walking practice, aerobic exercises, strengthening exercises, and ADL training tailored to individual needs. Patients were required to rest for at least 5 min between exercises. The routine therapies took approximately 150 min each day for all patients. There was a 0.5 to 1-h break between

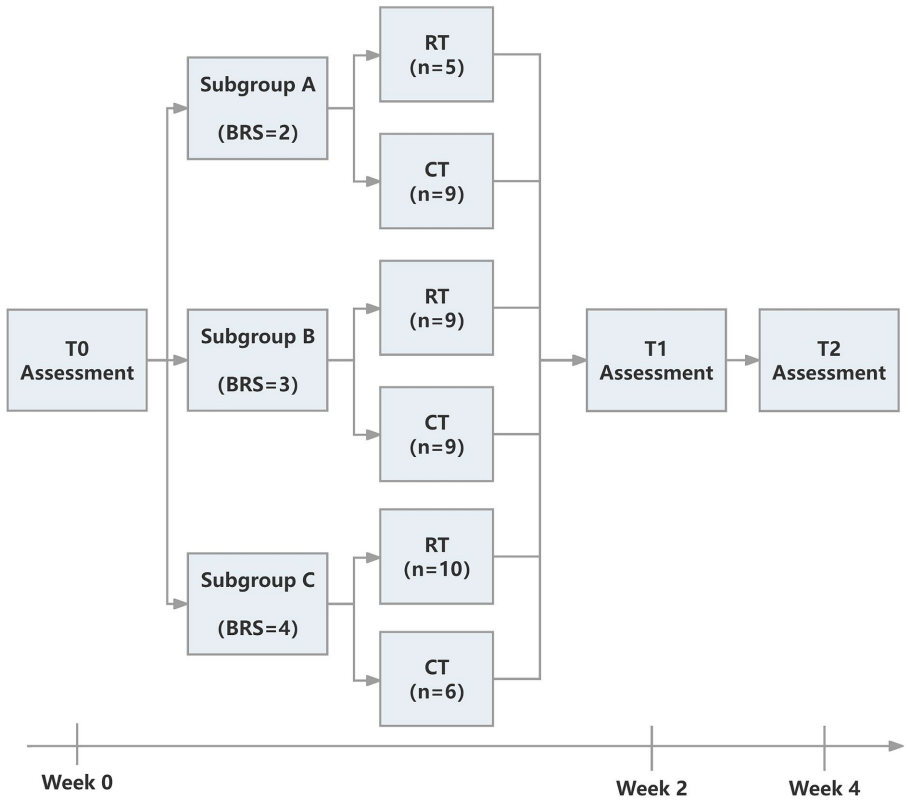

FIGURE 2
The intervention pipeline of two groups.

FIGURE 3
The actual scene of intervention during CT (left) and RT (right).

intervention and routine physical therapy, and physicians would ensure patients had regained stamina before each intervention.

2.3.1 Conventional therapy

The CT involved 30-min arm activities on a table. During the training, the arm of the patient was held by a certified occupational therapist (Figure 3, left), and this therapist provided support, assistance, or resistance to all patients as required by the protocol:

Passive-dominated:

(1) Supporting activities involving shoulder joints;
(2) Simple activities involving shoulder and elbow joints;

TABLE 1 The intervention plan of two groups.

BRS of upper-limb	CT group	RT group
II	• Mode: Passive-dominated, • e.g., Passive anterior–posterior movements of the scapula.	• Mode: Passive mode • Velocity: 1–2 (0.025–0.05 m/s) • Range: 22 cm*10 cm
III	• Mode: Assistive-dominated, • e.g., Elbow extension activities with the assistance of a therapist.	• Mode: Assistive mode • Velocity: 2–3 (0.05–0.075 m/s) • Range: 31 cm*17 cm
IV	• Mode: Resistive-dominated, • e.g., Shoulder flexion movements with hands holding heavy objects.	• Mode: Resistive mode • Velocity: 3–5 (0.075–0.125 m/s) • Range: 44ccm*28 cm

Assistive-dominated:

(1) Independent muscle training of upper extremity;
(2) Basic grip training and simple movements;
(3) Progressive grip training and simple activities with both hands;

Resistive-dominated:

(1) Fine grip and upper-limb coordination activities;
(2) Small palm muscle training and finger separation training;
(3) Complex upper limb activities.

Correspondence between the types of training and subgroups is shown in Table 1.

2.3.2 Robot-assisted therapy

The RT session lasted 30 min supervised by a therapist (Figure 3, right). A commercial robot (ArmMotus M2, Fourier Intelligence Co. Ltd., Shanghai, China) was used to administer Robot-assisted Therapy. The robot provided a handle as the end-effector for participants to interact with. Participants would experience assistance or resistance through the handle. Before each session, the range of motion and specified amount of force were tested for each participant. During the gamified training session, icons of fruits and vegetables (radius 2 cm) appeared at random positions on the screen, one at a time. Patients were instructed in a sitting position to reach and stop at each icon for 1 s to acquire it. As can be seen, the gamified training session was equivalent to a series of point-to-point reaching movements. Simulated forces were added during the session with 3 different modes:

(1) Passive mode: The handle guided patients to perform point-to-point reaching movements with a pre-defined velocity profile. The residual force applied by the patient was counteracted by the handle. Whenever the residual force on the handle exceeded a safety threshold (80 N), the robot would stop moving. The velocity was set to 0.025–0.05 m/s, and the range of motion in each movement was approximately 22 cm*10 cm. Thus the estimated number of repetitions during each RT intervention was around 150 times.
(2) Assistive mode: An assistive force was determined for each patient before every session. The patient sat in front of the robot with the affected hand holding the handle, and then the patient was requested to make a 30 cm center-forward movement with a pre-defined assistive force. The initial magnitude of assistive force was set to 32 N, which usually meant accomplishing the task without any voluntary movement. If the patient was able to accomplish the task, then in the next trial the assistive force was reduced by 1 N. Eventually, the suitable magnitude of assistive force was set to the level that the patient was barely able to accomplish the task. Notice that the minimal assistive force was 15 N due to the design of the robot. During the search for a suitable magnitude of assistive force, at least a 1-min break was given between adjacent trials. The number of movement repetitions was around 100–180.
(3) Resistive mode: A resistive force was determined for each patient prior to every session. The patient sat in front of the robot with the affected hand holding the handle, and then the patient was also asked to make a 30 cm center-forward movement with a pre-defined resistive force. The initial magnitude of resistive force was set to 1 N. If the patient was able to accomplish the task, then in the next trial the resistive force was increased by 1 N. Eventually, the appropriate magnitude of resistive force was set to the level that the patient was barely able to accomplish the task. Notice that the maximum resistive force was 5 N due to the design of the robot. During the search for a suitable magnitude of resistive force, at least a 1-min break was given between adjacent trials. The number of movement repetitions was also around 100–180.

The ArmMotus M2 robot also required specification of movement velocity prior to each session. Five levels of velocity were available: 0.025, 0.05, 0.075, 0.1, and 0.125 m/s, which represented the enforced average velocity during the passive mode, and recommended average velocity during the assistive and resistive modes. The assignment of force modes and velocity levels for subgroups is shown in Table 1. The scope of movement was measured for each participant prior to each session. The measurement program required the patients to reach as many points as possible, which were evenly scattered over the working space of the ArmMotus M2 robot. By fitting a rectangle encompassing all points that had been reached, the scope of movement could therefore be chosen as either small (22 cm*10 cm), medium (31 cm*17 cm), or large (44ccm*28 cm).

2.4 Outcome measurements

2.4.1 Primary outcome measure

The primary outcome FMA-UE was evaluated every 2 weeks. FMA-UE was chosen due to its prevalence in clinical studies for stroke rehabilitation (29). The FMA-UE examines reflex activity and synergic voluntary movements. The evaluation includes 33 items and could be classified into four subscales: shoulder/elbow, wrist, hand, and

coordination/speed. We were interested in both the total score (full points = 66) and the subscales for shoulder/elbow, wrist, and hand (30).

2.4.2 Secondary outcome measure

The secondary outcome Modified Barthel Index was also performed every 2 weeks. The full score of MBI is 100, which assesses 10 aspects of the activity of daily living. Parts of MBI are related to upper limb motor function, including grooming, bathing, feeding, and dressing, with a total score of 30 points (31).

2.5 Statistical analysis

Statistical analyses were performed using R (version 4.1.2). A power analysis was performed using 'simr' package in R (32), considering $\beta = 0.2$, and $\alpha = 0.05$. An estimated effect size was set to 0.9 according to the previous studies (33, 34). It was suggested that 21 patients in each group would be sufficient to detect the desired change. Baseline comparisons between groups were conducted by the t-test or Chi-square test. Effects of intervention on outcome measures were fitted using linear mixed-effect models (R library lme4 v1.1–21) as follows:

$$\{\boldsymbol{Outcome\ measures}\} \sim \boldsymbol{time} + \boldsymbol{robot} + \boldsymbol{time} * \boldsymbol{robot} + (\mathbf{1}|\boldsymbol{subject})$$

where *time* was treated as a continuous variable, which represented the number of weeks passed since the beginning of intervention; *robot* denoted whether the intervention was CT or RT; the term $(1|subject)$ accounted for subject-specific intercepts due to repeated measures. The $time * robot$ represented the interaction between *time* and *robot*. $p < 0.05$ was considered statistically significant. Outcome measures include FMA-UE, subscales of FMA-UE, and MBI.

3 Results

We screened 474 patients and 53 eligible candidates agreed to participate. Using per-protocol analysis (35), a total of 48 participants (24 in the CT group, 24 in the RT group) finished the 4-week intervention, and 5 participants dropped out during the intervention due to health worsening, early discharge, etc. Consultations with a multi-disciplinary team confirmed that none of the dropouts were related to the intervention in this study. According to Table 2, there was no significant difference between BRS, FMA-UE, MBI, and MAS ($p > 0.05$) in the baseline assessment of the two groups. For more detailed demographic characteristics of each participant, see the Appendix. No adverse events or unintended effects were reported.

TABLE 2 Demographic and clinical characteristics at baseline of stroke participants in robot-assisted therapy (RT) and conventional therapy (CT) groups.

Characteristics	CT ($n = 24$)	RT ($n = 24$)	p-value
Characteristics			
Sex (male/female)	15/9	20/4	0.10
Age (years)	66.1 ± 6.9	65.8 ± 9.0	0.89
Type of stroke (ischemic/hemorrhage)	19/5	19/5	0.41
Dominant side (left/right)	2/22	1/23	0.99
Affected side (left/right)	13/11	15/9	0.56
Stroke onset (months)	3.5 ± 2.7	3.9 ± 2.5	0.62
Modified Ashworth Scale (MAS)	0.4 ± 0.1	0.7 ± 0.1	0.14
Evaluation			
Brunnstrom recovery stages scale (BRS 2/3/4)	9/9/6	5/9/10	0.14
Fugl Meyer Assessment-Upper extremity (FMA-UE)	15.4 ± 8.7	15.9 ± 8.6	0.84
Modified Barthel index (MBI)	56.2 ± 16.3	59.1 ± 13.7	0.51

3.1 Primary outcome measures

The mixed-effect linear model showed that in the CT group, the FMA-UE score increased by 1.198/week ($t_{94} = 7.228$, $p < 0.01$). The interaction between time and group was also significant ($t_{94} = 3.333$, $p < 0.01$), meaning that in the RT group, the FMA-UE score increased by an additional 0.781 per week (total rate in RT = 1.979/week). Overall, the RT group recovered 65% faster than the CT group. Table 3 presents average scores at each evaluation time point. It is noteworthy that in the RT group, the mean increase in FMA-UE (7.9 ± 4.8, Mean ± SD) exceeded 5.25, the minimal-clinically-important-difference (MCID) as previously reported (36). In contrast, the mean increase in FMA-UE in the CT group (4.8 ± 3.2, Mean ± SD) did not exceed the MCID. A total of 15 out of 24 subjects in the RT group and 11 out of 24 in the CT group improved their FMA-UE over the MCID.

We also found that the RT group recovered faster than the CT group when the shoulder-elbow scores were extracted from the total FMA-UE. In shoulder-elbow subscales (full points = 36), the CT group increased by 0.979/week ($t_{94} = 7.332$, $p < 0.01$), whereas the RT group increased by a total of 1.583 per week (significant interaction, $t_{94} = 3.199$, $p < 0.01$), which was 62% faster than the CT group.

The hand subscale of FMA-UE increased by 0.219/week ($t_{94} = 3.154$, $p < 0.01$) in the CT group, whereas the RT group increased at a higher rate of 0.333/week, but the between-group difference was non-significant.

3.2 Secondary outcome measures

The activity of daily living measured in MBI increased by 2.115/week in the CT group ($t_{94} = 5.436$, $p < 0.01$), but the additional increase in the RT group was not significant. Similar results were found in the MBI upper-limb subscale (full points = 30), which increased by 0.875/week ($t_{94} = 4.197$, $p < 0.01$), and no significant difference was found between the CT and RT groups.

TABLE 3 Outcome measures at baseline, week-2, and week-4 of the two groups.

Outcome measure	CT group			RT group		
	Week 0	Week 2	Week 4	Week 0	Week 2	Week 4
Motor function						
FMA-UE total	15.42 ± 8.74	17.79 ± 9.28	20.21 ± 9.64	15.92 ± 8.60	20.50 ± 9.81	23.83 ± 11.02
FMA-UE Shoulder & Elbow	11.88 ± 5.14	13.92 ± 5.08	15.79 ± 5.27	12.00 ± 5.31	15.75 ± 6.15	18.33 ± 6.81
FMA-UE Wrist	0.75 ± 1.62	0.75 ± 1.75	0.79 ± 1.74	0.83 ± 1.86	0.96 ± 2.05	1.08 ± 2.50
FMA-UE Hand	2.46 ± 3.12	2.83 ± 3.33	3.33 ± 3.67	3.08 ± 3.41	3.75 ± 3.69	4.42 ± 3.92
Daily activity						
BI-total score	56.21 ± 16.26	61.21 ± 13.70	64.67 ± 14.59	59.13 ± 13.71	61.79 ± 12.30	66.33 ± 11.82
BI-Involving upper limbs	15.83 ± 5.20	18.13 ± 3.68	19.33 ± 4.85	17.21 ± 4.49	19.25 ± 3.69	20.58 ± 3.04

3.3 Subgroup analysis

We analyzed the effect of RT for each Brunnstrom subgroup. In subgroup A (BRS = 2), mixed-effect linear model found significant increase in FMA-UE total score (1.028/week, $t_{26} = 6.144$, $p < 0.01$, see Figure 4A), shoulder-elbow subscale (0.944/week, $t_{26} = 5.543$, $p < 0.01$, see Figure 5A), MBI (1.722/week, $t_{26} = 2.918$, $p < 0.01$) under CT, but no significant difference in between-group interaction was found in these outcomes, meaning that the RT did not incur faster motor recovery than did the CT for subgroup A.

In subgroup B (BRS = 3), the FMA-UE score increased by 1.306/week ($t_{34} = 5.327$, $p < 0.01$) under CT, compared to the 61% faster recovery of 2.111/week under RT (significant interaction, Figure 4B). Similarly, the shoulder/elbow FMA increased by 0.972/week ($t_{34} = 4.168$, $p < 0.01$) under CT, compared to an 86% faster recovery of 1.806/week under RT ($t_{34} = 2.526$, $p < 0.05$, see Figure 5B). The hand FMA and MBI scores showed no significant between-group interaction. Taken together, our results indicated that in subgroup B (BRS = 3), faster recovery of motor functions was observed under RT than CT.

In subgroup C (BRS = 4), FMA-UE total score (1.292 per week, $t_{30} = 3.056$, $p < 0.01$, see Figure 4C), shoulder-elbow subscale (1.042 per week, $t_{30} = 3.627$, $p < 0.01$, see Figure 5C), MBI (2.750 per week, $t_{30} = 3.104$, $p < 0.01$) were found significantly increased in the CT group, but the between-group interaction was not significant.

4 Discussion

Through this study, we found that both Robot-assisted Therapy and Conventional Therapy were likely to have a positive effect on post-stroke recovery of motor function. In comparison with conventional therapy, RT showed a higher rate of improvement in FMA-UE. Across all three subgroups, the added benefits of RT seemed the most prominent in patients with moderate motor impairment (BRS = 3). Taken together, our findings supported the hypothesis that even though both RT and CT groups received stratified intervention, the recovery of motor functions in the upper extremities would be faster with RT. Our results were consistent with these well-controlled RCTs, such as the RATULS trial, which demonstrated improvements in upper limb function within groups (26). However, our findings observed significant differences in the FMA scores between groups, which might be due to the stratified intervention or the different robot types. However, with a small sample size, caution must be applied, as our findings might not be extrapolated to all stroke patients.

A probable but noteworthy finding was that RT accelerated the motor recovery in the proximal joints of the upper limb (shoulder and elbow) but not distal ones (wrist and hand). Several possible explanations exist for this finding. Firstly, the participants moved the robot by contracting muscles around the shoulder and elbow, meanwhile, they kept the wrists and fingers strapped to the handle, therefore it could be the shoulder and elbow muscles that underwent the most training. It follows that the training ought to be extended to the wrist and hand, otherwise, it would leave a minimal chance for the wrist and hand to recover. Secondly, motor skills usually transfer from the proximal to the distal segments of the limb (37), thus the shoulder and elbow would lead the wrist and hand to show recovery. Thirdly, competition of adjacent joints in movement recovery suggests that proximal joints often recover better (38). In line with these findings, the end-effector robot employed in this study emphasized larger joint movements while fixing the hand at the terminal handle. In future studies, it might be possible to alter the type of robot to balance proximal and distal joints.

Another possible implication is that among the three subgroups, moderately impaired patients (BRS = 3, Subgroup B) recovered significantly faster when treated with RT compared to CT. In other two subgroups (BRS = 2 and 4) even though the between-group differences in FMA/week were not significant, the slopes were still steeper in RT, meaning that these two subgroups both contributed to the overall trend in pooled analysis. One reason why subgroup B (BRS = 3) outperformed the others was that patients in this stage might enjoy a higher capability of voluntary movement compared to subgroup A (BRS = 2). Therefore, the training may incur more afferent activity (i.e., the training signal) for motor re-learning (39). On the other hand, subgroups with better motor function (subgroup C, BRS = 4) might not be adequately challenged using the existing parameters, which inspires future studies on how much challenge is optimal for using robot-assisted therapy.

One limitation of this study was that it could not differentiate the contribution between assistive and resistive training, which required continuous monitoring of robot-applied force and the reaction from the participant. Note that the reaction might

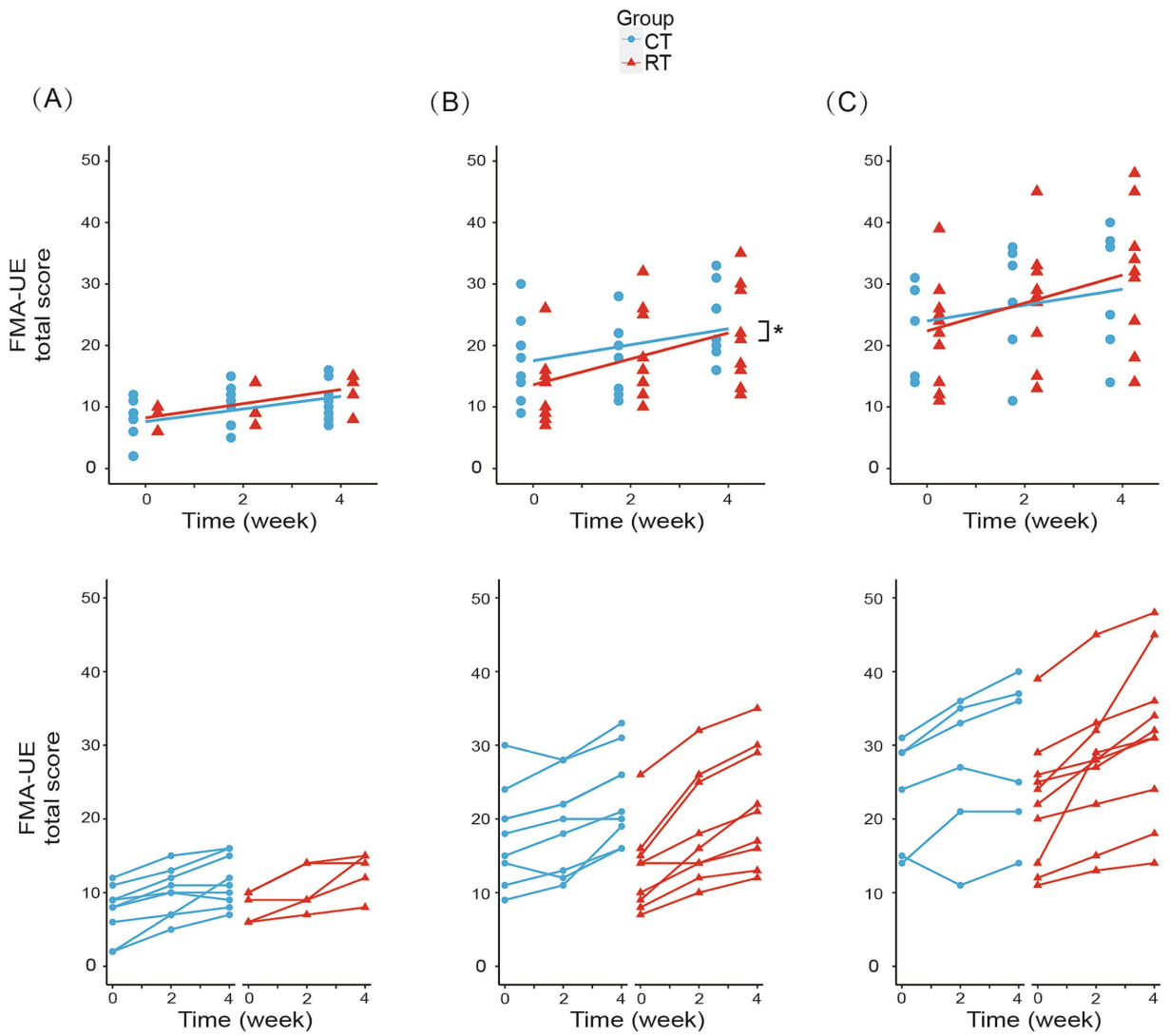

FIGURE 4
Change from baseline in FMA-UE total score in three subgroups. **(A)** In subgroup A (BRS = 2): RT group increased 1.150/week ($p < 0.01$), while CT group increased 1.028/week ($p < 0.01$). **(B)** In subgroup B (BRS = 3): RT group increased 2.111/week ($p < 0.01$), while CT group increased 1.306/week ($p < 0.01$). Between-group differences were significant ($p < 0.05$). **(C)** In subgroup C (BRS = 4): RT group increased 2.275/week ($p < 0.01$), while CT group increased 1.292/week ($p < 0.01$). The lines in the first row represent the arithmetic mean of the score. The lines in the second row represent the trend for the score of each patient in subgroups. *$p < 0.05$.

include a wide range of metrics, such as force, trajectory, electromyography, and brain activity. Another interesting but untested factor was whether the participants were compliant with the training, as has been shown critical for clinical outcome (40). Future robot-assistant studies could focus on finding more precise rehabilitation programs, such as the successful detection of voluntary muscle activity onset (41) and the utilization of brain-computer interfaces (BCI) system to achieve coordinated movements (42).

In clinic, our results support the application of robot-assisted therapy for the acceleration of post-stroke recovery in upper-extremity, especially with stratified intervention based on BRS. While this study was an initial, pilot study about the added benefits of robotics in stratified intervention for upper extremities poststroke. The clinical efficacy of our protocol was suggested by this pilot study, but it can only be asserted with larger-scale, multi-center trials.

5 Conclusion

Robot-assisted therapy showed promising clinical evidence in accelerating the poststroke recovery of upper-extremity motor performance following stratified intervention for 4 weeks. The improvements had been identified in general motor behaviors (Fugl-Meyer scores), especially in proximal parts of the upper limb. Among the tested (BRS II, III, and IV), individuals within Brunnstrom recovery stage III might benefit the most from robot-assisted training.

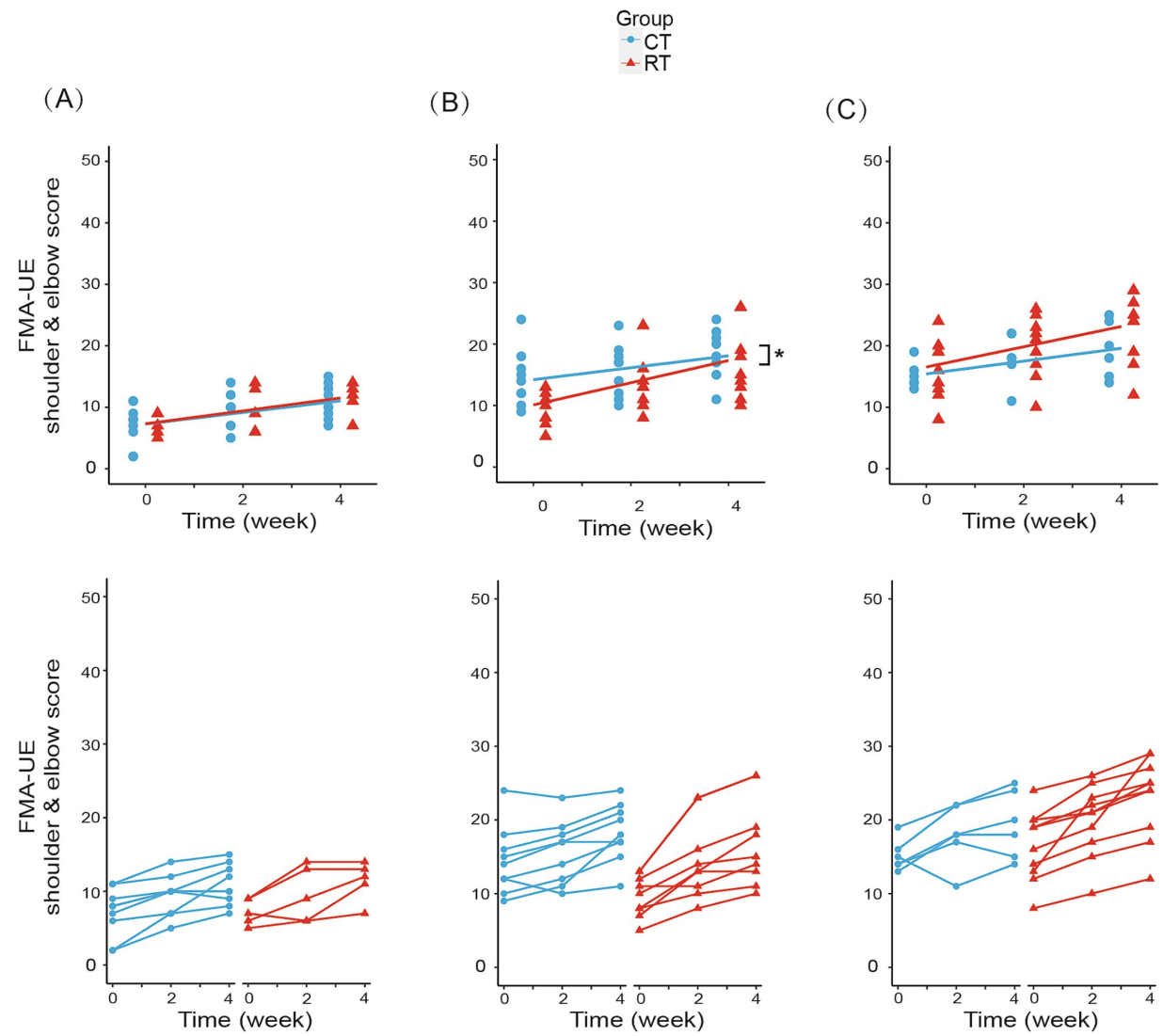

FIGURE 5
Change from baseline in FMA-UE shoulder and elbow score in three subgroups. **(A)** In subgroup A (BRS = 2): RT group increased 1.050/week ($p < 0.01$), while CT group increased 0.944/week ($p < 0.01$). **(B)** In subgroup B (BRS = 3): RT group increased 1.806/week ($p < 0.01$), while CT group increased 0.972/week ($p < 0.01$). Between-group differences were significant ($p < 0.05$). **(C)** In subgroup C (BRS = 4): RT group increased 1.650/week ($p < 0.01$), while CT group increased 1.042/week ($p < 0.01$). The lines in the first row represent the arithmetic mean of the score. The lines in the second row represent the trend for the score of each patient in subgroups. *$p < 0.05$.

However, with a small sample size, these findings cannot be extrapolated to all patients.

Data availability statement

The raw data supporting the conclusions of this article will be made available by the authors, without undue reservation.

Ethics statement

The studies involving humans were approved by the Ethics Committee of Ruijin Hospital, School of Medicine, Shanghai Jiao Tong University. The studies were conducted in accordance with the local legislation and institutional requirements. The participants provided their written informed consent to participate in this study. Written informed consent was obtained from the individual (s) for the publication of any potentially identifiable images or data included in this article.

Author contributions

YL: Data curation, Investigation, Writing – original draft, Writing – review & editing, Conceptualization, Methodology. LC: Formal analysis, Investigation, Project administration, Writing – original draft, Writing – review & editing. JW: Conceptualization, Formal analysis,

Supervision, Validation, Writing – review & editing. ZX: Data curation, Formal analysis, Investigation, Project administration, Writing – review & editing. ZC: Data curation, Investigation, Methodology, Writing – review & editing. JY: Formal Analysis, Validation, Writing – review & editing. CN: Formal analysis, Funding acquisition, Project administration, Supervision, Writing – original draft, Writing – review & editing. QX: Funding acquisition, Project administration, Supervision, Validation, Writing – original draft, Writing – review & editing.

Funding

The author(s) declare that financial support was received for the research, authorship, and/or publication of this article. This work has been supported by grants from the National Key R&D Program of China (2022YFC3602704), the National Natural Science Foundation of China (81971722), the Key disciplines construction project of Shanghai municipal (shslczdzk02701), Shanghai Municipal Health Commission (2019SY004), Shanghai Science and Technology Commission Project (19511105600), and Shanghai Jiao Tong University School of Medicine Yuan Shen Rehabilitation Research Institute Center Project (yskf3-23-1107-1).

Acknowledgments

The authors thank Jiaxi Tang for the technical support of Fourier ArmMotus M2 Robot, thank Zeyu Wang for the help in writing the manuscript, and thank Jie Zhang, Yunming Zhang, and Siyang Yu for the help during conventional therapy.

Conflict of interest

The authors declare that the research was conducted in the absence of any commercial or financial relationships that could be construed as a potential conflict of interest.

Publisher's note

Supplementary material

The Supplementary material for this article can be found online at: https://www.frontiersin.org/articles/10.3389/fneur.2024.1453508/full#supplementary-material

SUPPLEMENTARY DATA SHEET 1
The detailed demographic characteristics of participants.

References

1. Buma F, Kwakkel G, Ramsey N. Understanding upper limb recovery after stroke. *Restor Neurol Neurosci*. (2013) 31:707–22. doi: 10.3233/rnn-130332

2. Langhorne P, Coupar F, Pollock A. Motor recovery after stroke: a systematic review. *Lancet Neurol*. (2009) 8:741–54. doi: 10.1016/S1474-4422(09)70150-4

3. Saikaley M, Pauli G, Sun H, Serra JR, Iruthayarajah J, Teasell R. Network Meta-analysis of non-conventional therapies for improving upper limb motor impairment Poststroke. *Stroke*. (2022) 53:3717–27. doi: 10.1161/STROKEAHA.122.040687

4. Katsanos AH, Kamel H, Healey JS, Hart RG. Stroke prevention in atrial fibrillation: looking forward. *Circulation*. (2020) 142:2371–88. doi: 10.1161/CIRCULATIONAHA.120.049768

5. Lindsay MP, Norrving B, Sacco RL, Brainin M, Hacke W, Martins S, et al. World stroke organization (WSO): global stroke fact sheet 2019. *Int J Stroke*. (2019) 14:806–17. doi: 10.1177/1747493019881353

6. Alawieh A, Zhao J, Feng W. Factors affecting post-stroke motor recovery: implications on neurotherapy after brain injury. *Behav Brain Res*. (2018) 340:94–101. doi: 10.1016/j.bbr.2016.08.029

7. Boyd LA, Hayward KS, Ward NS, Stinear CM, Rosso C, Fisher RJ, et al. Biomarkers of stroke recovery: consensus-based core recommendations from the stroke recovery and rehabilitation roundtable. *Int J Stroke*. (2017) 12:480–93. doi: 10.1177/1747493017714176

8. Hara T, Niimi M, Yamada N, Shimamoto Y, Masuda G, Hara H, et al. Prognosis prediction of the effect of botulinum toxin therapy and intensive rehabilitation on the upper arm function in post-stroke patients using hierarchical cluster analysis. *Disabil Rehabil*. (2021) 44:6815–23. doi: 10.1080/09638288.2021.1977394

9. Rech KD, Salazar AP, Marchese RR, Schifino G, Cimolin V, Pagnussat AS. Fugl-Meyer assessment scores are related with kinematic measures in people with chronic hemiparesis after stroke. *J Stroke Cerebrovasc Dis*. (2020) 29:104463. doi: 10.1016/j.jstrokecerebrovasdis.2019.104463

10. Fugl-Meyer AR, Jääskö L, Leyman I, Olsson S, Steglind S. The post-stroke hemiplegic patient. 1. A method for evaluation of physical performance. *Scand J Rehabil Med*. (1975) 7:13–31.

11. Conroy SS, Wittenberg GF, Krebs HI, Zhan M, Bever CT, Whitall J. Robot-assisted arm training in chronic stroke: addition of transition-to-task practice. *Neurorehabil Neural Repair*. (2019) 33:751–61. doi: 10.1177/1545968319862558

12. Gladstone DJ, Danells CJ, Black SE. The Fugl-Meyer assessment of motor recovery after stroke: a critical review of its measurement properties. *Neurorehabil Neural Repair*. (2002) 16:232–40. doi: 10.1177/154596802401105171

13. Stinear CM, Lang CE, Zeiler S, Byblow WD. Advances and challenges in stroke rehabilitation. *Lancet Neurol*. (2020) 19:348–60. doi: 10.1016/S1474-4422(19)30415-6

14. Naghdi S, Ansari NN, Mansouri K, Hasson S. A neurophysiological and clinical study of Brunnstrom recovery stages in the upper limb following stroke. *Brain Inj*. (2010) 24:1372–8. doi: 10.3109/02699052.2010.506860

15. Huang C-Y, Lin G-H, Huang Y-J, Song C-Y, Lee Y-C, How M-J, et al. Improving the utility of the Brunnstrom recovery stages in patients with stroke: validation and quantification. *Medicine*. (2016) 95:e4508. doi: 10.1097/MD.0000000000004508

16. Nishimoto A, Kawakami M, Fujiwara T, Hiramoto M, Honaga K, Abe K, et al. Feasibility of task-specific brain-machine interface training for upper-extremity paralysis in patients with chronic hemiparetic stroke. *J Rehabil Med*. (2018) 50:52–8. doi: 10.2340/16501977-2275

17. Narayan Arya K, Verma R, Garg RK, Sharma VP, Agarwal M, Aggarwal GG. Meaningful task-specific training (MTST) for stroke rehabilitation: a randomized controlled trial. *Top Stroke Rehabil*. (2012) 19:193–211. doi: 10.1310/tsr1903-193

18. Yavuzer G, Selles R, Sezer N, Sütbeyaz S, Bussmann JB, Köseoğlu F, et al. Mirror therapy improves hand function in subacute stroke: a randomized controlled trial. *Arch Phys Med Rehabil*. (2008) 89:393–8. doi: 10.1016/j.apmr.2007.08.162

19. McLaren R, Signal N, Lord S, Taylor S, Henderson J, Taylor D. The volume and timing of upper limb movement in acute stroke rehabilitation: still room for improvement. *Disabil Rehabil*. (2020) 42:3237–42. doi: 10.1080/09638288.2019.1590471

20. Harris JE, Eng JJ. Strength training improves upper-limb function in individuals with stroke: a Meta-analysis. *Stroke*. (2010) 41:136–40. doi: 10.1161/STROKEAHA.109.567438

21. Saita K, Morishita T, Hyakutake K, Ogata T, Fukuda H, Kamada S, et al. Feasibility of robot-assisted rehabilitation in Poststroke recovery of upper limb function depending on the severity. *Neurol Med Chir (Tokyo)*. (2020) 60:217–22. doi: 10.2176/nmc.oa.2019-0268

22. Kwakkel G, Kollen BJ, Krebs HI. Effects of robot-assisted therapy on upper limb recovery after stroke: a systematic review. *Neurorehabil Neural Repair*. (2007) 22:111–21. doi: 10.1177/1545968307305457

23. Bertani R, Melegari C, De Cola MC, Bramanti A, Bramanti P, Calabrò RS. Effects of robot-assisted upper limb rehabilitation in stroke patients: a systematic review with meta-analysis. *Neurol Sci*. (2017) 38:1561–9. doi: 10.1007/s10072-017-2995-5

24. Mehrholz J, Pohl M, Platz T, Kugler J, Elsner B. Electromechanical and robot-assisted arm training for improving activities of daily living, arm function, and arm muscle strength after stroke. *Cochrane Database Syst Rev*. (2018) 9:CD006876. doi: 10.1002/14651858.CD006876.pub5

25. Chien W, Chong Y, Tse M, Chien C, Cheng H. Robot-assisted therapy for upper-limb rehabilitation in subacute stroke patients: a systematic review and meta-analysis. *Brain Behav*. (2020) 10:e01742. doi: 10.1002/brb3.1742

26. Rodgers H, Bosomworth H, Krebs HI, van Wijck F, Howel D, Wilson N, et al. Robot assisted training for the upper limb after stroke (RATULS): a multicentre randomised controlled trial. *Lancet*. (2019) 394:51–62. doi: 10.1016/S0140-6736(19)31055-4

27. Boutron I, Altman DG, Moher D, Schulz KF, Ravaud Pfor the CONSORT NPT Group. CONSORT statement for randomized trials of nonpharmacologic treatments: a 2017 update and a CONSORT extension for nonpharmacologic trial abstracts. *Ann Intern Med*. (2017) 167:40. doi: 10.7326/M17-0046

28. Winstein CJ, Stein J, Arena R, Bates B, Cherney LR, Cramer SC, et al. Guidelines for adult stroke rehabilitation and recovery. *Stroke*. (2016) 47:98–169. doi: 10.1161/str.0000000000000098

29. Chen Z, Wang C, Fan W, Gu M, Yasin G, Xiao S, et al. Robot-assisted arm training versus therapist-mediated training after stroke: a systematic review and Meta-analysis. *J Healthcare Eng*. (2020) 2020:1–10. doi: 10.1155/2020/8810867

30. Hernández E, Galeano C, Barbosa N, Forero S. Intra-and inter-rater reliability of Fugl-Meyer assessment of upper extremity in stroke. *J Rehabil Med*. (2019) 51:652–9. doi: 10.2340/16501977-2590

31. Ohura T, Hase K, Nakajima Y, Nakayama T. Validity and reliability of a performance evaluation tool based on the modified Barthel index for stroke patients. *BMC Med Res Methodol*. (2017) 17:131. doi: 10.1186/s12874-017-0409-2

32. Green P, Mac Leod CJ. SIMR: an R package for power analysis of generalized linear mixed models by simulation. *Methods Ecol Evol*. (2016) 7:493–8. doi: 10.1111/2041-210X.12504

33. Chinembiri B, Ming Z, Kai S, Xiu Fang Z, Wei C. The fourier M2 robotic machine combined with occupational therapy on post-stroke upper limb function and independence-related quality of life: a randomized clinical trial. *Top Stroke Rehabil*. (2020) 28:1–18. doi: 10.1080/10749357.2020.1755815

34. Lin C-H, Chou L-W, Luo H-J, Tsai P-Y, Lieu F-K, Chiang S-L, et al. Effects of computer-aided Interlimb force coupling training on paretic hand and arm motor control following chronic stroke: a randomized controlled trial. *PLoS One*. (2015) 10:e0131048. doi: 10.1371/journal.pone.0131048

35. Hernán MA, Robins JM. Per-protocol analyses of pragmatic trials. *N Engl J Med*. (2017) 377:1391–8. doi: 10.1056/NEJMsm1605385

36. Page SJ, Fulk GD, Boyne P. Clinically important differences for the upper-extremity Fugl-Meyer scale in people with minimal to moderate impairment due to chronic stroke. *Phys Ther*. (2012) 92:791–8. doi: 10.2522/ptj.20110009

37. Wilson R, Preethi R. *Stroke rehabilitation*. St. Louis, Missouri: Elsevier, (2019).

38. Hu X-L, Tong RK, Ho NSK, Xue J, Rong W, Li LSW. Wrist rehabilitation assisted by an electromyography-driven neuromuscular electrical stimulation robot after stroke. *Neurorehabil Neural Repair*. (2015) 29:767–76. doi: 10.1177/1545968314565510

39. van Dijk L, van der Sluis C, Bongers RM. Reductive and emergent views on motor learning in rehabilitation practice. *J Mot Behav*. (2016) 49:244–54. doi: 10.1080/00222895.2016.1191418

40. Mastos M, Miller K, Eliasson AC, Imms C. Goal-directed training: linking theories of treatment to clinical practice for improved functional activities in daily life. *Clin Rehabil*. (2007) 21:47–55. doi: 10.1177/0269215506073494

41. Li L, Wang X, Yao B, Zhang X, Zhou P. Sample entropy-based surface Electromyographic examination with a linear electrode Array in survivors with spinal cord injury. *IEEE Trans Neural Syst Rehabil Eng*. (2023) 31:2944–52. doi: 10.1109/TNSRE.2023.3290607

42. Li L, Zhang M, Chen Y, Wang K, Zhou G, Huang Q. TAGL: temporal-guided adaptive graph learning network for coordinated movement classification. *IEEE Trans Industr Inform*. (2024) 1–11. doi: 10.1109/TII.2024.3423311

frontiers | Frontiers in Neurorobotics

TYPE Original Research
PUBLISHED 11 October 2024
DOI 10.3389/fnbot.2024.1453571

OPEN ACCESS

EDITED BY
Yingbai Hu,
The Chinese University of Hong Kong, China

REVIEWED BY
Dan Huang,
South China University of Technology, China
Wing Yin Ng,
CUHK Department of Surgery,
Hong Kong SAR, China

*CORRESPONDENCE
Song GuanTing
✉ 19504356665@163.com

RECEIVED 23 June 2024
ACCEPTED 25 July 2024
PUBLISHED 11 October 2024

CITATION
LinLin H, Sangheang L and GuanTing S (2024) CAM-Vtrans: real-time sports training utilizing multi-modal robot data.
Front. Neurorobot. 18:1453571.
doi: 10.3389/fnbot.2024.1453571

CAM-Vtrans: real-time sports training utilizing multi-modal robot data

Hong LinLin[1], Lee Sangheang[1] and Song GuanTing[2]*

[1]College of Physical Education, Jeonju University, Jeonju, Jeollabuk-do, Republic of Korea, [2]Gongqing Institute of Science and Technology, Jiujiang, Jiangxi Province, China

Introduction: Assistive robots and human-robot interaction have become integral parts of sports training. However, existing methods often fail to provide real-time and accurate feedback, and they often lack integration of comprehensive multi-modal data.

Methods: To address these issues, we propose a groundbreaking and innovative approach: CAM-Vtrans—Cross-Attention Multi-modal Visual Transformer. By leveraging the strengths of state-of-the-art techniques such as Visual Transformers (ViT) and models like CLIP, along with cross-attention mechanisms, CAM-Vtrans harnesses the power of visual and textual information to provide athletes with highly accurate and timely feedback. Through the utilization of multi-modal robot data, CAM-Vtrans offers valuable assistance, enabling athletes to optimize their performance while minimizing potential injury risks. This novel approach represents a significant advancement in the field, offering an innovative solution to overcome the limitations of existing methods and enhance the precision and efficiency of sports training programs.

KEYWORDS

assistive robotics, human-machine interaction, balance control, movement recovery, vision-transformer, CLIP, cross-attention

1 Introduction

In the field of sports technology, the application of deep learning and machine learning techniques to enhance training efficiency and athlete performance has become a hot topic of research (Zheng et al., 2020). These technologies can accurately analyze athletes' movements and provide real-time feedback, helping athletes improve their skills more effectively (Pan et al., 2019). However, while existing technologies can handle single data sources such as video or biosensor data, their capabilities are still insufficient when it comes to integrating and processing multiple types of data (Herman et al., 2021), especially when simultaneously dealing with visual information and verbal instructions. This limitation highlights the need for the development of new methods to comprehensively understand and guide athlete training.

Traditional methods primarily rely on symbolic AI and knowledge representation for Taekwondo action recognition. Expert systems, for example, simulate human experts' decision-making processes by encoding their knowledge and provide explicit explanations for each recognition result. Yang et al. (2021) proposed a multi-knowledge representation framework for big data AI applications. Additionally, a comprehensive review by Himabindu et al. (2023) showcased the combination of symbolic reasoning and deep learning in neural-symbolic AI, highlighting its various applications and developments across different domains. Rule-based methods, on the other hand, utilize a set of predefined rules for action recognition. These methods demonstrate high determinism and reliability, performing well even in the face of complex or diverse actions. Jin et al. (2022) introduced

a deep reinforcement learning system for automatic symbol grounding discovery, while the research by Ilager et al. (2023) showcased the cost-saving benefits of symbolic representation in edge AI applications. Furthermore, logistic regression, as a statistical method, learns features from training data for classification decisions. It not only finds important applications in action recognition but also significantly improves classification accuracy. The study by Insuasti et al. (2023) demonstrated the application of logistic regression in sports action recognition, while Wu et al. (2022) further explored the use of fuzzy logic in symbolic representation, enhancing the symbolic foundations of AI. These methods offer advantages such as strong interpretability and transparency in the decision-making process. However, these methods have limitations in handling complex and diverse actions as well as limited capabilities in processing large-scale data.

To address the limitations of traditional algorithms, data-driven and machine learning-based approaches have been employed in multi-modal robot-assisted sports training. These approaches mainly utilize methods such as decision trees, random forests, and multi-layer perceptrons to tackle the challenges. This approach offers advantages such as efficient handling of large-scale data, high accuracy, and the ability to handle non-linear problems. For instance, Tjondronegoro and Chen (2006) automated event classification in sports videos using decision tree methods, while Jose et al. (2023) applied decision tree algorithms in predicting athlete performance. Furthermore, Morciano et al. (2023) used random forest algorithms to predict performance indicators of soccer players, demonstrating their superiority in handling biomechanical data, and Yagin et al. (2023) showcased the high accuracy of random forests in determining the positions of professional soccer players. Lastly, Aresta et al. (2022) highlighted the superior performance of multi-layer perceptrons in classifying elite and novice fencers based on biomechanical data, while Bakthavatchalam et al. (2022) demonstrated the efficient predictive performance of multi-layer perceptrons in agriculture. However, these methods have challenges such as overfitting, high computational costs, and strong reliance on large amounts of annotated data.

To overcome the limitations of statistical and machine learning algorithms, deep learning-based approaches have been used for Taekwondo action recognition, primarily employing Convolutional Neural Networks (CNN), reinforcement learning, and Transformer models. These methods offer higher accuracy and the ability to handle complex data. Firstly, Convolutional Neural Networks efficiently extract image features and have shown remarkable performance in predicting sports game outcomes and recognizing athlete actions. For example, Chen et al. (2020) used CNN to predict NBA game results with an accuracy of 91%, while Liu (2022) utilized CNN to improve action detection rates in sports videos. Secondly, reinforcement learning demonstrates significant potential in sports training by continuously adjusting strategies to optimize the decision-making process. The reinforcement learning approach proposed by Jia et al. (2020) improved players' winning rates in basketball training, and the research by Du et al. (2021) showcased the application of reinforcement learning in esports. Lastly, Transformer models, known for their advantages in handling sequential data, have been used for time-series analysis of motion signals, showing impressive performance. Dirgová Luptáková et al. (2022) achieved 99.2% accuracy in human activity recognition using the Transformer model, while Hauri and Vucetic (2023) combined Transformer with LSTM for team activity recognition in basketball games. However, these methods have challenges such as high computational complexity and a demand for large-scale training data.

Considering these challenges, this study proposes a novel approach, CAM-Vtrans: Real-time Sports Training Utilizing Multi-modal Robot Data, to address the limitations of traditional and machine learning algorithms, such as poor adaptability to complex environments, high computational costs, and dependency on large labeled datasets. CAM-Vtrans combines Vision Transformer (ViT), CLIP, and cross-attention mechanisms. ViT divides the image into multiple small patches and encodes them as a sequence, utilizing the self-attention mechanism to process these sequences and capture complex relationships within the image. This approach is particularly effective in handling sports activity images with rich details. The introduction of the CLIP model enables the system to understand training instructions in natural language and combines them with visual data to provide context-aware feedback. Through the cross-attention mechanism, this system further optimizes the fusion of different modalities, making the transformation from visual information to language descriptions more accurate and efficient. This integrated approach not only enhances the accuracy and efficiency of sports training analysis but also significantly reduces the computational burden and reliance on extensive labeled data.

The main contributions of this research can be summarized as follows:

- CAM-Vtrans is an innovative approach that combines Vision Transformer (ViT), the CLIP model, and cross-attention mechanisms to process and analyze multi-modal robot data in real-time, enhancing the accuracy of feedback in sports training.
- This method performs exceptionally well in various multi-scenario applications, efficiently handling complex sports activity images. It possesses broad applicability and adaptability, providing reliable support for different training requirements.
- Experimental results demonstrate that CAM-Vtrans significantly outperforms traditional methods in action recognition and feedback accuracy, greatly improving the effectiveness of sports training while reducing computational costs and reliance on large-scale annotated data.

2 Related work

2.1 Assisting sports training

In recent years, machine learning has made significant progress in assisting sports training tasks. Traditional sports training methods heavily rely on coaches' experience and intuition, which often suffer from subjectivity and lack of precision. The

introduction of machine learning has made the training process more scientific and systematic. Classic machine learning algorithms such as decision trees, random forests, and logistic regression have been widely applied in areas such as athlete performance prediction and injury risk assessment. For example, decision tree-based systems can provide personalized training recommendations by analyzing athletes' physiological and training data (Jose et al., 2023). However, these traditional machine learning methods also have some notable drawbacks and limitations (Tang et al., 2023). Firstly, these methods require high-quality and large quantities of labeled data to train models, which can be costly to acquire. Moreover, traditional machine learning algorithms exhibit limitations when dealing with complex and multi-dimensional sports data. For instance, while random forests can handle non-linear relationships to some extent, they still struggle with highly complex and dynamically changing sports data (Morciano et al., 2023). Additionally, these methods lack interpretability and explainability, making it difficult to provide clear explanations for training outcomes and limiting their practical applications (Dong et al., 2024). To overcome these limitations, deep learning methods have gradually become a research focus in the field of sports training. Deep learning, by constructing multi-layer neural networks, can better capture complex features and patterns, thus improving the predictive accuracy and robustness of models. However, deep learning methods also face challenges such as high computational costs, long training times, and dependence on large-scale annotated data, which still need to be further addressed in practical applications (Wang et al., 2024)

2.2 Transformer models

Since its introduction in 2017, the Transformer model has achieved groundbreaking advancements across multiple domains. Its unique self-attention mechanism and parallel processing capabilities have made Transformers particularly prominent in natural language processing (NLP) tasks. For instance, models like BERT and GPT, which are based on Transformer architecture, have demonstrated significant effectiveness in tasks such as language understanding, text generation, and machine translation. The Transformer model addresses the inefficiencies and vanishing gradient problems associated with traditional sequential models like RNNs and LSTMs by processing input sequences in parallel and dividing them into smaller chunks (Lu et al., 2024). Beyond NLP, the Transformer model has also shown strong capabilities in the field of computer vision (CV). Vision Transformer (ViT), by dividing images into fixed-size patches and processing these patches as input sequences, has achieved performance comparable to or even surpassing that of convolutional neural networks (CNNs). ViT has excelled in tasks such as image classification, object detection, and image segmentation, proving the potential of Transformers in handling visual data (Hu et al., 2019). In addition, the Transformer model has wide-ranging applications in time series data analysis, recommendation systems, and game AI. In time series data analysis, Transformers can effectively capture long-term dependencies, enhancing prediction accuracy. In recommendation systems, Transformers model user behavior sequences to provide more precise recommendations. In game AI, Transformers, combined with deep reinforcement learning, optimize strategy selection.

2.3 Sports action recognition

Sports action recognition is a crucial research area in sports science and computer vision, aiming to automatically identify and evaluate athletic performance by analyzing athletes' motion data. Traditional action recognition methods primarily rely on feature engineering-based machine learning algorithms, such as support vector machines, decision trees, and random forests. These methods extract features from motion data for classification and recognition, achieving certain levels of effectiveness (Zhao et al., 2020). With the development of deep learning technologies, the advantages of convolutional neural networks (CNNs) in image and video processing have become increasingly apparent, leading to their widespread application in sports action recognition. CNNs can automatically learn and extract high-level features from data, significantly improving the accuracy and robustness of action recognition (Zou et al., 2019). Additionally, temporal models in deep learning, such as long short-term memory networks (LSTMs) and Transformer models, have been applied to action recognition, better handling time series data and capturing dynamic changes in actions. However, despite the impressive performance of deep learning methods in action recognition, several challenges and limitations persist. First, deep learning models require large-scale annotated data, and acquiring and annotating sports action data is costly, limiting the effectiveness of model training. Second, deep learning models have high computational complexity, requiring substantial computational resources and time for training and inference, which can be a bottleneck in real-time applications. Moreover, existing action recognition models still face difficulties in handling complex and diverse actions, making it challenging to adapt to various sports scenarios and action types. To address these issues, researchers are exploring multi-modal data fusion methods, combining visual, auditory, and tactile data to enhance the accuracy and robustness of action recognition (Li et al., 2018). Additionally, emerging technologies such as reinforcement learning and self-supervised learning are being introduced to action recognition to reduce reliance on annotated data and improve model generalization. Despite these advancements, achieving efficient, accurate, and robust sports action recognition remains a challenging research topic, necessitating further exploration and innovation.

3 Methodology

3.1 Overview of our network

In this research, we propose a multimodal robotic system that combines Vision Transformer (ViT), CLIP, and cross-attention mechanisms for real-time feedback and guidance in sports training. The main innovation of this system lies in the use

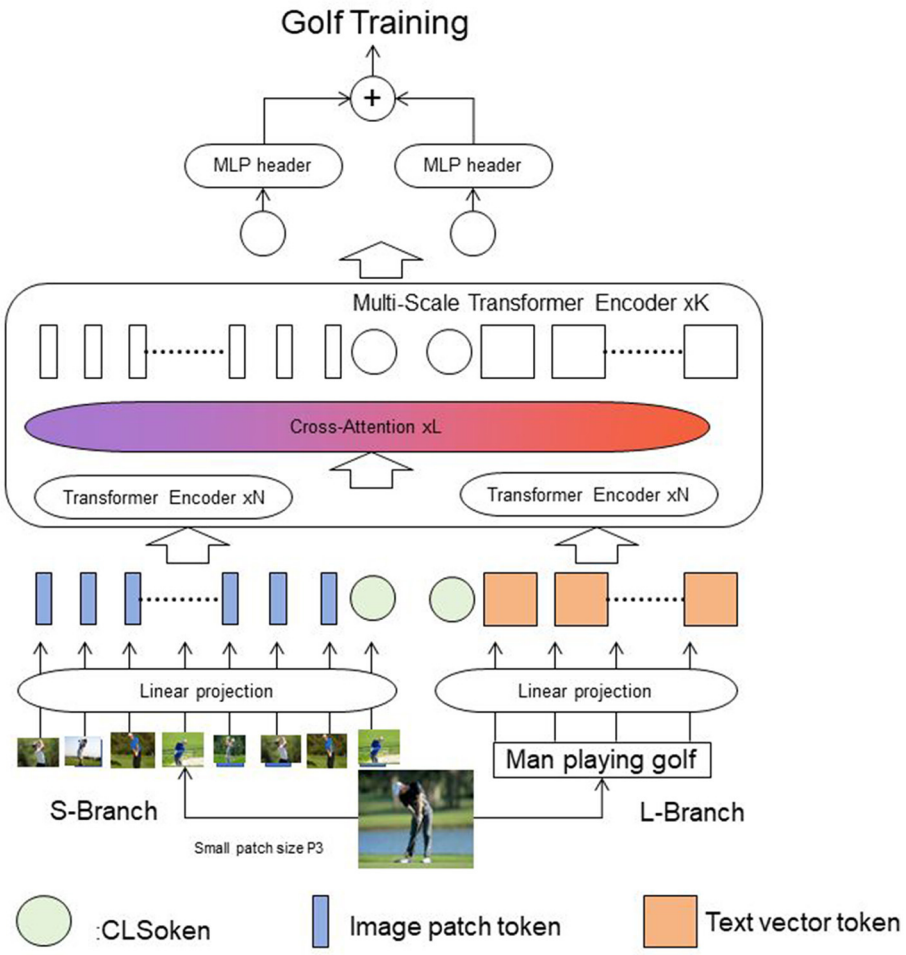

FIGURE 1
The overall framework diagram of the proposed method is presented.

of advanced visual and language processing models to analyze athletes' performances in-depth and provide immediate guidance and feedback.

Figure 1 shows the overall framework diagram of the proposed method.

Textual information is inputted from the L-Branch branch and is segmented into words or subwords. The text is then transformed into fixed-dimensional vector representations through an embedding layer. These text vectors are linearly projected and inputted into the corresponding Transformer Encoder. Images are inputted from the S-Branch, and each branch's image is divided into fixed-sized patches. After linear projection, the image patches are inputted into their respective Transformer Encoders. The image and text features interact and fuse through a Cross-Attention mechanism. The Cross-Attention layer takes features from the image and text encoders, calculates the correlation between them, and generates a fused multimodal feature representation. The fused multimodal features are further processed by a Multi-Scale Transformer Encoder layer to capture features at different scales, enhancing the expressive power of the features. Finally, a Multi-Layer Perceptron (MLP) head is used for tasks such as classification or regression. In the revised version, we will update Figure 1 to visually illustrate the processing and flow of textual information, including adding a schematic diagram of text input, demonstrating the processing of text through the embedding layer and linear projection layer, and clarifying the interaction between image and text features in the Section 3.4.

Differentiation from prior work: While the combination of ViT, CLIP, and Cross-Attention has been proposed in other domains, our research is the first to apply it to real-time sports coaching systems. Unlike previous studies, our research focuses on effectively integrating visual and textual data in dynamic and real-time sports training environments. Specifically, our proposed CAM-Vtrans system takes into account the continuity and complexity of sports actions during its design. Through optimized Cross-Attention mechanisms and multi-scale feature extraction modules, the system is able to provide stable and accurate feedback even with high-frequency inputs.

Overcoming limitations of previous methods: Previous methods often suffer from low computational efficiency and long feedback latency when dealing with real-time multimodal data.

In this research, we address these limitations by introducing the ViT-Adapter module, which enhances feature extraction efficiency. Through optimized Cross-Attention mechanisms, we achieve faster and more accurate multimodal data fusion. Compared to traditional single-modal or inefficient multimodal methods, the CAM-Vtrans system significantly reduces inference time and improves the accuracy of real-time feedback, overcoming the limitations of previous methods in terms of real-time performance and data fusion.

Reasons for method selection: We chose the combination of ViT, CLIP, and Cross-Attention because these techniques have demonstrated excellent performance in handling complex visual and textual data. ViT is renowned for its powerful visual feature extraction capabilities, while CLIP effectively maps visual and textual data to the same feature space, enabling cross-modal understanding. The Cross-Attention mechanism efficiently establishes correlations between different modalities, enhancing information fusion. These characteristics make them well-suited for application in sports training scenarios that involve large amounts of visual and textual data and require real-time feedback. Therefore, the selection of these methods is not random but based on their superiority in multimodal data processing and real-time performance.

Firstly, the Vision Transformer (ViT) is employed to process video data captured from multiple cameras. ViT divides each frame into several image patches, converts these patches into a sequence of vectors, and processes them with self-attention mechanisms to identify key visual information. This approach allows the model to focus on specific regions within the image that are relevant to the movement technique, improving the accuracy and granularity of motion analysis. Simultaneously, the CLIP model is utilized to process and parse natural language inputs such as coach instructions or verbal feedback from athletes. CLIP learns from a large corpus of image-text pairs, establishing intuitive associations between image content and textual descriptions. This enables CLIP to directly relate language descriptions to visual data, providing robust support for precise understanding of movement techniques and coach's intentions. In the implementation workflow, once the athlete starts training, the system collects video and audio data in real-time. The visual and language data are processed separately by ViT and CLIP, respectively, and then fed into the cross-attention layer. In this layer, the system analyzes the correlations and interactions between visual and language information, optimizing the fusion process to extract the most valuable insights from the inputs. The core of the cross-attention mechanism lies in its ability to dynamically adjust the focus on different data sources based on specific training scenarios, providing more personalized and goal-oriented training recommendations. After performing these analyses, the system generates specific feedback reports, including action correction guidelines, performance evaluations, and improvement suggestions. This feedback can be presented directly to the athlete through a graphical user interface or sent to the coach via mobile devices. Additionally, the system includes a feedback adjustment module that allows the coach to fine-tune the level and frequency of feedback as needed, ensuring training continuity and adaptability. The focal point of the entire system design is to ensure real-time and accurate feedback, making the training process more intelligent and efficient. The aim is to maximize athletes' performance and training effectiveness through technological means.

3.2 Vision-transformer

Vision Transformer (ViT) (Miyazawa et al., 2022) is a deep learning model that applies the Transformer architecture to process visual data. Traditionally, Convolutional Neural Networks (CNNs) have been the dominant approach for visual tasks,

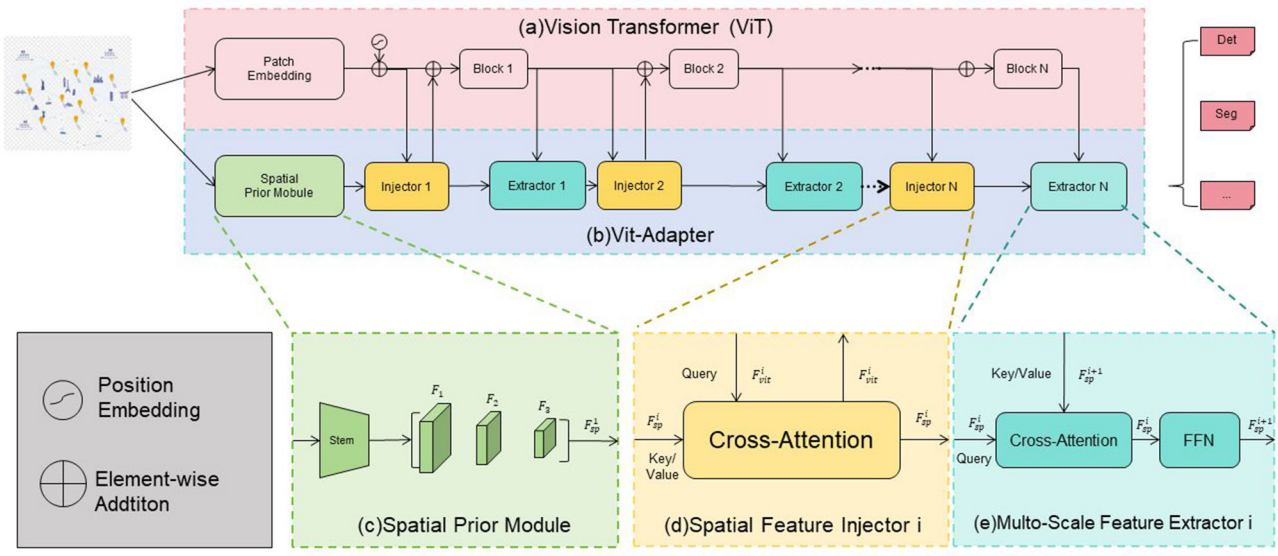

FIGURE 2
A schematic diagram of the principle of vision-transformer model.

but ViT introduces a novel paradigm by leveraging the self-attention mechanism of Transformers (Papadakis and Spyrou, 2024). Figure 2 is a schematic diagram of the principle of Vision-transformer Model.

The ViT-Adapter consists of the following components: Firstly, the Spatial Prior Module is responsible for initially extracting spatial features from the input image. The image first goes through the Stem layer, generating a series of feature maps (F1, F2, F3, ..., Fsp) that capture spatial information at different scales, preparing for the subsequent feature injection. Secondly, the Spatial Feature Injector is one of the key modules of the ViT-Adapter. It injects the spatial features (Fsp) extracted by the Spatial Prior Module into the intermediate features (Fvit) of the ViT using a Cross-Attention mechanism. Specifically, the intermediate features of the ViT serve as the Query, while the spatial features act as the Key and Value. The Cross-Attention calculates the fused features (Fsp + Fvit). Then, the Multi-Scale Feature Extractor further processes the fused features through multiple Cross-Attention layers and a Feed-Forward Neural Network (FFN) to enhance the expressive power of multi-scale features, enabling the model to better capture image details and global information. Additionally, the ViT-Adapter inserts Injector and Extractor modules between each block of the ViT. The Injector module injects the features from the Spatial Prior Module into the current ViT features, while the Extractor module extracts useful information from the fused features for the next Transformer Block to use. Finally, after being processed by multiple Transformer Blocks and ViT-Adapter modules, the final features are fed into a Multi-Layer Perceptron (MLP) head for tasks such as classification, detection, or segmentation. Through these improvements, the ViT-Adapter significantly enhances the ViT model's ability to capture spatial features when processing images, improving its performance in various visual tasks.

The Vision Transformer (ViT) model operates by dividing an input image into smaller patches, which are then flattened into a sequence of 1D vectors capturing local visual information. These patches are linearly projected into higher-dimensional embeddings, serving as the input to the Transformer model. The Transformer architecture, composed of multiple identical layers each containing a self-attention mechanism and a feed-forward neural network, captures both global and local dependencies within the sequence of patches. During self-attention, patches exchange information and capture long-range dependencies, with attended representations aggregated and combined with original patch representations using residual connections. This process refines the patch representations based on contextual information. After multiple layers, the final image representation is obtained, which can be used for tasks like image classification, object detection, or segmentation. ViT's advantages include capturing global and local information, scalability, and learning from raw pixels without hand-engineered features. However, its self-attention mechanism's quadratic computational complexity is a limitation. In real-time feedback for multimodal robots in sports training, ViT analyzes visual information to understand and provide guidance on body movements. Trained on annotated sports videos, ViT extracts relevant features and captures spatial relationships, enabling the robot to offer accurate, context-aware feedback by leveraging self-attention to focus on critical image regions and dependencies between patches.

The input image is divided into patches, resulting in a sequence of patches, denoted by x_i, where i represents the index of each patch. Each patch is then linearly projected to a higher-dimensional embedding space using a learnable linear transformation. Let's denote the projected embeddings as z_i.

The self-attention mechanism in ViT is defined by the following equations (Equation 1):

$$\text{Attention}(Q, K, V) = \text{softmax}\left(\frac{QK^T}{\sqrt{d_k}}\right)V \tag{1}$$

Here, Q, K, and V are the query, key, and value matrices, respectively. They are derived from the projected embeddings z_i as follows:

$$Q = ZW_Q\, K = ZW_K\, V = ZW_V \tag{2}$$

In these equations, Z is the matrix obtained by stacking the projected embeddings z_i, and W_Q, W_K, and W_V are learnable linear transformation matrices (Equation 2).

The self-attention mechanism calculates the attention weights between patches by computing the dot product similarity between the query and key matrices, scaled by the square root of the dimension d_k. The softmax function is applied to obtain the attention weights, which are then used to weight the values V.

The attended representations are computed as follows (Equation 3):

$$\text{SelfAtt}(Z) = \text{Attention}(Q, K, V) \tag{3}$$

The attended representations are then combined with the original patch embeddings using a residual connection, resulting in the intermediate representations:

$$\text{Intermediate}(Z) = \text{LayerNorm}(Z + \text{SelfAtt}(Z)) \tag{4}$$

Here, LayerNorm denotes layer normalization (Equation 4).

The intermediate representations are then passed through a feed-forward neural network (FFN) with two linear transformations and a non-linear activation function, typically a GELU activation:

$$\text{FFN}(Z) = \text{GELU}(\text{Intermediate}(Z)W_1 + b_1)W_2 + b_2 \tag{5}$$

W_1, W_2, b_1, and b_2 are learnable parameters of the feed-forward network (Equation 5).

The output of the ViT model is obtained by stacking multiple layers of self-attention and feed-forward networks. The final representation of the image is typically obtained by applying mean pooling to the patch embeddings.

In summary, Vision Transformer is a powerful model for visual processing that replaces traditional convolutional approaches with self-attention mechanisms. Its ability to capture global and local dependencies makes it well-suited for understanding and analyzing visual data in real-time feedback and guidance systems for multimodal robots in sports training.

3.3 CLIP

CLIP (Contrastive Language-Image Pretraining) is a deep learning model that learns to associate images and their corresponding text descriptions (Dobrzycki et al., 2023). It aims to bridge the gap between vision and language modalities, enabling cross-modal understanding and reasoning. The key idea behind CLIP is to leverage large-scale pretraining on a dataset of image-text pairs, allowing the model to learn rich representations that capture the semantic relationship between visual and textual information (Koh et al., 2024). The basic principle of the CLIP model involves jointly training a vision encoder and a text encoder. The vision encoder processes images and maps them to a high-dimensional latent space, while the text encoder processes textual descriptions and maps them to the same latent space. The encoders are trained to ensure that corresponding image-text pairs are closer to each other in the latent space compared to non-corresponding pairs. Figure 3 is a schematic diagram of the principle of CLIP Model.

The training process of CLIP involves several key steps: first, the input image is encoded by a vision encoder, typically a convolutional neural network (CNN), which extracts visual features and projects them into a latent space using a learnable linear transformation. Simultaneously, the input text description is encoded by a text encoder based on a Transformer architecture, which tokenizes the text, applies word embeddings, and processes it through multiple Transformer layers to produce the text's representation in the latent space. CLIP utilizes a contrastive loss function to maximize the similarity between corresponding image-text pairs while minimizing the similarity between non-corresponding pairs, achieved by measuring the cosine similarity between their latent representations. Pretraining on large-scale datasets, such as Conceptual Captions and ImageNet, enables CLIP to learn generalizable representations capturing the semantic relationship between images and texts. After pretraining, CLIP can be fine-tuned for downstream tasks like image classification, object detection, or image captioning. In real-time feedback and guidance for multimodal robots in sports training, CLIP is crucial for understanding and associating visual and textual information. By aligning and reasoning about sports movements based on annotated image-text pairs, CLIP allows the robot to understand textual annotations related to key movements, techniques, and performance indicators. Leveraging the pretrained CLIP model, the robot can generate real-time feedback and guidance based on its comprehension of the athlete's movements and the semantic context provided by textual information.

Let's consider an image-text pair with an image I and a text description T.

Image Encoding: The image I is processed by a vision encoder, typically a convolutional neural network (CNN), to extract visual features. Let's denote the image representation as v_I. Text Encoding: The text description T is processed by a text encoder, typically a Transformer-based architecture, to encode the textual information. Let's denote the text representation as v_T. Similarity Measurement: The similarity between the image and text representations is measured using cosine similarity. It can be calculated as:

$$\text{Similarity}(v_I, v_T) = \frac{v_I \cdot v_T}{|v_I| \cdot |v_T|} \tag{6}$$

Here, $\cdot$ denotes the dot product, and $|\cdot|$ represents the Euclidean norm (Equation 6).

Contrastive Loss: CLIP utilizes a contrastive loss function to train the model. Given a positive pair (an image-text pair that matches) and a set of negative pairs (image-text pairs that do not match), the contrastive loss encourages the positive pair to have a higher similarity than the negative pairs. The contrastive loss can be formulated as:

$$\text{Loss} = -\log\left(\frac{\exp(\text{Similarity}(v_I, v_T))}{\sum_{j=1}^{N}\exp(\text{Similarity}(v_I, v_{T_j}))}\right) \tag{7}$$

Here, N represents the number of negative pairs, and v_{T_j} denotes the text representation of the j-th negative pair (Equation 7).

The loss function aims to maximize the similarity between the positive image-text pair while minimizing the similarities between the positive pair and negative pairs. During training, the model optimizes the parameters of the image and text encoders to minimize the contrastive loss. This process enables the model to learn representations that associate images and their corresponding text descriptions. In summary, CLIP is a powerful model that combines image and text encoders to learn joint representations of visual and textual information. Its large-scale pretraining on image-text pairs enables it to capture the semantic relationship between these modalities. In the context of real-time feedback and guidance in sports training, CLIP enhances the multimodal robot's understanding and reasoning capabilities, facilitating personalized feedback and guidance based on the combination of visual and textual information.

3.4 Cross-Attention

Cross-Attention is a key component in models that handle multi-modal tasks, such as image captioning, visual question answering, and image-text matching (Kim et al., 2023). It enables the model to attend to relevant information from one modality (e.g., images) based on the input from another modality (e.g., text). The basic principle of Cross-Attention involves computing attention weights between elements in two different modalities and using these weights to combine the information effectively (Björkstrand et al., 2023).

Figure 4 is a schematic diagram of the principle of Cross-Attention.

Encoding: The image is typically encoded using a convolutional neural network (CNN), which extracts visual features from the image. The text description is encoded using a recurrent neural network (RNN) or a Transformer-based architecture, generating a sequence of hidden states. Query, Key, and Value: The hidden states from the text description serve as the query, while the visual features from the image act as the key and value. These query, key, and value representations are used to compute attention weights. Attention Calculation: The attention weights are computed by measuring the similarity between the query and key representations. This can be achieved through various methods, such as dot product, scaled dot product, or bilinear attention.

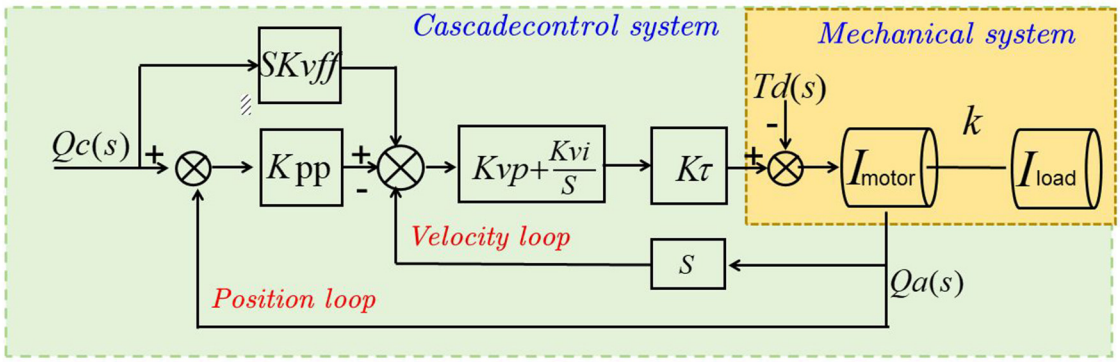

FIGURE 3
A schematic diagram of the principle of CLIP model.

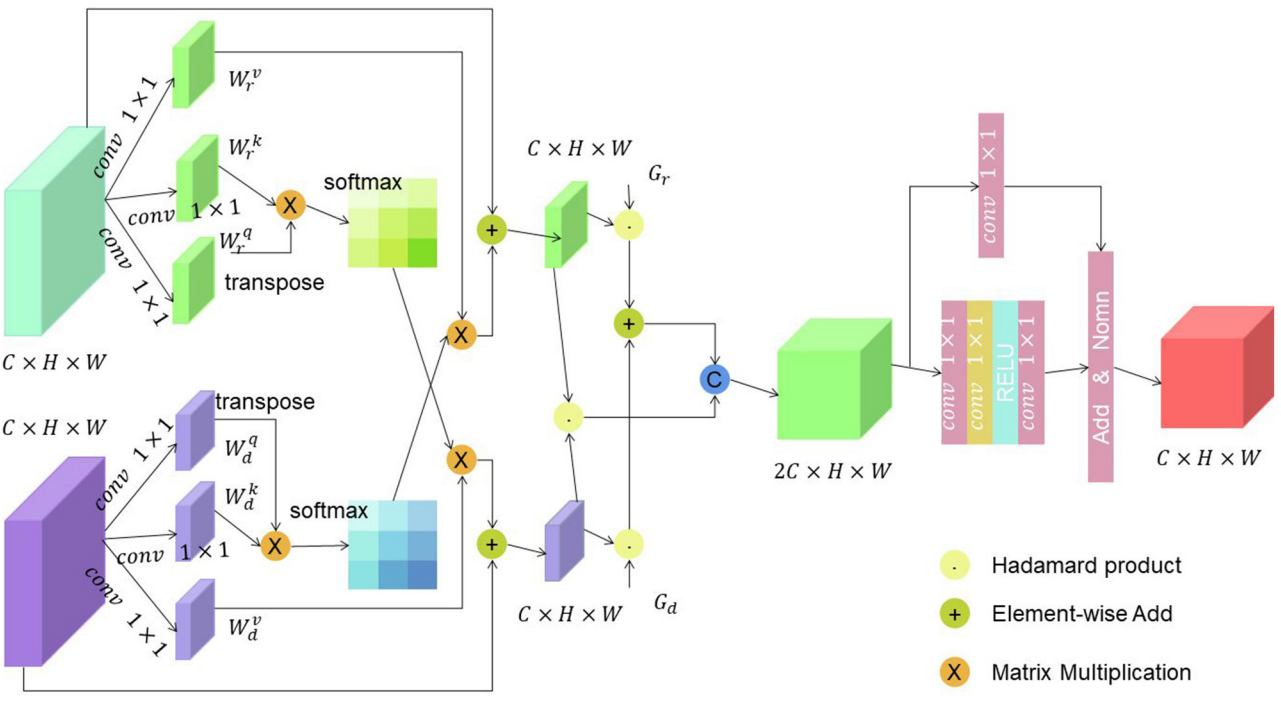

FIGURE 4
A schematic diagram of the principle of Cross-Attention.

The attention weights determine how much each visual feature should contribute to the final attended representation. Weighted Combination: The attention weights are used to weight the values (visual features) associated with each key. The weighted values are then combined to form the attended representation. This process allows the model to focus on the most relevant visual information based on the text query. Integration: The attended representation is integrated with the original text representation, typically through concatenation or element-wise addition. This integration step enables the model to capture the cross-modal interactions and create a fused representation that combines both text and visual information. The Cross-Attention mechanism plays a crucial role in multi-modal tasks by allowing the model to attend to relevant visual information conditioned on the textual input. It enables the model to align and associate the text and visual modalities, facilitating a comprehensive understanding and reasoning about the given input.

For example, in image captioning, the Cross-Attention mechanism helps the model generate descriptive captions by attending to relevant image regions while generating each word of the caption. In visual question answering, Cross-Attention allows the model to attend to specific image regions that are relevant to answering the question posed in the text. In image-text matching, Cross-Attention helps align and measure the similarity between image and text representations for tasks such as retrieval and ranking.

Let's consider two modalities, Modality A and Modality B, with their respective representations: Query (Q), Key (K), and Value (V).

The Cross-Attention mechanism involves the following steps:

Compute Attention Weights: The attention weights are calculated by measuring the similarity between the query representation (Q) and the key representation (K). One common approach is to use the dot product:

$$\text{AttentionWeights} = \text{softmax}\left(\frac{Q \cdot K^T}{\sqrt{d_k}}\right) \tag{8}$$

Here, d_k represents the dimensionality of the key representation (K). The softmax function ensures that the attention weights sum up to 1 (Equation 8).

Weighted Combination: The attention weights are used to weight the values (V) associated with each key. The weighted values are then combined to obtain the attended representation:

$$\text{AttendedRepresentation} = \text{AttentionWeights} \cdot V \tag{9}$$

The above Equation 9 represent a simplified version of Cross-Attention and assume single-head attention. In practice, multi-head attention is often employed to capture different aspects and provide richer representations. Cross-Attention allows the model to attend to relevant information in one modality based on the input from another modality. It enables the model to align and associate the information across modalities, facilitating tasks that involve multi-modal understanding, generation, and reasoning. Cross-Attention is a fundamental mechanism in multi-modal models that allows the model to attend to relevant information from one modality based on the input from another modality. It facilitates the fusion of text and visual information, enabling comprehensive understanding and reasoning in tasks involving multiple modalities.

4 Experiment

4.1 Datasets

This article uses the following four datasets:

OpenImages Dataset (Kuznetsova et al., 2020): OpenImages is a large-scale dataset consisting of annotated images from a wide range of categories. It contains over 9 million images with annotations for object detection, segmentation, and classification tasks. The dataset provides a diverse collection of visual data for training and evaluating computer vision models.

Objects365 Dataset (Shao et al., 2019): Objects365 is another comprehensive dataset that focuses on object detection and instance segmentation. It contains over 365 object categories, with more than 2 million labeled instances. The dataset is designed to cover a wide range of object classes and poses, providing a rich resource for training and evaluating object recognition models.

MSCOCO Dataset (Lin et al., 2014): MSCOCO (Microsoft Common Objects in Context) is a widely used benchmark dataset for object detection, segmentation, and captioning tasks. It consists of around 330,000 images, each annotated with object bounding boxes, segmentation masks, and image captions. MSCOCO offers a diverse set of images with multiple object instances and complex scenes, making it suitable for training and evaluating models in various visual tasks.

VG-Gap Dataset (Santana et al., 2015): VG-Gap is a dataset specifically focused on visual grounding and referring expression comprehension. It includes images from the Visual Genome dataset, accompanied by referring expressions that describe specific objects or regions within the images. The dataset is designed to facilitate research on understanding natural language instructions and grounding them to visual content.

4.2 Experimental details

In the experiment of our real-time feedback and guidance method for sports training based on a multimodal robot system, we utilized four widely recognized datasets: OpenImages, Objects365, MSCOCO, and VG-Gap, for training and validation of systems based on Vision Transformer (ViT), CLIP, and cross-attention mechanism. The training-validation split was set to 80% and 20% respectively. We designed two main experiments: metric comparison experiment and ablation experiment to evaluate and validate the performance and effectiveness of the systems. In the metric comparison experiment, we first established baseline models using traditional Convolutional Neural Networks (CNNs) and Long Short-Term Memory networks (LSTMs) as control groups for the same tasks. Subsequently, we deployed our multimodal system and focused on evaluating key performance metrics such as training time (in seconds), inference time (in milliseconds), model parameters (in millions), computational complexity (in billions of FLOPs), accuracy, AUC, recall, and F1 score. To ensure the experiment's accuracy, each model was run on the same hardware and software environment to eliminate the influence of external variables. Each model was trained and tested on an equal amount of data to ensure the comparability of results. Specifically, we utilized 8 A100 GPUs for training, employed the Adam optimizer, and set the following hyperparameters: learning rate of 0.001, batch size of 32, and 50 training epochs. We implemented the models using the Python programming language and the PyTorch framework. In the ablation experiment, we systematically removed key components from the system: first the cross-attention mechanism, then the CLIP module, and finally the Vision Transformer. We observed the impact of each modification on the model's performance. This approach helped us understand the contribution of each component to the overall system performance and identify indispensable parts in the system. Throughout the process, the aforementioned performance metrics were used to evaluate and quantify the importance and effectiveness of each component. Through these experiments, we gained detailed insights into the specific impact of different modules on the system's performance. We were also able to compare the efficiency and effectiveness of our approach in handling complex sports training scenarios with traditional methods. The in-depth analysis of the experimental results not only validated the effectiveness of our approach but also demonstrated the potential application value of multimodal interactive systems in real-time sports training guidance. Additionally, these experimental results

provide valuable data support and practical experience for future research in this field, contributing to further optimization and development of more efficient and accurate training assistance systems.

Algorithm 1 shows the training process of the proposed method.

Input: OpenImages Dataset, Objects365 Dataset, MSCOCO Dataset, VG-Gap Dataset
Output: Trained ViT-Net model

```
Initialize ViT-Net model with pre-trained weights;
Initialize optimizer with suitable learning rate;
Initialize loss function (e.g., cross-entropy);
while not converged do
    Sample a mini-batch of images and corresponding labels from the training dataset;
    for each image do
        Encode the image using Vision Transformer;
        for each object in the image do
            Encode the object using CLIP;
            Apply Cross-Attention mechanism to combine visual and textual features;
            Forward propagate the input through the ViT-Net;
            Compute the predicted probabilities for each class;
        end
        Calculate the loss between predicted probabilities and ground truth labels;
        Update the model parameters using backpropagation;
        Apply optimization step to update the weights;
    end
    Evaluate the model on the validation dataset;
    Calculate performance metrics (e.g., Accuracy, Recall, Precision);
    if performance metrics have improved then
        Save the current model weights as the best model;
    end
end
return Trained ViT-Net model
```

Algorithm 1. ViT-Net training.

4.3 Experimental results and analysis

Table 1 presents the performance comparison between our proposed model and models from other researchers on the OpenImages and Objects365 datasets. This comparison experiment focuses on four main performance metrics: Accuracy, Recall, F1 Score, and AUC (Area Under the Curve), which collectively evaluate the overall performance of the models in classification tasks. Accuracy measures the proportion of correct predictions made by the model, Recall focuses on the proportion of relevant instances identified by the model out of all relevant instances, F1 Score is the harmonic mean of Precision and Recall, providing an overall performance assessment, while AUC measures the overall performance of the model in predicting different classes. The results demonstrate that our model outperforms other methods in all metrics, particularly exhibiting outstanding performance on the Objects365 dataset, showcasing its superior image parsing and classification capabilities. This can be attributed to our model's ability to effectively combine the characteristics of Vision Transformer and CLIP, better understanding image content and contextual information through cross-attention mechanisms.

Table 2 showcases the comparison of computational efficiency on the MSCOCO and VG-Gap datasets, covering model parameters, computational complexity (FLOPs), inference time, and training time. Parameters and FLOPs reflect the complexity of the model and the computational resources required at runtime, with lower values indicating a lighter and more efficient model. Inference time and training time are directly related to the practical application of the model, with lower inference time and training time indicating real-time and cost-effective deployment. Our model demonstrates excellent performance in these metrics as well, particularly showcasing significant advantages in inference time and training time, proving its efficiency and practicality in real-world deployment.

We compared our method with GPT-3.5 using the OpenAI API, and the results are presented in Tables 1, 2. Our model outperforms GPT-3.5 in key metrics such as accuracy, recall, Inference Time(ms) and Training Time(s), as evaluated on the OpenImages, Objects365, MSCOCO, and VG-Gap datasets. In Table 2, the inference time is reported for every 10 images. Therefore, an inference time of 192 ms corresponds to every 10 images, which means the inference time per frame is 19.2 ms. This translates to approximately 52 frames per second (FPS), meeting the real-time requirement of 25 FPS. Additionally, by applying pruning and distillation techniques to our algorithm, we further optimized the model to achieve close to 60 FPS without significant loss in performance. Hence, our method satisfies the real-time demands in practical applications.

Table 3 focuses on the ablation experiment analyzing the impact of the Cross-Attention Module on the OpenImages and Objects365 datasets. The experimental setup involves removing or modifying the Cross-Attention Module and observing the changes in Accuracy, Recall, F1 Score, and AUC. AM (Attention Module), Seif-AM (Self-Attention Module), and Dynamic-AM (Dynamic Attention Module) represent different configurations of the Cross-Attention Module. By comparing these configurations, we discovered that the complete Cross-Attention Module significantly enhances all performance metrics, demonstrating its crucial role in integrating visual and textual information and improving the overall recognition capability of the model. Our model experiences a performance decline when the Cross-Attention mechanism

TABLE 1 Performance comparison on OpenImages and Objects365 datasets.

Model	OpenImages dataset				Objects365 dataset			
	Accuracy	Recall	F1 score	AUC	Accuracy	Recall	F1 score	AUC
MPR (Zheng et al., 2020)	96.44 ± 0.03	89.75 ± 0.02	84.51 ± 0.01	86.08 ± 0.02	93.62 ± 0.03	89.28 ± 0.02	88.03 ± 0.01	87.84 ± 0.02
STVE (Bergamasco et al., 2012)	92.88 ± 0.03	90.21 ± 0.02	91.18 ± 0.01	84.7 ± 0.02	95.08 ± 0.03	88.08 ± 0.02	88.67 ± 0.01	86.04 ± 0.02
ULR (Pan et al., 2019)	93.85 ± 0.03	87.11 ± 0.02	90.42 ± 0.01	84.39 ± 0.02	87.92 ± 0.03	91.28 ± 0.02	85.06 ± 0.01	87.25 ± 0.02
MIISE (Faria et al., 2016)	90.69 ± 0.03	84 ± 0.02	84.28 ± 0.01	91.8 ± 0.02	87.42 ± 0.03	92.19 ± 0.02	85.43 ± 0.01	88.49 ± 0.02
CMSRM (Wang and Liang, 2023)	93.26 ± 0.03	89.06 ± 0.02	90.3 ± 0.01	85.72 ± 0.02	86.34 ± 0.03	86.12 ± 0.02	83.78 ± 0.01	88.33 ± 0.02
MAT (Zou et al., 2019)	85.57 ± 0.03	85.73 ± 0.02	84.55 ± 0.01	84.72 ± 0.02	87.23 ± 0.03	87.38 ± 0.02	84.85 ± 0.01	87.83 ± 0.02
GPT-3.5	95.57 ± 0.03	95.73 ± 0.02	91.55 ± 0.01	89.32 ± 0.02	88.23 ± 0.03	90.38 ± 0.02	89.15 ± 0.01	87.73 ± 0.02
CAM-Vtrans	**96.97 ± 0.03**	**95.29 ± 0.02**	**94.03 ± 0.01**	**95.72 ± 0.02**	**98.26 ± 0.03**	**94.98 ± 0.02**	**92.84 ± 0.01**	**96.63 ± 0.02**

In the context of multimodal robot-assisted sports training, various methods have been proposed to enhance the effectiveness of training systems. The MPR model (Zheng et al., 2020) focuses on recognizing motion patterns of exoskeleton robots using a multimodal machine learning approach, which is crucial for understanding and improving athletic performance. The STVE method (Bergamasco et al., 2012) provides skill training within multimodal virtual environments, offering a simulated yet immersive training experience. The ULR system (Pan et al., 2019) is designed for upper limb rehabilitation using robot-aided feedback, combining multiple modalities to enhance recovery and training outcomes. The MIISE framework (Faria et al., 2016) enables multimodal interaction with robotic devices in simulated environments, facilitating a comprehensive training experience through various sensory inputs. The CMSRM model (Wang and Liang, 2023) leverages a cross-modal self-attention mechanism for controlling robot volleyball motion, which can be particularly beneficial for sports requiring precise control and coordination. Lastly, the MAT approach (Zou et al., 2019) focuses on passive force control in a multimodal astronaut training robot, aiming to improve training effectiveness in challenging environments by integrating different sensory and control modalities. The bold fonts in the table represent the best results.

TABLE 2 Computational efficiency on MSCOCO and VG-Gap datasets.

Method	MSCOCO dataset				VG-Gap dataset			
	Parameters(M)	Flops(G)	Inference time(ms)	Training time(s)	Parameters(M)	Flops(G)	Inference time(ms)	Training time(s)
MPR (Zheng et al., 2020)	246.98 ± 0.02	314.46 ± 0.03	337.79 ± 0.01	302.67 ± 0.02	387.91 ± 0.02	316.27 ± 0.03	380.31 ± 0.01	362.18 ± 0.02
STVE (Bergamasco et al., 2012)	265.50 ± 0.02	339.35 ± 0.03	282.47 ± 0.01	350.08 ± 0.02	320.78 ± 0.02	304.25 ± 0.03	273.47 ± 0.01	239.12 ± 0.02
ULR (Pan et al., 2019)	202.81 ± 0.02	380.08 ± 0.03	299.94 ± 0.01	237.91 ± 0.02	323.53 ± 0.02	381.44 ± 0.03	332.22 ± 0.01	390.26 ± 0.02
MIISE (Faria et al., 2016)	301.68 ± 0.02	237.67 ± 0.03	201.48 ± 0.01	347.54 ± 0.02	355.63 ± 0.02	315.60 ± 0.03	384.33 ± 0.01	263.49 ± 0.02
CMSRM (Wang and Liang, 2023)	230.91 ± 0.02	296.74 ± 0.03	381.06 ± 0.01	344.62 ± 0.02	370.59 ± 0.02	258.13 ± 0.03	278.78 ± 0.01	239.78 ± 0.02
MAT (Zou et al., 2019)	381.30 ± 0.02	381.89 ± 0.03	268.60 ± 0.01	362.22 ± 0.02	206.74 ± 0.02	372.37 ± 0.03	294.31 ± 0.01	317.34 ± 0.02
GPT-3.5	241.30 ± 0.02	331.39 ± 0.03	248.10 ± 0.01	252.22 ± 0.02	296.74 ± 0.02	182.37 ± 0.03	224.11 ± 0.01	267.36 ± 0.02
CAM-Vtrans	**194.13 ± 0.02**	**213.04 ± 0.03**	**192.35 ± 0.01**	**217.18 ± 0.02**	**132.25 ± 0.02**	**178.90 ± 0.03**	**117.04 ± 0.01**	**216.80 ± 0.02**

The MPR model (Zheng et al., 2020) focuses on recognizing motion patterns of exoskeleton robots using a multimodal machine learning approach, which is crucial for understanding and improving athletic performance. The STVE method (Bergamasco et al., 2012) provides skill training within multimodal virtual environments, offering a simulated yet immersive training experience. The ULR system (Pan et al., 2019) is designed for upper limb rehabilitation using robot-aided feedback, combining multiple modalities to enhance recovery and training outcomes. The MIISE framework (Faria et al., 2016) enables multimodal interaction with robotic devices in simulated environments, facilitating a comprehensive training experience through various sensory inputs. The CMSRM model (Wang and Liang, 2023) leverages a cross-modal self-attention mechanism for controlling robot volleyball motion, which can be particularly beneficial for sports requiring precise control and coordination. Lastly, the MAT approach (Zou et al., 2019) focuses on passive force control in a multimodal astronaut training robot, aiming to improve training effectiveness in challenging environments by integrating different sensory and control modalities. The bold fonts in the table represent the best results.

10.3389/fnbot.2024.1453571

TABLE 3 Ablation study of Cross-Attention module on OpenImages and Objects365 datasets.

Model	OpenImages dataset				Objects365 dataset			
	Accuracy	Recall	F1 score	AUC	Accuracy	Recall	F1 score	AUC
AM	91.59 ± 0.03	87.53 ± 0.02	86.1 ± 0.01	88.37 ± 0.02	95.45 ± 0.03	93.14 ± 0.02	90.24 ± 0.01	87.5 ± 0.02
Seif-AM	87.93 ± 0.03	85.41 ± 0.02	89.35 ± 0.01	92.55 ± 0.02	95.21 ± 0.03	85.76 ± 0.02	88.34 ± 0.01	92.73 ± 0.02
Dynamic-AM	90.48 ± 0.03	93.62 ± 0.02	84.88 ± 0.01	92.59 ± 0.02	86.36 ± 0.03	90.29 ± 0.02	89.53 ± 0.01	93.36 ± 0.02
CAM-Vtrans	**96.51 ± 0.03**	**94.27 ± 0.02**	**92.36 ± 0.01**	**93 ± 0.02**	**97.03 ± 0.03**	**95.28 ± 0.02**	**94.26 ± 0.01**	**92.81 ± 0.02**

The bold fonts in the table represent the best results.

TABLE 4 Computational efficiency in ablation study of Cross-Attention module on MSCOCO and VG-Gap datasets.

Method	MSCOCO dataset				VG-Gap dataset			
	Parameters(M)	Flops(G)	Inference time(ms)	Training time(s)	Parameters(M)	Flops(G)	Inference time(ms)	Training time(s)
AM	344.46 ± 0.02	225.62 ± 0.03	345.44 ± 0.01	228.51 ± 0.02	369.39 ± 0.02	266.69 ± 0.03	310.45 ± 0.01	286.33 ± 0.02
Seif-AM	369.19 ± 0.02	269.31 ± 0.03	263.81 ± 0.01	281.41 ± 0.02	303.00 ± 0.02	297.53 ± 0.03	201.25 ± 0.01	327.54 ± 0.02
Dynamic-AM	219.41 ± 0.02	360.93 ± 0.03	366.43 ± 0.01	303.11 ± 0.02	303.48 ± 0.02	267.01 ± 0.03	357.18 ± 0.01	256.34 ± 0.02
CAM-Vtrans	**172.13 ± 0.02**	**201.61 ± 0.03**	**165.47 ± 0.01**	**140.40 ± 0.02**	**162.70 ± 0.02**	**123.92 ± 0.03**	**229.97 ± 0.01**	**100.67 ± 0.02**

The bold fonts in the table represent the best results.

10.3389/fnbot.2024.1453571

is removed, but even in this case, it still outperforms other configurations, showcasing the robustness of our approach.

Table 4 further explores the impact of the Cross-Attention Module on computational efficiency, covering the MSCOCO and VG-Gap datasets. The experimental results show that after removing or modifying the Cross-Attention Module, our model performs best in terms of model parameters, computational complexity, inference time, and training time. This result not only reaffirms the efficiency of our model but also highlights the importance of the Cross-Attention mechanism in optimizing the model's computational path and reducing unnecessary computations. Overall, these experimental results thoroughly demonstrate the superiority of our proposed approach in handling complex multi-modal data, making it suitable for applications in scenarios such as sports training that require fast and accurate feedback.

Conducting validation in a real-world physical environment can indeed enhance the persuasiveness of the paper. However, we currently face some limitations and challenges. Firstly, high-quality video recording and processing require appropriate hardware devices, including high-definition cameras and powerful computational resources. We are actively seeking resource support to ensure access to the necessary equipment and computing capabilities. Secondly, it is necessary to establish a suitable video recording experimental setup to ensure data quality and consistency. We are planning and designing a standardized recording environment to capture high-quality motion training videos while minimizing the impact of environmental variables on experimental results. Additionally, self-recorded videos may introduce additional data processing and annotation work, increasing the complexity and workload of the experiments. To address this issue, we plan to develop semi-automated annotation tools and data preprocessing workflows to improve efficiency and reduce the workload. Lastly, factors such as lighting, background, and motion complexity in self-recorded videos may differ significantly from public datasets. This may require additional adjustments and optimizations to the model. We will fine-tune the model based on self-recorded videos to ensure its high performance and accuracy in different environments and conditions. In future work, we will continue to overcome these challenges and gradually achieve analysis and validation of self-recorded videos. We will report relevant results in subsequent research. Once again, thank you for the valuable suggestions provided by the reviewer, as they will help us further improve the research and enhance its practical value.

5 Conclusion and discussion

This research addresses the issue of real-time feedback and guidance in sports training and proposes a multimodal robotic system named CAM-Vtrans: Real-time Sports Training Utilizing Multi-modal Robot Data, which combines Vision Transformer (ViT), CLIP, and Cross-Attention mechanisms. This method leverages advanced deep learning techniques to process and integrate complex visual and textual data, aiming to provide more accurate and effective training feedback. The experiments are divided into performance comparison and ablation experiments, conducted on the OpenImages, Objects365, MSCOCO, and VG-Gap datasets. The results demonstrate that our model outperforms other state-of-the-art models in key metrics such as accuracy, recall, F1 score, and AUC. Additionally, it exhibits excellent computational efficiency, validating the effectiveness and practicality of the proposed approach.

Despite the positive outcomes, there are still some limitations to be addressed. Firstly, although the model performs well on multiple datasets, its generalization to other unseen types of sports activity data has not been validated, and further testing and optimization are needed in a broader range of sports activities. Secondly, while the current model exhibits real-time processing capability, there is still room for improvement in scenarios requiring extreme real-time performance. Future research should focus on reducing inference time and enhancing processing speed. Additionally, exploring the model's application across a wider array of sports activities and incorporating more diverse and complex datasets will be critical for ensuring its robustness and versatility. Further development of adaptive feedback mechanisms that tailor guidance to the specific needs of different sports disciplines could also enhance the system's effectiveness and user experience.

Data availability statement

The original contributions presented in the study are included in the article/supplementary material, further inquiries can be directed to the corresponding author.

Author contributions

HL: Conceptualization, Formal analysis, Investigation, Methodology, Project administration, Resources, Supervision, Visualization, Writing – original draft. LS: Data curation, Funding acquisition, Investigation, Methodology, Project administration, Resources, Software, Validation, Writing – review & editing. SG: Conceptualization, Data curation, Investigation, Methodology, Project administration, Resources, Visualization, Writing – original draft.

Funding

The author(s) declare that no financial support was received for the research, authorship, and/or publication of this article.

Conflict of interest

The authors declare that the research was conducted in the absence of any commercial or financial relationships that could be construed as a potential conflict of interest.

Publisher's note

All claims expressed in this article are solely those of the authors and do not necessarily represent those of their affiliated

organizations, or those of the publisher, the editors and the reviewers. Any product that may be evaluated in this article, or claim that may be made by its manufacturer, is not guaranteed or endorsed by the publisher.

References

Aresta, S., Bortone, I., Bottiglione, F., Di Noia, T., Di Sciascio, E., Lofù, D., et al. (2022). Combining biomechanical features and machine learning approaches to identify fencers levels for training support. *Appl. Sci.* 12:12350. doi: 10.3390/app122312350

Bakthavatchalam, K., Karthik, B., Thiruvengadam, V., Muthal, S., Jose, D., Kotecha, K., et al. (2022). IoT framework for measurement and precision agriculture: predicting the crop using machine learning algorithms. *Technologies* 10:13. doi: 10.3390/technologies10010013

Bergamasco, M., Bardy, B., and Gopher, D. (2012). *Skill Training in Multimodal Virtual Environments*. CRC Press. Available at: https://content.iospress.com/articles/work/wor0452

Björkstrand, D., Sullivan, J., Bretzner, L., Loy, G., and Wang, T. (2023). Cross-attention masked auto-encoder for human 3D motion infilling and denoising. Available at: https://papers.bmvc2023.org/0609.pdf

Chen, M.-Y., Chen, T.-H., and Lin, S.-H. (2020). "Using convolutional neural networks to forecast sporting event results," in *Deep Learning: Concepts and Architectures*, 269–285.

Dirgová Luptáková, I., Kubovčík, M., and Pospíchal, J. (2022). Wearable sensor-based human activity recognition with transformer model. *Sensors* 22:1911. doi: 10.3390/s22051911

Dobrzycki, A. D., Bernardos, A. M., Bergesio, L., Pomirski, A., and Sáez-Trigueros, D. (2023). Exploring the use of contrastive language-image pre-training for human posture classification: insights from yoga pose analysis. *Mathematics* 12:76. doi: 10.3390/math12010076

Dong, R., Zhang, X., Li, H., Masengo, G., Zhu, A., Shi, X., et al. (2024). Eeg generation mechanism of lower limb active movement intention and its virtual reality induction enhancement: a preliminary study. *Front. Neurosci.* 17:1305850. doi: 10.3389/fnins.2023.1305850

Du, X., Fuqian, X., Hu, J., Wang, Z., and Yang, D. (2021). "Uprising e-sports industry: machine learning/AI improve in-game performance using deep reinforcement learning," in *2021 International Conference on Machine Learning and Intelligent Systems Engineering (MLISE)*, 547–552. Available at: https://ieeexplore.ieee.org/abstract/document/9611712

Faria, B. M., Dias, D., and Reis, L. P. (2016). "Multimodal interaction robotic devices in a simulated environment," in *2016 11th Iberian Conference on Information Systems and Technologies (CISTI)* (IEEE), 1–6. Available at: https://ieeexplore.ieee.org/abstract/document/7521429

Hauri, S., and Vucetic, S. (2023). "Group activity recognition in basketball tracking data–neural embeddings in team sports (nets)," in *ECAI 2023* (IOS Press), 1012–1019. Available at: https://ebooks.iospress.nl/doi/10.3233/FAIA230373

Herman, J., Francis, J., Ganju, S., Chen, B., Koul, A., Gupta, A., et al. (2021). "Learn-to-race: a multimodal control environment for autonomous racing," in *Proceedings of the IEEE/CVF International Conference on Computer Vision*, 9793–9802. Available at: https://openaccess.thecvf.com/content/ICCV2021/html/Herman_Learn-To-Race_A_Multimodal_Control_Environment_for_Autonomous_Racing_ICCV_2021_paper.html

Himabindu, M., Revathi, V., Gupta, M., Rana, A., Chandra, P. K., and Abdulaali, H. S. (2023). "Neuro-symbolic AI: integrating symbolic reasoning with deep learning," in *2023 10th IEEE Uttar Pradesh Section International Conference on Electrical, Electronics and Computer Engineering (UPCON), Vol. 10*, 1587–1592. Available at: https://ieeexplore.ieee.org/abstract/document/10434380

Hu, Y., Wu, X., Geng, P., and Li, Z. (2019). Evolution strategies learning with variable impedance control for grasping under uncertainty. *IEEE Trans. Indus. Electron.* 66, 7788–7799. doi: 10.1109/TIE.2018.2884240

Ilager, S., De Maio, V., Lujic, I., and Brandic, I. (2023). "Data-centric edge-AI: a symbolic representation use case," in *2023 IEEE International Conference on Edge Computing and Communications (EDGE)*, 301–308.

Insuasti, J., Roa, F., and Zapata-Jaramillo, C. M. (2023). Computers' interpretations of knowledge representation using pre-conceptual schemas: an approach based on the bert and llama 2-chat models. *Big Data Cogn. Comput.* 7:182. doi: 10.3390/bdcc7040182

Jia, H., Ren, C., Hu, Y., Chen, Y., Lv, T., Fan, C., et al. (2020). "Mastering basketball with deep reinforcement learning: an integrated curriculum training approach," in *Proceedings of the 19th International Conference on Autonomous Agents and MultiAgent Systems*, 1872–1874. Available at: https://aamas.csc.liv.ac.uk/Proceedings/aamas2020/pdfs/p1872.pdf

Jin, M., Ma, Z., Jin, K., Zhuo, H. H., Chen, C., and Yu, C. (2022). "Creativity of AI: automatic symbolic option discovery for facilitating deep reinforcement learning," in *Proceedings of the AAAI Conference on Artificial Intelligence, Vol. 36*, 7042–7050. Available at: https://ojs.aaai.org/index.php/AAAI/article/view/20663

Jose, S., Maliackal, A. T., Sukumaran, A., Cyriac, J., and Varkey, R. M. (2023). "Machine learning technique to analyze the health condition of athletes and predict their performance," in *2023 International Conference on Circuit Power and Computing Technologies (ICCPCT)* (IEEE), 354–359. Available at: https://ieeexplore.ieee.org/abstract/document/10245401

Kim, S., Ahn, D., and Ko, B. C. (2023). "Cross-modal learning with 3D deformable attention for action recognition," in *Proceedings of the IEEE/CVF International Conference on Computer Vision*, 10265–10275. Available at: https://openaccess.thecvf.com/content/ICCV2023/html/Kim_Cross-Modal_Learning_with_3D_Deformable_Attention_for_Action_Recognition_ICCV_2023_paper.html

Koh, J. Y., Fried, D., and Salakhutdinov, R. R. (2024). "Generating images with multimodal language models," in *Advances in Neural Information Processing Systems*, 36. Available at: https://proceedings.neurips.cc/paper_files/paper/2023/hash/43a69d143273bd8215578bde887bb552-Abstract-Conference.html

Kuznetsova, A., Rom, H., Alldrin, N., Uijlings, J., Krasin, I., Pont-Tuset, J., et al. (2020). The open images dataset v4: unified image classification, object detection, and visual relationship detection at scale. *Int. J. Comput. Vis.* 128, 1956–1981. doi: 10.1007/s11263-020-01316-z

Li, Z., Zhao, T., Chen, F., Hu, Y., Su, C.-Y., and Fukuda, T. (2018). Reinforcement learning of manipulation and grasping using dynamical movement primitives for a humanoidlike mobile manipulator. *IEEE ASME Trans. Mechatron.* 23, 121–131. doi: 10.1109/TMECH.2017.2717461

Lin, T.-Y., Maire, M., Belongie, S., Hays, J., Perona, P., Ramanan, D., et al. (2014). "Microsoft coco: common objects in context," in *Computer Vision–ECCV 2014: 13th European Conference, Zurich, Switzerland, September 6-12, 2014, Proceedings, Part V 13* (Springer), 740–755. Available at: https://link.springer.com/chapter/10.1007/978-3-319-10602-1_48

Liu, L. (2022). Sports video motion direction detection and target tracking algorithm based on convolutional neural network. *Wireless Commun. Mobile Comput.* 2022:5760758. doi: 10.1155/2022/5760758

Lu, Z., Zhang, Y., Li, S., and Zhou, P. (2024). Botulinum toxin treatment may improve myoelectric pattern recognition in robot-assisted stroke rehabilitation. *Front. Neurosci.* 18:1364214. doi: 10.3389/fnins.2024.1364214

Miyazawa, K., Kyuragi, Y., and Nagai, T. (2022). Simple and effective multimodal learning based on pre-trained transformer models. *IEEE Access* 10, 29821–29833. doi: 10.1109/ACCESS.2022.3159346

Morciano, G., Zingoni, A., and Calabr, G. (2023). "Prediction of football players' performance indicators via random forest algorithm," in *2023 IEEE International Conference on Metrology for eXtended Reality, Artificial Intelligence and Neural Engineering (MetroXRAINE)*, 201–205. Available at: https://ieeexplore.ieee.org/abstract/document/10405671

Pan, L., Zhao, L., Song, A., Yin, Z., and She, S. (2019). A novel robot-aided upper limb rehabilitation training system based on multimodal feedback. *Front. Robot. AI* 6:102. doi: 10.3389/frobt.2019.00102

Papadakis, A., and Spyrou, E. (2024). A multi-modal egocentric activity recognition approach towards video domain generalization. *Sensors* 24:2491. doi: 10.3390/s24082491

Santana, R., Mendiburu, A., and Lozano, J. A. (2015). Multi-view classification of psychiatric conditions based on saccades. *Appl. Soft Comput.* 31, 308–316. doi: 10.1016/j.asoc.2015.02.038

Shao, S., Li, Z., Zhang, T., Peng, C., Yu, G., Zhang, X., et al. (2019). "Objects365: a large-scale, high-quality dataset for object detection," in *Proceedings of the IEEE/CVF International Conference on Computer Vision*, 8430–8439. Available at: https://openaccess.thecvf.com/content_ICCV_2019/html/Shao_Objects365_A_Large-Scale_High-Quality_Dataset_for_Object_Detection_ICCV_2019_paper.html

Tang, Q., Liang, J., and Zhu, F. (2023). A comparative review on multi-modal sensors fusion based on deep learning. *Signal Process.* 213:109165. doi: 10.1016/j.sigpro.2023.109165

Tjondronegoro, D., and Chen, Y.-P. P. (2006). "Using decision-tree to automatically construct learned-heuristics for events classification in sports video," in *2006 IEEE International Conference on Multimedia and Expo* (IEEE), 1465–1468. Available at: https://ieeexplore.ieee.org/abstract/document/4036887

Wang, M., and Liang, Z. (2023). Cross-modal self-attention mechanism for controlling robot volleyball motion. *Front. Neurorobot.* 17:1288463. doi: 10.3389/fnbot.2023.1288463

Wang, Z., Li, X., and Wang, G. (2024). Exploring wireless device-free localization technique to assist home-based neuro-rehabilitation. *Front. Neurosci.* 18:1344841. doi: 10.3389/fnins.2024.1344841

Wu, X., Zhu, X., Zhao, Y., and Dai, X. (2022). Differentiable fuzzy $\mathcal{LC}$: a neural-symbolic representation language for symbol grounding. *arXiv preprint* arXiv:2211.12006.

Yagin, F. H., Hasan, U. C., Clemente, F. M., Eken, O., Badicu, G., and Gulu, M. (2023). Using machine learning to determine the positions of professional soccer players in terms of biomechanical variables. *Proc. Inst. Mech. Eng. Part J. Sports Eng. Technol.* 17543371231199814. doi: 10.1177/17543371231199814

Yang, Y., Zhuang, Y., and Pan, Y. (2021). Multiple knowledge representation for big data artificial intelligence: framework, applications, and case studies. *Front. Inform. Technol. Electron. Eng.* 22, 1551–1558. doi: 10.1631/FITEE.2100463

Zhao, T., Deng, M., Li, Z., and Hu, Y. (2020). Cooperative manipulation for a mobile dual-arm robot using sequences of dynamic movement primitives. *IEEE Trans. Cogn. Dev. Syst.* 12, 18–29. doi: 10.1109/TCDS.2018.2868921

Zheng, Y., Song, Q., Liu, J., Song, Q., and Yue, Q. (2020). Research on motion pattern recognition of exoskeleton robot based on multimodal machine learning model. *Neural Comput. Appl.* 32, 1869–1877. doi: 10.1007/s00521-019-04567-1

Zou, Y., Qin, T., Wang, N., Li, J., and Xu, M. (2019). Passive force control of multimodal astronaut training robot. *Int. J. Adv. Robot. Syst.* 16:1729881419848261. doi: 10.1177/1729881419848261

frontiers | Frontiers in Neuroscience

TYPE Original Research
PUBLISHED 30 October 2024
DOI 10.3389/fnins.2024.1473755

OPEN ACCESS

EDITED BY
Longbin Zhang,
Nanyang Technological University, Singapore

REVIEWED BY
Zhongbo Sun,
Changchun University of Technology, China
Jie Zuo,
Wuhan University of Technology, China

*CORRESPONDENCE
Yi-Feng Chen
✉ chenyf6@sustech.edu.cn

RECEIVED 31 July 2024
ACCEPTED 01 October 2024
PUBLISHED 30 October 2024

CITATION
Miao Q, Min S, Wang C and Chen Y-F (2024) Integrating subject-specific workspace constraint and performance-based control strategy in robot-assisted rehabilitation. *Front. Neurosci.* 18:1473755. doi: 10.3389/fnins.2024.1473755

Integrating subject-specific workspace constraint and performance-based control strategy in robot-assisted rehabilitation

Qing Miao[1], Song Min[1], Cui Wang[2] and Yi-Feng Chen[2]*

[1]School of Electrical and Electronic Engineering, Wuhan Polytechnic University, Wuhan, China, [2]Shenzhen Key Laboratory of Smart Healthcare Engineering, Guangdong Provincial Key Laboratory of Advanced Biomaterials, Department of Biomedical Engineering, Southern University of Science and Technology, Shenzhen, China

Introduction: The robot-assistive technique has been widely developed in the field of neurorehabilitation for enhancement of neuroplasticity, muscle activity, and training positivity. To improve the reliability and feasibility in this patient–robot interactive context, motion constraint methods and adaptive assistance strategies have been developed to guarantee the movement safety and promote the training effectiveness based on the user's movement information. Unfortunately, few works focus on customizing quantitative and appropriate workspace for each subject in passive/active training mode, and how to provide the precise assistance by considering movement constraints to improve human active participation should be further delved as well.

Methods: This study proposes an integrated framework for robot-assisted upper-limb training. A human kinematic upper-limb model is built to achieve a quantitative human–robot interactive workspace, and an iterative learning-based repulsive force field is developed to balance the compliant degrees of movement freedom and constraint. On this basis, a radial basis function neural network (RBFNN)-based control structure is further explored to obtain appropriate robotic assistance. The proposed strategy was preliminarily validated for bilateral upper-limb training with an end-effector-based robotic system.

Results: Experiments on healthy subjects are enrolled to validate the safety and feasibility of the proposed framework. The results show that the framework is capable of providing personalized movement workspace to guarantee safe and natural motion, and the RBFNN-based control structure can rapidly converge to the appropriate robotic assistance for individuals to efficiently complete various training tasks.

Discussion: The integrated framework has the potential to improve outcomes in personalized movement constraint and optimized robotic assistance. Future studies are necessary to involve clinical application with a larger sample size of patients.

KEYWORDS

robot-assisted rehabilitation, integrated framework, compliant motion constraint, iterative learning, RBFNN control structure

1 Introduction

A large majority of patients with injuries to the nervous system suffer from motor disability of limbs, which gravely affects the quality of life. Exploring effective treatments, particularly rehabilitation strategies, is one of the challenging goals in medicine (Moore et al., 2020; Wright et al., 2020; Wingfield et al., 2022; Shi et al., 2024). In neurorehabilitation, bilateral upper-limb training is an effective adjunct treatment that has shown positive promise for neuroplasticity as it induces the remodeling of premotor cortex (Luft et al., 2004; Cauraugh and Summers, 2005; Chen et al., 2010; Xie et al., 2022; Norris et al., 2024) and prepares human subjects to return to activities of daily living (Lim et al., 2016).

Traditional rehabilitation intervention is to build a one-to-one training environment by means of physical therapists. This way has been extensively adopted but not adequately improved owing to its low efficiency and precision (Zhang and Cheah, 2015). Based on such limitations, robot-assisted therapy has been recently developed by the controllability and repeatability. For industrial robots, accuracy, rapidity, and stability of the operation are recognized as the paramount importance (Koç et al., 2019; Han et al., 2020; Sun et al., 2023a; Sun et al., 2023b). However, there exists an additional subject who needs to operate the robotic device during rehabilitation training. In this scenario, information perception on the user's movements becomes indispensable for a human–robot interaction, particularly in training safety and rehabilitation effectiveness.

When it comes to the human–robot interaction safety, a fundamental precondition is the estimation of suitable workspaces (Carbone et al., 2018). In general, some studies tend to drive the affected upper limb by referring the workspace of the unaffected side (Chunguang et al., 2009; Leonardis et al., 2015; Sarasola-Sanz et al., 2022), while the inconformity of both workspaces may result in strain injury. Other research studies prefer to try a standardized but small workspace according to the experience of the therapists (Squeri et al., 2009; Najafi et al., 2020). Although this one-size-fits-all approach can ensure the training safety by avoiding overstretch, the range of joint motion would not be sufficient, which may reduce the rehabilitation effectiveness. To address this problem, our previous study developed a subject-specific workspace determination method (Miao et al., 2020). The workspace was created based on a subject-specific upper-limb kinematic model. An attractive field was generated to guide the movement toward a predefined circle trajectory, and a repulsive field was defined to constrain deviated motion. Nevertheless, the diameter and position of the circle were set by the subjective opinion, which did not take into account individual adaptability. In addition, the variation of the resistance in the repulsive workspaces was uniformed rather than customized for the subjects. The inappropriate resistance levels may cause negative training, even "slacking" owing to the attractive field.

With regard to the training effectiveness, "assist-as-needed (AAN)" control techniques have been employed by providing only appropriate assistance during movement execution, which provides subjects more movement freedom. Pehlivan et al. (2016) proposed a minimal AAN controller for wrist rehabilitation robots in which the adaptive input estimation scheme included an extended Kalman filter with Lyapunov stability analysis. Zarrin et al. (2024) proposed a two-port admittance controller to address the lack of control frameworks for upper-limb rehabilitation exoskeletons. Cao et al. (2024) proposed a position-constrained AAN control method by introducing a constructed global continuous differentiable function incorporating dead zone and saturation characteristics to quantify the robotic assistance and facilitate seamless operation. It should be noted that the above-mentioned studies achieved good results; resorting to one-dimensional data, such as trajectory tracking error, movement velocity, or interactive force, is not comprehensive enough to support real estimation on subjects' motor functions. This case would misguide device's behavior of providing unsuitable assistance, which may cause patients' negative emotions or intermittent slack during the training. Thus, it is important to evaluate the motion state accurately to formulate robotic subject-specific assistance for maximizing active participation of the patients.

To address this issue, performance-based control strategies have been proposed. These strategies are dependent on multiple kinematic indicators to comprehensively evaluate subjects' motor functions, and adaptive controllers are designed to optimize robotic assistance based on the evaluation results. Krebs et al. detailed a concept of performance-based progressive robot therapy with MIT-MANUS, which included four diverse indicators in task-oriented training (Krebs et al., 2003). A piecewise function was adopted as an adaptive algorithm to tune the task difficulty. Similarly, Papaleo et al. presented a patient-tailored approach by using a seven degrees of freedom (DOFs) robot arm for three-dimensional (3D) upper-limb training (Papaleo et al., 2013). Three different performance indicators were developed to evaluate motor ability through a weighted sum method. Although these objective measures appear to be useful, they are not tightly linked to widely accepted clinical scales, such as the Fugl-Meyer Assessment (FMA), the Motor Status Score (MSS), or the modified Ashworth Scale, which may reduce the evaluation reliability of limbs' motor ability. In addition, little attention was paid to the combination of the training safety and effectiveness, which affects the development of user-centered robotics.

This article contributes to the bilateral upper-limb rehabilitation by proposing an integrated framework for safe and feasible neurorehabilitation training. On the one hand, the framework introduces a subject-specific workspace design method based on human's kinematic information at first; then, an iterative learning-based repulsive force field is established to perform optimal compliance motion constraints. On the other hand, a performance-based robotic assistance strategy is implemented to tailor subject-specific training task planning for various individuals. Three kinematic parameters of a clinical macro-metric model are applied as the performance indicators for accurate evaluation of subjects' motor functions, and a radial basis function neural network (RBFNN)-based multi-objective optimization method is implemented to tailor training difficulty level.

The article is organized as follows: In Section 2, a detailed robot-assisted bilateral upper-limb training system is described, a safe interactive workspace with an iterative learning strategy is analyzed based on an end-effector robotic device, and an overall control architecture of the robotic device is described, including performance indicator acquisition and robotic assistance decision. Section 3 gives the experimental protocol and experimental results, and discussions and conclusion are included at the last section.

2 Methods

2.1 Robotic system configuration

In this study, a robotic platform is applied for bilateral coordination training of human upper limbs, as shown in Figure 1 (Miao et al., 2021). The platform is a 6-DOF (two unilateral 3 DOF) end-effector device that comprises six linear modules and two handles with the aim of bilateral 3D

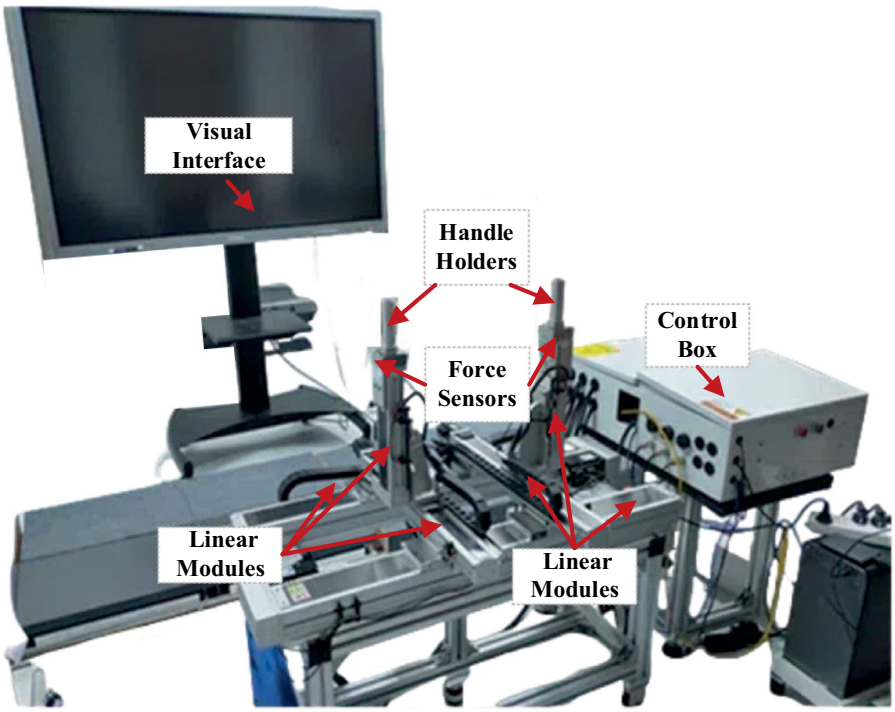

FIGURE 1
Bilateral upper-limb training system. It includes a visual interface, two handle holders, two three-axis force sensors, six linear modules, and a control box.

movement. Each end-effector device is equipped with a three-axis force sensor to acquire interactive force data. In terms of software, the host computer of the system adopts LabVIEW developed by the NI company to set the control parameters, and it communicates with the lower controller CompactRIO in real time through an Ethernet cable. The communication mode between the servo system and CompactRIO is based on analog signal transmission. Then, the servo system provides position feedback to the controller in the form of a pulse signal via a digital acquisition module. The device is not only furnished with a stop button for emergency braking but also integrated with photoelectric switches for safety limits.

2.2 Workspace constraint construction

The mirror symmetry training has been widely used through the bilateral upper-limb rehabilitation, particularly useful for people suffering from hemiparesis. There are clear clinical findings that mirror training can improve therapy effectiveness against unilateral neglect. A schematic diagram of the bilateral training pattern is presented in Figure 2.

The global coordinate directions are described as the orange arrows, and the origin of global coordinate (OGC) is defined at the center of the four modules (as well as the center of the table). It is assumed that the dimensional positions of the robot and the subject are fixed. D_1 and D_2 indicate width and height of the table, respectively. During the training, the subject is asked to stand on the designated location (the center of the shoulder joints and OGC are on the same YZ plane), keep the body straight, grasp the handles, and focus on the training task presented on the visual interface. D_3 represents the distance between the shoulder joints and the table. D_4 is the height of the shoulder joint. L_a is the distance between the handle center and the table. L_b is the initial length between the modules on Y-axis. In this case, the reachable workspace of the handles can be obtained by coordinate transformation of the positions of the shoulders as given in Equations 1, 2.

$$\begin{cases} P_{lx} = {}^{S}P_{lx} - S + 0.5L_b \\ P_{ly} = {}^{S}P_{ly} + 0.5D_1 + D_3 \\ P_{lz} = {}^{S}P_{lz} + L_a - D_4 \end{cases} \tag{1}$$

$$\begin{cases} P_{rx} = {}^{S}P_{rx} + S - 0.5L_b \\ P_{ry} = {}^{S}P_{ry} + 0.5D_1 + D_3 \\ P_{rz} = {}^{S}P_{rz} + L_a - D_4 \end{cases} \tag{2}$$

where ${}^{S}P_l = \left[{}^{S}P_{lx}, {}^{S}P_{ly}, {}^{S}P_{lz} \right]$ denotes the coordinates of the left shoulder joint, and ${}^{S}P_r = \left[{}^{S}P_{rx}, {}^{S}P_{ry}, {}^{S}P_{rz} \right]$ denotes the coordinates of the right shoulder joint. S is the horizontal distance between each shoulder joint to the body center, which can be expressed as 0.179 times as the body height (Miao et al., 2018).

Therefore, the reachable interactive workspace can be described by quantitative upper-limb workspace. Our previous study proposed a three-stage method to determine human hands' workspace on a subject-specific basis (Miao et al., 2018). This considered the human upper limb as a model with seven degrees of freedom and used the Denavit–Hartenberg (D-H) method to derive the human left-hand workspace ${}^{S}P_l$ and the right-hand workspace ${}^{S}P_r$ as given in Equation 3.

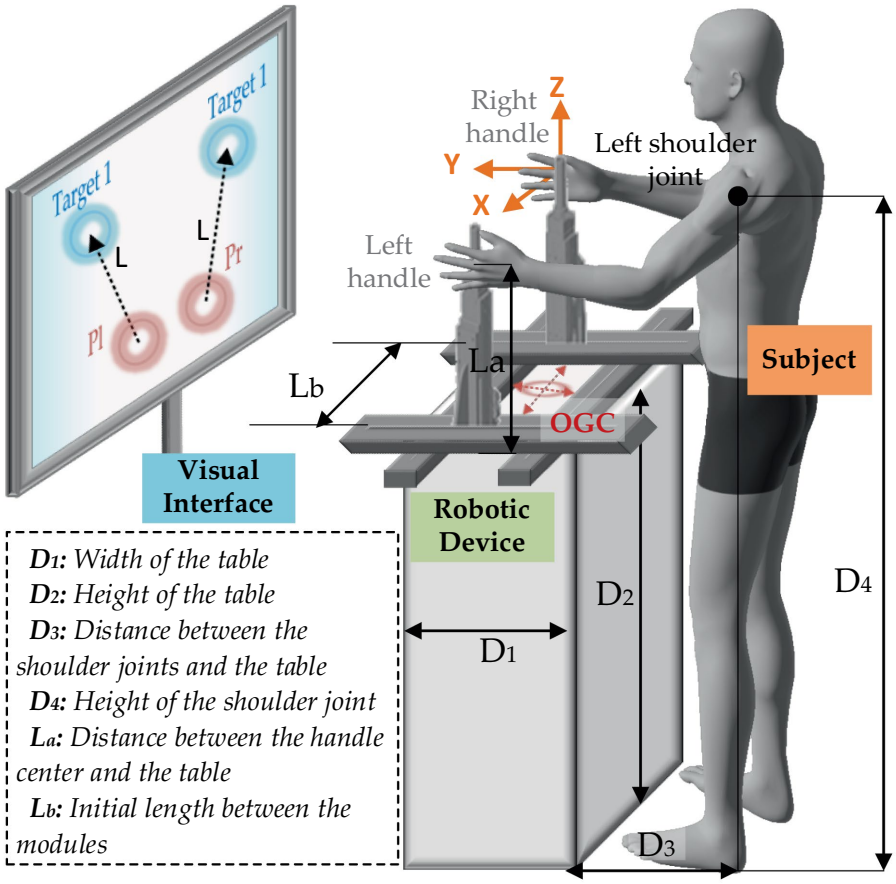

FIGURE 2
Schematic diagram of the proposed training strategy.

$$\prod_{i=1}^{7} {}^{i-1}A_i = \begin{bmatrix} n_{lx} & o_{lx} & \alpha_{lx} & {}^{S}P_x \\ n_{ly} & o_{ly} & \alpha_{ly} & {}^{S}P_y \\ n_{lz} & o_{lz} & \alpha_{lz} & {}^{S}P_z \\ 0 & 0 & 0 & 1 \end{bmatrix} \tag{3}$$

$${}^{i-1}A_i = \begin{bmatrix} \cos\theta_i & -\cos\alpha_i \sin\theta_i & \sin\alpha_i \sin\theta_i & a_i \cos\theta_i \\ \sin\theta_i & \cos\alpha_i \cos\theta_i & -\sin\alpha_i \cos\theta_i & a_i \sin\theta_i \\ 0 & \sin\alpha_i & \cos\alpha_i & d_i \\ 0 & 0 & 0 & 1 \end{bmatrix} \tag{4}$$

where α_i, a_i, d_i, and θ_i are the D-H parameters of the ith upper-limb joint. ${}^{i-1}A_i$ is the homogeneous transformation matrix, as given in Equation 4. Then, the reachable interactive workspace can be plotted as shown in Figure 3.

To limit the movement into this workspace in safety, an optimized repulsive potential field concept is adopted to yield compliant constraint. Take the X-Y plane as an instance. It is assumed that the current position of the left handle is $P_l = (P_{lx}, P_{ly})$, and the right side is $P_r = (P_{rx}, P_{ry})$. To extend the line segment between handles and the geometric centers of the workspaces they located, we can obtain two points of intersections on the boundaries, and the ones positioning closer the boundaries are corresponding obstacles, denoted as ${}^{O}P_l = ({}^{O}P_{lx}, {}^{O}P_{ly})$ for the left side and ${}^{O}P_r = ({}^{O}P_{rx}, {}^{O}P_{ry})$ for the right side. The repulsive potential function can be presented as given in Equations 5, 6.

$$U_l = \begin{cases} e^{-\eta\left[\left(P_{lx} - {}^{o}P_{lx}\right)^2 + \left(P_{ly} - {}^{o}P_{ly}\right)^2\right]}, \sqrt{\left(P_{lx} - {}^{O}P_{lx}\right)^2 + \left(P_{ly} - {}^{O}P_{ly}\right)^2} \le d_0 \\ 0, \sqrt{\left(P_{lx} - {}^{O}P_{lx}\right)^2 + \left(P_{ly} - {}^{O}P_{ly}\right)^2} > d_0 \end{cases} \tag{5}$$

$$U_r = \begin{cases} e^{-\eta\left[\left(P_{rx} - {}^{o}P_{rx}\right)^2 + \left(P_{ry} - {}^{o}P_{ry}\right)^2\right]}, \sqrt{\left(P_{rx} - {}^{O}P_{rx}\right)^2 + \left(P_{ry} - {}^{O}P_{ry}\right)^2} \le d_0 \\ 0, \sqrt{\left(P_{rx} - {}^{O}P_{rx}\right)^2 + \left(P_{ry} - {}^{O}P_{ry}\right)^2} > d_0 \end{cases} \tag{6}$$

where d_0 is the maximum influence length of each obstacle, and η is a positive scalar. Afterward, the repulsive forces can be calculated by the gradient descent method as given in Equation 7.

$$\begin{cases} F_{lrep} = -\nabla U_l \\ F_{rrep} = -\nabla U_r \end{cases} \tag{7}$$

In the context of rehabilitation training, d_0 is generally fixed, while the parameter η should be customized to individual subjects based on their control ability of muscular strength. A big ηgenerates an extensive but flat repulsive potential field, which limits interference range for a freedom movement and affects activities of limbs. However, a small ηwill form a narrow but steep repulsive potential field, which may reduce the compliance of the movement. As a consequence, it is essential to explore

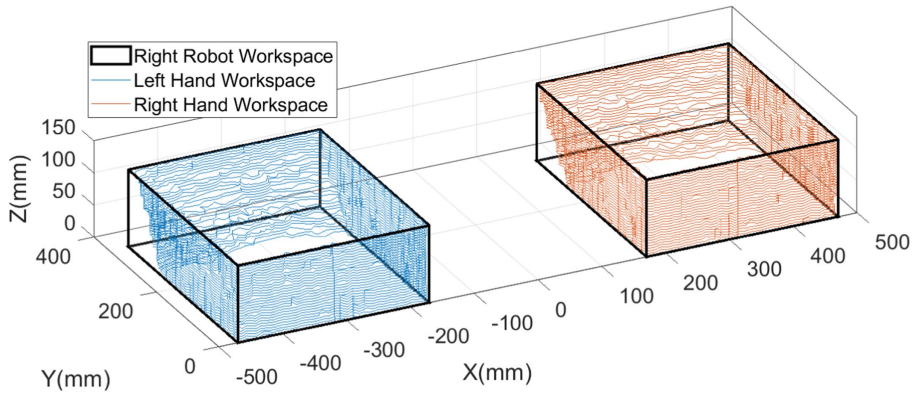

FIGURE 3
Workspaces of the handles.

the most appropriate η that leads the trajectories of the handles stabilizing in a certain area. We assume that each repulsive force field consists of numerous repulsive force lines, as shown in Figure 4a. It is observed that the maximum curvatures of the lines, as well as the inflection points, are capable of balancing the repulsive force gradient and its range of influence. Hence, it needs to quantify the maximum curvature regions, which are described by colored surfaces, as shown in Figure 4b.

In response to this problem, an iterative learning method is used to hunt for the optimal η round by round, which can be described as given in Equation 8.

$$\eta_{k+1} = \eta_k + \delta\Delta\eta \tag{8}$$

where δ is the learning rate, and subscript k means the kth positive scalar.

Denoting $d_l\big|_{\eta=\eta_k} = \sqrt{\left(P_{lx} - {}_i^O P_{lx}\right)^2 + \left(P_{ly} - {}_i^O P_{ly}\right)^2}$ and $d_r\big|_{\eta=\eta_k} = \sqrt{\left(P_{rx} - {}_i^O P_{rx}\right)^2 + \left(P_{ry} - {}_i^O P_{ry}\right)^2}$, the maximum curvature of the ith line for each side can be calculated as given in Equation 9.

$$\begin{cases} {}^iC_{l\max}\big|_{\eta=\eta_k} = \max\limits_{d_l\big|_{\eta=\eta_k} \le d_0\big|_{\eta=\eta_k}} \left\{ \dfrac{F_l''}{\left(1+F_l'^2\right)^{2/3}} \right\} \\ {}^iC_{r\max}\big|_{\eta=\eta_k} = \max\limits_{d_r\big|_{\eta=\eta_k} \le d_0\big|_{\eta=\eta_k}} \left\{ \dfrac{F_r''}{\left(1+F_r'^2\right)^{2/3}} \right\} \end{cases} \tag{9}$$

The corresponding plane coordinates of the maximum curvatures can be expressed as ${}_i^C P_l = \left({}_i^C P_{lx}, {}_i^C P_{ly}\right)$ for the left side and ${}_i^C P_r = \left({}_i^C P_{rx}, {}_i^C P_{ry}\right)$ for the right side. Then, the distances between the maximum curvature points and the boundary points are obtained as follows:

$$\begin{cases} {}^C d_l\big|_{\eta=\eta_k} = \sqrt{\left({}_i^C P_{lx} - {}_i^O P_{lx}\right)^2 + \left({}_i^C P_{ly} - {}_i^O P_{ly}\right)^2} \\ {}^C d_r\big|_{\eta=\eta_k} = \sqrt{\left({}_i^C P_{rx} - {}_i^O P_{rx}\right)^2 + \left({}_i^C P_{ry} - {}_i^O P_{ry}\right)^2} \end{cases} \tag{10}$$

The subject who intends to train is asked to move the handles along the workspace boundary, and sampling distances $\left(d_l\big|_{\eta=\eta_k}, d_r\big|_{\eta=\eta_k}\right)$ will be recorded to compare with distances given in Equation 10 as follows:

$$\frac{1}{n}\sum_{i=1}^{n} \| {}^C d_l\big|_{\eta=\eta_k} - {}_i d_l\big|_{\eta=\eta_k} \| < \varepsilon \tag{11}$$

where ε is a predefined deviation threshold. If the inequality in Equation 11 is not satisfied, η_k will not be used; then, the iteration continues ($k \to k+1$); otherwise, the iteration stops, which means η_k is the optimal scalar.

2.3 Training strategy and performance indicators

In mirror symmetry rehabilitation, reaching-task training is commonly implemented. To precisely evaluate the training performance, one clinical study established a linear regression model based on hundreds of stroke patients' behavior information in Fugl-Meyer Assessment (FMA) scales. It emphasized three key indicators, including peak speed, smoothness, and duration (Bosecker et al., 2010). The peak speed represented the maximum velocity in one reaching training round, as defined in Equation 12. The smoothness signified the ratio of mean to peak speed, as denoted in Equation 13. The duration is the completion time of one target-to-target task, as described in Equation 14.

$$P_n = \max_{1\le i\le n}\left\{\frac{\Delta d_i}{\Delta t_i}\right\} \tag{12}$$

$$S_n = \frac{\sum_{i=1}^{m}\Delta d_i}{\sum_{i=1}^{m}\Delta t_i \cdot \max\limits_{1\le i\le m}\left\{\dfrac{\Delta d_i}{\Delta t_i}\right\}} \tag{13}$$

$$D_n = \sum_{i=1}^{m}\Delta t_i \tag{14}$$

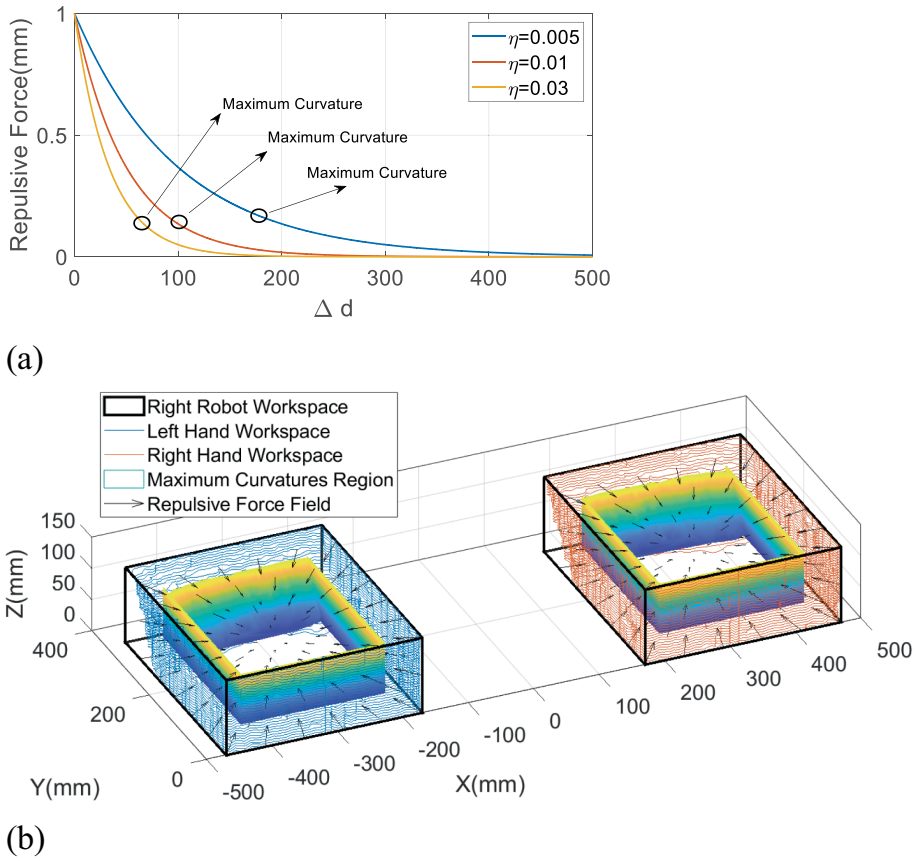

FIGURE 4
Maximum curvature dots of the repulsive potential field. (a) The maximum curvature dots of the different repulsive curves. (b) The repulsive potential field.

where the subscript n means the nth raining round, and the parameter m represents the sample number in one round. $\ddot{A}d_i$ is the displacement deviation between two contiguous samples, denoted as follows: $\Delta d_i = \sqrt{\left({}_iP_x - {}_{i-1}P_x\right)^2 + \left({}_iP_y - {}_{i-1}P_y\right)^2}$. Δt_i is the corresponding time deviation.

To scientifically define standard performance indicators, Fitts's law was involved to determine desired duration at first (Fitts and Peterson, 1964), as given in Equation 15.

$$D_d = a + b \cdot \log_2\left(\frac{L}{R} + 1\right) \tag{15}$$

where R denotes the radius of the targets, and L represents the distance between any two targets. The parameters a and b are constant values, which are commonly set according to clinical training requirements.

Because desired peak speed and smoothness are both dependent on velocity, it is significant to define an appropriate trajectory between the two targets. There is clear evidence that the minimum jerk principle is able to characterize the reaching trajectory of upper limbs, which can be expressed as given in Equation 16 (Flash and Hogan, 1985).

$$q(t) = L\left(10\tau^3 - 15\tau^4 + 6\tau^5\right) \tag{16}$$

where the parameter $\tau = t / D_d$. Then, the first-order derivative of Equation 16 can be acquired as given in Equation 17.

$$v(t) = \frac{L}{D_d}\left(30\tau^2 - 60\tau^3 + 30\tau^4\right) \tag{17}$$

Furthermore, the parameter P_d can be calculated as given in Equation 18.

$$P_d = \max_{0 \le t \le D_d} \{v(t)\} \tag{18}$$

Finally, the desired smoothness can be written as given in Equation 19.

$$S_d = \frac{\int_0^{D_d} v(t)dt}{D_d P_d} \tag{19}$$

2.4 Control system design

Based on the above concepts, it is obvious that the smaller the gap between the desired and the measured performance indicators, the better the training effectiveness. For this purpose, the difficulty of training should be subject-specific. We assume that there exists the nth difficulty level $k_n \in \mathbb{R}^+$ such that the nth comprehensive performance error is minimum in each indicator's limited range of variation, as given in Equation 20.

$$\exists k_n \in \mathbb{R}^+, s.t. \min\{\Delta P_n, \Delta S_n, \Delta D_n\} \tag{20}$$

$$\begin{cases} \Delta P_n \in [-P_{thr}, P_{thr}] \\ \Delta S_n \in [-S_{thr}, S_{thr}] \\ \Delta D_n \in [-D_{thr}, D_{thr}] \end{cases} \tag{21}$$

where $\Delta P_n = P_d - P_n$, $\Delta S_n = S_d - S_n$ and $\Delta D_n = D_d - D_n$ are the performance indicator errors, as given in Equation 21. P_{thr}, S_{thr}, and D_{thr} are the threshold values of the corresponding variations. To make the thresholds appropriate, a physiotherapist is involved to give basic references at first. Then, they are further adjusted according to the feedbacks of the subjects after a series of previous experiments. Therefore, the mapping from the human functional ability to the robot resistance level and the multi-objective optimization should be considered. Based on this, the RBFNN method is employed to obtain the optimal difficulty level, as shown in Figure 5.

It assumed that $x = [\Delta P_n, \Delta S_n, \Delta D_n]$, the input is the single performance indicator error $x_i \in \Re^n$. The output of the network is the difficulty level, which is the scalar function of the input indicator as given in Equation 22.

$$f_i(x_i) = \sum_{j=1}^{N} \omega_j \rho(\| x_i - \mu_j \|), i = 1,2,3 \tag{22}$$

where N is the number of the nodes in the hidden layer, which is set at 20. μ_j is the center field, and ω_j is the jth weight. The radial basis function is defined as Gaussian form as given in Equation 23.

$$\rho(\| x - c_j \|) = e^{\frac{-\|x_i - \mu_j\|^2}{2\sigma^2}} \tag{23}$$

where σ is the standard deviation of the function. The RBF networks are trained by indicators, and the difficulty levels are sampled from previous experiments. Specifically, the chosen μ_j is the k-means clustering, and the σ can be obtained as given in Equation 24.

$$\sigma = \frac{\mu_{\max}}{\sqrt{2N}} \tag{24}$$

The least squares function is used to calculate the weights between the hidden layer and the output layer as given in Equation 25.

$$\omega = e^{\|x_i - \mu_j\|^2 \cdot \frac{N}{\mu_{\max}^2}} \tag{25}$$

The technique for order of preference by similarity to ideal solution (TOPSIS) method is employed for multi-objective optimization. It is assumed that the desired minimum errors are ΔP_n^*, ΔS_n^*, and ΔD_n^*. The model can be written as in Equation 26.

$$\tilde{k}_n = \sum_{i=1}^{3} \lambda_i \left(x_i - x_i^*\right)^2 = \sum_{i=1}^{3} \lambda_i \left[f_i^{-1}(x_i) - x_i^*\right]^2 \tag{26}$$

where $x^* = [\Delta P_n^*, \Delta S_n^*, \Delta D_n^*]$, and λ_i is the ith weight of the ith objective function. $f_i^{-1}(x_i)$ is the ith inverse function of the ith performance indicator error.

The admittance law module makes the device operate with specific inertia, specific damping, and unfixed stiffness by measuring and controlling the force from two force sensors. These parameters are equal on the X-axis and the Y-axis. The admittance equation is written as given in Equation 27.

$$\begin{cases} F_l = m_l \ddot{q}_l + b_l \dot{q}_l + k_l q_l \\ F_r = m_r \ddot{q}_r + b_r \dot{q}_r + k_r q_r \end{cases} \tag{27}$$

where $F_l = \left[F_l^x, F_l^y\right]^T$ denotes the measured interactive force vector on the left handle along the X-axis and the Y-axis, and $F_r = \left[F_r^x, F_r^y\right]^T$ corresponds to the right handle. The parameters (m_l, m_r), (b_l, b_r), and (k_l, k_r) represent the predefined robotic handle's mass, damping, and stiffness factors depending on specific tasks, respectively. Setting the trajectories caused by the interactive forces, the admittance law can be simplified into Equation 28 as a linear spring, where the acceleration and the velocity are ignored (Ott et al., 2015).

$$\begin{cases} F_l = k_l q_l \\ F_r = k_r q_r \end{cases} \tag{28}$$

Combined with the repulsive potential function and the training difficulty level, Equation 28 can be modified as given in Equation 29.

$$\begin{cases} F_l = \tilde{k}_l q_l + F_{lrep} \\ F_r = \tilde{k}_r q_r + F_{rrep} \end{cases} \tag{29}$$

3 Experimental results

3.1 Experimental protocol

The experiments were conducted with the end-effector-based bilateral robot to validate the feasibility of the developed safety metrics. Two healthy subjects (two male participants: age 29.00 ± 4.24 years, height 1765.00 ± 21.21 mm, and weight 83.00 ± 9.90 kg) volunteered to participate in this study. The study was approved by the Southern University of Science and Technology, Human Participants Ethics Committee (20190004), and consent was obtained from the participant.

To test the performance of the proposed safety strategy, the experiments were divided into two blocks. The first experiment was conducted to search for the most appropriate η values of each subject. The subjects were required to execute a reaching-task training between two pre-set points for the first 20 rounds. Then, the subjects needed to move the left handle along the workspace boundary in an anticlockwise direction and synchronously move the right side in an anticlockwise direction (mirror symmetry training mode) during the next 20 rounds. In this context, the positions of the targets were set at [−400.00 mm, 200.00 mm] and [−230.00 mm, 50.00 mm] for the left side and [400.00 mm, 200.00 mm] and [230.00 mm, 50.00 mm] for the right side. The admittance parameters were fixed as $k_l = k_r = 0.08$, which could make subjects' movements more compliant. The starting η value was set at 400. The deviation $\Delta\eta$ was set at 30. Due to the large learning rate δ causing large η that limits interference range for

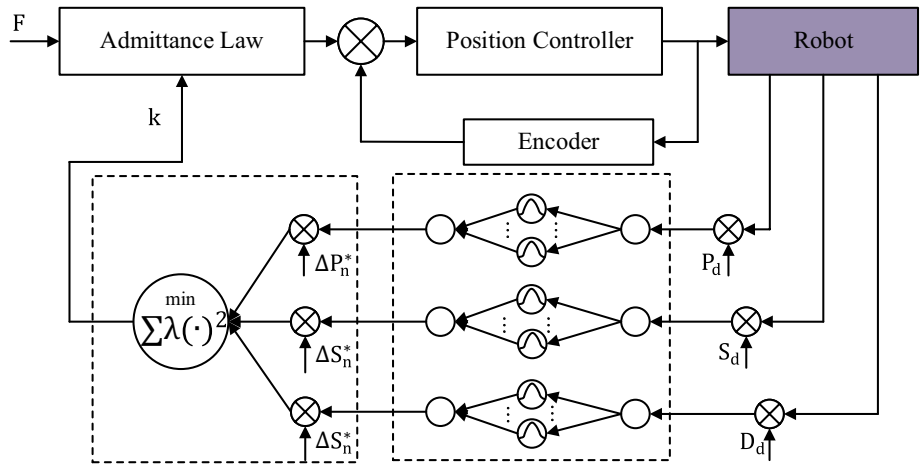

FIGURE 5
Overall control architecture of the robotic system.

TABLE 1 Definition of the desired performance indicators and the training results of the admittance parameters for the first subject.

Round (No.)	P_d (mm/s)	S_d	D_d (s)	k_l	k_r
0–10	94.46	0.53	4.5	0.0159	0.0166
10–20	121.45	0.53	4.5	0.0231	0.0241
20–30	170.05	0.53	4.5	0.0492	0.0498
30–40	283.39	0.53	4.5	0.0764	0.0791

TABLE 2 Definition of the desired performance indicators and the training results of the admittance parameters for the second subject.

Round (No.)	P_d (mm/s)	S_d	D_d (s)	k_l	k_r
0–10	94.46	0.53	4.5	0.0232	0.0245
10–20	121.45	0.53	4.5	0.0312	0.0337
20–30	170.05	0.53	4.5	0.0582	0.0611
30–40	283.39	0.53	4.5	0.0776	0.0808

a freedom movement but the small learning rate δ extending the optimization time, the learning rate δ was finally set at 0.5 to combine the rate of convergence of η and the training efficiency after proceeding numbers of preliminary experiments and seeking advice from a physical therapist.

In the second experiment, the performance-based robotic assistance strategy was added to validate whether it is effective to approximate the training tasks, including four difficulty levels with 40 rounds of training (each for 10 rounds). The positions of the targets were set as in the first experiment. According to a series of preliminary training tests, the parameters a and b in Fitts's law were set both at 1. Combined with Equations 15 to 19, the desired performance indicators can be worked out, as shown in Table 1. Due to all the subjects being healthy individuals, the initial k_l and k_r were set at 0.1, and the range of admittance values was limited in [0, 0.12]. The desired minimum errors were set as ΔP_n^* =15 mm/s, ΔS_n^* =0.15, and ΔD_n^* =0.5 s. After acquiring 1,200 groups of the performance indicators of each subject and corresponding admittance parameter, the customized values can be obtained (as shown in Table 1 for the first subject and Table 2 for the second subject).

3.2 Experimental results

Figure 6 reports the results of the first experiment, where Figures 6a,b the trajectories, respectively, being generated by two subjects. Figures 6c,d display their interactive forces (red lines) and repulsive forces (blue lines) on X-axis, while Figures 6e,f correspond to the forces on Y-axis.

It is found that the trajectories in the first 20th training rounds consist of straight lines, which reflect that the subjects adapted well to the mirror symmetry training, and repulsive forces appear only if the handles approach the targets. Owing to the small η, the repulsive forces exponentially increase when the handles are close to the boundaries of the workspaces at the beginning of the last 40 rounds. However, the repulsive forces gradually reduce with the η continuously modulating in approximately 8–10 rounds, which verifies that the trajectories can converge to maximum curvature points.

In detail, the iterative processes of the η are given in Figure 7, where the blue bars represent the position deviations, and the gray dots are corresponding η. To make it clearer to analyze, the values of η in Figure 7 are multiplied by 0.02. The data are recorded from the 21th round and provided in Table 1. The results in Figure 7a show that the position deviations from the 21th rounds to the 29th rounds are far more beyond the predefined ε=30 mm, so the η increases from 400 to 530. In contrast, the η holds when the position deviation is below 30 mm, which means iteration stops, and η=530 ought to be the optimal scalar for the first subject. Although some position deviations, such as in the 33–35th round, are not completely smaller than ε=30 mm, their difference values are in few millimeters, which can be assumed to be effective. Similarly, the most appropriate η for the second subject can be determined as 560 in Figure 7b.

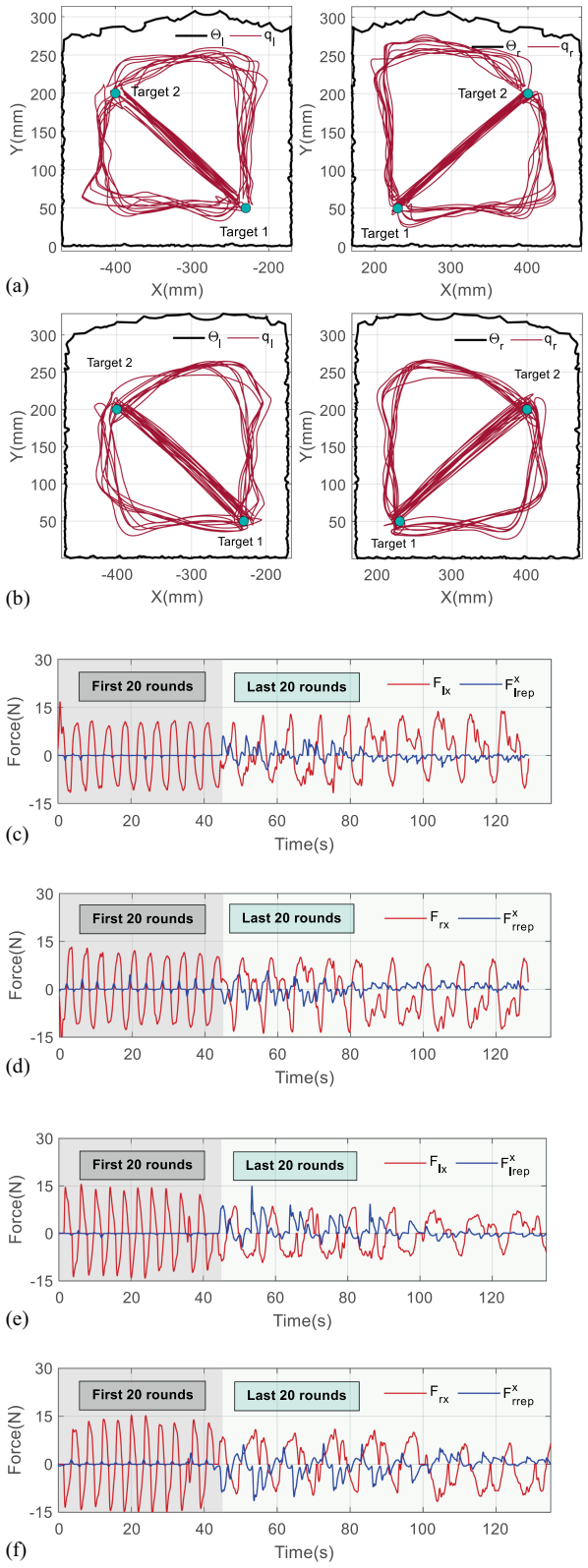

FIGURE 6
Results of the first experiment. (a) The trajectories being generated by the first subject. (b) The trajectories being generated by the second subject. (c) The interactive and repulsive forces performed by the first subject on X-axis. (d) The interactive and repulsive forces performed by the first subject on Y-axis. (e) The interactive and repulsive forces performed by the second subject on X-axis. (f) The interactive and repulsive forces performed by the second subject on Y-axis.

Figures 8,9 present the results of the second experiment, where Figure 8 shows the measured performance indicators applied by the subjects in the second experiment. The black and gray imaginary lines represent different desired performance indicators. Figure 8a uses blue lines to represent the measured performance indicators of the first subject and applies light blue shadows to describe the standard deviations. Figure 8b represents the results performed by the second subject. Figure 9 gives measured interactive forces in the second experiment.

A statistical analysis with a paired *t*-test is used for comparisons among the trials. It is denoted that four training tasks correspond to T1, T2, T3, and T4. The results given in Figure 10 show that the *p*-values of the *t*-test are all larger than 0.05, which means there are no significant differences represented between any two tasks, either for the left hand or the right side.

Overall, it can be seen that the measured indicators approximate the desired values. For more specific information, in a total of 40 rounds, the values of the root-mean-square error (RMSE) for the first subject are 26.24 mm/s, 0.06, and 0.02 s, and 22.41 mm/s, 0.04, and 0.12 s for the second subject, which shows the feasibility of the RBFNN-based method. The average forces in Figure 8 vary steadily during the whole training, which implies that the training difficulty levels fit the subjects well, and the training effectiveness tends to be positive.

4 Discussion

Robot-assisted upper-limb training plays an important role in reducing the burden of labor and improving the training efficiency. To guarantee the safety of the robotic system and provide appropriate assistance, previous studies preferred to define uniformed workspace and rigid motion restraint as the safe metrics. However, these strategies ignored the human specificity and motion smoothness. To improve the accuracy of performance evaluation, some studies used multi-performance-based control methods to synthetically adjust parameters of the robotic system (Krebs et al., 2003; Papaleo et al., 2013), while few studies focus on exploring subject-specific training methods to maximize subject participation.

The developed integrated framework can benefit robot-assisted rehabilitation training in three aspects. First, this study developed subject-specific workspaces based on human kinematic information and the robot characteristic to ensure the training safety. Second, the proposed iterative learning-based repulsive force field is capable of providing optimal motion constraints, which can reduce the risk of secondary injury and avoid unbalance between movement freedom and compliance. Finally, the designed robotic assistance strategy introduces three performance measures that are closely linked to clinical scales to improve the evaluation accuracy of training, and a learning method combined with the repulsive force field is developed to obtain customized control parameters for various that can approximate any training requirements.

Experiments on healthy subjects are enrolled to validate the safety and feasibility of the proposed framework. The results show that the framework is capable of guaranteeing safe and natural movements and providing different subject-specific parameters for individuals to conduct various training tasks. Furthermore, the results shown in Figure 8 in this article present better rapidity than the results in our previous study (Miao et al., 2023). The fuzzy-based methods need several iteration times to lock appropriate robotic assistance, while the

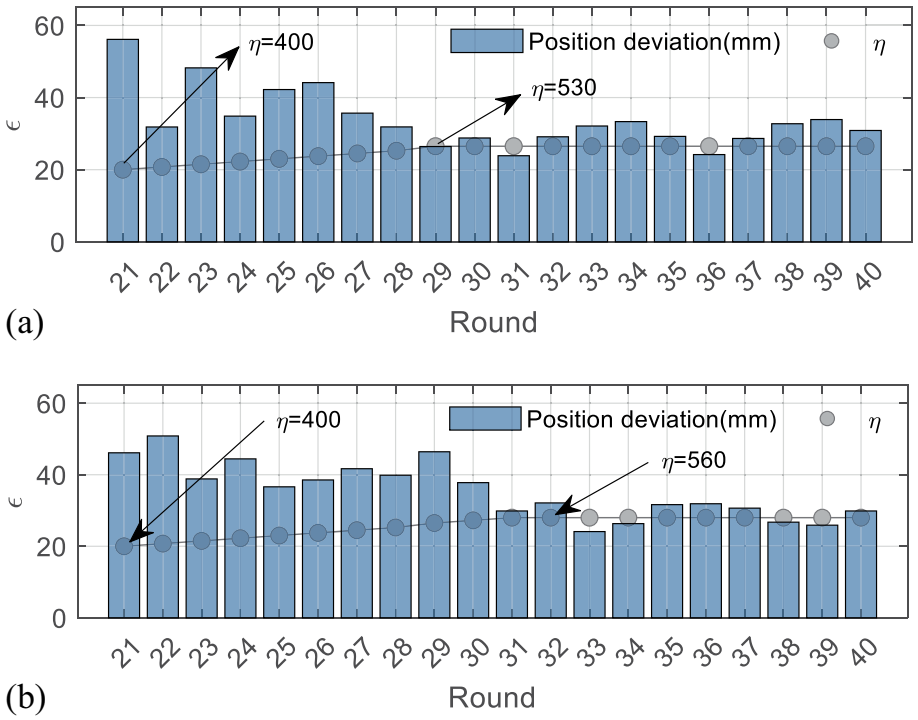

FIGURE 7
Iterative process of the first experiment. (a) The results of the first subject. (b) The results of the second subject.

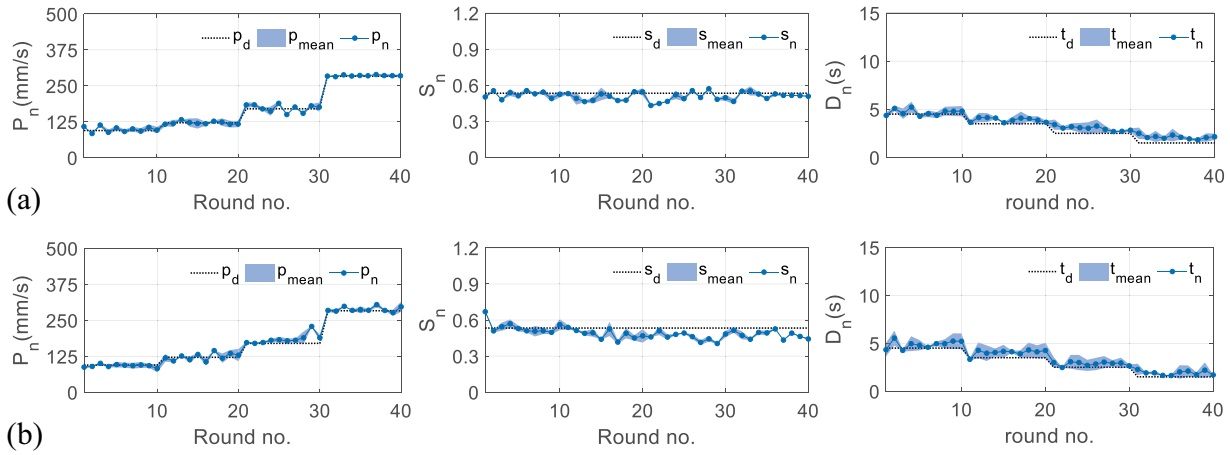

FIGURE 8
Results of measured performance indicators applied by the subjects in the second experiment. (a) The results of the first subject. (b) The results of the second subject.

RBFNN-based control structure can skip the convergence procedure, which can increase training efficiency.

However, there are still some limitations to this study. First, the training tasks are defined only in a two-dimensional space, while most activities of daily living belong to the category of three-dimensional space. Second, the learning strategy relies on long time for offline training. Third, the experiments only include healthy individuals. However, it should be noted that the human kinematic upper-limb model can be achieved according to the FMA scales, and all involved control parameters are able to be trained or further optimized for various groups of subjects; hence, the system is also applicable to patients.

5 Conclusion

This study proposes an integrated framework for robot-assisted upper-limb training, which not only includes human kinematic-based

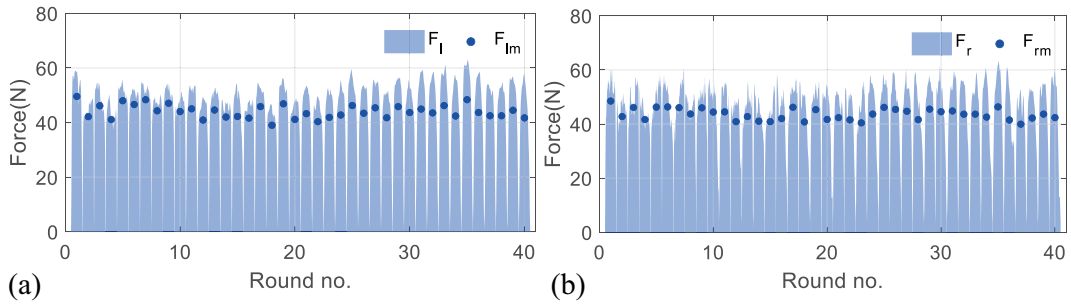

FIGURE 9
Results of measured interactive forces in the second experiment. Figure 9 (a) represents the mean interactive forces performed by the left hands of both subjects. The light blue shadows represent measured forces, and the blue dots represent corresponding mean values. Figure 9 (b) shows the results of the right side.

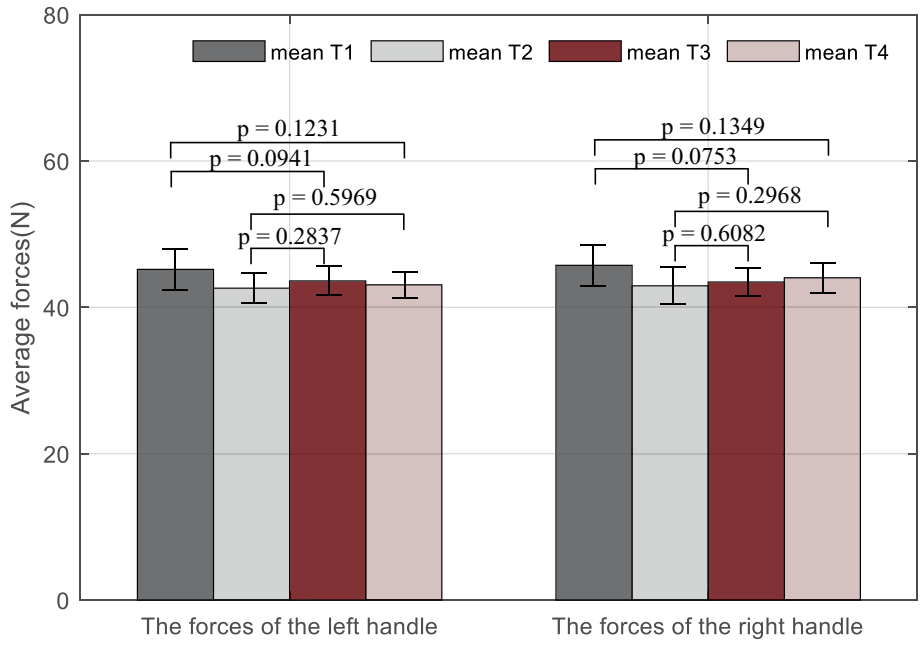

FIGURE 10
Statistical analysis results of average measured forces on the left handle and the right handle during the training. Mean Ti (i = 1,2,..., 4) represents the mean force performed by both subjects during the ith trial.

compliant motion constraints for safe interactive training but also develops a performance-based adaptive control strategy to provide appropriate robotic assistance. Experimental results demonstrated that the proposed framework can avoid unsafe motion and prompt the acquisition of appropriate subject-specific parameters. Future studies will consider the optimization of the proposed framework with advanced algorithms, as well as its clinical application with a larger sample size of patients.

Data availability statement

The original contributions presented in the study are included in the article/supplementary material, further inquiries can be directed to the corresponding authors.

Ethics statement

The studies involving humans were approved by the Southern University of Science and Technology, Human Participants Ethics Committee (20190004). The studies were conducted in accordance with the local legislation and institutional requirements. The participants provided their written informed consent to participate in this study.

Author contributions

QM: Formal analysis, Investigation, Methodology, Writing – original draft, Writing – review & editing. SM: Data curation, Writing – original draft. CW: Software, Validation, Writing

– original draft. YC: Formal analysis, Supervision, Validation, Writing – original draft.

Funding

The author(s) declare that financial support was received for the research, authorship, and/or publication of this article. We acknowledge the funding support from the National Natural Science Foundation of China (Grant no. 62303211), the Guangdong Basic and Applied Basic Research Foundation (Grant no. 2024A1515012308), the Shenzhen Science and Technology Program (Grant no. JCYJ20220530113811027), and the Natural Science Foundation of Hubei Province (Grant no. B2022330).

Conflict of interest

The authors declare that the research was conducted in the absence of any commercial or financial relationships that could be construed as a potential conflict of interest.

Publisher's note

References

Bosecker, C., Dipietro, L., Volpe, B., and Krebs, H. I. (2010). Kinematic robot-based evaluation scales and clinical counterparts to measure upper limb motor performance in patients with chronic stroke. *Neurorehabil. Neural Repair* 24, 62–69. doi: 10.1177/1545968309343214

Cao, Y., Chen, X. K., Zhang, M. S., and Huang, J. (2024). Adaptive position constrained assist-as-needed control for rehabilitation robots. *IEEE Trans. Ind. Electron.* 71, 4059–4068. doi: 10.1109/tie.2023.3273270

Carbone, G., Gherman, B., Ulinici, I., Vaida, C., and Pisla, D. (2018). "Design issues for an inherently safe robotic rehabilitation device" in Advances in service and industrial robotics. eds. C. Ferraresi and G. Quaglia (Cham: Springer International Publishing Ag), 1025–1032.

Cauraugh, J. H., and Summers, J. J. (2005). Neural plasticity and bilateral movements: a rehabilitation approach for chronic stroke. *Prog. Neurobiol.* 75, 309–320. doi: 10.1016/j.pneurobio.2005.04.001

Chen, H. W., Epstein, J., and Stern, E. (2010). Neural plasticity after acquired brain injury: evidence from functional neuroimaging. *Pm&R* 2, S306–S312. doi: 10.1016/j.pmrj.2010.10.006

Chunguang, L., Tao, L., Kyoko, S., and Yoshio, I. (2009). A master-slave control system with energy recycling and force sensing for upper limb rehabilitation robots. in: *2009 IEEE/ASME International Conference on Advanced Intelligent Mechatronics (AIM)*, Singapore, pp. 36–41.

Fitts, P. M., and Peterson, J. R. (1964). Information capacity of discrete motor-responses. *J. Exp. Psychol.* 67:103-+. doi: 10.1037/h0045689

Flash, T., and Hogan, N. (1985). The coordination of arm movements - an experimentally confirmed mathematical-model. *J. Neurosci.* 5, 1688–1703. doi: 10.1523/jneurosci.05-07-01688.1985

Han, Y., Wu, J. H., Liu, C., and Xiong, Z. H. (2020). An iterative approach for accurate dynamic model identification of industrial robots. *IEEE Trans. Robot.* 36, 1577–1594. doi: 10.1109/tro.2020.2990368

Koç, O., Maeda, G., and Peters, J. (2019). Optimizing the execution of dynamic robot movements with learning control. *IEEE Trans. Robot.* 35, 909–924. doi: 10.1109/tro.2019.2906558

Krebs, H. I., Palazzolo, J. J., Dipietro, L., Volpe, B. T., and Hogan, N. (2003). Rehabilitation robotics: performance-based progressive robot-assisted therapy. *Auton. Robot.* 15, 7–20. doi: 10.1023/a:1024494031121

Leonardis, D., Barsotti, M., Loconsole, C., Solazzi, M., Troncossi, M., Mazzotti, C., et al. (2015). An EMG-controlled robotic hand exoskeleton for bilateral rehabilitation. *IEEE Trans. Haptics* 8, 140–151. doi: 10.1109/toh.2015.2417570

Lim, K. M., Jung, J., and Shim, S. (2016). The effect of bilateral trainings on upper extremities muscle activation on level of motor function in stroke patients. *J. Phys. Ther. Sci.* 28, 3427–3431. doi: 10.1589/jpts.28.3427

Luft, A. R., McCombe-Waller, S., Whitall, J., Forrester, L. W., Macko, R., Sorkin, J. D., et al. (2004). Repetitive bilateral arm training and motor cortex activation in chronic stroke - a randomized controlled trial. *JAMA* 292, 1853–1861. doi: 10.1001/jama.292.15.1853

Miao, Q., Li, Z. J., Chu, K. Y., Liu, Y. D., Peng, Y. X., Xie, S. Q., et al. (2023). Performance-based iterative learning control for task-oriented rehabilitation: a pilot study in robot-assisted bilateral training. *IEEE Trans. Cogn. Dev. Syst.* 15, 2031–2040. doi: 10.1109/tcds.2021.3072096

Miao, Q., McDaid, A., Zhang, M. M., Kebria, P., and Li, H. S. (2018). A three-stage trajectory generation method for robot-assisted bilateral upper limb training with subject-specific adaptation. *Robot. Auton. Syst.* 105, 38–46. doi: 10.1016/j.robot.2018.03.010

Miao, Q., Peng, Y. X., Liu, L., McDaid, A., and Zhang, M. M. (2020). Subject-specific compliance control of an upper-limb bilateral robotic system. *Robot. Auton. Syst.* 126:103478. doi: 10.1016/j.robot.2020.103478

Miao, Q., Sun, C. Y., Zhong, B., Guo, K. Q., and Zhang, M. M. (2021). *Improving human-robot interaction safety through compliant motion constraints in bilateral upper limb rehabilitation*. In: IEEE International Conference on Robotics and Biomimetics (IEEE ROBIO), (New York, pp. 379–385.

Moore, J. L., Nordvik, J. E., Erichsen, A., Rosseland, I., Bo, E., Hornby, T. G., et al. (2020). Implementation of high-intensity stepping training during inpatient stroke rehabilitation improves functional outcomes. *Stroke* 51, 563–570. doi: 10.1161/strokeaha.119.027450

Najafi, M., Rossa, C., Adams, K., and Tavakoli, M. (2020). Using potential field function with a velocity field controller to learn and reproduce the Therapist's assistance in robot-assisted rehabilitation. *IEEE ASME Trans. Mechatron.* 25, 1622–1633. doi: 10.1109/tmech.2020.2981625

Norris, T. A., Augenstein, T. E., Rodriguez, K. M., Claflin, E. S., and Krishnan, C. (2024). Shaping corticospinal pathways in virtual reality: effects of task complexity and sensory feedback during mirror therapy in neurologically intact individuals. *J. Neuroeng. Rehabil.* 21:154. doi: 10.1186/s12984-024-01454-2

Ott, C., Mukherjee, R., and Nakamura, Y. (2015). A hybrid system framework for unified impedance and admittance control. *J. Intell. Robot. Syst.* 78, 359–375. doi: 10.1007/s10846-014-0082-1

Papaleo, E., Zollo, L., Spedaliere, L., and Guglielmelli, E. (2013). *Patient-tailored adaptive robotic system for upper-limb rehabilitation*. In: 2013 IEEE international conference on robotics and automation. New York: IEEE, pp. 3860–3865.

Pehlivan, A. U., Losey, D. P., and O'Malley, M. K. (2016). Minimal assist-as-needed controller for upper limb robotic rehabilitation. *IEEE Trans. Robot.* 32, 113–124. doi: 10.1109/tro.2015.2503726

Sarasola-Sanz, A., López-Larraz, E., Irastorza-Landa, N., Rossi, G., Figueiredo, T., McIntyre, J., et al. (2022). Real-time control of a multi-degree-of-freedom Mirror myoelectric Interface during functional task training. *Front. Neurosci.* 16:12. doi: 10.3389/fnins.2022.764936

Shi, X. Q., Ti, C. H. E., Lu, H. Y., Hu, C. P., Xie, D. S., Yuan, K., et al. (2024). Task-oriented training by a personalized electromyography-driven soft robotic hand in chronic stroke: a randomized controlled trial. *Neurorehabil. Neural Repair* 38, 595–606. doi: 10.1177/15459683241257519

Squeri, V., Casadio, M., Vergaro, E., Giannoni, P., Morasso, P., and Sanguineti, V. (2009). Bilateral robot therapy based on HAPTICS and reinforcement learning: feasibility study of a new concept for treatment of patients after stroke. *J. Rehabil. Med.* 41, 961–965. doi: 10.2340/16501977-0400

Sun, Z. B., Tang, S. J., Jin, L., Zhang, J. L., and Yu, J. Z. (2023a). Nonconvex activation noise-suppressing neural network for time-varying quadratic programming: application to omnidirectional Mobile manipulator. *IEEE Trans. Industr. Inform.* 19, 10786–10798. doi: 10.1109/tii.2023.3241683

Sun, Z. B., Tang, S. J., Zhang, J. L., and Yu, J. Z. (2023b). Nonconvex noise-tolerant neural model for repetitive motion of omnidirectional Mobile manipulators. *IEEE CAA J. Autom. Sin.* 10, 1766–1768. doi: 10.1109/jas.2023.123273

Wingfield, M., Fini, N. A., Brodtmann, A., Williams, G., Churilov, L., and Hayward, K. S. (2022). Upper-limb motor intervention elements that drive improvement in biomarkers and clinical measures post-stroke: a systematic review in a systems paradigm. *Neurorehabil. Neural Repair* 36, 726–739. doi: 10.1177/15459683221129273

Wright, Z. A., Majeed, Y. A., Patton, J. L., and Huang, F. C. (2020). Key components of mechanical work predict outcomes in robotic stroke therapy. *J. Neuroeng. Rehabil.* 17:53. doi: 10.1186/s12984-020-00672-8

Xie, H., Li, X., Huang, W. H., Yin, J. H., Luo, C. L., Li, Z. Y., et al. (2022). Effects of robot-assisted task-oriented upper limb motor training on neuroplasticity in stroke patients with different degrees of motor dysfunction: a neuroimaging motor evaluation index. *Front. Neurosci.* 16:13. doi: 10.3389/fnins.2022.957972

Zarrin, R. S., Zeiaee, A., and Langari, R. (2024). A variable-admittance assist-as-needed controller for upper-limb rehabilitation exoskeletons. *IEEE Robot. Autom. Lett.* 9, 5903–5910. doi: 10.1109/lra.2024.3398565

Zhang, J. J., and Cheah, C. C. (2015). Passivity and stability of human-robot interaction control for upper-limb rehabilitation robots. *IEEE Trans. Robot.* 31, 233–245. doi: 10.1109/tro.2015.2392451

frontiers | Frontiers in Neuroscience

TYPE Original Research
PUBLISHED 04 December 2024
DOI 10.3389/fnins.2024.1485066

OPEN ACCESS

EDITED BY
Yingbai Hu,
The Chinese University of Hong Kong, China

REVIEWED BY
Rajat Emanuel Singh,
Northwestern College, United States
Flavie Bompaire,
Hôpital d'instruction des Armées Percy, France

*CORRESPONDENCE
Tomofumi Yamaguchi
✉ yamaguchi.tomofumi.3i@kyoto-u.ac.jp

RECEIVED 23 August 2024
ACCEPTED 04 November 2024
PUBLISHED 04 December 2024

CITATION
Tsuchiya J, Momose K, Saito H, Watanabe K and Yamaguchi T (2024) Comparison of muscle synergies in walking and pedaling: the influence of rotation direction and speed.
Front. Neurosci. 18:1485066.
doi: 10.3389/fnins.2024.1485066

Comparison of muscle synergies in walking and pedaling: the influence of rotation direction and speed

Junko Tsuchiya[1,2], Kimito Momose[3], Hiroki Saito[1,4], Koji Watanabe[5] and Tomofumi Yamaguchi[6,7]*

[1]Major of Physical Therapy, Department of Rehabilitation, School of Health Sciences, Tokyo University of Technology, Tokyo, Japan, [2]Department of Health Sciences, Graduate School of Medicine, Shinshu University, Nagano, Japan, [3]Department of Physical Therapy, School of Health Science, Shinshu University, Nagano, Japan, [4]Centre for Human Movement at Tokyo University of Technology, Tokyo, Japan, [5]Department of Rehabilitation Medicine, Juntendo University Graduate School of Medicine, Tokyo, Japan, [6]Department of Physical Therapy, Human Health Sciences, Graduate School of Medicine, Kyoto University, Kyoto, Japan, [7]Department of Physical Therapy, Faculty of Health Science, Juntendo University, Tokyo, Japan

Background: Understanding the muscle synergies shared between pedaling and walking is crucial for elucidating the mechanisms of human motor control and establishing highly individualized rehabilitation strategies. This study investigated how pedaling direction and speed influence the recruitment of walking-like muscle synergies.

Methods: Twelve healthy male participants pedaled at three speeds (60 RPM, 30 RPM, and 80 RPM) in two rotational directions (forward and backward). Additionally, they completed walking tasks at three different speeds (slow, comfortable, and fast). Surface electromyography (EMG) was recorded on 10 lower limb muscles during movement, and muscle synergies were extracted from each condition using non-negative matrix factorization. The similarities between the muscle synergies during walking and each pedaling condition were examined using cosine similarity.

Results: The results confirmed that the composition of muscle synergies during pedaling varied depending on the rotational direction and speed. Furthermore, one to three muscle synergies, similar to those observed during walking, were recruited in each pedaling condition, with specific synergies dependent on direction and speed. For instance, synergy involving the quadriceps and hip extensors was predominantly observed during pedaling at 30 RPM, regardless of the direction of rotation. Meanwhile, synergy involving the hamstrings was more pronounced during forward pedaling at 60 RPM and backward pedaling at 80 RPM.

Conclusion: These findings suggest that walking-like muscle synergies can be selectively recruited during pedaling, depending on the rotational direction and speed.

KEYWORDS

locomotor modules, gait, cycling, electromyography (EMG), motor control, rehabilitation, central nervous system (CNS)

1 Introduction

Human motor control is a highly complex behavior, with the central nervous system (CNS) controlling vast degrees of freedom of the musculoskeletal system (Bernstein, 1967). Muscle synergies are functional units consisting of groups of muscles that work together in a coordinated manner to control specific motor tasks. To address the excessive redundancy in motor control, the CNS has been suggested to achieve complex movements by flexibly combining a small number of fundamental muscle synergies (Tresch and Jarc, 2009; Bizzi and Cheung, 2013; Ting et al., 2015).

Walking and cycling involve rhythmic movements of the lower limbs and exhibit similar muscle activity patterns (Raasch and Zajac, 1999) and neural modulation (Zehr et al., 2007). This similarity suggests a shared neural control mechanism and comparable muscle synergies between walking and pedaling have also been noted (Hug et al., 2010; De Marchis et al., 2013; Barroso et al., 2013, 2014). The activity of multiple muscle groups during walking can be explained by four or five muscle synergies (Ivanenko et al., 2004; Ivanenko et al., 2005; Cappellini et al., 2006; Neptune et al., 2009; Clark et al., 2010). Additionally, muscle activity during pedaling is often explained by three or four muscle synergies (Hug et al., 2010; Hug et al., 2011; De Marchis et al., 2013; Barroso et al., 2013, 2014; Ambrosini et al., 2016). However, a study investigating muscle synergies during pedaling at various cadences showed that although the number of required synergies remains consistent across different cadences, the composition of the recruited muscle synergies varies with speed (Barroso et al., 2014).

Barroso et al. (2014) compared muscle synergies between walking and pedaling at four different speeds and reported that similar muscle synergies were observed between these two motor tasks. However, they noted that a muscle synergy in which the soleus muscle contributed independently was only observed during low-speed pedaling (Barroso et al., 2014). Alternatively, during walking, a muscle synergy involving the ankle plantar flexors, which contribute to forward propulsion during the late stance phase, has been observed across all speeds from low to high (Ivanenko et al., 2004; Clark et al., 2010; Yokoyama et al., 2016). Barroso's study investigated muscle synergies in pedaling at four speeds, comparing them with walking synergies at matched speeds. Their findings suggest that muscle synergies essential for walking may be observed only during pedaling at specific speeds. Therefore, it is important to investigate the similarity of muscle synergies during walking and during pedaling at different speeds.

Furthermore, a simulation study examining the contribution of functional muscle groups in different pedaling directions (forward and backward) reported that smooth backward pedaling was achieved by splitting the pairs of the rectus femoris (RF)/tibialis anterior (TA) and hamstrings (HAM)/ankle plantar flexors (TS) observed in forward pedaling into two distinct pairs: RF-HAM and TA-TS pair (Raasch and Zajac, 1999). However, given the findings of previous studies that the composition of muscle synergies during pedaling varies with movement direction and speed (Barroso et al., 2014), it is possible that the composition of walking-like muscle synergies recruited during pedaling may also differ depending on these factors.

Pedaling exercises are widely used in the rehabilitation of patients with stroke as an effective method for regaining walking function, including improvements in walking speed, distance, and asymmetry (Barbosa et al., 2015). Clarifying the details of the shared muscle synergies between pedaling and walking is essential for assessing motor function impairments and establishing highly individualized rehabilitation strategies. This study aimed to investigate the similarities between muscle synergies obtained from six pedaling conditions, combining forward and backward pedaling at three different speeds and walking muscle synergies, to elucidate the composition of walking-like muscle synergies recruited during pedaling based on direction and speed.

Abbreviations: EMG, Electromyography; CNS, Central nervous system; TDC, Top dead center; TA, Tibialis anterior; SOL, Soleus; LG, Lateral gastrocnemius; RF, Rectus femoris; VM, Vastus medialis; VL, Vastus lateralis; MH, Medial hamstrings; LH, Lateral hamstrings; Gmed, Gluteus medius; Gmax, Gluteus maximus; NMF, Non-negative matrix factorization; VAF, Variance accounted for.

2 Materials and methods

2.1 Subjects

Twelve healthy male volunteers (age, 25 ± 2; height, 1.71 ± 0.06 m; weight, 68.0 ± 7.5 kg) participated in this study. These individuals met the inclusion criteria of no history of CNS disorders or orthopedic conditions that would impair walking or pedaling movements. Individuals with training experience as cyclists were excluded.

They were informed about all procedures and the potential discomfort associated with the experimental procedures before providing written consent to participate. The study protocol was approved by the Institutional Review Board of Shinshu University, Nagano, Japan (Approval No. 4473) and adhered to the standards of the latest revision of the Declaration of Helsinki.

2.2 Experimental procedure

The participants completed three sessions. In the first session, the participants walked on flat ground at three speeds: comfortable, slow, and fast. Next, forward pedaling was performed on a recumbent ergometer (StrengthErgo240; Mitsubishi Electric Co., Tokyo, Japan) at three speeds: comfortable, slow, and fast. Finally, they pedaled backward on the same ergometer at three speeds.

2.3 Gait

The participants walked on flat ground at three different speeds, and each speed was recorded once after the preparer practiced. Measurements were conducted using a 16 m walking path, which included three meters before and after the acceleration and deceleration sections. Pressure signals during walking were recorded from a foot switch attached to the right heel during a 10 m section where the walking speed was constant. The timing of the heel strike was used to identify one walking cycle and cadence.

2.4 Pedaling

Pedaling was performed using a recumbent ergometer with an adjustable seat height of 51 cm and a crank length of 18 cm. The backrest

angle was set to 10°, and the distance from the seat to the crank axis and the height of the pedal axis were adjusted to ensure the knee extension angle was −10° when the knee was maximally extended during pedaling.

The participants pedaled during all tasks using an isometric contraction mode of 10 Nm. Pedaling speeds (expressed in revolutions per minute, RPM) were selected at 60 RPM, 30 RPM, and 80 RPM, with the aim of capturing a wide range of differences in muscle synergies induced by pedaling speed. The rationale for selecting these specific speeds was based on previous studies involving stroke patients that employed slower pedaling speeds, ranging from 20 to 50 RPM (Ambrosini et al., 2016), while research on trained cyclists utilized higher speeds, ranging from 60 to 140 RPM (Wakeling and Horn, 2009). Based on these methodologies and considering the ability of our participants to maintain a steady pedaling cadence without undue strain, we selected 30 RPM as a slower speed and 80 RPM as a faster speed. Additionally, the comfortable cadence was set at 60 RPM, per previously established methods (De Marchis et al., 2013). The order of the speeds in each session was randomized. A 30 s trial was conducted for each speed of forward and backward pedaling. Real-time measurement of the crank angle during pedaling was made possible by recording voltage changes from the left crank. Since all participants in this study were right-leg dominant, the right-side profiles were shifted by 180°. The pedaling cycle in this study was defined as starting when the right knee transitioned from the extension phase to the flexion phase (the right crank angle at 135°) and ending after the completion of one full revolution (Figure 1).

2.5 Electromyogram

Surface electromyography (EMG) was recorded from the following 10 muscles of the dominant lower limb: tibialis anterior (TA), soleus (SOL), lateral gastrocnemius (LG), rectus femoris (RF), vastus medialis (VM), vastus lateralis (VL), medial hamstrings (MH), lateral hamstrings (LH), gluteus medius (Gmed), and gluteus maximus (Gmax). Based on previous studies (Barroso et al., 2014) investigating muscle synergies during cycling, which demonstrated consistent EMG patterns from the dominant leg, this study also focused on measuring muscle activity from the dominant leg. Participants underwent gait and pedaling tasks focusing on their dominant side, and each participant's dominant leg was established using the Footedness Questionnaire (Chapman et al., 1987). Electrode placement followed the SENIAM (surface electromyography for the noninvasive assessment of muscles) guidelines (Hermens et al., 2000). EMG activity was recorded during a stable performance of each task using a wireless EMG system (Trigno Wireless System; DELSYS, Boston, MA, United States). The EMG signals were bandpass-filtered (20–450 Hz), amplified (with a 300-gain preamplifier), and sampled at 2000 Hz. Data analysis was conducted offline using MATLAB R2022b (MathWorks, Natick, MA, United States) and IBM SPSS Statistics 25 software (IBM).

2.6 EMG processing

Before commencing EMG processing, a meticulous visual inspection of the EMG recordings from all muscles was conducted. A continuous series of six strides/pedaling cycles devoid of noise artifacts was carefully selected for analysis in each trial. Selected EMG signals underwent full-wave rectification and were smoothed using a Butterworth zero-phase low-pass filter with a cutoff frequency of 5 Hz (Clark et al., 2010; Hug et al., 2010; Barroso et al., 2014).

The smoothed EMG data were normalized to the average of the peaks from each muscle's six strides/pedaling cycles to facilitate comparisons across subjects, motor tasks, and speeds. Additionally,

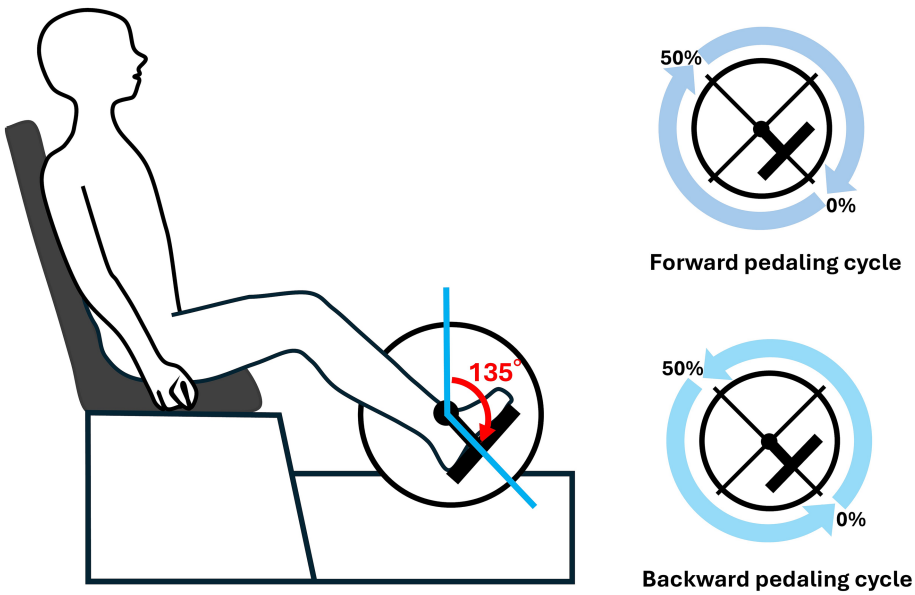

FIGURE 1
Experimental setup. As illustrated in the figure, the starting position of the pedaling cycle was defined as the right crank angle at 135°. Both forward and backward pedaling were recorded. One segment was defined as the period from the initial 135° position until it reached 135° again, and this segment was represented as 100% of the pedaling cycle.

the EMG signals were resampled at intervals of 200 points for each stride/pedaling cycle (Barroso et al., 2014). Furthermore, we subtracted the minimum value for each cycle to ensure a zero value for all cycles (Barroso et al., 2014). For each subject, motor task, and speed, the normalized EMG signals were combined into an $m \times t$ matrix, where m represents the number of muscles (10 in this case), and t indicates the time base (t = number of strides (6) × 200 timepoints) (Barroso et al., 2014).

2.7 Muscle synergy analysis

To extract the motor modules, non-negative matrix factorization (NMF) was performed on the EMG matrices (EMG_0) obtained from each trial, consisting of six continuous cycles for each participant (Clark et al., 2010; Hug et al., 2010; Barroso et al., 2014). NMF is a linear decomposition technique that decomposes a given data matrix into two non-negative matrices, as represented by the following equation (Lee and Seung, 1999; Tresch et al., 2006):

$$M = W \cdot C + e$$

where M represents an $m \times t$ matrix (i.e., 10 muscles × 1,200 time points, comprising six cycles × 200-time points), W is an $m \times n$ matrix representing the weighting components (where n is the number of modules), C is an $n \times t$ matrix representing the temporal pattern components, and e is the residual matrix. When the matrices W and C are multiplied, an $m \times t$ matrix is generated that attempts to reconstruct the EMG for all consecutive cycles.

At each iteration, the algorithm updates W and C to minimize the Frobenius norm representing the residual between the reconstructed EMG (EMG_r) and original EMG matrix (EMG_0) (Lee and Seung, 1999). NMF was applied to all possible n values, ranging from 1 to 10, for module extraction. Muscle synergy vectors (columns of matrix W) were normalized by the maximum value of each column to enable comparisons among the subjects, speeds, and motor tasks (Hug et al., 2010; Barroso et al., 2014). In addition, each row of matrix C was normalized to its peak for all cycles.

As the algorithm iteratively updates based on random initial estimates of W and C, it converges to a locally optimal matrix factorization. To avoid the local minima, the algorithm was repeated 100 times for each participant. The variance accounted for (VAF) was calculated at each iteration, and only the iteration with the maximum VAF was retained. VAF is defined as follows:

$$\mathrm{VAF} = 1 - \frac{\sum_{i=1}^{m}\sum_{j=1}^{l}\left(\mathrm{EMG0}(i,j) - \mathrm{EMGr}(i,j)\right)^2}{\sum_{i=1}^{m}\sum_{j=1}^{l}\left(\mathrm{EMG0}(i,j)\right)^2}$$

We defined the optimal number of modules, n, as meeting the following criteria: first, n was selected as the smallest number of modules, explaining more than 90% of the VAF (Torres-Oviedo et al., 2006). Second, n was the smallest number, and adding another module did not increase the VAF by more than 5% (Frère and Hug, 2012).

Daily life requires walking at a wide range of speeds, from slow to fast, and stroke patients undergoing rehabilitation need to regain their walking ability across this range of speeds. Therefore, in this study, we compared walking across a broad range of speeds with pedaling at various speeds, considering its potential application for rehabilitation.

To this end, we concatenated the EMG matrices obtained from each subject walking at three speeds (comfortable, slow, and fast) along the time points in the direction. Subsequently, NMF was performed on the concatenated EMG matrix of walking at all speeds (i.e., the matrix consisted of 10 muscles × 3 speed conditions × 1,200 time points) to extract the synergies across all walking speeds (Yokoyama et al., 2016; Saito et al., 2021).

2.8 Clustering the muscle synergy across participants

To elucidate the characteristics of muscle synergy vectors among the different conditions, hierarchical clustering analysis (Ward's method, Euclidean distance) was conducted on the weighting components of the muscle synergies for all subjects in each condition (Yokoyama et al., 2016; Saito et al., 2021). Clustering was performed for each of the seven conditions: three velocities for forward pedaling, three velocities for backward pedaling, and whole-speed walking. The optimal number of clusters was determined using a gap statistic (Tibshirani et al., 2001). Subsequently, the muscle synergy vectors within the clusters were averaged across the subjects. Synergies possessed by more than half of the subjects were defined as representative synergies for each condition (Funato et al., 2022) and were adopted for further examination of similarities with walking synergies. The similarity between walking and representative synergies for each pedaling condition was assessed using cosine similarity, and synergies were considered similar when the cosine similarity was more significant than 0.85.

2.9 Statistical analyses

All statistical analyses were performed using IBM SPSS Statistics 25 software (IBM). The Wilcoxon signed-rank test, which is appropriate for paired data, was used to compare the differences in cadence across the walking speed conditions (comfortable, slow, fast). All statistical significance levels were set at $p \leq 0.05$.

3 Results

3.1 Walking cadences

The cadences (mean ± standard deviation) at each walking speed (comfortable, slow, fast) were 59 ± 2 strides/min, 51 ± 4 strides/min, and 69 ± 4 strides/min, respectively. Significant differences among the cadence conditions were observed in the comfortable vs. slow, slow vs. fast, and comfortable vs. fast conditions ($p < 0.001$, Wilcoxon signed-rank test).

3.2 Muscle synergies extracted from whole-speed walking EMG matrices

Table 1 presents the VAF values of the 12 subjects for each condition. The median number of muscle synergies required to meet

10.3389/fnins.2024.1485066

TABLE 1 The number of muscle synergies and VAF in each condition.

	Whole-speed walking	Forward pedaling			Backward pedaling		
		60 RPM	30 RPM	80 RPM	60 RPM	30 RPM	80 RPM
Median (min, max)	4.5 (3, 5)	4 (4, 5)	4 (3, 5)	4 (4, 5)	4 (2, 5)	4 (2, 5)	4 (3, 5)
VAF	94.2 ± 2.2	97.9 ± 1.1	96.9 ± 1.1	98.5 ± 1.0	96.9 ± 2.0	96.9 ± 2.1	97.3 ± 1.2

This table shows the number of muscle synergies required to explain the electromyogram (EMG) patterns during whole-speed walking and each pedaling condition, along with the corresponding variance accounted for (VAF) values. The number of muscle synergies is presented as the median (maximum, minimum) across all subjects, and the VAF is presented as the mean ± standard deviation (SD).

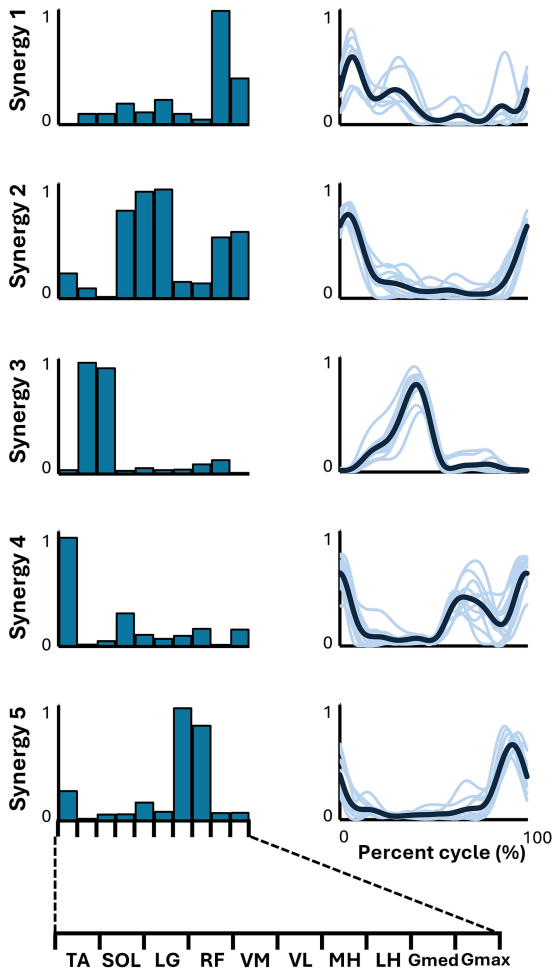

FIGURE 2
Synergies from whole-speed walking. The representative muscle synergies (bar graphs) and corresponding temporal patterns (bold lines) during whole-speed walking are shown. The representative muscle synergies for each condition are arranged based on the timing of the peak in the temporal patterns. The thin lines in the temporal patterns indicate the mean values over six cycles for each subject.

the criteria for whole-speed walking was 4.5, and the mean VAF for the optimal number of synergies across all subjects was 94.2 ± 2.2%.

Figure 2 illustrates the representative synergies (mean muscle synergy vectors within each cluster) and corresponding average temporal pattern components during whole-speed walking. Table 2 lists the muscles that primarily contribute to each representative synergy based on visual inspection and the number of subjects within each cluster.

The lower limb EMG activities during walking, encompassing speeds from slow to fast, were adequately explained by five muscle synergies for all participants. Additionally, all five muscle synergies were shared by more than half of the participants. Therefore, for the comparison of similarities with each pedaling condition, we adopted the five muscle synergies as representative muscle synergies for whole-speed walking.

3.3 Muscle synergies in various pedaling conditions

In all six pedaling conditions, the median number of synergies required to meet the criterion was consistently four (Table 1). Figure 3 shows the representative synergies and corresponding average temporal pattern components for each speed during forward pedaling. The muscle synergy vectors from all subjects during each forward pedaling condition were clustered into seven groups at 60 RPM and 30 RPM and into eight groups at 80 RPM. Among these, four representative synergies were identified at 60 and 30 RPM and five at 80 RPM.

Figure 4 presents the representative synergies and corresponding average temporal pattern components for each speed during backward pedaling. Muscle synergy vectors from all subjects during each backward pedaling condition were clustered into six, eight, and five groups at 60, 30, and 80 RPM, respectively. Among these, four representative synergies were observed at 60 and 30 RPM and five at 80 RPM.

Pedaling conditions, except for backward pedaling at 80 RPM, exhibited subject-specific muscle synergies. Notably, numerous subject-specific muscle synergies were observed at backward pedaling at 30 RPM. This suggests that the muscle synergies recruited during pedaling are less robust and show greater variability among individuals compared to those during walking.

3.4 The similarity between walking muscle synergies and pedaling muscle synergies

Figure 5 summarizes the representative synergies of whole-speed walking as a reference and the representative and subject-dependent muscle synergies for each pedaling condition (forward and backward pedaling), sorted by cosine similarity. Table 2 shows the representative muscle synergies of walking, the primary contributing muscles, and the number of participants contributing to the pedaling muscle synergies sorted for each walking synergy. In each of the six pedaling conditions, one to three sets of muscle synergies similar to those of walking were identified, with the composition within each set varying

TABLE 2 Characteristics of muscle synergies and the number of subjects within the cluster synergies.

		Number of participants within clusters		
Whole-speed walking			Forward pedaling	Backward pedaling
Synergy	Major muscles	Whole-speed walking	60 RPM/30 RPM/80 RPM	60 RPM/30 RPM/80 RPM
Synergy1	Gmed	7	-/-/-	-/3/-
Synergy2	Quad, Gmed, Gmax	11	-/12/-	-/12/-
Synergy3	SOL, LG	10	5/8/5	5/7/7
Synergy4	TA	12	11/10/12	6/6/9
Synergy5	MH, LH	12	6/-/-	5/4/11

This table shows the muscles with the greatest contribution to each synergy during whole-speed walking, the number of subjects in which each synergy was observed, and the number of subjects in which walking-like muscle synergies were observed under each pedaling condition.

depending on the combination of rotation direction and speed. Muscle synergies similar to walking synergy 2 were observed only at a rotational speed of 30 RPM in both forward and backward pedaling. In contrast, muscle synergies similar to synergy 5 were observed only during forward pedaling at 60 RPM and backward pedaling at 80 RPM.

Synergies 2–5 of whole-speed walking showed similar muscle synergies across pedaling conditions, whereas synergy 1 did not exhibit similar muscle synergies in any pedaling condition.

3.5 Functions of representative muscle synergies for each condition

The functions of each representative muscle synergy for each condition are associated with their corresponding temporal patterns by classifying the primary muscle functions ($W \geq 0.5$) (Rimini et al., 2017; Abd et al., 2022).

For whole-speed walking, synergy 1 was composed of the activity of Gmed during the early to mid-stance phase. Synergy 2 was characterized by the activity of the quadriceps group, Gmed, and Gmax during the early stance phase. Synergy 3 consisted of the activity of SOL and LG during the late stance phase. Synergy 4 involved the activity of TA during the swing phase, while synergy 5 included the activity of the hamstrings from the late swing to the early stance phase.

In pedaling, the cycle was divided into two phases: 0–50% for flexion and 50–100% for extension. Each synergy's function was identified accordingly. In forward pedaling, synergy 1 showed increased activity during the early part of the flexion phase across all speeds. At 60 RPM, the hamstrings were the primary muscle, while at 30 RPM, both the hamstrings and Gmed contributed significantly. Conversely, synergy 1 at 80 RPM showed a significant contribution from RF, which differed from the other speeds. Synergy 2 consistently highlighted TA as the primary contributor across all speeds, with increased activity during the latter part of the flexion phase. Notably, at 30 RPM, RF also contributed significantly alongside TA. Synergies 3 at 60 RPM and 30 RPM, as well as synergy 4 at 80 RPM, primarily involved VM and VL, with activity increasing from the end of the flexion phase to the early part of the extension phase. Synergy 3 at 80 RPM exhibited isolated activity of VM. Synergies 4 at 60 RPM and 30 RPM, and synergy 5 at 80 RPM, primarily involved LG, functioning from the latter part of the extension phase to the early part of the flexion phase.

In backward pedaling, synergy 1 for each speed was mainly contributed by TA, remaining active from the flexion phase to the early part of the extension phase. Synergies 2 at 30 RPM and 80 RPM showed activity during the early part of the flexion phase, with the plantar flexor muscles contributing predominantly, although SOL's contribution was minimal at 80 RPM. Synergy 2 at 60 RPM and synergy 3 at 80 RPM showed activity throughout the flexion phase, with significant contributions from the hamstrings. Synergies 3 at 60 RPM and 30 RPM, and synergy 4 at 80 RPM, primarily involved VM and VL, being active during the extension phase. Finally, synergy 4 at 60 RPM and 30 RPM, along with synergy 5 at 80 RPM, showed RF as the primary muscle, functioning from the latter part of the extension phase to the early part of the flexion phase.

4 Discussion

The novel finding of this study is that among the six pedaling conditions, comprising three rotational speeds (30 RPM, 60 RPM, and 80 RPM) and both forward and backward rotations, the identified muscle synergies included those similar to the muscle synergies observed during walking for each condition. The results of this study support the hypothesis that the majority of synergies are shared between walking and pedaling.

Different muscle synergies are associated with rotational direction and speed. In many subjects, the muscle synergy resembling that of walking, with predominant contributions from the plantar flexor muscles of the ankle, was recruited only during pedaling at 30 RPM, regardless of the direction of rotation. In contrast, the muscle synergy resembling that of walking, with predominant contributions from the hamstrings, was observed only during forward pedaling at 60 RPM and backward pedaling at 80 RPM. These findings reveal that specific walking-like muscle synergies are recruited only in certain directions and speeds.

4.1 Representative muscle synergies in whole-speed walking

This study identified five muscle synergies in walking. Among these, synergies 2–5 closely matched the characteristics of the four walking muscle synergies reported in previous studies (Neptune et al., 2009; Clark et al., 2010). Synergy 1, on the other hand, was uniquely identified in this study and primarily represented Gmed activity during the early to mid-stance phases. Because different sets of recorded muscles can result in different muscle synergy vectors (Turpin et al., 2021), the discrepancies between this study and previous studies may be due to the differences in the recorded muscle sets. Furthermore, given that the Gmed module is typically extracted during slow-to-moderate walking (Yokoyama et al., 2016), its inclusion in the synergies extracted from the EMG data encompassing a range of walking speeds in this study is considered valid.

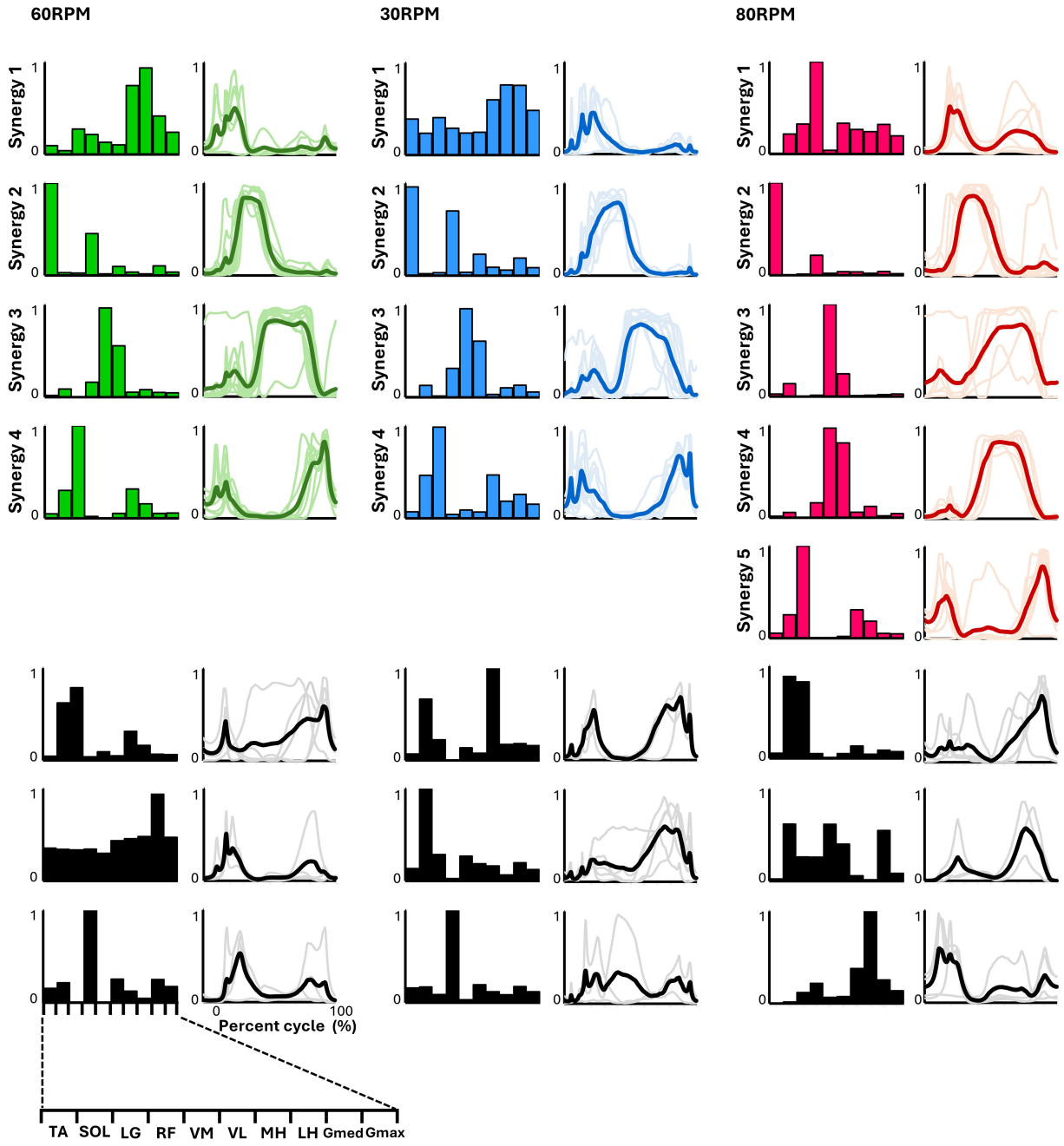

FIGURE 3
Synergies from forward pedaling. The representative muscle synergies (bar graphs) and corresponding temporal patterns (bold lines) during forward pedaling are shown. The representative muscle synergies for each condition are arranged based on the timing of the peak in the temporal patterns. The thin lines in the temporal patterns indicate the mean values over six cycles for each subject. The black graphs shown represent subject-dependent muscle synergies, which were observed in fewer than half of the subjects.

4.2 Representative muscle synergies in forward pedaling

In forward pedaling, four representative muscle synergies were identified at 60 RPM and 30 RPM and five at 80 RPM, indicating variations in the number and composition of synergies depending on pedaling speed (Figure 3). In contrast to our study, previous research involving trained cyclists (Hug et al., 2011) reported that the number of synergies required to explain muscle activity during pedaling remained consistent at three, regardless of pedaling speed, and the synergy compositions were similar.

Cheung et al. (2020) reported that the number and composition of muscle synergies change plastically in response to developmental and training adaptations, suggesting that the differences in subjects between our study and previous studies might have influenced the number and composition of muscle synergies. Another study by Barroso et al. (2014) found that the EMG of all subjects while pedaling at four different speeds could be explained by four muscle synergies for untrained cyclists. Compared to the maximum speed of 70 RPM

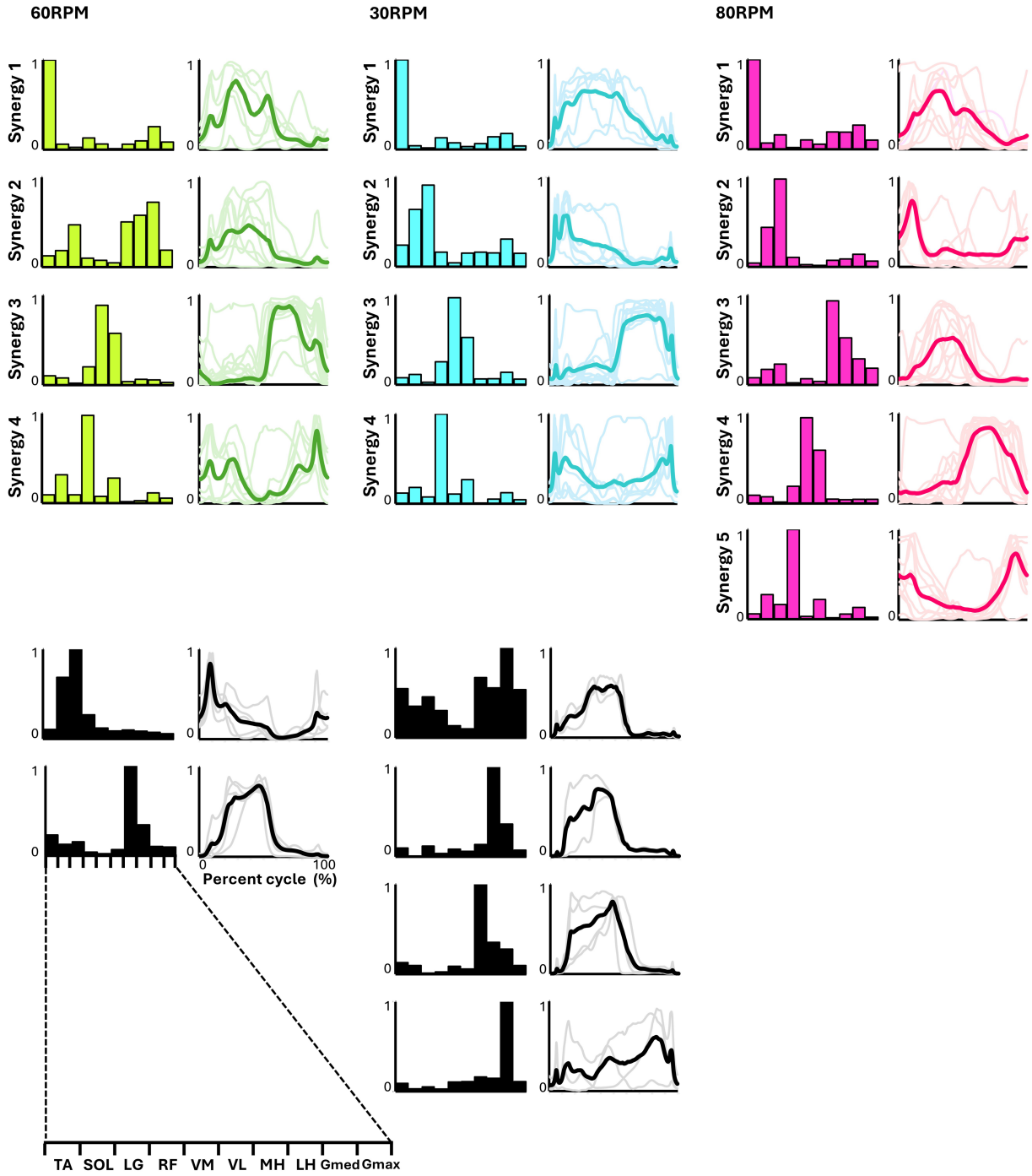

FIGURE 4
Synergies from backward pedaling. The representative muscle synergies (bar graphs) and corresponding temporal patterns (bold lines) during backward pedaling are shown. The representative muscle synergies for each condition are arranged based on the timing of the peak in the temporal patterns. The thin lines in the temporal patterns indicate the mean values over six cycles for each subject. The black graphs shown represent subject-dependent muscle synergies, which were observed in fewer than half of the subjects.

in the study by Barroso et al. (2014), our study included a higher pedaling speed of 80 RPM. This may explain the identification of a greater number of representative muscle synergies at higher speeds. Nevertheless, Barroso et al. (2014) reported distinct muscle synergy profiles at high and low speeds, which is consistent with our findings.

The composition of the muscle synergies identified at 30 and 60 RPM in our study closely resembled the four muscle synergies reported in previous pedaling studies (De Marchis et al., 2013; Barroso et al., 2014). At 80 RPM, muscle synergy involving the hamstrings, which are typically active during the early phase of the upstroke as observed at other speeds, was absent. Instead, the muscle synergy involving the rectus femoris (RF), which contributes to thigh lifting, appears during the early upstroke phase. Additionally, the muscle synergies of the knee extensors that were active during the downstroke phase were divided into two separate synergies. Previous research by De Marchis et al. (2013) indicated that inexperienced subjects

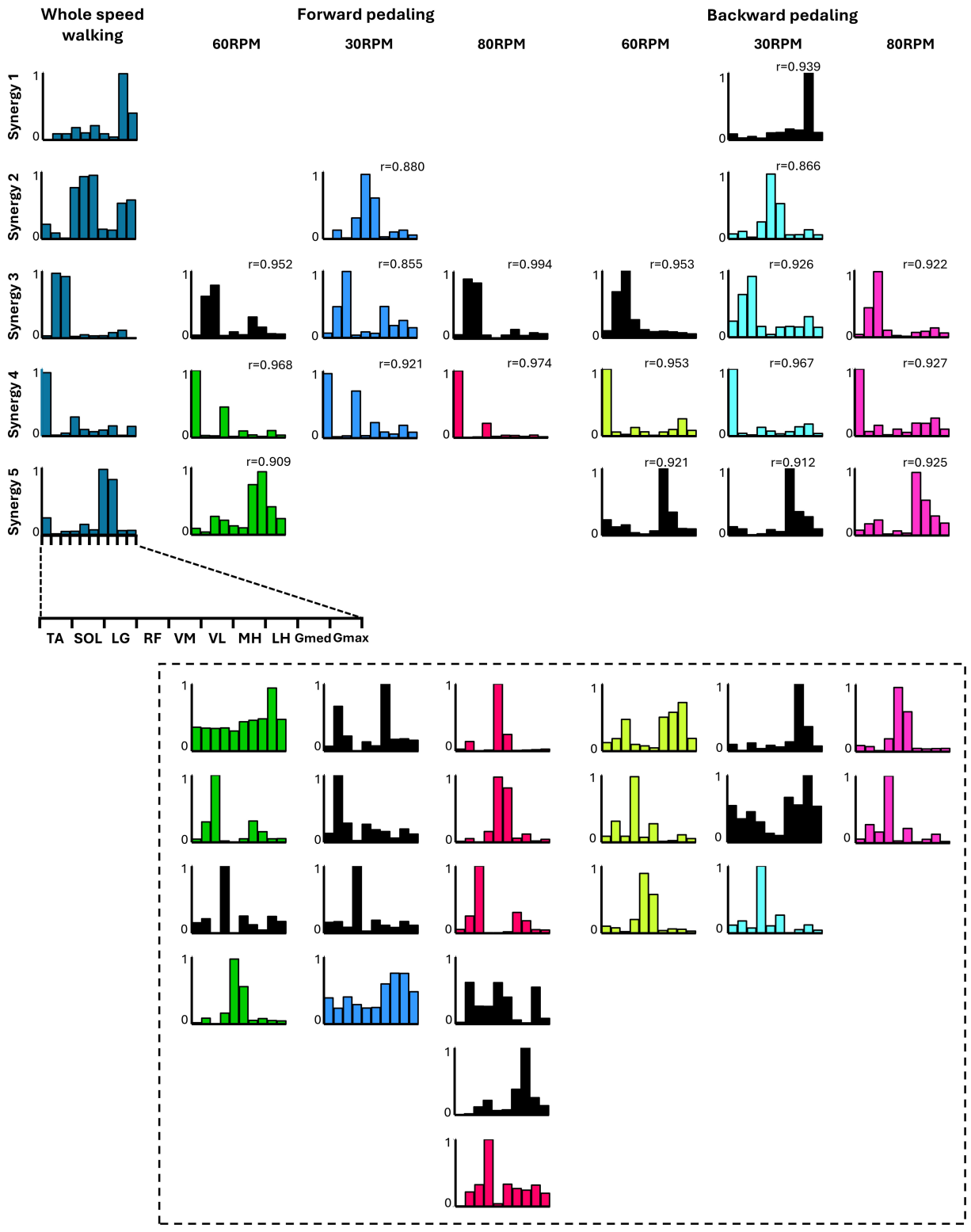

FIGURE 5
The similarity between the five muscle synergies from the whole-speed walking dataset of all subjects and the weighting components of each pedaling condition. For each condition, while the required number of essential modules remained the same, the composition of the weighting component of representative muscle synergies differed. Each bar graph represents the centroid of each cluster of weighting components obtained from each condition. Within each column, synergies obtained from each condition are arranged with bars of the same color. The black graph represents synergies specific to individual subjects (i.e., observed in less than half of the samples). The leftmost column represents the representative synergies (synergy 1 to synergy 5) of whole-speed walking. Synergy 1 consisted of the activation of the Gmed and Gmax during the early to mid-stance phase.

(Continued)

FIGURE 5 (Continued)
Synergy 2 was characterized by the activity of the quadriceps group, Gmed, and Gmax during the early stance phase. Synergy 3 involved the activation of SOL and LG during the late stance phase. Synergy 4 was composed of TA and RF activities during both the early and late swing phases. Finally, synergy 5 included the activity of the hamstrings and TA from the late swing to early stance phase. The *r* value in the graph represents the cosine similarity between each synergy and the corresponding representative muscle synergy from whole-speed walking. Similar synergies obtained from each pedaling condition ($r \geq 0.85$) are displayed in correspondence with the rows of synergies 1 to 5. Synergies enclosed by dashed lines below are those with low similarity to walking synergies, indicating task-specific synergies.

predominantly adopt a pedaling strategy that adds propulsive force during the downstroke. Similar to previous research, our findings suggest that at a more demanding speed of 80 RPM, a propulsive force is generated by the activity of the knee extensors during the downstroke phase.

4.3 Representative muscle synergies in backward pedaling

The representative muscle synergies identified from backward pedaling also showed variations in the number and composition of muscle synergies depending on the pedaling speed (Figure 4). Additionally, four representative muscle synergies were identified at both 30 and 60 RPM. However, at 30 RPM, there was a larger individual variability in the composition of muscle synergies compared to other speeds, with many subject-specific muscle synergies observed. When examining the composition of the muscle synergy vectors at each backward pedaling speed, it appeared that the muscle synergy indicating the activity of the TA and RF observed in forward pedaling was split. At 80 RPM, five representative muscle synergies were identified, with the composition of muscle synergy vectors showing distinct synergies representing the activity of the TA, RF, plantar flexors, and hamstrings. A simulation study by Raasch and Zajac (1999) stated that the biarticular muscles of the thigh (rectus femoris and hamstrings) changed roles depending on the direction of movement, and smooth backward pedaling was achieved by controlling the pairs of TA/RF and hamstrings/plantar flexors separately, which were observed in forward pedaling. These results are consistent with the findings of the simulation study.

4.4 The similarity between walking muscle synergies and pedaling muscle synergies

In this study, 1–3 walking-like muscle synergies were present under all six pedaling conditions. The use of similar muscle synergies associated with different kinematic and kinetic patterns provides further evidence that the CNS generates movements through a flexible combination of muscle synergies (Tresch and Jarc, 2009). Similar to previous studies (Hug et al., 2010; De Marchis et al., 2013; Barroso et al., 2013, 2014), the results of this study suggest the existence of shared neural networks between walking and pedaling.

Furthermore, the results indicated that the composition of walking-like muscle synergies observed during pedaling depends on the direction and speed of pedaling. As shown in Figure 5, the muscle synergy associated with the activation of the quadriceps and hip extensors during whole-speed walking (synergy 2) was recruited during pedaling at 30 RPM, regardless of the direction of rotation. Meanwhile, the muscle synergy associated with the activation of the hamstrings (synergy 5) was recruited during forward pedaling at 60 RPM and backward pedaling at 80 RPM. Additionally, a muscle synergy similar to synergy 1, representing the activity of the Gmed and Gmax muscles during walking, was not observed under any pedaling condition. Walking synergy 1 is thought to contribute to pelvic stability during the stance phase. It is speculated that the minimal postural control required during pedaling may explain the lack of synergy 1 recruitment.

In contrast to the findings of this study, previous research on muscle synergies during upper-limb cycling reported a high degree of similarity and consistency in the number and structure of upper-limb synergies, regardless of power levels (Abd et al., 2022). One possible reason for the discrepancy between these studies is the difference in neural control between the upper and lower limbs. The upper limbs are involved in fine and diverse motor tasks, requiring precise control, whereas the lower limbs are specialized for posture control, weight-bearing, and cyclic movements, like walking and running. These differences in function may result in distinct neural control strategies, contributing to the different outcomes observed. Additionally, Abd et al. (2022) varied resistance load, while the present study examined the effect of rotational speed on muscle synergies under a constant resistance load. Since muscle synergies are recruited to optimize task performance (Tresch and Jarc, 2009; Bizzi and Cheung, 2013; Ting et al., 2015), differences in task conditions could explain the variation in results. Given the functional roles of the upper and lower limbs, further investigation into how rotational speed affects muscle synergies in the upper limbs is warranted.

4.5 Clinical application

Pedaling exercises, which involve muscle activity in the lower limbs similar to walking (Raasch and Zajac, 1999) and require minimal postural control, are a promising rehabilitation method for improving the walking ability of patients with stroke in the early stages of recovery when gait training is challenging (Barbosa et al., 2015). The results of this study suggest the importance of considering the direction and speed of rotation when adopting pedaling as a gait training method. For example, previous studies reported that changes in the recruitment of two synergies (TA and RF, TFL muscle synergy; hamstrings and plantar flexors, Gmax muscle synergy) characterizing the upstroke phase of forward pedaling on the paretic side of patients with stroke are positively correlated with indicators of gait asymmetry (Ambrosini et al., 2016). The results of this study suggest that forward pedaling is effective for selectively recruiting the TA and RF muscle synergy (synergy 4), regardless of speed (Figure 5). Alternatively, forward pedaling at 60 RPM and backward pedaling at 80 RPM may be more suitable for selectively recruiting the hamstrings and MG muscle synergy (synergy 5). Therefore, by considering the direction

and speed of pedaling according to the patient's impairment, it may be possible to enhance its effect on improving walking function.

4.6 Limitations

The EMG activity of each muscle was normalized to the average peak value across six cycles for each condition. This method is similar to those used in previous studies involving muscle synergies (Hug et al., 2011; Barroso et al., 2014; Ambrosini et al., 2016), but since the muscle activity levels are provided only as relative information to the peak values, it is not possible to directly quantify the contribution of power output from each muscle synergy. However, a standardized normalization method that accurately quantifies the contribution of the output from each muscle synergy has not yet been established (Ambrosini et al., 2016). Moreover, because the number and composition of muscle synergies during pedaling in patients with stroke differ from those in healthy individuals (Ambrosini et al., 2016), it is necessary for future research to elucidate how walking-like muscle synergies observed during pedaling are affected by the speed and direction of rotation in these patients.

5 Conclusion

The present study indicated common muscle synergies between walking and pedaling. However, the composition of similar muscle synergies varied with pedaling speed and direction. Our results suggest that it is crucial to consider muscle synergy when performing pedaling exercises for gait rehabilitation.

Data availability statement

The raw data supporting the conclusions of this article will be made available by the authors, without undue reservation.

Ethics statement

The studies involving humans were approved by the Institutional Review Board of Shinshu University, Nagano, Japan. The studies were conducted in accordance with the local legislation and institutional requirements. The participants provided their written informed consent to participate in this study.

Author contributions

JT: Conceptualization, Data curation, Formal analysis, Funding acquisition, Investigation, Methodology, Project administration, Resources, Software, Supervision, Validation, Visualization, Writing – original draft, Writing – review & editing. KM: Conceptualization, Data curation, Formal analysis, Investigation, Methodology, Project administration, Resources, Software, Supervision, Validation, Writing – original draft, Writing – review & editing. HS: Data curation, Formal analysis, Methodology, Software, Validation, Writing – original draft, Writing – review & editing. KW: Data curation, Investigation, Resources, Validation, Writing – original draft, Writing – review & editing. TY: Conceptualization, Data curation, Formal analysis, Funding acquisition, Investigation, Methodology, Project administration, Resources, Software, Supervision, Validation, Visualization, Writing – original draft, Writing – review & editing.

Funding

The author(s) declare that financial support was received for the research, authorship, and/or publication of this article. This work was supported by grants from the funds for JSPS KAKENHI (Grant Nos. JP21K11298 to JT and 23K27943 to TY).

Conflict of interest

The authors declare that the research was conducted in the absence of any commercial or financial relationships that could be construed as a potential conflict of interest.

Publisher's note

References

Abd, A. T., Singh, R. E., Iqbal, K., and White, G. (2022). Investigation of power specific motor primitives in an upper limb rotational motion. *J. Mot. Behav.* 54, 80–91. doi: 10.1080/00222895.2021.1916424

Ambrosini, E., De Marchis, C., Pedrocchi, A., Ferrigno, G., Monticone, M., Schmid, M., et al. (2016). Neuro-mechanics of recumbent leg cycling in post-acute stroke patients. *Ann. Biomed. Eng.* 44, 3238–3251. doi: 10.1007/s10439-016-1660-0

Barbosa, D., Santos, C. P., and Martins, M. (2015). The application of cycling and cycling combined with feedback in the rehabilitation of stroke patients: a review. *J. Stroke Cerebrovasc. Dis.* 24, 253–273. doi: 10.1016/j.jstrokecerebrovasdis.2014.09.006

Barroso, F. O., Torricelli, D., Moreno, J. C., Taylor, J., Gómez-Soriano, J., Bravo-Esteban, E., et al. (2014). Shared muscle synergies in human walking and cycling. *J. Neurophysiol.* 112, 1984–1998. doi: 10.1152/jn.00220.2014

Barroso, F., Torricelli, D., Moreno, J. C., Taylor, J., Gómez-Soriano, J., Esteban, E. B., et al. (2013). Similarity of muscle synergies in human walking and cycling: preliminary results. *Conf. Proc. IEEE Eng. Med. Biol. Soc.* 2013, 6933–6936. doi: 10.1109/EMBC.2013.6611152

Bernstein, N. A. (1967). The co-ordination and regulation of movements. New York: Pergamon Press.

Bizzi, E., and Cheung, V. C. K. (2013). The neural origin of muscle synergies. *Front. Comput. Neurosci.* 7:51. doi: 10.3389/fncom.2013.00051

Cappellini, G., Ivanenko, Y. P., Poppele, R. E., and Lacquanit, F. (2006). Motor patterns in human walking and running. *J. Neurophysiol.* 95, 3426–3437. doi: 10.1152/jn.00081.2006

Chapman, J. P., Chapman, L. J., and Allen, J. J. (1987). The measurement of foot preference. *Neuropsychologia* 25, 579–584. doi: 10.1016/0028-3932(87)90082-0

Cheung, V. C. K., Cheung, B. M. F., Zhang, J. H., Chan, Z. Y. S., Ha, S. C. W., Chen, C. Y., et al. (2020). Plasticity of muscle synergies through fractionation and merging during development and training of human runners. *Nat. Commun.* 11:4356. doi: 10.1038/s41467-020-18210-4

Clark, D. J., Ting, L. H., Zajac, F. E., Neptune, R. R., and Kautz, S. A. (2010). Merging of healthy motor modules predicts reduced locomotor performance and muscle coordination complexity post-stroke. *J. Neurophysiol.* 103, 844–857. doi: 10.1152/jn.00825.2009

De Marchis, C., Schmid, M., Bibbo, D., Bernabucci, I., and Conforto, S. (2013). Inter-individual variability of forces and modular muscle coordination in cycling: a study on untrained subjects. *Hum. Mov. Sci.* 32, 1480–1494. doi: 10.1016/j.humov.2013.07.018

Frère, J., and Hug, F. (2012). Between-subject variability of muscle synergies during a complex motor skill. *Front. Comput. Neurosci.* 6:99. doi: 10.3389/fncom.2012.00099

Funato, T., Hattori, N., Yozu, A., An, Q., Oya, T., Shirafuji, S., et al. (2022). Muscle synergy analysis yields an efficient and physiologically relevant method of assessing stroke. *Brain Commun.* 4:200. doi: 10.1093/braincomms/fcac200

Hermens, H. J., Freriks, B., Disselhorst-Klug, C., and Rau, G. (2000). Development of recommendations for SEMG sensors and sensor placement procedures. *J. Electromyogr. Kinesiol.* 10, 361–374. doi: 10.1016/S1050-6411(00)00027-4

Hug, F., Turpin, N. A., Couturier, A., and Dorel, S. (2011). Consistency of muscle synergies during pedaling across different mechanical constraints. *J. Neurophysiol.* 106, 91–103. doi: 10.1152/jn.01096.2010

Hug, F., Turpin, N. A., Guével, A., and Dorel, S. (2010). Is interindividual variability of EMG patterns in trained cyclists related to different muscle synergies? *J. Appl. Physiol.* 108, 1727–1736. doi: 10.1152/japplphysiol.01305.2009

Ivanenko, Y. P., Cappellini, G., Dominici, N., Poppele, R., and Lacquaniti, F. (2005). Coordination of locomotion with voluntary movements in humans. *J. Neurosci.* 25, 7238–7253. doi: 10.1523/JNEUROSCI.1327-05.2005

Ivanenko, Y. P., Poppele, R. E., and Lacquaniti, F. (2004). Five basic muscle activation patterns account for muscle activity during human locomotion. *J. Physiol.* 556, 267–282. doi: 10.1113/jphysiol.2003.057174

Lee, D. D., and Seung, H. S. (1999). Learning the parts of objects by non-negative matrix factorization. *Nature* 401, 788–791. doi: 10.1038/44565

Neptune, R. R., Clark, D. J., and Kautz, S. A. (2009). Modular control of human walking: a simulation study. *J. Biomech.* 42, 1282–1287. doi: 10.1016/j.jbiomech.2009.03.009

Raasch, C. C., and Zajac, F. E. (1999). Locomotor strategy for pedaling: muscle groups and biomechanical functions. *J. Neurophysiol.* 82, 515–525. doi: 10.1152/jn.1999.82.2.515

Rimini, D., Agostini, V., and Knaflitz, M. (2017). Intra-subject consistency during locomotion: similarity in shared and subject-specific muscle synergies. *Front. Hum. Neurosci.* 11:586. doi: 10.3389/fnhum.2017.00586

Saito, H., Yokoyama, H., Sasaki, A., Kato, T., and Nakazawa, K. (2021). Flexible recruitments of fundamental muscle synergies in the trunk and lower limbs for highly variable movements and postures. *Sensors* 21:6186. doi: 10.3390/s21186186

Tibshirani, R., Walther, G., and Hastie, T. (2001). Estimating the number of clusters in a data set via the gap statistic. *J. R. Stat. Soc. B* 63, 411–423. doi: 10.1111/1467-9868.00293

Ting, L. H., Chiel, H. J., Trumbower, R. D., Allen, J. L., McKay, J. L., Hackney, M. E., et al. (2015). Neuromechanical principles underlying movement modularity and their implications for rehabilitation. *Neuron* 86, 38–54. doi: 10.1016/j.neuron.2015.02.042

Torres-Oviedo, G., Macpherson, J. M., and Ting, L. H. (2006). Muscle synergy organization is robust across a variety of postural perturbations. *J. Neurophysiol.* 96, 1530–1546. doi: 10.1152/jn.00810.2005

Tresch, M. C., Cheung, V. C. K., and d'Avella, A. (2006). Matrix factorization algorithms for the identification of muscle synergies: evaluation on simulated and experimental data sets. *J. Neurophysiol.* 95, 2199–2212. doi: 10.1152/jn.00222.2005

Tresch, M. C., and Jarc, A. (2009). The case for and against muscle synergies. *Curr. Opin. Neurobiol.* 19, 601–607. doi: 10.1016/j.conb.2009.09.002

Turpin, N. A., Uriac, S., and Dalleau, G. (2021). How to improve the muscle synergy analysis methodology? *Eur. J. Appl. Physiol.* 121, 1009–1025. doi: 10.1007/s00421-021-04604-9

Wakeling, J. M., and Horn, T. (2009). Neuromechanics of muscle synergies during cycling. *J. Neurophysiol.* 101, 843–854. doi: 10.1152/jn.90679.2008

Yokoyama, H., Ogawa, T., Kawashima, N., Shinya, M., and Nakazawa, K. (2016). Distinct sets of locomotor modules control the speed and modes of human locomotion. *Sci. Rep.* 6:36275. doi: 10.1038/srep36275

Zehr, E. P., Balter, J. E., Ferris, D. P., Hundza, S. R., Loadman, P. M., and Stoloff, R. H. (2007). Neural regulation of rhythmic arm and leg movement is conserved across human locomotor tasks. *J. Physiol.* 582, 209–227. doi: 10.1113/jphysiol.2007.133843

Frontiers in Neuroscience

Provides a holistic understanding of brain function from genes to behavior

Part of the most cited neuroscience journal series which explores the brain - from the new eras of causation and anatomical neurosciences to neuroeconomics and neuroenergetics.

Discover the latest Research Topics

See more →

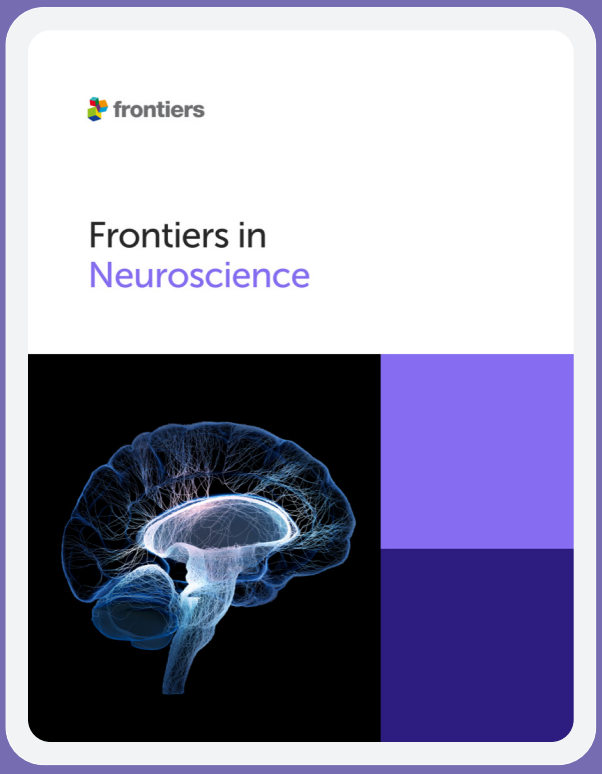

Frontiers

Avenue du Tribunal-Fédéral 34
1005 Lausanne, Switzerland
frontiersin.org

Contact us

+41 (0)21 510 17 00
frontiersin.org/about/contact